MTA Doktori Értekezés

A hippokampális gamma oszcillációk keletkezésének sejtszintű mechanizmusai és kannabinoidok által történő szabályozása

Dr. HÁJOS NORBERT

MTA Kísérleti Orvostudományi Kutatóintézet
Celluláris- és Hálózat-Neurobiológiai Osztály
Hálózat-Idegélettan Kutatócsoport

Budapest, 2010

dc_71_10

TARTALOMJEGYZÉK

I. BEVEZETÉS

I/1. A hippokampusz

Evolúciós értelemben a hippokampusz egy olyan ősi agykérgi terület, amely az egyrétegbe rendeződött fősejtjeivel és hálózati elemeinek kapcsolatrendszereivel ideális modell a tágabb értelemben vett agykérgi idegsejthálózatokban lezajló folyamatok felderítéséhez, megértéséhez. Emlősökben ez az agyterület döntő szerepet játszik a memóriafolyamatokban és a térbeli tájékozódásban. Az agykéreg az entorhinális kérgen keresztül reciprok kapcsolatban áll a hippokampusszal. A kérgi információ feldolgozását a hippokampusz szintjén jelentősen szabályozzák a kéreg alatti területekről érkező felszálló pályák, mint pl. a kolinerg afferensek a mediális szeptumból. A kérgi és kéreg alatti területek együttes, időben összehangolt működése elengedhetetlen a hippokampusz élettani szerepének a betöltéséhez (Andersen és mtsai, 2007).

A hippokampális idegsejthálózatokat, mint az agykérgi hálózatokat általában, döntően serkentő fősejtek alkotják (a gyrus dentatus-ban a szemcsesejtek, míg a cornu ammonis (CA) régióiban a piramissejtek) (Lorente de Nó, 1934). Hasonlóan az agykéreghez, a hippokampusz CA3 régiójában a piramissejtek jelentős mennyiségű lokális axon kollaterálissal rendelkeznek, melyeken keresztül reciprok kapcsolatban állnak egymással (Li és mtsai, 1994). A lokális szinaptikus serkentéssel történő kommunikáció nem jellemzi sem a gyrus dentatus-t, sem a CA1 régiót (Tamamaki és mtsai, 1987; Acsády és mtsai, 1998). Ez a hippokampális régiók közti alapvető strukturális különbség lehet az oka, hogy a térben lokalizált szinkron idegi aktivitások kialakulhatnak a CA3 régióban (hasonlóan a többi agykérgi régióhoz), míg a CA1-ben, ill. a gyrus dentatusban nem. A serkentősejtek mellett, melyek számos tulajdonságaikban nagyfokú hasonlóságot mutatnak, a kérgi neuronhálózatokban számos morfológiailag és funkcionálisan elkülönülő gátlósejttípus található (Freund és Buzsáki, 1996). Axon arborizációjuk alapján négy fő csoportba oszthatóak a gátlósejtek: 1) a fősejtek szóma körüli régióját idegzik be a *periszomatikus gátlósejtek*; 2) a serkentősejtek dendritjeit innerválják a *dendritikus gátlósejtek*; 3) elsősorban más gátlósejteken végződnek az *interneuron-szelektív gátlósejtek,* ill. 4) a hippokampuszból különböző agyi régiókba küldik axonjaikat az ún. *projekciós GABAerg sejtek*. Ezen csoportok közül a periszomatikus gátlósejtek játszanak főszerepet a fősejtek tüzelésének szabályozásában, így a szinkron idegi aktivitások kialakításában is (Cobb és mtsai, 1995; Miles és mtsai, 1996). A periszomatikus gátlósejtek megnevezés is egy tovább osztható sejtpopulációt fed le, hiszen ezen sejtek közé funkcionális szempontból legalább három, jól

elkülöníthető sejtcsoport tartozik a kérgi neuronhálózatokban: 1) egy Ca^{2+} kötő fehérjét, a parvalbumint (PV) kifejező kosársejtek, amelyek a fősejtek szómáit és proximális dendritjeit innerválják, 2) a PV tartalmú axoaxonikus sejtek, amelyek specifikusan a fősejtek axon iniciális szegmentumain végződnek, és 3) egy neuropeptidet, a kolecisztokinint (CCK) expresszáló kosársejtek, amelyek szintén a fősejtek sejttestein és proximális dendritjein szinaptizálnak. A PV- ill. a CCK-tartalmú interneuronok számos anatómiai, elektrofiziológiai és molekuláris biológiai jellemzőben különböznek egymástól, amelyek alapján eltérő szerepet tölthetnek be az idegsejthálózatok működésében (Freund és Katona, 2007). Megjegyzendő, hogy a periszomatikus gátlósejteknek ez a diverzitása csak a kérgi neuronhálózatokra jellemző, mert pl. a kisagyban vagy a striátumban csak egy periszomatikus gátlósejttípus van, amelyik PV tartalmú és az itt található fősejtek szómáinak és axon iniciális szegmentumainak a működését egyaránt szabályozza (Shepherd, 2004).

Számos idegrendszeri folyamat mögött az idegsejtek időben összehangolt működése ismerhető fel. Ez a szinkronizált idegi működés hozza létre az elektroenkefalogramban (EEG) azonosítható ritmikus aktivitásokat. A jellegzetes frekvenciatartományú ritmikus aktivitásokhoz, amelyek gyakran mint oszcillációk detektálhatók a hagyományos mintavétellel készült EEG-n, más-más funkciót társítható. A rágcsálók hippokampuszában is elvezethetőek különböző EEG mintázatok, amelyek a viselkedéssel változnak. Az egyik ilyen mintázat egy szinuszoid alakú ritmikus aktivitás, az ún. théta hullám, mely frekvenciája 4-9 Hz, és az állat explorációs tevékenysége (pl. ágaskodás, futás) alatt vezethető el, ill. ez figyelhető meg REM alvás alatt is (Vanderwolf, 1988). A másik jellegzetes EEG aktivitás nem-explorációs-viselkedések (pl. evés, ivás, tisztálkodás), mozdulatlan ébrenlét, és lassú hullámú alvás alatt jelentkezik, amelyre jellemező egy alacsony amplitúdójú irreguláris aktivitás, amit időről-időre megszakít egy nagy amplitúdójú, 50-150 ms időtartamú szinkron idegi tevékenység, az ún. éleshullámmal (Buzsáki, 1986). Amíg a théta ritmust több agyterület (hippokampusz, mediális szeptum, entorhinális kéreg) közös működése hozza létre, az éleshullám a hippokampusz CA3 régiójában keletkezik a piramissejtek populációs kisülése eredményeként, tehát lokális eredetű (Buzsáki, 2006). Buzsáki György elmélete szerint a théta aktivitás alatt a hippokampális neuronhálózatba elsősorban az entorhinális bemenet hordozta szenzoros infomációk „gyűjtése” történik, míg az éleshullámok alatt a releváns információk összekapcsolására és bevésésére tevődik át a hangsúly (Buzsáki, 1989). Ezen jellegzetes hullámformákon kívül még egy 30-100 Hz frekvenciával jellemezhető ritmikus aktivitás, az ún. gamma oszcilláció is felismerhető a hippokampuszban mért lokális mezőpotneciálban (Bragin és mtsai, 1995). A megfigyelések szerint a gamma oszcillációk ereje jelentősen növekszik figyelem, észlelés és munkamemória alatt, azaz a kognitív idegi tevékenységek

során (Engel és msai, 2001). Nem meglepő, hogy a kognitív képességek csökkenésével jellemezhető betegekben (mint pl. a skizofrének esetében) a gamma oszcillációk ritkábban és kisebb amplitúdóval jelentkeznek. Ennek az oszcillációnak a szerepére először Prof. Wolf Singer tett javaslatot, miszerint a kérgi rendszerekben a szenzoros információ különböző modalitásainak időbeli összekapcsolását végezhetnék a gamma frekvenciatartományú oszcillatorikus aktivitások (Singer, 1993). Megjegyzendő, hogy a gamma oszcilláció frekvenciatartománya egybeesik a tüzelési időtől függő plaszticitási folyamatok (spike time dependent plasticity) kritikus idejével (~25 ms), amely időtartományban a legnagyobb hatékonyságú a szinaptikus súlyok megváltoztathatósága, azaz a szinaptikus erősségek aktivitásfüggő átrendezése. Ezért a gamma oszcillációknak szerepe tulajdonítanak a sejtszintű tanulási folyamatokban is (Paulsen és Moser, 1998).

I/2 A hippokampális gamma oszcillációk

A hippokampális gamma oszcillációk mind a théta ritmusba ágyazva megfigyelhetőek exploráció alatt, mind a nyugalmi állapotra jellemző irreguláris aktivitás alatt az éleshullámoktól függetlenül vagy azokat időben követve (Traub és mtsai, 1996; Buzsaki és mtsai, 2003). Az *in vivo* kísérletek kiderítették, hogy a CA3 régió neuronhálózata képes önmaga generálni gamma oszcillációt, amelyre az alacsonyabb (25-50 Hz közötti) frekvencia-tartomány jellemző és a keletkezés helyéről, a CA3 régióból ez az oszcilláció átterjed a CA1 régióba (Bragin és mtsai, 1995; Csicsvari és mtsai, 2003; Colgin és mtsai, 2009). Hasonló vizsgálatok felfedték, hogy az entorhinális kéregben keletkező magasabb (65-140 Hz közötti) frekvencia-tartománnyal jellemezhető gamma oszcillációk képesek mind a gyrus dentatus, mind a CA1 régió neuronhálózatában azonos frekvenciával oszcillációt kialakítani (Bragin és mtsai, 1995; Colgin és mtsai, 2009). A CA1 régióban az alacsonyabb és magasabb frekvenciájú gamma oszcillációk, azaz a CA3 régióból ill. az entorhinális kéregből eredő ritmikus aktivitások, időben váltakozva mérhetőek, azaz egymást kölcsönösen kizárják. Ezáltal egyszer a hippokampális, másszor a kérgi eredetű információ feldolgozása valósulhat meg a különböző frekvenciával oszcilláló idegsejthálózat működése során (Colgin és mtsai, 2009). Hogy ezeket a folyamatokat részleteiben megértsük, ill. a gamma oszcillációk idegi tevékenységekben betöltött szerepét tisztázzuk, fel kell tárni a ritmusgenerálás sejt- és hálózatszintű mechanizmusait. Ezt a célt ma még *in vivo* technikák alkalmazásával nem, csak *in vitro* mérésekkel lehet elérni, azaz túlélő hippokampusz-szeletekben létrehozott gamma oszcillációs modellek tanulmányozásával.

A vizsgálataink kezdetén, amelynek az volt a célja, hogy a hippokampális gamma oszcillációk sejt- és hálózatszintű mechanizmusait felderítsük, három *in vitro* oszcillációs modell célozta meg az *in vivo* gamma oszcillációk tulajdonságait megragadni a hippokampusz-szeletekben. Az első modellt Prof. Miles Whittington és mtsai 1995-ben publikálták a Nature hasábjain (Whittington és mtsai, 1995). Itt a gamma oszcillációt elektromos stimulálással váltották ki a hippokampusz CA1 régiójában, amely oszcillációra jellemző a magasabb frekvencia-tartomány. Ezt az oszcillációt az elektromos stimulálás következtében az extracelluláris térben megnövekedet glutamát váltja ki, amely a metabotrópos receptorokon keresztül serkenti a lokális gátlósejteket ionotróp glutamát receptor blokkolók jelenlétében is. A gátlósejtek szinaptikus és réskapcsolataikon keresztül szinkronizálják a tüzelésüket kb. 40 Hz-es csúcsfrekvenciával 100-300 ms hosszan. A szerzők szerint gátlósejtek ritmikus kisülése következtében keletkező gátló szinaptikus áramok alakíthatják ki a lokális mezőpotenciálban mérhető tranziens gamma oszcillációt, tehát egy gátlósejtekből álló neuronhálózat önmaga lenne képes gamma frekvenciás oszcilláció létrehozására a CA1 régióban. Ez a modell talán megfeleltethető a viselkedő állatban az éleshullámot követő, rövid ideig tartó gamma oszcilláció kialakulásának. Ekkor a CA3 régió piramissejtjeinek szinkron kisülése nagymértékű glutamát ürülést okoz a CA1 régióban, ami lehetővé teszi a metabotrópos glutamát receptorok által indukált gamma oszcillációk kialakulását *in vivo* körülmények között (Traub és mtsai, 1996). A második gamma oszcillációs modellt Dr. Ole Paulsen és mtsai 1998-ban szintén a Nature-ben közölték (Fisahn és mtsai, 1998). Ők a 30 Hz körüli oszcillációt egy kolinerg receptor agonistával, a karbakollal indukálták a hippokampusz-szelet CA3 régiójában, amely oszcilláció át tudott terjedni a CA1 régióra is. A kísérleteik felderítették, hogy ezt az oszcillációt a CA3 piramissejtek és a lokális gátlósejtek szinkronizált kisülése hozza létre. A piramissejtek lokális kollaterálisaikon keresztül serkentik a GABAerg interneuronokat, amelyek az őket innerváló piramissejtekre visszacsatolva meggátolják azok további kisülését. Amikor a szinaptikus gátlás lecseng, a piramissejtek újra tudnak akciós potenciált generálni, és újból kisütik a lokális gátlósejteket, ami egy újabb oszcillációs ciklust eredményez. Az oszcilláció tehát ebben a modellben a piramissejtek és a gátlósejtek időben pontosan összehangolt működése alakítja ki. Ez az oszcilláció, ellentétben a stimulációval kiváltott oszcillációval, időben stabilan fenntartható az acetilkolin receptor agonista jelenlétében. A karbakol indukált oszcilláció a hippokampusz-szeletben megfeleltethető a viselkedő állatban mért, théta ritmusba ágyazott gamma oszcillációnak. Ezen EEG mintázat alatt a hippokampusz acetilkolin szintje magas, megteremtve az előfeltételtét a kolinerg receptorok aktiválásával létrehozható gamma oszcillációk kialakulásának (Marrosu és mtsai, 1995). A harmadik

gamma oszcillációs modellt a hippokampusz-szeletben egy ionotróp glutamát receptor agonista a káinsav hozzáadásával hoztuk létre (Hájos és mtsai, 2000). Ez a modell nagy hasonlóságot mutat a karbakol indukált *in vitro* oszcillációval, ahogy az Dr. Fisahn és Dr. Gloveli munkacsoportjainak későbbi kutatásaiból is kiderült (Fisahn és mtsai, 2004; Gloveli és mtsai, 2005). A káinsavval kiváltott oszcilláció a hippokampusz-szeletben modellezheti azt az *in vivo* állapotot, amikor a hippokampuszban alacsony az acetilkolin szint, pl. az alacsony amplitúdójú irreguláris aktivitás alatt, de mégis megfigyelhető gamma oszcilláció az éleshullámtól függetlenül (Senior és mtsai, 2008). Összefoglalva, a hippokampusz-szeletben kiváltható három típusú gamma oszcilláció az éber állatban más-más EEG mintázat alatt megfigyelhető gamma oszcillációnak lehet a modellje. A modellek részletes elektrofiziológiai vizsgálatával felderíthetjük az azokat létrehozó sejtszintű folyamatokat, így közelebb kerülhetünk a gamma oszcillációk funkciójának megértéséhez.

I/3 Az endokannabinoid jelátviteli rendszer

A sejtek közti szinaptikus kommunikáció hatékonyságát számos jelátviteli rendszer szabályozza. Ezek egyike az endokannabinoidok által közvetített szignalizációs útvonal. 1971-ben Prof. Raphael Mechoulam izolálta a marihuána hatóanyagát, a Δ^9-tetrahidrokannabinolt (THC-t), amely a pszichotikus hatásokért nagymértékben felelős (Gaoni és Mechoulam, 1971). Ezzel az eredménnyel kezdődött a kannabinoid szignalizációs rendszer feltárása. Közel húsz évvel később, 1990-ben Lisa Matsuda és mtsai azonosították a központi idegrendszerben a kannabinoidok jelfelfogó molekuláit, az egyes típusú (CB1) kannabinoid receptorokat (Matsuda és mtsai, 1990). Ezek a receptorok igen nagy mennyiségben megtalálhatóak az idegszövetben, ahol G-fehérjéken keresztül számos effektor molekulára hathatnak (Herkenham és mtsai, 1990). Ma már tudjuk, hogy a CB1 receptorok aktiválásának hatására bezáródhatnak a feszültségfüggő Ca^{2+} csatornák, kinyithatnak a feszültségfüggő K^+ csatornákat, gátolódhat az adenilát cikláz aktivitás vagy fokozódhat jó néhány proteinkináz működése. Tehát ezek a receptorok mind rövid távon (azaz az ioncsatornák nyitásának közvetlen modulálásával), mind hosszú távon (azaz az enzimek aktivitásának szabályozásával) képesek befolyásolni az idegsejtek működését (Freund és mtsai, 2003; Piomelli, 2003). Az anatómiai vizsgálatok felfedték, hogy legnagyobb mennyiségben az idegsejtek axonvégződésein találhatóak a CB1 receptorok, ahol ideális helyzetben vannak a neurotranszmitter molekulák felszabadulásának szabályozásához (Freund és mtsai, 2003). De mi aktiválja az élettani folyamatok során a CB1 receptorokat? A kutatások kiderítették, hogy a CB1 receptorok endogén ligandumai zsírsavszármazékok, amelyek közül elsőként 1992-ben

izolálták az N-arachidonoil-etanolamidot (vagy elterjedtebb nevén az anandamide-ot), majd öt évvel később a 2-arachidonoil-glicerolt (2-AG-t)(Devane és mtsai, 1992; Stella és mtsai, 1997). Ezeket az ún. endokannabinoidokat Ca^{2+} függő enzimek szintetizálják, pl. az anandamide-ot a preszinaptikus terminálisokban található N-acil-etanolamin foszfolipáz D (NAPE-PLD) vagy a 2-AG-t a posztszinaptikus membránokban lokalizálódó diacil-glicerol lipáz α enzim (DGL- α)(Okamoto és mtsai, 2004; Katona és mtsai, 2006; Jung és mtsai, 2007; Nyilas és mtsai, 2008). Az endokannabinoidok lebontását, azaz a jelátvitel időtartamának szabályzását számos enzim végezheti, amelyek mind a preszinaptikus (pl. N-acil-etanolamin(NAE)-sav-amidáz vagy monoacil-glicerin lipáz), mind a posztszinaptikus (pl. zsírsavamid-hidroláz vagy ABDH6) oldalon megtalálhatóak (Marrs és mtsai, 2010; Gulyas és mtsai, 2004; Nyilas és mtsai, 2008). Az endokannabinoidok membránokon keresztül történő átjutását a ma még nem azonosított transzportermolekulák segíthetik (Beltramo és msai, 1997). A legelfogadottabb elmélet szerint a 2-AG egy retrográd jelátvivő molekula, amely a posztszinaptikus membránban aktivitásfüggő módon szintetizálódik. Kijutva a sejtből az extracelluláris térben hozzákötődik a preszinaptikus axonvégződésen található receptorához, amely ennek következtében aktiválódik és jelentősen lecsökkenti a neurotranszmitter molekulák ürülésének valószínűségét. Alacsony aktivitási szint mellett ez a visszacsatoló mechanizmus nem működik, csak felfokozott aktivitás esetén kapcsol be (Katona és Freund, 2008). Ezzel szemben az anandamide a neuronhálózatokban inkább egy intracelluláris jelátvivő szerepét töltheti be, hiszen a mai ismereteink szerint mind a szintetizáló (NAPE-PLD), mind a lebontó (NAE-sav-amidáz) enzime a preszinaptikus axonvégződésekben lokalizálódik belső membránokhoz kötve (Nyilas és mtsai, 2008).

II. CÉLKITŰZÉSEK

Kísérleteink fő célja, hogy megértsük azokat a sejt- és hálózatszintű mechanizmusokat, amelyek kialakítják a gamma oszcillációkat a hippokampális neuronhálózatokban, ill. hogy e szinkron idegi tevékenységet hogyan módosítja a kannabinoid receptorok aktiválása. Kutatásainkkal az alábbi konkrét kérdésekre kerestünk választ:

A különböző gamma oszcillációs modellek tulajdonságai és azok módosíthatósága a hippokampusz CA3 régiójában (1, 6)

- Milyen tulajdonságokban térnek el az egyes transzmitter-rendszerek aktiválásával kiváltott gamma oszcillációk a hippokampusz-szeletben?
- Eltérő neuronhálózatok működése hozza létre a különböző típusú gamma oszcillációkat a hippokampuszban?
- Hogyan szabályozza a gátló szinaptikus transzmissziót a zolpidem, egy benzodiazepin származék, és ez milyen hatással van a gamma oszcillációkra?

A neuronhálózati oszcillációk vizsgálatának kombinálása képalkotó eljárásokkal (12, 13)

- Milyen technikai feltételek szükségesek ahhoz, hogy a hálózati oszcillációkat az ún. *submerged* szeletkamrákban is tudjuk tanulmányozni, ahol a vizsgálatok összekapcsolhatóak optikai módszerek alkalmazásával?

A kolinerg receptorok aktiválásával kiváltott oszcillációk sejt- és hálózatszintű mechanizmusai a hippokampuszban (7-10, 14-19)

- Mennyire jól modellezi egy kolinerg receptor agonistával, a karbakollal kiváltott oszcilláció a hippokampusz-szeletben az *in vivo* körülmények közt megfigyelhető gamma oszcillációkat?
- Hogyan tüzelnek ez egyes idegsejttípusok a karbakol indukált gamma oszcillációk alatt és ezt mennyiben határozzák meg a rájuk érkező szinaptikus bemenetek?
- Mi a periszomatikus és dendritikus gátlósejtek szerepe az oszcillációk kialakításában?
- Mi az áramgenerátor a karbakol indukált oszcillációban?
- A periszomatikus gátlósejtek egyes típusai hogyan járulnak hozzá az oszcilláció generálásához?
- Milyen hatással van a karbakol az egyes periszomatikus gátlósejttípusoktól eredő szinaptikus gátlásra?

- Milyen hálózati mechanizmussal terjed a gamma oszcilláció a hippokampusz CA3 régiójából a CA1 régióba?
- Mennyire határozzák meg a szinaptikus bemenetek és mennyire az egyes sejtek rezonancia-tulajdonságai az idegsejtek aktivitását a gamma oszcilláció alatt a hippokampusz CA1 régiójában?

A hippokampális szinaptikus jelátvitel szabályozása kannabinoidokkal (2-5, 11)

- Hogyan szabályozza a CB1 kannabinoid receptorok aktiválása a hippokampális szinaptikus transzmissziót?
- Farmakológiai szempontból eltérnek-e a serkentő, ill. a gátló axonvégződéseken található CB1 receptorok?
- Van-e az exogén kannabinoidoknak CB1 receptoroktól független hatása, amely modulálhatja a szinaptikus neurotranszmissziót?
- Milyen mértékben szabályozza a transzport az endokannabinoidok hatását?

A kannabinoidok hatásai a hippokampális gamma oszcillációkra (2, 20)

- Milyen mechanizmusokon keresztül szabályozzák a kannabinoid receptor agonisták a gamma oszcillációkat a hippokampusz-szeletekben?

III. MÓDSZEREK

Az értekezésben bemutatott kísérletek részletes leírása a mellékletben található dolgozatokban megtalálhatóak a megfelelő hivatkozásokkal együtt. Itt csak vázlatosan kerülnek ismertetésre az egyes alkalmazott módszerek.

III/1. *In vitro* elektrofiziológiai módszerek (1-20)

A kísérleteinkhez 15-36 napos Wistar patkányokat, 15-60 napos CD1 ill. C57BL/6 egereket, CB1 receptor hiányos egereket, ill. ezek homozigóta kontrolljait (Ledent és mtsai, 1999; Zimmer és mtsai, 1999), valamint olyan transzgenikus egereket használtunk, amelyekben az EGFP (enhanced green fluorescent protein) expresszióját a parvalbumin (PV-EGFP) vagy a GAD65 promóter (GAD65-EGFP) szabályozta (Meyer és mtsai, 2002; Lopez-Bendito és mtsai, 2004). Az állatokat nátrium pentobarbitallal (i.p. 70 mg/kg) vagy izoflurránnal mélyen elaltattuk, majd a koponyából eltávolítottuk az agyat. Az agyból szikével olyan blokkot készítettünk, amely tartalmazta a hippokampuszt, ill. az azt körülvevő agyrészeket. Ebből a blokkból Vibratom segítségével 300-450 μm vastag szeleteket készítettünk, és a hippokampuszt körülvevő agyterületeket eltávolítottuk. Az így nyert hippokampusz-szeleteket min. 1 óra inkubálás után tettük át a szelettartó kamrából a mérőkamrába. A szeletek tartására, ill. a méréshez olyan mesterséges cerebrospinális folyadékot (ACSF) használtunk, amelyet 95% O_2 és 5% CO_2 gázeleggyel telítettünk. A 2. és 6. mellékletként feltüntetett dolgozaton kívül, ahol a gamma oszcillációkat ún. *interface* kamrákban vizsgáltuk, minden mérés ún. *submerged* típusú szeletkamrában történt, ahol az idegsejtek sejttestjei infravörös differenciál interferencia kontraszt mikorszkópia segítségével láthatóvá tehetők. Ilyen körülmények közt célzottan lehet elvezetni vizuális kontroll mellett az élő sejtekből. Epifluoreszcens feltét alkalmazásával tettük láthatóvá az egyes élő gátlósejtek EGFP tartalmát a hippokampusz-szeletekben, amely sejtekből aztán célzottan vezettünk el elektromos jeleket.

A szinaptikus, ill. a hiperpolarizációra aktiválódó nem-szelektív kationcsatornák (HCN-csatornák) által közvetített áramok mérését, és az idegsejtekben történő akciós potenciál kiváltását *whole-cell patch-clamp* technikával végeztük. A boroszilikát üvegből készült pipettákat a kísérleti paradigmáknak megfelelő oldatokkal töltöttük fel. A helyi mezőpotenciálokat, ill. az oszcillációk alatt elvezetett idegsejtaktivitásokat ACSF-el töltött üvegelektróddal extracellulárisan detektáltuk. A jeleket Axopatch 200B, Multiclamp 700 vagy 700B típusú erősítőkkel vezettük el, az így nyert analóg jeleket 1-3 kHz-es aluláteresztő

szűrővel megszűrtük, majd 5-10 kHz-es mintavételi frekvenciával digitalizáltuk, és számítógépen tároltuk, majd az elvezetés után kielemzetük. Az adatok számítégépes rögzítésére és az adatok analíziséhez CDR, SCAN (J. Dempster, University of Strathclyde), EVAN (Módy I., UCLA), Stimulog (Nusser Z., MTA KOKI), IGOR, MatLab, Origin szoftvereket használtunk.

Az oszcillációk alatti áramforrás-sűrűség változások tér- és időbeli alakulását úgy állapítottuk meg, hogy a helyi mezőpotenciálokat olyan 64-csatornás elektródrendszerrel detektáltuk, amelyben az elektródok egy 8X8-as kiosztásban, síkban egymástól 100 µm távolságra helyezkedtek el (Panasonic MED-P2105; Tensor Biosciences, Irvine, CA). Erre az elektródmátrixra helyeztük rá a hippokampusz-szeletet, és az elvezetett elektromos jelekből térképeztük fel az áramforrás eloszlást. Ahhoz, hogy megállapítsuk, hogy az áramforrások közül melyek az aktív, és melyek a passzív áramok, a 64-csatornás elvezetéseket kombináltuk egy feszültségfüggő festék fluoreszcenciájának a detektálásával. Ehhez a szeleteket 200 µM Di-4-ANEPPS festék tartalmú oldatban inkubáltuk, majd a festék feszültségingadozásra bekövetkező fluoreszcencia-változását egy MiCAM01 CCD kamerával követtük nyomon (BrainVision; SciMedia Ltd., Tokyo, Japán). Ezeket a kísérleteket döntően Dr. Edward Mann kollégám végezte Dr. Ole Paulsen oxfordi laboratóriumában.

III/2. *In vitro* jelölt sejtek megjelenítése (1, 7-10, 14-20)

Intracelluláris méréseink során biocitin tartalmú oldattal vezettünk el, amely egy biológiailag inert anyag. A biocitin szabadon diffundál a sejt dendritágaiba és axonkollaterálisaiba. Az elektrofiziológiai elvezetés után 4% paraformaldehid tartalmú pufferben fixáltuk a szövetszeleteket, majd a sejteket immunperixodáz módszert használva nikkellel intenzifikált diaminobenzidin-tetrahidroklorid (DAB-Ni) csapadékkal tettük láthatóvá. A reakció után dehidráltuk a szeleteket, és műgyantába ágyaztuk. A sejteket fénymikroszkóppal azonosítottuk, axon- és dendritfájuk alapján. Az egyes sejttípusok jellegzetes képviselőit rajzolócső (*camera lucida*) segítségével rekonstruáltuk.

III/3. Hisztológia (2, 10)

A állatokat minden esetben mély narkózisban, a szíven keresztül paraformaldehid tartalmú fixálóval perfundáltuk. Az optimális fixálás elérése érdekében a hagyományos Zamboni-féle fixáló (4% paraformaldehid, 15% pikrinsav, 0,05% glutáraldehid) mellett, 1% paraformaldehid tartalmú foszfát pufferrel vagy 4% paraformaldehid tartalmú Na-acetát alapú

pufferrel (pH=6) perfundáltunk, amit 4% paraformaldehid tartalmú bórax puffer alapú fixálóval (pH=8,5) történő perfúzió követett. A fixálást követően az agyakat Vibratommal 60 μm vastagságú szeletekre metszettük.

III/4. Beágyazás előtti (preembedding) immuncitokémia (2, 10)

A kísérleteinkben arra kerestük a választ, hogy a CB1 kannabinoid receptorok mely típusú gátlósejtek axonvégződésein lokalizálódnak (2), ill. hogy ezen axonvégződések által létrehozott szinapszisoknál milyen a nitrogén monoxid (NO) szignalizációs útvonal elemeinek lokalizációja (10).

A metszetek alapos mosása után az antitestek penetrációjának a növeléséhez a szeleteket fagyasztottuk, majd az aspecifikus kötődést csökkentettük a megfelelő szérumfehérjék alkalmazásával (blokkolás). Az egyik kísérletsorozatban (2) a metszeteket CB1 receptor ill. PV ellen termeltetett antitestekkel kezeltük, majd az előbbit immunarany, míg az utóbbit immunperoxidáz módszerrel tettük láthatóvá. A CB1 receptor ellen termeltetett antitest specifikusságát teszteltük CB1 receptor hiányos egérben, amit összehasonlítottunk a vadtípusú egérben, ill. patkányban történt immunfestés eredményével. A másik kísérletsorozatban (10) a neuronális nitrogén monoxid szintázt (nNOS) immunarannyal jelenítettük meg, míg a CB1 receptorokat immunperoxidáz módszerrel. Az nNOS ellen termeltetett antitest specificitását is teszteltük nNOS-t nem expresszáló génkiütött egérből származó metszeteken. Az NO szignalizációs útvonal másik kulcsenzimét, a NO-érzékeny guanilát ciklázt (NO-sGC) annak alfa1 alegysége ellen termeltetett antitesttel tettük láthatóvá. Ezekben a kolokalizációs kísérletekben az NO-sGC-t immunperoxidáz módszerrel, míg a CB1 receptorokat immunarannyal jelenítettük meg.

Mindkét kísérletsorozatban a festéseket követte a metszetek OsO_4-el történő kezelése, majd dehidrálása, amely procedúra közben a metszeteket uranil-acetát alkoholos oldatában is inkubáltuk. A dehidrálást követte a metszetek műgyantába ágyazása, majd a szövetminták elektronmikroszkópos vizsgálata.

III/5. Kettős immunfluoreszcens vizsgálatok (10, 17, 18, 20)

Ezeket a vizsgálatokat olyan szöveteken végeztük, amelyeket az *in vitro* elektrofiziológiai mérések után fixáltunk 4% paraformaldehidet tartalmazó foszfát pufferben. Az első kísérletsorozatban az NO donor indukált cGMP növekedést vizsgáltuk a CB1 receptort, ill. a PV-t kifejező axonvégződésekben. Az anti-cGMP és anti-CB1 receptor, ill.

anti-PV ellenanyagokat használtuk a vizsgálatainkban, melyeket zöld (Alexa Fluor 488) és piros (Alexa Fluor 594) hullámhosszon emittáló anyagokhoz kötött másodlagos ellenanyaggal tettünk láthatóvá. A másik kísérletsorozatban a biocitinnel töltött PV tartalmú gátlósejtek típusát határoztuk meg, azaz elkülönítettük a kosársejteket az axoaxonikus sejtektől. A vizsgálatokban az axoaxonikus sejtek célelemét az axon iniciális szegmentumot anti-Ankyrin G ellenanyaggal tettük láthatóvá Cy3 konjugált másodlagos ellenanyaggal, míg a biocitin tartalmú axonkollaterálisokat streptavidinhez kötött Alexa 488-al. Mindkét kísérletsorozatban az eredményeket epifluoreszcens feltéttel rendelkező Zeiss mikroszkóppal értékeltük ki.

III/6. *In vivo* elektrofiziológiai mérések (18)

Az *in vivo* méréseket ketamin/xilazin keverékkel altatott felnőtt egereken végeztük. Sztereotaxis segítségével a 16 csatornás multielektrodót, amely két belső, drogadagolásra szolgáló kanüllel volt felszerelve, a ventrális hippokampusz CA3 régiójába helyeztük. A kontroll periódus alatt regisztráltuk a gamma frekvencia-tartománnyal jellemezhető lokális mezőpotenciálokat, amely regisztrátumokat összehasonlítottuk egy mu-opioid receptor agonista, a DAMGO lokális adagolása után bekövetkező változásokkal. Kontroll oldatként 0,9 %-os NaCl tartalmú oldatot adtunk hasonló térfogatban, amely kezelés nem befolyásolta a mezőpotenciálok tulajdonságait. Az *in vivo* méréseket Dr. Ulbert István végezte a Pázmány Péter Katolikus Egyetem Információs Technológiai Karán.

III/7. Az oxigén koncentrációjának meghatározása az oldatban, ill. a hippokampusz-szeletben (12)

A tápoldat oxigén koncentrációját 50-100 µm-rel a hippokampusz-szelet felett mértük a *submerged* szeletkamrában. A méréshez ún. optode-t használtunk, amelynek az átmérője 50 µm volt (Microx TX3, PreSens GmbH, Németország). Az optode függőleges irányban történő mozgatása, sem a perfúzió sebességének változása nem befolyásolta a mérést. A kalibrálásnál a nulla pontot 2-3 mM nátrium szulfitot tartalmazó nem oxigenált tápoldattal, míg a max. értéket 1 óra hosszat 95% O_2 és 5% CO_2 gázeleggyel telítettünk oldattal állítottuk be. A kísérletek közben az oxigén koncentrációjának a változtatását 95% N_2 és 5% CO_2 gázelegy hozzákeverésével értük el. A szövetszeletben az oxigén koncentrációjának mélység szerinti függését ciklikus voltammetriával határoztuk meg. Ebben az esetben a mérőelektród egy 7 µm átmérőjű, 20-30 µm hosszú szénszál volt, amely egy Millar voltamméterhez csatlakozott. A voltammetriás méréseket Dr. Richard Exley végezte az Oxfordi Egyetemen.

IV. EREDMÉNYEK ÉS KÖVETKEZTETÉSEK

IV/1. A különböző gamma oszcillációs modellek tulajdonságai és azok módosíthatósága a hippokampusz CA3 régiójában (1, 6)

A vizsgálataink kezdetekor három típusú *in vitro* gamma oszcillációs modell állt rendelkezésre, melyeket két csoportba lehetett osztani. Az egyik csoportba tartoztak azok a modellek, melyeket Miles Whittington munkacsoportja fejlesztett ki (Traub és mtsai, 1998). Ezekben a vizsgálatokban a metabotrópos glutamát receptorok (mGluR) aktiválásával indukálták a 40 Hz körüli ritmikus aktivitásokat a hippokampusz CA1 régiójában. A másik csoportba tartozó modellekben a gamma aktivitást a hippokampusz CA3 régiójában indukáltak karbakollal (Fisahn és mtsai, 1998), ill. káinsavval (2). A két utóbbi modellben az volt a közös, hogy a nagyon hasonló alakú hullámforma mellett az oszcillációk frekvenciája 30 Hz körül volt, és mindkét esetben az oszcilláció a CA3-ban generálódott és átterjedt a CA1-be. Ahhoz, hogy eldöntsük, melyik oszcillációs modellt érdemes részleteiben vizsgálni, azaz melyik áll közelebb az *in vivo* megfigyelt gamma oszcillációkhoz, összehasonlítást végeztünk. Mivel ismert volt, hogy a hippokampusz CA3 régiójának neuronhálózata az élő állatban mért eredmények alapján képes önmaga gamma oszcillációt létrehozni (Bragin és mtsai, 1995; Csicsvari és mtsai, 2003), ezért az *in vitro* vizsgálatainkat e régióra koncentráltuk. Az oszcillációkat egy metabotrópos glutamát receptor agonistával, a DHPG-el, ill. egy kolinerg agonistával, a karbakollal indukáltuk a hippokampusz-szeletekben. Az így kiváltott ritmikus aktivitások a CA3 régióban számos tulajdonságukban különböztek. A karbakol indukált oszcillációk csúcsfrekvenciája 30 Hz körül volt és kisebb spektrális tartományt ölelt fel e nagy amplitúdójú oszcilláció. Ezzel szemben a DHPG indukált oszcillációk csúcsfrekvenciája 40 Hz körül volt és az alacsonyabb amplitúdójú oszcillációk igen szeles spektrális tartományt fedtek le (6/1. ábra). Ezek alapján felmerül a kérdés, hogy ezeket a számos tulajdonságban eltérő oszcillációkat más- más neuronhálózatok működése hozza-e létre. Ennek eldöntésére farmakológiai megközelítést választottunk. A tesztelt neurotranszmitter rendszerek közül négy esetben találtunk eltérést az oszcillációkra gyakorolt hatásban. Egy M1/3 típusú muszkarinikus acetilkolin receptor antagonista, a pirenzepine, egy neurokinin-1 receptor agonista, a substance P fragmentum, ill. egy benzodiazepin származék a zolpidem jelentősen csökkentette, ill. megszüntette a karbakol indukált oszcillációt, míg a DHPG-el indukáltat megerősítette (6/6. ábra). Ezzel szemben egy mGluR antagonista, az LY341495 blokkolta a DHPG indukált oszcillációt, míg a karbakol indukált oszcillációra nem

volt hatása (6/2. ábra). Mindkét oszcillációs típust blokkolta egy AMPA típusú ionotróp glutamát receptor antagonista, a GYKI 53655, ill. egy $GABA_A$ receptor antagonista, a bicuculline (6/3. ábra).

Ezen farmakológiai eredmények alapján azt a következtetést vontuk le, hogy mindkét oszcillációs modellt a piramissejtek és gátlósejtek közös aktivitása hozza létre, de az eltérő tulajdonságok és különböző farmakológiai profil alapján feltehető, hogy más-más gátló neuronhálózatok vesznek részt a ritmikus aktivitások kialakításában. Összehasonlítva e kísérleti eredményeket az *in vivo* mért eredményekkel (Bragin és mtsai, 1995; Csicsvari és mtsai, 2003) úgy döntöttünk, hogy a továbbiakban a karbakol indukált hálózati oszcillációkat fogjuk a tanulmányozni, ami jól modellezheti az élő állatban mért, a théta aktivitás alatt detektálható gamma oszcillációkat.

Mind a pirenzepine, mind a zolpidem hatására bekövetkező amplitúdó növekedés a DHPG indukált oszcilláció esetében együtt járt az oszcilláció frekvenciájának jelentős csökkenésével is. Mivel a korábbi kísérletek azt vetették fel, hogy szinaptikus gátlás elhalási ideje lehet az egyik fő szabályozója az oszcillációk frekvenciájának, azaz a ritmusgenerálásnak (Fisahn és mtsai, 1998; Whittington és mtsai, 2000), ezért a $GABA_A$ receptorok nyitvatartási idejének a fokozása szükségszerűen a ritmikus aktivitás gyakoriságának a csökkenését kell eredményeznie. Ha a GABA kötve van a receptorához, a zolpidem képes a $GABA_A$ receptorok nyitvatartási idejét megnövelni, így a gátló szinaptikus áramok (IPSC) elhalási idejét megnyújtani, ahogy azt az agykéreg V. rétegi piramissejtjein feltárták (Perrais és Ropert, 1999). Vajon a hippokampális oszcilláció lassulásának hátterében is hasonló mechanizmusok állnak? A korábbi kísérleteink megmutatták, hogy mind a piramissejtekre, mind a gátlósejtekre érkező IPSC-k elhalási ideje jelentősen megnövelhető zolpidemmel a hippokampuszban (1/1. ábra). Ez az eredmény alátámasztja azt a hipotézist, hogy a gamma oszcillációk frekvenciája alapvetően függhet a szinaptikus gátlás elhalási idejétől. Ezen vizsgálatok másik kérdése az volt, hogy a zolpidem az IPSC-k elhalási idején túl képes-e növelni azok amplitúdóját szobahőmérsékleten mért kísérletek esetében. Perrais és Ropert (1999) megmutatták, hogy a zolpidem akkor képes az IPSC-k amplitúdóját növelni, ha a szinapszisok résébe ürült GABA még nem telíti a posztszinaptikus részen elhelyezkedő $GABA_A$ receptorokat, azaz vannak olyan receptorok, amelyekhez a kiürült neurotranszmitter molekulák nem megfelelő számban kötődtek. A telítettség kérdése azért izgalmas, mert a szinaptikus jelátvitel rövidtávú hatékonyságának a fokozása csak olyan kapcsolatok esetében valósítható meg, ahol a neurotranszmitter molekulák nem telítik azok posztszinaptikus receptorait. A zolpidem azon képessége, hogy a szinaptikus receptorok GABA-val történő telítettségét felfedje, csak szobahőmérsékleten érvényesül, magasabb hőmérsékleten nem.

Kísérleteink megmutatták, hogy a neuronhálózatok különböző elemeire érkező gátló bementeknél a $GABA_A$ receptorok más-más telítettségűek, sőt egyes sejtekre érkeznek olyan szinapszisok, amelyekben a kiürülő GABA telíti, míg más szinapszisoknál nem a posztszinaptikusan elhelyezkedő receptorait (1). Tehát számos gátló szinapszis esetében is fokozható a jelátvitel hatékonyság rövidtávon, azaz a szinaptikus gátlás plasztikus lehet, hasonlóan a serkentő szinapszisoknál tapasztaltakhoz (Liu és mtsai, 1999; Mainen és mtsai, 1999).

IV/2. A neuronhálózati oszcillációk vizsgálatának kombinálása képalkotó eljárásokkal (12, 13)

A hálózati oszcillációk sejtszintű mechanizmusainak felderítésére ma leginkább az *in vitro* méréstechnikák alkalmasak, melyek segítségével tanulmányozzák az egyes sejtek tüzelési sajátosságai, bemeneti és kimeneti tulajdonságaik. Az eddigi tanulmányokban csak az ún. *interface* típusú szeletkamrában tartott agyszeletekben tudtak oszcillációkat létrehozni, amely elvezetési körülmények nem kombinálhatóak különböző képalkotó eljárásokkal, mivel ebben a kamrában az agyszeletek a tápoldat és a nedvesített karbogén gáz közti határterületen helyezkednek el (Yamamoto és McIlwain, 1966; Skrede és Westgaard, 1971; Schwartzkroin és Andersen, 1975; Andersen és mtsai, 1977). Ahhoz, hogy az optikai technikák segítségével vizsgálni tudjuk az oszcillációk mechanizmusait, az ún. *submerged* szeletkamrában kell hálózati oszcillációkat létrehozni, és időben stabilan fenntartani. Ebben a szeletkamrában tartott túlélő agyszeletekben alkalmazható a vizualizált *patch-clamp* méréstechnika és/ vagy a különböző fluoreszcens festékek jeleinek detektálása, hiszen itt az agyszeletek egy üveglapon fekszenek, és felettük áramlik át a tápoldat, miközben a mikroszkóp objektíve az oldatban van (Edwards és mtsai, 1989). De milyen körülményeket kell teremteni ahhoz, hogy a *submerged* szeletkamrában tartott szeletekben is lehessen gamma oszcillációkat, ill. más ritmikus aktivitásokat vizsgálni? A munkánk megkezdésekor erre a kérdésre nem volt válasz. A feltételezésünk az volt, hogy a *submerged* szeletkamrákban a tápoldat általánosan használt perfúzió sebessége alacsony (2-3 ml/perc), ami nem képes az idegsejtek nagy energiaigényű működését megfelelő oxigénnel ellátni. Ezen túlmenően a sokak által használt kör alakú szeletkamrában a tápoldat áramlása elsősorban a kamra szélein történik, és nem éri el közvetlenül az agyszeletet. Az újításunk egyik lényege, hogy a szeletkamrát jelentősen le kell szűkíteni, mintegy „rákényszerítve” az oxigenáltatott tápoldatot, hogy közvetlenül a szelet felett áramoljon át. Egy másik lényegi elem, hogy ha a leszűkített kamrában megemeljük a folyási sebességet 5-6 ml/percre, akkor tartós oszcillációkat kapunk, hiszen több oxigént

tudunk az idegsejtekhez juttatni. Összhangban e feltételezéssel, Dr. Ole Paulsen oxfordi laboratóriumában kimértük, hogy a kamra leszűkítése és a folyadék perfúziós sebességének megemelése azt eredményezi, hogy a szeletkamrában detektált oldott oxigén mennyisége a szokásos mérési körülmények közt mérthez képest magasabb lesz, elégséges ahhoz, hogy az oszcillatorikus aktivitások stabilan vizsgálhatóak legyenek az agyszeletekben (12/3. ábra). Tehát sikerült olyan *in vitro* mérési körülményeket kialakítanunk, amelyek lehetővé teszik a hálózati oszcillációk vizsgálatát agyszelet-preparátumokban, miközben a szeletben lévő sejtek, ill. azok nyúlványai vizualizálhatóak (13/1. ábra). Kísérleteink során azonban szembesültünk azzal a problémával, hogy a lokálisan generálódó oszcillációk a leszűkített kamrában gyorsabb folyadékáramlás mellett ugyan kiválóan tanulmányozhatóak, de az oszcillációk terjedésének a mechanizmusai pl. a hippokampusz CA3 régiójából a CA1 régiójába már csak korlátozottan vizsgálhatóak. Amíg a CA3 régióban az oszcilláció létrehozásában olyan fősejtek is résztvesznek, amelyeknek csak lokális kollaterálisai vannak, de a szeletkészítés közben a CA1 régióba vetülő axonjaikat levágtuk, addig az oszcillációk terjedése a CA3 régióból a CA1-be csak ép axonú piramissejtek tüzélésével lehetséges. Az üveglapon tartott szeletekben lévő idegsejteket csak egyik oldalról látjuk el megfelelő oxigénmennyiséggel (12/3. ábra), azaz a szelet felső egyharmadában, felében található neuronhálózat hozza létre a lokális oszcillációt, amelynek csak kevés fősejtje rendelkezik a CA1 régióba vetülő axonnal. Tehát, ha növelni akarjuk az ép vetítőaxonú fősejtek számát, melyek ritmikusan tüzelnek a CA3-ban oszcilláció alatt, akkor növelni kell a megfelelő oxigénellátású szövet nagyságát is. Ezért kifejlesztettünk Budapesten egy olyan szövetszeletkamrát, amelyben a szeletek egy hálóra vannak helyezve, és mind a szelet alatt, mind a szelet felett áramlik az oxigenáltatott tápoldat, tehát a szeletben található sejtek mindkét oldalról el vannak látva megfelelő mennyiségű oxigénnel, ill. tápanyagokkal, így megduplázható a megfelelően oxigenált szövet mennyisége az üveglapon tartott szeletekhez képest. Ez a kamra is behelyezhető a mikroszkóp objektíve alá, így a hálózati oszcillációk terjedése vizsgálható vizualizált *patch-clamp* elvezetésekkel és/ vagy képalkotó technikákkal (12/1. ábra). Összefoglalva, ezekkel a megoldásokkal elegendő oxigént tudunk biztosítani a szövetszeletekben található sejtek nagy energiafelhasználást igénylő működéséhez, így tanulmányozni tudjuk a szinkron idegi tevékenységek mechanizmusainak (12). Az *in vitro* szeletek oxigénellátásának fontosságáról és a tápoldat összetételének a lehetséges módosításáról egy külön közleményben hívtuk fel e technikák használóinak a figyelmét (13). A kísérleti eredményeink közlése óta számos külföldi laboratóriumban sikerrel meghonosodott a dupla perfúzióra kialakított szövetszeletkamra (pl. Dr. A. Fisahn stockholmi, Dr. K. Lamsa oxfordi, Dr. R. Miles párizsi laboratóriumában).

IV/3. A kolinerg receptorok aktiválásával kiváltott oszcillációk sejt- és hálózatszintű mechanizmusai a hippokampuszban (7-10, 14-19)

Az in vitro kolinerg oszcillációs modell összevetése az in vivo mért gamma oszcillációkkal a hippokampusz CA3 régiójában. Az első és legfontosabb kérdés, hogy mennyire jól modellezik az *in vivo* regisztrált gamma oszcillációkat az agyszeletben farmakológiailag kiváltott gamma oszcillációk. Kísérleteinket a hippokampuszban végeztük, amely agyterület CA3 régiójának neuronhálózata önmagában képes gamma oszcillációt generálni az eddigi *in vivo* és *in vitro* mérések alapján (Bragin és mtsai, 1995; Fisahn és mtsai, 1998; Csicsvari és mtsai, 2003). Ha összehasonlítjuk a szabadon mozgó patkány hippokampuszában mért gamma oszcilláció jellemző tulajdonságait a hippokampusz-szeletben egy kolinerg receptor agonista, a karbakol applikációjával kiváltott gamma oszcilláció tulajdonságaival, akkor sok hasonlóságot találunk. A CA3 régió lokális mezőpotenciáljában regisztrálható gamma oszcilláció fázisainak rétegek szerinti változása, az áramsűrűség mintázatának eloszlása, ill. a piramissejtek és gátlósejtek tüzelési sajátosságai nagyon hasonlóak, szinte teljesen megegyeznek az *in vivo* körülmények között tapasztaltakkal (7/2. ábra; 14/1. ábra). Ez a három makroszkópikus tulajdonság nagyfokú hasonlósága azt sugallja, hogy a hippokampusz CA3 régiójában az *in vitro* körülmények között kiváltható gamma oszcilláció jól modellezi az ezen agyterületen *in vivo* mért gamma oszcilláció számos tulajdonságát. Tehát feltehető, hogy a hippokampusz-szeletekben felderíthető sejt- és hálózatszintű mechanizmusokhoz hasonló, esetleg velük azonos módon generálódik az élő állat hippokampuszában is e ritmikus aktivitás.

Az idegsejtek bemeneti és kimeneti tulajdonságai a CA3 régióban kiváltott oszcillácókban. Az *in vitro* oszcillációs modellünk alkalmasságának megerősítése után, megvizsgáltuk az egyes idegsejttípusok tüzelési sajátosságait a karbakollal indukált gamma oszcillációk alatt. A kísérleteinkben a tápoldathoz adtuk a karbakolt, majd két üvegelektród segítségével extracellulárisan detektáltuk a ritmikusan változó lokális mezőpotenciált a CA3 piramissejtek rétegéből és ezzel párhuzamosan vizuális kontroll alatt egy adott idegsejt akciós potenciáljait. Az adatgyűjtés után intracellulárisan biocitint juttattunk az elvezetett idegsejtbe, amit immuncitokémiai módszerekkel láthatóvá tettünk, majd anatómiailag azonosítottuk a sejteket. Eredményeink azt mutatták, hogy a piramissejtek rétegéből elvezetett mezőpotenciál negatív csúcsán tüzelnek a piramissejtek, amit 2-3 ms késéssel követ a fáziskapcsolt gátlósejtek kisülése (7/7. ábra). Ez az időbeni késés megfelel a monoszinaptikus transzmisszió idejének. Ezen eredmények alapján feltételezhetjük, hogy a gamma oszcilláció alatt a

piramissejtek a lokális kollaterálisaik révén aktiválják a gátló interneuronokat, amely idegsejtek visszacsatoló módon szabályozzák a piramissejtek szinkron kisülését. Tehát a CA3 régióban keletkező gamma oszcillációkat egy visszacsatoló (feed-back) szinaptikus kör működése hozza létre, megerősítve a korábbi eredményeket (Fisahn és mtsai, 1998). Ezen túlmenően azt állapítottuk meg, hogy szinte az összes gátlósejttípus tüzelése fáziskapcsolt volt a gamma oszcillációhoz. A sejttípusok közti eltérés elsősorban a tüzelési frekvenciában, ill. a fáziskapcsoltságban mutatkozott meg (7/7. ábra). Vajon mi az oka az egyes neurontípusok tüzelési viselkedésében mutatkozó különbségeknek az oszcillációk alatt, azaz mi határozza meg a sejtek kisülésének gyakoriságát, fázisát és fáziskapcsoltságát? A kérdés megválaszolásához először elvezettük az idegsejtek aktivitását extracellulárisan, majd *whole-cell patch-clamp* technikával intracellulárisan detektáltuk a sejtre érkező serkentő, ill. gátló posztszinaptikus áramokat. A sejtek típusát az elvezetés után anatómiailag azonosítottuk. Az elektrofiziológiai elvezetések analízisénél a sejtek tüzelési frekvenciáját és fáziskapcsoltságát korreláltattuk a sejtre érkező áramok amplitúdójával, ill. időzítettségével. Azt találtuk, hogy az oszcilláció alatt a sejtre érkező szinaptikus bemenetek különböztek a sejttípusok között. Míg a piramissejtek esetében a fáziskapcsolt szinaptikus gátlás dominált, addig a fáziskapcsoltan tüzelő periszomatikus gátlósejtek erős, fáziskapcsolt szinaptikus serkentésben részesültek (9/2. ábra). Erős pozitív korrelációt találtunk a sejtekre adott fázisban érkező serkentő és gátló áramok aránya és a sejt tüzelési frekvenciája között, valamint - interneuronok esetén - a sejtre érkező serkentés fáziskapcsoltsága és a generált akciós potenciálok fáziskapcsoltságának pontossága között (9/5-6. ábra). Ezek az eredmények szintén alátámasztják a hipotézisünket, miszerint a karbakol indukált gamma oszcillációért a hippokampusz CA3 régiójában egy rekurrens mechanizmus a felelős, ahol a piramissejtek tüzelését elsősorban a rájuk érkező szinaptikus gátlás, míg a gátlósejtek kisülését a CA3 piramissejtektől eredő serkentés időzíti (9/7. ábra). Hasonló eredményeket kaptak Dr. Gloveli munkacsoportjában a káinsav indukált gamma oszcillációk vizsgálata során (Gloveli és mtsai, 2005), ami még jobban alátámasztja a karbakol, ill. a káinsav által indukált gamma oszcillációk közti hasonlóságot.

Az in vitro oszcillációkban a periszomatikus gátlósejtek játszák a kulcsszerep. Az eddigi eredményeinkből látható, hogy számos gátlósejttípus fáziskapcsoltan tüzel az oszcilláció alatt. A következőkben azt a kérdést vizsgáltuk, hogy melyik gátlósejttípusok játszanak főszerepet az oszcillációk generálásában, azaz a periszomatikus vagy a dendritikus gátlósejtek alakítják-e ki a ritmikus aktivitást a CA3 régióban, avagy e funkcionálisan elváló sejtcsoportok együttes működése szükséges ehhez. A kísérletek során az elektrofiziológiai

méréseket kombináltuk képalkotó eljárásokkal, ahol feszültségfüggő festékek fluoreszcenciáját analizáltuk az oszcillációk alatt. Megállapítottuk, hogy a karbakol indukált hálózati oszcillációkban az aktív folyamatok (a sejtek tüzelése, ill. szinkronizált gátlás) a periszomatikus régióra szorítkoznak (8/3. ábra). Ezzel párhuzamosan a farmakológiai kísérleteink megerősítették, hogy a dendritikus régió csak passzívan vesz részt az oszcillációban (8/7. ábra). Összegezve e munka eredményeit elmondhatjuk, hogy a CA3 régióban a kolinerg receptorok aktiválásával kiváltott oszcillációk kialakításáért a piramissejtek és a periszomatikus gátlósejtek időben összerendezett tüzelése a felelős (14/5. ábra). Ez az eredményünk ellentétben áll a korábbi kísérleteikből levont következtetésekkel (Shimono és mtsai, 2000), ahol az aktív áramokat a dendritikus régióba lokalizálták áramforrás-sűrűség analízis alapján, igaz, azokat a vizsgálatokat nem egészítették ki feszültségfüggő festékek fluoreszcenciájának a mérésével, ami megmutatja az aktív és passzív áramforrások eloszlását térben és időben. Tehát a biológiai eredményeken túl fontos kiemelni, hogy az áramforrás-sürüség analízis eredményének független megerésítése elengedhetetlen a helyes következtetések levonásához.

Az in vitro oszcillációk áramgenerátorának azonosítása. Minden oszcillációra jellemző egy frekvencia-tartomány és egy amplitúdó eloszlás. A korábbi vizsgálatok azt mutatták, hogy a $GABA_A$ receptorok nyitvatartási idejét megnövelő farmakonok, pl. a barbiturátok lecsökkentik a gamma oszcillációk frekvenciáját, tehát a gátló szinaptikus transzmisszió időállandója lenne az oszcilláció frekvenciájának meghatározója, azaz a ritmusgenerátor (Fisahn és mtsai, 1998; Whittington és mtsai, 2000). De mi a gamma oszcilláció áramgenerátora? Milyen sejtszintű folyamatok határozzák meg a periodikus jelek amplitúdóját a piramissejtek rétegében gamma oszcilláció alatt? Ennek a kérdésnek a megválaszolására korrelációs vizsgálatokat végeztünk. Összevetettük az oszcilláció pillanatnyi amplitúdójának a változását az egyes sejtek tüzelési valószínűségével és a rájuk érkező szinaptikus bemenetekkel (15/2-5. ábra). Azt kaptuk eredményül, hogy a periszomatikus eredetű posztszinaptikus gátló áramok teszik ki annak az áramnak közel 90%-át, ami generálja a gamma oszcillációt a hippokampusz-szeletben, míg az oszcillációt generáló áram kb. 10%-a a piramissejtek akciós potenciáljait létrehozó áramokból adódik (15/6. ábra). Összegezve, a karbakol indukált gamma oszcilláció ritmusgenerátora a $GABA_A$ receptorok által közvetített periszomatikus gátlás elhalási ideje, míg az áramgenerátora döntően ezen szinaptikus áramok amplitúdója. Ezen eredmények közlésével közel egyidőben megjelent egy *in vivo* munka, amelyben hasonló következtetésekre jutottak a szerzők (Atallah és Scanziani, 2009), azaz a gátló szinaptikus áramok fluktuálása jelenti a periodikus változást

a lokális mezőpotenciálban. Andrew Trevelyan hasonló következtetésre jutott, amikor az epileptikus aktivitások extracellulárisan detektálható feszültségingadozások mögött meghúzódó áramgenerátorként a gátló szinaptikus áramokat azonosította (Trevelyan, 2009). Tehát ezek a munkák együttesen azt sugallják, hogy az EEG-ben regisztrálható számos oszcillatorikus jelet a szinaptikus, elsősorban a $GABA_A$ receptorokon keresztül folyó áramok generálhatják.

A CA3 régióban karbakollal indukálható oszcillációk kialakításához a gátlósejtek közül a gyorsan tüzelő kosársejtek szinkronizált működése elégséges. Miután a fent vázolt kísérleti eredmények tisztán a periszomatikus gátlósejtek kulcsszerepére utaltak, felmerült, hogy a periszomatikus gátlósejtek típusai közül melyek felelősek az oszcilláció generálásáért a hippokampusz CA3 régiójában. A piramissejtek periszomatikus régióját három típusú gátlósejt idegzi be: (1) a gyorsan tüzelő, PV-t expresszáló kosársejtek (FS-BC), amelyek a sejttesteket és a proximális dendriteket innerválják; (2) a gyorsan tüzelő, PV-t expresszáló axoaxonikus sejtek (AAC), amelyek a piramissejtek axon iniciális szegmentumait idegzik be, és (3) a szabályosan tüzelő, CCK-t tartalmazó kosársejtek (RS-BC), amelyek axonterminálisai elsősorban sejttesteken és proximális dendriteken végződnek (17/1. ábra; 18/1. ábra)(Freund és Buzsáki, 1996). Első lépésként meghatároztuk ezen sejttípusok tüzelési tulajdonságait a karbakollal kiváltott oszcilláció alatt szobahőmérsékleten, amikor az oszcilláció jellemző frekvenciája 15-20 Hz a $GABA_A$ receptorok közvetített szinaptikus áramok lassúbb elhalási ideje miatt. (Megjegyzendő, hogy a fiziológiás és a szobahőmérsékleten kiváltott *in vitro* oszcillációk generálásának mechanizmusai azonosak (18).) Azt találtuk, hogy az FS-BC-k az oszcilláció szinte minden ciklusában kisültek és erős fáziskapcsoltságot mutattak az oszcilláció adott fázisához, míg az AAC-k és az RS-BC-k általában minden második ciklusban tüzeltek és szignifikánsan gyengébben voltak fáziskapcsoltak. Minden sejttípus ugyanabban a fázisban tüzelt, a piramissejtek kisülése után. Ezek az eredmények azt sugallják, hogy mindhárom sejttípus részt vehet a periszomatikus gátlás kialakításában a karbakol indukált oszcilláció alatt (18/2. ábra).

Az oszcilláció erőssége és a $GABA_A$ receptor mediált szinaptikus áramok nagysága közt szoros összefüggés van (15)(Atallah és Scanziani, 2009). Ismert, hogy az FS-BC-k és az AAC-k axonvégződésein lokalizálódó M2 muszkarinikus acetilkolin receptorok (Hájos és mtsai, 1998), és az RS-BC-k axonterminálisain található CB1 kannabinoid receptorok (2) karbakollal történő direkt, ill. indirekt aktiválása igen hatékonyan képes csökkenteni a GABA felszabadulását a periszomatikus gátlósejtek axonvégződéseikből (Hefft és mtsai, 2002; Neu és mtsai, 2007). Ezért arra voltunk kíváncsiak, hogy vajon milyen mértékű lehet ezen sejtektől

eredő gátló szinaptikus áramok (IPSC) csökkenése olyan koncentrációjú karbakol mellett, ami elégséges az oszcilláció kiváltásához. Tehát, ha meghatározzuk az egyes periszomatikus gátlósejtek által kiváltotott IPSC-k amplitúdóját adott koncentrációjú karbakol jelenlétében, akkor közelebb kerülhetünk ahhoz, hogy tisztázzuk ezen gátlósejttípusok szerepét az oszcillogenezisben, hiszen ezen sejtek axonvégződéseiből periodikusan felszabaduló GABA generálja azt az áramot a $GABA_A$ receptorain keresztül, amit oszcillációként detektálunk a piramissejtek rétegében (15)(Atallah és Scanziani, 2009). Hogy kiderítsük milyen hatékonysággal csökkenti a karbakol az IPSC-k amplitúdóját, párelvezetéseket végeztünk hippokampusz-szeletekben. Kísérleteinkben a preszinaptikus gátlósejtben 10 akciós potenciált váltottunk ki az oszcillációban tapasztalt, az adott sejttípusra jellemző frekvenciával (FS-BC 15 Hz-el, míg az AAC és a RS-BC esetében 10 Hz-el), és mértük a posztszinaptikus CA3 piramissejtben kiváltott IPSC-ket, majd a szeleteket karbakollal kezeltük, és összehasonlítottuk a kiváltott IPSC-k amplitúdóját a drogkezelés előtt és után. Azt találtuk, hogy az egyes sejttípusok ingerlésével kiváltott IPSC-k eltérő mértékben gátolhatóak karbakollal. Az FS-BC – piramissejt párokban a gátlás mértéke kb. 50%-os volt, azaz felére csökkent a kiváltott IPSC-k amplitúdója, az AAC – piramissejt párokban a gátlás mértéke nagyobb volt, míg az RS-BC-piramissejt párokban karbakol hatására gyakorlatilag megszűnt a mérhető IPSC (18/7. ábra). Tehát, ezek az eredmények azt mutatják, hogy a karbakollal kiváltott oszcillációk generálásában az RS-BC-k nem vehetnek részt, attól függetlenül, hogy fáziskapcsoltan tüzelnek az oszcillációk alatt, hiszen ilyen körülmények közt az axonvégződéseikből nem szabadul fel GABA. A következőkben azt szerettük volna megállapítani, vajon milyen mértékben függ az oszcillogenezis az FS-BC-k és az AAC-k működésétől. Ezt úgy próbáltuk megválaszolni, hogy e sejtek axonvégződésein lokalizálódó mu-opioid receptorok aktiválhatóságát vizsgáltuk (Glickfeld és mtsai, 2008). Párelvezetésekben a karbakol kezelés után a szeletekhez DAMGO-t, egy mu-opioid receptor agonistát adtunk, és megmértük az IPSC-k amplitúdójában bekövetkező csökkenés mértékét. Azt kaptuk, hogy amíg az FS-BC-k által kiváltott IPSC-k amplitúdója karbakol jelenlétében tovább csökkent DAMGO hatására, addig az AAC-k által kiváltott IPSC-k tovább már nem változtak (18/8. ábra). Tehát, ha karbakol kiváltott oszcillációt a DAMGO megszünteti, akkor a periszomatikus gátlósejtek közül az FS-BC-k egyedül képesek létrehozni az oszcillációt a hippokampusz CA3 régiójában. Ezzel szemben, ha a DAMGO applikációja nem befolyásolja az oszcillációt, akkor az FS-BC-k és az AAC-k közösen generálják a ritmikus aktivitást. A kísérletek során azt állapítottuk meg, hogy a DAMGO megszünteti a karbakol által generált oszcillációt a hippokampusz-szelet CA3 régiójában (18/4. ábra). Hogy ezen *in vitro* kísérleteink eredményeinkből levont következtetések helyességét megerősítsük *in vivo*

mérésekkel is, Dr. Ulbert Istvánnal az MTA Pszichológiai Intézetéből kollaborációba kezdtünk. A közös mérésekben azt vizsgáltuk, hogy vajon a DAMGO lokális applikációja a hippokampusz CA3 régiójába képes-e az altatott állatban elvezetett gamma oszcillációt is csökkenteni. A vizsgálataink azt mutatták, hogy az *in vitro* mérési eredményeinkkel összhangban, a DAMGO jelentősen lecsökkentette az *in vivo* gamma oszcillációt (18/3. ábra). Ezekből a kísérletekből azt a következtetést vontuk le, hogy a mu-opioid receptorok aktiválása gátolja a gamma oszcilláció keletkezését feltehetően periszomatikus gátlósejttípusok közül az FS-BC-k axonvégződéseiből felszabaduló GABA ürülésének a csökkentésével, tehát az FS-BC-k szinkronizált működése a hippokampusz CA3 régiójában önmagában elégséges a gamma oszcillációk kialakításához. A DAMGO-val történő vizsgálataink eredménye jól összecseng a korábbi CA1 régióban leírt eredményekkel, ahol az elektromos stimulálással kiváltott gamma oszcillációk esetében bizonyították, hogy a mu-opioid receptorok aktiválása jelentősen csökkenti a gamma oszcillációkat (Whittington és mtsai, 1998). A korábbi molekuláris biológiai és optogenetikai kísérletekben tisztázták, hogy a PV tartalmú gátlósejtek mind a kérgi, mind a hippokampális gamma oszcillációk létrehozásában kulcszerepet játszanak (Fuchs és msai, 2007; Sohal és msai, 2009). A módszerből fakadóan viszont ezek a kísérletek nem adtak egyértlemű választ arra, hogy melyik gátlósejttípusok felelősek az oszcillogenezisért, hiszen a PV promóterrel az kosársejteken kívül mind az axoaxonikus, mind a bistratified gátlósejtek működését befolyásolták (Somogyi és Klausberger, 2005). Erre a kérdésre először direkt választ a mi kísérleteink adtak, hiszen kimértük, hogy a bistratified sejtektől származó szinaptikus gátlás is szinte teljesen megszűnik karbakol kezelés hatására (18). Tehát összegezve a méréseink eredményei alapján elmondhatjuk, hogy a karbakol indukált oszcilláció kialakításában döntő szerepük a PV tartalmú kosársejteknek van.

A karbakol eltérő hatása a különböző típusú periszomatikus gátlósejtektől eredő szinaptikus gátlásra. A következő kérdésünk az volt, hogy a hippokampusz CA3 régiójában milyen mechanizmusokon keresztül csökkenti a karbakol a periszomatikus eredetű IPSC-k amplitúdóját. Amint azt a korábbi anatómiai eredményeink sugallták (Hájos és mtsai, 1998), az FS-BC-k és az AAC-k axonvégződésein lokalizálódó M2 muszkarinikus receptorok aktiválása szabályozhatja a GABA ürülését a hippokampusz CA3 régiójában is, hasonlóan a CA1 régióban megfigyeltekhez (Fukudome és mtsai, 2004). Ezt a hipotézist igazolták a farmakológiai kísérleteink, miszerint egy M2 receptor antagonista, az AFDX 116 teljes mértékben visszaállította az FS-BC-, ill. az AAC-piramissejt párokban mért IPSC-k amplitúdójának a nagyságát a karbakol okozta csökkenés után. Ezzel szemben az RS-BC-

piramissejt párokban a karbakol a CB1 kannabinoid receptorok aktiválásán keresztül gátolta a neurotranszmissziót, mert egy CB1 receptor antagonista, az AM251 hozzáadása a tápoldathoz a kontroll értékekre állította vissza az IPSC-k amplitúdóját (17/3. ábra). Ezek az eredmények megerősítették a CA1 régióban mért eredményeket (Fukudome és mtsai, 2004; Neu és mtsai, 2007). További részletes vizsgálatokkal azt szerettük volna kideríteni, hogy a karbakol milyen mechanizmuson keresztül aktiválja a gátló szinapszisoknál található CB1 receptorokat. A farmakológiai kísérleteinket alátámasztva neuroanatómiai eredményekkel igazoltuk, hogy a karbakol jelenléte szükséges a piramissejtek posztszinaptikus oldalán található nitrogén monoxid (NO) szintáz működésének bekapcsolásához (10/1., 5. 7. ábra). Az ennek hatására keletkező NO átjutva a sejtek membránján az RS-BC axonvégződéseiben megemeli a cGMP szintet a NO-sGC aktiválásán keresztül (10/2., 6. ábra). A cGMP szint növekedése egy ma még ismeretlen lipáz aktiválásán keresztül endokannabinoidok szintézisét indukálhat, amely endokannabinoid molekulák aktiválják az axonvégződéseken található CB1 receptorokat (10/4. ábra), ami meggátolja a GABA felszabadulását ezen terminálisokból (10/1. ábra). Ez a szignalizciós útvonal csak karbakol jelenlétében működik M1/3 muszkarinikus acetilkolin receptorok aktiválásán keresztül (Fukudome és mtsai, 2004). Az a folyamat még nem ismert a piramissejtekben, ami az M1/3 receptorok aktiválásától az NO szintéziséig vezet. Az endotélium sejtjeiben egy hasonló útvonalat már feltártak. Ott a kutatásokból az körvonalazódik, hogy az endothélium sejtmembránjában a caveolin-1 fehérjék protein-protein kapcsolattal limitálják az endotheliális NOS aktivitását. Az intracelluláris Ca^{2+} emelkedése csak akkor indukál NO szintézist, ha az M3 receptorok aktiválására felbomlik a caveolin-1 és az endotehliális NOS közti kapcsolat (Michel és Vanhoutte, 2010). Mivel a caveolin-1 nagy mennyiségben expresszálódik a piramissejtekben (Gaudreault és msai, 2004), és a vázolt szignalizációs útvonal többi eleme is megtalálható a hippokampusz fősejtjeiben, így elképzelhető, hogy a neuronokban nagyon hasonló mechanizmuson keresztül szabályozzák a muszkarin receptorok az NO szintézisét. Összefoglalva ezeket a kísérleti eredményeket elmondhatjuk, hogy mind a három periszomatikus gátlósejttípus transzmitter-ürülését szabályozza a karbakol. Az FS-BC-k és az AAC-k esetében ez a szabályzás M2 receptorok aktiválásán keresztül történik, míg az RS-BC-k axonvégződéseiből a GABA felszabadulásának gátlása az M1/3 receptor-NO-cGMP-CB1 receptor szignalizációs útvonal aktiválásával valósul meg.

Hogyan terjed át a hippokampusz CA3 régiójából a CA1 régióba a gamma oszcilláció? Mind az *in vivo*, mind az *in vitro* vizsgálatok azt mutatták (Bragin és mtsai, 1995; Fisahn és mtsai, 1998; Csicsvari és mtsai, 2003), hogy a hippokampusz CA1 régiója önmaga

nem képes gamma oszcillációt generálni, hanem az itt regisztrálható gamma oszcillációt más régiókból érkező ritmikus bemenet hozza létre. Egyes *in vivo* kísérleti eredmények azt sugallták, hogy a gamma oszcilláció beterjedése előrecsatoló gátláson keresztül valósul meg (Csicsvari és mtsai, 2003), azaz a más agyterületről érkező ritmikus serkentés a lokális gátlósejtek közvetlen aktiválásával alakítja ki az oszcillációt. Mások inkább az előrecsatoló serkentést tartották a lehetséges sejtszintű mechanizmusnak, amikor egy másik agyterületről érkező ritmikus serkentés a lokális piramissejtek tüzelését szinkronizálja, s ezen idegsejtek serkentik e régió lokális gátlósejtjeit, mely eredményeként kialakul a gamma oszcilláció (Fries és mtsai, 2007). A következő kísérletsorozatban azt vizsgáltuk meg, melyik mechanizmussal terjed át a gamma oszcilláció a CA3-ból a hippokampusz CA1 régiójába. A karbakollal létrehozott gamma oszcillációknak a CA3 és a CA1 régióban hasonló frekvenciájuk volt, de az oszcillációk erőssége jelentősen kisebb volt a CA1-ben a CA3-ban mért értékekhez képest (19/1. ábra). Az *in vitro* kísérleteinkben meghatároztuk a CA1 régió különböző típusú idegsejtjeinek tüzelési tulajdonságait, ill. a rájuk érkező szinaptikus bemenetek sajátságait (19/2. ábra). Az eredményeink azt mutatják, hogy a CA1 piramissejtek csak kevéssé fáziskapcsoltan tüzeltek (19/3. ábra). Ezzel szemben a lokális gátlósejtek tüzelése erősen fáziskapcsolt volt (19/3. ábra). Mind a piramissejtekre, mind a gátlósejtekre a szinaptikus áramok fáziskapcsoltan érkeztek. A CA1 piramissejtekre a domináns szinaptikus bemenet a gátló volt, míg a gátlósejteken a serkentő szinaptikus bemenet volt a jellemző, hasonlóan a CA3 régióban mértekhez (19/2. ábra, 8). A CA1, ill. a CA3 piramissejtek és a CA1, ill. a CA3 gátlósejtek tüzelésének és a szinaptikus bemeneteinek időbeni viszonyaiból azt a következtetést vontuk le (19/4. ábra), hogy a CA1 régióban keletkezett gamma oszcillációt a lokális gátlósejtek szinkron aktivitása hozza létre, amely szinkron aktivitást a CA3 piramissejtek időben összehangolt tüzelése biztosítja (19/4. ábra). Tehát összefoglalva, a CA3 régióban a gamma oszcilláció létrejötte visszacsatoló (feed-back) szinaptikus mechanizmuson alapul, a hippokampusz CA1 régiójában pedig a gamma oszcilláció előrecsatoló (feed-forward) gátláson keresztül jön létre. A CA3-ban, ill. a CA1-ben a serkentő és gátlósejtek általunk megfigyelt tüzelési sajátosságai összhangban vannak az éber állatból mért eredményekkel (Csicsvari és mtsai, 2003), ami tovább erősíti az *in vitro* modellünk *in vivo* relevanciáját.

Az idegsejtek belső membrántulajdonságainak lehetségese szerepe az oszcillációk keletkezésében. Azért, hogy felderítsük, pontosan miként is valósul meg a piramissejtek és a gátlósejtek időben összerendezett aktivitása, tovább vizsgáltuk a sejtek tüzelési tulajdonságai mögött álló mechanizmusokat. Ehhez nélkülözhetetlen az oszcillációk során a sejtekre érkező

posztszinaptikus áramok pontos feltérképezése, ahogy azt korábban leírtuk. A sejtek tüzelési tulajdonságait a rájuk érkező szinaptikus bemenetek mellett saját membrántulajdonságaik is meghatározhatják. A különféle sejttípusok passzív és aktív membrántulajdonságai eltérhetnek egymástól, és ez hatással lehet az oszcillációban betöltött szerepükre is. Ezért a posztszinaptikus áramok mellett megvizsgáltuk a sejtek ún. rezonancia-tulajdonságait is. A „rezonancia" mutatja meg, hogy mely frekvencia-tartományban bír a sejt nagyobb bemenő ellenállással, így e frekvenciával érkező jelekre a sejt nagyobb valószínűséggel tüzel (Hutcheon és Yarom, 2000). Vizsgálataink azt mutatták, hogy mind a piramissejtekben, mind a gátlósejtek egy csoportjában megfigyelhető rezonancia a 4-9 Hz-es, ún. théta frekvencia-tartományba esik (16/3. ábra). A sejtszintű elektrofiziológiai vizsgálataink kimutatták, hogy a jelenség kialakításában fontos szerepet tölt be a hiperpolarizációra aktiválódó nem-szelektív kationcsatornák (HCN) által létrehozott áram, a h-áram (I(h)), és a sejtek rezonancia-sajátságai korrelálnak a h-áram tulajdonságaival (16/4-5. ábra)(Hu és msai, 2002). Idegsejtmodellek segítségével is vizsgáltuk a különböző hippokampális neurontípusok impedancia-tulajdonságait meghatározó tényezőket. Az elektrofiziológiai méréseken alapuló modellezést Dr. Káli Szabolcs kollégánk végezte. Sikerült zárt alakban felírható matematikai képletet találni a több feszültségfüggő konduktanciát tartalmazó, egyszerű dendritfával rendelkező neuronális modellek impedanciájára. Ennek segítségével megjósolható, hogy az egyes neurontípusok impedanciáját milyen feszültségfüggő konduktanciák határozzák meg. Azt találtuk, hogy mind a CA1 piramissejtek, mind a startum oriensben található és stratum lacunosum-moleculare-ba vetítő (O-LM) gátlósejtek és a stratum oriensben található projekciós GABAerg sejtek impedancia-profilját a I(h) mellett a sejtek passzív membrántulajdonságai is meghatározzák (16/6-8. ábra). Mivel a théta frekvencia-tartományú rezonanciával rendelkező idegsejtek magasabb frekvenciával tüzeltek a gamma oszcillációk alatt (10-30 Hz közt)(19), mint ahogy az a rezonancia-tulajdonságaikból következne, ezért azt a következtetést vontuk le, hogy a sejtek tüzelési gyakoriságát elsősorban a rájuk érkező szinaptikus bemenetek, és nem a belső tulajdonságaik határozzák meg a karbakol indukált oszcillációs modellben. A kísérleteink eredményei azt jósolják, hogy a rezonancia-tulajdonságok alapvetően alacsony aktivitási szint mellett szabályozhatják az idegsejtek tüzelési sajátságait.

IV/4. A hippokampális szinaptikus jelátvitel szabályozása kannabinoidokkal (2-5, 11)

Az anatómiai eredmények azt mutatták (Katona és mtsai, 1999), hogy a CB1 receptorok nagy mennyiségben megtalálhatóak a CCK-t, de nem a PV-t expresszáló gátlósejtek axonvégződésein a hippokampuszban. Először Dr. Katona István kollégámmal

megismételtük ezen vizsgálatokat egy újabb CB1 receptorok ellen termeltetett antitesttel, amely specificitását CB1 receptor hiányos egereken igazoltuk (2/1. ábra). Az eredmények megerősítették a korábbi anatómiai eredményeket. Majd kombinált elektrofiziológiai és farmakológiai kísérleteinkben megvizsgáltuk, hogy milyen hatása van a CB1 receptorok aktiválásának a gátló szinaptikus transzmisszióra a hippokampuszban. CB1 receptor agonistákkal bizonyítottuk, hogy a gátló rostok elektromos ingerlésével kiváltott IPSC-k amplitúdóját jelentősen csökkenti a CB1 receptorok aktiválása (2/3. ábra). Ez a hatás rostspecifikus volt, azaz találtunk olyan rostokat, amelyekből a GABA felszabadulását az agonisták teljesen gátolták, míg voltak olyan rostok, amely nem voltak érzékenyek a CB1 receptor agonistákra (2/4. ábra). Ezek az elektrofiziológiai eredmények jól összecsengenek az anatómiai eredményeinkkel, miszerint a gátlórostok csak egy részén, a CCK-t is tartalmazó terminálisokon találhatóak a CB1 receptorok, míg a PV-t expresszáló axonvégződéseken nem (2/2. ábra). További kísérleteinkben bizonyítottuk, hogy a CB1 receptorok aktiválása csak az akciós potenciál-függő GABA ürülést gátolja, az akciós potenciál független transzmitterfelszabadulást nem (2/5-6. ábra). Összegezve, a CB1 receptorok aktiválására feltehetően a feszültségfüggő Ca^{2+} csatornákon keresztül történő Ca^{2+} ionok beáramlása csökken, ami a GABA felszabadulását gátolja. Ezek az eredmények számos más munkában megerősítést nyertek mind a hippokampuszban (Hoffman és Lupica, 2000; Ohno-Shosaku és mtsai, 2002), mind más agyterületen (Freund és mtsai, 2003).

A hippokampális szinaptikus gátláson kívül, a szinaptikus serkentést is képesek a CB1 receptorok szabályozni. Először ezt Misner és Sullivan 1999-ben megjelent munkája igazolta (Misner és Sullivan, 1999), melyet számos további tanulmány megerősített a hippokampuszban (Straiker és Mackie, 2005), köztünk a saját vizsgálatunk is (3/1. ábra; 4/2. ábra; 11/1. ábra), ill. más agyterületen (Freund és mtsai, 2003). A CB1 receptorok jelenlétét a serkentő axonterminálisokon a későbbi anatómiai eredmények is alátámasztották (Katona és mtsai, 2006; Kawamura és mtsai, 2006). Mi a különbség a hippokampális serkentő, ill. a gátló terminálisokon lokalizálódó CB1 receptorok között? Az anatómiai vizsgálatokból egyértelmű, hogy CB1 receptorok sokkal nagyobb számban találhatóak a gátló axonvégződéseken, mint a serkentőkön (2/2. ábra)(Nyiri és mtsai, 2005; Katona és mtsai, 2006; Kawamura és mtsai, 2006). Ez a számbeli eltérés funkcionális különbségben is megjelenik, hiszen a CCK-t expresszáló gátlósejtektől eredő IPSC-ket teljesen gátolni lehet CB1 receptor agonistákkal (2/4. ábra)(17)(Fukudome és mtsai, 2004; Neu és mtsai, 2007), míg a serkentő posztszinaptikus áramok (EPSC) amplitúdója csak a felére csökken ugyan ilyen körülmények közt elvégzett kísérletekeben (3/1. ábra; 4/1. ábra; 11/1. ábra)(Misner és Sullivan, 1999). További kérdés, hogy van-e farmakológiai különbség is a gátló, ill. a serkentő terminálisokon

található CB1 receptorok közt. A vizsgálataink azt mutatták, hogy két olyan farmakológiai eszköz is van, amelyre a CB1 receptorok érzékenysége különböző. A serkentő axonokon található CB1 receptorok aktiválására bekövetkező EPSC-k amplitúdójának csökkenése nem antagonizálható AM251-el, de a csökkenés kivédhető egy vanilloid receptor antagonista, a kapszazepin jelenlétében, ha 1µM feletti koncentrációban adtunk egy CB1 receptor agonistát, a WIN55,212-2-t (4/2. ábra). Ezzel szemben ez a CB1 receptor agonista ugyan ilyen koncentrációja mellett okozta IPSC-k csökkenése kivédhető AM251-el, de nem kapszazepinnel (4/2. ábra). Hasonló megfigyelést tettünk egy másik CB1 receptor agonistával, a CP55,940-el (4/3. ábra). Tehát elmondható, hogy mind a serkentő, mind a gátló szinaptikus transzmisszió a hippokampuszban szabályozható CB1 receptorokon keresztül, de e szabályozás eltérő farmakológiai profilt mutat. Ez az eredmény számos viselkedéskutatási eredményt megmagyaráz (Haller és mtsai, 2007).

Ahhoz, hogy a kívülről adott farmakológiai szerek okozta változásokat megfelelően értelmezni tudjuk egy adott kísérleti felállásban, tudnunk kell, hogy vannak-e, és ha igen, akkor milyen más hatásaik a farmakonoknak a kívánt hatáson kívül. Annak érdekében, hogy kiderítsük, hogy az általunk, ill. a világ számos laboratóriumában használt CB1 receptor agonisták közül a WIN55,212-2-nek milyen CB1 receptoroktól független hatásai vannak, megvizsgáltuk az EPSC-k amplitúdójára gyakorolt hatását ennek a kannabinoid receptor agonsitának olyan hippokampális szeletekben, amelyek CB1 receptor hiányos egerekből készültek, ill. patkány hippokampuszából készült szeletekben AM251 jelenlétében. Az eredményeink azt mutatták, hogy µM-os koncentráció alatt adva a WIN55,212-2 specifikusan CB1 receptorokon hat, de ez felett már csökkentheti az EPSC-k amplitúdóját az N-típusú feszültségfüggő Ca^{2+} csatornák működésének direkt gátlásával (11/1-3. ábra). Összefoglalva elmondhatjuk, hogy sikerült olyan koncentráció-tartományt meghatározni, ahol a WIN55,212-2 adagolása specifikusan a CB1 receptorok funkcióját szabályozza.

További kísérleteinkben azt tanulmányoztuk, hogy az endokannabinoidok transzportja mennyire befolyásolja a tápoldathoz adott egyik endokannabinoid molekula, a 2-AG hatását a szinaptikus gátlásra. A 2-AG adagolása fiziológiai hőmérséklet közelében kb 20%-kal csökkentette az elektromos stimulálással kiváltott IPSC-k amplitúdóját (5/1. ábra), amely hatás jóval kisebb mértékű volt, mindha WIN55,212-2 vagy CP55,940 agonistákat használtunk volna hasonló körülmények közt (2/3. ábra, 3/1 ábra, 4/2 ábra). Ha ugyan ezt a kísérletet szobahőmérsékleten végeztük el 2-AG-vel, azaz olyan körülményeket teremtettünk, amikor a transzporterek funkciója gátolt, akkor kétszer akkora csökkenés volt megfigyelhető az IPSC-k amplitúdójában, mint fiziológiás hőmérsékleten (5/1. ábra). Ez a kísérlet valószínűsíti a transzporterek szabályozó szerepét az endokannabinoidok funkcióinak a

betöltésében. Egy ma még nem azonosított fehérje (vagy fehérjék) lehet(nek) felelős(ek) az endokannabinoidok transzportjáért (Beltramo és msai, 1997). Az endokannabinoidok transzportjának több gátlószere is ismert. Ezek közül egy gátlószert alkalmazva azt találtuk, hogy fiziológiás hőmérsékleten a 2-AG okozta csökkenése a szinaptikus gátlásnak olyan mértékü volt, mindha szobahőmérsékleten végeztük volna a kísérleteket (5/2. ábra). Tehát a 2-AG hatékonyságát jelentősen befolyásolják transzport folyamatok. Ezt a következtetést uptake kísérletekkel támasztottak alá Dr. Danielle Piomelli Irvine-i laboratóriumában (5/3. ábra). Ezek az eredmények egyrészt mutatják, hogy az endokannabinoid szignalizácós útvonal egy fontos szabályozásai pontja lehet az endokannabinoidok transzportja, másrészt mutatja a szobahőmérsékleten végzett kannabinoid kutatások limitáltságát.

IV/5. A kannabinoidok hatásai a hippokampális gamma oszcillációkra (2, 20)

Az *in vitro* kísérleteink (2) és *in vivo* mérések (Robbe és mtsai, 2006) eredményei azt mutatták, hogy a CB1 receptorok ingerlése a szinkron idegi aktivitást hatékonyan gátolja, ami magyarázhatja a marihuána káros hatását a rövidtávú memóriafolyamatokra (Murray és mtsai, 2007). Hogy megértsük a sejtszintű folyamatokat, amin keresztül a CB1 kannabinoid receptorok aktivációja csökkenti a CA3 régióban keletkezett gamma oszcillációkat, azt vizsgáltuk, hogy a 14/5. ábrán bemutatott neuronhálózat mely szinapszisainak működését szabályozzák a kannabinoid receptor agonisták. Ez különösen azon eredmények fényében vált izgalmas kérdéssé, miszerint az RS-BC-k axonvégződéseiből, ahol a legnagyobb mennyiségben találhatóak a CB1 receptorok (2/2. ábra), nem szabadul fel az oszcilláció közben GABA (18/7. ábra), tehát nem e szinapszisok működésének gátlásán keresztül csökkentik a kannabinoidok a gamma oszcilláció erejét (2/7. ábra). De akkor milyen mechanizmuson keresztül fejtik ki a hatásukat a kannabinoid származékok? Mivel az FS-BC-k és az AAC-k axonvégződésein nem kimutatható a CB1 receptorok jelenléte (2/2. ábra) (Katona és mtsai, 1999), ezért feltételeztük, hogy a serkentő idegvégződéseken található CB1 receptorok aktiválása csökkentheti az oszcillációt. Az anatómiai és farmakológiai kísérletek bizonyították, hogy a piramissejtek egymást innerváló axonterminálisaikon vannak CB1 receptorok (11/1. ábra) (Katona és mtsai, 1999; Kawamura és mtsai, 2006), ill. más elektrofiziológiai mérések azt mutatták, hogy a gátlósejtekre érkező serkentő szinapszisok nem érzékenyek kannabinoidokra (Hoffman és mtsai, 2003). Ezekből az eredményekből azt vártuk, hogy a piramissejtekre, és nem az FS-BC-kre érkező EPSC-k amplitúdóját fogják csökkenteni a CB1 receptor agonisták karbakol jelenlétében, ami megmagyarázná a kannabinoidok az oszcillációkra gyakorolt hatását, hiszen a piramissejtek közti rekurrens

serkentés hozzájárulhat az idegi szinkronitás kialakításához (Buzsáki, 2006). Kísérleteinkben először meghatároztuk, hogy az általunk tesztelt két kannabinoid receptor agonista (WIN55,212-2, CP55,940) CB1 receptorfüggő módon csökkenti a karbakol indukált gamma oszcillációt. Ez a következtetésünk azon a kísérleti megfigyelésen alapult, hogy mind a két kannabinoid származék közel felére csökkentette a gamma oszcilláció amplitúdóját vad típusú egerek hippokampuszából készült szeletekben, míg a CB1 receptort nem expresszáló egerek hippokampusz-szeleteiben kiváltott gamma oszcillációk tulajdonságai nem változtak (20/1. ábra). További kísérletekben meghatároztuk, hogy a gamma oszcilláció amplitúdójának csökkenésével párhuzamosan csökkent mind a piramissejtek, mind az FS-BC-k tüzelési frekvenciája (20/2. ábra). De mi okozhatja a tüzelés csökkenését? Az okok meghatározásához megvizsgáltuk az egyes szinaptikus kapcsolatok kannabinoid érzékenységét karbakol jelenlétében, hiszen a szinaptikus áramok határozzák meg elsősorban az idegsejtek aktivitását gamma oszcillációk alatt (9/5-6. ábra). Összhangban az eddig eredményekkel azt találtuk, hogy a karbakol mellett mérhető periszomatikus gátlás nem volt kannabinoid szenzitív (20/3. ábra), hiszen már csak a PV-tartalmú gátlósejtektől eredő szinaptikus áramokat detektálhattuk karbakol jelenlétében, mivel az RS-BC-k axonvégződéseiből ilyen körülmények közt nem szabadul fel GABA (17/3. ábra; 18/7. ábra). További kísérletekben meghatároztuk, hogy a kannabinoidok közel egyharmadával csökkentették a CA3 piramissejtekre érkező EPSC-k amplitúdóját karbakol mellett (20/3. ábra). Az irodalmi adatokkal szemben viszont azt találtuk, hogy azonos mérési körülmények közt az FS-BC-kre érkező EPSC-k amplitúdója is egyharmadával csökkent kannabinoidok adagolásának a következtében (20/3. ábra). Tehát a kannabinoid-származékok mind a piramissejtekre, mind az FS-BC-kre érkező szinaptikus serkentést csökkentették. Ezekből az eredményekből azt a következtetést vontuk le, hogy a CB1 receptorok ingerlésének következtében gátlódik a serkentő terminálisokból felszabaduló glutamát mennyisége, ami mind a piramissejtek, mind az FS-BC-k tüzelési gyakoriságának csökkenését okozhatja az oszcillációk alatt. A tüzelési frekvencia csökkenése kisebb detektálható áramot generál az extracelluláris térben, ezért ez megmagyarázza az oszcilláció amplitúdójának a csökkenését a CB1 receptorok aktiválásának a következtében. Mivel a gamma oszcillációknak fontos szerepet tulajdonítanak a rövidtávú memóriafolyamatokban (Paulsen és Moser, 1998), így kannabinoidok okozta memóriazavarok egyik magyarázata lehet a gamma oszcillációra gyakorolt hatásuk.

V. ÖSSZEFOGLALÁS

Az egyik célkitűzésünk az volt, hogy megértsük azokat a sejt- és hálózatszintű mechanizmusokat, amelyek kialakítják a gamma oszcillációkat a hippokampális neuronhálózatokban. A kísérleteink alapján elmondhatjuk, hogy a hippokampusz-szeletekben karbakollal indukált gamma oszcillációk számos tulajdonsága megegyezik az éber állat hippokampuszában mért gamma oszcillációk jellegzetességeivel. A karbakol indukált oszcillációkat a piramissejtek és a gyorsan tüzelő kosársejtek időben összehangolt periodikus tüzelése hozza létre a hippokampusz CA3 régiójában. A piramissejtek szinkron kisülése visszacsatoló mechanizmuson keresztül aktiválja a gyorsan tüzelő kosársejteket, amelyek nagy időbeni pontossággal kisülnek a rájuk fázikusan érkező serkentés következtében, és egyszerre kiürítik az axonvégződéseikből a GABA-t. A szinaptikus gátlás lecsengésével újraindul a piramissejtek tüzelése, amely egy újabb oszcillációs ciklus kezdetét jelenti. A periodikusan és időben nagy pontossággal felszabaduló GABA a posztszinaptikus piramissejteken nagy amplitúdójú gátló szinaptikus áramokat hoz létre, amely áramok periodikus fluktuálása okozza elsősorban a piramissejtek rétegéből elvezethető ritmikus feszültségváltozást, amelyet mint oszcillációt regisztrálunk. Ezek az oszcillációk lokálisan a CA3 régióban keletkeznek, és előrecsatoló gátláson keresztül terjednek a hippokampusz CA1 régiójába. Az *in vitro* oszcillációk alatt az idegsejtek tüzelését döntően a rájuk érkező szinaptikus bemenetek határozzák meg.

A másik cékitűzésünk az volt, hogy felderítsük azokat a mechanizmusokat, amin keresztül a kannabinoidok szabályozzák a ritmikus aktivitásokat. A kannabinoidok, amelyek receptorai mind a piramissejtek, mind a szabályosan tüzelő kosársejtek axonvégződésein megtalálhatóak és aktiválásuk jelentősen csökkenti a neurotranszmitterek felszabadulását, hatékonyan csökkentik az *in vitro* oszcillációk amplitúdóját is CB1 kannabinoid receptorokon keresztül. Vizsgálataink megmutatták, hogy a kannabinoidok gamma oszcillációkra gyakorolt hatása abból adódik, hogy mind a piramissejtek közti, mind a gyorsan tüzelő kosársejtekre érkező szinaptikus serkentést jelentősen csökkentik, ami eredményezi e hálózati aktivitást létrehozó idegsejtek tüzelésének a csökkenését. A neuronok kisebb aktivitási szintje pedig alacsonyabb amplitúdójú oszcillációt eredményez.

Összefoglalva, a kutatási eredményeink tisztázták a hippokampális gamma oszcillációk keletkezésének és tovaterjedésének folyamatait, amely eredmények segíthetnek olyan pszichés betegségek mögött meghúzódó jelenségek megfejtésében, mint pl. a skizofrénia tünetcsoport, amivel kapcsolatban megfigyelték, hogy a gamma oszcillácók jelentősen eltérnek a normális agyi működésben tapasztaltaktól.

VI. IRODALOM

VI/1 Az értekezés általános irodalomjegyzéke:

Acsády L, Kamondi A, Sik A, Freund T, Buzsáki G (1998) GABAergic cells are the major postsynaptic targets of mossy fibers in the rat hippocampus. J Neurosci 18:3386-3403.

Andersen P, Sundberg SH, Sveen O, Wigström H (1977) Specific long-lasting potentiation of synaptic transmission in hippocampal slices. Nature 266:737-739.

Andersen P, Morris R, Amaral D, Bliss T, O'Keefe J (2007) The Hippocampus Book.: Oxford University Press.

Atallah BV, Scanziani M (2009) Instantaneous modulation of gamma oscillation frequency by balancing excitation with inhibition. Neuron 62:566-577.

Beltramo M, Stella N, Calignano A, Lin SY, Makriyannis A, Piomelli D (1997) Functional role of high-affinity anandamide transport, as revealed by selective inhibition. Science 277:1094-1097.

Bragin A, Jando G, Nadasdy Z, Hetke J, Wise K, Buzsaki G (1995) Gamma (40-100 Hz) oscillation in the hippocampus of the behaving rat. J Neurosci 15:47-60.

Buzsaki G, Buhl DL, Harris KD, Csicsvari J, Czh B, Morozov A (2003) Hippocampal network patterns of activity in the mouse. Neuroscience 116:201-211.

Buzsáki G (1986) Hippocampal sharp waves: their origin and significance. Brain Res 398:242-252.

Buzsáki G (1989) Two-stage model of memory trace formation: A role for 'noisy' brain states. Neuroscience 310:551-570.

Buzsáki G (2006) Rhythms of the brain: Oxford University Press.

Cobb SR, Buhl EH, Halasy K, Paulsen O, Somogyi P (1995) Synchronization of neuronal activity in hippocampus by individual GABAergic interneurons. Nature 378:75-78.

Colgin LL, Denninger T, Fyhn M, Hafting T, Bonnevie T, Jensen O, Moser MB, Moser EI (2009) Frequency of gamma oscillations routes flow of information in the hippocampus. Nature 462:353-357.

Csicsvari J, Jamieson B, Wise KD, Buzsaki G (2003) Mechanisms of gamma oscillations in the hippocampus of the behaving rat. Neuron 37:311-322.

Devane WA, Hanus L, Breuer A, Pertwee RG, Stevenson LA, Griffin G, Gibson D, Mandelbaum A, Etinger A, Mechoulam R (1992) Isolation and structure of a brain constituent that binds to the cannabinoid receptor. Science 258:1946-1949.

Edwards FA, Konnerth A, Sakmann B, Takahashi T (1989) A thin slice preparation for patch clamp recordings from neurones of the mammalian central nervous system. Pflugers Arch 414:600-612.

Engel AK, Fries P, Singer W (2001) Dynamic predictions: oscillations and synchrony in top-down processing. Nat Rev Neurosci 2:704-716.

Fisahn A, Pike FG, Buhl E, Paulsen O (1998) Cholinergic induction of network oscillations at 40 Hz in the hippocampus in vitro. Nature 394:186-189.

Fisahn A, Contractor A, Traub RD, Buhl EH, Heinemann SF, McBain CJ (2004) Distinct roles for the kainate receptor subunits GluR5 and GluR6 in kainate-induced hippocampal gamma oscillations. The Journal of neuroscience 24:9658-9668.

Freund TF, Buzsáki G (1996) Interneurons of the hippocampus. Hippocampus 6:345 - 470.

Freund TF, Katona I (2007) Perisomatic inhibition. Neuron 56:33-42.

Freund TF, Katona I, Piomelli D (2003) Role of endogenous cannabinoids in synaptic signaling. Physiol Rev 83:1017-1066.

Fries P, Nikolic D, Singer W (2007) The gamma cycle. Trends Neurosci 30:309-316.

Fuchs EC, Zivkovic AR, Cunningham MO, Middleton S, Lebeau FE, Bannerman DM, Rozov A, Whittington MA, Traub RD, Rawlins JN, Monyer H (2007) Recruitment of parvalbumin-positive interneurons determines hippocampal function and associated behavior. Neuron 53:591-604.

Fukudome Y, Ohno-Shosaku T, Matsui M, Omori Y, Fukaya M, Tsubokawa H, Taketo MM, Watanabe M, Manabe T, Kano M (2004) Two distinct classes of muscarinic action on hippocampal inhibitory synapses: M2-mediated direct suppression and M1/M3-mediated indirect suppression through endocannabinoid signalling. Eur J Neurosci 19:2682-2692.

Gaoni Y, Mechoulam R (1971) The isolation and structure of delta-1-tetrahydrocannabinol and other neutral cannabinoids from hashish. J Am Chem Soc 93:217-224.

Gaudreault SB, Dea D, Poirier J (2004) Increased caveolin-1 expression in Alzheimer's disease brain. Neurobiol Aging 25:753-759.

Glickfeld LL, Atallah BV, Scanziani M (2008) Complementary modulation of somatic inhibition by opioids and cannabinoids. The Journal of neuroscience 28:1824-1832.

Gloveli T, Dugladze T, Saha S, Monyer H, Heinemann U, Traub RD, Whittington MA, Buhl EH (2005) Differential involvement of oriens/pyramidale interneurones in hippocampal network oscillations in vitro. The Journal of physiology 562:131-147.

Gulyas AI, Cravatt BF, Bracey MH, Dinh TP, Piomelli D, Boscia F, Freund TF (2004) Segregation of two endocannabinoid-hydrolyzing enzymes into pre- and postsynaptic compartments in the rat hippocampus, cerebellum and amygdala. Eur J Neurosci 20:441-458.

Hájos N, Papp EC, Acsady L, Levey AI, Freund TF (1998) Distinct interneuron types express m2 muscarinic receptor immunoreactivity on their dendrites or axon terminals in the hippocampus. Neuroscience 82:355-376.

Hájos N, Katona I, Naiem SS, MacKie K, Ledent C, Mody I, Freund TF (2000) Cannabinoids inhibit hippocampal GABAergic transmission and network oscillations. Eur J Neurosci 12:3239-3249.

Haller J, Matyas F, Soproni K, Varga B, Barsy B, Nemeth B, Mikics E, Freund TF, Hajos N (2007) Correlated species differences in the effects of cannabinoid ligands on anxiety and on GABAergic and glutamatergic synaptic transmission. Eur J Neurosci 25:2445-2456.

Hefft S, Kraushaar U, Geiger JR, Jonas P (2002) Presynaptic short-term depression is maintained during regulation of transmitter release at a GABAergic synapse in rat hippocampus. J Physiol 539:201-208.

Herkenham M, Lynn AB, Little MD, Johnson MR, Melvin LS, de Costa BR, Rice KC (1990) Cannabinoid receptor localization in brain. Proc Natl Acad Sci U S A 87:1932-1936.

Hoffman AF, Lupica CR (2000) Mechanisms of cannabinoid inhibition of GABA(A) synaptic transmission in the hippocampus. J Neurosci 20:2470-2479.

Hoffman AF, Riegel AC, Lupica CR (2003) Functional localization of cannabinoid receptors and endogenous cannabinoid production in distinct neuron populations of the hippocampus. Eur J Neurosci 18:524-534.

Hu H, Vervaeke K, Storm JF (2002) Two forms of electrical resonance at theta frequencies, generated by M-current, h-current and persistent Na+ current in rat hippocampal pyramidal cells. J Physiol 545:783-805.

Hutcheon B, Yarom Y (2000) Resonance, oscillation and the intrinsic frequency preferences of neurons. Trends Neurosci 23:216-222.

Jung KM, Astarita G, Zhu C, Wallace M, Mackie K, Piomelli D (2007) A key role for diacylglycerol lipase-alpha in metabotropic glutamate receptor-dependent endocannabinoid mobilization. Mol Pharmacol 72:612-621.

Katona I, Freund TF (2008) Endocannabinoid signaling as a synaptic circuit breaker in neurological disease. Nat Med 14:923-930.

Katona I, Sperlagh B, Sik A, Kafalvi A, Vizi ES, Mackie K, Freund TF (1999) Presynaptically located CB1 cannabinoid receptors regulate GABA release from axon terminals of specific hippocampal interneurons. J Neurosci 19:4544-4558.

Katona I, Urban GM, Wallace M, Ledent C, Jung KM, Piomelli D, Mackie K, Freund TF (2006) Molecular composition of the endocannabinoid system at glutamatergic synapses. J Neurosci 26:5628-5637.

Kawamura Y, Fukaya M, Maejima T, Yoshida T, Miura E, Watanabe M, Ohno-Shosaku T, Kano M (2006) The CB1 cannabinoid receptor is the major cannabinoid receptor at excitatory presynaptic sites in the hippocampus and cerebellum. J Neurosci 26:2991-3001.

Ledent C, Valverde O, Cossu G, Petitet F, Aubert JF, Beslot F, Bohme GA, Imperato A, Pedrazzini T, Roques BP, Vassart G, Fratta W, Parmentier M (1999) Unresponsiveness to cannabinoids and reduced addictive effects of opiates in CB1 receptor knockout mice. Science 283:401-404.

Li XG, Somogyi P, Ylinen A, Buzsáki G (1994) The hippocampal ca3 network - an in vivo intracellular labeling study. Journal of Comparative Neurology 339:181-208.

Liu G, Choi S, Tsien RW (1999) Variability of neurotransmitter concentration and nonsaturation of postsynaptic AMPA receptors at synapses in hippocampal cultures and slices. Neuron 22:395-409.

Lopez-Bendito G, Sturgess K, Erdelyi F, Szabo G, Molnar Z, Paulsen O (2004) Preferential origin and layer destination of GAD65-GFP cortical interneurons. Cereb Cortex 14:1122-1133.

Lorente de Nó R (1934) Studies on the structure of the cerebral cortex. II. Continuation of the study of the ammonic system. JPsycholNeur(Leipzig).

Mainen ZF, Malinow R, Svoboda K (1999) Synaptic calcium transients in single spines indicate that NMDA receptors are not saturated. Nature 399:151-155.

Marrosu F, Portas C, Mascia MS, Casu MA, Fa M, Giagheddu M, Imperato A, Gessa GL (1995) Microdialysis measurement of cortical and hippocampal acetylcholine release during sleep-wake cycle in freely moving cats. Brain Res 671:329-332.

Marrs WR, Blankman JL, Horne EA, Thomazeau A, Lin YH, Coy J, Bodor AL, Muccioli GG, Hu SS, Woodruff G, Fung S, Lafourcade M, Alexander JP, Long JZ, Li W, Xu C, Moller T, Mackie K, Manzoni OJ, Cravatt BF, Stella N (2010) The serine hydrolase ABHD6 controls the accumulation and efficacy of 2-AG at cannabinoid receptors. Nat Neurosci 13:951-957.

Matsuda LA, Lolait SJ, Brownstein MJ, Young AC, Bonner TI (1990) Structure of a cannabinoid receptor and functional expression of the cloned cDNA. Nature 346:561-564.

Meyer AH, Katona I, Blatow M, Rozov A, Monyer H (2002) In vivo labeling of parvalbumin-positive interneurons and analysis of electrical coupling in identified neurons. J Neurosci 22:7055-7064.

Michel T, Vanhoutte PM (2010) Cellular signaling and NO production. Pflugers Arch 459:807-816.

Miles R, Toth K, Gulyás AI, Hajos N, Freund TF (1996) Differences between somatic and dendritic inhibition in the hippocampus. Neuron 16:815-823.

Misner DL, Sullivan JM (1999) Mechanism of cannabinoid effects on long-term potentiation and depression in hippocampal CA1 neurons. J Neurosci 19:6795-6805.

Murray RM, Morrison PD, Henquet C, Di Forti M (2007) Cannabis, the mind and society: the hash realities. Nat Rev Neurosci 8:885-895.

Neu A, Foldy C, Soltesz I (2007) Postsynaptic origin of CB1-dependent tonic inhibition of GABA release at cholecystokinin-positive basket cell to pyramidal cell synapses in the CA1 region of the rat hippocampus. J Physiol 578:233-247.

Nyilas R, Dudok B, Urban GM, Mackie K, Watanabe M, Cravatt BF, Freund TF, Katona I (2008) Enzymatic machinery for endocannabinoid biosynthesis associated with calcium stores in glutamatergic axon terminals. J Neurosci 28:1058-1063.

Nyiri G, Cserep C, Szabadits E, Mackie K, Freund TF (2005) CB1 cannabinoid receptors are enriched in the perisynaptic annulus and on preterminal segments of hippocampal GABAergic axons. Neuroscience 136:811-822.

Ohno-Shosaku T, Tsubokawa H, Mizushima I, Yoneda N, Zimmer A, Kano M (2002) Presynaptic cannabinoid sensitivity is a major determinant of depolarization-induced retrograde suppression at hippocampal synapses. J Neurosci 22:3864-3872.

Okamoto Y, Morishita J, Tsuboi K, Tonai T, Ueda N (2004) Molecular characterization of a phospholipase D generating anandamide and its congeners. J Biol Chem 279:5298-5305.

Paulsen O, Moser EI (1998) A model of hippocampal memory encoding and retrieval: GABAergic control of synaptic plasticity. Trends Neurosci 21:273-278.

Perrais D, Ropert N (1999) Effect of zolpidem on miniature IPSCs and occupancy of postsynaptic GABAA receptors in central synapses. J Neurosci 19:578-588.

Piomelli D (2003) The molecular logic of endocannabinoid signalling. Nat Rev Neurosci 4:873-884.

Robbe D, Montgomery SM, Thome A, Rueda-Orozco PE, McNaughton BL, Buzsaki G (2006) Cannabinoids reveal importance of spike timing coordination in hippocampal function. Nat Neurosci 9:1526-1533.

Schwartzkroin PA, Andersen P (1975) Glutamic acid sensitivity of dendrites in hippocampal slices in vitro. Adv Neurol 12:45-51.

Senior TJ, Huxter JR, Allen K, O'Neill J, Csicsvari J (2008) Gamma oscillatory firing reveals distinct populations of pyramidal cells in the CA1 region of the hippocampus. J Neurosci 28:2274-2286.

Shepherd GM (2004) The synaptic organization of the brain.: Oxford University Press.

Shimono K, Brucher F, Granger R, Lynch G, Taketani M (2000) Origins and distribution of cholinergically induced beta rhythms in hippocampal slices. J Neurosci 20:8462-8473.

Singer W (1993) Synchronization of cortical activity and its putative role in information processing and learning. Annu Rev Physiol 55:349-374.

Skrede KK, Westgaard RH (1971) The transverse hippocampal slice: a well-defined cortical structure maintained in vitro. Brain research 35:589-593.

Sohal VS, Zhang F, Yizhar O, Deisseroth K (2009) Parvalbumin neurons and gamma rhythms enhance cortical circuit performance. Nature 459:698-702.

Somogyi P, Klausberger T (2005) Defined types of cortical interneurone structure space and spike timing in the hippocampus. J Physiol 562:9-26.

Stella N, Schweitzer P, Piomelli D (1997) A second endogenous cannabinoid that modulates long-term potentiation. Nature 388:773-778.

Straiker A, Mackie K (2005) Depolarization-induced suppression of excitation in murine autaptic hippocampal neurones. J Physiol 569:501-517.

Tamamaki N, Abe K, Nojyo Y (1987) Columnar organization in the subiculum formed by axon branches originating from single CA1 pyramidal neurons in the rat hippocampus. Brain Res 412:156-160.

Traub RD, Whittington MA, Colling SB, Buzsaki G, Jefferys JG (1996) Analysis of gamma rhythms in the rat hippocampus in vitro and in vivo. J Physiol (Lond) 493:471-484.

Traub RD, Spruston N, Soltesz I, Konnerth A, Whittington MA, Jefferys GR (1998) Gamma-frequency oscillations: a neuronal population phenomenon, regulated by synaptic and intrinsic cellular processes, and inducing synaptic plasticity. Prog Neurobiol 55:563-575.

Trevelyan AJ (2009) The direct relationship between inhibitory currents and local field potentials. J Neurosci 29:15299-15307.

Vanderwolf CH (1988) Cerebral activity and behaviour: control by central cholinergic and serotonergic systems. Int Rev Neurobiol 30:225-340.

Whittington MA, Traub RD, Jefferys JG (1995) Synchronized oscillations in interneuron networks driven by metabotropic glutamate receptor activation. Nature 373:612-615.

Whittington MA, Faulkner HJ, Doheny HC, Traub RD (2000) Neuronal fast oscillations as a target site for psychoactive drugs. Pharmacol Ther 86:171-190.

Whittington MA, Traub RD, Faulkner HJ, Jefferys JG, Chettiar K (1998) Morphine disrupts long-range synchrony of gamma oscillations in hippocampal slices. Proc Natl Acad Sci U S A 95:5807-5811.

Yamamoto C, McIlwain H (1966) Potentials evoked in vitro in preparations from the mammalian brain. Nature 210:1055-1056.

Zimmer A, Zimmer AM, Hohmann AG, Herkenham M, Bonner TI (1999) Increased mortality, hypoactivity, and hypoalgesia in cannabinoid CB1 receptor knockout mice. Proc Natl Acad Sci U S A 96:5780-5785.

VI/2 Az értekezés alapjául szolgáló saját közlemények

Eredeti közlemények

1. Hájos N, Nusser Z, Rancz EA, Freund TF, Mody I. Cell type- and synapse-specific variability in synaptic GABAA receptor occupancy. **Eur J Neurosci.** *12:* 810-8. (2000)

2. Hájos N, Katona I, Naiem SS, MacKie K, Ledent C, Mody I, Freund TF. Cannabinoids inhibit hippocampal GABAergic transmission and network oscillations. **Eur J Neurosci**. *12:* 3239-49. (2000)

3. Hájos N, Ledent C, Freund TF. Novel cannabinoid-sensitive receptor mediates inhibition of glutamatergic synaptic transmission in the hippocampus. **Neuroscience** *106:* 1-4. (2001)

4. Hájos N, Freund TF. Pharmacological separation of cannabinoid sensitive receptors on hippocampal excitatory and inhibitory fibers, **Neuropharmacology** *43*: 503-510. (2002)

5. Hájos N, Kathuria S, Dinh T, Piomelli D, Freund TF. Endocannabinoid transport tightly controls 2-arachidonoyl glycerol actions in the hippocampus: effects of low temperature and the transport inhibitor AM404. **Eur. J. Neurosci**. *19:* 2991-6. (2004)

6. Pálhalmi J, Paulsen O, Freund TF, Hájos N. Distinct properties of carbachol- and DHPG-induced network oscillations in hippocampal slices. **Neuropharmacology**. *47:*381-9. (2004)

7. Hájos N, Pálhalmi J, Mann EO, Németh B, Paulsen O, Freund TF. (2004) Spike timing of distinct types of GABAergic interneurons during hippocampal gamma oscillations *in vitro*. **J. Neurosci**. *24:* 9127-37.

8. Mann EO, Suckling JM, Hájos N, Greenfield SA, Paulsen O. Perisomatic feedback inhibition underlies cholinergically induced fast network oscillations in the rat hippocampus in vitro. **Neuron**, *45:* 105-17. (2005)

9. Oren I, Mann EO, Paulsen O, Hájos N. Synaptic currents in anatomically identified CA3 neurons during hippocampal gamma oscillations in vitro. **J Neurosci.** *26:* 9923-34. (2006)

10. Makara JK, Katona I, Nyíri G, Németh B, Ledent C, Watanabe M, de Vente J, Freund TF, Hájos N. Involvement of nitric oxide in depolarization-induced suppression of inhibition in hippocampal pyramidal cells during activation of cholinergic receptors. **J Neurosci.** *27:* 10211-22. (2007)

11. Németh B, Ledent C, Freund TF, Hájos N. CB(1) receptor-dependent and -independent inhibition of excitatory postsynaptic currents in the hippocampus by WIN 55,212-2. **Neuropharmacology** *54:* 51-7. (2008)

12. Hájos N, Ellender TJ, Zemankovics R, Mann EO, Exley R, Cragg SJ, Freund TF, Paulsen O. Maintaining network activity in submerged hippocampal slices: importance of oxygen supply. **Eur J Neurosci.** *29:* 319-27. (2009)

13. Hájos N, Mody I Establishing a physiological environment for visualized in vitro brain slice recordings by increasing oxygen supply and modifying aCSF content. **J Neurosci Meth.** *183:* 107-13. (2009)

14. Hájos N, Paulsen O, Network mechanisms of gamma oscillations in the CA3 region of the hippocampus. **Neural Networks** *22:* 1113-9. (2009)

15. Oren I, Hájos N, Paulsen O. Identification of the current generator underlying cholinergically induced gamma frequency field potential oscillations in the hippocampal CA3 region. **J Physiol.** *588:* 785-97. (2010)

16. Zemankovics R, Káli S, Paulsen O, Freund TF, Hájos N. Differences in subthreshold resonance of hippocampal pyramidal cells and interneurons: the role of h-current and passive membrane characteristics. **J Physiol.** *588:* 2109-32. (2010)

17. Szabó GG, Holderith N, Gulyás AI, Freund TF, Hájos N. Distinct synaptic properties of perisomatic inhibitory cell types and their different modulation by cholinergic receptor activation in the CA3 region of the mouse hippocampus. **Eur J Neurosci.** *31:* 2234-46. (2010)

18. Gulyás AI, Szabó GG, Ulbert I, Holderith N, Monyer H, Erdéyi F, Szabó G, Freund TF, Hájos N. Parvalbumin-containing fast-spiking basket cells generate the field potential oscillations induced by cholinergic receptor activation in the hippocampus. **J Neurosci.** (elfogadva).

19. Zemankovics R, Veres J, Oren I, Hájos N. Feed-forward inhibition underlies the propagation of cholinergically induced gamma oscillations from CA3 to CA1 hippocampal region (előkészülőben).

20. Holderith N, Németh B, Veres J, Nagy GA, Szabó GG, Hájos N. Impairment of gamma oscillation by cannabinoids is due to a mutual suppression of excitatory inputs onto CA3 pyramidal cells and fast spiking interneurons (előkészülőben).

VI/3. Egyéb a doktori fokozat óta megjelelent saját közlemény
Eredeti közlemények:

21. Papp EC, Hájos N**,** Acsády L, Freund TF. Medial septal and median raphe innervation of vasoactive intestinal polypeptide-containing interneurons in the hippocampus. **Neuroscience**. *90:* 369-82. (1999)

22. Katona I, Rancz EA, Acsády L, Ledent C, Mackie K, Hájos N and Freund TF. Distribution of CB1 cannabinoid receptors in the amygdala and their role in the control of GABAergic transmission. **J Neurosci**. *2123:* 9506-9518. (2001)

23. Hájos N, Freund TF. Distinct cannabinoid sensitive receptors regulate hippocampal excitation and inhibition. **Chemistry and Physics of Lipids** *121*:73-82. (2002)

24. Hájos N, Freund TF, Mody I. Comparison of single NMDA receptor channels recorded on hippocampal principal cells and oriens/alveus interneurons projecting to stratum lacunosum-moleculare (O-LM cells). **Acta Biol Hung**. *53:* 465-72. (2002)

25. Gulyás AI, Hájos N, Katona I, Freund TF. Interneurons are the local targets of hippocampal inhibitory cells which project to the medial septum. **Eur J Neurosci**. *17:* 1861-72. (2003)

26. Freund TF, Hájos N. Excitement Reduces Inhibition via Endocannabinoids. **Neuron.** *38:* 362-5. (2003)

27. Bodor AL, Katona I, Nyíri G, Mackie K, Ledent C, Hájos N, Freund TF. Endocannabinoid signaling in rat somatosensory cortex: laminar differences and involvement of specific interneuron types. **J Neurosci.** *25:* 6845-56. (2005)

28. Haller J, Mátyás F, Soproni K, Varga B, Barsy B, Németh B, Mikics E, Freund TF, Hájos N. Correlated species differences in the effects of cannabinoid ligands on anxiety and on GABAergic and glutamatergic synaptic transmission. **Eur. J. Neurosci**. *25:* 2445-56. (2007)

29. Benninger F, Freund TF, Hájos N. Control of excitatory synaptic transmission by capsaicin is unaltered in TRPV(1) vanilloid receptor knockout mice. **Neurochem Int.** *52:* 89-94. (2008)

Könyvfejezet:

Gulyás AI, Hájos N, Borhegyi Zs, Freund TF. Anatomical and physiological properties of hippocampak GABAergic neurons projecting to the medial septum.: La anatomia fina del conocimiento. In: Garcia CL, Olucha-Bordonau FE, Blasco Ibanez JM, Rosello JN, Rupérez CC (szerk.) Citoquimica de los microcircuitos neuronales. Valéncia: Universitat de Valéncia, 2008. pp. 159-180.

VI/4. Publikációs mutatók a tézisek beadásakor:

Eredeti közlemények száma: 36
Összegzett impakt faktor: 218,7
Könyvfejezetek száma: 1
Összes független idézetek száma: 2222

dc_71_10

VII. KÖSZÖNETNYILVÁNÍTÁS

Legelőször szeretném köszönetemet kifejezni tanítómesteremnek, Freund Tamás akadémikusnak, aki a kutatói pályán elindított, vezetett, és azóta is önzetlenül támogatja a kutatómunkámat.

A sejtélettani technikák elsajátítását Módy István professzornak köszönhetem, akinek a laboratóriumában Los Angeleseben tanulhattam, és aki nagy hatással volt a tudományos gondolkodásom kialakítására. A hálózat-idegélettan iránti érdeklődésemet Ole Paulsen professzor keltette fel, aki nagyfokú kritikai érzékével mindig élesen rávilágított a kísérleteink korlátaira.

Szeretnék itt köszönetet mondani Acsády Lászlónak, Gulyás Attilának, Tóth Katalinnak, és Katona Istvánnak, akikkel igazi élmény volt együtt kísérletezni, együtt gondolkodni.

A bemutatott kísérletek többségét a közvetlen tanítványaimmal közösen végeztük, akiknek ezúton is szeretnék köszönetet mondani kimagasló színvonalú munkájukért, név szerint Rancz Edének, Zemankovics Ritának, Németh Beátának, Szabó Gergelynek, Veres Juditnak és Nagy Gergelynek.

A doktori értekezésben tárgyalt munkákban számos hazai és külföldi kollégám vett részt, akiknek hálával tartozom ezért. Nusser Zoltán, Makara Judit, Pálhalmi János, Nyiri Gábor, Holderith Noémi és Káli Szabolcs kollégáimnak az MTA KOKI-ból, illetve Ed Mann-nek és Iris Oren-nek az oxfordi laboratóriumból.

Az értekezésben szereplő eredmények technikai hátterét Iványi Katalin, Lengyel Katalin, Gregori Erzsébet, Simon Emőke, és Goda Győző biztosította.

Végül, de nem utolsósorban szeretném megköszönni szüleimnek, hogy megteremtették a feltételeit annak, hogy a kutatói életpályát választhassam, és szeretetükkel, életbölcsességeikkel mindig támogatták, egyengették a sokszor rögös úton való haladásomat.

dc_71_10

1. számú melléklet

dc_71_10
European Journal of Neuroscience, Vol. 12, pp. 810–818, 2000

Cell type- and synapse-specific variability in synaptic $GABA_A$ receptor occupancy

Norbert Hájos, Zoltan Nusser,[1]* Ede A. Rancz, Tamás F. Freund and Istvan Mody[1]
Institute of Experimental Medicine, Hungarian Academy of Sciences, Budapest, Hungary
[1]Departments of Neurology and Physiology, UCLA School of Medicine, 710 Westwood Plz., Los Angeles, CA 90095-1769, USA

Keywords: benzodiazepines, electrophysiology, mouse, rat, receptor saturation

Abstract

The degree of postsynaptic type A γ-aminobutyric acid receptor ($GABA_A$ receptor) occupancy was investigated by using the benzodiazepine agonist zolpidem. This drug increases the affinity of $GABA_A$ receptors for γ-aminobutyric acid (GABA) at room temperature (Perrais & Ropert, 1999, *J. Neurosci.*, **19**, 578) leading to an enhancement of synaptic current amplitudes if receptors are not fully occupied by the released transmitter. We recorded miniature inhibitory postsynaptic currents (mIPSCs) from eight different cell types in three brain regions of rats and mice. Receptors in every cell type were benzodiazepine sensitive, as 10–20 μM zolpidem prolonged the decays of mIPSCs (151–184% of control). The amplitude of the $GABA_A$ receptor-mediated events was significantly enhanced in dentate granule cells, CA1 pyramidal cells, hippocampal GABAergic interneurons, cortical layer V pyramidal cells, cortical layer V interneurons, and in cortical layer II/III interneurons. An incomplete postsynaptic $GABA_A$ receptor occupancy is thus predicted in these cells. In contrast, zolpidem induced no significant change in mIPSC amplitudes recorded from layer II/III pyramidal cells, suggesting full $GABA_A$ receptor occupancy. Moreover, different degrees of receptor occupancy could be found at distinct GABAergic synapses on a given cell. For example, of the two distinct populations of zolpidem-sensitive mIPSCs recorded in olfactory bulb granule cells, the amplitude of only one type was significantly enhanced by the drug. Thus, at synapses that generate mIPSCs, postsynaptic receptor occupancy is cell type and synapse specific, reflecting local differences in the number of receptors or in the transmitter concentration in the synaptic cleft.

Introduction

A packet of neurotransmitter released from a presynaptic terminal evokes variable responses in a postsynaptic cell. The trial-to-trial variability in the postsynaptic response at a single release site mainly originates from the stochastic behaviour of the channels if postsynaptic receptors are fully occupied by the released transmitter (Faber *et al*., 1992) or from variations in the concentration of neurotransmitter in the synaptic cleft if receptor saturation does not occur (Frerking *et al*., 1995). Thus, a maximal receptor occupancy, i.e. receptor saturation, will result in a lower coefficient of variation (CV) of the postsynaptic responses. Indeed, a low CV was shown for inhibitory postsynaptic potentials or currents (IPSPs or IPSCs) evoked with focal stimulation in principal cells of the hippocampal formation (Edwards *et al*., 1990; Ropert *et al*., 1990; Nusser *et al*., 1998). Considering the high maximal open probability of type A γ-aminobutyric acid ($GABA_A$) receptors ($P_{o,max} = 0.6–0.8$; Jones & Westbrook, 1995; Auger & Marty, 1997; Perrais & Ropert, 1999), saturation of $GABA_A$ receptors by released γ-aminobutyric acid (GABA) was inferred at these synapses. The effect of benzodiazepines on miniature inhibitory postsynaptic currents (IPSCs), events that occur spontaneously in an action potential-independent manner, also supported this conclusion. After application of benzodiazepine agonists, modulators of $GABA_A$ receptors were thought to increase receptor affinity (Macdonald & Olsen, 1994; Lavoie & Twyman, 1996; Mellor & Randall, 1997; Perrais & Ropert, 1999), the decays of mIPSCs were prolonged with no change in their amplitude at physiological temperature (Otis & Mody, 1992; Soltesz & Mody, 1994; Poisbeau *et al*., 1997). However, the degree of receptor occupancy and the use of benzodiazepines for determining postsynaptic $GABA_A$ receptor occupancy remained controversial. Using rapid agonist applications to outside-out patches and recording the effect of benzodiazepines on mIPSCs at room temperature, an incomplete $GABA_A$ receptor occupancy was suggested in various preparations (Frerking *et al*., 1995; Galarreta & Hestrin, 1997; Defazio & Hablitz, 1998). In addition, two studies suggested that postsynaptic $GABA_A$ receptor occupancy may vary within a single cell and that the occupancy of the receptors is inversely related to the initial size of the synaptic current (Auger & Marty, 1997; Nusser *et al*., 1997). A recent study (Perrais & Ropert, 1999) using fast application of GABA to outside-out patches, has demonstrated that at room temperature the benzodiazepine agonist zolpidem (1–10 μM) increased the amplitude of currents elicited by subsaturating concentrations of GABA (100–300 μM), but not by saturating GABA concentrations (10 mM). The increase in amplitude was a direct consequence of the change in the number of $GABA_A$ receptors that bind GABA without changing the single channel conductance or the maximal open probability of the receptors. Using zolpidem at room temperature, Perrais & Ropert (1999) demonstrated that $GABA_A$ receptors are not saturated by the synaptically released GABA in rat layer V pyramidal cells. They have also shown that

Correspondence: Dr I. Mody, as above.
E-mail: mody@ucla.edu

**Present address*: Institute of Experimental Medicine, Budapest, Hungary

Received 4 August 1999, revised 15 November 1999, accepted 18 November 1999

zolpidem has an anomalous effect at physiological temperatures, making it inadequate as a tool to determine $GABA_A$ receptor occupancy at these temperatures. In light of these results, we have systematically studied the degree of postsynaptic $GABA_A$ receptor occupancy by examining the effect of 10–20 μM zolpidem on mIPSCs recorded from eight different cell types in three brain regions at room temperature.

Materials and methods

Slice preparation

Male mice (15–38 days old, C57/Bl 6) were deeply anaesthetized with either ether or halothane and were decapitated. Male Wistar rats (16–20 days old) were anaesthetized with sodium pentobarbital (70 mg/kg, i.p.) and then decapitated. After opening of the skull, the brain was removed and immersed into ice-cold (~ 4 °C) modified artificial cerebrospinal fluid (ACSF), which contained (in mM): NaCl, 126; KCl, 2.5; $NaHCO_3$, 26; $CaCl_2$, 0.5; $MgCl_2$, 5; NaH_2PO_4, 1.25; glucose, 10. Coronal slices of the hippocampus and primary visual cortex, and sagittal slices of the main olfactory bulb (300–350 μm in thickness) were prepared using a Lancer Series 1000 Vibratome. The slices were incubated in ACSF [containing (in mM): NaCl, 126; KCl, 2.5; $NaHCO_3$, 26; $CaCl_2$, 2; $MgCl_2$, 2; NaH_2PO_4, 1.25; glucose, 10] for 30 min at 32 °C, followed by incubation at room temperature (22–23 °C).

Whole-cell recordings and data analysis

Whole-cell voltage-clamp recordings were obtained from neurons visualized using infrared DIC (Zeiss, Axioscope) videomicroscopy. Cell types in the hippocampus and neocortex were identified based on the location of their soma and their morphology (shape of the soma and the origin of the primary dendrites). The identity of the cells was *post hoc* confirmed after the development of biocytin. Patch electrodes were pulled from borosilicate glass capillaries with an inner filament (KG-33, 1.5 mm O.D.; Garner Glass, Claremont, CA) using either a two-stage vertical Narashige PP-83 or a Sutter P-87 puller, and had resistances of 2–8 MΩ when filled with the intracellular solution. Intracellular solution was prepared from Omnisolve water (EM Science, Gibbstown, NJ, USA) and contained (in mM): CsCl, 140; NaCl, 4; HEPES, 10; $MgCl_2$, 1; Mg-ATP, 2; EGTA, 0.05 at pH 7.2–7.3 adjusted with CsOH. In some cases, 0.3–0.5% biocytin (Molecular Probes) was added to the solution. The final osmolarity was 285–300 mOsm.

During experiments, slices were superfused continuously with oxygenated (95% O_2 : 5% CO_2) ACSF containing 2–5 mM kynurenic acid (Sigma) and 0.5–1 μM tetrodotoxin (TTX, Alomone Labs) to block ionotropic glutamate receptors and voltage-gated sodium channels, respectively. All experiments were performed at room temperature (22–23 °C). Recordings were made with an Axopatch 200B amplifier (Axon Instruments), digitized at 88 kHz (Neurocorder, NeuroData, New York) and stored on videotape, or digitized at 44 kHz and stored on a DAT recorder (DTR-1202, Biologic, Claix, France). The data were filtered at 2 kHz (eight-pole Bessel, Frequency Devices 902 or FLA-01, Cygnus Technology, Fredericton, Canada), digitized at 5–20 kHz (National Instruments LabPC+A/D or PCI-MIO-16E-4 board), and were analysed using either the Strathclyde Electrophysiology Software (courtesy of Dr J. Dempster) or an in-house software written in LabView (National Instruments, Austin, TX, USA). The threshold for event detection was set to two to three times the signal-to-noise-ratio, where the noise (3–4 pA) was the standard deviation of the baseline recorded before the events. Series resistance and whole-cell capacitance were estimated by correcting the fast current transients evoked at the onset and offset of 8 ms 5 mV voltage-command steps, and were checked every 2 min during the recording. If the series resistance increased by more than 25%, the recording was discontinued.

Amplitudes, 10–90% rise times, 50% or 67% decay times, inter-event intervals were measured for each IPSC. The decays of the averaged currents were fitted with a single or the sum of two exponential functions. A weighted decay time constant (τ_w) was calculated as $\tau_w = \tau_1 \times A_1 + \tau_2 \times (1 - A_1)$, where τ_1 and τ_2 are the time constants of the first and second exponential functions, respectively, and A_1 is the proportion of the first exponential function contributing to the amplitude of the IPSC. The Kolmogorov–Smirnov (K–S) test was used to compare two cumulative distributions, and Student's paired *t*-test was used to compare the changes in the mean conductance, rise time, decay time and frequency after zolpidem application. Data are presented as mean ± SEM.

Anatomical identification of neurons

After the recordings, slices were fixed overnight in 4% paraformaldehyde, 0.05% glutaraldehyde and 15% picric acid in 0.1 M phosphate buffer (PB, pH 7.4). The slices were then incubated in cryoprotecting solution (0.1 M PB containing 12% glycerol and 25% sucrose) for 1 h, freeze-thawed once in liquid nitrogen, and treated with 0.5% H_2O_2 in 0.1 M PB for 30 min to reduce endogenous peroxidase activity. Recorded neurons were visualized using avidin–biotinylated horseradish peroxidase complex reaction (ABC, Vector, Burlingame, CA, USA) with nickel-intensified 3,3′-diaminobenzidine (Sigma) as chromogen (dark blue reaction product). The slices were then re-sectioned at 80 μm thickness with a Vibratome, followed by dehydration and embedding in Durcupan.

Reagents

Bicuculline methiodide (Sigma) was applied by bath perfusion in final concentrations of 10 and 30 μM. Zolpidem (Tocris) was either dissolved in ethanol (100 mM stock solution) or polyethylene glycol (20 mM stock solution), and was diluted to the final concentration of 10 or 20 μM.

Results

In the presence of kynurenic acid (2–5 mM) and TTX (0.5 or 1 μM), spontaneously occurring inward currents were observed at holding potentials ranging between –60 and –70 mV using high Cl^--containing intracellular solution in eight different cell types of three distinct brain areas of mice ($n = 48$, P15–36) and from hippocampal CA1 pyramidal cells and CA1 GABAergic interneurons of young rats ($n = 12$, P16–20). Recorded currents were completely blocked by the $GABA_A$ receptor antagonist bicuculline methiodide (10–30 μM, data not shown), indicating that the TTX-resistant synaptic currents (mIPSCs) were mediated by $GABA_A$ receptors. The frequency of mIPSCs varied between different cell types and had a range of 0.4–5.4 Hz.

$GABA_A$ receptor occupancy in the hippocampus and dentate gyrus

We first addressed possible differences between the properties of mIPSCs in rat and mouse neurons in the hippocampal CA1 area. Two representative CA1 pyramidal cells are shown in Fig. 1. There were no significant differences in the frequency, peak conductance and weighted decay time of mIPSCs recorded in CA1 pyramidal cells between the two species ($P > 0.05$, Mann–Whitney *U*-test). In

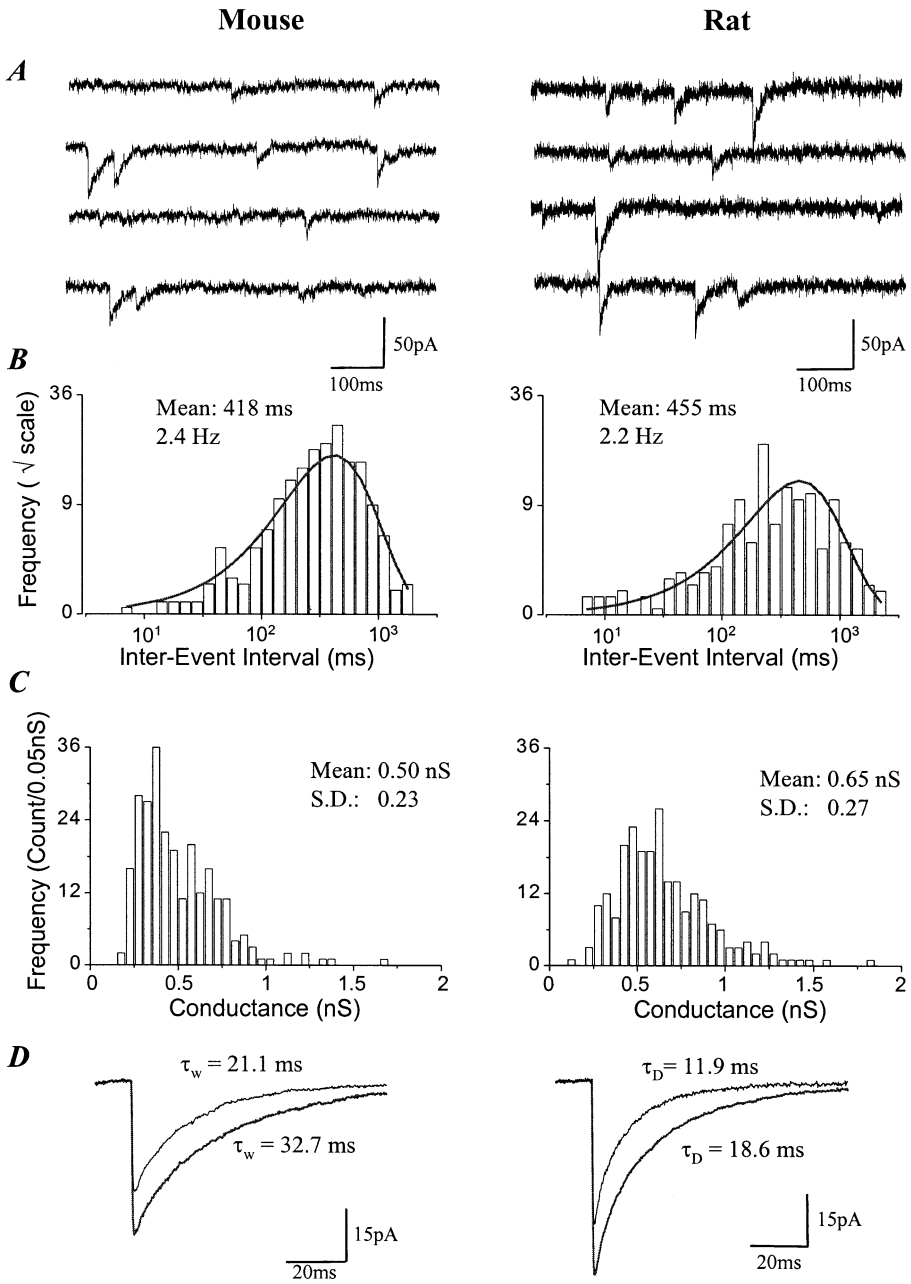

FIG. 1. Comparison of mIPSCs recorded at room temperature from CA1 mouse (P35) and rat (P18) hippocampal pyramidal cells. (A) Whole-cell patch-clamp recordings from CA1 pyramidal cells held at –65 mV in the presence of 2 mM kynurenic acid and 0.5 μM TTX. Miniature IPSCs are inward currents as the intracellular solution contained 135 mM CsCl. (B) Log-binned (10 bins per decade) inter-event intervals are plotted on a square root ordinate and illustrate similar mIPSC frequencies in pyramidal cells of mouse and rat. The fitted lines represent exponential probability density functions with means of 418 and 455 ms, corresponding to an average mIPSC frequency of 2.4 and 2.2 Hz, respectively. (C) In both neurons, the distributions of mIPSC conductances are skewed toward large values and have similar means and standard deviations ($n = 252$ in mouse and $n = 238$ in rat, respectively). (D) The decay time constant of averaged mIPSCs is faster in rats than in mice. In the mouse, the decay of the averaged mIPSC is best described by the sum of two exponentials [$\tau_1 = 10.7$ ms (36%), $\tau_2 = 26.9$ ms, $\tau_W = 21.1$ ms], whereas in the rat neuron it is adequately described by a single exponential function ($\tau_D = 11.9$ ms). Application of 10 μM zolpidem (thick traces) increased the amplitude (by 35 and 31% in mouse and rat, respectively) and the duration (by 55 and 56%) of the synaptic currents to a similar extent in both species.

contrast to pyramidal cells, the decay time course of mIPSCs in interneurons was significantly ($P < 0.05$, Mann–Whitney *U*-test) faster (rat, $\tau_w = 10.9 \pm 1.2$ ms, $n = 7$; mouse, $\tau_w = 19.6 \pm 2.6$ ms, $n = 5$), and the peak conductance was larger in rats than in mice (rat, 668 ± 49 pS; mouse, 510 ± 32 pS). Despite the differences in the amplitude and the decay kinetics of synaptic currents in CA1 interneurons, the effect of zolpidem was indistinguishable between the different species both in interneurons and in CA1 pyramidal cells (see below). Therefore, in the remaining cell types, postsynaptic $GABA_A$ receptor occupancy was only examined in mouse neurons.

Bath application of zolpidem (10 μM) significantly increased both the peak conductance (39 ± 11%, $P < 0.001$, *t*-test) and the decay time constant (52 ± 9%, $P < 0.001$) of mIPSCs recorded in mouse CA1 pyramidal cells (Fig. 1 and Table 1). A similar change in mIPSC amplitudes and kinetics was detected in rat neurons of the same type; a 35 ± 6% increase in the conductance and 73 ± 7% prolongation of the decay was observed ($P < 0.001$, Fig. 1D).

Hippocampal CA1 interneuron types were identified after the development of the biocytin labelling and comprised striatum oriens-lacunosum-molecurare cells ($n = 3$), horizontal and radial trilaminar cells ($n = 4$), or interneurons projecting to strata radiatum and lacunosum-moleculare ($n = 2$, Freund & Buzsáki, 1996; Hájos & Mody, 1997). As each interneuron type comprised a relatively small number of cells, we pooled all the interneurons for the description of the zolpidem effect on mIPSCs in these cells. Much like in principal cells, 10 μM zolpidem significantly ($P < 0.001$, Table 1) enhanced both the amplitude and decay of mIPSCs in mice (42 ± 4% and 61 ± 5%, respectively) and in rats (40 ± 5% and 84 ± 10%, respectively). In contrast to principal cells, however, the shift to the right of the cumulative distributions of mIPSC conductances was not always parallel (data not shown). In three out of five mouse interneurons, 20–40% of the events, in particular those with small amplitudes, showed no increase in their amplitudes following zolpidem application, but the prolongation of the decay of these

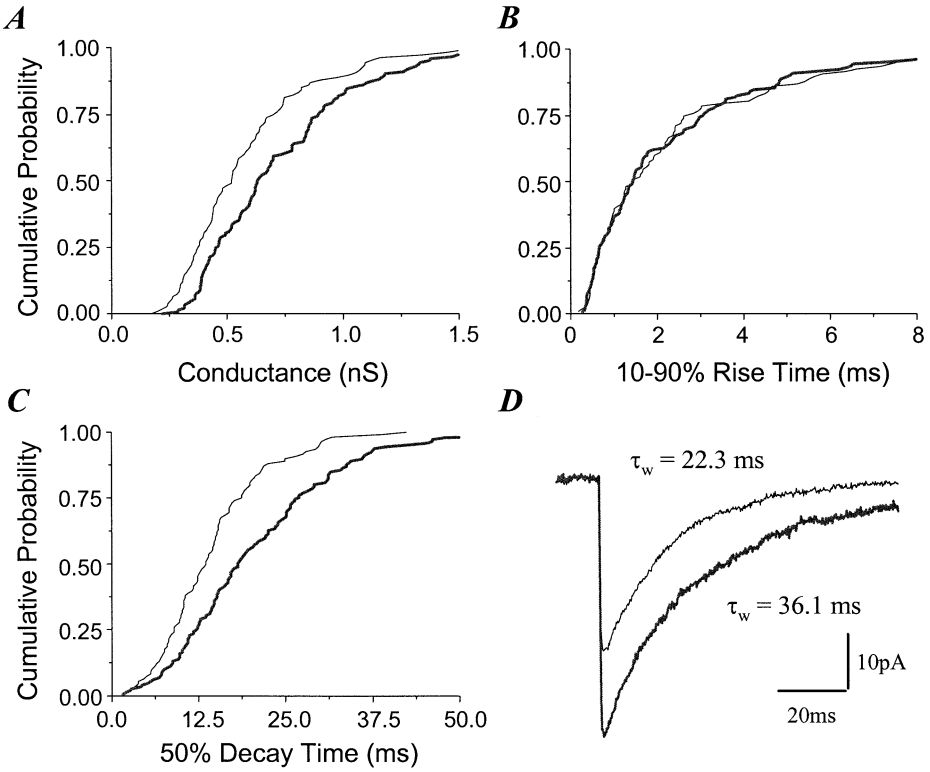

FIG. 2. Effects of 10 μM zolpidem on mIPSC properties recorded in a mouse dentate granule cell. Cumulative probability plots of mIPSC conductances (A), 10–90% rise times (B) and 50% decay times (C) before (thin lines) and after (thick lines) the application of zolpidem. The distributions of mIPSC conductances and 50% decay times in zolpidem are significantly different from those in the control (K–S test; $P < 0.001$), but no significant change was observed in the rise time distributions (K–S test, $P > 0.05$). (D) Averaged current waveforms in control (thin trace) and 10 μM zolpidem (thick trace) show that zolpidem increased both the peak amplitude and the decay time course of the synaptic currents. The decay phase of averaged mIPSCs can be well described by the sum of two exponential functions in the control [$\tau_1 = 16.5$ ms (74%), $\tau_2 = 38.8$ ms, $\tau_W = 22.3$ ms] and in zolpidem [$\tau_1 = 13.9$ ms (36%), $\tau_2 = 48.6$ ms, $\tau_W = 36.1$ ms].

mIPSCs was similar to that seen for events displaying a large amplitude enhancement (> 40%). These three cells did not belong to a single anatomical category of interneurons. A similar enhancement of mIPSC amplitudes has recently been described in cerebellar molecular layer interneurons (Nusser *et al*., 1997). Accordingly, a different degree of $GABA_A$ receptor occupancy is predicted at distinct synapses of some hippocampal interneurons. More detailed investigations will be necessary to identify the precise origin of the distinct IPSCs.

Several previous studies examined the effect of zolpidem on mIPSCs of dentate granule cells at physiological temperature (33–36 °C) and reported the prolongation of decay times without a change in the amplitudes of the events (De Koninck & Mody, 1994; Hollrigel & Soltesz, 1997). However, as zolpidem should only be used to probe $GABA_A$ receptor occupancy at room temperature (Perrais & Ropert, 1999), we have re-examined its effect on mIPSCs in mouse dentate granule cells at room temperature. As shown in Fig. 2, mIPSC conductances (mIPSGs) as well as their durations were significantly increased, as indicated by a rightward shift of the cumulative distributions. The 10–90% rise times of mIPSCs remained constant (Fig. 2B). The significant enhancement of mIPSC amplitudes ($41 \pm 9\%$, $P < 0.001$) is consistent with an incomplete occupancy of the receptors in principal cells of the hippocampal formation.

Enhancement of mIPSC amplitudes by zolpidem is cell type specific in the neocortex

As previously shown, zolpidem increased the amplitude of mIPSCs in layer V pyramidal cells of young rats (Perrais & Ropert, 1999). We have confirmed this result in layer V pyramidal cells of mice. Following the application of zolpidem, the conductance of the synaptic currents increased from 581 ± 51 to 735 ± 74 pS, and their duration was also prolonged from 14.3 ± 1.9 to 23.9 ± 2.6 ms ($P < 0.001$, Table 1), an effect similar to that seen in layer V pyramidal cells of rats (Perrais & Ropert, 1999). Recordings were also obtained from GABAergic interneurons located in layer V of the neocortex. As the anatomical identification of cortical interneuron types was not performed for every cell, we pooled the layer V interneurons and presented the effects of zolpidem on the whole population. Compared with the effect of zolpidem on mIPSCs in layer V pyramidal cells, the mIPSG increase was somewhat larger ($38 \pm 3\%$ versus $26 \pm 4\%$), but the decay was less prolonged ($51 \pm 9\%$ versus $69 \pm 9\%$) in layer V interneurons.

To investigate whether zolpidem has a similar effect on mIPSCs recorded from neurons in supragranular layers, we obtained whole-cell voltage-clamp recordings from pyramidal cells and GABAergic interneurons in layer II/III. Application of 10–20 μM zolpidem had no significant effect on the peak conductance of the synaptic events recorded in layer II/III pyramidal cells ($102 \pm 4\%$ of control, $P > 0.4$). However, $GABA_A$ receptors underlying mIPSCs in layer II/III pyramidal cells were benzodiazepine sensitive, as 10–20 μM zolpidem significantly prolonged their decay kinetics ($56 \pm 6\%$, $P < 0.001$, Fig. 3). Figure 3 shows a representative cell. As seen on the cumulative distributions, zolpidem failed to change the conductance and 10–90% rise time of the events (K–S test, $P > 0.05$, Fig. 3A and B), but significantly prolonged their duration (K–S test, $P < 0.001$, Fig. 3C). In contrast to pyramidal cells in layer II/III, interneurons in the same layers responded to the administration of zolpidem by an increase in mIPSG and by the prolongation of the decay time ($22 \pm 3\%$ and $67 \pm 17\%$, respectively, $P < 0.001$, Table 1). Our results demonstrate that in most cell types of the neocortex, postsynaptic $GABA_A$ receptors are not fully occupied by the synaptically released GABA, similar to most cells of the hippocampus. However, postsynaptic $GABA_A$ receptor saturation does occur in some cell types (e.g. layer II/III pyramidal cells), consistent with a cell type-specific variation in the degree of occupancy.

Different degrees of receptor occupancy at GABAergic synapses of olfactory bulb granule cells

In olfactory bulb granule cells, the 10–90% rise times of mIPSCs have a bimodal distribution with a modal separation at ~ 1 ms,

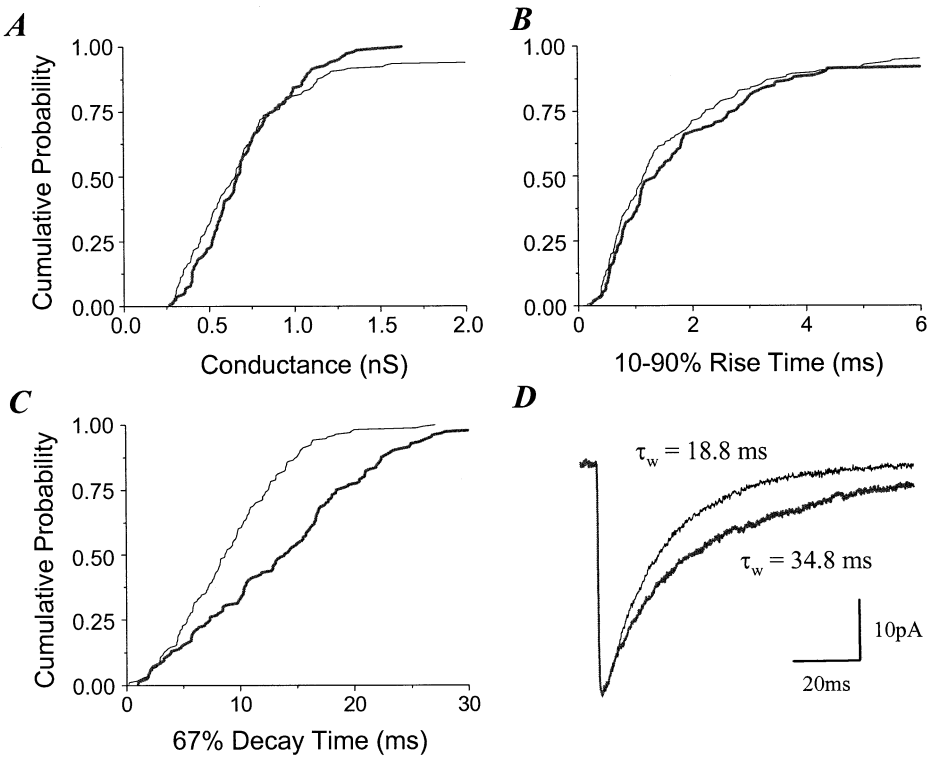

FIG. 3. Zolpidem increases the duration but not the peak conductance of mIPSCs in a mouse layer II/III pyramidal cell. Cumulative distributions of mIPSC conductances (A), 10–90% rise times (B) and 67% decay times (C) in control (thin lines) and in the presence of 20 μM zolpidem (thick lines). The distributions of mIPSC conductances and 10–90% rise times in zolpidem are not significantly different from those in the control (K–S test, $P > 0.05$). Zolpidem, however, significantly increased the decay time of mIPSCs, as indicated by a shift to the right on the cumulative distributions (K–S test, $P < 0.001$). (D) Superimposed averaged mIPSCs before (thin trace) and after the application of zolpidem (thick trace) demonstrate no change in the peak amplitude of the synaptic currents. In both cases, the decay was best fitted with the sum of two exponentials [control, $\tau_1 = 11.7$ ms (43%), $\tau_2 = 24.2$ ms, $\tau_W = 18.8$ ms; zolpidem, $\tau_1 = 10.8$ ms (37%), $\tau_2 = 49$ ms, $\tau_W = 34.9$ ms].

suggesting two distinct populations of events (Nusser *et al.*, 1999). Miniature IPSCs with 10–90% rise times faster than 1 ms ($mIPSC_{FR}$, 0.63 ± 0.07 ms) have three times faster rise times and almost twofold larger peak conductances (Table 1) than those with rise times slower than 1 ms ($mIPSC_{SR}$, 2.1 ± 0.35 ms). However, the weighted decay time constant of the slow rising mIPSCs ($\tau_w = 42.9 \pm 4.6$ ms) was similar to that of the $mIPSC_{FR}$ ($\tau_w = 45.9 \pm 6.5$ ms), indicating that dendritic filtering alone cannot be responsible for the differences between $mIPSC_{FR}$ and $mIPSC_{SR}$. The two types of event must have different kinetics at their site of generation, consistent with the possibility of originating from two functionally distinct types of synapses.

To examine whether postsynaptic $GABA_A$ receptor occupancy is similar at synapses generating these two types of synaptic current, we examined the effect of zolpidem (10–20 μM) on mIPSCs recorded from olfactory bulb granule cells at room temperature. $GABA_A$ receptors at synapses generating both $mIPSC_{FR}$ and $mIPSC_{SR}$ showed benzodiazepine sensitivity, as the decay of the synaptic currents was significantly prolonged after the bath application of zolpidem ($61 \pm 5\%$ and $76 \pm 16\%$, respectively, Fig. 4 and Table 1). In contrast, zolpidem significantly ($P < 0.02$) increased the amplitude of only the fast rising currents ($117 \pm 4\%$ of control, Fig. 4 and Table 1), but not that of the $mIPSC_{SR}$ ($102 \pm 4\%$ of control, Fig. 4 and Table 1). This result shows that the postsynaptic receptor occupancy could vary at different synapses on a given cell, in agreement with the result of previous studies in cerebellar neurons (Auger & Marty, 1997; Nusser *et al.*, 1997).

Discussion

Cell type-dependent variability in postsynaptic $GABA_A$ receptor occupancy

The effect of 10–20 μM zolpidem on the peak amplitude of mIPSCs was cell type specific, regardless of the subunit composition of the receptors. Zolpidem displaces Ro15-1788 from α1β3γ2, α2β3γ2, α3β3γ2 and α5β3γ2 $GABA_A$ receptors with K_i values of 20, 450, 400 and 15 000 nM, respectively (Pritchett & Seeburg, 1990), but we eliminated the impact of various subunits on zolpidem affinity by using 10–20 μM zolpidem, which should exert a similar effect on most BZ-sensitive $GABA_A$ receptor assemblies. Consequently, zolpidem increased the duration of all mIPSCs to a similar extent in every cell type studied. Thus, the cell type- and synapse-specific modulation of mIPSC peak conductances by zolpidem should reflect a varying degree of occupancy rather than differences in the zolpidem sensitivity of $GABA_A$ receptors. If 10–20 μM zolpidem increases postsynaptic receptor occupancy to near 1.0 following the synaptic release of GABA, the initial occupancy must vary between 0.7 and 0.8 at synapses with incomplete occupancy, and should be ~1.0 in layer II/III pyramidal cells. With a maximal open probability ($P_{o,max}$; as defined by Silver *et al.*, 1996) of $GABA_A$ receptors of 0.6–0.8 (Jones & Westbrook, 1997; Perrais & Ropert, 1999), the lower limit of the open probability ($P_o = P_{o,max} \times$ occupancy) is 0.42 and the upper limit is 0.8. If 10–20 μM zolpidem did not cause full occupancy, the lower limit of $P_o = 0.42$ is obviously an overestimate. As neither $P_{o,max}$ nor $GABA_A$ receptor occupancy depends on temperature (Perrais & Ropert, 1999), the values obtained at room temperature should hold true at physiological temperatures as well.

Occupancy is mainly determined by the postsynaptic target cell

Postsynaptic $GABA_A$ receptor saturation (full occupancy) occurs at synapses generating mIPSCs in layer II/III pyramidal neurons. In other cells of the same cortical layer, i.e. in GABAergic interneurons, the miniature inhibitory postsynaptic conductances (mIPSG) were enhanced by zolpidem, consistent with an incomplete occupancy. Yet, both pyramidal cells and interneurons of this layer are likely to be innervated by the same local inhibitory cells (Somogyi *et al.*, 1983; Kisvarday *et al.*, 1993; Thomson *et al.*, 1996; Tamas *et al.*, 1997,

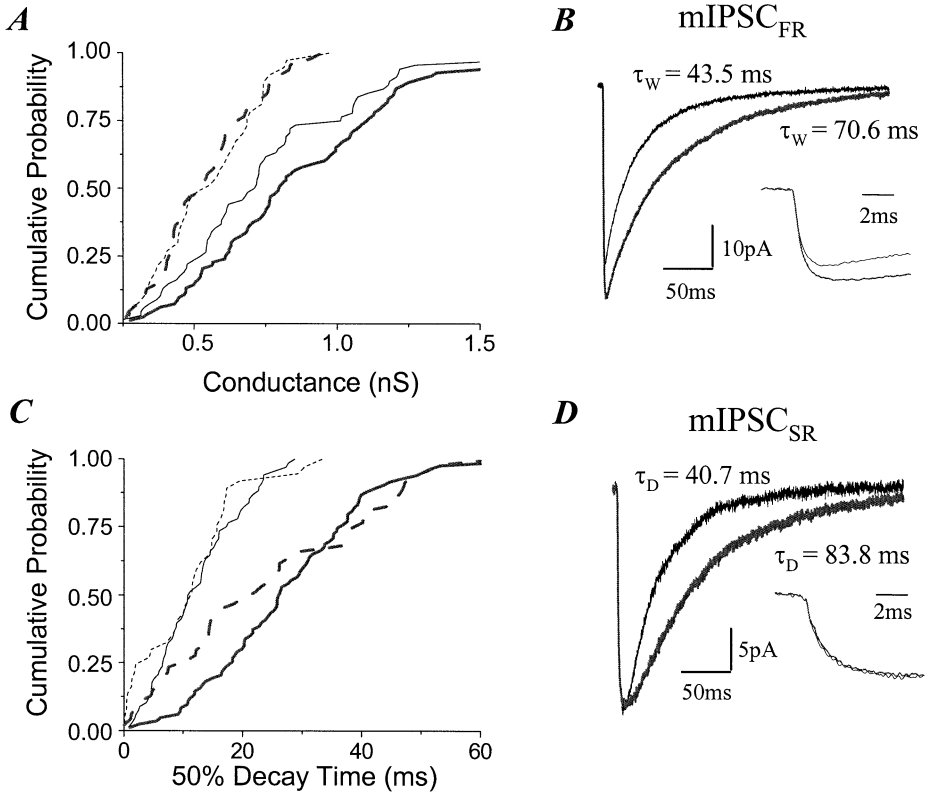

FIG. 4. The effect of zolpidem on mIPSCs is synapse specific in olfactory bulb granule cells. Miniature synaptic currents are grouped according to their rise times. mIPSCs with less than 1 ms 10–90% rise time comprise the fast rising currents ($mIPSC_{FR}$) while slow rising mIPSCs ($mIPSC_{SR}$) include those with slower rise times. (A) Cumulative distributions of mIPSC conductances demonstrate that the peak conductance of the $mIPSC_{SR}$ (thin dotted line in control) did not change significantly ($P > 0.1$, K–S test) after zolpidem application (thick dashed line), but that of $mIPSC_{FR}$ is increased (control, thin line; zolpidem, thick line; $P < 0.1$, K–S test). (B) Superimposed averaged $mIPSC_{FR}$ in control and in 10 μM zolpidem show that zolpidem increased both the peak amplitude and the decay time course of the synaptic currents. The decay phase of averaged $mIPSC_{FR}$ is best described by the sum of two exponential functions both in control [$\tau_1 = 26.7$ ms (79%), $\tau_2 = 106$ ms, $\tau_W = 43.5$ ms] and zolpidem [$\tau_1 = 35.8$ ms (45%), $\tau_2 = 107$ ms, $\tau_W = 70.6$ ms]. (C) Cumulative probability plots of the 50% decay times of $mIPSC_{FR}$ and $mIPSC_{SR}$ demonstrate an increase in the decay time of both slow and fast rising mIPSCs after zolpidem application (control $mIPSC_{SR}$, thin dotted line; control $mIPSC_{FR}$, thin line; zolpidem $mIPSC_{SR}$, thick dashed line; zolpidem $mIPSC_{FR}$, thick line). (D) Averaged slow rising mIPSCs show that only the decay time course of these events is prolonged by zolpidem without effecting the peak amplitude. The decay of the slow rising synaptic currents is well described by a single exponential function with time constants of 40.7 ms in control and 83.8 ms in zolpidem. (B and D) Insets show the rising phase of the synaptic currents on an expanded time scale.

TABLE 1. Effect of 10–20 μM zolpidem on mIPSCs recorded in eight different cell types of three brain regions of mice and rats

				Conductance (pS)			CV			τ_w (ms)		
Cell type	*n*	Age (days)	Species	Control	Zolpidem	Z/C ratio (%)	Control	Zolpidem	Z/C ratio (%)	Control	Zolpidem	Z/C ratio (%)
Olfactory GC $IPSC_{FR}$	5	20.4 ± 1.3	Mouse	1018 ± 189	1176 ± 4	117 ± 4*	0.51 ± 0.03	0.47 ± 0.02	93 ± 7	45.9 ± 6.5	74.4 ± 11.1	161 ± 5*
Olfactory GC $IPSC_{SR}$	5	20.4 ± 1.3	Mouse	577 ± 83	595 ± 95	102 ± 4	0.39 ± 0.03	0.49 ± 0.07	126 ± 21	42.9 ± 4.6	76.9 ± 12.3	176 ± 16*
Layer II/III PC	8	21.4 ± 3.3	Mouse	606 ± 58	606 ± 46	102 ± 4	0.42 ± 0.03	0.42 ± 0.02	101 ± 6	21.2 ± 1.4	32.9 ± 2.1	156 ± 6*
Layer II/III IN	6	32.4 ± 0.7	Mouse	513 ± 92	633 ± 127	122 ± 3*	0.45 ± 0.04	0.5 ± 0.04	114 ± 5	19.6 ± 2.4	33.3 ± 5.6	167 ± 17*
Layer V PC	6	24.2 ± 3.0	Mouse	581 ± 51	735 ± 74	126 ± 4*	0.44 ± 0.04	0.47 ± 0.03	110 ± 7	14.3 ± 1.9	23.0 ± 2.6	169 ± 9*
Layer V IN	6	37.7 ± 0.8	Mouse	566 ± 41	779 ± 48	138 ± 3*	0.52 ± 0.03	0.54 ± 0.04	104 ± 3	17.0 ± 2.0	25.6 ± 3.0	151 ± 9*
Dentate GC	6	29.7 ± 2.8	Mouse	499 ± 34	691 ± 32	141 ± 9*	0.48 ± 0.03	0.55 ± 0.05	114 ± 10	20.3 ± 1.5	33.2 ± 3.0	163 ± 6*
CA1 PC	6	33.7 ± 2.6	Mouse	508 ± 31	693 ± 19	139 ± 11*	0.45 ± 0.01	0.48 ± 0.01	107 ± 4	20.1 ± 1.7	29.9 ± 1.3	152 ± 9*
CA1 IN	5	24.4 ± 1.1	Mouse	510 ± 32	719 ± 34	142 ± 4*	0.5 ± 0.04	0.6 ± 0.05	120 ± 6	19.6 ± 2.6	31.2 ± 4.1	161 ± 5*
CA1 PC	5	17.6 ± 0.2	Rat	614 ± 35	834 ± 78	135 ± 6*	0.42 ± 0.02	0.47 ± 0.02	112 ± 6	17.8 ± 1.8	30.6 ± 2.9	173 ± 7*
CA1 IN	7	17.8 ± 0.3	Rat	668 ± 49	940 ± 79	140 ± 5*	0.5 ± 0.01	0.54 ± 0.03	109 ± 4	10.9 ± 1.2	19.9 ± 2.1	184 ± 10*

Conductance values are obtained as the mean of the mIPSC conductance distributions. The coefficient of variation (CV) is calculated by dividing the SD of the mIPSC conductance distribution with its mean. The weighted decay time constant (τ_w) is calculated as the weighted average of the time constants of fast and slow exponential components fitted to the averaged synaptic currents. Data are given as mean ± SEM. *n* indicates the number of recorded cells. The ratio Z/C (%) denotes the mean ± SEM of the corresponding parameters in zolpidem relative to the control values. The age of the animals is given in days. Olfactory GC, granule cells of the olfactory bulb; PC, pyramidal cell; IN, interneuron; dentate GC, granule cell of the dentate gyrus.

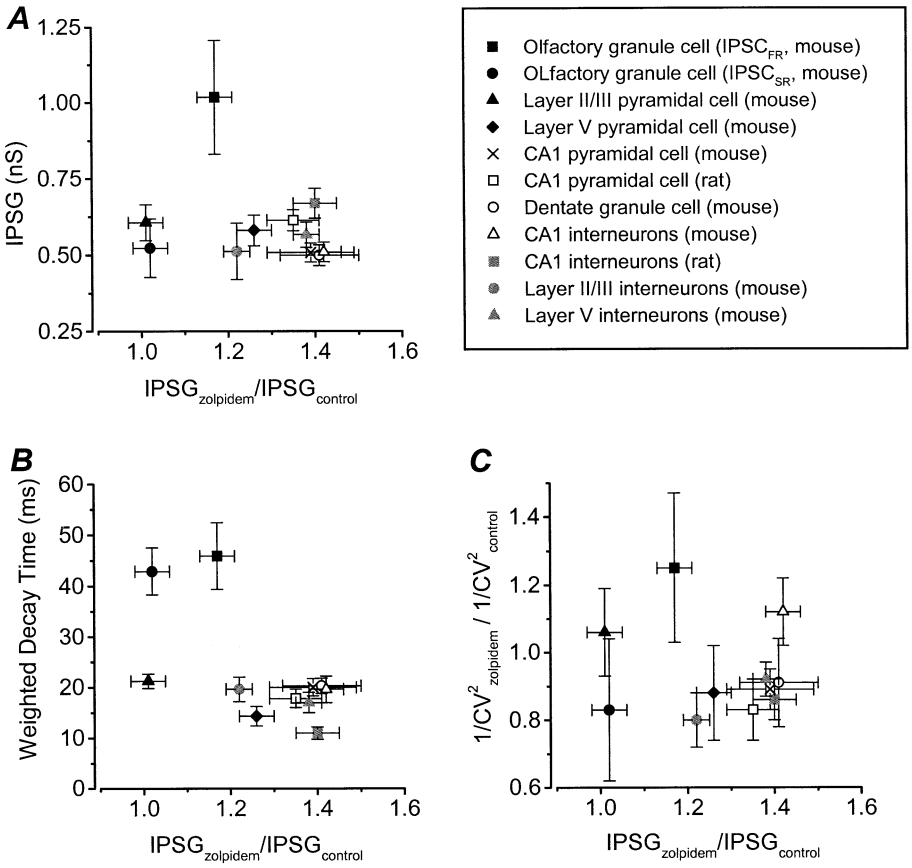

FIG. 5. The degree of synaptic $GABA_A$ receptor occupancy shows no significant correlation with mIPSC conductances (A) or decay times (B) in different cell types. The $mIPSG_{zolpidem}$: $mIPSG_{control}$ ratio indicates the degree of occupancy under control conditions, such that a larger ratio corresponds to a smaller postsynaptic receptor occupancy. (C) The $1/CV^2_{zolpidem}$: $1/CV^2_{control}$ ratio is a measure of the change in the variability of the peak amplitudes after zolpidem application. This ratio is independent of the initial occupancy of the postsynaptic receptors, suggesting that the main variability in the peak amplitude does not originate from the variation of the transmitter concentration in the cleft.

1998). Thus, $GABA_A$ receptor occupancy appears to be predominantly determined by the identity of the postsynaptic target cell. In most cell types, zolpidem increased the peak conductance of mIPSCs, indicating an incomplete postsynaptic receptor occupancy (Frerking *et al*., 1995; Defazio & Hablitz, 1998; Perrais & Ropert, 1999). The parallel shift in the cumulative mIPSG distributions caused by zolpidem in most cells indicates a similar degree of receptor occupancy at all synapses responsible for generating mIPSCs, and is also consistent with receptor occupancy being controlled by some postsynaptic mechanism. In dentate granule cells mIPSCs originate from perisomatic synapses (Soltesz *et al*., 1995), and at least three interneuron types form synapses in this region (Freund & Buzsáki, 1996) having $GABA_A$ receptors with different subunit compositions depending on the identity of the presynaptic neuron (Nusser *et al*., 1996). Yet, according to the parallel shift in mIPSG distributions in zolpidem, at each mIPSC-generating synapse receptors have a similar degree of occupancy regardless of the origin of the presynaptic terminals.

In most cells the degree of occupancy seems to be determined by the postsynaptic target cell, but a synapse-specific variation in the occupancy within a single cell might mean that in such cells other (e.g. presynaptic) factors also contribute to the control of postsynaptic receptor occupancy. Two previous studies have suggested that at distinct synapses of a single cell (cerebellar stellate cells), postsynaptic $GABA_A$ receptor occupancy could vary (Auger & Marty, 1997; Nusser *et al*., 1997). In three out of five GABAergic interneurons of the hippocampal CA1 area, zolpidem caused a non-parallel shift in the cumulative distribution of mIPSGs. Furthermore, of the two distinct populations of zolpidem-sensitive mIPSCs recorded in olfactory bulb granule cells, the drug significantly enhanced the amplitude of only one type of event ($mIPSC_{FR}$).

Variation in postsynaptic $GABA_A$ receptor occupancy is not solely the consequence of variation in the number of postsynaptic receptors

The following three possibilities can be envisaged to explain differences between synapses with complete versus incomplete receptor occupancy: (i) different numbers of receptors are present at synapses of distinct sizes; (ii) synapses contain $GABA_A$ receptors with distinct GABA affinities; and (iii) different concentrations of GABA are released into the synaptic cleft.

In cerebellar stellate cells, the P_o of $GABA_A$ receptors at large synapses, containing many $GABA_A$ receptors, is lower than that at small synapses with few receptors (Auger & Marty, 1997; Nusser *et al*., 1997). Accordingly, $GABA_A$ receptor occupancy may be determined by the number of postsynaptic receptors. At small synapses with only a few $GABA_A$ receptors (<80), the receptors should be saturated by the released GABA, whereas at large synapses the hundreds of postsynaptic receptors are not fully occupied. It follows that large-amplitude mIPSCs should be increased by zolpidem more than those with small amplitudes. Inconsistent with the possibility that the number of postsynaptic receptors alone is responsible for determining receptor occupancy, we found no significant correlation between the peak conductance of mIPSCs and the initial occupancy of the receptors (reflected by the $IPSG_{zolpidem}$: $IPSG_{control}$ ratio; Fig. 5A) in eight different cell types of three brain regions.

Variation in postsynaptic $GABA_A$ receptor occupancy is not solely the consequence of receptors with different GABA affinity

The variation in the degree of occupancy between cells and synapses may be the consequence of different $GABA_A$ receptors with distinct

affinity for GABA. The microscopic binding rate is inversely proportional to the unbinding rate at $GABA_A$ receptors (Jones *et al*., 1998). As the agonist unbinding rate strongly influences deactivation and consequently synaptic current decay, lower affinity receptors should produce more rapidly decaying synaptic currents (Jones *et al*., 1998). If the variation in synaptic GABA receptor occupancy results from the presence of receptors with different affinities for GABA, IPSCs with fast decays (i.e. those generated by low-affinity receptors) should be more strongly potentiated by zolpidem. Yet our data show no correlation between the decay of the synaptic currents and the initial receptor occupancy (Fig. 5B). Provided that the binding and unbinding rates are indeed inversely proportional (Jones *et al*., 1998) for every $GABA_A$ receptor subtype, our results suggest that the varying degrees of occupancy seen at different synapses are not simply a consequence of receptors with diverse GABA affinities.

Variability in the transmitter concentration may be the major contributor to the variation of postsynaptic receptor occupancy between cells and synapses

The estimates of peak GABA concentrations in the synaptic cleft range from 0.3 to 3 mM (Maconochie *et al*., 1994; Jones & Westbrook, 1995; Mozrzymas *et al*., 1999; Perrais & Ropert, 1999). This large range in the estimates may stem from studying diverse synapses. Morphological data also predict large differences in the GABA concentration at synapses. The volume of GABAergic synapses varies by 20-fold in cerebellar interneurons (Nusser *et al*., 1997) and by over 10-fold in dentate gyrus granule cells (Nusser *et al*., 1998). Because our data do not support the dependence of occupancy on GABA receptor number or affinity, the variation in transmitter concentration in the cleft could be responsible for the variation in the postsynaptic receptor occupancy. Clearly, future experiments are required to directly test this hypothesis, including the manner in which the postsynaptic cell matches the cleft GABA concentration to the number and type of receptors to produce a relatively constant occupancy across different synapses.

The variation in the GABA concentration in the cleft was also proposed to underlie the amplitude variability of postsynaptic responses (Frerking *et al*., 1995). Other studies identified differences in the postsynaptic receptor number as determining the variability in quantal amplitude (Edwards *et al*., 1990; De Koninck & Mody, 1994; Nusser *et al*., 1997, 1998; Lim *et al*., 1999). If the variance in quantal amplitude within a cell solely results from the trial-to-trial fluctuation of the transmitter concentration at synapses with unsaturated receptors, an increase in occupancy, e.g. caused by zolpidem, should reduce quantal variance. We monitored (Fig. 5C) possible changes in the variability of the peak amplitudes after zolpidem application (given by the ratio $1/CV^2_{zolpidem} : 1/CV^2_{control}$) as a function of the degree of occupancy (described by the ratio $IPSG_{zolpidem} : IPSG_{control}$). According to the lack of a correlation (Fig. 5C), variation in cleft transmitter concentration cannot be the major determinant of the quantal variance. Rather than the trial-to-trial fluctuation of GABA concentration in the synaptic cleft, the 20–30-fold variability in postsynaptic $GABA_A$ receptor number shown to exist in cerebellar stellate cells and dentate gyrus granule cells (Nusser *et al*., 1997, 1998) is more likely to produce the amplitude variance of IPSCs.

Acknowledgements

This research was supported by the Wellcome Trust (International Prize Travelling Fellowship to Z.N.), NINDS grant (NS 30549) and the Coelho Endowment to I.M.

Abbreviations

ACSF, artificial cerebrospinal fluid; CV, coefficient of variation; GABA, γ-aminobutyric acid; $GABA_A$ receptor, type A γ-aminobutyric acid receptor; IPSCs, inhibitory postsynaptic currents; mIPSCs, miniature inhibitory postsynaptic currents; $mIPSC_{FR}$, fast rising miniature inhibitory postsynaptic current; $mIPSC_{SR}$, slow rising miniature inhibitory postsynaptic current; mIPSGs, miniature inhibitory postsynaptic conductances; P_o, channel open probability; $P_{o,max}$, maximal channel open probability; PB, phosphate buffer; TTX, tetrodotoxin; τ_w, weighted decay time constant.

References

Auger, C. & Marty, A. (1997) Heterogeneity of functional synaptic parameters among single release sites. *Neuron*, **19**, 139–150.

De Koninck, Y. & Mody, I. (1994) Noise analysis of miniature IPSCs in adult rat brain slices: properties and modulation of synaptic $GABA_A$ receptor channels. *J. Neurophysiol.*, **71**, 1318–1335.

Defazio, T. & Hablitz, J.J. (1998) Zinc and zolpidem modulate mIPSCs in rat neocortical pyramidal neurons. *J. Neurophysiol.*, **80**, 1670–1677.

Edwards, F.A., Konnerth, A., Sakmann, B. & Busch, C. (1990) Quantal analysis of inhibitory synaptic transmission in the dentate gyrus of rat hippocampal slices: a patch-clamp study. *J. Physiol.* (*Lond.*), **430**, 213–213.

Faber, D.S., Young, W.S., Legendre, P. & Korn, H. (1992) Intrinsic quantal variability due to stochastic properties of receptor– transmitter interactions. *Science*, **258**, 1494–1498.

Frerking, M., Borges, S. & Wilson, M. (1995) Variation in GABA mini amplitude is the consequence of variation in transmitter concentration. *Neuron*, **15**, 885–895.

Freund, T.F. & Buzsáki, G. (1996) Interneurons of the hippocampus. *Hippocampus*, **6**, 345–470.

Galarreta, M. & Hestrin, S. (1997) Properties of $GABA_A$ receptors underlying inhibitory synaptic currents in neocortical pyramidal neurons. *J. Neurosci.*, **17**, 7220–7227.

Hájos, N. & Mody, I. (1997) Synaptic communication among hippocampal interneurons: properties of spontaneous IPSCs in morphologically identified cells. *J. Neurosci.*, **17**, 8427–8442.

Hollrigel, G.S. & Soltesz, I. (1997) Slow kinetics of miniature IPSCs during early postnatal development in granule cells of the dentate gyrus. *J. Neurosci.*, **17**, 5119–5128.

Jones, M.V., Sahara, Y., Dzubay, J.A. & Westbrook, G.L. (1998) Defining affinity with the $GABA_A$ receptor. *J. Neurosci.*, **18**, 8590–8604.

Jones, M.V. & Westbrook, G.L. (1995) Desensitized states prolong $GABA_A$ channel responses to brief agonist pulses. *Neuron*, **15**, 181–191.

Jones, M.V. & Westbrook, G.L. (1997) Shaping of IPSCs by endogenous calcineurin activity. *J. Neurosci.*, **17**, 7626–7633.

Kisvarday, Z.F., Beaulieu, C. & Eysel, U.T. (1993) Network of GABAergic large basket cells in cat visual cortex (area 18) – implication for lateral disinhibition. *J. Comp. Neurol.*, **327**, 398–415.

Lavoie, A.M. & Twyman, R.E. (1996) Direct evidence for diazepam modulation of $GABA_A$ receptor microscopic affinity. *Neuropharmacology*, **35**, 1383–1392.

Lim, R., Alvarez, F.J. & Walmsley, B. (1999) Quantal size is correlated with receptor cluster area at glycinergic synapses in the rat brainstem. *J. Physiol.* (*Lond.*), **516**, 505–512.

Macdonald, R.L. & Olsen, R.W. (1994) $GABA_A$ receptor channels. *Annu. Rev. Neurosci.*, **17**, 569–602.

Maconochie, D.J., Zempel, J.M. & Steinbach, J.H. (1994) How quickly can $GABA_A$ receptors open? *Neuron*, **12**, 61–71.

Mellor, J.R. & Randall, A.D. (1997) Frequency-dependent actions of benzodiazepines on $GABA_A$ receptors in cultured murine cerebellar granule cells. *J. Physiol.* (*Lond.*), **503**, 353–369.

Mozrzymas, J.W., Barberis, A., Michalak, K. & Cherubini, E. (1999) Chlorpromazine inhibits miniature GABAergic currents by reducing the binding and by increasing the unbinding rate of $GABA_A$ receptors. *J. Neurosci.*, **19**, 2474–2488.

Nusser, Z., Cull-Candy, S. & Farrant, M. (1997) Differences in synaptic $GABA_A$ receptor number underlie variation in GABA mini amplitude. *Neuron*, **19**, 697–709.

Nusser, Z., Sieghart, W., Benke, D., Fritschy, J.-M. & Somogyi, P. (1996) Differential synaptic localization of two major γ-aminobutyric acid type A receptor α subunits on hippocampal pyramidal cells. *Proc. Natl Acad. Sci.* (*USA*), **93**, 11 939–11 944.

Nusser, Z., Hajos, N., Somogyi, P. & Mody, I. (1998) Increased number of

synaptic $GABA_A$ receptors underlies potentiation at hippocampal inhibitory synapses. *Nature*, **395**, 172–177.

Nusser, Z., Sieghart, W. & Mody, I. (1999) Differential regulation of synaptic $GABA_A$ receptors by cAMP-dependent protein kinase in mouse cerebellar and olfactory bulb neurones. *J. Physiol.* (*Lond.*), **521**, 421–435.

Otis, T.S. & Mody, I. (1992) Modulation of decay kinetics and frequency of $GABA_A$ receptor-mediated spontaneous inhibitory postsynaptic currents in hippocampal neurons. *Neuroscience*, **49**, 13–32.

Perrais, D. & Ropert, N. (1999) Effect of zolpidem on miniature IPSCs and occupancy of postsynaptic $GABA_A$ receptors in central synapses. *J. Neurosci.*, **19**, 578–588.

Poisbeau, P., Williams, S.R. & Mody, I. (1997) Silent $GABA_A$ synapses during flurazepam withdrawal are region-specific in the hippocampal formation. *J. Neurosci.*, **17**, 3467–3475.

Pritchett, D.B. & Seeburg, P.H. (1990) γ-Aminobutyric $acid_A$ receptor α5-subunit creates novel type II benzodiazepine receptor pharmacology. *J. Neurochem.*, **54**, 1802–1804.

Ropert, N., Miles, R. & Korn, H. (1990) Characteristics of miniature inhibitory postsynaptic currents in CA1 pyramidal neurones of rat hippocampus. *J. Physiol.* (*Lond.*), **428**, 707–722.

Silver, R.A., Cull-Candy, S.G. & Takahashi, T. (1996) Non-NMDA glutamate receptor occupancy and open probability at a rat cerebellar synapse with single and multiple release sites. *J. Physiol.* (*Lond.*), **494**, 231–250.

Soltesz, I. & Mody, I. (1994) Patch-clamp recordings reveal powerful GABAergic inhibition in dentate hilar neurons. *J. Neurosci.*, **14**, 2365–2376.

Soltesz, I., Smetters, D.K. & Mody, I. (1995) Tonic inhibition originates from synapses close to the soma. *Neuron*, **14**, 1273–1283.

Somogyi, P., Kisvárday, Z.F., Martin, K.A.C. & Whitteridge, D. (1983) Synaptic connections of morphologically identified and physiologically characterized large basket cells in the striate cortex of cat. *Neuroscience*, **10**, 261–294.

Tamas, G., Buhl, E.H. & Somogyi, P. (1997) Fast IPSPs elicited via multiple synaptic release sites by different types of GABAergic neurone in the cat visual cortex. *J. Physiol.* (*Lond.*), **500**, 715–738.

Tamas, G., Somogyi, P. & Buhl, E.H. (1998) Differentially interconnected networks of GABAergic interneurons in the visual cortex of the cat. *J. Neurosci.*, **18**, 4255–4270.

Thomson, A.M., West, D.C., Hahn, J. & Deuchars, J. (1996) Single axon IPSPs elicited in pyramidal cells by three classes of interneurones in slices of rat neocortex. *J. Physiol.* (*Lond.*), **496**, 81–102.

dc_71_10

2. számú melléklet

dc_71_10
European Journal of Neuroscience, Vol. 12, pp. 3239–3249, 2000

Cannabinoids inhibit hippocampal GABAergic transmission and network oscillations

N. Hájos,[1]* I. Katona,[1]* S. S. Naiem,[2] K. Mackie,[3] C. Ledent,[4] I. Mody[2] and T. F. Freund[1]
[1]Institute of Experimental Medicine, Hungarian Academy of Sciences, Budapest, Szigony u. 43, 1083 Hungary,
[2] Departments of Neurology and Physiology, UCLA School of Medicine, Los Angeles, California 90095–1769, USA
[3] Departments of Anaesthesiology, and Physiology and Biophysics, University of Washington, Seattle, Washington 98195, USA
[4] IRIBHN, Université libre de Bruxelles, Brussels, Belgium

Keywords: granule cell, interneuron, mouse, pyramidal cell, rat

Abstract

Using a new antibody developed against the C-terminus of the cannabinoid receptor (CB1), the immunostaining in the hippocampus revealed additional axon terminals relative to the pattern reported previously with an N-terminus antibody. Due to a greater sensitivity of this antibody, a large proportion of boutons in the dendritic layers displaying symmetrical (GABAergic) synapses were also strongly immunoreactive for CB1 receptors, as were axon terminals of perisomatic inhibitory cells containing cholecystokinin. Asymmetrical (glutamatergic) synapses, however, were always negative for CB1. To investigate the effect of presynaptic CB1 receptor activation on hippocampal inhibition, we recorded inhibitory postsynaptic currents (IPSCs) from principal cells. Bath application of CB1 receptor agonists (WIN55,212-2 and CP55,940) suppressed IPSCs evoked by local electrical stimulation, which could be prevented or reversed by the CB1 receptor antagonist SR141716A. Action potential-driven IPSCs, evoked by pharmacological stimulation of a subset of interneurons, were also decreased by CB1 receptor activation. We also examined the effects of CB1 receptor agonists on Ca^{2+}-independent miniature IPSCs (mIPSC). Both agonists were without significant effect on the frequency or amplitude of mIPSCs. Synchronous gamma oscillations induced by kainic acid in the CA3 region of hippocampal slices were reversibly reduced in amplitude by the CB1 receptor agonist CP 55,940, which is consistent with an action on IPSCs. We used $CB1^{-/-}$ knock-out mice to confirm the specificity of the antibody and of the agonist (WIN55,212-2) action. We conclude that activation of presynaptic CB1 receptors decreases Ca^{2+}-dependent GABA release, and thereby reduces the power of hippocampal network oscillations.

Introduction

Our knowledge of the mechanisms of cannabinoid actions and the possible roles of the endogenous cannabinoid system is rapidly expanding in recent years due to the discovery of two distinct cannabinoid receptors, as well as their endogenous and synthetic ligands (for review see: Pertwee, 1997; Di Marzo *et al*., 1998). The type 1 cannabinoid receptor (CB1 receptor) is predominantly expressed in the central nervous system (Matsuda *et al*., 1990), and is responsible for the most prominent behavioural effects of cannabinoids (Ledent *et al*., 1999) including an impairment of memory formation in the hippocampus (Hampson & Deadwyler, 1998). However, the mechanisms involved and the precise sites of cannabinoid actions in the brain are still largely unknown. Before functional predictions can be made, or mechanisms of drug actions can be revealed in complex integrative centres of the brain, one has to identify the types of neurons (e.g. excitatory principal cells or inhibitory interneurons) and the cellular membrane compartments (axon terminals, cell bodies, dendrites or dendritic spines) expressing the particular receptor. Earlier receptor binding studies were of insufficient resolution to identify cannabinoid binding sites at the cellular and subcellular level. Nevertheless, they have shown that one of the areas with the highest density of cannabinoid binding sites is the hippocampal formation, with all of its subfields and layers showing intense labelling (Herkenham *et al*., 1991). Recent physiological experiments suggested that presynaptic CB1 receptors may be located on glutamatergic axon terminals (Ameri *et al*., 1999; Misner & Sullivan, 1999). This could explain the robust binding found in all hippocampal layers, as well as the mechanisms by which cannabinoids may disrupt memory formation. In contrast, recent immunocytochemical studies found no evidence for CB1 localization on glutamatergic neurons but revealed the selective expression of this receptor protein in the axon terminal membrane and perinuclear cytoplasm of GABAergic interneurons (Katona *et al*., 1999; Tsou *et al*., 1999). In agreement with the prediction of these anatomical data, cannabinoid agonists inhibited the release of radiolabelled GABA from hippocampal slices (Katona *et al*., 1999), the mechanisms of which have been recently uncovered (Hoffman & Lupica, 2000). These experiments imply that the major site of action of cannabinoids will be on GABAergic neurons. The striking discrepancy with the physiological results may be explained by the possible existence of mRNA splice variants differing in the N-terminus region in mice and humans (Shire *et al*., 1995). Therefore, we used a novel antibody directed against the C-terminal tail of the CB1 receptor, which is identical in both described splice variants, to gain insight into the cellular and subcellular localization of CB1 receptors in

Correspondence: Tamás F. Freund, as above.
E-mail: freund@koki.hu

*These authors contributed equally to this study.

Received 24 April 2000, revised 9 June 2000, accepted 12 June 2000

hippocampal neurons. In the second, electrophysiological, part of the study we used whole-cell patch-clamp and field potential recordings to establish the functional role of these receptors in the modulation of GABAergic transmission and to determine how cannabinoids interfere with a form of experimental network oscillations.

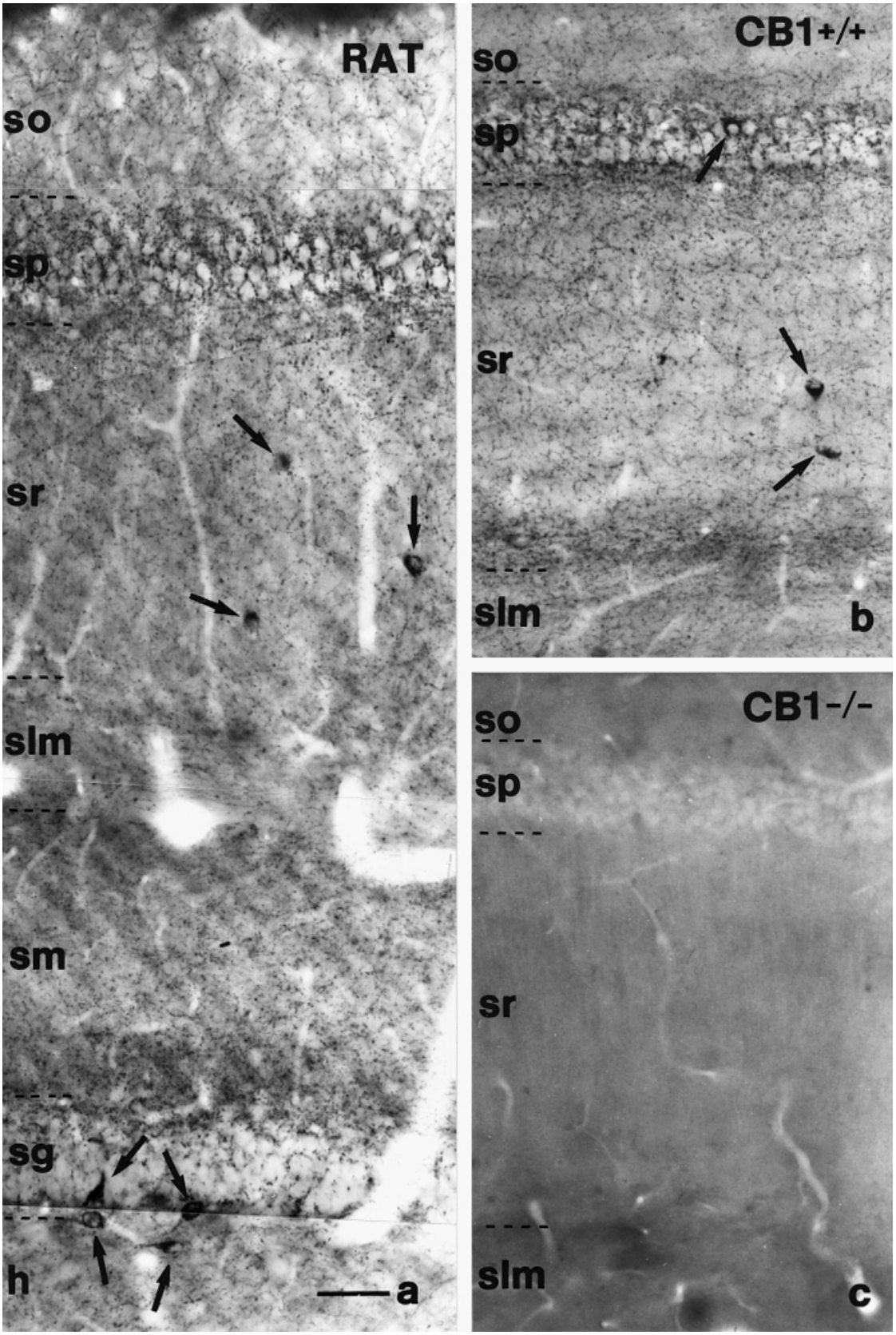

Materials and methods

Immunocytochemistry

For CB1 immunostaining, Wistar rats, CB1 wild-type control (+/+) and CB1 knockout (–/–) mice were used (Ledent *et al*., 1999). The single- and double-staining protocols were identical to those described in Katona *et al*. (1999). The specificity of the affinity-purified C-terminal antibody (used at 1 : 5000) for the CB1 cannabinoid receptor was verified in several ways, i.e. by the lack of any immunostaining in the $CB1^{-/-}$ mice (Fig. 1), by Western blotting, transfection experiments in ATt20 cells, and expression pattern correlation analysis with the previously charaterized CB1 N-terminal antibody (Tsou *et al*., 1998 and see Results). The other antisera used in the present study were: rabbit anti-CB1 receptor N-terminal end (1 : 1000, Tsou *et al*., 1998), rabbit antiparvalbumin (1 : 2000, Baimbridge & Miller, 1982), rabbit anticholecystokinin (1 : 10000 Gulyas *et al*., 1990), and rabbit anti-substance P (SP) receptor (1 : 1000, Shigemoto *et al*., 1993). The specificity of these antisera were extensively investigated in the laboratories of origin. For immunofluorescence double-staining, the rabbit antibodies against CB1 were used together with monoclonal mouse antisera against parvalbumin (PV; 1 : 1000; Sigma, St. Louis, MO, USA). Cy3-conjugated antirabbit IgG made in donkey (1 : 200) and FITC-conjugated antimouse IgG made in goat (1 : 100; both from Jackson ImmunoResearch, West Grove, PA, USA) were used as secondary antibodies.

Electrophysiology

Male Wistar rats (16–22-day-old) were deeply anaesthetized with sodium pentobarbital (70 mg/kg, i.p.) and then decapitated. Adult male mice (CB1 wild-type or knock-out) were anaesthetized with ether and then decapitated. After opening the skull, the brain was removed and immersed into ice-cold (≈ 4 °C) modified artificial cerebrospinal fluid (ACSF), which contained (in mM) NaCl, 126; KCl, 2.5; $NaHCO_3$, 26; $CaCl_2$, 0.5; $MgCl_2$, 5; NaH_2PO_4, 1.25; and glucose, 10. Coronal slices of the hippocampus (300–350 µm in thickness) were prepared using a Lancer Series 1000 Vibratome. The slices were incubated in ACSF (containing $CaCl_2$ and $MgCl_2$ at 2 mM) for at least an hour before recordings. Whole-cell patch-clamp recordings were obtained at 32–34 °C from rat CA1 pyramidal cells or mouse dentate granule cells visualized by infrared DIC videomicroscopy (Zeiss Axioscope, Germany). In all experiments, slices were superfused with ACSF containing 2–3 mM kynurenic acid to eliminate the ionotropic glutamatergic transmission. Recorded currents were completely and reversibly blocked by the $GABA_A$ receptor antagonist bicuculline methiodide (10–20 µM, $n = 4$, data not shown). Patch electrodes were pulled from borosilicate glass capillaries with an inner filament (KG-33, 1.5 mm OD; Garner Glass, Claremont, CA, USA) using a Sutter P-87 puller, and had resistances of 3–6 MΩ when filled with the intracellular solution. For stimulation experiments the intracellular solution contained (in mM): Cs-gluconate, 140; CsCl, 2; $MgCl_2$, 2; HEPES, 10; QX-314, 5; and Mg-ATP, 2 (pH 7.2–7.3 adjusted with CsOH; osmolarity 290–300 mOsm). Recordings were made at a holding potential of +10 ± 5 mV. For spontaneous IPSC recordings, the pipette was filled with (in mM) CsCl, 145; $MgCl_2$, 2; HEPES, 10; QX-314, 5; and Mg-ATP, 2. Recordings were performed at a holding potential of –65 mV. Access resistances (between 5 and 15 MΩ, compensated 70–75%) were frequently monitored and remained constant (± 20%) during the analysed period. Signals were recorded with an Axopatch 200B amplifier (Axon Instruments, CA, USA), filtered at 1–2 kHz (eight-pole Bessel, FLA-01, Cygnus Technology, Fredericton, Canada), digitized at 5–10 kHz (National Instruments LabPC + A/D board, Austin, TX, USA) and analysed off-line with CDR or SCAN software (courtesy of J. Dempster). Student's paired *t*-test was used to compare the changes in the mean conductance and frequency after CB1 receptor agonist application; $P < 0.05$ was considered significant. Data are presented as mean ± SEM.

Extracellular field recordings were obtained in 350-µm-thick hippocampal slices cut in the horizontal plane prepared from 28–36-day-old rats. The recording chamber was an interface type, but the surface of the slices was covered with a layer of ACSF (containing no receptor blockers) approximately 100 µm deep. Recordings were made at 34 °C in the pyramidal cell layer of the CA3 region. The γ oscillations were induced by perfusion of 100–200 nM kainic acid (Buhl *et al*., 1998), which resulted in steady oscillations within 15 min following its perfusion. The power of the oscillations was measured by performing fast Fourier transformations on 5-s-long epochs sampled at 2500 Hz, after being bandpass filtered between 1 and 200 Hz (eight-pole Bessel, Brownlee, CA, USA). The peak of the power at a certain frequency was established from at least four averaged fast Fourier transformations of 5-s epochs. These measurements were repeated in the presence of the CB1 agonists, and following washout.

Reagents

CP55,940 and WIN55,212-2 were obtained from Tocris (UK) and were dissolved in DMSO (100 mM stock solution for both agonists). SR141716A (dissolved as 10 mM stock) was provided by NIDA drug supply service. DMSO by itself had no effect on IPSCs up to 0.01% concentration ($n = 3$). Bicuculline, SP fragment (Acetyl-[Arg^6, Sar^9, $Met(O_2)^{11}$]-fragment 6–11) and kynurenic acid were purchased from Sigma and tetrodotoxin (TTX) was purchased from Alomone Labs, Israel.

Results

Presynaptic CB1 cannabinoid receptors are localized on GABAergic axon terminals

Immunostaining with antibodies directed against the intracellular C-terminal tail of the rat CB1 cannabinoid receptor (residues 401–473) visualized interneuron somata scattered in all hippocampal layers (Fig. 1a), similar to the pattern obtained by using another antibody against the extracellular N-terminal domain of CB1. Indeed, colocalization by the mirror technique confirmed that the two antibodies labelled the same interneuron population (n = 33). Pyramidal and granule cell somata were always negative for CB1. The C-terminal antibody revealed a far more extensive axonal meshwork than the N-terminal antibody both in rats and in $CB1^{+/+}$

FIG. 1. Light microscopy of CB1 cannabinoid receptor localization in the rodent hippocampus. (a) CB1 receptor immunostaining with the C-terminus antibody labels a dense axon meshwork in all layers of the rat hippocampus. A subpopulation of interneurons (arrows) are positive for CB1, but neither granule cells in str. granulosum (sg) of the dentate gyrus, nor pyramidal cells in str. pyramidale (sp.) of the CA1 subfield, are CB1-immunoreactive. (b) $CB1^{+/+}$ mice have an identical CB1 receptor localization pattern to rats. The highest density of CB1-positive axons is found at the border of str. pyramidale (sp) and str. radiatum (sr) of the CA1 subfield, whereas str. lacunosum-moleculare (slm) is sparsely stained for CB1. (c) In contrast, immunostaining for CB1 cannabinoid receptor in $CB1^{-/-}$ mice gave rise to no staining at all, which confirms the selectivity of the C-terminus antibody. Abbreviations: so, stratum oriens; sp, stratum pyramidale; sr, stratum radiatum; slm, stratum lacunosum-moleculare; sm, stratum moleculare; sg, stratum granulosum; h, hilus. Scale bar, 80 µm (a–c).

mice (Fig. 1a,b). The labelled axon density was most pronounced in the stratum moleculare of the dentate gyrus and in the stratum pyramidale of CA1–3, but all other layers were also covered by CB1-immunoreactive axons except for the stratum lacunosum-moleculare, where they were sparse. This staining shows a perfect overlap with the cannabinoid receptor-binding pattern described in the hippocampus earlier (Herkenham *et al.*, 1991). In the CB1$^{-/-}$ mice, no staining was found for CB1 receptors (Fig. 1c), whereas immunostainings for PV or cholecystokinin (CCK) showed the same pattern as in wild-type mice (data not shown).

Electron microscopy of stained sections revealed that all CB1-positive boutons formed symmetrical synapses characteristic of GABAergic terminals, whereas axon terminals forming asymmetric synapses never showed CB1 immunoreactivity (Fig. 2). CB1-positive

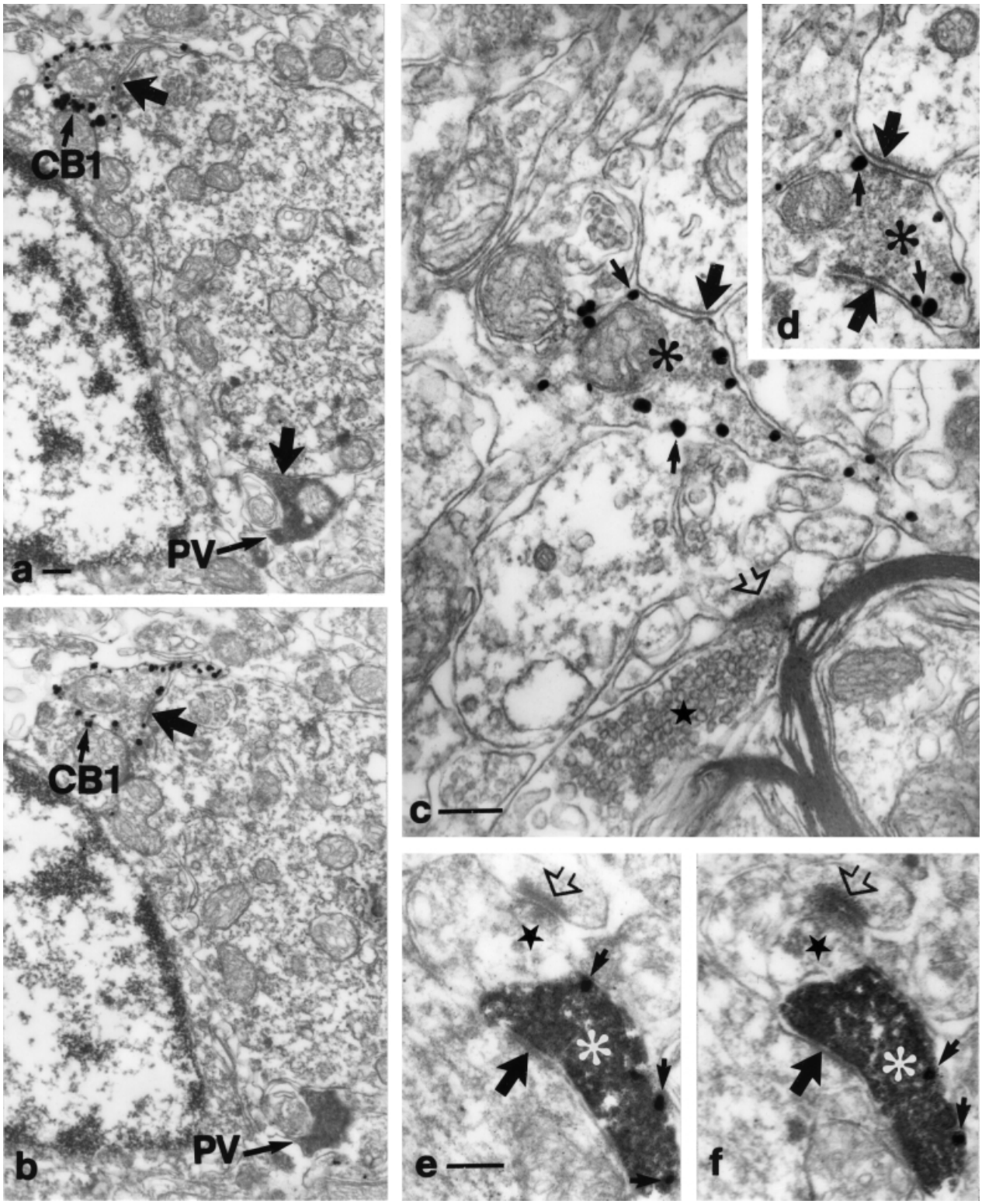

GABAergic boutons were found to terminate on somata of principal cells (Fig. 2a,b), thick proximal dendrites, and thin, distal dendrites in strata radiatum and moleculare (Fig. 2c,d). CB1 expression was restricted to certain interneuron types characterized by different neurochemical markers. Double-labelling by immunofluorescence or the combined immunogold–immunoperoxidase approach showed that CB1 was not present either in the somata ($n = 42$) or in the axon terminals of the most characteristic perisomatic inhibitory cell types, the basket and axo-axonic cells that express the calcium-binding protein PV (Kosaka *et al*., 1987). On the other hand, most of the CB1-positive boutons contained the neuropeptide CCK especially in the cell body layers, but also in the other laminae of the hippocampus (Fig. 2e,f). We visualized a large portion of hippocampal interneurons by SP receptor immunostaining which outlines interneuron dendritic trees in the greatest details (Acsady *et al*., 1997). The multiple contacts formed by CB1-positive fibres on SP receptor-immunoreactive interneuron dendrites suggest that interneuron-specific interneurons are also among the CB1-containing cells.

Immunogold staining with the antibody against the C-terminal domain of CB1 revealed an unexpectedly high concentration of presynaptic CB1 receptors (Fig. 2). Gold particles representing CB1-immunoreactive sites covered the entire intracellular surface of some axon terminals. No labelling was associated with the extracellular surface of the membrane, which also confirmed the specificity of the antibody. Frequently, preterminal axon segments were also strongly immunoreactive (Fig. 2b,c). By counting several sections, we estimated roughly 60–100 silver-intensified gold particles per axon terminal, but this should be considered an underestimate due to the poor and uneven penetration of the antibodies and the loss of some labelling during dehydration.

Hippocampal slices used for patch-clamp recordings (see below) were also fixed and immunostained for CB1 after spending 0.5, 3, 6 or 9 h in the slice chamber or medium. The pattern of CB1 immunostaining was identical to that seen in perfused animals both at the light and electron microscopic levels.

CB1 receptor activation depresses monosynaptically evoked IPSCs

The coverage of GABAergic boutons by CB1 receptors strongly suggests that cannabinoid action should alter inhibitory synaptic transmission in the hippocampus. This prediction was tested by investigating the effect of the potent cannabinoid receptor agonists, WIN55,212-2 and CP55,940, on inhibitory postsynaptic currents (IPSCs) evoked in rat CA1 pyramidal cells. As shown in Fig. 3a, the amplitudes of monosynaptic IPSCs were considerably depressed ($59 \pm 5\%$ of control, $P < 0.01$, *t*-test) after bath application of 1 μM WIN55,212-2, which lasted for the whole duration of the recording. The reduction of evoked IPSCs (eIPSCs) by the agonist could be prevented ($99 \pm 5\%$ of control, $P > 0.5$, Fig. 3b,d) or reversed ($96 \pm 4\%$ of control, $P > 0.5$, Fig. 3c,d) by the specific CB1 receptor antagonist SR141716A (1 μM). Using another CB1 receptor agonist, CP55,940 (1 μM), a similar reduction of IPSC amplitude was observed ($66 \pm 5\%$ of control, $P < 0.01$). This effect was reversed or could be antagonized by 1 μM SR141716A ($103 \pm 8\%$ of control, $P > 0.05$, Fig. 3d). We also tested the effect of WIN55,212-2 on eIPSCs recorded in dentate granule cells of both wild-type ($CB1^{+/+}$) and CB1 receptor knock-out ($CB1^{-/-}$) mice. Bath application of 1 μM WIN55,212-2 significantly reduced the eIPSC amplitude ($64 \pm 6\%$ of control, $P < 0.05$, Fig. 3d,e) in the wild-type, but failed to change it in $CB1^{-/-}$ mice ($97 \pm 2\%$ of control, $P > 0.1$, Fig. 3d,f).

Selectivity of CB1 receptor-mediated effects on a subset of inhibitory afferents

According to our anatomical findings, only a subpopulation of GABAergic terminals contain CB1 receptors. To provide physiological evidence for this striking selectivity, we used minimal stimulation, which aims to activate a single presynaptic axon. In this case, the mean amplitude of IPSCs should show a clear threshold without further changes with increasing stimulus intensity (Raastad, 1995) (Fig. 4a). In eight out of 17 cases, IPSCs evoked by minimal stimulation in the close vicinity of somata or proximal dendrites showed a large reduction of their release probability upon application of CP55,940 (0.5–1 μM), as indicated by a massive increase of the failure rate (Fig. 4c). The effect could be reversed by washing out the agonist. In the remaining nine cases, however, IPSCs were not altered during application of the agonist (Fig. 4c). Thus, the selective presence of CB1 receptors on some but not all GABAergic boutons manifests physiologically as a selective modulation of GABAergic IPSCs evoked by a specific subset of inhibitory interneurons, but a lack of effect on others.

Action potential-dependent spontaneous IPSCs are suppressed by CB1 receptor activation

Under the present recording conditions the majority of spontaneously occurring IPSCs were action potential-independent (i.e. TTX only slightly reduced the frequency of IPSCs; data not shown), therefore firing was induced in a subset of hippocampal interneurons by pharmacological tools. As shown earlier (Acsady *et al*., 1997), CCK-containing hippocampal interneurons (which give rise to the majority of axon terminals expressing CB1 receptors) also express SP receptors on their soma–dendritic surface. To examine the effect of CB1 receptor agonist on IPSCs evoked by spontaneous action potential discharge, we activated these CCK-containing (and CB1 receptor-expressing) interneurons by bath application of a highly selective SP receptor agonist, an SP fragment. Compared to controls, 50 nM SP fragment application caused a large increase in both IPSC amplitude ($155 \pm 2\%$ of control, $P < 0.05$) and IPSC frequency ($195 \pm 43\%$ of control, $P < 0.01$) recorded in CA1 pyramidal cells

FIG. 2. CB1 cannabinoid receptors are restricted to axon terminals forming symmetrical (presumed GABAergic) synapses. (a and b) Serial sections cut from axon terminals of two different basket cell types forming symmetrical synapses (thick arrows) on a cell body in the CA3 subfield of the hippocampus. The upper bouton is immunoreactive for CB1 (see dense immunogold labelling around the membrane), whereas the lower terminal is positive for the calcium-binding protein parvalbumin (PV; see the dark, diffuse DAB precipitate of immunoperoxidase staining), but negative for CB1. Note that silver–gold particles representing CB1 protein nearly completely cover the axon terminal, as well as the preterminal segment, but appear to avoid synaptic active zone. Labelling is restricted to the inner surface of the bouton, where the intracellular C-terminus epitope of CB1 is located (see also c–f). (c and d) Thin, distal dendrites of pyramidal cells are also innervated by CB1-positive axon terminals (asterisks) as shown here in serial sections from the border of str. radiatum and str. lacunosum-moleculare in the CA1 subfield. In contrast, boutons (stars) forming asymmetrical (mostly glutamatergic) synapses (open arrows in e and f) on spine heads are always avoided by silver–gold particles (small arrows), and are therefore considered CB1-negative. (e and f) Combined immunogold (for CB1) and immunoperoxidase (for the neuropeptide cholecystokinin, CCK) staining reveals that the axon terminals of CCK-containing interneurons bear presynaptic CB1 receptors. Serial sections in the stratum moleculare of the dentate gyrus show that gold particles (small arrows) representing CB1 are confined to a CCK-positive axon terminal (white asterisks) and avoid excitatory terminals (stars). Scale bars, 0.2 μm (in a for a and b; in c for c and d; in e for e and f).

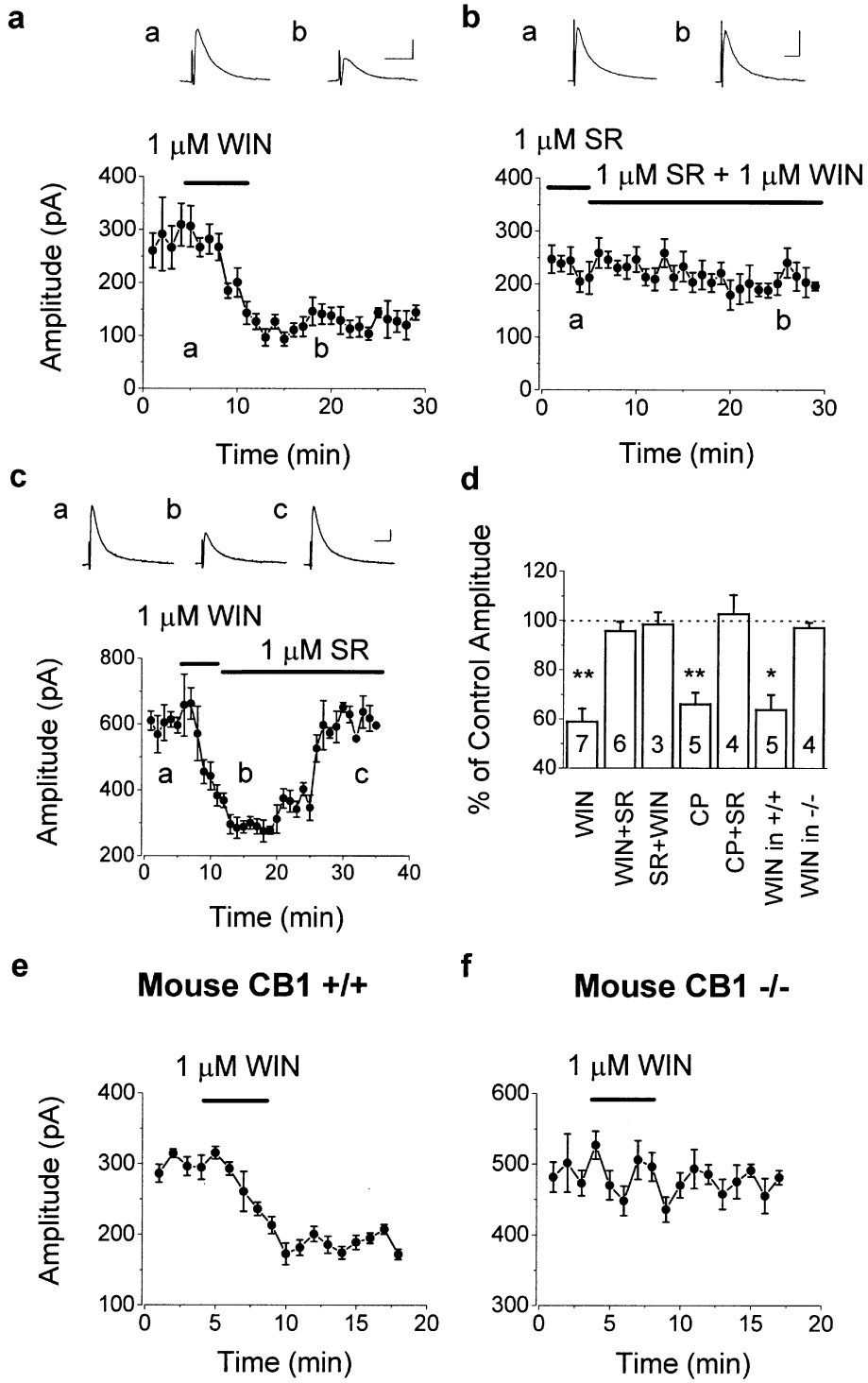

FIG. 3. Specific CB1 receptor agonists suppress IPSCs evoked by electrical stimulation. Whole-cell patch-clamp recordings were obtained from the hippocampal principal cells. (a) Plot of the eIPSC amplitude shows an ≈50% reduction of monosynaptic responses following bath application of the CB1 receptor agonist WIN55,212-2 (1 μM). (b) Pretreatment with a CB1 receptor antagonist, SR141716A, and its coapplication with WIN55,212-2, prevents the suppression of the eIPSC amplitude. (c) The CB1 receptor antagonist, SR141716A, reversed the reduction of eIPSC amplitude caused by WIN55,212-2. All data points on the plots represent a mean ± SEM of six consecutive events recorded in rat CA1 pyramidal cells. Inserts in a, b and c are averaged records of 6–8 consecutive IPSCs taken at the labelled time points. The events were evoked by stimulation in strata pyramidale or radiatum by 0.1 Hz (holding potential +10 mV). The lower panels show data from dentate granule cells of wild-type and CB1 receptor (–/–) knock-out mice. The stimulation was delivered at the border of strata moleculare and granulosum. (e) In the wild-type animals eIPSCs are sensitive to WIN55,212-2. (f) In contrast, the CB1 receptor agonist has no effect in cells from mice that lack CB1 receptors. (d) Summary plot of effects of CB1 receptor agonists (WIN55,212-2 and CP55,940) and antagonist (SR141716A) on eIPSC amplitude in both species. All data were normalized to the control values, and are represented as percentages. The numbers of neurons recorded under different experimental conditions are shown within the columns (+/+, wild-type; –/–, CB1 receptor knock-out mice). $^{**}P<0.01$, $^{*}P<0.05$. Scale bars, 25 ms and 100 pA.

(Fig. 5a,b). This increase of inhibitory activity could be observed 3–5 min after drug application and was sustained for up to 20 min ($n=3$). When the enhanced inhibitory activity was established, we washed in 1 μM WIN55,221–2. Within 5–8 min the CB1 agonist largely reversed the increases in both the amplitude (116 ± 18% of control, $P>0.1$) and frequency (115 ± 8% of control, $P>0.1$) of IPSCs (Fig. 5a,b). The results were similar in all seven cells tested (Fig. 5c,d). To rule out the possibility that SP fragment acts directly on the presynaptic side of inhibitory terminals, we applied SP fragment in the presence of TTX, which prevents action potential generation. In agreement with previous results (Kouznetsova & Nistri, 1998), SP fragment had no effect on either the conductance (102 ± 2% of control, $P>0.5$) or the frequency (104 ± 15 of control, $P>0.5$) of miniature IPSCs (mIPSC; $n=4$). We conclude that CB1 receptor activation can also diminish action potential-driven IPSCs generated by the SP receptor-rich CCK-containing interneurons.

Action potential-independent GABA release is unaffected by CB1 receptor agonists

Under our experimental conditions, mIPSCs recorded in CA1 pyramidal cells were independent of external Ca^{2+} influx, because perfusion of 100 μM Cd^{2+} (a blocker of voltage-gated Ca^{2+} channels)

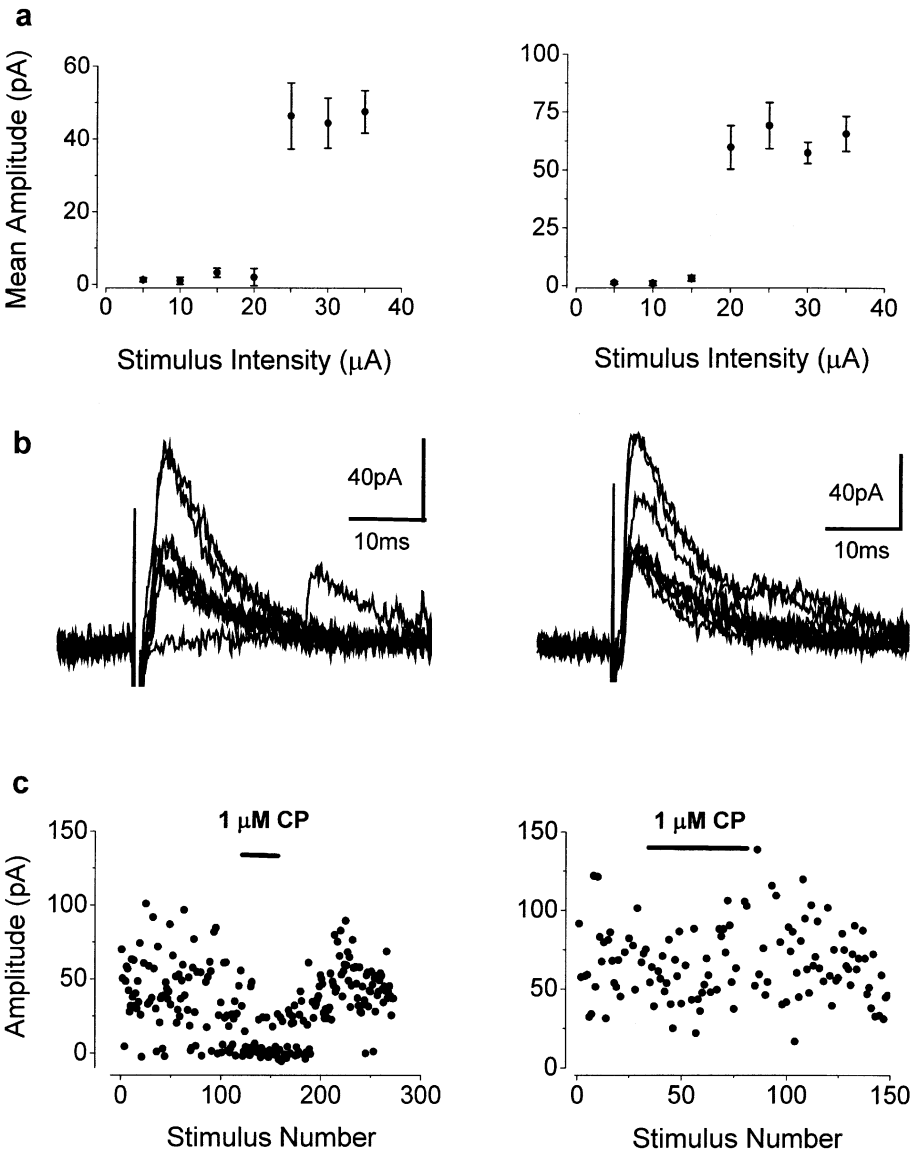

FIG. 4. Only a subset of inhibitory axons are responsive to CB1 receptor activation, consistent with our anatomical results. IPSCs were evoked by minimal stimulation (0.25–0.3 Hz) at two different sites in the close vicinity of a CA1 pyramidal cell. (a) Plots of mean amplitude (± SEM) as a function of stimulus intensity show a sharp threshold of synaptic responses as the stimulus strength is elevated, then no further increases are observed indicating that there is no recruitment of additional axons. (b) Representative traces evoked from two different stimulus sites (holding potential +10 mV). (c) As the amplitude plot shows, one of the eIPSCs (left panel) was sensitive to the CB1 agonist CP55,940 as indicated by the increased number of transmission failures. After washout, the synaptic responses returned to control levels. The IPSCs evoked with stimulation of a different site (right panel) were insensitive to the agonist application because there was no obvious change in their failure rate during the CP55,940 treatment.

in the presence of 0.5 μM TTX failed to change either the frequency (99 ± 2% of control, $P > 0.1$) or the conductance (96 ± 4% of control, $P > 0.1$) of mIPSCs ($n = 5$). Similarly, application of 1 μM CP55,940 did not significantly alter either the frequency (124 ± 14%, $P > 0.05$) or the size (108 ± 4%, $P > 0.1$) of the mIPSCs ($n = 8$, Fig. 6a–c). The results were confirmed by the use of another CB1 agonist WIN55,212-2 (frequency: 130 ± 19%, $P > 0.05$; conductance: 107 ± 2%, $P > 0.1$, $n = 5$). These data suggest that CB1 receptor agonists do not directly affect the action potential-independent release machinery of GABA from terminals, and do not influence the postsynaptic sensitivity to GABA.

The effect of CB1 receptor activation on hippocampal gamma oscillations

Gamma (γ) oscillations in the frequency range of 30–100 Hz can be elicited in brain slice preparations by perfusion of the muscarinic agonist carbachol or of the ionotropic glutamate receptor agonist kainic acid (Buhl *et al.*, 1998; Fisahn *et al.*, 1998). We have used the latter method to induce γ oscillations in hippocampal slices in order to avoid the direct activation of G-protein-coupled receptors during the induction phase. Within 15 min of its perfusion, kainic acid (100–200 nM) induced robust γ oscillations that could be recorded in the CA3 pyramidal cell layer (Fig. 7). As determined by fast Fourier transformations of the raw recordings, the average frequency of the oscillations was 36.7 ± 3.6 Hz (mean ± SD, $n = 7$ slices). Addition of the CB1 receptor agonist (CP55,940, 250 nM) to the bath significantly diminished the power of the oscillations (54.5 ± 20.6% of control at 250 nM, $P < 0.005$, paired *t*-test). While the power became gradually reduced, there was no shift in the peak frequency of the oscillations as the drug washed in (35.1 ± 7.5 Hz; $P = 0.63$, two-tailed *t*-test). In three slices exposed to the agonist we were able to wash out the drug effect, whereupon the oscillations returned to control levels (Fig. 7).

Discussion

The present study demonstrates (i) a selective, dense coverage of GABAergic axon terminals of functionally distinct interneuron types by CB1 cannabinoid receptors (Miles *et al.*, 1996), i.e. of both dendritic and perisomatic inhibitory cells. These anatomical data represent the structural basis for (ii) the observed massive reduction

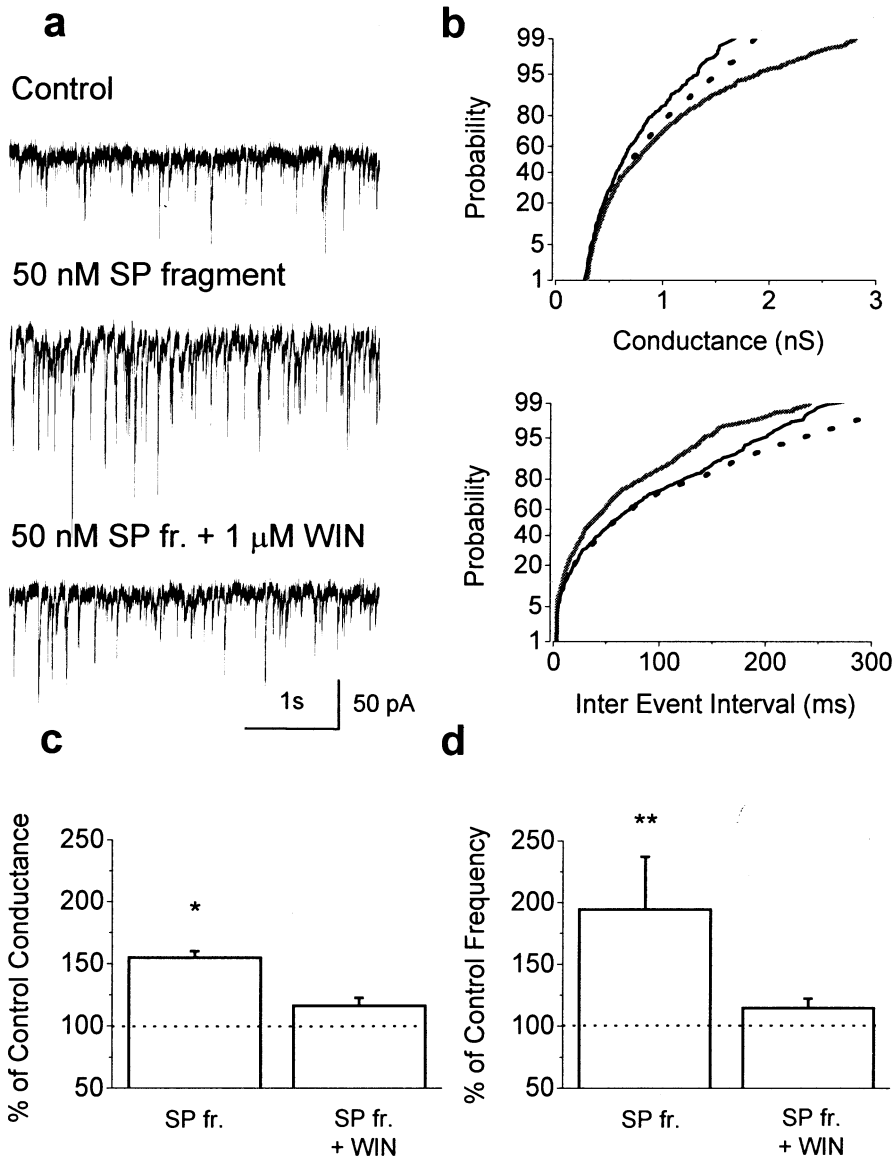

FIG. 5. Spontaneous, action potential-dependent IPSCs are also reduced by CB1 receptor activation in CA1 pyramidal cells. (a) Representative recordings before and after bath application of a potent SP receptor agonist, and after the addition of WIN55,212-2 (1 μM). Glutamatergic transmission was blocked throughout the recordings (holding potential – 65 mV). (b) Cumulative probability distributions of IPSC peak conductances (upper panel) and interevent intervals (lower panel) under the three different experimental conditions are shown from the same neuron as in (a). The application of SP fragment (thick grey line) increased both the conductance (right shift of the distribution curve) and the frequency of IPSCs (left shift) compared to control (thin black line), whereas the addition of WIN55,212-2 (dashed line) reversed this increment almost to control level. The bar graphs summarize the data from seven recorded cells for (c) conductance and (d) frequency. $^{**}P < 0.01$, $^{*}P < 0.05$.

of IPSCs evoked by focal microstimulation or pharmacologically induced action potential firing of interneurons, and for (iii) the reduction in the amplitude of kainate-induced γ oscillations.

Localization of CB1 receptors by a novel antibody directed against a C-terminus epitope

Compared to our previous results obtained with an antibody developed against an N-terminal epitope of the CB1 receptor (Katona *et al*., 1999), staining with the C-terminus antibody revealed a much stronger axonal staining, even outside the cell body layers, in agreement with earlier binding studies (Herkenham *et al*., 1991). However, the two antibodies were shown here to label the same population of CB1 receptor-positive somata. Thus, the colocalization data we published earlier with the N-terminus antiserum (Katona *et al*., 1999) are valid for the cell bodies visualized by the C-terminus antibody as well, i.e. the vast majority (≈ 85%) of CB1-positive somata contained CCK. As shown with the N-terminus antibody (Katona *et al*., 1999), the immunogold labelling in the cell bodies was restricted to the Golgi apparatus or the endoplasmic reticulum, and completely avoided the cell membrane. Electron microscopic examination of immunoreactive profiles in serial ultrathin sections confirmed our earlier observation that, if considering only plasma membrane localization, CB1 receptors are located solely on axon terminals forming symmetrical (presumed GABAergic) synapses in all layers of the hippocampus. Based on our data showing CB1 receptor-immunoreactive axon endings also in strata radiatum and oriens, and sparsely in lacunosum-moleculare, we conclude that, in addition to the previously described CCK-containing basket cells, CB1 receptors are also expressed in interneurons exerting dendritic inhibition. Some of these may belong to the calbindin-containing subset (Gulyas & Freund, 1996; Marsicano & Lutz, 1999; Tsou *et al*., 1999), whereas others could still contain CCK, because this neuropeptide is not confined to perisomatic interneurons (I. Katona, T.F. Freund, unpublished observations). Previous studies together with our results obtained from CB1 and SP receptor double-immunostaining suggest that some axon terminals in the dendritic layers may belong to interneurons containing calretinin (Marsicano & Lutz, 1999; Tsou *et al*., 1999), which selectively innervate other interneurons (Freund & Buzsaki, 1996; Gulyas *et al*., 1996). In summary, CB1 receptors are expressed in a more heterogenous interneuron population than suggested earlier using the N-terminus antiserum (Katona *et al*., 1999). CB1-positive neurons include both

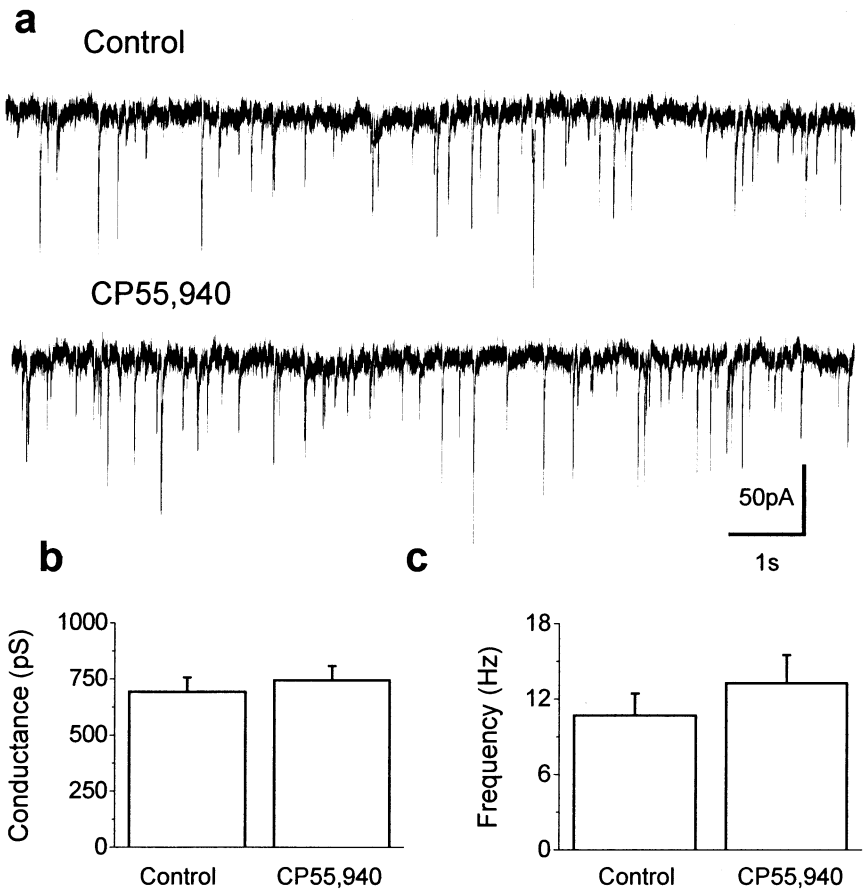

FIG. 6. Activation of CB1 receptors does not significantly alter the action potential-independent IPSCs. (a) Raw traces depicting mIPSCs in the presence of 3 mM kynurenic acid and 0.5 μM TTX in a CA1 pyramidal cell are shown before (upper panel) and after (lower panel) bath application of the CB1 receptor agonist CP55,940 (1 μM) (holding potential –65 mV). (b) The averaged mIPSC conductance or (c) the averaged frequency, recorded from eight neurons, did not differ significantly before or after applying CP55,940.

perisomatic and dendritic inhibitory cells, most of which contain CCK, but some CB1-positive axons in the dendritic layers may originate from calbindin- and calretinin-containing interneurons as well.

The C-terminus antibody should have uncovered the hippocampal localization of all possible N-terminal splice variants. Inconsistent with recent physiological observations (Ameri *et al*., 1999; Misner & Sullivan, 1999) proposing direct CB1 receptor action on glutamatergic transmission, the new C-terminus antibody failed to reveal any labelling on boutons forming asymmetric (i.e. glutamatergic) synapses. This apparent contradiction of anatomical and physiological data may possibly be explained by the presence of an as yet unknown cannabinoid receptor type on glutamatergic endings.

Besides selectivity, another impressive and functionally important aspect of CB1 localization is the extremely high density of receptor immunoreactivity around the axon terminal membrane and spreading further down the preterminal collaterals. The 60–100 receptors per terminal calculated from serial electron microscopic sections are probably an underestimate, because some degree of false-negative staining always occurs in immunocytochemistry for various technical reasons. For example, in postembedding immunogold studies, a gold particle is likely to correspond to ≈2.5 functional AMPA-type glutamate or $GABA_A$ receptors (Nusser *et al*., 1998a,b). In spite of the large number of CB1 receptors, the synaptic active zones did not contain silver–gold particles, which suggests that the endogenous ligand is unlikely to approach the boutons from the postsynaptic neuron via the synaptic cleft. Alternatively, CB1 receptors in the cleft may be masked by other proteins, or are in a conformational state not recognized by these antibodies.

Presynaptic inhibition of GABAergic synaptic transmission by CB1 receptors

Previous results have suggested the potential involvement of cannabinoids in the modulation of hippocampal GABAergic transmission (Paton *et al*., 1998; Katona *et al*., 1999). Here we provide direct evidence for the depression of monosynaptic IPSCs by CB1 receptor activation in the hippocampus. Our pharmacological and anatomical results strongly support a presynaptic site of action. Based on previously published data, this effect probably results from the inhibition of N- or P/Q-type voltage-gated Ca^{2+} channels (Twitchell *et al*., 1997; Hoffman & Lupica, 2000), which play a major role in vesicle release (Matthews, 1996). The lack of significant changes in mIPSC properties after applying the CB1 receptor agonists (Fig. 6; Hoffman & Lupica, 2000) further strengthens this hypothesis, because mIPSCs in our preparations were independent of Ca^{2+} influx into the terminals. However, when the barrage of IPSCs was enhanced as a consequence of increased interneuronal firing known to elevate Ca^{2+} levels in boutons (Tan & Llano, 1999), the IPCSs were markedly depressed by CB1 activation (Fig. 5).

Cannabinoids regulate gamma oscillations via a subset of inhibitory interneurons

Highly synchronous oscillations in the gamma frequency range resembling those recorded *in vivo* can be induced pharmacologically in slices of the hippocampus (Fisahn *et al*., 1998) and of the neocortex (Buhl *et al*., 1998). Our study provides the first direct evidence that cannabinoids interfere with kainate-induced synchronous γ oscillations in the *in vitro* hippocampus. Several lines of evidence support the critical involvement of basket cell-mediated inhibition in the

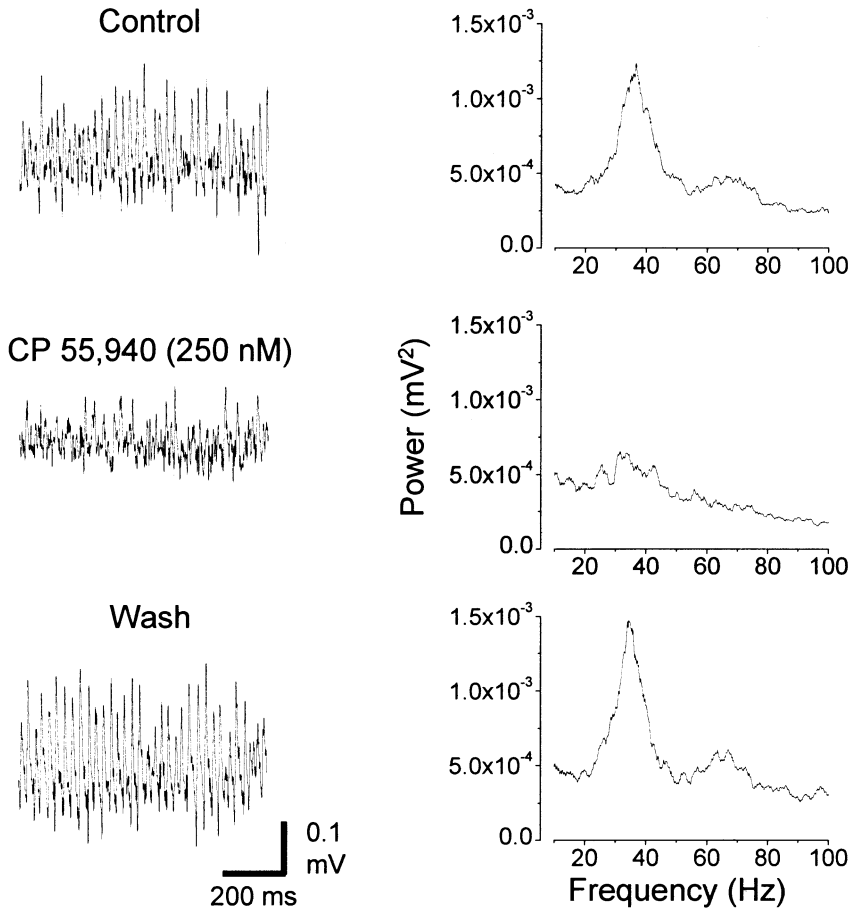

FIG. 7. CB1 receptor activation reduces the power of gamma oscillations in the hippocampus. Example traces of extracellular local field recordings in the CA3 pyramidal cell layer (left panel). After bath application of 200 nM kainate, a steady rhythmic activity at ≈ 40 Hz was maintained in the hippocampal slice preparation. The power of the oscillations was reversibly decreased by the CB1 receptor agonist CP55,940 (250 nM). The right panels indicate the corresponding averaged fast Fourier transformations (four epochs of 5-s recordings) of the extracellular field responses showing the reduction in the power of the gamma oscillations during the cannabinoid agonist application.

generation of principal cell synchrony in the theta and gamma frequency ranges (Whittington *et al*., 1995; Ylinen *et al*., 1995; Traub *et al*., 1996; Wang & Buzsaki, 1996). Interneurons containing CCK may synchronize via direct connections with each other (Nunzi *et al*., 1985), or could be governed by 'supernetworks' of interneuron-selective GABAergic cells that are coupled via gap junctions or conventional synapses, and contain the calcium binding protein calretinin (Freund & Buzsaki, 1996; Gulyas *et al*., 1996). Our data demonstrate that the CCK-immunoreactive basket cells and some of the calretinin-containing neurons (Katona *et al*., 1999; Tsou *et al*., 1999) express CB1 receptors, so there are at least two potential sites where cannabinoids may interfere with population oscillations. Interestingly, the power of the 40 Hz activity decreased following CB1 agonist application. The degree of activation of CB1 receptors by either their endogenous agonist or by exogenous cannabinoids is not known. Therefore, it is possible for PV-containing basket cells, which lack presynaptic CB1 receptors (see Results and Katona *et al*., 1999), to still be operational in the presence of CB1 ligands, and through their release of GABA to maintain a low level of oscillatory activity. The CCK-containing and CB1 receptor-endowed interneuron network may be responsible for the fine tuning of the oscillations, which may explain the psychoactive effects of marijuana on associative and memory processes (Felder & Glass, 1998).

Acknowledgements

This work was supported by the Howard Hughes Medical Institute, the McDonnell Foundation (T.F.F.), NIH (NS 30549) (T.F.F. and I.M.), and NIH (DA 00286, DA 11322) (K.M.). C.L. is Chercheur Qualifié of the Fonds National de la Recherche Scientifique. N.H. was supported by Bolyai Scholarship. We are grateful to Drs T.J. Görcs and K.G. Baimbridge for antisera against cholecystokinin and parvalbumin, and to E. Oszwald, Gy. Goda, K. Lengyel and B. Oyama for excellent technical assistance.

Abbreviations

ACSF, artificial cerebrospinal fluid; CB1 receptor, type 1 cannabinoid receptor; CCK, cholecystokinin; eIPSC, evoked inhibitory postsynaptic current; IPSC, inhibitory postsynaptic current; mIPSC, miniature inhibitory postsynaptic current; PV, parvalbumin; SP, substance P; TTX, tetrodotoxin.

References

Acsady, L., Katona, I., Gulyas, A.I., Shigemoto, R. & Freund, T.F. (1997) Immunostaining for substance P receptor labels GABAergic cells with distinct termination patterns in the hippocampus. *J. Comp Neurol.*, **378**, 320–336.

Ameri, A., Wilhelm, A. & Simmet, T. (1999) Effects of the endogeneous cannabinoid, anandamide, on neuronal activity in rat hippocampal slices. *Br. J. Pharmacol.*, **126**, 1831–1839.

Baimbridge, K.G. & Miller, J.J. (1982) Immunohistochemical localization of calcium-binding protein in the cerebellum, hippocampal formation and olfactory bulb of the rat. *Brain Res.*, **245**, 223–229.

Buhl, E.H., Tamas, G. & Fisahn, A. (1998) Cholinergic activation and tonic excitation induce persistent gamma oscillations in mouse somatosensory cortex *in vitro*. *J. Physiol. (Lond.)*, **513**, 117–126.

Di Marzo, V., Melck, D., Bisogno, T. & De Petrocellis, L. (1998) Endocannabinoids: endogenous cannabinoid receptor ligands with neuromodulatory action. *Trends Neurosci.*, **21**, 521–528.

Felder, C.C. & Glass, M. (1998) Cannabinoid receptors and their endogenous agonists. *Annu. Rev. Pharmacol. Toxicol.*, **38**, 179–200.

Fisahn, A., Pike, F.G., Buhl, E.H. & Paulsen, O. (1998) Cholinergic induction of network oscillations at 40 Hz in the hippocampus *in vitro*. *Nature*, **394**, 186–189.

Freund, T.F. & Buzsaki, G. (1996) Interneurons of the hippocampus. *Hippocampus*, **6**, 347–470.

Gulyas, A.I., Gorcs, T.J. & Freund, T.F. (1990) Innervation of different peptide-containing neurons in the hippocampus by GABAergic septal afferents. *Neuroscience*, **37**, 31–44.

Gulyas, A.I. & Freund, T.F. (1996) Pyramidal cell dendrites are the primary targets of calbindin D28k-immunoreactive interneurons in the hippocampus. *Hippocampus*, **6**, 525–534.

Gulyas, A.I., Hajos, N. & Freund, T.F. (1996) Interneurons containing calretinin are specialized to control other interneurons in the rat hippocampus. *J. Neurosci.*, **16**, 3397–3411.

Hampson, R.E. & Deadwyler, S.A. (1998) Role of cannabinoid receptors in memory storage. *Neurobiol. Dis.*, **5**, 474–482.

Herkenham, M., Lynn, A.B., Johnson, M.R., Melvin, L.S., de Costa, B.R. & Rice, K.C. (1991) Characterization and localization of cannabinoid receptors in rat brain: a quantitative *in vitro* autoradiographic study. *J. Neurosci.*, **11**, 563–583.

Hoffman, A.F. & Lupica, C.R. (2000) Mechanisms of cannabinoid inhibition of GABA (A) synaptic transmission in the hippocampus. *J. Neurosci.*, **20**, 2470–2479.

Katona, I., Sperlagh, B., Sik, A., Kafalvi, A., Vizi, E.S., Mackie, K. & Freund, T.F. (1999) Presynaptically located CB1 cannabinoid receptors regulate GABA release from axon terminals of specific hippocampal interneurons. *J. Neurosci.*, **19**, 4544–4558.

Kosaka, T., Katsumaru, H., Hama, K., Wu, J.Y. & Heizmann, C.W. (1987) GABAergic neurons containing the Ca^{2+}-binding protein parvalbumin in the rat hippocampus and dentate gyrus. *Brain Res.*, **419**, 119–130.

Kouznetsova, M. & Nistri, A. (1998) Modulation by substance P of synaptic transmission in the mouse hippocampal slice. *Eur. J. Neurosci.*, **10**, 3076–3084.

Ledent, C., Valverde, O., Cossu, G., Petitet, F., Aubert, J.F., Beslot, F., Bohme, G.A., Imperato, A., Pedrazzini, T., Roques, B.P., Vassart, G., Fratta, W. & Parmentier, M. (1999) Unresponsiveness to cannabinoids and reduced addictive effects of opiates in CB1 receptor knockout mice. *Science*, **283**, 401–404.

Marsicano, G. & Lutz, B. (1999) Expression of the cannabinoid receptor CB1 in distinct neuronal subpopulations in the adult mouse forebrain. *Eur. J. Neurosci.*, **11**, 4213–4225.

Matsuda, L.A., Lolait, S.J., Brownstein, M.J., Young, A.C. & Bonner, T.I. (1990) Structure of a cannabinoid receptor and functional expression of the cloned cDNA. *Nature*, **346**, 561–564.

Matthews, G. (1996) Neurotransmitter release. *Annu. Rev. Neurosci.*, **19**, 219–233.

Miles, R., Toth, K., Gulyas, A.I., Hajos, N. & Freund, T.F. (1996) Differences between somatic and dendritic inhibition in the hippocampus. *Neuron*, **16**, 815–823.

Misner, D.L. & Sullivan, J.M. (1999) Mechanism of cannabinoid effects on long-term potentiation and depression in hippocampal CA1 neurons. *J. Neurosci.*, **19**, 6795–6805.

Nunzi, M.G., Gorio, A., Milan, F., Freund, T.F., Somogyi, P. & Smith, A.D. (1985) Cholecystokinin-immunoreactive cells form symmetrical synaptic contacts with pyramidal and nonpyramidal neurons in the hippocampus. *J. Comp. Neurol.*, **237**, 485–505.

Nusser, Z., Lujan, R., Laube, G., Roberts, J.D., Molnar, E. & Somogyi, P. (1998a) Cell type and pathway dependence of synaptic AMPA receptor number and variability in the hippocampus. *Neuron*, **21**, 545–559.

Nusser, Z., Hajos, N., Somogyi, P. & Mody, I. (1998b) Increased number of synaptic GABA (A) receptors underlies potentiation at hippocampal inhibitory synapses. *Nature*, **395**, 172–177.

Paton, G.S., Pertwee, R.G. & Davies, S.N. (1998) Correlation between cannabinoid mediated effects on paired pulse depression and induction of long term potentiation in the rat hippocampal slice. *Neuropharmacology*, **37**, 1123–1130.

Pertwee, R.G. (1997) Pharmacology of cannabinoid CB1 and CB2 receptors. *Pharmacol. Ther.*, **74**, 129–180.

Raastad, M. (1995) Extracellular activation of unitary excitatory synapses between hippocampal CA3 and CA1 pyramidal cells. *Eur. J. Neurosci.*, **7**, 1882–1888.

Shigemoto, R., Nakaya, Y., Nomura, S., Ogawa-Meguro, R., Ohishi, H., Kaneko, T., Nakanishi, S. & Mizuno, N. (1993) Immunocytochemical localization of rat substance P receptor in the striatum. *Neurosci. Lett*, **153**, 157–160.

Shire, D., Carillon, C., Kaghad, M., Calandra, B., Rinaldi-Carmona, M., Le Fur, G., Caput, D. & Ferrara, P. (1995) An amino-terminal variant of the central cannabinoid receptor resulting from alternative splicing. *J. Biol. Chem.*, **270**, 3726–3731.

Tan, Y.P. & Llano, I. (1999) Modulation by K^+ channels of action potential-evoked intracellular Ca^{2+} concentration rises in rat cerebellar basket cell axons. *J. Physiol. (Lond.)*, **520**, 65–78.

Traub, R.D., Whittington, M.A., Colling, S.B., Buzsaki, G. & Jefferys, J.G. (1996) Analysis of gamma rhythms in the rat hippocampus *in vitro* and *in vivo*. *J. Physiol. (Lond.)*, **493**, 471–484.

Tsou, K., Brown, S., Sanudo-Pena, M.C., Mackie, K. & Walker, J.M. (1998) Immunohistochemical distribution of cannabinoid CB1 receptors in the rat central nervous system. *Neuroscience*, **83**, 393–411.

Tsou, K., Mackie, K., Sanudo-Pena, M.C. & Walker, J.M. (1999) Cannabinoid CB1 receptors are localized primarily on cholecystokinin-containing GABAergic interneurons in the rat hippocampal formation. *Neuroscience*, **93**, 969–975.

Twitchell, W., Brown, S. & Mackie, K. (1997) Cannabinoids inhibit N- and P/Q-type calcium channels in cultured rat hippocampal neurons. *J. Neurophysiol.*, **78**, 43–50.

Wang, X.J. & Buzsaki, G. (1996) Gamma oscillation by synaptic inhibition in a hippocampal interneuronal network model. *J. Neurosci.*, **16**, 6402–6413.

Whittington, M.A., Traub, R.D. & Jefferys, J.G. (1995) Synchronized oscillations in interneuron networks driven by metabotropic glutamate receptor activation. *Nature*, **373**, 612–615.

Ylinen, A., Soltesz, I., Bragin, A., Penttonen, M., Sik, A. & Buzsaki, G. (1995) Intracellular correlates of hippocampal theta rhythm in identified pyramidal cells, granule cells, and basket cells. *Hippocampus*, **5**, 78–90.

dc_71_10

3. számú melléklet

Pergamon

dc_71_10

PII: S0306-4522(01)00287-1

www.elsevier.com/locate/neuroscience

Neuroscience Vol. 106, No. 1, pp. 1–4, 2001

0306-4522/01 $20.00+0.00

Letter to Neuroscience

NOVEL CANNABINOID-SENSITIVE RECEPTOR MEDIATES INHIBITION OF GLUTAMATERGIC SYNAPTIC TRANSMISSION IN THE HIPPOCAMPUS

N. HÁJOS,[a] C. LEDENT[b] and T. F. FREUND[a]*

[a]Institute of Experimental Medicine, Hungarian Academy of Sciences, Budapest H-1450, Hungary

[b]IRIBHN, Université libre de Bruxelles, Brussels B-1070, Belgium

Key words: CB1 cannabinoid receptor, GABAergic transmission, mouse, paired pulse, pyramidal cell.

Psychoactive effects of cannabinoids are thought to be mediated, at least in part, by suppression of both glutamate and GABA release via CB1 cannabinoid receptor. Two types of cannabinoid receptor (CB1 and CB2) have been cloned so far. The CB1 receptors are abundantly expressed in the nervous system, whereas CB2 receptors are limited to lymphoid organs (Matsuda et al., 1990; Munro et al., 1993). Immunocytochemical and electrophysiological studies revealed that in the hippocampus CB1 receptors are expressed on axon terminals of GABAergic inhibitory interneurons (Tsou et al., 1999; Katona et al., 1999) and activation of these receptors decreases GABA release (Hájos et al., 2000). Other physiological studies pointed out the involvement of CB1 receptors in the modulation of hippocampal glutamatergic synaptic transmission and long-term potentiation (Stella et al., 1997; Misner and Sullivan, 1999), but anatomical studies could not confirm the existence of CB1 receptors on glutamatergic terminals. Here we examined cannabinoid actions on both glutamatergic and GABAergic synaptic transmission in the hippocampus of wild type (CB1+/+) and CB1 receptor knockout mice (CB1−/−). The synthetic cannabinoid agonist WIN55,212-2 reduced the amplitudes of excitatory postsynaptic currents in both wild type and CB1−/− mice, while inhibitory postsynaptic currents were decreased only in wild type mice, but not in CB1−/− animals. Our findings are consistent with a CB1 cannabinoid receptor-dependent modulation of GABAergic postsynaptic currents, but a novel cannabinoid-sensitive receptor must be responsible for the inhibition of glutamatergic neurotransmission. © 2001 IBRO. Published by Elsevier Science Ltd. All rights reserved.

*Corresponding author. Tel.: +36-1-2109400; fax: +36-1-3139498.
E-mail address: freund@koki.hu (T. F. Freund).

Abbreviations: ACSF, artificial cerebrospinal fluid; (e)EPSC, (evoked) excitatory postsynaptic current; HEPES, *N*-(2-hydroxyethyl)piperazine-*N*′-(2-ethanesulphonic acid); (e)IPSC, (evoked) inhibitory postsynaptic current; PPD, paired pulse depression; PPF, paired pulse facilitation.

We investigated cannabinoid actions on synaptic transmission in hippocampal slices prepared from CB1 cannabinoid receptor knockout (CB1−/−) and wild type mice (CB1+/+). Using whole-cell patch-clamp techniques monosynaptically evoked currents were recorded from CA1 pyramidal cells (Hájos et al., 2000). We first examined the effect of the potent cannabinoid agonist WIN55,212-2 (WIN) on glutamatergic transmission. Excitatory postsynaptic currents (EPSC) were evoked in the presence of a GABA-A receptor blocker (50 μM picrotoxin) by focal electrical stimulation delivered via a patch pipette placed into the stratum radiatum where Schaffer collaterals of CA3 pyramidal cells terminate on the dendritic spines of CA1 pyramidal cells. Bath application of 1 μM WIN caused a significant reduction (49%, $P < 0.01$) in the amplitude of eEPSCs in wild type mice (Fig. 1, Table 1) as previously reported (Ameri et al., 1999; Misner and Sullivan, 1999). Application of 1μM WIN produced a similar decrease of eEPSCs (50%, $P < 0.01$) in mice lacking CB1 (Fig. 1, Table 1). In both types of mice the widely used cannabinoid receptor antagonist SR141716A (1 μM) reversed the amplitude decrement of eEPSCs (Fig. 1, Table 1).

Subsequently we examined the effects of the same cannabinoid agonist on GABAergic neurotransmission in the CA1 region. Inhibitory postsynaptic currents (eIPSC) were evoked in the presence of an ionotropic glutamate receptor blocker (2 mM kynurenic acid) by stimulating GABAergic fibers in the perisomatic region of pyramidal cells. Similarly to the findings in dentate granule cells (Hájos et al., 2000), 1μM WIN produced a significant decrement (33%, $P < 0.01$) in the amplitude of eIPSCs in wild type, but not in CB1−/− mice (Fig. 1, Table 1).

In general, an alteration in the paired pulse facilitation (PPF) or depression (PPD) ratio by a drug indicates a presynaptic site of drug action. Such a mechanism of action has been suggested for cannabinoids by both physiological (Paton et al., 1998; Ameri et al., 1999; Misner and Sullivan, 1999) and anatomical (Katona et

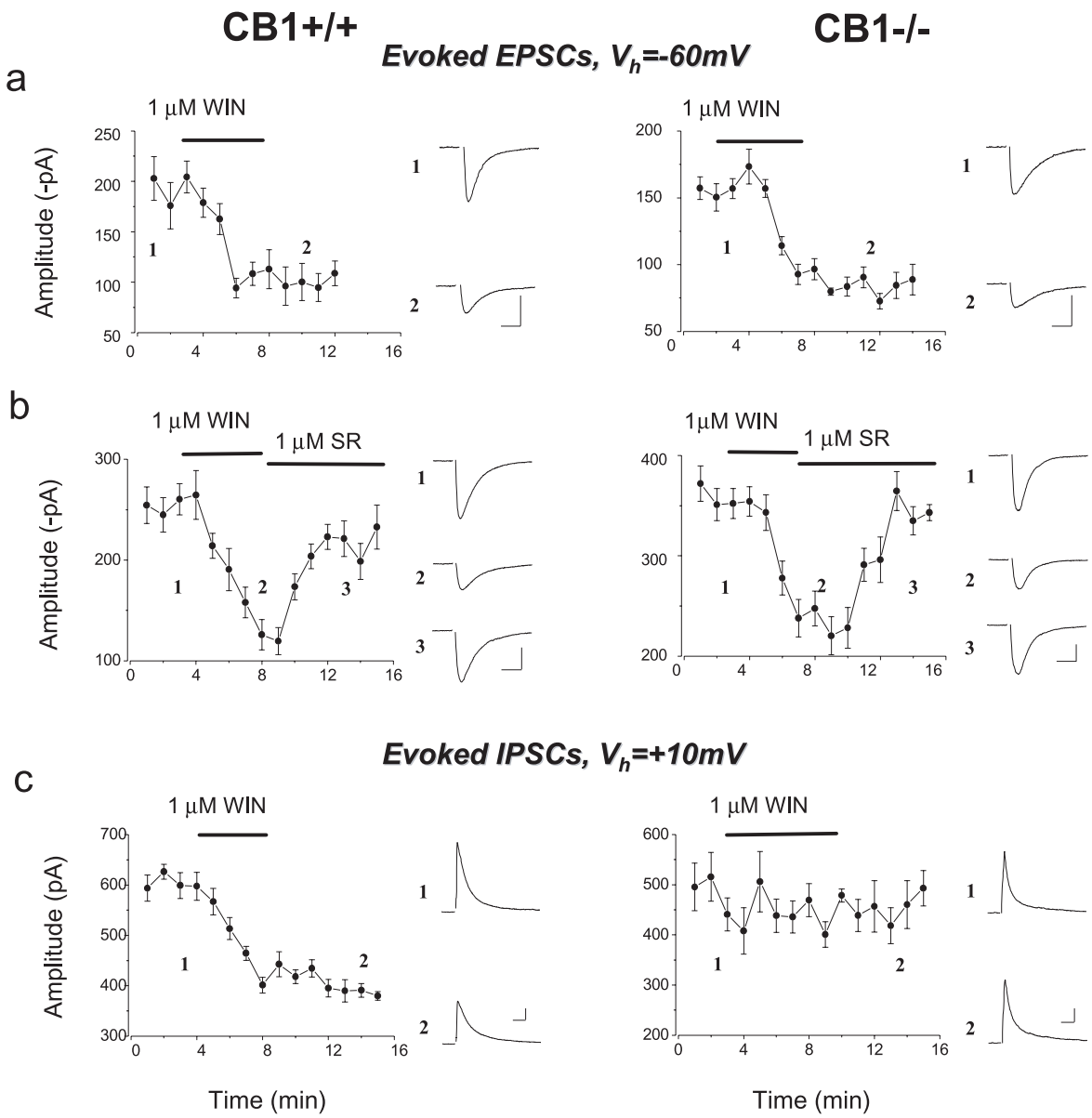

Fig. 1. The CB agonist WIN inhibits glutamatergic synaptic transmission, but not GABA release in CB1 receptor knockout mice. (a) In CA1 pyramidal neurons of both CB1+/+ and CB1−/− mice the amplitudes of monosynaptically evoked EPSCs were reduced in a similar manner by bath application of 1 μM WIN. (b) The effects of WIN could be reversed by 1 μM SR141716A (SR), a cannabinoid receptor antagonist. (c) WIN (1 μM) decreased the amplitudes of eIPSCs in CB1+/+ mice, but had no effect in CB1−/− animals. Data points represent a mean ± S.E.M. of 6 or 12 consecutive events recorded in pyramidal cells. Inserts are averaged records of 6–10 consecutive events taken at the labeled time points. The stimulus artifacts were removed from the traces. Scale bars = 100 pA and 10 ms.

al., 1999, 2000; Hájos et al., 2000) studies. We measured cannabinoid effects on PPF of EPSCs evoked at 50-ms intervals. As reported previously (Misner and Sullivan, 1999), in wild type mice 1 μM WIN significantly increased PPF (2.09 ± 0.17 in WIN compared with 1.54 ± 0.07 in control artificial cerebrospinal fluid (ACSF), respectively; $P < 0.001$, paired t-test, $n = 10$; Fig. 2). A comparable increment in PPF was observed after WIN application in mice lacking CB1 receptors (2.08 ± 0.16 in WIN compared with 1.67 ± 0.12 in control ACSF, respectively; $P < 0.001$, paired t-test, $n = 11$; Fig. 2). We next investigated cannabinoid actions on PPD of IPSCs evoked at 200-ms intervals. In wild type mice the PPD was significantly decreased after cannabinoid application (1 μM WIN) (control ACSF, 0.63 ± 0.04; in WIN, 0.75 ± 0.06; $P < 0.01$, paired t-test, $n = 4$; Fig. 2). In CB1−/− mice, no change was found in PPD before and after drug application (control ACSF, 0.78 ± 0.05; in WIN, 0.77 ± 0.04; $P > 0.05$, paired t-test, $n = 4$; Fig. 2). The PPF of eEPSCs recorded in control ACSF was similar between CB1+/+ and CB1−/− mice (1.54 ± 0.07 and 1.67 ± 0.12, respectively, Mann–Whitney U-test, $P > 0.1$). In contrast, the PPD of eIPSCs under control conditions was significantly less in knockouts compared to that recorded in wild type mice (i.e., 0.63 ± 0.04 for CB1+/+ and 0.78 ± 0.05 for CB1−/−,

Table 1. Effect of cannabinoid agonist (WIN; 1 μM) and antagonist SR141716A (SR; 1 μM) on the amplitude of evoked postsynaptic currents recorded in CA1 hippocampal pyramidal cells of adult wild type (CB1+/+) and knockout (CB1−/−) mice

Current	Mouse type	*N*	Drugs	Amplitude (pA)		Ratio D/C (%)
				Control	Drug	
eEPSC	CB1+/+	10	WIN	242.1 ± 20.9	120.9 ± 9.1	50.9 ± 2.6*
	CB1+/+	3	WIN+SR	293.7 ± 34.6	258.8 ± 25.9	88.8 ± 6.1
	CB1−/−	11	WIN	289.9 ± 29.9	144.1 ± 17.2	50.1 ± 2.8*
	CB1−/−	4	WIN+SR	324.7 ± 55.3	304.4 ± 42.4	96.5 ± 6.3
eIPSC	CB1+/+	5	WIN	415.9 ± 60.6	280.6 ± 36.7	66.9 ± 5.5*
	CB1−/−	4	WIN	495.7 ± 70.0	480.7 ± 73.9	96.3 ± 2.1

Data are the mean ± S.E.M. *Significant decrement after drug application (paired *t*-test, $P < 0.01$). The drug/control (D/C) ratio represents the decrement of the amplitude induced by WIN application.

Mann–Whitney *U*-test, $P < 0.05$). This difference was abolished by WIN application (CB1+/+ in WIN, 0.75 ± 0.06, and CB1−/− in control ACSF 0.78 ± 0.05, Mann–Whitney *U*-test, $P > 0.5$). Thus, deletion of CB1 receptors in mice altered only the action of the cannabinoid agonist on inhibitory transmission, but left its effect on glutamate release unchanged.

Earlier studies have shown the hippocampal formation to be one of the brain regions with the highest density of cannabinoid receptor binding (Herkenham et al., 1991). Recent immunocytochemical studies using specific antibodies developed against either the N- or C-terminus of the CB1 receptor showed that in the hippocampus these receptors are abundantly expressed on axon terminals of GABAergic inhibitory interneurons containing the neuropeptide cholecystokinin (Katona et al., 1999, 2000; Hájos et al., 2000). In addition, electrophysiological and pharmacological experiments confirmed the predictions of these anatomical observations by demonstrating the reduction of hippocampal GABAergic postsynaptic currents and GABA release by cannabinoids in both rodents and humans (Katona et al., 1999, 2000; Hájos et al., 2000; Hoffman and Lupica, 2000). Several physiological studies have emphasized the modulatory action of CB1 receptors in hippocampal glutamatergic synaptic transmission and long-term potentiation (Stella et al., 1997; Paton et al., 1998; Ameri et al., 1999; Misner and Sullivan, 1999). In sharp contrast with these latter observations, even the most painstaking analysis at the electron microscopic level using sensitive antibodies and techniques was unable to reliably detect CB1 receptor immunostaining in axon terminals forming asymmetric (mostly glutamatergic) synapses in the hippocampus (Katona et al., 1999, 2000; Hájos et al., 2000).

Our recent anatomical data showing the absence of CB1 receptor immunostaining in CB1−/− knockout mice in parallel with the lack of suppression of IPSC by cannabinoids strongly suggest that CB1 receptors are involved in the modulation of hippocampal GABAergic synaptic transmission (present study and Hájos et al., 2000). In contrast, the persistent cannabinoid-mediated reduction of excitatory neurotransmission in mice lacking CB1 receptors clearly indicates that a different, so far unknown receptor type must mediate cannabinoid actions in glutamatergic terminals.

Recent studies suggested that endocannabinoids, produced by postsynaptic neurons, may serve as retrograde signaling molecules inhibiting the release of both GABA (Wilson and Nicoll, 2001; Ohno-Shosaku et al., 2001)

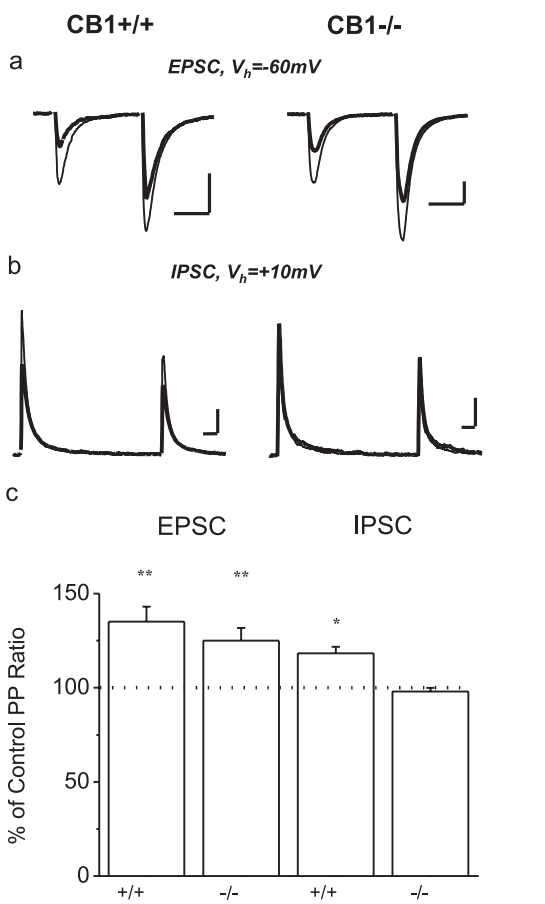

Fig. 2. PPF of EPSCs is equally enhanced by the synthetic cannabinoid (1 μM WIN) in both CB1+/+ and CB1−/− mice (a). In contrast, 1 μM WIN modifies PPD of IPSCs in wild type mice, but not in CB1 knockouts (b). The averaged traces under control conditions (thin lines) are superimposed onto those recorded after drug application (thick lines). Note that the superimposed averaged traces of eIPSCs in CB1−/− completely overlap. The stimulus artifacts were removed from the traces. Scale bars = 100 pA and 20 ms. (c) Summary plot of WIN effects on the paired pulse (PP) ratio in CB1+/+ and CB1−/− animals. All data are normalized to the PP ratios obtained in control ACSF, and are expressed as a percentage of these respective ratios (+/+, wild type; −/−, CB1 knockout mice). $^{**}P < 0.001$, $^{*}P < 0.01$.

and glutamate (Kreitzer and Regehr, 2001) from axon terminals. Thus, according to the present results, GABAergic transmission in the hippocampus will lose endogenous cannabinergic control in the CB1 knockout animals (Wilson et al., 2001), but glutamatergic transmission will not, which may introduce an imbalance in the postsynaptic activity-dependent regulation of excitation and inhibition.

EXPERIMENTAL PROCEDURES

CB1 receptor knockout and wild type mice were generated as described (Ledent et al., 1999). The genotype of mice was tested by conventional polymerase chain reaction (PCR) technique. In this study, 14th generation heterozygotes were bred together in order to generate the CB1 knockout and control mice. Adult male mice (CB1 wild type or knockout) were anaesthetized with ether and then decapitated. After opening the skull, the brain was removed and immersed into ice-cold ($\sim$4°C) modified ACSF, which contained (in mM): 126 NaCl, 2.5 KCl, 26 $NaHCO_3$, 0.5 $CaCl_2$, 5 $MgCl_2$, 1.25 NaH_2PO_4, and 10 glucose. Coronal slices of the hippocampus (300 μm in thickness) were prepared using a Lancer Series 1000 Vibratome. The slices were incubated in ACSF (containing (in mM): 126 NaCl, 2.5 KCl, 26 $NaHCO_3$, 2 $CaCl_2$, 2 $MgCl_2$, 1.25 NaH_2PO_4, and 10 glucose) for at least an hour before recordings. Whole-cell patch-clamp recordings were obtained at 34–36°C from mouse CA1 pyramidal cells visualized by infrared DIC video microscopy (Zeiss Axioscope, Germany). The intracellular solution contained (mM): 140 Cs-gluconate, 2 CsCl, 2 $MgCl_2$, 10 HEPES, 5 QX-314 and 2 Mg-ATP (pH 7.2–7.3 adjusted with CsOH; osmolarity 290–300 mOsm). Stimulation was delivered via a patch pipette. IPSCs were evoked by 0.1 Hz, while EPSCs by 0.1- or 0.2-Hz stimulation. Recordings of IPSCs were done at a holding potential of $+10 \pm 5$ mV. EPSCs were recorded at a holding potential of -60 ± 5 mV. Access resistances (between 5 and 15 MΩ, compensated 70–75%) were frequently monitored and remained constant ($\pm 20\%$) during the analyzed period. Signals were recorded with an Axopatch 200B amplifier (Axon Instruments, CA, USA), filtered at 1–2 kHz (eight-pole Bessel, FLA-01, Cygnus Technology, Fredericton, Canada), digitized at 5–10 kHz (National Instruments LabPC+A/D board, Austin, TX, USA) and analyzed off-line with SCAN software (courtesy of J. Dempster, University of Strathclyde, Glasgow, UK). Data are presented as mean $\pm$ S.E.M.

Reagents: WIN was obtained from Tocris (UK) and were dissolved in dimethyl sulphoxide (100 mM stock solution for both agonists). SR141716A (dissolved as 10 mM stock) was provided by NIDA drug supply service. Dimethyl sulphoxide by itself had no effect on postsynaptic currents up to 0.01% concentration ($n = 3$).

Acknowledgements—This work was supported by the Howard Hughes Medical Institute, the McDonnell Foundation, NIH (NS 30549), and OTKA (T32251). N.H. was supported by the Bolyai Scholarschip. C.L. is Chercheur Qualifié of the Fonds National de la Recherche Scientifique. We thank Drs I. Katona, K. Mackie, and I. Mody for comments and suggestions on the manuscript.

REFERENCES

Ameri, A., Wilhelm, A., Simmet, T., 1999. Effects of the endogeneous cannabinoid, anandamide, on neuronal activity in rat hippocampal slices. Br. J. Pharmacol. 126, 1831–1839.

Hájos, N., Katona, I., Naiem, S.S., MacKie, K., Ledent, C., Mody, I., Freund, T.F., 2000. Cannabinoids inhibit hippocampal GABAergic transmission and network oscillations. Eur. J. Neurosci. 12, 3239–3249.

Herkenham, M., Lynn, A.B., Johnson, M.R., Melvin, L.S., de Costa, B.R., Rice, K.C., 1991. Characterization and localization of cannabinoid receptors in rat brain: a quantitative *in vitro* autoradiographic study. J. Neurosci. 11, 563–583.

Hoffman, A.F., Lupica, C.R., 2000. Mechanisms of cannabinoid inhibition of GABA(A) synaptic transmission in the hippocampus. J. Neurosci. 20, 2470–2479.

Katona, I., Sperlágh, B., Sik, A., Kõfalvi, A., Vizi, E.S., Mackie, K., Freund, T.F., 1999. Presynaptically located CB1 cannabinoid receptors regulate GABA release from axon terminals of specific hippocampal interneurons. J. Neurosci. 19, 4544–4558.

Katona, I., Sperlágh, B., Maglóczky, Z., Sántha, E., Kõfalvi, A., Czirják, S., Mackie, K., Vizi, E.S., Freund, T.F., 2000. GABAergic interneurons are the targets of cannabinoid actions in the human hippocampus. Neuroscience 100, 797–804.

Kreitzer, A.C., Regehr, W.G., 2001. Retrograde inhibition of presynaptic calcium influx by endogenous cannabinoids at excitatory synapses onto Purkinje cells. Neuron 29, 717–727.

Ledent, C., Valverde, O., Cossu, G., Petitet, F., Aubert, J.F., Beslot, F., Bohme, G.A., Imperato, A., Pedrazzini, T., Roques, B.P., Vassart, G., Fratta, W., Parmentier, M., 1999. Unresponsiveness to cannabinoids and reduced addictive effects of opiates in CB1 receptor knockout mice. Science 283, 401–404.

Matsuda, L.A., Lolait, S.J., Brownstein, M.J., Young, A.C., Bonner, T.I., 1990. Structure of a cannabinoid receptor and functional expression of the cloned cDNA. Nature 346, 561–564.

Misner, D.L., Sullivan, J.M., 1999. Mechanism of cannabinoid effects on long-term potentiation and depression in hippocampal CA1 neurons. J. Neurosci. 19, 6795–6805.

Munro, S., Thomas, K.L., Abu-Shaar, M., 1993. Molecular characterization of a peripheral receptor for cannabinoids. Nature 365, 61–65.

Ohno-Shosaku, T., Maejima, T., Kano, M., 2001. Endogenous cannabinoids mediate retrograde signals from depolarized postsynaptic neurons to presynaptic terminals. Neuron 29, 729–738.

Paton, G.S., Pertwee, R.G., Davies, S.N., 1998. Correlation between cannabinoid mediated effects on paired pulse depression and induction of long-term potentiation in the rat hippocampal slice. Neuropharmacology 37, 1123–1130.

Stella, N., Schweitzer, P., Piomelli, D., 1997. A second endogenous cannabinoid that modulates long-term potentiation. Nature 388, 773–778.

Tsou, K., Mackie, K., Sanudo-Pena, M.C., Walker, J.M., 1999. Cannabinoid CB1 receptors are localized primarily on cholecystokinin-containing GABAergic interneurons in the rat hippocampal formation. Neuroscience 93, 969–975.

Wilson, R.I., Nicoll, R.A., 2001. Endogenous cannabinoids mediate retrograde signaling at hippocampal synapses. Nature 410, 588–592.

Wilson, R.I., Kunos, G., Nicoll, R.A. (2001) Presynaptic specificity of endocannabinoid signaling in the hippocampus. Neuron, in press.

(*Accepted* 8 *July* 2001)

dc_71_10

4. számú melléklet

dc_71_10

Pergamon

Neuropharmacology 43 (2002) 503–510

NEURO PHARMACOLOGY

www.elsevier.com/locate/neuropharm

Pharmacological separation of cannabinoid sensitive receptors on hippocampal excitatory and inhibitory fibers

N. Hájos, T.F. Freund *

Department of Functional Neuroanatomy, Institute of Experimental Medicine, Hungarian Academy of Sciences, Budapest, H-1450 Hungary

Received 10 May 2002; received in revised form 11 July 2002; accepted 16 July 2002

Abstract

Our earlier studies demonstrated that in the hippocampus, cannabinoids suppress inhibitory synaptic transmission via CB_1 cannabinoid receptors, whereas a novel cannabinoid-sensitive receptor modulates excitatory synapses (Katona, I. et al., Journal of Neuroscience 19 (1999) 4544; Hájos, N. et al., European Journal of Neuroscience 12 (2000) 3239; Hájos, N. et al., Neuroscience 106 (2001) 1). The novel receptor does not correspond to CB_2, since this receptor type is not expressed in the brain (Munro, S. et al., Nature 365 (1993) 61). Recent binding experiments revealed that the synthetic cannabinoid WIN 55,212-2 binds with lower affinity to brain membranes of CB_1 receptor-knockout mice indicating that pharmacological differences exist between these two types of cannabinoid receptors in the hippocampus (Breivogel et al., Molecular Pharmacology 60 (2001) 155). To analyze this difference in detail, we first determined the EC_{50} values of WIN 55,212-2 for excitatory and inhibitory transmission in rat hippocampal slices using whole-cell patch-clamp recordings. The estimated EC_{50} value for inhibitory postsynaptic currents (IPSC) evoked by electrical stimulation in CA1 pyramidal cells was 0.24 μM, whereas for excitatory postsynaptic currents (EPSC) it was 2.01 μM, respectively. The cannabinoid antagonist, AM251, blocked the WIN 55,212-2-induced inhibition of evoked IPSCs, but not of EPSCs, providing evidence for its selectivity for CB_1. We then tested the hypothesis of whether the cannabinoid effect on hippocampal excitatory neurotransmission is mediated via receptors with an affinity for vanilloid ligands. Co-application of the vanilloid receptor antagonist capsazepine (10 μM) with cannabinoids (WIN55,212-2 or CP55,940) prevented the reduction of EPSCs, but not of IPSCs. The amplitude of evoked EPSCs was also suppressed by superfusion of the vanilloid receptor agonist capsaicin (10 μM), an effect which could also be antagonized by capsazepine. In contrast, capsaicin did not change the amplitude of evoked IPSCs.

These results demonstrate that WIN 55,212-2 is an order of magnitude more potent in reducing GABAergic currents via CB_1 than in inhibiting glutamatergic transmission via the new CB receptor. The sensitivity of the new CB receptor (and EPSCs) to vanilloid ligands, but not to the cannabinoid antagonist AM251, represents another pharmacological tool to distinguish the two receptors, since CB_1 (and its effect on IPSCs) is not modulated by vanilloids, but is antagonized by AM251.

Keywords: GABA; Glutamate; Cannabinoids; CB_1 receptor; Hippocampus; Rat

1. Introduction

A well-known effect of a synthetic cannabinoid WIN 55,212-2 is the inhibition of both glutamatergic and GABAergic neurotransmission in several brain regions, including the hippocampus, by acting on presynaptic terminals (Misner and Sullivan, 1999; Hájos et al., 2000; Hoffman and Lupica, 2000). To date, only one cloned cannabinoid receptor (CB_1) has been identified in the CNS (Matsuda et al., 1990). Using light and electron microscopic techniques, immunocytochemical analyses revealed that CB_1 receptors are present on a subset of GABAergic axon terminals in the hippocampus (Katona et al., 1999; Hájos et al., 2000) and in the basolateral amygdala (Katona et al., 2001). Glutamatergic terminals, however, were found to be immunonegative for CB_1. Combined physiological and pharmacological studies in CB_1 receptor knockout mice verified that cannabinoids suppress hippocampal inhibition via CB_1 receptors (Hájos et al., 2000, 2001; Wilson et al., 2001). In contrast, the reduction of glutamatergic transmission by WIN 55,212-2 was unchanged in mice lacking CB_1

* Corresponding author. Tel.: +36-1-2109410; fax: +36-1-2109412.
E-mail address: freund@koki.hu (T.F. Freund).

0028-3908/02/$ - see front matter © 2002 Elsevier Science Ltd. All rights reserved.
PII: S0028-3908(02)00157-0

receptors compared to wild types (Hájos et al., 2001). In agreement with these findings, binding studies in CB_1 receptor knockout mice have demonstrated that WIN 55,212-2 could still stimulate GTPγS binding in brain membranes, although with reduced efficacy (Breivogel et al., 2001). Taken together, in the hippocampus, CB_1 receptors mediate inhibition of GABA release, while a different, so far unidentified cannabinoid sensitive receptor should be responsible for the modulation of glutamatergic synaptic transmission**.** The routinely used cannabinoid antagonist SR 141716A does not distinguish between CB_1 and the new CB receptor, as it was shown to antagonize WIN 55,212-2-induced inhibition of both eIPSCs and EPCSs (Misner and Sullivan, 1999; Hájos et al., 2000; Hoffman and Lupica, 2000; Hájos et al., 2001)**.**

One of the putative endogenous ligands of cannabinoid receptors is anandamide (Devane et al., 1992). Recent data, however, indicate that anandamide can also act as a full agonist on VR1 vanilloid receptors (Zygmunt et al., 1999; Smart et al., 2000), and has a substantial structural similarity to vanilloid ligands such as capsaicin (Szallasi and Di Marzo, 2000). The presence of VR1 receptors in the brain, including the hippocampus, has been shown by both binding studies and immunostaining (Acs et al., 1996; Mezey et al., 2000; Sanchez et al., 2001), although other studies have found no VR1 expression in the CNS (e.g. Caterina et al., 1997). In addition, recently published data indicated that anandamide and vanilloid ligands might act at the same site in the hippocampus (Al-Hayani et al., 2001). Thus, it seems possible that vanilloid ligands can differentially modulate the effects of cannabinoids on hippocampal excitation and inhibition. To elucidate whether these differences underlie a possible pharmacological separation between two distinct types of cannabinoid receptor present on excitatory and inhibitory axon terminals, we first compared the potency of WIN 55,212-2 to reduce excitatory and inhibitory postsynaptic currents (EPSC, IPSC) and demonstrated that—unlike SR 141716A—the cannabinoid antagonist AM251 is selective for CB_1, and does not affect cannabinoid-induced reduction of EPSCs. The effect of vanilloid ligands was then tested on both types of neurotransmission, which turned out to be another tool to distinguish CB_1 and the new CB receptor.

2. Materials and methods

Experiments were carried out according to the guidelines of the institutional ethical codex and the Hungarian Act of Animal Care and Experimentation (1998. XXVIII. section 243/1998), which is in full agreement with the regulation of animal experiments in the European Union. All efforts were made to minimize pain and suffering and to reduce the number of animals used.

Male Wistar rats (15–22 days old) were deeply anaesthetized with sodium pentobarbital (70 mg/kg, i.p.) or with isoflurane followed by decapitation. After opening the skull, the brain was quickly removed and immersed into ice-cold (~4°C) artificial cerebrospinal fluid (ACSF), which contained (in mM) 126 NaCl, 2.5 KCl, 26 $NaHCO_3$, 2 $CaCl_2$, 2 $MgCl_2$, 1.25 NaH_2PO_4, and 10 glucose. Coronal or horizontal slices of the hippocampus (350–400 μm in thickness) were prepared using a Lancer Series 1000 Vibratome or a Leica VT1000S Vibratome. Then the slices were incubated in ACSF at 32–33°C for at least 1 h before recordings. Whole-cell patch-clamp recordings were obtained at 33–35°C from CA1 pyramidal cells or dentate granule cells visualized by infrared DIC videomicroscopy (Zeiss Axioscope, Germany) using a submerged type chamber. To isolate the excitatory postsynaptic currents (EPSCs), slices were perfused with ACSF containing either 10–30 μM bicuculline methiodide or 50–70 μM picrotoxin to block $GABA_A$ receptor mediated transmission. To record inhibitory postsynaptic currents (IPSCs), the ACSF contained 2–3 mM kynurenic acid to eliminate ionotropic glutamatergic transmission. Patch electrodes were pulled from borosilicate glass capillaries with an inner filament (1.5 mm O.D.; 1.1 mm I.D., Sutter Instruments Co., CA, or 1.5 mm O.D.; 1.12 mm I.D., Hilgenberg, Germany) using a Sutter P-87 puller, and had resistances of 3–6 MΩ when filled with the intracellular solution. The intracellular solution contained (in mM) either 140 Cs-gluconate, 2 CsCl, 2 $MgCl_2$, 10 HEPES, 5 QX-314 and 2 Mg-ATP or 140 CsCl 4 NaCl, 1 $MgCl_2$, 10 HEPES, 3 Mg-ATP, 0.05 EGTA, and 5 QX-314 (pH 7.2–7.3 adjusted with CsOH; osmolarity 285–300 mOsm). For EPSCs, recordings were done at a holding potential of −65 mV. At the beginning of our study, IPSCs were recorded at +10 mV using Cs-gluconate based solution, but it has been shown that endocannabinoids could be released from the postsynaptic cell as a result of depolarization, therefore we repeated our experiments using CsCl based solution at a holding potential of −65 mV. Beacuse no differences were noticed in the inhibitory potency of cannabinoids on IPSCs recorded at −65mV compared to those found at +10 mV, the data were pooled**.** Data were corrected for the pipette offset that varied between ±5 mV. Access resistances (between 4–15 MΩ, compensated 70–75%) were frequently monitored and remained constant (±25%) during the period of analysis. Electrical stimulation was delivered via a patch pipette or a theta glass pipette (Sutter Instruments) containing ACSF at 0.1 or 0.2 Hz using a Supertech timer and isolator (Supertech LTD, Pécs, Hungary). To evoke EPSCs, the pipette was placed either into the stratum radiatum (for CA1 pyramidal cells) or into the middle part of the stratum moleculare (for granule cells). IPSCs were evoked by an electrode placed into the perisomatic region of principal cells. Signals were recorded

with an Axopatch 200B amplifier (Axon Instruments, CA), filtered at 2 kHz (eight-pole Bessel, FLA-01, Cygnus Technology, Fredericton, Canada), digitized at 5–10 kHz (National Instruments LabPC+ A/D board, Austin, TX) and analyzed off-line with SCAN software (courtesy of J. Dempster) or with the EVAN program (courtesy of I. Mody). Student's paired *t*-test was used to compare changes in the mean amplitude after drug application, $p < 0.05$ was considered significant. Data are presented as mean ± SEM.

The drugs were perfused until the maximal effect was seen. The time needed for the maximal inhibition (4–7 min) correlated with the depth of the recorded cells and the solvent used for the dilution of different drugs (see below). Each stock solution was tested on both EPSCs and IPSCs. Antagonists and agonists were co-perfused for at least 7–9 min.

The concentration response relationship for WIN 55,212-2 was obtained as follows: in the case of evoked EPSCs, axons of CA3 pyramidal cells with presumably homogenous characteristics were stimulated. The stimulation of inhibitory fibers, however, gives rise to mixed IPSCs originating from both CB_1 receptor positive and negative axon terminals (Katona et al., 1999; Hájos et al., 2000). In a given experiment, WIN 55,212-2 was usually added to the bath in two different concentrations consecutively. The inhibition was calculated as the amplitude of PSCs after WIN 55,212-2 treatment divided by the control amplitude, and the value was subtracted from 1. EC_{50} values were estimated by fitting a sigmoid curve to the points of the dose response plot using the Prism 3.0 version of GraphPad software (San Diego, CA). In these experiments, only WIN 55,212-2 dissolved in 0.1N HCl was used.

Reagents: WIN55,212-2 (RBI) and CP55,940 (Tocris) were dissolved either in DMSO (100 mM stock solution for both agonists) or in 2-hydroxypropyl-β-cyclodextrin (RBI, 10mM stock for both agonists). Later on we found that WIN 55,212-2 can be dissolved in 0.1N HCl giving a 10 mM stock solution. We observed that the time needed for the inhibition of postsynaptic currents in slice preparation using the WIN 55,212-2 dissolved in 0.1N HCl was much shorter compared to those found in the cases of WIN 55,212-2 dissolved in DMSO or in 2-hydroxypropyl-β-cyclodextrin. Adding 0.1N HCl to the ACSF caused a small decrement in the pH (0.1–0.15), but to ensure that this pH change has no effect on the reduction of EPSCs or IPSCs, we added the same amount of HCl into the control solution as well. AM251, capsaicin, and capsazepine (100 mM stock solution in DMSO) were obtained from Tocris. DMSO or 2-hydroxypropyl-β-cyclodextrin by itself had no effect on postsynaptic currents up to 0.01% concentration ($n = 6$). The perfusion of the drugs did not change the holding current during the recordings**.** Bicuculline, picrotoxin, and kynurenic acid were purchased from Sigma.

3. Results

3.1. The synthetic cannabinoid WIN 55,212-2 reduces monosynaptically evoked EPSCs and IPCSs with different affinity

Binding studies obtained in CB_1 receptor knockout mice (Breivogel et al., 2001) suggest that the cannabinoid ligand WIN 55,212-2 may have a lower affinity to cannabinoid sensitive receptors present on glutamatergic axon terminals compared to CB_1 receptors located on GABAergic axon endings. Therefore we performed concentration response analyses for the inhibitory effect of WIN 55,212-2 on both EPSCs and IPSCs evoked by focal electrical stimulation in CA1 pyramidal cells. As shown in Fig. 1, WIN 55,212-2 inhibited the evoked currents in a dose dependent manner, with different estimated EC_{50} values. The estimated values of EC_{50} for evoked EPSCs was 2.01 μM, while for evoked IPSCs it was 0.24 μM.

3.2. The vanilloid receptor antagonist, capsazepine, but not the CB1 receptor specific antagonist AM251, prevents the cannabinoid-mediated inhibition of EPSCs

As earlier data showed (Misner and Sullivan, 1999; Hájos et al., 2000; Hoffman and Lupica, 2000; Hájos et al., 2001), bath application of 1–2 μM WIN 55,212-2 significantly reduced the amplitude of both evoked EPSCs (eEPSCs; 46%, $p < 0.01$) and IPSCs (eIPSCs; 37%, $p < 0.01$) in CA1 pyramidal cells (Fig. 2A, B; Tables 1 and 2). These studies confirmed that the cannabinoid receptor antagonist, SR 141716A, blocked WIN

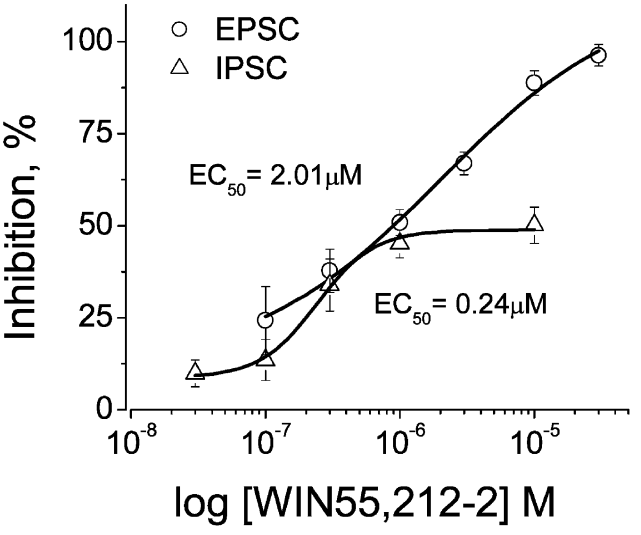

Fig. 1. Concentration response relationship for the inhibitory effect of WIN 55,212-2 on evoked IPSCs and EPSCs in CA1 pyramidal cells. Each point represents a mean ± S.E.M. for 3-8 individual cells. The estimated values of EC_{50} from the fitted curves are 0.24 μM for IPSCs and 2.01 μM for EPSCs, respectively.

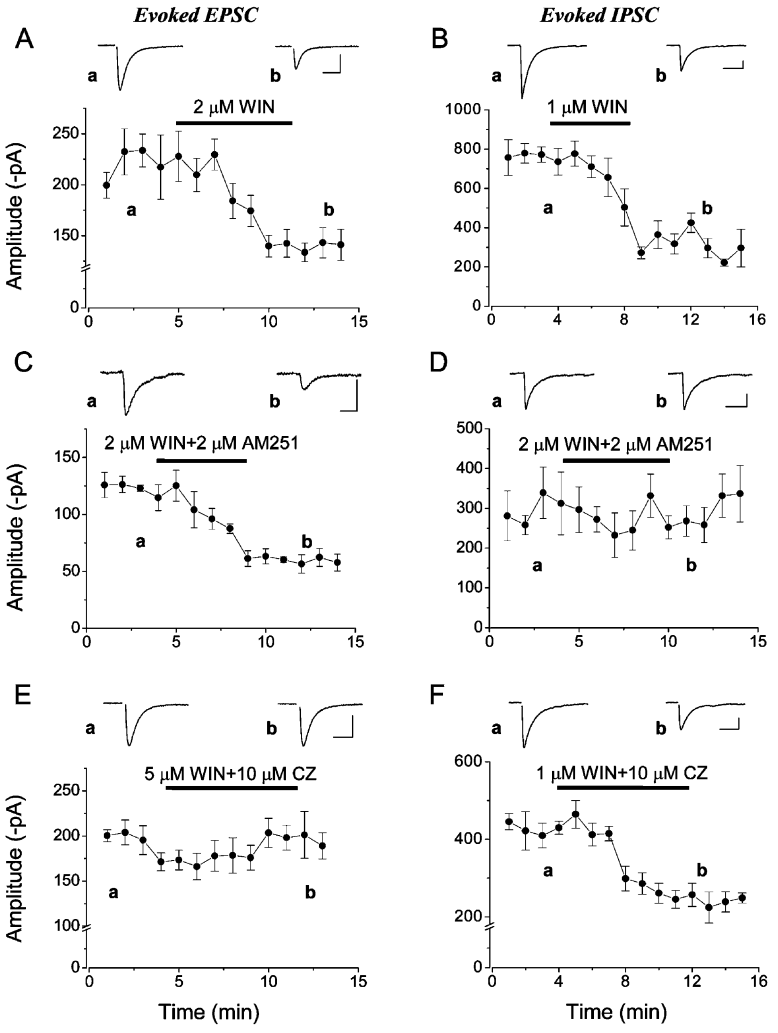

Fig. 2. Effect of cannabinoid receptor agonist and vanilloid receptor antagonist on postsynatic currents evoked by local electrical stimulation. Whole-cell patch-clamp recordings were obtained from CA1 pyramidal cells using CsCl based intrapipette solution. Both EPSCs and IPSCs, appearing as inward currents, were recorded at a holding potential of −65 mV. (A, B) Bath application of a synthetic cannabinoid WIN 55,212-2 (1–2 μM, WIN) reduced the amplitude of both the monosynaptically evoked EPSCs and IPSCs. (C, D) Co-application of the cannabinoid agonist with the antagonist AM251 (2 μM) prevented the suppression of eIPSC, but not the eEPSCs amplitude. (E, F) In contrast, co-application of WIN 55,212-2 with the vanilloid receptor antagonist capsazepine (10 μM, CZ) blocked the inhibition of eEPSCs, but not of eIPSCs. All data points on the plots represent a mean ± SEM of six or twelve consecutive events recorded in pyramidal cells (IPSCs were evoked by 0.1Hz, while EPSCs by 0.1 or 0.2 Hz). Inserts are averaged records of 6–8 consecutive events taken at the labeled time points. Scale bars, 10 ms and 100 pA for EPSCs, and 25 ms and 100 pA for IPSCs, respectively.

55,212-2-induced inhibition of both EPSCs and IPSCs (see e.g. Fig. 1 in Hájos et al., 2001). Thus, SR 141716A was unable to distinguish between CB_1 and the new CB receptor. In our search for an antagonist with a potential selectivity for CB_1 (Gatley et al., 1996), we first employed AM251. This experiment was successful, since co-application of AM251 (2μM) with WIN 55,212-2 blocked the inhibition of eIPSCs (1-2 μM WIN 55,212-2), but not of eEPSCs (2-5 μM WIN 55,212-2; Fig. 2C, D; Tables 1 and 2).

We then tested the modulation of cannabinoid effects by vanilloid receptor antaginist. Co-application of a vanilloid receptor antagonist, capsazepine (10 μM), with WIN 55,212-2 prevented the reduction of eEPSCs (2–5 μM WIN 55,212-2), but not of eIPSCs (1 μM WIN 55,212-2; Fig. 2E, F; Tables 1 and 2). We also tested the effect of another frequently used cannabinoid agonist, CP 55,940 on EPSCs of Schaffer collaterals. 1 μM CP 55,940 significantly inhibited the amplitude of eEPSCs recorded in CA1 pyramidal cells (53%, $p < 0.05$; Table 1).

3.3. The cannabinoid agonist, CP 55,940, inhibits EPSCs in dentate gyrus, which can be blocked by vanilloid receptor antagonist, capsazepine

The majority of cortical excitation enters the hippocampus via the dentate gyrus. To investigate the canna-

Table 1
Pharmacological properties of EPSCs evoked by local electrical stimulation in hippocampal principal cells

Cell types	N	Drugs	Amplitude (pA)		Ratio D/C, %
			Control	Drug	
CA1 PC	8	WIN	246.1±28.6	141.1±25.6	**54.4±6.3∗**
CA1 PC	4	WIN+AM251	172.6±50.6	79.1±17.3	**48.6±6.5#**
CA1 PC	8	WIN+CZ	210.6±54.0	206.9±59.7	94.2±4.1
CA1 PC	6	CP	186.1±33.1	84.6±13.9	**46.8±3.3#**
GC	7	CP	102.3±17.0	52.9±10.5	**50.2±4.5∗**
GC	6	CP+CZ	269.1±73.9	271.4±73.6	100.3±3.4
CA1 PC	10	Capsaicin	199.9±33.7	124.7±24.8	**58.5±3.7∗**
CA1 PC	4	Caps.+CZ	110.3±16.7	105.4±14.0	96.7±5.0
GC	7	Capsaicin	257.8±41.8	153.5±36.9	**55.8±6.9∗**
GC	4	Caps.+CZ	202.9±28.0	188.5±23.9	93.3±1.9

Data are the mean ± SEM. Significant decrement after drug application indicated in bold (paired *t*-test, ∗ for $p < 0.01$ and # for $p < 0.05$). The drug/control (D/C) ratio represents the decrement of the amplitude induced by drug application. PC, pyramidal cell; GC, granule cells; CZ, capsazepine; Caps., capsaicin.

Table 2
Pharmacological properties of IPSCs evoked by local electrical stimulation in hippocampal principal cells

Cell types	N	Drugs	Amplitude (pA)		Ratio D/C, %
			Control	Drug	
CA1 PC	8	WIN	620.3±104.3	389.3±69.2	**63.3±3.8∗**
CA1 PC	4	WIN+AM251	348.4±67.6	344.5±69.9	98.9±3.1
CA1 PC	6	WIN+CZ	442.3±67.7	305.4±54.9	**68.1±2.7∗**
GC	5	CP	330.5±39.5	239.4±22.9	**62.5±9.1∗**
GC	4	CP+CZ	277.0±82.0	168.5±56.8	**58.2±4.1#**
CA1 PC	4	Capsaicin	448.3±56.3	431.8±46.0	97.3±3.7
GC	4	Capsaicin	406.7±36.3	400.2±35.6	98.5±1.9

Data are the mean ± SEM. Significant decrement after drug application indicated in bold (paired *t*-test, ∗ for $p < 0.01$ and # for $p < 0.05$). The drug/control (D/C) ratio represents the decrement of the amplitude induced by drug application. PC, pyramidal cell; GC, granule cells; CZ, capsazepine.

binoid sensitivity of cortical afferents in addition to the local GABAergic fibers at this important stage of the trisynaptic loop, evoked currents were recorded in dentate granule cells. 1 μM CP 55,940 suppressed both EPSC and IPSC amplitudes in dentate granule cells (50% for EPSCs and 37% for IPSCs, respectively, $p < 0.01$; Fig. 3A, B; Tables 1 and 2), which could be reversed by washout. We also examined the blocking effect of capsazepine on CP 55,940-induced reduction of evoked currents in dentate granule cells. Comparable to the observation in CA1 pyramidal cells, co-application of 10 μM capsazepine with 1 μM CP 55,940 abolished the reduction of eEPSCs, but not of eIPSCs (42%, $p < 0.05$; Fig. 3C, D; Tables 1 and 2). These data suggest that cannabinoid suppression of evoked EPSCs, but not of evoked IPSCs, can be selectively blocked by the vanilloid receptor antagonist capsazepine in both the CA1 region and the dentate gyrus.

3.4. The vanilloid receptor agonist capsaicin reduces evoked EPSCs, but not IPSCs

As a next step, we investigated the effect of a widely used vanilloid receptor agonist capsaicin on evoked currents. Bath application of 10 μM capsaicin significantly reduced the amplitude of eEPSCs in both CA1 pyramidal cells (42%, $p < 0.01$; Fig. 4A, Table 1) and dentate granule cells (45%, $p < 0.01$; Table 1), and washout reversed the reduction of the EPSC amplitude. Desensitization of the response was tested by the subsequent application of capsaicin after washout, which caused a similar magnitude of inhibition ($57.4 \pm 0.03\%$ for the first, and $53.3 \pm 0.04\%$ for the second application, respectively; $n = 3$). The effect of capsaicin could be prevented by co-application of 10 μM capsazepine (Fig. 4B; Table 1). In contrast, the amplitude of eIPSCs was unaffected by 10 μM capsaicin application (Fig. 4C;

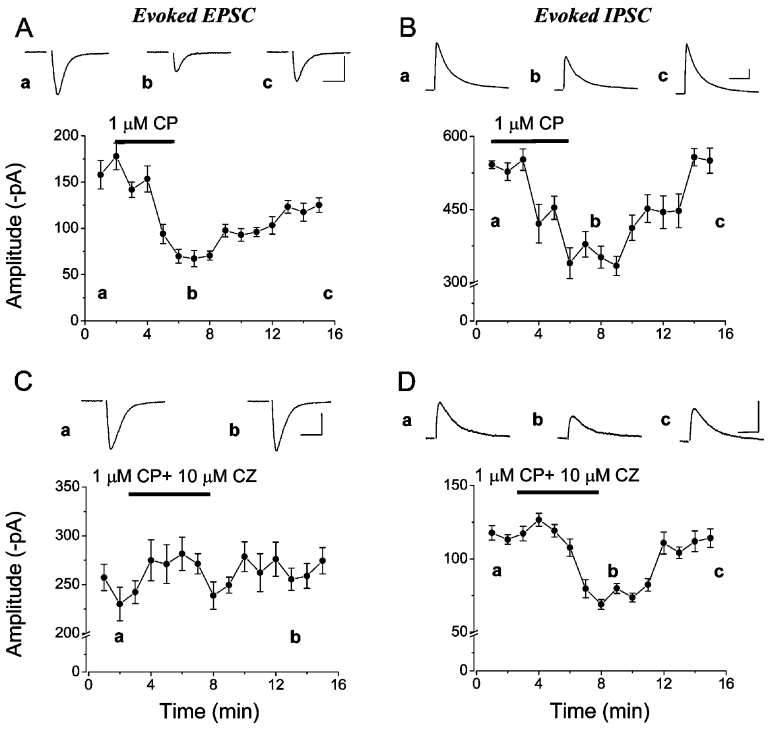

Fig. 3. Effect of synthetic cannabinoid agonist and vanilloid receptor antagonist on the amplitude of evoked postsynaptic currents in dentate granule cells using Cs-gluconate based intrapipette solution. EPSCs recorded at a holding potential of −65 mV and IPSCs measured at +10 mV appear as inward or outward currents, respectively. (A, B) After bath application of the cannabinoid receptor agonist CP 55,940 (1 μM, CP), the amplitude of both evoked EPSCs and IPSCs was suppressed, which could be reversed by washout. (C, D) Co-application of the vanilloid receptor antagonist capsazepine (10 μM, CZ) with 1 μM CP 55,940 abolished the reduction of the eEPSC amplitude, but did not prevent the suppression of amplitude of eIPSCs. Presentation of data is the same as for Fig. 2. Scale bars, 10 ms and 100 pA for EPSCs, and 25 ms and 100 pA for IPSCs, respectively.

Table 2). Taken together, these data indicate that the vanilloid receptor agonist, capsaicin, modulates EPSCs, but not IPSCs, in the hippocampus and dentate gyrus showing the same selectivity as the capsazepine antagonism of cannabinoid effects.

4. Discussion

The ten-fold difference in EC_{50} values of WIN 55,212-2 mediated inhibition of evoked EPSCs and IPSCs strongly support our previous conclusion that distinct receptors regulate cannabinoid inhibition of hippocampal glutamatergic and GABAergic synaptic transmission. An EC_{50} value for inhibition of IPSCs (0.138 μM) comparable to that obtained in our present study (0.24 μM) was estimated in hippocampal slice preparation by Hoffman and Lupica (2000). Furthermore, [^{35}S]GTPγS binding stimulated by WIN 55,212-2 has given an EC_{50} value of 0.17 μM in wild type mice (Breivogel et al., 2001), also in agreement with the above data. In addition, our estimated EC_{50} value for EPSCs (2.01 μM) was a magnitude higher, which agrees well with the value (EC_{50} of 1.8 μM) obtained from the [^{35}S]GTPγS binding study using CB_1 receptor knockout mice (Breivogel et al., 2001). Remarkably, only glutamatergic, but not GABAergic, transmission could be modulated by WIN 55,212-2 in the hippocampus of these mice (Hájos et al., 2001).

In the binding study of Breivogel et al. (2001), other synthetic cannabinoids (e.g. CP 55,940) had no effect on stimulation of [^{35}S]GTPγS binding in brain membranes of CB_1 knockouts. Our recent finding that CP 55,940 was able to reduce the glutamatergic transmission both in the CA1 region of the hippocampus and in the dentate gyrus seems to disagree with the binding data. The discrepancy could be explained by the possibility that the ratio of membranes derived from the hippocampus and/or cortex in the total brain membrane preparations was insufficient to give a significant value for the [^{35}S]GTPγS binding (membranes from hippocampus were not directly tested). Alternatively, the receptors identified by Breivogel et al. (2001) and the present study may be different.

Earlier electrophysiological data demonstrating cannabinoid-mediated reduction in evoked EPSC amplitude, which could be antagonized by SR 141716A, were misinterpreted as being mediated by CB_1 receptors (Ameri et al., 1999; Misner and Sullivan, 1999), because at that time SR 141716A was thought to be a selective antagon-

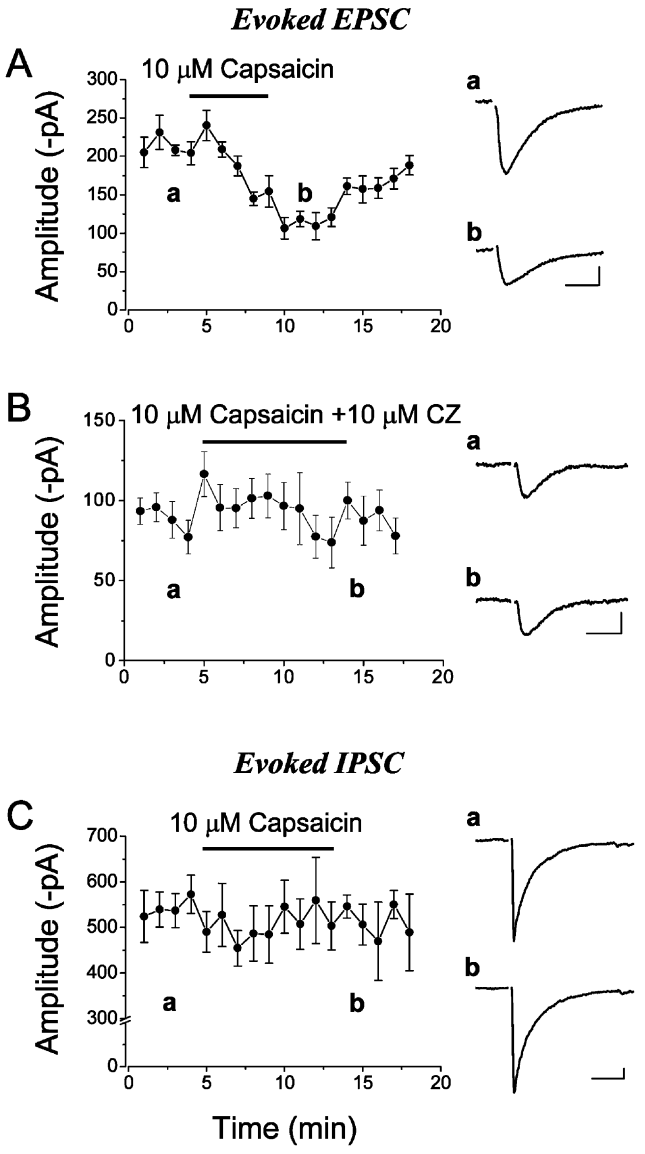

Fig. 4. Vanilloid receptor ligands alter the amplitude of evoked EPSCs but not of evoked IPSCs. 10 μM capsaicin, a vanilloid receptor agonist, suppressed the amplitude of evoked EPSCs (A) but not of evoked IPSCs (C) in CA1 pyramidal cells using CsCl based intracellular solution. (B) The reduction of eEPSC amplitude could be prevented by co-application of the vanilloid receptor antagonist capsazepine (10 μM, CZ). Presentation of data is the same as for Fig. 2. Scale bars, 10 ms and 50 pA for EPSCs, and 10 ms and 100 pA for IPSCs, respectively.

ist of CB_1. Our data clearly showed that cannabinoid effects on glutamatergic transmission survive in CB_1 receptor knockout mice, and can still be antagonized by SR 141716A, thus in cannot be selective for CB_1 (Hájos et al., 2001). In the present study, our quest for an antagonist that is selective for the CB_1 cannabinoid receptor was successful, since AM251 proved to have no effect on the cannabinergic reduction of evoked EPSCs, while it readily antagonized the reduction of eIPSCs.

In addition, our further results clearly suggest that vanilloid receptor ligands act selectively on glutamatergic, but not on GABAergic, neurotransmission. The question arises whether these ligands bind to VR1 receptors or to a novel, pharmacologically different, cannabinoid-sensitive receptor type present on the excitatory axon terminals. We suggest that the latter possibility is more likely for several reasons. First, VR1 receptors do not bind WIN 55,212-2 on sensory nerves (Zygmunt et al., 1999), which is the opposite of our results in the hippocampus. The second argument is the well-known desensitization effect of capsaicin (Jancsó and Jancsó, 1949). Bath application of capsaicin significantly desensitizes VR1 receptors on the periphery, therefore only a much smaller response is observed on the second application of this agonist (e.g. Dray et al., 1989; Docherty et al., 1991; Caterina et al., 1997), which does not match with our measurements (see Results). Third, the VR1 receptor forms a non-selective cation channel (Caterina et al., 1997), whereas cannabinoid action on hippocampal glutamatergic terminals is mediated via pertussis toxin-sensitive G-proteins (Misner and Sullivan, 1999). Thus, both the synthetic cannabinoids and vanilloid ligands in the hippocampus might act on glutamatergic transmission via a novel receptor, which is different from VR1 or CB_1.

A recent paper by Al-Hayani et al. (2001) showed that the endocannabinoid anandamide decreased the second of a pair of population spikes evoked in the hippocampus, which could be blocked by capsazepine, and mimicked by the vanilloid receptor agonists (capsaicin and resiniferatoxin). Furthermore, anandamide is able to reduce the field EPSPs evoked by Schaffer collaterals (Ameri et al., 1999), whereas in the binding study of Breivogel et al. (2001), this endocannabinoid could still stimulate [^{35}S]GTPγS binding in mice lacking CB_1 receptors. In summary, these observations together with our data showing the selective modulation of glutamatergic neurotransmission by vanilloids implies that a novel presynaptic G-protein coupled receptor regulates glutamate release from axon terminals of hippocampal and cortical pyramidal neurons. This receptor is sensitive to both cannabinoid (anandamide, WIN 55,212-2, CP 55,940, and SR141716A) and vanilloid (capsaicin and capsazepine) ligands, but is not affected by the apparently CB_1 selective antagonist, AM251.

Acknowledgements

This work was supported by OTKA (No: T32251), the Howard Hughes Medical Institute, and NIH (NS30549). N.H. was supported by Bolyai Scholarship. We thank Drs I. Mody and I. Katona for comments on the manuscript.

References

Acs, G., Palkovits, M., Blumberg, P.M., 1996. Specific binding of [3H]resiniferatoxin by human and rat preoptic area, locus ceruleus, medial hypothalamus, reticular formation and ventral thalamus membrane preparations. Life Sciences 59, 1899–1908.

Al-Hayani, A., Wease, K.N., Ross, R.A., Pertwee, R.G., Davies, S.N., 2001. The endogenous cannabinoid anandamide activates vanilloid receptors in the rat hippocampal slice. Neuropharmacology 41, 1000–1005.

Ameri, A., Wilhelm, A., Simmet, T., 1999. Effects of the endogeneous cannabinoid, anandamide, on neuronal activity in rat hippocampal slices. British Journal of Pharmacology 126, 1831–1839.

Breivogel, C.S., Griffin, G., Di Marzo, V., Martin, B.R., 2001. Evidence for a new G protein-coupled cannabinoid receptor in mouse brain. Molecular Pharmacology 60, 155–163.

Caterina, M.J., Schumacher, M.A., Tominaga, M., Rosen, T.A., Levine, J.D., Julius, D., 1997. The capsaicin receptor: a heat-activated ion channel in the pain pathway. Nature 389, 816–824.

Devane, W.A., Hanus, L., Breuer, A., Pertwee, R.G., Stevenson, L.A., Griffin, G., Gibson, D., Mandelbaum, A., Etinger, A., Mechoulam, R., 1992. Isolation and structure of a brain constituent that binds to the cannabinoid receptor. Science 258, 1946–1949.

Docherty, R.J., Robertson, B., Bevan, S., 1991. Capsaicin causes prolonged inhibition of voltage-activated calcium currents in adult rat dorsal root ganglion neurons in culture. Neuroscience 40, 513–521.

Dray, A., Bettaney, J., Forster, P., 1989. Capsaicin desensitization of peripheral nociceptive fibres does not impair sensitivity to other noxious stimuli. Neuroscience Letters 99, 50–54.

Gatley, S.J., Gifford, A.N., Volkow, N.D., Lan, R., Makriyannis, A., 1996. 123I-labeled AM251: a radioiodinated ligand which binds in vivo to mouse brain cannabinoid CB1 receptors. European Journal of Pharmacology 307, 331–338.

Hájos, N., Katona, I., Naiem, S.S., MacKie, K., Ledent, C., Mody, I., Freund, T.F., 2000. Cannabinoids inhibit hippocampal GABAergic transmission and network oscillations. European Journal of Neuroscience 12, 3239–3249.

Hájos, N., Ledent, C., Freund, T.F., 2001. Novel cannabinoid-sensitive receptor mediates inhibition of glutamatergic synaptic transmission in the hippocampus. Neuroscience 106, 1–4.

Hoffman, A.F., Lupica, C.R., 2000. Mechanisms of cannabinoid inhibition of GABA(A) synaptic transmission in the hippocampus. Journal of Neuroscience 20, 2470–2479.

Jancsó, N., Jancsó, A., 1949. Desensitization of sensory nerve endings (in Hungarian). Kísérletes Orvostudomány 2, 15.

Katona, I., Rancz, E.A., Acsády, L., Ledent, C., Mackie, K., Hájos, N., Freund, T.F., 2001. Distribution of CB1 cannabinoid receptors in the amygdala and their role in the control of GABAergic transmission. Journal of Neuroscience 21, 9506–9518.

Katona, I., Sperlagh, B., Sik, A., Kafalvi, A., Vizi, E.S., Mackie, K., Freund, T.F., 1999. Presynaptically located CB1 cannabinoid receptors regulate GABA release from axon terminals of specific hippocampal interneurons. Journal of Neuroscience 19, 4544–4558.

Matsuda, L.A., Lolait, S.J., Brownstein, M.J., Young, A.C., Bonner, T.I., 1990. Structure of a cannabinoid receptor and functional expression of the cloned. Nature 346, 561–564.

Mezey, E., Toth, Z.E., Cortright, D.N., Arzubi, M.K., Krause, J.E., Elde, R., Guo, A., Blumberg, P.M., Szallasi, A., 2000. Distribution of mRNA for vanilloid receptor subtype 1 (VR1) and VR1-like immunoreactivity, in the central nervous system of the rat and human. Proceedings of the National Academy of Sciences of the United States of America 97, 3655–3660.

Misner, D.L., Sullivan, J.M., 1999. Mechanism of cannabinoid effects on long-term potentiation and depression in hippocampal CA1 neurons. Journal of Neuroscience 19, 6795–6805.

Sanchez, J.F., Krause, J.E., Cortright, D.N., 2001. The distribution and regulation of vanilloid receptor VR1 and VR1 5′ splice variant RNA expression in rat. Neuroscience 107, 373–381.

Smart, D., Gunthorpe, M.J., Jerman, J.C., Nasir, S., Gray, J., Muir, A.I., Chambers, J.K., Randall, A.D., Davis, J.B., 2000. The endogenous lipid anandamide is a full agonist at the human vanilloid receptor (hVR1). British Journal of Pharmacology 129, 227–230.

Szallasi, A., Di Marzo, V., 2000. New perspectives on enigmatic vanilloid receptors. Trends in Neurosciences 23, 491–497.

Wilson, R.I., Kunos, G., Nicoll, R.A., 2001. Presynaptic specificity of endocannabinoid signaling in the hippocampus. Neuron 31, 453–462.

Zygmunt, P.M., Petersson, J., Andersson, D.A., Chuang, H., Sorgard, M., Di Marzo, V., Julius, D., Hogestatt, E.D., 1999. Vanilloid receptors on sensory nerves mediate the vasodilator action of anandamide. Nature 400, 452–457.

dc_71_10

5. számú melléklet

European Journal of Neuroscience, Vol. 19, pp. 2991–2996, 2004
dc_71_10

Endocannabinoid transport tightly controls 2-arachidonoyl glycerol actions in the hippocampus: effects of low temperature and the transport inhibitor AM404

Norbert Hájos,[1] Satish Kathuria,[2] Thien Dinh,[2] Daniele Piomelli[2] and Tamás F. Freund[1]
[1]Institute of Experimental Medicine, Hungarian Academy of Sciences, Szigony u. 43, Budapest, H-1083 Hungary
[2]Department of Pharmacology, University of California Irvine, Irvine, CA, USA

Keywords: CB_1 receptor, endocannabinoids, GABA, *in vitro*, rat, synaptic transmission

Abstract

The control of endocannabinoid actions on cortical neurons by a putative carrier-mediated uptake is still poorly understood at the level of synaptic transmission. We investigated the effect of an endocannabinoid, 2-arachidonoyl glycerol (2-AG), on inhibitory postsynaptic currents (IPSCs) in hippocampal slices under physiological conditions, and when uptake was altered by a selective blocker or lower temperature. Bath application of 2-AG (20 μM) caused a 40% reduction in the amplitude of IPSCs evoked in the perisomatic region of CA1 pyramidal neurons at room temperature; this effect could be blocked by a specific CB_1 receptor antagonist, AM251. By contrast, a smaller (20%) but significant suppression of inhibitory transmission was found by 2-AG at 33–35 °C. This reduced blocking effect at physiological temperature could be brought back to 40% by coapplying the endocannabinoid uptake blocker, AM404 (10 or 20 μM) with 2-AG. In parallel experiments, we measured [^{3}H]2-AG uptake at different temperatures in primary cultures prepared from cortical neurons. These data confirmed a striking inhibition of [^{3}H]2-AG uptake at room temperature compared with values observed at 37 °C. Uptake could be significantly modified by anandamide, 2-AG and AM404, suggesting a common transporter for the two endocannabinoids. These findings together demonstrate the presence of an effective endocannabinoid uptake in cortical neurons, which could considerably alter the spatial and temporal constraints of endocannabinoid signalling at physiological temperature, and which may critically change the interpretation of findings at room temperature.

Introduction

The brain endocannabinoid system consists of signal molecules (endocannabinoids), enzymes for their synthesis and degradation, specific cell-surface receptors and a putative transport system (see for review Freund *et al*., 2003). Most studies have investigated the functional roles of this signalling system in normal and pathological neuronal activity using plant-derived or synthetic cannabinoid agonists such as delta-9-tetrahydrocannabinol or WIN55,212-2. The main advantage of these compounds is that they are resistant to deactivation, whereas endocannabinoid substances are rapidly eliminated by uptake and intracellular hydrolysis (Freund *et al*., 2003). Two endocannabinoids have been extensively characterized – anandamide and 2-arachidonoyl glycerol (2-AG). Both activate CB_1 cannabinoid receptors (Devane *et al*., 1992; Sugiura *et al*., 1995) and are taken up by neurons and astrocytes (Beltramo *et al*., 1997; Beltramo & Piomelli, 2000; Hillard & Jarrahian, 2000; Bisogno *et al*., 2001) *en route* to intracellular degradation by distinct serine hydrolase enzymes: anandamide is broken down by fatty acid amide hydrolase (FAAH), and 2-AG by a monoglyceride lipase (MGL) (Cravatt *et al*., 1996; Dinh *et al*., 2002).

In the hippocampus, the endocannabinoid system is thought to play a role in important signalling events such as depolarization-induced suppression of inhibition (DSI; Ohno-Shosaku *et al*., 2001; Wilson & Nicoll, 2001) or regulation of neuronal excitability via long-term depression of inhibition (I-LTD; Chevaleyre & Castillo, 2003). In these events, the endocannabinoids may act as retrograde messengers, suppressing GABA release and inhibitory postsynaptic currents by engaging CB_1 receptors present on axon terminals of cholecystokinin-containing GABAergic interneurons (Katona *et al*., 1999; Hájos *et al*., 2000).

The clearance of endocannabinoids via uptake and/or degradation is a critical factor in determining the spatial and temporal constraints of their actions. The time-course of DSI is considerably shorter at physiological temperature than at room temperature (Kreitzer & Regehr, 2001), which may reflect the temperature dependence of uptake (Vizi, 1998). By contrast, the induction of I-LTD requires the presence of 2-AG for at least 5–10 min, which may be possible if uptake is slowed by subphysiological temperature. Indeed, the I-LTD experiments of Chevaleyre & Castillo (2003) were carried out at 25 °C. For a better prediction of the significance of endocannabinoid-mediated phenomena under physiological conditions, the temperature dependence of 2-AG uptake and action on GABAergic currents should be investigated.

In the present report, we have used freshly dissected slices of rat hippocampus to investigate the effects of ambient temperature and endocannabinoid transport blockade on the ability of 2-AG to inhibit GABAergic transmission. We have selected 2-AG for these experiments because of its higher abundance in the hippocampus relative to

Correspondence: Dr N. Hájos, as above.
E-mail: hajos@koki.hu

Received 17 November 2003, revised 6 April 2004, accepted 14 April 2004

doi:10.1111/j.1460-9568.2004.03433.x

anandamide (Stella *et al*., 1997) and its possible roles in I-LTD (Chevaleyre & Castillo, 2003). Moreover, we have used primary cultures of rat cortical neurons to examine how ambient temperature affects [^{3}H]2-AG transport.

Materials and methods

Experiments were carried out in accordance with the guidelines of the institutional ethical codex and the Hungarian Act of Animal Care and Experimentation (1998. XXVIII. section 243/1998), which is in full agreement with the regulation of animal experiments in the European Union. All efforts were made to minimize the number of animals used.

Electrophysiology

Male Wistar rats (16–22 days old) were deeply anaesthetized with isoflurane and decapitated. After opening the skull, the brain was quickly removed and immersed in ice-cold (~4 °C) modified artificial cerebrospinal fluid (ACSF), which contained (in mM): 252 sucrose, 2.5 KCl, 26 $NaHCO_3$, 2 $CaCl_2$, 2 $MgCl_2$, 1.25 NaH_2PO_4 and 10 glucose. Horizontal slices of the hippocampus (350–400 μm in thickness) were prepared using a Leica VT1000S Vibratome. The slices were then incubated in ACSF containing 126 mM NaCl instead of sucrose at room temperature for at least 1 h before recordings. Whole-cell patch-clamp recordings were obtained at 22–25 °C or at 33–35 °C from CA1 pyramidal cells visualized by infrared DIC videomicroscopy (Zeiss Axioscope, Germany) using a submerged type chamber. The extracellular solution had a composition of (in mM): 126 NaCl, 2.5 KCl, 26 $NaHCO_3$, 2 $CaCl_2$, 2 $MgCl_2$, 1.25 NaH_2PO_4 and 10 glucose, and the intrapipette solution contained (in mM): 80 CsCl, 60 Cs-gluconate, 3 NaCl, 1 $MgCl_2$, 10 HEPES, 2 Mg-ATP and 5 QX-314 (pH 7.2–7.3 adjusted with CsOH; osmolarity 275–290 mOsm). Patch electrodes were pulled from borosilicate glass capillaries with an inner filament (1.5 mm O.D.; 1.1 mm I.D., Sutter Instruments Co., CA, USA, or 1.5 mm O.D.; 1.12 mm I.D., Hilgenberg, Germany) using a Sutter P-87 puller, and had resistances of 3–6 MΩ when filled with the intrapipette solution. Access resistances (between 4 and 15 MΩ, compensated 70–75%) were frequently monitored and remained constant (± 20%) during the period of analysis. Signals were recorded with an Axopatch 200B amplifier or a Multiclamp 700A (Axon Instruments, CA, USA), filtered at 2 kHz, digitized at 6–10 kHz (National Instruments LabPC+ or PCI-6024E A/D board, Austin, TX, USA) and analysed off-line with the EVAN program (courtesy of Professor I. Mody, UCLA, CA, USA). Student's paired *t*-test and Mann–Whitney *U*-test were used to compare changes in the mean amplitude after drug application; a value of $P < 0.05$ was considered significant. Data are presented as mean ± SEM.

The drugs were perfused until the maximal effect was seen. The time needed for the maximal inhibition (at least 3–5 min) correlated with the depth of the recorded cells. In some cases, we applied 2-AG for 7–15 min at 33–35 °C. The longer application did not cause further change in the amplitude compared with the effect seen after 5 min, suggesting that this time period was enough at a flow rate of 3.5–4.0 mL/min to equilibrate the drug effect. To quantify the drug effects, control IPSC amplitudes in a 2–3 min time window were compared with those measured after 5 min drug application for the same period of time.

Reagents for electrophysiological recordings

2-AG (26.4 mM stock solution in acetonitrile) was purchased from Sigma or Cayman Chemical. AM251 and AM404 [100 mM stock solution in dimethylsulphoxide (DMSO) or 50 mM in ethanol, respectively] were obtained from Tocris (UK). AM374 and URB597 were dissolved in DMSO. Solvents on their own had no effect on postsynaptic currents ($n = 8$). The perfusion of the drugs did not change the holding current during the recordings. Kynurenic acid was purchased from Sigma.

Uptake experiments

We prepared primary cultures of rat cortical neurons from 18-day-old Wistar rat embryos in 24-well plates, as described by Stella & Piomelli (2001). We incubated the neurons in Krebs'–Tris buffer containing [^{3}H]2-AG (American Radiolabelled Chemicals, 200 Ci/mol; 0.45 nM, brought to 30 nM with nonradioactive 2-AG) for 2–20 min at 37, 22 and 4 °C, rinsed them three times with 0.5 mL Krebs'–Tris buffer containing fatty acid-free bovine serum albumin (BSA, 0.1%), and extracted internalized tracer with 0.5 mL sodium hydroxide (0.1 M). We measured radioactivity by liquid scintillation counting.

Results

Temperature-dependence of the suppression of monosynaptically evoked inhibitory postsynaptic currents by 2-AG

We investigated the action of 2-AG on inhibitory neurotransmission in the hippocampal slice preparation. Inhibitory postsynaptic currents (IPSCs) recorded in CA1 pyramidal cells were evoked in the presence of an ionotropic glutamate receptor blocker, kynurenic acid (2–3 mM), by stimulating GABAergic fibres terminating in the perisomatic region (Hájos *et al*., 2000). First we tested the effect of 2-AG on GABAergic inhibition at room temperature (22–25 °C), at which transporter activity for various transmitters is known to be considerably reduced or even blocked (Vizi, 1998). Bath application of 2-AG (20 μM) significantly reduced the amplitude of evoked IPSCs (eIPSCs) ($58.9 \pm 6.5\%$, $n = 7$, $P < 0.001$), an effect that was reversed upon washout (Fig. 1A and D). Pretreatment with or concomitant application of the CB_1 receptor antagonist AM251 (2 μM) abolished the effect of 2-AG ($98.5 \pm 4.8\%$, $n = 3$, $P > 0.05$; Fig. 1B and D). Next, we examined the action of 2-AG on inhibitory synaptic transmission at 33–35 °C. Application of 20 μM 2-AG produced a substantially smaller, albeit significant decrease of eIPSCs ($78.9 \pm 2.7\%$, $n = 9$, $P < 0.01$; Fig. 1C and D), which contrasted with the change observed at room temperature (Mann–Whitney *U*-test, $P < 0.02$).

The endocannabinoid uptake inhibitor, AM404, enhances the suppression of evoked IPSCs by 2-AG at physiological temperature

In further investigations, we examined the effect of the endocannabinoid transport inhibitor AM404 on the action of 2-AG at 33–35 °C. In these experiments, 2-AG was applied at 10 μM, which reduced eIPSC amplitude ($78.1 \pm 2.5\%$, $n = 12$, $P < 0.001$; Fig. 2A and D) to a similar extent as at 20 μM (Mann–Whitney *U*-test, $P > 0.05$; Fig. 1D). When 2-AG (10 μM) application was either followed by a washing in of 2-AG together with AM404 (10 or 20 μM; Fig. 2C), or this mixture was directly applied (Fig. 2B), the inhibition of eIPSC amplitude was markedly enhanced at physiological temperature ($63.1 \pm 3.9\%$, $n = 7$, $P < 0.001$; $61.1 \pm 4.7\%$, $n = 12$, $P < 0.01$, respectively), an effect that could be fully reversed by AM251 ($102.3 \pm 4.6\%$ of control, $n = 3$, $P > 0.05$). Irrespective of the application method, 10 or 20 μM AM404 enhanced the effect of 2-AG to a similar degree (10 μM, $62.1 \pm 5.4\%$; 20 μM, $62.8 \pm 4.5\%$; Mann–Whitney *U*-test, $P > 0.05$; Fig. 2D). Application of AM404 alone had no significant impact on the amplitude of eIPSC (10 μM, $94.8 \pm 5\%$; 20 μM, $102.5 \pm 8.1\%$; $P > 0.05$; Fig. 2D). To exclude the possibility that the enhancement of the action of 2-AG with AM404 is not due to its impact on FAAH

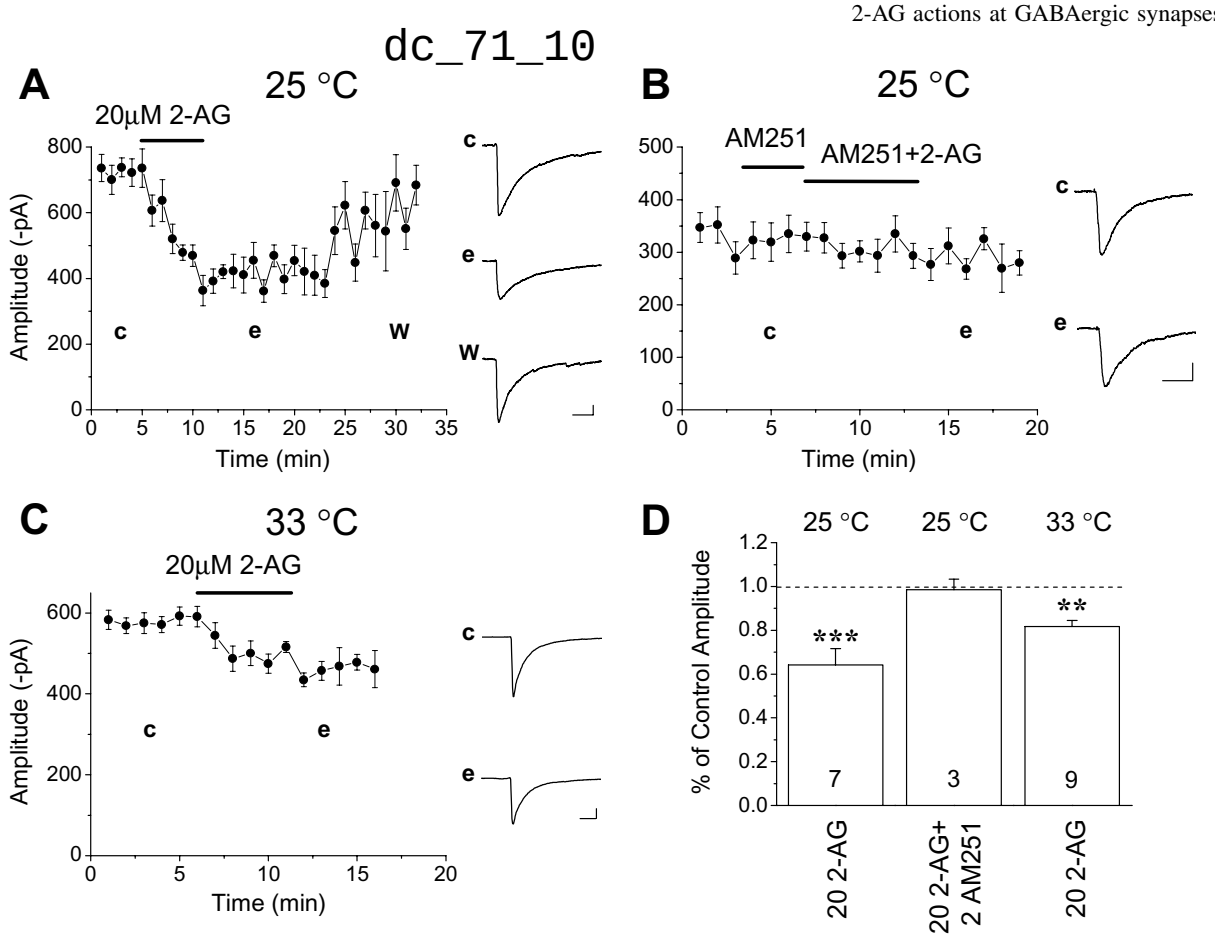

FIG. 1. The efficacy of 2-arachidonoyl glycerol (2-AG), an endocannabinoid ligand, in suppressing evoked inhibitory postsynaptic currents (eIPSCs) in the hippocampus is temperature-dependent. Whole-cell patch-clamp recordings were obtained from CA1 pyramidal cells using a CsCl-based intrapipette solution. IPSCs recorded at a holding potential of −60 mV appear as inward currents. (A) Bath application of 2-AG (20 μM) for 5–7 min markedly reduced the amplitude of IPSCs evoked at room temperature, a reduction that could be reversed by washout. (B) Pretreatment with the CB_1 cannabinoid receptor agonist, AM251 (2 μM), and its coapplication with 2-AG (20 μM) prevented reduction of eIPSC amplitude. (C) At 33 °C, 2-AG application caused only a modest, but significant reduction in the amplitude of eIPSCs. All data points on the plots represent a mean ± SEM of six consecutive events evoked by focal electrical stimulation with 0.1 Hz at the border of strata pyramidale and radiatum. Insets are averaged records of six consecutive events taken at the indicated time points. The stimulus artefacts were removed from the traces. Scale bars = 100 pA and 25 ms for A and B, respectively, and 5 ms for C. (D) Summary plot of the effects of 2-AG at different temperatures and its coapplication with the CB_1 receptor antagonist (AM251) on eIPSC amplitudes. All data are normalized to the control values and presented as percentages. The numbers of experiments performed under different conditions are indicated within the columns. $^{***}P < 0.001$, $^{**}P < 0.01$.

activity, we coapplied 2-AG (10 μM) with a specific FAAH inhibitor, URB597 (100–200 nM). The perfusion of this mixture caused a similar reduction in IPSC amplitude (76.2 ± 1.6%, $n = 4$, $P < 0.05$) as with 2-AG application alone, indicating that the enhancement produced by AM404 is most likely mediated by inhibition of the transporter rather than reducing FAAH activity. The IPSC amplitude was not affected by URB597 application alone (96.7 ± 2.2% of control, $n = 4$, $P > 0.05$). In summary, these results demonstrate that there is no significant difference in the 2-AG-induced reduction of eIPSC amplitude at physiological temperature and at room temperature, if at the former AM404 is applied together with 2-AG (Mann–Whitney *U*-test, $P > 0.05$). These data imply that 2-AG uptake is considerably reduced at room temperature in slice preparations.

2-AG uptake by cortical neurons in culture is highly temperature-dependent

Human astrocytoma cells accumulate exogenous [^{3}H]2-AG through a saturable and temperature-dependent process (Beltramo & Piomelli, 2000). The fact that this process is inhibited by either nonradioactive 2-AG or anandamide, as well as by the anandamide transport inhibitor AM404, suggests that astrocytoma cells may accumulate both endocannabinoids through a common carrier-mediated mechanism. To determine whether neurons internalize 2-AG, we incubated primary cultures of rat cortical neurons in Krebs' buffer containing [^{3}H]2-AG (30 nM). After incubation, which lasted 2–20 min, we rinsed the cultures with buffer containing fatty-acid-free BSA, to eliminate residual tracer, and measured radioactivity in the cell extracts. The results of these experiments indicate that cortical neurons rapidly accumulate [^{3}H]2-AG in a strikingly temperature-dependent manner (Fig. 3A). Next, we incubated the neurons for 4 min in Krebs' buffer containing [^{3}H]2-AG (30 nM) plus a large excess of nonradioactive 2-AG or anandamide (10 or 50 μM). Both compounds prevented [^{3}H]2-AG internalization in a concentration-dependent manner (Fig. 3B). Moreover, AM404 (10 μM) significantly reduced [^{3}H]2-AG accumulation (Fig. 3B). This effect cannot be attributed to inhibition of FAAH activity by AM404, because two potent FAAH inhibitors, AM374 and URB597, had no effect on [^{3}H]2-AG accumulation (AM374, 112%; URB597, 99% of control; $n = 8$). These findings indicate that rat brain neurons may internalize 2-AG via a carrier-mediated process similar to that previously described for

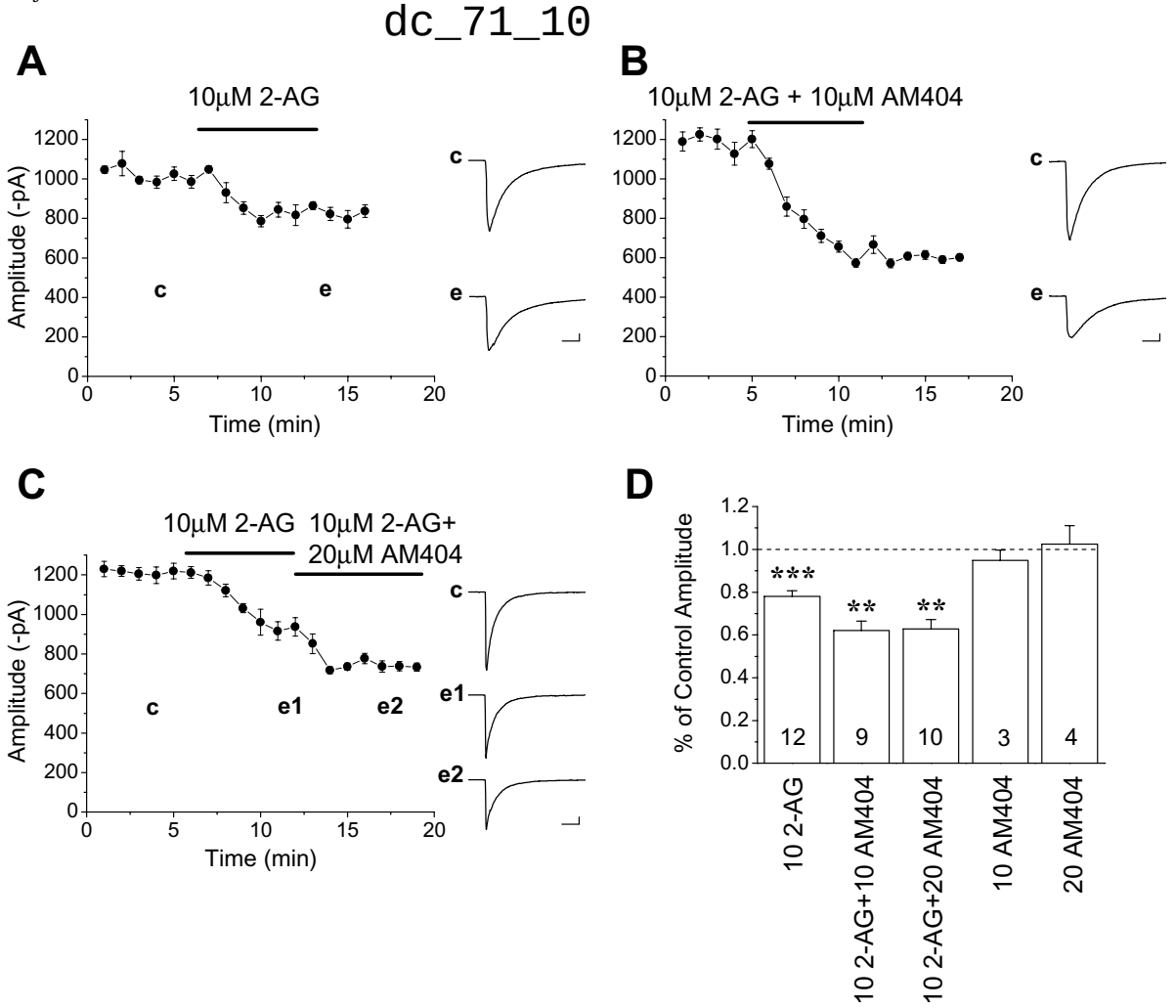

FIG. 2. The endocannabinoid uptake blocker, AM404, enhances the effect of 2-arachidonoyl glycerol (2-AG) on inhibitory postsynaptic currents (IPSCs) recorded at 33–35 °C. (A) Bath application of 10 μM 2-AG caused a similar, modest (~20%) reduction in the amplitude of evoked IPSCs as was noted after treatment with 20 μM 2-AG. (B) Coapplication of 2-AG (10 μM) with 10 μM AM404 resulted in a larger (~50%) suppression of eIPSC amplitude. (C) Application of the 2-AG/AM404 mix after 2-AG treatment alone further reduced the amplitudes of evoked IPSCs. (D) Summary plot of the effects of 2-AG and AM404 at 33–35 °C on eIPSC amplitudes. Presentation of data is the same as for Fig. 1. Scale bar = 100 pA and 10 ms. $^{***}P < 0.001$, $^{**}P < 0.01$.

astrocytoma cells (Beltramo & Piomelli, 2000), and that this uptake is highly temperature-dependent.

Discussion

The 2-AG-mediated suppression of inhibitory synaptic transmission in the hippocampus is probably due to the activation of CB_1 cannabinoid receptors. Our previous observations showed that CB_1 receptors are selectively present on axon terminals and preterminal axon segments of a subset of GABAergic interneurons expressing cholecystokinin, and their activation reduces GABA release as well as inhibitory postsynaptic currents (Katona *et al.*, 1999; Hájos *et al.*, 2000). In addition, our electrophysiological recordings provided direct evidence that cannabinoid actions on GABAergic IPSCs are entirely mediated by CB_1 receptors, because cannabinoid ligands have no effect on GABAergic currents in CB_1 knockout mice (Hájos *et al.*, 2000).

The temperature dependence of [^{3}H]2-AG transport has been demonstrated in astrocytoma and other cells (Beltramo & Piomelli, 2000; Bisogno *et al.*, 2001). Here we provide the first measurements of [^{3}H]2-AG uptake in primary neuronal cultures. Our results indicate that [^{3}H]2-AG uptake is almost abolished at room temperature, providing a likely explanation for our electrophysiological results. AM404, an uptake blocker without any direct effect on CB_1 receptors, inhibited [^{3}H]2-AG uptake at low micromolar concentrations and enhanced the 2-AG-mediated reduction of hippocampal IPSCs at physiological temperature. This enhancement of IPSC reduction at 33 °C was similar to those observed at room temperature. Although the putative endocannabinoid transporter(s) have not yet been identified, uptake studies *in vitro* have provided evidence for the presence of endocannabinoid transport in several brain regions including the hippocampus (Giuffrida *et al.*, 2001). Together, our physiological and biochemical data indicate that the effect of 2-AG is profoundly reduced by its uptake at physiological, but not at ambient temperature. A similar finding has been reported for anandamide in the midbrain (Vaughan *et al.*, 2000).

As suggested by biochemical studies, endocannabinoid uptake can be saturated (Bisogno *et al.*, 2001). Therefore, the question arises as to why we did not see a larger reduction in IPSC amplitude after longer (7–15 min) applications of 2-AG at physiological temperature, as

dc_71_10

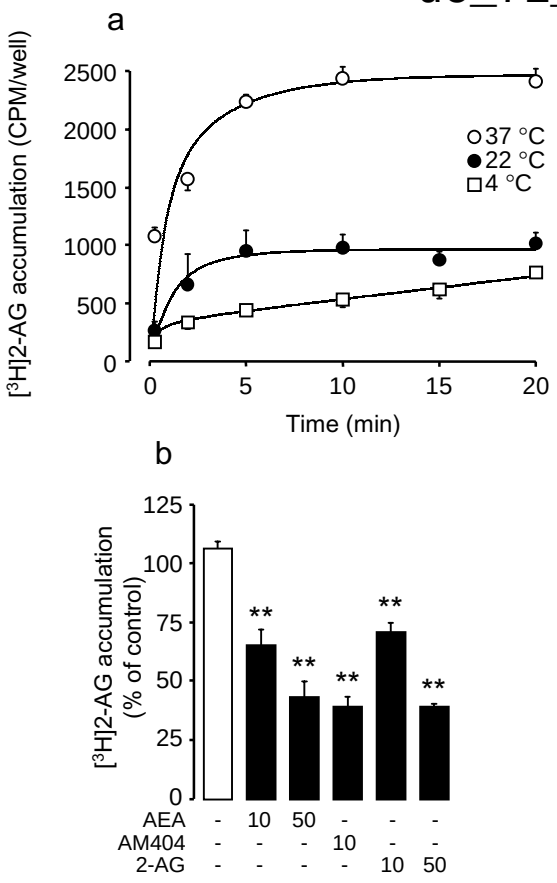

FIG. 3. [^{3}H]2-AG accumulation in rat cortical neurons. (A) Time-course of [^{3}H]2-AG accumulation at 37 °C, 22 °C and 4 °C. (B) Effects of various agents on [^{3}H]2-AG accumulation. AEA, anandamide. $^{**}P < 0.01$; $n = 4$.

could be predicted from the saturation of uptake. One possibility might be that after uptake 2-AG is metabolized intracellularly, which may allow a constant siphoning of 2-AG from the extracellular space (Beltramo & Piomelli, 2000). Kinetic analyses of anandamide internalization have led to the suggestion that uptake in neuroblastoma and astrocytoma cell lines requires FAAH activity and that no anandamide transporter exists in these cells (Glaser *et al*., 2003). These findings cannot be generalized to the brain, however, because pharmacological inhibition of FAAH activity in neurons or astrocytes has no effect on anandamide transport (Beltramo *et al*., 1997; Kathuria *et al*., 2003).

Most studies on the short- (DSI) or long-term (I-LTD) effects of endocannabinoids at inhibitory synapses have been performed at room temperature (Wilson & Nicoll, 2001; Chevaleyre & Castillo, 2003), at which, according to the present results, endocannabinoid uptake is greatly reduced. This might explain why AM404 increases the magnitude and time course of DSI at 33 °C (Trettel & Levine, 2003) but not at 22 °C (Wilson & Nicoll, 2001). Considering these results, the time window for DSI or for I-LTD at inhibitory synapses in the central nervous system should be narrower than suggested by the experiments performed at room temperature (Wilson & Nicoll, 2001; Chevaleyre & Castillo, 2003). Data by Kreitzer & Regehr (2001) and our present findings imply that this time period, when the CB_1-expressing subset of inhibitory afferents is temporarily silenced by endocannabinoids, is likely to be in the range of 1–2 s *in vivo*. This time might still be long enough to allow short- or long-term modifications to take place at certain excitatory inputs (Carlson *et al*., 2002), but may also ensure specificity in space and time.

Acknowledgements

This work was supported by OTKA (No. T32251; T.F.F.), ETT (474/2003; N.H.), the Howard Hughes Medical Institute (T.F.F.), Philip Morris External Research Program (T.F.F.) and NIH (NS30549 for T.F.F. and DA12447 for D.P.). N.H. is a recipient of the Bolyai János Scholarship. We thank Drs I. Katona and J. Makara for comments on the manuscript.

Abbreviations

2-AG, 2-arachidonoyl glycerol; CB_1, cannabinoid receptor type 1; DSI, depolarization-induced suppression of inhibition; FAAH, fatty acid amide hydrolase; I-LTD, long-term depression of inhibition; IPSC, inhibitory postsynaptic current; MGL, monoglyceride lipase.

References

Beltramo, M. & Piomelli, D. (2000) Carrier-mediated transport and enzymatic hydrolysis of the endogenous cannabinoid 2-arachidonylglycerol. *Neuroreport*, **11**, 1231–1235.

Beltramo, M., Stella, N., Calignano, A., Lin, S.Y., Makriyannis, A. & Piomelli, D. (1997) Functional role of high-affinity anandamide transport, as revealed by selective inhibition. *Science*, **277**, 1094–1097.

Bisogno, T., MacCarrone, M., De Petrocellis, L., Jarrahian, A., Finazzi-Agro, A., Hillard, C. & Di Marzo, V. (2001) The uptake by cells of 2-arachidonoylglycerol, an endogenous agonist of cannabinoid receptors. *Eur. J. Biochem.*, **268**, 1982–1989.

Carlson, G., Wang, Y. & Alger, B.E. (2002) Endocannabinoids facilitate the induction of LTP in the hippocampus. *Nat. Neurosci.*, **5**, 723–724.

Chevaleyre, V. & Castillo, P.E. (2003) Heterosynaptic LTD of hippocampal GABAergic synapses: a novel role of endocannabinoids in regulating excitability. *Neuron*, **38**, 461–472.

Cravatt, B.F., Giang, D.K., Mayfield, S.P., Boger, D.L., Lerner, R.A. & Gilula, N.B. (1996) Molecular characterization of an enzyme that degrades neuromodulatory fatty-acid amides. *Nature*, **384**, 83–87.

Devane, W.A., Hanus, L., Breuer, A., Pertwee, R.G., Stevenson, L.A., Griffin, G., Gibson, D., Mandelbaum, A., Etinger, A. & Mechoulam, R. (1992) Isolation and structure of a brain constituent that binds to the cannabinoid receptor. *Science*, **258**, 1946–1949.

Dinh, T.P., Carpenter, D., Leslie, F.M., Freund, T.F., Katona, I., Sensi, S.L., Kathuria, S. & Piomelli, D. (2002) Brain monoglyceride lipase participating in endocannabinoid inactivation. *Proc. Natl Acad. Sci. USA*, **99**, 10819–10824.

Freund, T.F., Katona, I. & Piomelli, D. (2003) The role of endogenous cannabinoids in synaptic signaling. *Physiol. Rev.*, **83**, 1017–1066.

Giuffrida, A., Beltramo, M. & Piomelli, D. (2001) Mechanisms of endocannabinoid inactivation: biochemistry and pharmacology. *J. Pharmacol. Exp. Ther.*, **298**, 7–14.

Glaser, S.T., Abumrad, N.A., Fatade, F., Kaczocha, M., Studholme, K.M. & Deutsch, D.G. (2003) Evidence against the presence of an anandamide transporter. *Proc. Natl Acad. Sci. USA*, **100**, 4269–4274.

Hájos, N., Katona, I., Naiem, S.S., MacKie, K., Ledent, C., Mody, I. & Freund, T.F. (2000) Cannabinoids inhibit hippocampal GABAergic transmission and network oscillations. *Eur. J. Neurosci.*, **12**, 3239–3249.

Hillard, C.J. & Jarrahian, A. (2000) The movement of N-arachidonoylethanolamine (anandamide) across cellular membranes. *Chem. Phys. Lipids*, **108**, 123–134.

Kathuria, S., Gaetani, S., Fegley, D., Valino, F., Duranti, A., Tontini, A., Mor, M., Tarzia, G., Rana, G.L., Calignano, A., Giustino, A., Tattoli, M., Palmery, M., Cuomo, V. & Piomelli, D. (2003) Modulation of anxiety through blockade of anandamide hydrolysis. *Nat. Med.*, **9**, 76–81.

Katona, I., Sperlagh, B., Sik, A., Kafalvi, A., Vizi, E.S., Mackie, K. & Freund, T.F. (1999) Presynaptically located CB1 cannabinoid receptors regulate GABA release from axon terminals of specific hippocampal interneurons. *J. Neurosci.*, **19**, 4544–4558.

Kreitzer, A.C. & Regehr, W.G. (2001) Retrograde inhibition of presynaptic calcium influx by endogenous cannabinoids at excitatory synapses onto Purkinje cells. *Neuron*, **29**, 717–727.

Ohno-Shosaku, T., Maejima, T. & Kano, M. (2001) Endogenous cannabinoids mediate retrograde signals from depolarized postsynaptic neurons to presynaptic terminals. *Neuron*, **29**, 729–738.

Stella, N. & Piomelli, D. (2001) Receptor-dependent formation of endogenous cannabinoids in cortical neurons. *Eur. J. Pharmacol.*, **425**, 189–196.

Stella, N., Schweitzer, P. & Piomelli, D. (1997) A second endogenous cannabinoid that modulates long-term potentiation. *Nature*, **388**, 773–778.

Sugiura, T., Kondo, S., Sukagawa, A., Nakane, S., Shinoda, A., Itoh, K., Yamashita, A. & Waku, K. (1995) 2-Arachidonoylglycerol: a possible endogenous cannabinoid receptor ligand in brain. *Biochem. Biophys. Res. Commun.*, **215**, 89–97.

Trettel, J. & Levine, E.S. (2003) Endocannabinoids mediate rapid retrograde signaling at interneuron right-arrow pyramidal neuron synapses of the neocortex. *J. Neurophysiol.*, **89**, 2334–2338.

Vaughan, C.W., Connor, M., Bagley, E.E. & Christie, M.J. (2000) Actions of cannabinoids on membrane properties and synaptic transmission in rat periaqueductal gray neurons in vitro. *Mol. Pharmacol.*, **57**, 288–295.

Vizi, E.S. (1998) Different temperature dependence of carrier-mediated (cytoplasmic) and stimulus-evoked (exocytotic) release of transmitter: a simple method to separate the two types of release. *Neurochem. Int.*, **33**, 359–366.

Wilson, R.I. & Nicoll, R.A. (2001) Endogenous cannabinoids mediate retrograde signalling at hippocampal synapses. *Nature*, **410**, 588–592.

dc_71_10

6. számú melléklet

Available online at www.sciencedirect.com
SCIENCE DIRECT®
ELSEVIER
Neuropharmacology 47 (2004) 381–389
NEURO PHARMACOLOGY
www.elsevier.com/locate/neuropharm

Distinct properties of carbachol- and DHPG-induced network oscillations in hippocampal slices

J. Pálhalmi [a], O. Paulsen [b], T.F. Freund [a], N. Hájos [a,*]

[a] *Department of Cellular and Network Neurobiology, Institute of Experimental Medicine, Hungarian Academy of Sciences, Szigony u. 43, 1083 Budapest, Hungary*

[b] *Department of Physiology, Oxford University, Parks Road, Oxford OX1 3PT, UK*

Received 8 February 2004; received in revised form 24 March 2004; accepted 22 April 2004

Abstract

The aim of this study was to compare and contrast the properties of gamma oscillations induced by activation of muscarinic acetylcholine or metabotropic glutamate receptors in the CA3 region of rat hippocampal slices. Both carbachol and the group I metabotropic glutamate receptor agonist, (*RS*)-3,5-dihydroxyphenylglycine (DHPG), induced network oscillations in the gamma-frequency range (30–100 Hz). The M1 muscarinic receptor antagonist, pirenzepine, blocked carbachol-, but enhanced DHPG-induced oscillations, whereas LY 341495, an antagonist at metabotropic glutamate receptors, abolished DHPG-, but left carbachol-induced oscillations unchanged. There were significant differences in the peak frequency, maximal power, and spectral width of the two oscillations. Pharmacological experiments showed that both types of oscillation depend on fast excitatory and inhibitory synaptic transmission. Interestingly, activation of neurokinin-1 receptors by substance P fragment or enhancement of inhibitory synaptic currents by the benzodiazepine ligand, zolpidem, boosted DHPG-, but reduced the power of carbachol-induced oscillations.

These results suggest that, although carbachol and DHPG might activate similar conductances in individual pyramidal cells, the oscillations they induce in slices involve different network mechanisms, most likely by recruiting distinct types of GABAergic interneuron.

Keywords: Rat; Hippocampus; Carbachol; DHPG; Muscarinic acetylcholine receptor; Metabotropic glutamate receptor

1. Introduction

Various patterns of rhythmic neuronal activity have been recorded in the hippocampus during different behavioural states including exploration, REM sleep and consummatory behaviour (Buzsaki, 1989). Of these network activities, gamma-frequency oscillations have been subject to much interest, as they are hypothesised to be important in memory processes and control of the temporal relationship between pre- and post-synaptic activity during induction of spike timing-dependent synaptic plasticity (Traub et al., 1998; Paulsen and Sejnowski, 2000; Engel and Singer, 2001; Whittington and Traub, 2003).

Hippocampal slice preparations have been widely used to explore the mechanisms of both electrically evoked, transient and pharmacologically induced, persistent oscillations in the frequency range of 10–50 Hz. Thus, activation of either muscarinic acetylcholine (mAChR) or metabotropic glutamate receptors (mGluRs) induces robust, persistent beta and gamma oscillations (Boddeke et al., 1997; Fisahn et al., 1998). Previous studies showed that mAChR- and mGluR-induced synchronous activities are driven by the complex network of the CA3 region involving both excitatory and inhibitory synaptic transmission (Fisahn et al., 1998; Cobb et al., 2000). There is good evidence that GABAergic inhibitory transmission has a major function in gamma oscillations (Whittington et al., 1995; Boddeke et al., 1997; Fisahn et al., 1998; Traub et al., 1998), however, the contribution by different

* Corresponding author. Tel.: +36-12109416; fax: +36-12109412.
E-mail address: hajos@koki.hu (N. Hájos).

0028-3908/$ - see front matter © 2004 Elsevier Ltd. All rights reserved.
doi:10.1016/j.neuropharm.2004.04.010

interneuron subtypes expressing distinct combinations of pre- and postsynaptic receptors is poorly understood.

Hippocampal interneuron classes differ not only in the expression pattern of mAChRs and mGluRs (Freund and Buzsaki, 1996; Freund, 2003), but also in their response to activation of these receptors (McBain et al., 1994; McQuiston and Madison, 1999; van Hooft et al., 2000). These anatomical and electrophysiological data suggest that different populations of interneurons might be differentially involved in mAChR- and mGluR-induced gamma oscillations, and modulated by distinct pre- and postsynaptic receptors.

The aim of this study was to investigate whether cholinergic and mGluR-induced gamma oscillations can be dissociated pharmacologically. We found that these oscillations depend on both excitatory and inhibitory synaptic transmission but differ with respect to frequency and power of oscillatory activity, as well as by the effect of drugs acting via different classes of interneurons.

2. Methods

2.1. Slice preparation

All experiments were carried out in accordance with the guidelines of the Institutional Ethical Codex and the Hungarian Act of Animal Care and Experimentation (1998. XXVIII. section 243/1998). Male Wistar rats (P14-20) were deeply anaesthetised with isoflurane. Following decapitation, the brain was quickly removed into ice-cold artificial cerebrospinal fluid (ACSF), containing (in mM): NaCl, 126; KCl, 2.5; $NaHCO_3$, 26; $CaCl_2$, 2; $MgCl_2$, 2; NaH_2PO_4, 1.25; glucose, 10, and bubbled with 95% O_2/5% CO_2. Four-hundred-micrometer thick horizontal slices were prepared using a Leica VT1000S microtome. Slices containing the hippocampal formation were trimmed from other brain regions and were kept in interface-style holding chamber at room temperature for at least 60 min before recordings commenced.

2.2. Electrophysiological recordings and data analysis

Extracellular field potentials were recorded in the stratum pyramidale of the CA3 region in an interface-style recording chamber using patch pipettes filled with ACSF at a resistance of 3–6 MΩ. All experiments were done at 28–30 °C, and flow rate was 2 ml min^{-1}. Data were recorded in AC mode with a Multiclamp 700A amplifier (Axon Instruments, Foster City, CA), using an amplification of 1000. Signals were lowpass filtered at 400 Hz. Analog-to-digital conversion was done by a PCI-6024E data acquisition board (National Instruments, Austin, TX) with either EVAN 6.0 (courtesy of Dr. I. Mody) or WCR software (courtesy of Dr. J. Dempster). Detailed data analysis was carried out off-line using Origin 7.0 and Matlab 6.0 software. Power spectra were estimated from one-minute-long traces with the Welch method using one-second-wide time windows with 50% overlap. Peak frequencies and summated power in the frequency range of 20–47 Hz were used for statistical analyses, unless otherwise indicated. This frequency range, measured at 28–30 °C, includes frequencies below the gamma-frequency range (30–70 Hz) of the EEG in intact brain. However, because of the temperature dependence of network oscillations in vitro (Ecker et al., 2001; Dickinson et al., 2003), the peak frequencies of the oscillations studied in this paper would most likely fall within the gamma-frequency band at body temperature, and we have thus referred to oscillations in the whole of this frequency range as gamma-band oscillations. In a few experiments, line noise was picked up that could interfere with the gamma-band power estimates. For consistency, we therefore restricted the power measurements upward to 47 Hz. Although this would slightly underestimate the total power, the estimated change in power would be only minimally affected. All values are given as percentages relative to control.

In the pharmacological experiments, following the induction of stable gamma-frequency oscillations, one-minute long recordings were obtained every 5 min. Stable recording of at least 15 min was required before bath application of different drugs, and the recordings continued every 5 min for at least 25 min. Peak frequencies and gamma-band powers were expressed relative to the average of control. Data are presented as mean ± standard error of the mean (SEM). N values refer to the number of slices recorded. Statistical significance was assessed using Student's t-test ($p < 0.05$).

2.3. Chemicals and drugs

Bicuculline, substance P fragment, MK 801, atropine, and carbachol were purchased from Sigma (St. Louis, MO, USA), whereas (*RS*)-3,5-dihydroxyphenylglycine (DHPG), (2*S*)-2-amino-2-[(1*S*,2*S*)-2-carboxycycloprop-1-yl]-3-(xanth-9-yl)propanoic acid (LY 341495), pirenzepine, methoctramine, 6,7-dinitro-quinoxaline-2,3-dione (DNQX), DL-2-amino-5-phosphonopentanoic acid (AP5), and zolpidem were obtained from Tocris (Bristol, UK). 1-(4-aminophenyl)-3-methyl-carbamyl-4-methyl-7,8-methylenedioxy-3,4-dihydro-5H-2,3-benzodiazepine (GYKI 53655) was generously provided by Ivax Drug Research Institute Ltd. (Budapest, Hungary).

3. Results

3.1. Different properties of carbachol- and DHPG-induced oscillations

Synchronous network activity was recorded in the CA3 region of the hippocampus after bath application of either the cholinergic agonist, carbachol (20 μM), or the group I specific mGluR agonist, DHPG (10 μM). Both agonists induced robust and persistent field oscillations in the gamma-frequency range (Fig. 1). Similar to what has been shown earlier for carbachol-induced oscillations (Fisahn et al., 1998), both the peak frequency and the gamma-band power of DHPG-induced oscillations depend on the applied agonist concentration (Fig. 1(D)).

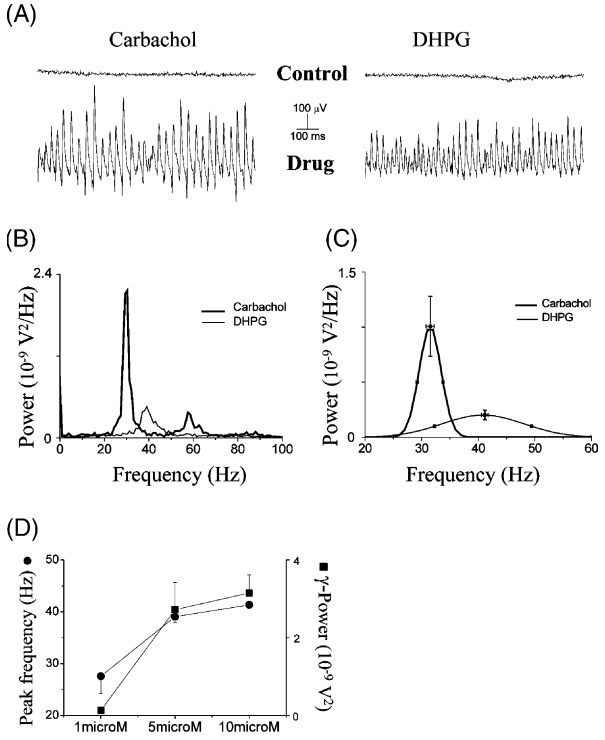

Fig. 1. Different properties of carbachol (CCh)- and DHPG-induced gamma-frequency network oscillations in hippocampal slices. (A) Representative traces recorded in the stratum pyramidale of the CA3 region showing synchronous oscillatory activity after bath application of 20 μM carbachol (left) or 10 μM DHPG (right). (B) Corresponding power spectra of these gamma oscillations calculated from one-minute long epochs. (C) Averaged data for the main gamma-band peak of carbachol- and DHPG-induced oscillation. A Gaussian function was fitted through the average of the peak and half maximal widths of the main power spectral density peak for each type of oscillation. Note the higher peak frequency and wider power spectrum for DHPG-induced oscillations compared with carbachol-induced synchronous activity. The horizontal bars indicate the standard error of the mean (SEM) of the peak frequency, the vertical bars indicate the SEM of the peak gamma-band power for each oscillation. (D) Concentration dependence of frequency (squares) and gamma-band power (circles) of DHPG-induced oscillation.

Comparison of the oscillations induced by carbachol (20 μM) and DHPG (10 μM) at concentrations above the EC50 values for M1 muscarinic and mGluR group I receptors, respectively (Ito et al., 1992; Rhee et al., 2000), revealed significant differences in peak frequency (31.5 ± 0.7 Hz, $n = 11$ for carbachol- and 41.2 ± 0.6 Hz, $n = 13$ for DHPG-induced oscillations) and peak gamma-band power density ($1.01 \pm 0.27 \times 10^{-9}$ V^2/Hz, $n = 11$ for carbachol- and $2.02 \pm 0.43 \times 10^{-10}$ V^2/Hz, $n = 13$ for DHPG-induced oscillations) ($p < 0.01$; Fig. 1(B, C)). The half-widths of the power spectra also differed significantly (4.6 ± 0.3 Hz, $n = 11$ for carbachol- and 16.1 ± 2 Hz, $n = 13$ for DHPG-induced oscillations, $p < 0.01$, Fig. 1(C)). Together, these data suggested that different neuronal circuits might be involved in carbachol- and DHPG-induced oscillations and we proceeded to investigate whether they could be further dissociated pharmacologically.

3.2. Pharmacological dissociation of carbachol- and DHPG-induced oscillations

To investigate whether the induction and maintenance of the oscillations are specific to the activation of each type of receptor or whether the mechanisms involved might interact, we bath-applied selective antagonists at mAChR and mGluRs during on-going oscillations. An M1 subtype-selective mAChR antagonist, pirenzepine (10 μM), blocked the gamma-band activity of carbachol-induced oscillations ($9.7 \pm 4.3\%$, $n = 5$), but caused a significant elevation of the gamma-band power of DHPG-induced oscillations ($234.6 \pm 36.5\%$, $p < 0.05$; $n = 9$; Fig. 2(A), Table 1). The peak frequency of the DHPG-induced oscillations was not affected by pirenzepine ($96 \pm 2.4\%$). To strengthen the conclusion that mAChRs are tonically activated in DHPG-induced synchronous activity, we also tested the effect of the broad-spectrum mAChR antagonist atropine (5 μM). A similar effect to that of pirenzepine on DHPG-induced oscillation was seen by application of atropine (gamma power: $286.9 \pm 54.2\%$; peak frequency: $101.9 \pm 4.3\%$, $n = 4$). A broad-spectrum antagonist at mGluRs, LY 341495 (50 μM), completely blocked the gamma-band activity of DHPG-induced oscillations ($3.5 \pm 0.4\%$, $n = 3$), but did not significantly change either the gamma-band power ($116.3 \pm 14.3\%$, $n = 7$) or the peak frequency ($98.4 \pm 2.5\%$, $n = 7$) of carbachol-induced oscillations (Fig. 2(B), Table 1). These results indicate that not only the induction, but also the maintenance of oscillation depend on metabotropic receptor activation. In addition, the results suggest that muscarinic receptors are tonically activated in DHPG-induced oscillations, whereas mGluRs are not activated during carbachol-induced oscillations.

To investigate whether excitatory synaptic mechanisms might differ between carbachol- and

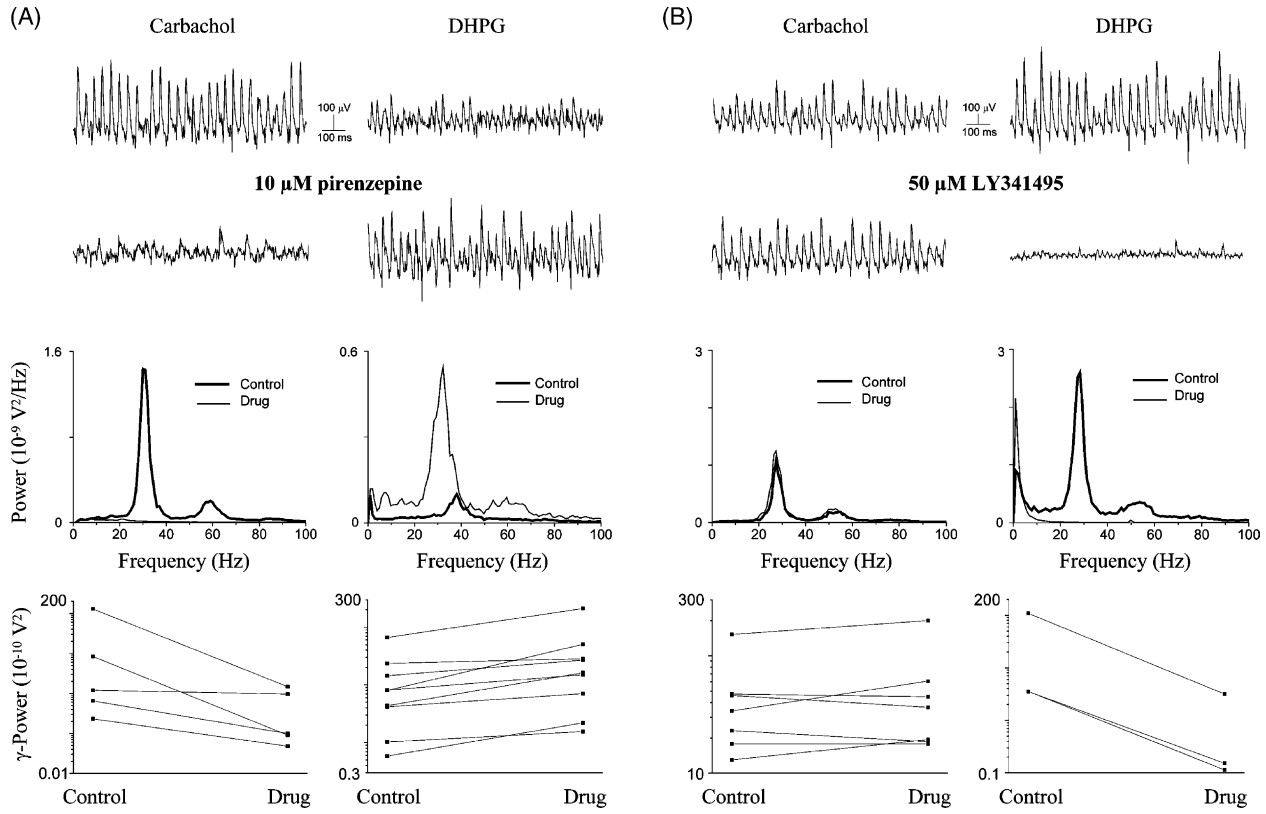

Fig. 2. Effect of muscarinic and metabotropic glutamate receptor antagonists on carbachol- and DHPG-induced oscillations. (A) Pirenzepine, an M1 type muscarinic receptor antagonist, blocked carbachol-induced gamma oscillation, but increased the power of DHPG-induced network activity. Upper panel, representative traces; middle panel, power spectra; lower panel, results from individual experiments. No significant change in the peak frequency of DHPG-induced oscillations was observed. (B) LY 341495, a metabotropic glutamate receptor antagonist, completely blocked DHPG-induced oscillation, but did not change either the power or the frequency of carbachol-induced gamma oscillation as shown by representative traces (upper panel) and power spectra (middle panel). Gamma-band powers for individual slices are shown in the bottom panel (logarithmic *y*-axis).

DHPG-induced oscillation, we tested the contribution of AMPA receptor-mediated synaptic transmission in both oscillations using the selective antagonist at AMPA receptors, GYKI 53655 (50 μM; Tarnawa et al., 1993; Bleakman et al., 1996). GYKI 53655 almost completely blocked gamma-band oscillations in both models (Fig. 3(A)). Gamma-band power decreased to $18.9 \pm 12.5\%$ for carbachol ($n = 3$) and to $14 \pm 4.1\%$ for DHPG-induced oscillation ($n = 7$, Table 1). Whereas all cholinergically induced oscillatory activity was blocked by GYKI 53655 ($n = 3$), prolonged blockade of fast excitatory synaptic transmission unmasked

Table 1
Changes in gamma-band power of carbachol- and DHPG-induced oscillations produced by different drugs. Gamma-band power was estimated from one-minute long traces. Data are mean ± SEM. Significant changes after drug applications are indicated with asterisks ($^{*}p < 0.05$ and $^{**}p < 0.01$). *N* refers to the number of slices for a given drug. The drug/control (D/C) ratio represents the change in gamma-band power induced by drug application

	Gamma power of carbachol-induced oscillation (10^{-9} V^2)				Gamma power of DHPG-induced oscillation (10^{-9} V^2)			
	N	Control	Drug	D/C (%)	*N*	Control	Drug	D/C (%)
Pirenzepine	5	2.8 ± 2.5	0.053 ± 0.029	$9.7 \pm 4.3^{**}$	9	1.4 ± 0.69	3.9 ± 2.2	$234.6 \pm 36.5^{*}$
LY 341495	7	4.8 ± 1.8	5.7 ± 2.5	116.3 ± 14.3	3	3.9 ± 3.5	0.11 ± 0.10	$3.5 \pm 0.4^{**}$
GYKI 53655	3	1.9 ± 1.1	0.19 ± 0.092	$18.9 \pm 12.5^{*}$	7	7.2 ± 5.5	0.904 ± 0.42	$14 \pm 4.1^{**}$
Bicuculline	3	5.9 ± 1.8	0.23 ± 0.13	$5.8 \pm 3.5^{**}$	4	1.5 ± 0.50	0.13 ± 0.038	$8.4 \pm 1.8^{**}$
Zolpidem	8	2.03 ± 0.60	1.2 ± 0.51	$56.1 \pm 9.4^{**}$	6	8.5 ± 3.6	16 ± 4.6	$194.5 \pm 27.3^{*}$
Methoctramine	8	3.7 ± 1.7	4.1 ± 1.5	191.2 ± 50.8	10	6.1 ± 2.9	7.2 ± 2.4	222.2 ± 76.4
Substance P fragment	9	4.6 ± 1.3	2.7 ± 0.82	$67.6 \pm 10.5^{*}$	8	6.5 ± 2.01	9.6 ± 2.4	$159 \pm 15.6^{**}$

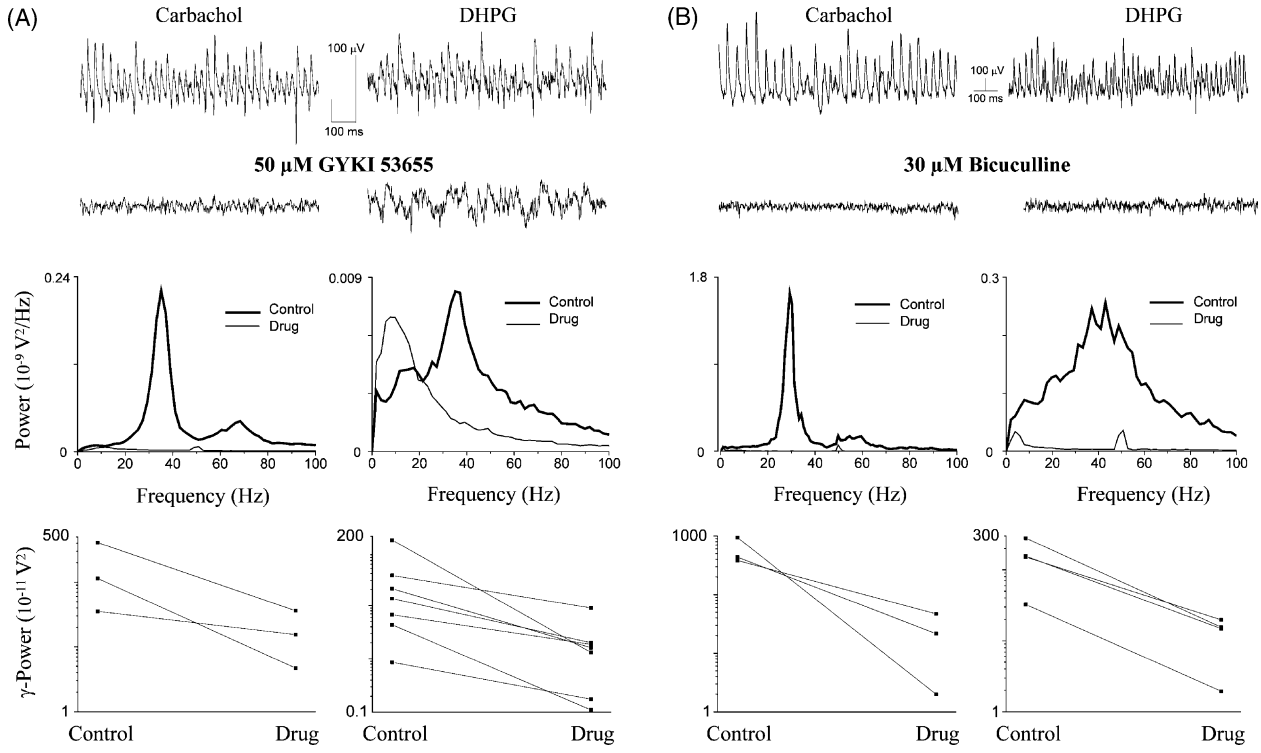

Fig. 3. Effect of AMPA and $GABA_A$ receptor antagonists on gamma oscillations induced by carbachol or DHPG. (A) GYKI 53655, a selective AMPA receptor antagonist, completely blocks both carbachol- and DHPG-induced gamma oscillations, but residual theta-band activity becomes apparent in the presence of DHPG as seen from the representative traces (upper panel) and corresponding power spectra (middle panel). The change of gamma-band power in each individual experiment is shown in the lower panel. (B) Bicuculline, a $GABA_A$ receptor antagonist, abolished both types of oscillations, as shown by example traces (upper panel) and power spectra (middle panel). Power spectra were calculated from one-minute long recording. The effect of bicuculline on the gamma-band power for individual slices is shown in the bottom panel. Note that values are presented on a logarithmic *y*-axis.

a low-frequency network activity (5–15 Hz) in four out of seven experiments in the presence of DHPG ($156.6 \pm 39.8\%$, $n = 7$, $p < 0.05$, Fig. 3(A)), in agreement with a recent study by Gillies et al. (2002). Similarly, combined application of DNQX (10 μM), AP5 (20 μM) and MK 801 (40 μM) significantly reduced the gamma-band power ($13.6 \pm 4.9\%$, $n = 9$) but increased low-frequency power in eight out of nine experiments with DHPG ($288.1 \pm 60.3\%$, $n = 9$, $p < 0.05$).

In addition to fast excitatory transmission, several reports indicate an important role for $GABA_A$ receptors during in vitro gamma oscillations (Whittington et al., 1995; Boddeke et al., 1997; Fisahn et al., 1998). As predicted, the antagonist at $GABA_A$ receptors, bicuculline (30 μM), blocked the gamma oscillation induced by both carbachol ($5.8 \pm 3.5\%$, $n = 3$) and DHPG ($8.4 \pm 1.8\%$, $n = 4$; Fig. 3(B), Table 1). Together, these data support the suggestion that in both models, both excitatory and inhibitory synaptic transmission are important to maintain gamma-band oscillations in the CA3.

To investigate whether more subtle differences in GABAergic transmission might distinguish between carbachol- and DHPG-induced oscillations, we also examined the effect of enhancing $GABA_A$ receptor-mediated synaptic transmission with the benzodiazepine ligand, zolpidem. Zolpidem (10 μM) significantly decreased the power in the gamma band of carbachol-induced oscillations ($56.1 \pm 9.4\%$, $n = 8$), while significantly increased the power of DHPG-induced oscillations ($194.5 \pm 27.3\%$, $n = 6$; Fig. 4, Table 1). The peak frequency of the carbachol-induced oscillations was not modified by zolpidem ($97 \pm 3.3\%$), but the peak frequency of DHPG-induced oscillations was significantly decreased from 35.5 ± 0.7 to 32.03 ± 0.9 Hz ($p < 0.05$). Thus, these experiments showed differential effect of modulation of GABAergic inhibition in these two models of hippocampal gamma oscillations, suggestive of differential involvement of interneuron classes.

As different subclasses of GABAergic interneurons express different modulatory receptors, we finally wanted to dissociate the two oscillations on the basis of possible differential effects of activating or blocking such receptors. We focused on the M2 type of mAChRs and neurokinin-1 (NK-1) receptors. A specific M2 receptor antagonist, methoctramine (5 μM) caused in some slices an elevation of gamma-band

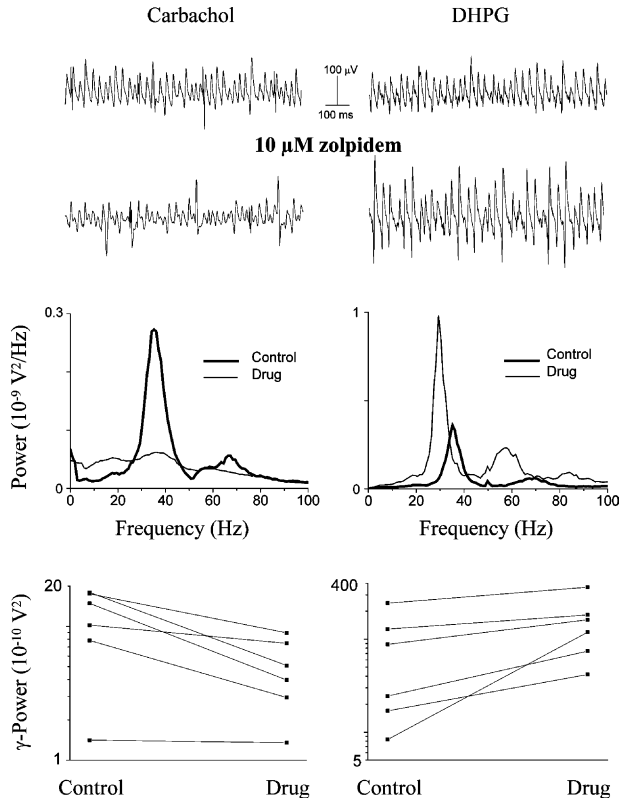

Fig. 4. Enhancement of inhibitory synaptic transmission differentially alters carbachol- and DHPG-induced oscillations. (A) Application of zolpidem, a benzodiazepine ligand, significantly decreased the power of the carbachol-induced network activity without changing the peak frequency, as shown by representative recordings (upper panel) and power spectra (middle panel). (B) In contrast, zolpidem caused a significant increase in the power and a decrease in the peak frequency of the DHPG-induced oscillation. The corresponding gamma-band powers for single slices before and after drug application are shown in the plots with logarithmic *y*-axis in the bottom panel.

power in both carbachol- and DHPG-induced oscillations (in three of eight, on average: $191.2 \pm 50.8\%$ for carbachol, $n = 8$; in four of 10, on average: $222.2 \pm 76.4\%$ for DHPG, $n = 10$, Table 1) without changing their peak frequencies ($95.9 \pm 3.5\%$ for carbachol; $92.3 \pm 5.1\%$ for DHPG; Fig. 5(A)). This effect did not reach overall significance, however. In contrast, substance P fragment (50 nM), a specific NK-1 receptor agonist, significantly decreased the gamma power of carbachol-induced oscillations ($67.6 \pm 10.5\%$, $n = 9$), while significantly increased the gamma power of DHPG-induced oscillations ($159 \pm 15.6\%$, $n = 8$; Fig. 5(B), Table 1). This NK-1 receptor agonist also caused a small, but significant shift in the peak frequency of carbachol-induced oscillations from 29.3 ± 1.2 to 31.4 ± 1.3 Hz ($107.1 \pm 1.8\%$, $p < 0.01$) without changing the peak frequency of DHPG-induced oscillations ($102.3 \pm 2.5\%$; Fig. 5(B)). Thus, blocking M2 type of mAChRs had similar effects on the two oscillations, while substance P fragment differentially altered them, which might indicate the involvement of distinct neuronal circuits in these models. A summary plot of the main results is shown in Fig. 6.

4. Discussion

Previous studies reported peak frequencies of network oscillations in slices induced by bath application of mAChR or mGluR agonists varying between 0.5 and 70 Hz (Boddeke et al., 1997; Fisahn et al., 1998; Fellous and Sejnowski, 2000; Shimono et al., 2000; Fisahn et al., 2002; Gillies et al., 2002; Colgin et al., 2003). Comparison of these data is rather difficult, since the oscillation frequency varies with many factors, including recording temperature (Ecker et al., 2001; Dickinson et al., 2003) and the cutting angle of hippocampal slices (Whittington et al., 1995; Cobb et al., 2000; Lanneau et al., 2002).

Under our experimental conditions, both metabotropic agonists (carbachol and DHPG) induced gamma-frequency network oscillations in the CA3 region. The DHPG-induced oscillations were significantly faster than the cholinergically-induced oscillations. A similar difference was reported by Boddeke et al. (1997) between network oscillations induced by the broad spectrum mGluR agonist 1-aminocyclopentane-(1*S*,3*R*)-dicarboxylate ((1*S*,3*R*)-ACPD) and carbachol in the CA1 region of the hippocampus. An in vivo study also found a faster (1*S*,3*R*)-ACPD–induced gamma oscillation in the dentate gyrus compared to those induced by mAChR activation (Martin, 2001). The former oscillation in this study had a wider power spectrum compared to mAChR-induced oscillations, which is similar to our finding, suggesting different network mechanisms in the generation of mAChR- and mGluR-induced gamma activities.

Different results have been reported for the effect of blockers of fast excitatory synaptic transmission on hippocampal gamma oscillations in vitro (Whittington et al., 1995; Boddeke et al., 1997; Fisahn et al., 1998; Gillies et al., 2002). In our model in CA3, both fast excitatory and inhibitory synaptic transmission are necessary for the maintenance of gamma oscillations. These observations indicate that the activity of both pyramidal cells and GABAergic interneurons is crucial. In contrast, both the (1*S*,3*R*)-ACPD-induced oscillations in CA1 (Boddeke et al., 1997) and electrically evoked transient oscillations (Whittington et al., 1995) were independent of fast excitatory synaptic transmission suggesting that these rhythmic activities were dependent solely on inhibitory interneuronal circuits. The apparent discrepancy between these studies and our observations might reflect the difference in the ana-

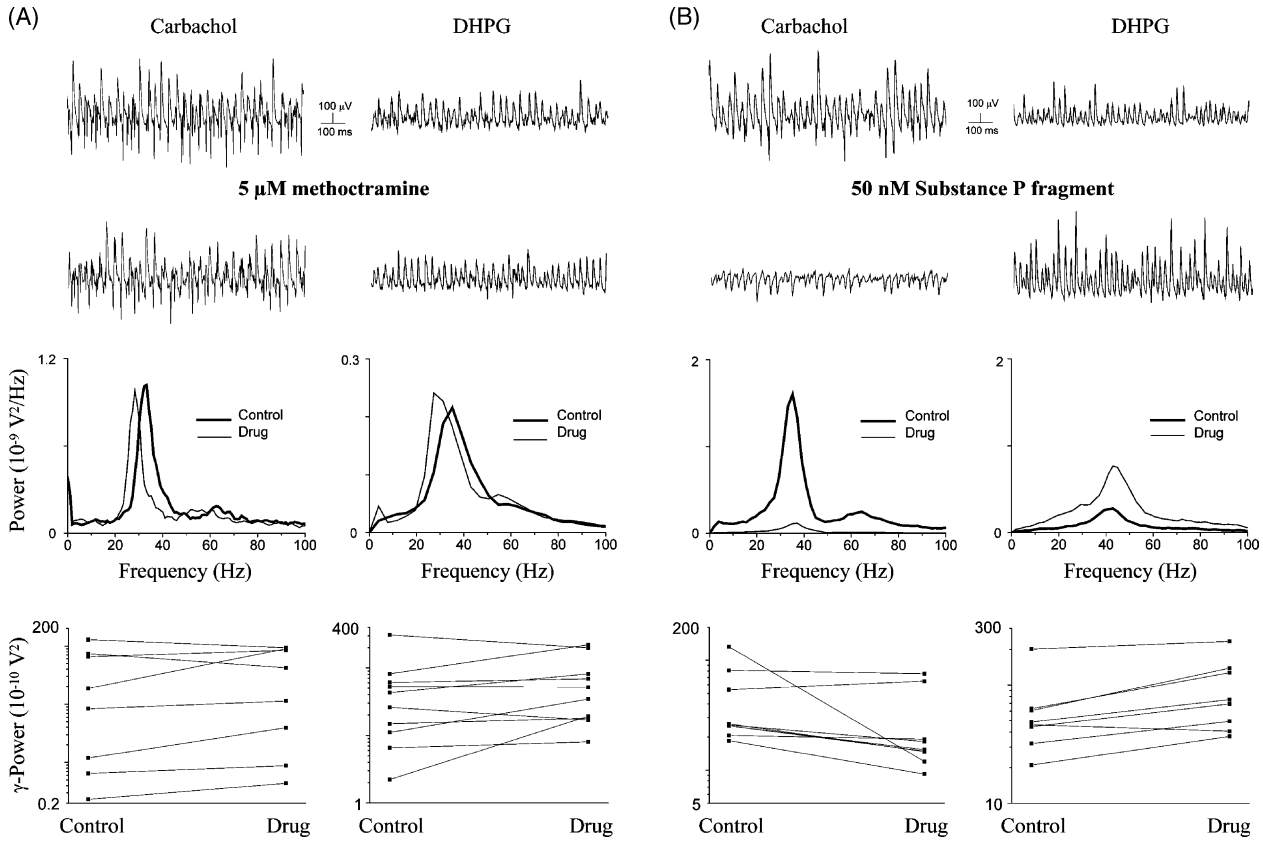

Fig. 5. Modulation of gamma oscillations by antagonism at M2 type of muscarinic receptors and by activation of neurokinin-1 (NK-1) receptors. (A) Methoctramine, a selective M2 muscarinic receptor antagonist, in some slices, but not all, produced an increment in the power of both types of gamma oscillations, but this effect did not reach overall significance. Methoctramine did not alter the peak frequencies. (B) Substance P fragment, acting selectively on NK-1 receptors, significantly decreased the power and increased the frequency of the carbachol-induced oscillation, while significantly increased the power without changing the peak frequency of the DHPG-induced oscillation. Plots with logarithmic *y*-axis in the bottom row show the change in gamma-band power in individual slices.

tomical connectivity in the CA3 and CA1 subfields (Freund and Buzsaki, 1996).

Our data are consistent with the recent observation by Gillies et al. (2002), that blocking fast excitatory synaptic transmission blocked the gamma-band activity of DHPG-induced oscillations, unmasking residual theta-frequency network activity in the stratum pyramidale of the CA3 region.

Both theoretical models and experimental evidence indicate that IPSC kinetics influence the frequency of gamma oscillations (Whittington et al., 1995; Fisahn et al., 1998; Traub et al., 1998). Application of 10 µM zolpidem, a concentration that prolongs IPSC decay times in both CA1 pyramidal cells and interneurons (Hájos et al., 2000a), significantly decreased the frequency and increased the power of DHPG-induced oscillations. In contrast, carbachol-induced oscillations were reduced in power with no change in frequency. Theoretical predictions (Whittington et al., 2000) suggest that oscillations depending predominantly on GABAergic transmission would show stronger sensitivity to the alteration of IPSC decay times compared to those where both inhibitory and excitatory fast synaptic transmissions are equally important. These considerations suggest that in DHPG-induced oscillations interneuronal circuits might have a more prominent role than in carbachol-induced oscillations.

Addition of an acetylcholine esterase inhibitor was shown to induce synchronous gamma activity in hippocampal slices (Engel et al., 2002), indicating that endogenous ACh levels in slices could be high enough to activate muscarinic receptors (Fig. 6). This is in agreement with our results showing that in DHPG-induced oscillations muscarinic receptor antagonists (pirenzepine and atropine) did increase the power, thus these receptors might have been tonically activated. In contrast, LY 341495 had no effect on carbachol-induced oscillations suggesting no tonic activation of mGluRs in these synchronous network activities. Methoctramine (an M2 type of mAChR antagonist) elevated the power of gamma oscillations in some slices. Muscarinic receptor protein type 2 (belonging to pharmacologically defined M2 receptors) was demonstrated to be selectively expressed on the axon term-

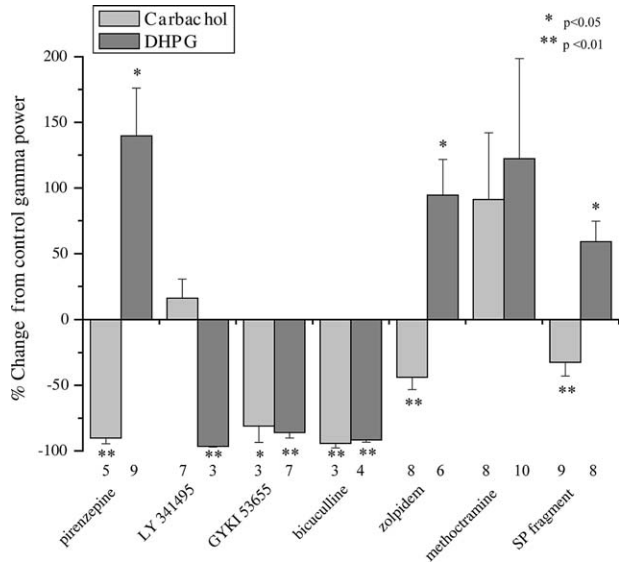

Fig. 6. Summary plot of effects of distinct receptor agonists and antagonists on gamma-band power in both oscillation models. All data are expressed as percent change relative to control (means and SEM). The number of slices in different conditions is shown under each column.

inals of parvalbumin-containing perisomatic inhibitory interneurons in the hippocampus (Hájos et al., 1998). As physiological experiments revealed, activation of presynaptic muscarinic receptors could decrease GABA release (Behrends and ten Bruggencate, 1993; Hefft et al., 2002). Thus, blocking of M2 receptors, which should increase the potency of perisomatic inhibition, could enhance the oscillation power as our results showed. Similar increment in the oscillation power was recently noticed in parvalbumin knockout mice, where the short-term depression of perisomatic inhibitory currents was significantly smaller at gamma frequencies causing larger GABAergic currents (Vreugdenhil et al., 2003). Taken together these data imply that parvalbumin-containing perisomatic inhibitory cells might be involved in both types of gamma oscillations (Freund, 2003).

Previous data indicated that substance P receptor (NK-1 receptor) activation increased both the frequency and amplitude of spontaneous inhibitory postsynaptic currents or potentials recorded in CA1 pyramidal cells leading to a decrease in the excitatory synaptic transmission (Kouznetsova and Nistri, 1998; Hájos et al., 2000b). Anatomical observations indicated that NK-1 receptors are expressed in different types of hippocampal interneurons including those containing somatostatin, cholecystokinin, neuropeptide-Y or calretinin, but not parvalbumin (Acsády et al., 1997). Pyramidal cells were found to be immunonegative for NK-1 receptors (Acsády et al., 1997). Since activation of these receptors had opposite effect on carbachol- and DHPG-induced oscillations, we propose that different networks of pyramidal cell–interneuron circuitries might operate in these two in vitro models.

The question arises whether these two in vitro models of gamma oscillation have any correspondence to the oscillations in the gamma-frequency band recorded in vivo. Our working hypothesis is that the carbachol model could be related to those gamma oscillations that are recorded during exploratory behaviour (Bragin et al., 1995), when acetylcholine concentration is the highest in the extracellular space (Marrosu et al., 1995). Conversely, DHPG-induced oscillations might be related to sharp-wave activity during immobility, when populations of CA3 pyramidal cells fire action potentials synchronously (Csicsvári et al., 1999). This population activity could elevate the glutamate level in the extracellular space sufficiently to stimulate mGluRs inducing gamma oscillations. Indeed, short-term gamma oscillations, so-called 'tail gamma', have been shown to occur after sharp waves in the CA1 region in vivo (Traub et al., 1996). Both theta modulated and tail gamma could have similar roles but in different physiological situations: the precise timing of firing in specific neuronal assemblies.

In summary, our results suggest that, although the two metabotropic receptors (mAChR and mGluR) could affect similar conductances in pyramidal neurons (Chuang et al., 2002; Fisahn et al., 2002), their activation at the network level generates population oscillation with different properties, which are likely to involve distinct interneuronal circuits.

Acknowledgements

This work was supported by OTKA (No: T32251), the Howard Hughes Medical Institute, NIH (NS30549), and the British Council. N.H. is a grantee of the Bolyai János Scholarship.

References

Acsády, L., Katona, I., Gulyas, A.I., Shigemoto, R., Freund, T.F., 1997. Immunostaining for substance P receptor labels GABAergic cells with distinct termination patterns in the hippocampus. J. Comp. Neurol. 378, 320–336.

Behrends, J.C., ten Bruggencate, G., 1993. Cholinergic modulation of synaptic inhibition in the guinea pig hippocampus in vitro: excitation of GABAergic interneurons and inhibition of GABA-release. J. Neurophysiol. 69, 626–629.

Bleakman, D., Ballyk, B.A., Schoepp, D.D., Palmer, A.J., Bath, C.P., Sharpe, E.F., Woolley, M.L., Bufton, H.R., Kamboj, R.K., Tarnawa, I., Lodge, D., 1996. Activity of 2,3-benzodiazepines at native rat and recombinant human glutamate receptors in vitro: stereospecificity and selectivity profiles. Neuropharmacology 35, 1689–1702.

Boddeke, H.W., Best, R., Boeijinga, P.H., 1997. Synchronous 20 Hz rhythmic activity in hippocampal networks induced by activation

of metabotropic glutamate receptors in vitro. Neuroscience 76, 653–658.

Bragin, A., Jando, G., Nadasdy, Z., Hetke, J., Wise, K., Buzsaki, G., 1995. Gamma (40–100 Hz) oscillation in the hippocampus of the behaving rat. J. Neurosci. 15, 47–60.

Buzsaki, G., 1989. Two-stage model of memory trace formation: a role for "noisy" brain states. Neuroscience 31, 551–570.

Chuang, S.C., Zhao, W., Young, S.R., Conquet, F., Bianchi, R., Wong, R.K., 2002. Activation of group I mGluRs elicits different responses in murine CA1 and CA3 pyramidal cells. J. Physiol. 541, 113–121.

Cobb, S.R., Bulters, D.O., Davies, C.H., 2000. Coincident activation of mGluRs and mAChRs imposes theta frequency patterning on synchronised network activity in the hippocampal CA3 region. Neuropharmacology 39, 1933–1942.

Colgin, L.L., Kubota, D., Lynch, G., 2003. Cholinergic plasticity in the hippocampus. Proc. Natl. Acad. Sci. USA 100, 2872–2877.

Csicsvári, J., Hirase, H., Czurko, A., Mamiya, A., Buzsaki, G., 1999. Fast network oscillations in the hippocampal CA1 region of the behaving rat. J. Neurosci. 19, RC20.

Dickinson, R., Awaiz, S., Whittington, M.A., Lieb, W.R., Franks, N.P., 2003. The effects of general anaesthetics on carbachol-evoked gamma oscillations in the rat hippocampus in vitro. Neuropharmacology 44, 864–872.

Ecker, C., Suckling, J.M., Paulsen, O., 2001. Temperature dependence of cholinergically induced network oscillations in the CA1 region of the hippocampus. Soc. Neurosci. Abstr. 27, 47.

Engel, A.K., Singer, W., 2001. Temporal binding and the neural correlates of sensory awareness. Trends Cogn. Sci. 5, 16–25.

Engel, D., Robson, A.A., Gloveli, T., Whittington, M.A., Buhl, E.H., 2002. Acetylcholinesterase inhibitors elicit cholinergic gamma frequency network oscillations in the rodent hippocampus in vitro. FENS Abstr. 1, A146.

Fellous, J.-M., Sejnowski, T.J., 2000. Cholinergic induction of oscillations in the hippocampal slice in the slow (0.5–2 Hz), theta (5–12 Hz), and gamma (35–70 Hz) bands. Hippocampus 10, 187–197.

Fisahn, A., Pike, F.G., Buhl, E.H., Paulsen, O., 1998. Cholinergic induction of network oscillations at 40 Hz in the hippocampus in vitro. Nature 394, 186–189.

Fisahn, A., Yamada, M., Duttaroy, A., Gan, J.W., Deng, C.X., McBain, C.J., Wess, J., 2002. Muscarinic induction of hippocampal gamma oscillations requires coupling of the M1 receptor to two mixed cation currents. Neuron 33, 615–624.

Freund, T.F., Buzsaki, G., 1996. Interneurons of the hippocampus. Hippocampus 6, 347–470.

Freund, T.F., 2003. Interneuron diversity series: rhythm and mood in perisomatic inhibition. Trends Neurosci. 26, 489–495.

Gillies, M.J., Traub, R.D., LeBeau, F.E., Davies, C.H., Gloveli, T., Buhl, E.H., Whittington, M.A., 2002. A model of atropine-resistant theta oscillations in rat hippocampal area CA1. J. Physiol. 543, 779–793.

Hájos, N., Papp, E.C., Acsady, L., Levey, A.I., Freund, T.F., 1998. Distinct interneuron types express m2 muscarinic receptor immunoreactivity on their dendrites or axon terminals in the hippocampus. Neuroscience 82, 355–376.

Hájos, N., Nusser, Z., Rancz, E.A., Freund, T.F., Mody, I., 2000a. Cell type- and synapse-specific variability in synaptic GABAA receptor occupancy. Eur. J. Neurosci. 12, 810–818.

Hájos, N., Katona, I., Naiem, S.S., MacKie, K., Ledent, C., Mody, I., Freund, T.F., 2000b. Cannabinoids inhibit hippocampal GABAergic transmission and network oscillations. Eur. J. Neurosci. 12, 3239–3249.

Hefft, S., Kraushaar, U., Geiger, J.R., Jonas, P., 2002. Presynaptic short-term depression is maintained during regulation of transmitter release at a GABAergic synapse in rat hippocampus. J. Physiol. 539, 201–208.

Ito, I., Kohda, A., Tanabe, S., Hirose, E., Hayashi, M., Mitsunaga, S., Sugiyama, H., 1992. 3,5-Dihydroxyphenyl-glycine: a potent agonist of metabotropic glutamate receptors. Neuroreport 3, 1013–1016.

Kouznetsova, M., Nistri, A., 1998. Modulation by substance P of synaptic transmission in the mouse hippocampal slice. Eur. J. Neurosci. 10, 3076–3084.

Lanneau, C., Harries, M.H., Ray, A.M., Cobb, S.R., Randall, A., Davies, C.H., 2002. Complex interactions between mGluR1 and mGluR5 shape neuronal network activity in the rat hippocampus. Neuropharmacology 43, 131–140.

Marrosu, F., Portas, C., Mascia, M.S., Casu, M.A., Fa, M., Giagheddu, M., Imperato, A., Gessa, G.L., 1995. Microdialysis measurement of cortical and hippocampal acetylcholine release during sleep-wake cycle in freely moving cats. Brain Res. 671, 329–332.

Martin, S.J., 2001. Activation of metabotropic glutamate receptors induces gamma frequency oscillations in the rat dentate gyrus in vivo. Neuropharmacology 40, 634–637.

McBain, C.J., DiChiara, T.J., Kauer, J.A., 1994. Activation of metabotropic glutamate receptors differentially affects two classes of hippocampal interneurons and potentiates excitatory synaptic transmission. J. Neurosci. 14, 4433–4445.

McQuiston, A.R., Madison, D.V., 1999. Muscarinic receptor activity has multiple effects on the resting membrane potentials of CA1 hippocampal interneurons. J. Neurosci. 19, 5693–5702.

Paulsen, O., Sejnowski, T.J., 2000. Natural patterns of activity and long-term synaptic plasticity. Curr. Opin. Neurobiol. 10, 172–179.

Rhee, J.C., Rhee, P.L., Park, M.K., So, I., Uhm, D.Y., Kim, K.W., Kang, T.M., 2000. Muscarinic receptors controlling the carbachol-activated nonselective cationic current in guinea pig gastric smooth muscle cells. Jpn J. Pharmacol. 82, 331–337.

Shimono, K., Brucher, F., Granger, R., Lynch, G., Taketani, M., 2000. Origins and distribution of cholinergically induced β rhythms in hippocampal slices. J. Neurosci. 20, 8462–8473.

Tarnawa, I., Berzsenyi, P., Andrási, F., Botka, P., Hámori, T., Ling, I., Kõrösi, J., 1993. Structure-activity relationships of 2,3-benzodiazepine compounds with glutamate antagonist action. Bioorg. Med. Chem. 3, 99–104.

Traub, R.D., Whittington, M.A., Colling, S.B., Buzsaki, G., Jefferys, J.G., 1996. Analysis of gamma rhythms in the rat hippocampus in vitro and in vivo. J. Physiol. 493, 471–484.

Traub, R.D., Spruston, N., Soltesz, I., Konnerth, A., Whittington, M.A., Jefferys, G.R., 1998. Gamma-frequency oscillations: a neuronal population phenomenon, regulated by synaptic and intrinsic cellular processes, and inducing synaptic plasticity. Prog. Neurobiol. 55, 563–575.

van Hooft, J.A., Giuffrida, R., Blatow, M., Monyer, H., 2000. Differential expression of group I metabotropic glutamate receptors in functionally distinct hippocampal interneurons. J. Neurosci. 20, 3544–3551.

Vreugdenhil, M., Jefferys, J.G., Celio, M.R., Schwaller, B., 2003. Parvalbumin-deficiency facilitates repetitive IPSCs and gamma oscillations in the hippocampus. J. Neurophysiol. 89, 1414–1422.

Whittington, M.A., Traub, R.D., Jefferys, J.G., 1995. Synchronized oscillations in interneuron networks driven by metabotropic glutamate receptor activation. Nature 373, 612–615.

Whittington, M.A., Faulkner, H.J., Doheny, H.C., Traub, R.D., 2000. Neuronal fast oscillations as a target site for psychoactive drugs. Pharmacol. Ther. 86, 171–190.

Whittington, M.A., Traub, R.D., 2003. Interneuron diversity series: inhibitory interneurons and network oscillations in vitro. Trends Neurosci. 26, 676–682.

dc_71_10

7. számú melléklet

The Journal of Neuroscience, October 13, 2004 • 24(41):9127–9137 • 9127

Behavioral/Systems/Cognitive

Spike Timing of Distinct Types of GABAergic Interneuron during Hippocampal Gamma Oscillations *In Vitro*

Norbert Hájos,[1] János Pálhalmi,[1] Edward O. Mann,[2] Beáta Németh,[1] Ole Paulsen,[2] and Tamas F. Freund[1]

[1]Institute of Experimental Medicine, Hungarian Academy of Sciences, Budapest H-1450, Hungary, and [2]Department of Physiology, University of Oxford, Parks Road, Oxford OX1 3PT, United Kingdom

Gamma frequency (30–100 Hz) network oscillations occur in the intact hippocampus during awake, attentive behavior. Here, we explored the underlying cellular mechanisms in an *in vitro* model of persistent gamma-frequency oscillations, induced by bath application of 20 μM carbachol in submerged hippocampal slices at 30 ± 1°C. Current-source density analysis of the field oscillation revealed a prominent alternating sink-source pair in the perisomatic and apical dendritic regions of CA3. To elucidate the active events generating these extracellular dipoles, we examined the firing properties of distinct neuron types. Visually guided unit recordings were obtained from individual CA3 neurons followed by intracellular labeling for anatomical identification. Pyramidal cells fired at 2.82 ± 0.7 Hz, close to the negative peak of the oscillation (0.03 ± 0.65 msec), and often in conjunction with a negative spike-like component of the field potential. In contrast, all phase-coupled interneurons fired after this negative peak. Perisomatic inhibitory interneurons fired at high frequency (18.1 ± 2.7 Hz), shortly after the negative peak (1.97 ± 0.95 msec) and were strongly phase-coupled. Dendritic inhibitory interneurons fired at lower frequency (8.4 ± 2.4 Hz) and with less fidelity and a longer delay after the negative peak (4.3 ± 1.1 msec), whereas interneurons with cell body in the stratum radiatum often showed no phase relationship with the field oscillation. The phase and spike time data of individual neurons, together with the current-source density analysis, support a synaptic feedback model of gamma oscillations primarily involving pyramidal cells and inhibitory cells targeting their perisomatic region.

Key words: **hippocampus; carbachol; gamma oscillation; GABAergic cells; phase-coupling; rat**

Introduction

Oscillatory activity in the gamma-frequency band (30–100 Hz) occurs in multiple brain regions and has been implicated in different cognitive functions, including sensory processing (Singer, 1993; Gray, 1994), selective attention (Fries et al., 2001), and memory (Fell et al., 2001). Gamma oscillations are prominent in the hippocampal formation (Leung, 1979; Bragin et al., 1995; Chrobak and Buzsáki, 1998; Csicsvari et al., 2003), where they have been suggested to contribute to encoding and retrieval of memory (Hasselmo et al., 1996; Varela et al., 2001). Despite extensive investigation of gamma oscillations *in vivo*, the cellular mechanisms underlying the generation and maintenance of this network activity are largely unknown.

The hippocampal circuitry comprises excitatory principal cells and inhibitory interneurons. The former cell type is thought to encode, process, store, and retrieve information (cf. Engel et al., 2001), whereas the latter controls spike timing of principal neurons, synaptic plasticity, and network oscillations (Buzsáki and Chrobak, 1995; Paulsen and Moser, 1998; Whittington and Traub, 2003). Although principal neurons are rather uniform within each hippocampal subfield, a large morphological and functional heterogeneity is typical of GABAergic interneurons (Freund and Buzsáki, 1996). Functionally, at least three main GABAergic cell types coexist in cortical networks: perisomatic inhibitory neurons controlling the firing of principal cells, dendritic inhibitory interneurons regulating synaptic input and Ca^{2+} signaling, and GABAergic cells specifically innervating other inhibitory interneurons (Gulyás et al., 1996; Miles et al., 1996). Information about the activity of different types of interneuron during oscillations should facilitate our understanding of how these network oscillations are generated, and may shed light on their different functions. To date, the firing patterns of some anatomically identified cell types have been correlated with θ and ripple oscillations, but not to gamma oscillations. Moreover, only a limited number of neurons from each cell class has been reported (Soltesz et al., 1993; Sik et al., 1995; Ylinen et al., 1995; Klausberger et al., 2003, 2004).

To study the cellular mechanisms underlying gamma activity, *in vitro* models of gamma oscillation have been introduced (Whittington et al., 1995; Fisahn et al., 1998). Cholinergically induced gamma-frequency network oscillations in hippocampal slices (Fisahn et al., 1998) are a model of hippocampal gamma oscillations during wakefulness, when extracellular acetylcholine levels are high (Marrosu et al., 1995). Similar to *in vivo* gamma oscillations, these *in vitro* oscillations are generated within the

Received June 1, 2004; revised Aug. 12, 2004; accepted Aug. 31, 2004.

This work was supported by Országos Tudományos Kutatási Alapprogramok (Grant T046820), the Howard Hughes Medical Institute, National Institutes of Health Grant NS30549, the Biotechnology and Biological Sciences Research Council, and the British Council. N.H. is a grantee of the Bolyai János Scholarship. We thank Dr. V. Varga for helping in data analysis. The technical assistance of Katalin Lengyel is gratefully acknowledged.

Correspondence should be addressed to Norbert Hájos, Department of Cellular and Network Neurobiology, Institute of Experimental Medicine, Hungarian Academy of Sciences, Szigony u. 43, Budapest 1083, Hungary. E-mail: hajos@koki.hu.

DOI:10.1523/JNEUROSCI.2113-04.2004

 0270-6474/04/249127-11$15.00/0

CA3 subfield, and at each oscillatory cycle pyramidal cell firing is followed by the discharge of local GABAergic interneurons (Bragin et al., 1995; Csicsvari et al., 2003).

The aim of this study was to investigate the firing properties of different types of anatomically identified hippocampal neuron in the CA3 region during cholinergically induced gamma oscillations *in vitro*. We were able to record persistent gamma oscillations in the submerged slice allowing a more detailed investigation of the mechanisms underlying synchronous activity. Using visually guided single-unit and patch-clamp recordings during these persistent network oscillations, we compared the firing activity and spike timing of distinct types of interneuron and pyramidal cells.

Materials and Methods

Slice preparation. All experiments were performed in accordance with British and Hungarian legislation and institutional guidelines. Male Wistar rats [postnatal day 14 (P14)–P20] were deeply anesthetized with isoflurane. After decapitation, the brain was quickly removed and placed into ice-cold artificial CSF (ACSF) containing (in mM): sucrose, 252; KCl, 2.5; $NaHCO_3$, 26; $CaCl_2$, 2; $MgCl_2$, 2; NaH_2PO_4, 1.25; glucose, 10, and bubbled with 95% O_2 and 5% CO_2 (carbogen gas). We prepared 400-μm-thick horizontal slices using a Leica (Nussloch, Germany) VT1000S microtome. Slices containing the hippocampal formation were trimmed from other brain regions and kept in an interface-type holding chamber at room temperature for at least 60 min before recording.

Electrophysiological recordings and data analysis. Experiments were performed in the CA3 region of the hippocampus using a submerged-type recording chamber at 30 ± 1°C. Extracellular solution had content as above, but with 126 mM NaCl instead of sucrose. The solution, constantly bubbled with carbogen gas at room temperature, was superfused at a flow rate of at least 3.5–4.5 ml/min, crucial for oscillations in submerged slices (Hájos et al., 2004). Oscillations were induced by bath application of 20 μM carbachol, which was present throughout the experiments (Sigma, St. Louis, MO). Two patch pipettes filled with ACSF (resistance 3–6 MΩ) were used during the recording. The tip of one electrode was placed within the pyramidal cell layer of the CA3b region at a depth of 100–200 μm to monitor extracellular field oscillations. The other pipette was used to detect action potentials extracellularly from a visually identified neuron. Recorded neurons located no deeper than 100–120 μm from the surface were sampled in the close vicinity (<200 μm) of the field electrode, but for some cells in the stratum radiatum the distance between the electrodes exceeded 300 μm. After the extracellular recording, the same cell was labeled with a different pipette using the whole-cell patch-clamp technique. For intracellular labeling, this pipette contained (in mM): 138 K-gluconate, 2 NaCl, 10 creatine phosphate, 10 HEPES, 4 ATP, 0.4 GTP, and 0.3–0.5% biocytin. Only recordings obtained extracellularly were analyzed in this work. All data were recorded with a Multiclamp 700A amplifier (Axon Instruments, Foster City, CA), except signals for current-source density (CSD) analysis, which were acquired on a planar multielectrode array using the Panasonic (Matsushita, Osaka, Japan) MED64-system (Oka et al., 1999). Multielectrode recordings were performed with an 8 × 8 array of planar microelectrodes, each 20 x 20 μm in size, with an interpolar distance of 100 μm (MED-P2105, Panasonic; Tensor Biosciences, Irvine, CA). Slices were positioned on the array and maintained in a submerged condition. ACSF containing 20 μM carbachol, bubbled with carbogen, was superfused at 4–6 ml/min. Signals were low-pass filtered at 2 kHz for both field and unit recordings. Data acquisition was done with a PCI-6024E board (National Instruments, Austin, TX) using either EVAN 1.3 (courtesy of Dr. I. Mody, Departments of Neurology and Physiology, University of California Los Angeles, Los Angeles, CA) or IGOR (WaveMetrics, Lake Oswego, OR) software and analyzed offline using Origin 7.0, Igor Pro 4.0, and Matlab 6.0 software. For investigation of stability of oscillations in submerged slices, power spectra were estimated from 1-min-long traces with the Welch method using 1-sec-wide time windows with 50% overlap. Peak frequencies and summated power in the frequency range of 20–47 Hz were used for comparison. Peak-to-peak averages were made by averaging successive peak-to-peak signals interpolated to a 100-point wave. One-dimensional CSD profiles were calculated as the second spatial derivative of these peak-to-peak averages. To examine the firing properties of neurons relative to the ongoing field oscillation, stationary 1- to 3-min-long recording epochs were analyzed, to collect a minimum of 200 spikes. Absolute spike times were calculated using threshold detection for high-pass filtered (>100 Hz) single-unit recordings, with spike detection threshold adjusted by visual inspection. Spike timing was analyzed using spike time histograms, calculated relative to the negative peak of the peak-to-peak averages. Because in several examples spike time distributions showed clear asymmetry, the mode of the histograms was used for the comparison. To enable comparison of our *in vitro* data with those obtained in freely moving animals (Csicsvari et al., 2003), spike phase was calculated relative to the negative peak of a cycle of the bandpass-filtered field recording in the frequency range of 15–45 Hz using a high-order digital Finite Impulse Response (FIR) filter. Field signal was filtered in both directions to conserve the phase of the oscillations. Phase values of individual cells were analyzed by circular statistical methods using Oriana 2.0 software (Kovach Computing Services, Anglesey, UK). Significant deviation from uniform (random) phase distribution along the circle indicates directionality. This was tested with Rao's spacing test and Rayleigh's uniformity test (both calculates the probability of the null hypothesis that the data are distributed in a uniform manner). To characterize a nonuniform distribution, two parameters of its mean vector (calculated from individual observations) were used, i.e., the mean angle and the length of the mean vector. The length, a measure of disparity, ranges from 0 to 1; larger values indicate that the observations are clustered more closely around the mean than lower ones. To illustrate the precision of spiking during oscillations, we used values of angular SD, where lower numbers indicate stronger phase-coupling. Note that field oscillations recorded at 2 kHz and the peak-to-peak averages (used for calculation of spike times) clearly deviated from the sinusoidal waveforms obtained after bandpass filtering of field signals (used for calculation of spike phases). Because of this difference, the negative peaks of the peak-to-peak averages (0 msec) and the bandpass filtered signals (0°) did not correspond to each other (see Fig. 3). Data are presented as mean ± SEM. Statistical significance was assessed using *t* test ($p < 0.05$).

Anatomical identification of cells. After intracellular recording and biocytin filling, the slices were fixed in 4% paraformaldehyde in 0.1 M phosphate buffer (PB; pH 7.4) for at least 30 min, followed by washout with PB several times, and incubation in cryoprotecting solution (30% sucrose in 0.01 M PB) for 2 hr. Then slices were freeze-thawed three times above liquid nitrogen and treated with 1% H_2O_2 in PB for 15 min to reduce endogenous peroxidase activity. Filled cells were visualized using avidin-biotinylated horseradish peroxidase complex reaction (ABC; Vector Laboratories, Burlingame, CA) with nickel-intensified 3,3′-diaminobenzidine (Sigma) as chromogen giving a dark blue reaction product. After dehydration and embedding in Durcupan, representative neurons were reconstructed with the aid of a drawing tube using a 40 or 63× objective.

Results

Persistent network oscillations at gamma frequency were induced in hippocampal slices under submerged condition by bath application of 20 μM carbachol (Fig. 1*A*). Network oscillations were monitored by an extracellular recording electrode in the pyramidal cell layer of the CA3b region. First, we characterized the properties and temporal stability of carbachol-induced gamma oscillations under these conditions. Both the frequency (34.6 ± 0.9 Hz) and the gamma-band power ($9.2 \pm 1.2 \times 10^{-9}$ V^2; $n = 6$) of the oscillations, which showed only minor fluctuations during the recording period (up to 1 hr) (Fig. 1*B*), were comparable with those reported earlier in interface chamber (Fisahn et al., 1998; Pálhalmi et al., 2004). Thus, gamma oscillations with properties similar to those found under interface conditions can be investigated in submerged slices.

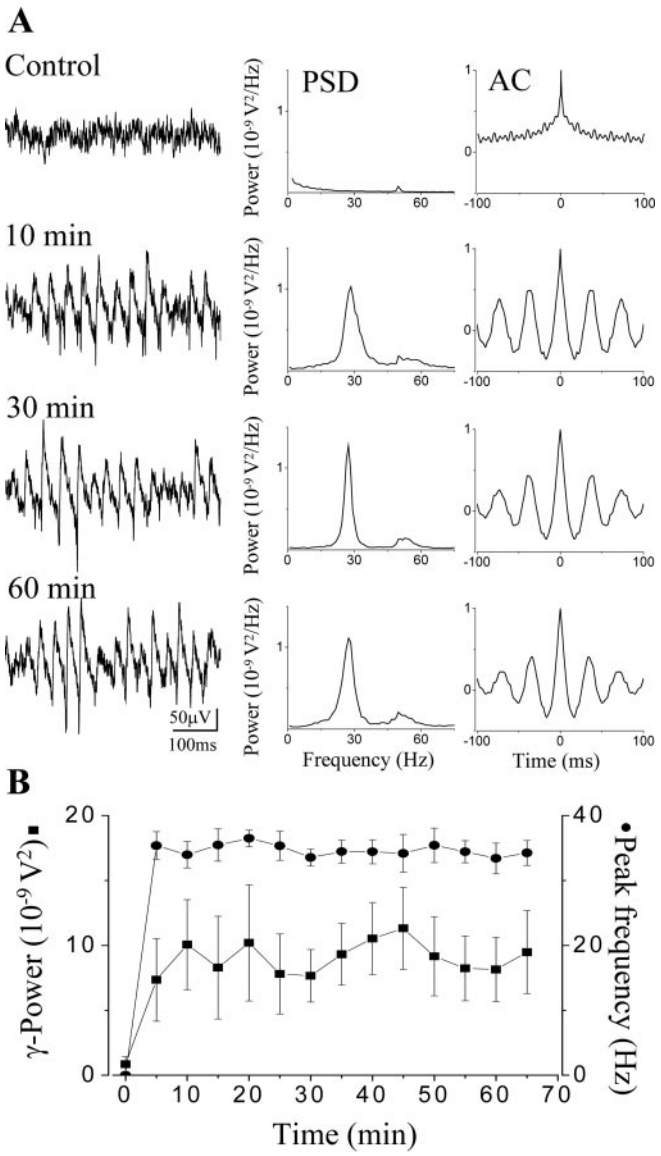

Figure 1. Carbachol-induced gamma oscillations in submerged hippocampal slices. *A*, A representative experiment of synchronous activity after bath application of 20 μM carbachol, a cholinergic agonist, demonstrating the temporal stability of the oscillation. Field potential recordings were obtained in the stratum pyramidale of the CA3 hippocampal region. During the control period, no rhythmicity can be seen. Drug application induced a stable oscillation in 10 min that was sustained for at least 1 hr. Corresponding power spectra (PSD) and autocorrelation (AC) of the recordings at different time points were calculated from 1-min-long epochs. *B*, Stability of the gamma oscillations (gamma power, square; peak frequency, circle) in submerged slices illustrated on a summary graph obtained from six different experiments. Data points represent mean ± SEM.

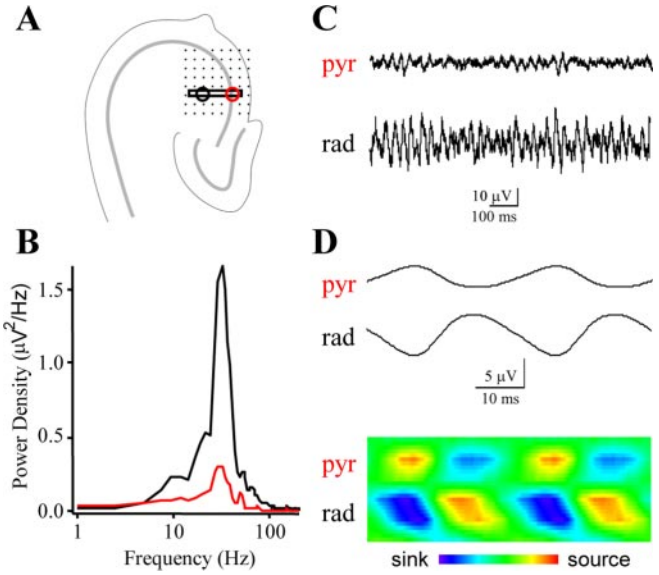

Figure 2. CSD analysis of cholinergically induced oscillations in submerged slices. *A*, Network oscillations induced by 20 μM carbachol were recorded across the CA3 subfield from slices mounted on 64-electrode arrays. The sample recordings from the stratum pyramidale and stratum radiatum shown in *C* and *D* were taken from the electrodes marked by the red and black circles, respectively. The black box marks the electrodes used for calculating the current source density profile in *D*. *B*, The power spectral density functions of the field oscillation in the stratum pyramidale (red) and stratum radiatum (black) both revealed peaks at 32 Hz. *C*, Example traces from the stratum pyramidale (top) and stratum radiatum (bottom) show a clear reversal in the polarity of the field oscillation between these layers. *D*, Peak-to-peak cycle averages were calculated for the gamma-frequency oscillations, using a reference from the stratum pyramidale (marked with red circle in *A*). The average period was 29 msec. The peak-to-peak averages were used to construct CSD profiles for the gamma-frequency oscillations, which revealed alternating sink (blue) and source (red) pairs in the stratum pyramidale and stratum radiatum.

Next, we performed CSD analysis of the carbachol-induced field oscillation acquired on a 64-channel planar multielectrode probe organized in an 8-by-8 array (interelectrode center-to-center distance of 100 μm) (Fig. 2*A*). The peak frequency of the oscillations was 31.6 ± 2.1 Hz (n = 5) (Fig. 2*B*). The largest-amplitude oscillations in local field potentials were recorded in the proximal stratum radiatum (Fig. 2*C*) with clear phase reversal compared with oscillations in the stratum pyramidale as seen on the corresponding peak-to-peak averages (Fig. 2*D*). The CSD analysis uncovered sink-source pairs in strata radiatum and pyramidale that were alternating periodically (Fig. 2*D*), similar to what has been reported *in vivo* (Bragin et al., 1995; Csicsvari et al., 2003). This CSD profile raises the question of whether different sources could be produced by distinct sets of interneurons with different laminar and target selectivity of their axon terminals. We therefore performed a detailed analysis of the spiking properties of distinct types of interneurons, with identified axonal and dendritic arbors, relative to ongoing gamma-frequency network oscillations.

After induction of stable network oscillations, action potentials were recorded extracellularly from visually identified neurons followed by intracellular labeling via a different patch pipette to enable *post hoc* anatomical identification. Results are reported only for those neurons that could be unequivocally classified based on their synaptic input and output characteristics (i.e., dendritic and axonal arborizations) (n = 54 from a total of 101 recorded neurons).

Relative to the extracellularly recorded field oscillation, all pyramidal cells (n = 10 of 10) and a proportion of interneurons (n = 31 of 44) showed phase-related firing. Two different methods were used to quantify the phase-related firing. First, a peak-to-peak average of the oscillation was made between consecutive negative peaks, and a spike time histogram constructed based on the spike timing relative to each peak-to-peak interval, normalized to the overall mean length of the peak-to-peak interval. Second, to facilitate comparison to earlier reports *in vivo* (Csicsvari et al., 2003), the field oscillation was bandpass-filtered between 15 and 45 Hz and the phase of firing was calculated relative to the negative peak of the bandpass-filtered oscillation. The phase histogram of those cells that could not be distinguished from a uniform distribution using both Rayleigh's uniformity test and Rao's

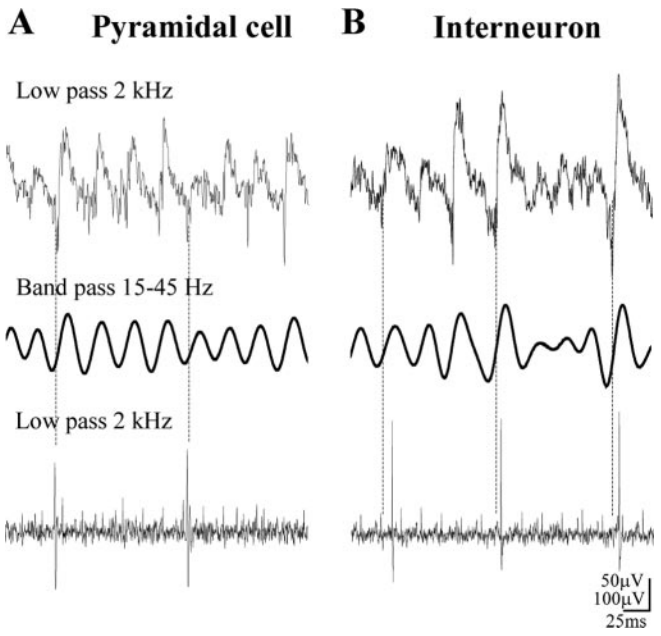

Figure 3. Cholinergically induced gamma oscillations in the pyramidal cell layer consist of slow and fast components. Field recordings low-pass-filtered at 2 kHz contain an oscillatory component, which is often decorated at the negative part with spike-like elements (top row). For the detailed analysis of gamma oscillations, traces were bandpass filtered in the frequency range of 15–45 Hz using a high-order FIR filter in both directions to conserve the phase of the oscillation. Note that negative peaks of the oscillation on filtered signals are shifted compared with those seen in the raw recordings (dashed line). Comparison of unit recordings during oscillations obtained from a pyramidal cell (*A*) and from an interneuron [*post hoc* identified as an OLM cell (*B*)] revealed that firing of the pyramidal cell took place at the negative peak of the gamma oscillation (dashed line), whereas the OLM cell discharged with a short delay (bottom row).

spacing test were classified as nonphase-coupled neurons and not included in the further analysis.

Pyramidal cells fired action potentials around the negative peak of the oscillations with an average spike time of 0.03 ± 0.65 msec after the negative peak ($n = 10$) (Figs. 3*A*, 4*A*). The field oscillation as recorded in the pyramidal cell layer was regular but deviated significantly from a purely sinusoidal waveform. On a proportion of cycles, a variable negative spike-like component followed by a positive wave was observed. Pyramidal neuron firing tended to be close to the negative peak of the oscillation, coinciding with this spike-like component when present, suggesting that these spikes of the field recording reflect population discharges of pyramidal cell ensembles of variable size (Fig. 3*A*). All pyramidal neurons showed significant phase-coupling (length of the mean vector calculated from the phase histograms for each cell >0.2, $p < 0.05$, Rao's spacing test and Rayleigh's uniformity test). The mean angle of their spike times relative to the bandpass-filtered field signal was 58.1 ± 5.3° (mean ± 95% confidence interval). The phase coupling of pyramidal cells was weaker than that of the majority of interneurons, as indicated by an angular SD of 59.1 ± 6.1° (Fig. 4*A*). The average frequency of pyramidal cell firing was 2.82 ± 0.7 Hz (Fig. 4*A*). Because the spiking of phase-coupled cells varies with the oscillation frequency, we divided the firing rate with the oscillation frequency to compare the activity of different cell types. For the pyramidal cells, the firing rate divided by the oscillation frequency was 0.09 ± 0.02 (i.e., these neurons fired on fewer than every 10th cycle of the oscillation).

Relative to the pyramidal cells, all interneurons that were phase-coupled to the oscillation fired significantly later, on the ascending phase of the field potential, as recorded in the pyramidal cell layer (Figs. 3*B*, 4*B*, *C*, 5, 6). Perisomatic inhibitory cells were the most abundant cell group among the sampled interneurons ($n = 14$ of 31). Among them, 12 basket cells and 2 putative axo-axonic cells were distinguished based on their axonal arborizations. Both cell types had either multipolar or bitufted dendritic tree. The axon of the basket cells arborized rather evenly in the stratum pyramidale with some collaterals penetrating into strata oriens and lucidum, and only occasionally into the stratum radiatum (Fig. 4*B*), whereas axon branches of the putative axo-axonic cells were restricted to the bottom part of the stratum pyramidale and the top part of the stratum oriens, often giving rise to short bouton-laden collaterals with vertical or oblique orientation (Fig. 4*C*). Because some axo-axonic cells might have been misclassified as basket cells, and we were unable to provide electron microscopic evidence to unequivocally identify the two putative axo-axonic cells, we decided to pool data from all perisomatic inhibitory cells and analyze them together. One example for each cell type is shown in Figure 4, *B* and *C*. Eleven of fourteen perisomatic inhibitory neurons showed significant phase coupling (length of the mean vector >0.2; $p < 0.05$; Rao's spacing test and Rayleigh's uniformity test) (Fig. 7*B,C*). In comparison with other cell types, the perisomatic inhibitory cells discharged action potentials at a high rate (18.1 ± 2.7 Hz) (Fig. 7*A,G*). The spike rate divided by the oscillation frequency was 0.62 ± 0.09 for this cell type (Fig. 7*D*), meaning that on average they fired on more than every second cycle of the oscillation. Their average spike time was 1.97 ± 0.95 msec after the negative peak of the oscillation (Figs. 4*B,C*, 8*A,C*). Relative to the bandpass-filtered oscillation signal, the average phase of firing was 93 ± 2.1° ($n = 11$) (Fig. 7*E,G*). The firing of perisomatic inhibitory cells was tightly coupled to the oscillation, as shown by a mean angular SD of 51.1 ± 5° (Figs. 4*B,C*, 7*F*). Correlation of discharge frequency with spike times indicated that more active cells tended to fire earlier on an oscillation cycle ($r = -0.581$; $p = 0.06$) (Fig. 8*B*). In one putative axo-axonic and three basket cells, two spikes per cycle ("doublets") were often observed.

Among the dendritic inhibitory cells, we classified OLM cells (interneurons with dendritic tree in stratum oriens and axonal projection into stratum lacunosum-moleculare) (Fig. 5A), radiatum cells (RCs) (both the dendritic and axonal arborization localized in the stratum radiatum) (Fig. 5*B*), and RLM cells (dendritic tree found primarily in stratum radiatum with axon restricted to stratum lacunosum-moleculare) (Fig. 5*C*). The firing properties of dendritic inhibitory neurons varied between these subtypes. All but one OLM cell was phase-coupled ($n = 4$ of 5) (Fig. 7*B*). Their discharge rate was relatively high (12.9 ± 1.8 Hz) (Figs. 5*A*, 7*A*). Spike rate divided by oscillation frequency was 0.4 ± 0.07 (Fig. 7*D*), i.e., these cells fired on almost every second cycle of the oscillation. Their spikes also occurred after the negative peak of the oscillations with an average spike time of 2.95 ± 0.44 msec after the negative peak (Fig. 8*A,C*). The mean angle of the firing (obtained from the filtered signal) was 88.1 ± 6.1° (Fig. 7*E,G*). The phase coupling of OLM cells showed large variability with a mean angular SD of 59.8 ± 14.5° (Figs. 5*A*, 7*F*). Radiatum cells showed the most heterogeneous behavior. Only three of seven radiatum cells showed significant phase-coupling (Fig. 7*B*). These radiatum cells had the lowest firing rate among all neurons (2.3 ± 0.6 Hz, $n = 3$) (Figs. 5*B*, 7*A*, *G*) as also indicated by their spike rate divided by oscillation frequency (0.07 ± 0.02) (Fig. 7*D*). Of all cells recorded, the radiatum cells discharged with the

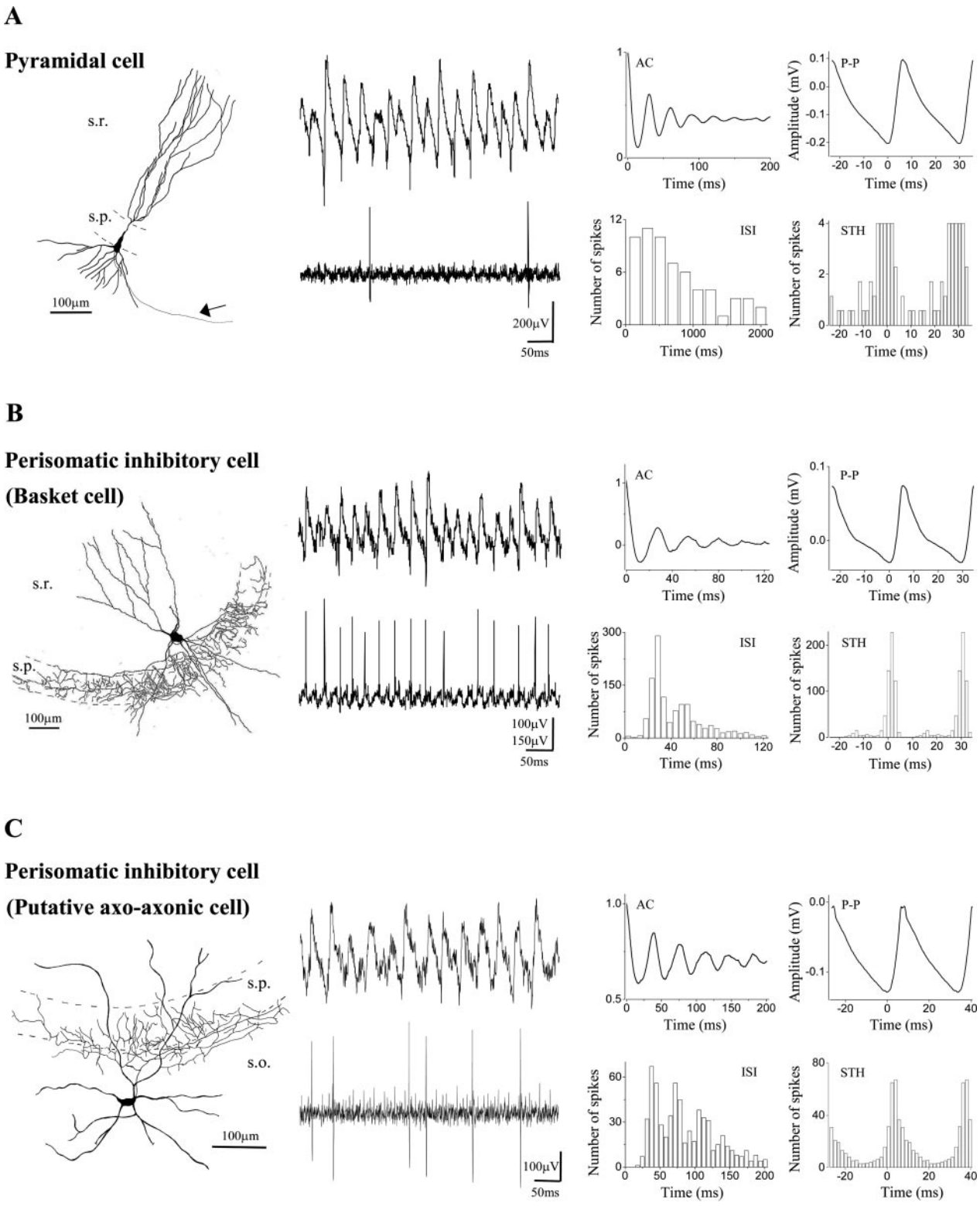

Figure 4. Firing properties of pyramidal cells and perisomatic inhibitory neurons during cholinergically induced gamma oscillations. Camera lucida reconstructions of intracellularly labeled neurons are shown in the left column. *A*, Pyramidal cell located at the border of strata pyramidale and oriens had an extensive dendritic arborization outside the pyramidal cell layer. In this case, only the main axon projecting toward the fimbria-fornix (arrow) could be followed. *B*, Multipolar basket cell with soma in the stratum lucidum gave rise to a dense axonal ramification almost completely restricted to the stratum pyramidale. *C*, A putative axo-axonic cell with axon collaterals at the border of strata pyramidale and oriens, showing short vertical and oblique axon segments studded with boutons. The cell body and the large part of the dendritic arbor were found in the stratum oriens, but some dendrites also penetrated into the strata pyramidale and lucidum. The middle panel of the figure shows representative traces for each cell illustrating the different firing activity during gamma oscillations. The pyramidal cell discharged at 1.1 Hz, the basket cell at 22.8 Hz, and the axo-axonic cell at 11.8 Hz. The right panels show autocorrelograms (AC), interspike interval histograms (ISI), peak-to-peak averages (P-P), and spike time histograms (STH) for each cell type calculated from a 3-min-long epoch for the pyramidal cell and from 1-min-long epochs for interneurons. Spike time histograms show that the pyramidal cell fired at the negative peak of the oscillations, whereas interneurons fired with a short delay. Note that perisomatic inhibitory cells follow the oscillations with high fidelity, as can be seen by comparing the ISI histograms with the autocorrelograms. s.r., Stratum radiatum; s.p., stratum pyramidale; s.o., stratum oriens.

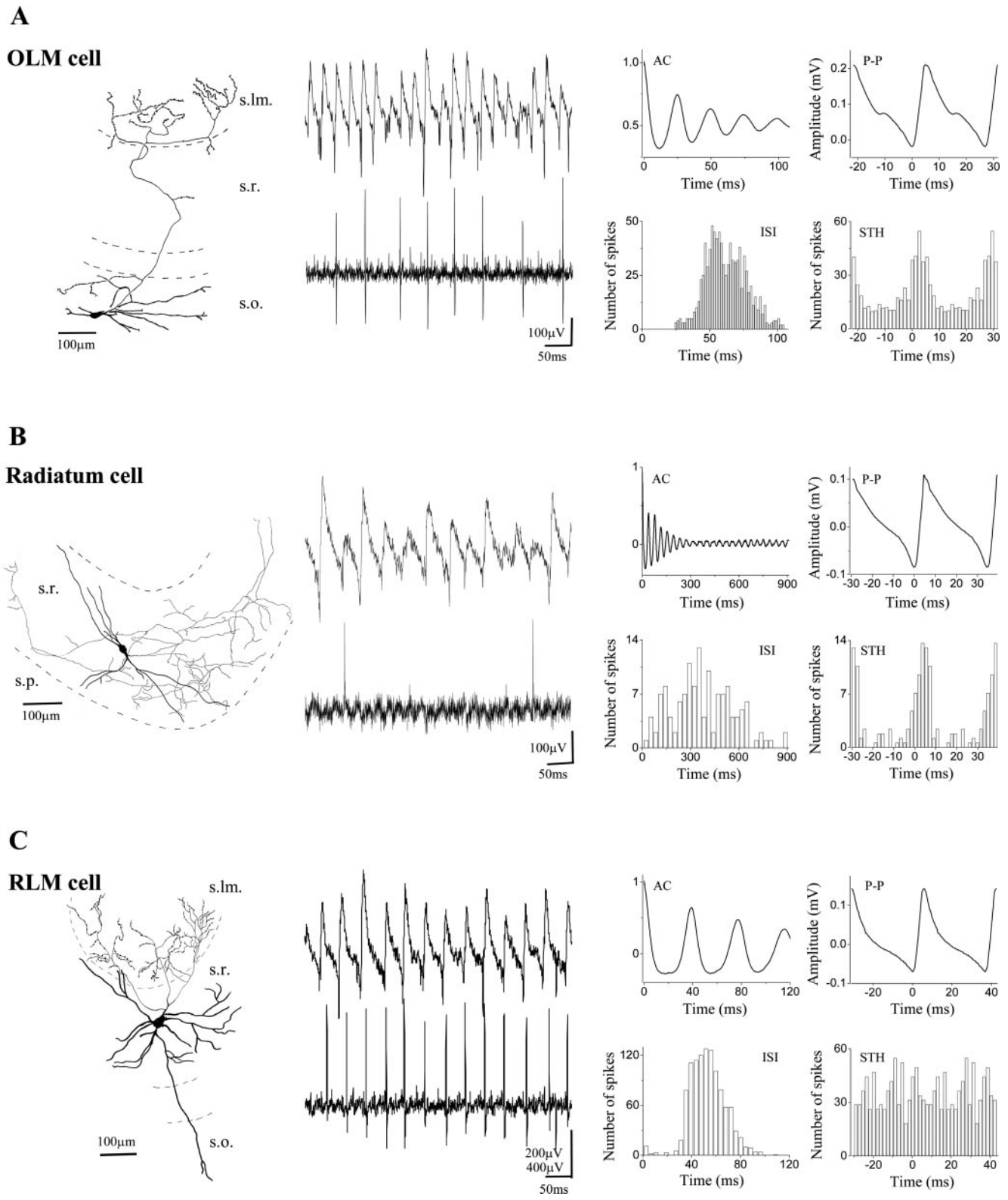

Figure 5. Behavior of dendritic inhibitory interneurons during carbachol-induced network oscillations. Camera lucida reconstructions of an OLM cell (*A*), a radiatum cell (*B*), and an RLM cell (*C*) are shown. *A*, Both the cell body and the dendritic arbor of the OLM cell were found in the stratum oriens, whereas most of the varicose axon collaterals were restricted to the stratum lacunosum-moleculare. *B*, The dendritic tree, as well as the axon cloud of the radiatum cell, were located in the stratum radiatum. *C*, The RLM cell with the majority of dendrites in the stratum radiatum exclusively projected to the stratum lacunosum-moleculare. Representative recordings for each cell type demonstrate the different firing characteristics (middle panel). The spike frequency was 15.7 Hz for the OLM cell, 2.5 Hz for the radiatum cell, and 18.5 Hz for the RLM cell. The corresponding data calculated from 1-min-long recording epochs are illustrated in the right column. As seen on the STHs compared with the P-P, both the OLM cell and the radiatum cell fired phased-coupled to the oscillations after the negative peak. The ISIs together with ACs indicate that the OLM cell discharged on every second or third cycle, whereas the radiatum cell was much less active. In contrast, the firing of the RLM cell showed no phase relationship indicated by uniform distribution in the spike time histogram, although both the oscillations and the discharge of the neuron were prominent shown by the AC and ISI histogram, respectively. s.lm., Stratum lacunosum-moleculare.

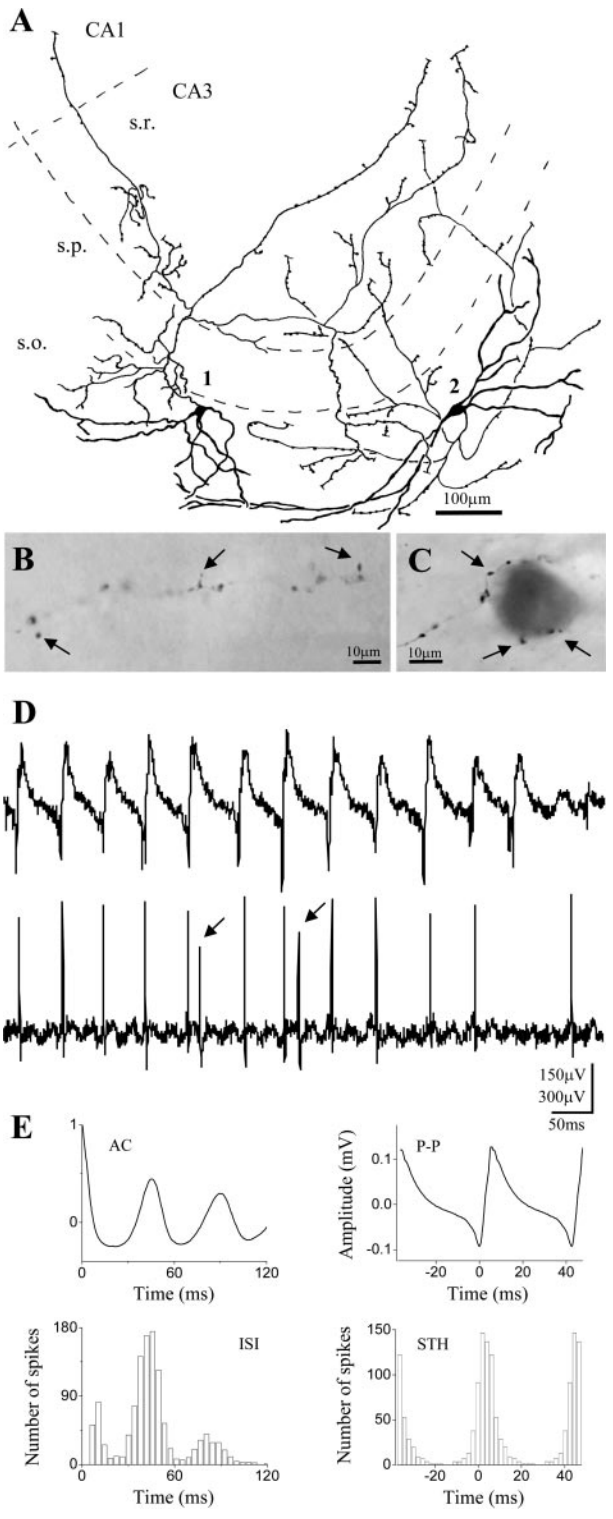

Figure 6. Firing of IS cells is tightly coupled to gamma oscillation. *A–C*, Light microscopic reconstruction of two intracellularly filled putative IS cells. The cell bodies and the dendritic arbors for both neurons were found in the stratum oriens (*A*). The main axon originating from the somata gave rise to several collaterals predominantly arborizing in strata oriens and radiatum. Long axon branches reaching the CA3c region as well as penetrating into the CA1 were often decorated by drumstick-like boutons (*B*, arrows), whereas other varicose collaterals formed multiple appositions (arrows) with nonpyramidal cell bodies in the strata oriens or radiatum (*C*). *D*, Raw traces showing the firing activity of cell 2 during the oscillation (20.8 Hz). Arrows mark the second spike within an oscillation cycle. *E*, Results calculated from a 1-min-long recording epoch showing that the neuron discharged on the ascending phase of the oscillation as indicated on the STH in conjunction with the P-P. Its spiking followed the oscillation with a high fidelity as demonstrated by the ISI together with the AC.

greatest delay after the negative peak of the oscillation (6.23 ± 2.14 msec) (Fig. 8*A,C*). The mean angle of the spike times was 128.4 ± 12.4° (Fig. 7*E,G*) with weak coupling to the oscillations (mean angular SD, 58.3 ± 7.3°) (Fig. 7*F*). Those radiatum cells that were not recruited in the synchronous activity had significantly higher firing frequency (8.7 ± 1.1 Hz; $n = 4$; $p < 0.01$). None of the recorded RLM cells showed significant phase coupling (Figs. 5*C*, 7*B*), but they showed relatively high firing frequency (13.2 ± 3.9 Hz; $n = 4$) (Figs. 5*C*, 7*A*).

A third main group of interneurons was identified on the basis of the following light microscopic criteria: (1) long axon collaterals with infrequent branching, sometimes penetrating into the CA1 region (Fig. 6*A*); (2) axon terminals were irregularly spaced often with drumstick-like appendages (Fig. 6*B*), and (3) labeled terminals consistently formed close appositions with unlabelled cell bodies outside of the stratum pyramidale resembling GABAergic somata (Fig. 6*C*). These morphological features were found to be characteristic of interneuron-selective (IS) cells, i.e., interneurons that were shown to selectivity innervate other local GABAergic cells in the hippocampus (Acsády et al., 1996; Gulyás et al., 1996; Gulyás et al., 2003), but were considerably different from horizontal bistratified cells in the stratum oriens (Maccaferri et al., 2000). Based on the criteria described above, we would refer to these neurons as IS cells. According to the laminar distribution of their axons, IS cells belong to the so-called trilaminar cells (Sik et al., 1995), which, however, do not represent a functional category. In addition to IS cells (Gulyás et al., 2003), they appear to include also cells that widely innervate pyramidal neurons (Sik et al., 1995). The light microscopic characteristics of IS cells described above unequivocally distinguish these two cell types with distinct target selectivity. In the present study, IS cells were labeled in the stratum oriens with long dendrites restricted to this layer (Fig. 6*A*). All but one IS cell fired with high frequency (18.2 ± 2.7 Hz) (Figs. 6*D*, 7*A,G*) and were strongly phase-coupled (Figs. 6*E,* 7*B*). The spike rate divided by the oscillation frequency was 0.6 ± 0.09 (Fig. 7*D*), i.e., these neurons also discharged on more than every second cycle of the oscillation. In three cells doublet spikes were also noticed (Fig. 6*D*). The average spike time of the first spike for these cells was 1.51 ± 0.37 msec (Fig. 8*A,C*). The mean angle obtained from the bandpass-filtered signal was 96.8 ± 2.2° ($n = 7$) (Fig. 7*E,G*). As indicated by their angular SD (46.1 ± 5.5°) (Fig. 7*F*), IS cells followed the gamma oscillations with high fidelity.

Comparison of the firing phase between interneurons and pyramidal cells revealed that pyramidal cells fired significantly earlier than all types of interneuron (Fig. 7*G*) (Watson-Williams *F* test, $p < 0.05$), similar to data obtained in freely moving rat (Csicsvari et al., 2003). In addition, radiatum cells fired significantly later than perisomatic inhibitory cells, OLM cells, and IS cells (Fig. 7*G*) (Watson-Williams *F* test; $p < 0.05$), whereas the firing phase of these latter three cell types was indistinguishable. The average time difference of spiking between pyramidal cells and interneurons (excluding radiatum cells) was 2.1 ± 0.5 msec ($n = 22$) (Fig. 8*C*), consistent with monosynaptic neurotransmission at 30°C.

Discussion

The main findings of the present study are the following: (1) long-lasting, temporally stable oscillatory activity can be induced in submerged hippocampal slices; (2) in the carbachol model of gamma oscillations, pyramidal cells fire at the negative peak of

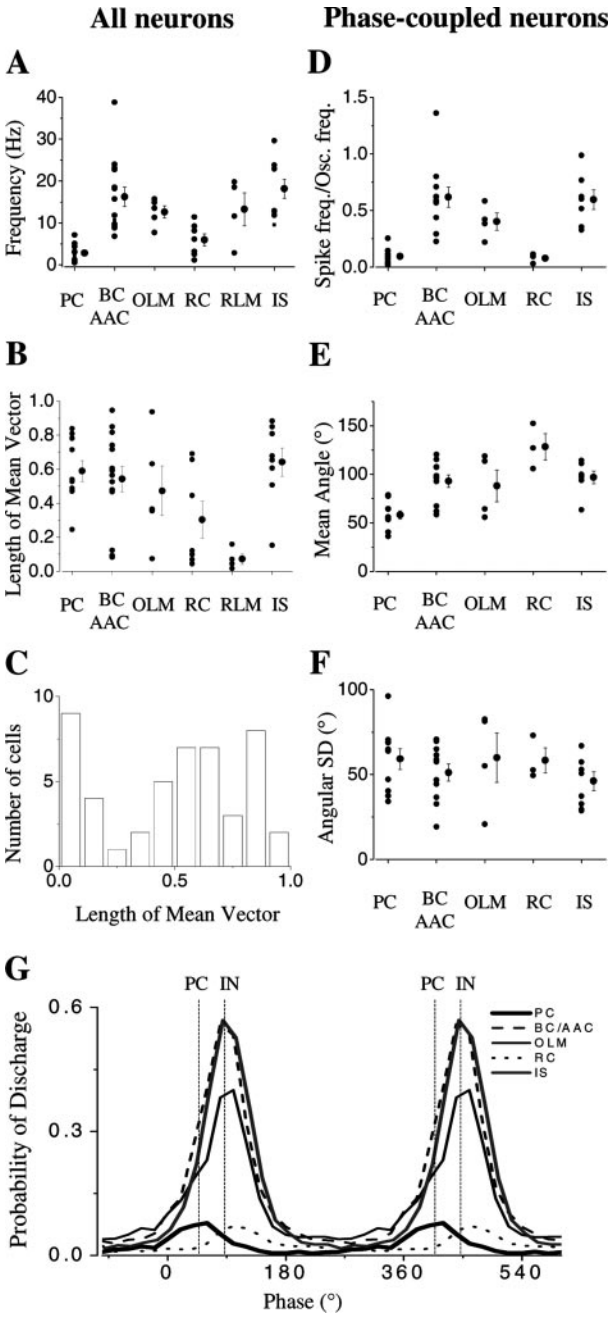

Figure 7. Phase relationship between field oscillations and spiking of identified neurons during cholinergically induced gamma oscillations. *A–C*, Analysis in all neurons. *A*, *B*, Frequency and length of mean vector plotted for all morphologically identified neurons in each cell category. Note that in all interneuron groups, at least one cell was found not to be significantly phase-coupled. *C*, Histogram of the length of mean vector, including data for all cells showing a bimodal distribution. Values of the mean vector <0.2 suggested a uniform distribution (Rao's spacing test and Rayleigh's uniformity test, $p > 0.05$). Further detailed analysis was performed only on phase-coupled neurons. *D–F*, Firing rate divided by oscillation frequency (*D*), mean angle (*E*), and angular SD, indicating the precision of phase-coupling (*F*) varied substantially among the cell types. Individual points on the plots represent data for individual cells, whereas the mean ± SEM is indicated on the right for each neuron type. PC, Pyramidal cell; BC, basket cell; AAC, axo-axonic cell; OLM, interneurons in the stratum oriens projecting to the stratum lacunosum-moleculare; RC, interneurons with both dendritic and axonal arborizations restricted to the stratum radiatum; RLM, interneurons with dendritic tree in the stratum radiatum projecting into the stratum lacunosum-moleculare; IS, cells with morphological appearance resembling interneuron-selective interneurons. *G*, Average phase histograms of unit activity during gamma oscillations showing that PC discharge is followed by discharge of the various types of interneuron (IN). Dotted vertical lines indicate the mean of the mode of the phase angle for pyramidal cells and all classes of interneurons, respectively.

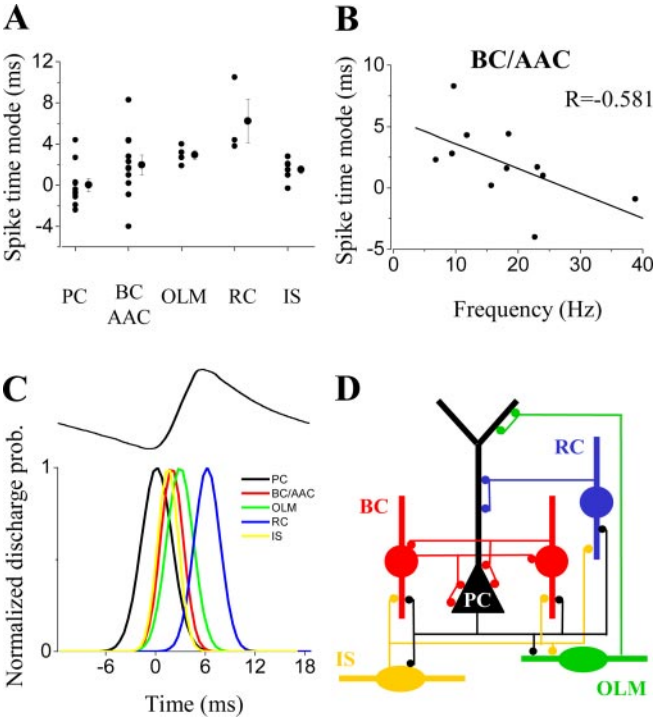

Figure 8. Time relationship between field potentials and spiking activity of identified hippocampal neurons during oscillations. *A*, Mode of the spike time histograms relative to the time of the negative peak of the average oscillation plotted for the different types of hippocampal neurons. The individual points on the plot represent data for individual cells, whereas the mean ± SEM is indicated on the right for each type of neuron. *B*, Negative correlation between the rate of firing of individual perisomatic inhibitory neurons (basket and axo-axonic cells) and their relative spike times. Cells with higher discharge rate tend to fire closer to the negative peak. *C*, Time sequence of firing of different neuron types during an oscillatory cycle. Top trace shows representative average field oscillatory wave. Pyramidal cells fired at the negative peak of the oscillation followed by the interneurons. Gaussian functions were fitted to the spike time distribution for each type of neuron, and the average mean and SD were used to represent each cell class as a Gaussian function. *D*, Schematic diagram of the connectivity among phase-coupled neuron types in the CA3 hippocampal circuitry taking part in the gamma oscillation.

the oscillations followed by the discharge of interneurons; and (3) perisomatic inhibitory neurons and IS cells are the most active cell types during this type of oscillation with strong phase coupling, whereas dendritic-targeting interneurons show less or sometimes no significant phase coupling.

Previous *in vitro* studies showed that gamma-frequency network oscillations lasting for tens of minutes could be routinely induced in hippocampal slices in an interface-type of recording chamber (Whittington et al., 1995; Boddeke et al., 1997; Fisahn et al., 1998; Pálhalmi et al., 2004). In contrast, oscillations evoked in submerged-type of slice chambers, designed for visually guided patch-clamp recordings using infrared DIC optics, lasted for only some seconds and were qualitatively different from those recorded in interface conditions (McMahon et al., 1998; Kawaguchi, 2001). Here, we combine the advantages of both techniques, i.e., maintenance of long-lasting stable oscillations with visualization of individual neurons, by improving the recording conditions in submerged chamber to allow us to study the behavior of different types of neuron during network oscillations. The possibility of obtaining stable oscillations for >1 hr suggests that these conditions may be appropriate for exploring many aspects of network physiology *in vitro*.

Different *in vitro* models of gamma oscillations have been introduced that suggest that distinct mechanisms could lead to fast synchronous oscillatory activity in the hippocampal subfields. In the CA1 region, but not in CA3, both chemically and electrically interconnected interneuronal networks could generate 40 Hz oscillations without any contribution of pyramidal cells (Whittington et al., 1995; Boddeke et al., 1997; Hormuzdi et al., 2001; Traub et al., 2001a). On the other hand, different protocols that excite both pyramidal cells and interneurons (Fisahn et al., 1998; LeBeau et al., 2002; Cunningham et al., 2003; Pálhalmi et al., 2004) were found to induce *in vitro* gamma oscillations in both CA1 and CA3, implying that synchronization could also occur as an interplay between excitatory cells and GABAergic interneurons. Both *in vitro* and *in vivo* studies (Fisahn et al., 1998; Csicsvari et al., 2003; Pálhalmi et al., 2004) suggested that during gamma oscillations in CA3, pyramidal cells drive local interneurons in a feedback manner. Here we tested predictions of this hypothesis by measuring the firing properties and phase relationship of anatomically identified interneurons and compared them to those of pyramidal cells. Our data show that most interneuron subtypes do indeed discharge with a delay after pyramidal cells consistent with monosynaptic transmission. Although our values are somewhat different from those predicted by a study in the olfactory system (Eeckman and Freeman, 1990), they are in good agreement with data obtained in the hippocampus of freely moving rats (Csicsvari et al., 2003).

In addition, our experiments revealed that functionally distinct interneuron subtypes show different firing properties during *in vitro* oscillations. Perisomatic inhibitory interneurons were found to fire with high discharge rate, strongly phase-coupled to the network oscillation. In contrast, OLM cells showed phase-coupled firing at somewhat lower frequency, whereas the majority of interneurons in the stratum radiatum targeting the dendritic region of pyramidal cells (radiatum and RLM cells) did not show significant phase-related firing. Cells belonging to a third functional category of GABAergic neurons, the IS cells, which share several morphological similarities with GABAergic cells projecting to the medial septum (Gulyás et al., 2003), also fired with high discharge rate, tightly locked to the oscillation. This heterogeneity in the firing patterns of different types of interneuron raises the question of what is the main determining factor of their distinct behavior. One explanation might be that different interneurons have a distinct firing preference for a given oscillatory input. As suggested by Pike et al. (2000), hippocampal fast-spiking cells (corresponding, at least partly, to perisomatic inhibitory cells) are "tuned" to gamma frequency range. In contrast, some cells in stratum oriens (that may correspond to OLM cells) as well as pyramidal cells showed firing preference at θ frequencies. Our results showed that perisomatic inhibitory cells can follow gamma oscillations with high fidelity, whereas OLM cells and pyramidal cells fired at a lower rate, suggesting that intrinsic membrane properties might indeed contribute to the different firing properties during oscillations.

Another explanation for the heterogeneity in firing might be that excitatory input from CA3 pyramidal cells could drive interneurons with different efficacy. Given that the axons of CA3 pyramidal cells first enter the stratum oriens where they give rise to all their recurrent collaterals, some of which turn to penetrate into the stratum radiatum projecting toward the CA1 region (Sik et al., 1993; Li et al., 1994), one might assume that in slices, the chance of preserving intact axon collaterals from pyramidal cells in the stratum oriens is higher than in the stratum radiatum. In fact, we found that the vast majority of interneurons in the stratum oriens were phase-coupled (86%; 56 of 65), whereas <50% of the neurons in the strata radiatum or lucidum had any phase relationship (44%; 14 of 32), regardless of the axon arborization pattern. The timing and the kinetics of excitation received by different interneuron types could also contribute to their distinct firing reliability and frequency (Jonas et al., 2004; Pouille and Scanziani, 2004). Studies are underway to establish whether the intrinsic properties of interneurons or the magnitude and integration of synaptic input are the more important factors in determining firing properties during network oscillations.

The finding that most interneurons in carbachol-induced oscillations were excited in a feedback manner raises the question of which inhibitory cell types are more important for synchronization. We suggest that perisomatic inhibitory cells, including both basket and axo-axonic cells, are in a key position to synchronize the network, because they effectively control spike timing of pyramidal cells (Cobb et al., 1995; Miles et al., 1996), which in turn could reliably excite them via monosynaptic connections (Gulyás et al., 1993; Sik et al., 1993). Thus, a pyramidal cell-perisomatic inhibitory neuron loop could generate fast oscillations in the CA3 network, as suggested by modeling studies (Traub et al., 2000). These suggestions are also supported by the results obtained with CSD analysis, which showed periodic sources in the stratum pyramidale after the peak discharge phase of perisomatic inhibitory interneurons. Conversely, there were no dendritic current sources that could be attributed to fast inhibition after the peak discharge of dendritic interneurons. Indeed, the firing phase and frequency of pyramidal cells and inhibitory interneurons imply that sinks and sources in the stratum pyramidale are active processes paralleled by passive currents in proximal stratum radiatum. Another question relates to the events that terminate the firing of basket cells after discharging a single spike (or sometimes doublets). The control of basket cell firing might derive from two independent sources. First, it has been shown that basket cells are mutually interconnected (Sik et al., 1995; Klausberger et al., 2002) and communicate via IPSCs of large amplitude and fast kinetics (Bartos et al., 2002), providing a possibility to effectively regulate the firing of one another. Second, IS cells, another cell type that fired tightly coupled to the oscillation, may also be able to terminate the firing of perisomatic inhibitory neurons (Fig. 8*D*).

Several studies showed (for review, see Traub et al., 2001b) that bath application of carbachol could induce seizure-like activity in hippocampal slices. Under our circumstances, appearance of interictal spikes was present in <5% of slices in conjunction with gamma oscillations. These slices were excluded from the study.

A comparison of *in vitro* gamma oscillations induced by carbachol in the CA3 region of hippocampal slices with those obtained in freely moving animals (Bragin et al., 1995; Csicsvari et al., 2003) reveals striking similarities. First, the origin of gamma oscillations is intrinsic to the CA3 neuronal network (Fisahn et al., 1998). Second, there is a phase reversal in stratum lucidum of CA3 (Fig. 2*C*) (Fisahn et al., 1998; Shimono et al., 2000). Third, CA3 pyramidal cell firing is followed by the discharge of CA3 interneurons with a delay consistent with monosynaptic transmission (present study). These observations suggest that carbachol-induced oscillations in the CA3 region represent a physiologically relevant model and can be used to study the cellular mechanisms underlying the generation, maintenance, and

termination of synchronous activity at 40 Hz. It should be noted, however, that gamma oscillations recorded in other regions of the hippocampus may rely on different mechanisms, because neuronal circuitries of the CA3 subfield have some unique features such as the recurrent collateral system.

In summary, in the cholinergic model of gamma oscillations, recurrent excitation of inhibitory interneurons by CA3 pyramidal cells could give rise to synchronization of the local neuronal network (Fig. 8*D*). Based on previous data and our current results, perisomatic inhibitory cells are likely to play an instrumental role during gamma oscillations by controlling the precise timing of firing of pyramidal cell assemblies.

References

Acsády L, Gorcs TJ, Freund TF (1996) Different populations of vasoactive intestinal polypeptide-immunoreactive interneurons are specialized to control pyramidal cells or interneurons in the hippocampus. Neuroscience 73:317–334.

Bartos M, Vida I, Frotscher M, Meyer A, Monyer H, Geiger JR, Jonas P (2002) Fast synaptic inhibition promotes synchronized gamma oscillations in hippocampal interneuron networks. Proc Natl Acad Sci USA 99:13222–13227.

Boddeke HW, Best R, Boeijinga PH (1997) Synchronous 20 Hz rhythmic activity in hippocampal networks induced by activation of metabotropic glutamate receptors in vitro. Neuroscience 76:653–658.

Bragin A, Jando G, Nadasdy Z, Hetke J, Wise K, Buzsáki G (1995) Gamma (40–100 Hz) oscillation in the hippocampus of the behaving rat. J Neurosci 15:47–60.

Buzsáki G, Chrobak JJ (1995) Temporal structure in spatially organized neuronal ensembles: a role for interneuronal networks. Curr Opin Neurobiol 5:504–510.

Chrobak JJ, Buzsáki G (1998) Gamma oscillations in the entorhinal cortex of the freely behaving rat. J Neurosci 18:388–398.

Cobb SR, Buhl EH, Halasy K, Paulsen O, Somogyi P (1995) Synchronization of neuronal activity in hippocampus by individual GABAergic interneurons. Nature 378:75–78.

Cunningham MO, Davies CH, Buhl EH, Kopell N, Whittington MA (2003) Gamma oscillations induced by kainate receptor activation in the entorhinal cortex in vitro. J Neurosci 23:9761–9769.

Csicsvari J, Jamieson B, Wise KD, Buzsáki G (2003) Mechanisms of gamma oscillations in the hippocampus of the behaving rat. Neuron 37:311–322.

Eeckman FH, Freeman WJ (1990) Correlations between unit firing and EEG in the rat olfactory system. Brain Res 528:238–244.

Engel AK, Fries P, Singer W (2001) Dynamic predictions: oscillations and synchrony in top-down processing. Nat Rev Neurosci 2:704–716.

Fell J, Klaver P, Lehnertz K, Grunwald T, Schaller C, Elger CE, Fernandez G (2001) Human memory formation is accompanied by rhinal-hippocampal coupling and decoupling. Nat Neurosci 4:1259–1264.

Fisahn A, Pike FG, Buhl EH, Paulsen O (1998) Cholinergic induction of network oscillations at 40 Hz in the hippocampus in vitro. Nature 394:186–189.

Freund TF, Buzsáki G (1996) Interneurons of the hippocampus. Hippocampus 6:347–470.

Fries P, Reynolds JH, Rorie AE, Desimone R (2001) Modulation of oscillatory neuronal synchronization by selective visual attention. Science 291:1560–1563.

Gray CM (1994) Synchronous oscillations in neuronal systems: mechanisms and functions. J Comput Neurosci 1:11–38.

Gulyás AI, Miles R, Sik A, Toth K, Tamamaki N, Freund TF (1993) Hippocampal pyramidal cells excite inhibitory neurons through a single release site. Nature 366:683–687.

Gulyás AI, Hájos N, Freund TF (1996) Interneurons containing calretinin are specialized to control other interneurons in the rat hippocampus. J Neurosci 16:3397–3411.

Gulyás AI, Hájos N, Katona I, Freund TF (2003) Interneurons are the local targets of hippocampal inhibitory cells which project to the medial septum. Eur J Neurosci 17:1861–1872.

Hájos N, Mann EO, Freund TF, Paulsen O (2004) Increased oxygen supply enables cholinergically-induced network oscillations in submerged hippocampal slices. Fed European Neurosci Soc Abstr 2:A009.013.

Hasselmo ME, Wyble BP, Wallenstein GV (1996) Encoding and retrieval of episodic memories: role of cholinergic and GABAergic modulation in the hippocampus. Hippocampus 6:693–708.

Hormuzdi SG, Pais I, LeBeau FE, Towers SK, Rozov A, Buhl EH, Whittington MA, Monyer H (2001) Impaired electrical signaling disrupts gamma frequency oscillations in connexin 36-deficient mice. Neuron 31:487–495.

Jonas P, Bischofberger J, Fricker D, Miles R (2004) Interneuron diversity series: fast in, fast out–temporal and spatial signal processing in hippocampal interneurons. Trends Neurosci 27:30–40.

Kawaguchi Y (2001) Distinct firing patterns of neuronal subtypes in cortical synchronized activities. J Neurosci 21:7261–7272.

Klausberger T, Roberts JD, Somogyi P (2002) Cell type- and input-specific differences in the number and subtypes of synaptic GABA(A) receptors in the hippocampus. J Neurosci 22:2513–2521.

Klausberger T, Magill PJ, Marton LF, Roberts JD, Cobden PM, Buzsáki G, Somogyi P (2003) Brain-state- and cell-type-specific firing of hippocampal interneurons in vivo. Nature 421:844–848.

Klausberger T, Marton LF, Baude A, Roberts JD, Magill PJ, Somogyi P (2004) Spike timing of dendrite-targeting bistratified cells during hippocampal network oscillations in vivo. Nat Neurosci 7:41–47.

LeBeau FE, Towers SK, Traub RD, Whittington MA, Buhl EH (2002) Fast network oscillations induced by potassium transients in the rat hippocampus in vitro. J Physiol (Lond) 542:167–179.

Leung SW (1979) Potentials evoked by alvear tract in hippocampal CA1 region of rats. II. Spatial field analysis. J Neurophysiol 42:1571–1589.

Li XG, Somogyi P, Ylinen A, Buzsáki G (1994) The hippocampal CA3 network: an in vivo intracellular labeling study. J Comp Neurol 339:181–208.

Maccaferri G, Roberts JD, Szucs P, Cottingham CA, Somogyi P (2000) Cell surface domain specific postsynaptic currents evoked by identified GABAergic neurones in rat hippocampus in vitro. J Physiol (Lond) 524:91–116.

Marrosu F, Portas C, Mascia MS, Casu MA, Fa M, Giagheddu M, Imperato A, Gessa GL (1995) Microdialysis measurement of cortical and hippocampal acetylcholine release during sleep-wake cycle in freely moving cats. Brain Res 671:329–332.

McMahon LL, Williams JH, Kauer JA (1998) Functionally distinct groups of interneurons identified during rhythmic carbachol oscillations in hippocampus *in vitro*. J Neurosci 18:5640–5651.

Miles R, Toth K, Gulyás AI, Hájos N, Freund TF (1996) Differences between somatic and dendritic inhibition in the hippocampus. Neuron 16:815–823.

Oka H, Shimono K, Ogawa R, Sugihara H, Taketani M (1999) A new planar multielectrode array for extracellular recording: application to hippocampal acute slice. J Neurosci Methods 93:61–67.

Pálhalmi J, Paulsen O, Freund TF, Hájos N (2004) Distinct properties of carbachol- and DHPG-induced network oscillations in hippocampal slices. Neuropharmacology 47:381–389.

Paulsen O, Moser EI (1998) A model of hippocampal memory encoding and retrieval: GABAergic control of synaptic plasticity. Trends Neurosci 21:273–278.

Pike FG, Goddard RS, Suckling JM, Ganter P, Kasthuri N, Paulsen O (2000) Distinct frequency preferences of different types of rat hippocampal neurones in response to oscillatory input currents. J Physiol (Lond) 529:205–213.

Pouille F, Scanziani M (2004) Routing of spike series by dynamic circuits in the hippocampus. Nature 429:717–723.

Shimono K, Brucher F, Granger R, Lynch G, Taketani M (2000) Origins and distribution of cholinergically induced beta rhythms in hippocampal slices. J Neurosci 20:8462–8473.

Sik A, Tamamaki N, Freund TF (1993) Complete axon arborization of a single CA3 pyramidal cell in the rat hippocampus, and its relationship with postsynaptic parvalbumin-containing interneurons. Eur J Neurosci 5:1719–1728.

Sik A, Penttonen M, Ylinen A, Buzsáki G (1995) Hippocampal CA1 interneurons: an in vivo intracellular labeling study. J Neurosci 15:6651–6665.

Singer W (1993) Synchronization of cortical activity and its putative role in information processing and learning. Annu Rev Physiol 55:349–374.

Soltesz I, Bourassa J, Deschenes M (1993) The behavior of mossy cells of the

rat dentate gyrus during theta oscillations in vivo. Neuroscience 57:555–564.

Traub RD, Bibbig A, Fisahn A, LeBeau FE, Whittington MA, Buhl EH (2000) A model of gamma-frequency network oscillations induced in the rat CA3 region by carbachol in vitro. Eur J Neurosci 12:4093–4106.

Traub RD, Kopell N, Bibbig A, Buhl EH, LeBeau FE, Whittington MA (2001a) Gap junctions between interneuron dendrites can enhance synchrony of gamma oscillations in distributed networks. J Neurosci 21:9478–9486.

Traub RD, Whittington MA, Buhl EH, LeBeau FE, Bibbig A, Boyd S, Cross H, Baldeweg T (2001b) A possible role for gap junctions in generation of very fast EEG oscillations preceding the onset of, and perhaps initiating, seizures. Epilepsia 42:153–170.

Varela F, Lachaux JP, Rodriguez E, Martinerie J (2001) The brainweb: phase synchronization and large-scale integration. Nat Rev Neurosci 2:229–239.

Whittington MA, Traub RD (2003) Interneuron diversity series: inhibitory interneurons and network oscillations in vitro. Trends Neurosci 26:676–682.

Whittington MA, Traub RD, Jefferys JG (1995) Synchronized oscillations in interneuron networks driven by metabotropic glutamate receptor activation. Nature 373:612–615.

Ylinen A, Soltesz I, Bragin A, Penttonen M, Sik A, Buzsáki G (1995) Intracellular correlates of hippocampal theta rhythm in identified pyramidal cells, granule cells, and basket cells. Hippocampus 5:78–90.

dc_71_10

8. számú melléklet

Neuron, Vol. 45, 105–117, January 6, 2005, Copyright ©2005 by Elsevier Inc. DOI 10.1016/j.neuron.2004.12.016

Perisomatic Feedback Inhibition Underlies Cholinergically Induced Fast Network Oscillations in the Rat Hippocampus In Vitro

Edward O. Mann,[1,*] Jillian M. Suckling,[1,2] Norbert Hajos,[1,3] Susan A. Greenfield,[2] and Ole Paulsen[1]

[1]University Laboratory of Physiology
Oxford University
Parks Road
Oxford OX1 3PT
United Kingdom

[2]Department of Pharmacology
Oxford University
Mansfield Road
Oxford OX1 3QT
United Kingdom

[3]Institute of Experimental Medicine
Hungarian Academy of Sciences
P.O. Box 67
Budapest H-1450
Hungary

Summary

Gamma frequency network oscillations are assumed to be important in cognitive processes, including hippocampal memory operations, but the precise functions of these oscillations remain unknown. Here, we examine the cellular and network mechanisms underlying carbachol-induced fast network oscillations in the hippocampus in vitro, which closely resemble hippocampal gamma oscillations in the behaving rat. Using a combination of planar multielectrode array recordings, imaging with voltage-sensitive dyes, and recordings from single hippocampal neurons within the CA3 gamma generator, active current sinks and sources were localized to the stratum pyramidale. These proximal currents were driven by phase-locked rhythmic inhibitory inputs to pyramidal cells from identified perisomatic-targeting interneurons. AMPA receptor-mediated recurrent excitation was necessary for the synchronization of interneuronal discharge, which strongly supports a synaptic feedback model for the generation of hippocampal gamma oscillations.

Introduction

Network oscillations in the gamma frequency range (~30–100 Hz), which are a characteristic feature of the awake brain during attention, have been proposed to provide a temporal structure for various cognitive processes, including sensory binding (Singer, 1993), selective attention (Fries et al., 2001), and consciousness (Llinas et al., 1998). In the hippocampus, gamma activity has been implicated in memory processing (Jensen and Lisman, 1996; Lisman and Idiart, 1995) and is commonly observed superposed on theta-frequency oscillations (4–12 Hz) (Bragin et al., 1995; Lisman and Idiart, 1995; Hasselmo et al., 1996; Buzsaki et al., 2003; Csicsvari et al., 2003). To establish more precisely what functional role gamma oscillations may subserve, it will be necessary to elucidate the underlying mechanisms. Given the extensive knowledge of hippocampal connectivity, physiology, and neurochemical anatomy, hippocampal gamma oscillations offer an attractive opportunity to investigate the cellular processes involved.

Two largely independent gamma generators have been identified in the hippocampal formation in vivo: the dentate gyrus and the CA3-CA1 system (Bragin et al., 1995; Csicsvari et al., 2003). The gamma oscillations in the dentate gyrus are driven by extrahippocampal cortical inputs and are virtually abolished by lesions of the entorhinal cortex (Bragin et al., 1995). In contrast, the CA3-CA1 system appears to form an intrinsic intrahippocampal gamma generator, in which the oscillation is generated in the recurrent CA3 network and then propagates to CA1 (Csicsvari et al., 2003). Intrahippocampal gamma activity is associated with alternating pairs of current sinks and sources in the pyramidal cell layer and the stratum radiatum (Bragin et al., 1995; Csicsvari et al., 2003), but the precise cellular and synaptic events that generate these extracellular currents have not been determined. While it has been demonstrated that both pyramidal cells and interneurons fire phase locked to the gamma oscillation (Bragin et al., 1995; Penttonen et al., 1998; Csicsvari et al., 2003) and that CA1 pyramidal cells receive gamma frequency rhythmic inhibition (Penttonen et al., 1998), the relative contributions of recurrent excitation and somatodendritic inhibition to the extracellular sink/source distribution have not been established. Furthermore, it is not yet clear whether gamma frequency synchronization in the CA3 network arises via entrainment by an interneuronal network (Whittington et al., 1995) or from synaptic recurrent feedback loops (Freeman, 1968). Therefore, what cellular currents are being recorded as gamma oscillations in the field potential and how this activity is synchronized remain uncertain. Understanding such "current" and "rhythm" generation is necessary to determine the network state during gamma oscillations and, thus, the computational roles that this rhythm could fulfill (Buzsaki, 2002).

Network oscillations in the gamma frequency range can be induced in the hippocampus in vitro by muscarinic acetylcholine receptor (mAChR) activation (Fisahn et al., 1998; Fellous and Sejnowski, 2000). At room temperature, these oscillations can be in the beta frequency range as defined in vivo (~15–30 Hz), but fall clearly in the gamma frequency band when recorded at or above 32°C (C. Ecker et al., 2001, Soc. Neurosci., abstract; Dickinson et al., 2003). They will subsequently be referred to as fast network oscillations. Such cholinergically induced fast network oscillations share many of the features of intrahippocampal gamma oscillations in vivo, including pyramidal neurons firing at low frequencies (<5 Hz) phase locked to the oscillation and the oscillation being generated in CA3 and propagating to CA1 (Fisahn et al., 1998; Csicsvari et al., 2003). Such a model has some inherent appeal, since the hippocampus re-

*Correspondence: ed.mann@physiol.ox.ac.uk

dc_71_10

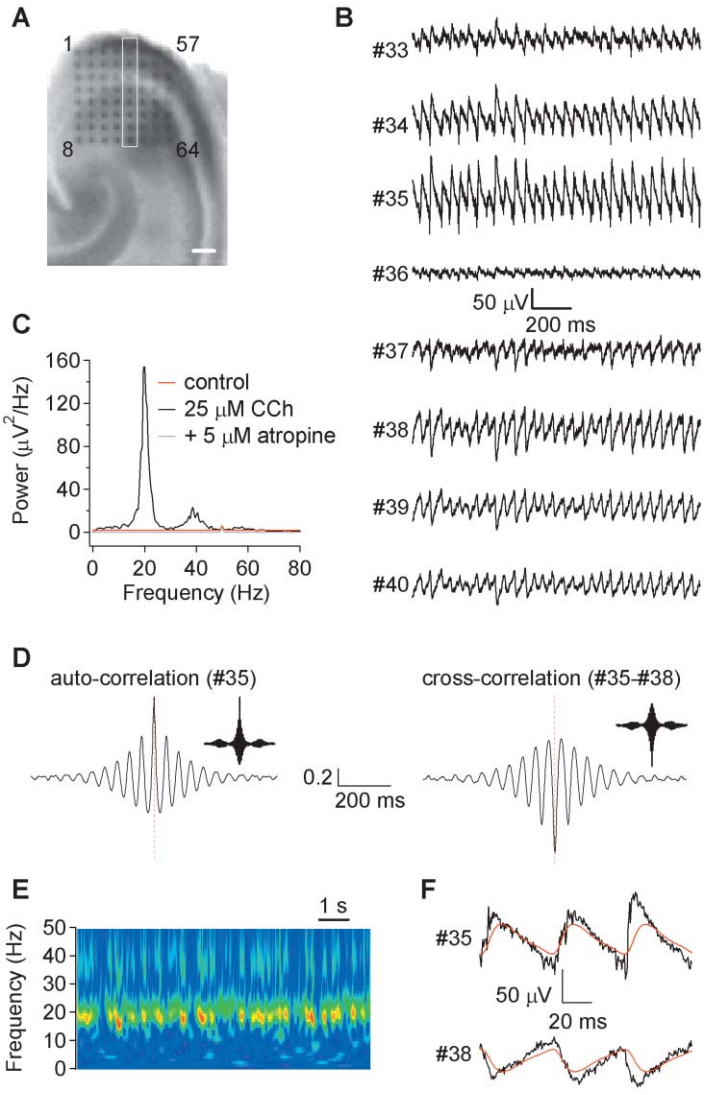

Figure 1. Carbachol-Induced Fast Network Oscillations Recorded on Multielectrode Arrays

(A) Slice mounted on 64 electrode array recording from CA3. The white box marks the column of electrodes used for presentation in (B). Electrode numbers are provided for references in the remaining panels of the figure. Scale bar, 200 μm. (B) Application of 25 μM carbachol induced oscillations in the field potentials across the different layers of CA3, with reversal of the polarity of the field oscillation in stratum lucidum (#36). (C) The power spectral density of the field oscillation in the stratum pyramidale (#35) revealed a peak at 20 Hz, with a harmonic at 40 Hz. There was no rhythmic activity prior to carbachol application (control), and the network oscillation was completely blocked by 5 μM atropine. (D) The autocorrelogram of the oscillation recorded in the stratum pyramidale (left) demonstrates robust rhythmicity in the fast network oscillation, with a period of 50 ms. The cross-correlogram between the oscillation recorded in the stratum pyramidale and distal stratum radiatum (right) reveals that these signals were π radians (180°) out of phase. Both the autocorrelogram and the cross-correlogram display side bands at ~0.86 s (inset), showing that the fast network oscillations were amplitude modulated at low frequencies (1–2 Hz). (E) The stability of the fast network oscillation over time, analyzed using wavelet transform [normalized Morlet wavelet; $\omega_0 = 6$; scales chosen to reflect unit frequencies (f) between 1 and 50 Hz; scale = $(\omega_0 + \sqrt{(2 + \omega_0^2)})/4\pi f$]. The magnitude of the wavelet transform was plotted as a function of time and frequency (corresponding to scale), with warmer colors representing increasing magnitude.

(F) Peak-to-peak cycle averages for the fast network oscillation (red traces) with an average period of 48 ms. These peak-to-peak averages fitted the time course of the underlying oscillation (black traces).

ceives a dense cholinergic projection from the medial septum/diagonal band of Broca, which plays a permissive role in the generation of hippocampal network activity (Leung, 1985; but see Lee et al., 1994). To elucidate the cellular and synaptic mechanisms underlying gamma frequency "current" and "rhythm" generation within the hippocampus, we analyzed fast network oscillations in vitro, using a combination of field recordings with planar multielectrode arrays, imaging with voltage-sensitive dyes (VSD), and recordings from individual pyramidal cells and interneurons. Our data demonstrate that cholinergically induced fast network oscillations are mediated by rhythmic perisomatic inhibition, which is synchronized by recurrent synaptic excitation.

Results

Muscarinic Receptor Activation Induces Fast Network Oscillations in the CA3 Region of the Hippocampus

To monitor field potentials, hippocampal slices were mounted on 8 × 8 planar multielectrode arrays with 100 μm spacing (Oka et al., 1999; Shimono et al., 2000) oriented across the different layers of hippocampal CA3 (see Figure 1A). Application of 25 μM carbachol induced persistent oscillations that could be recorded in all layers of the CA3 (Figure 1B), with a mean frequency of 18.9 ± 0.5 Hz at room temperature and a mean peak power of 55 ± 18 μV^2/Hz (n = 25; see Figure 1C), and often could be amplitude modulated at low frequencies (1–2 Hz; 11 of 25 slices; Figure 1D). The carbachol-induced fast network oscillations were completely blocked by the selective mAChR antagonist atropine (n = 12; Figure 1C).

The phase of the carbachol-induced oscillations reversed steeply across the stratum lucidum of the CA3 subfield (Figure 1B), with oscillations in the stratum pyramidale and distal stratum radiatum being π radians (180 degrees) out of phase (Figure 1D). Such phase reversal is expected, as changes in the extracellular field potential predominantly reflect the flow of currents in circuits along the somatodendritic axis of pyramidal cells. To analyze the mechanisms underlying these currents, peak-to-peak cycle averages were calculated for the

fast network oscillations (see Experimental Procedures). Such calculation of cycle averages assumes that the oscillation is stable and persistent. Consequently, the time-frequency characteristics of fast network oscillations were analyzed using wavelet analysis (Morlet wavelet, $\omega_0 = 6$), which does not assume stationarity and is sensitive to discontinuities (Torrence and Compo, 1998). The wavelet magnitude spectrum revealed that the oscillation frequency was stable over time and that the oscillation amplitude often showed low-frequency modulation (Figure 1E), consistent with the results from the Fourier power spectrum and autocorrelation analysis (see Figures 1C and 1D). Peak-to-peak averaging was therefore justified, and the resulting cycle averages fitted closely to the recorded responses (mean period, 48.2 ± 1.3 ms; Figure 1F).

Distribution of Current Sinks and Sources in the CA3 Region during Fast Network Oscillations

To accurately localize the sinks and sources of extracellular currents within the CA3, current-source density (CSD) profiles were constructed from cycle averages (Mitzdorf, 1985). CSD analysis of gamma oscillations in the hippocampus in vivo has been performed mainly in one dimension (1D) across the strata, assuming that extracellular currents orthogonal to the recording probe have a minimal effect on the spatial sink/source profile (see Holsheimer, 1987). This might not necessarily be justified in the centripetally organized CA3, so we started by comparing 1D and 2D CSD profiles. Both CSD methods revealed alternating sink and source pairs in the stratum pyramidale and distal stratum radiatum (Figure 2). There were small quantitative differences in the CSD analysis between the two methods (Supplemental Figure S1 [http://www.neuron.org/cgi/content/full/45/1/105/DC1/]), but as CSD analysis was subsequently used only for qualitative comparisons, 1D and 2D CSD were considered interchangeable.

Perisomatic Currents Are the Active Events Driving Sink-Source Pairs in the CA3 Region during Fast Network Oscillations

Analysis of the CSD profiles of network oscillations reveals the sinks and sources of extracellular currents, but does not distinguish between the active current generators and passive return currents. For example, a sink in the stratum pyramidale and its corresponding source in the stratum radiatum could reflect somatic excitation and/or dendritic inhibition. To elucidate the active events, CSD analysis was combined with imaging using a neuronally selective voltage-sensitive dye, Di-4-ANEPPS (Tominaga et al., 2000), to reveal the voltage changes accompanying the extracellular currents. It was found that current sinks in the stratum pyramidale with corresponding sources in the distal stratum radiatum were followed by depolarization in the perisomatic regions of CA3 pyramidal neurons, which then propagated into the apical dendrites (Figure 3A). The opposite sink/source pair preceded a hyperpolarization at perisomatic sites, with a subsequent hyperpolarization in the apical dendrites (Figure 3A). This pattern was consistent over all 25 slices tested (Figure 3B), with changes in fractional fluorescence during fast network activity, representing

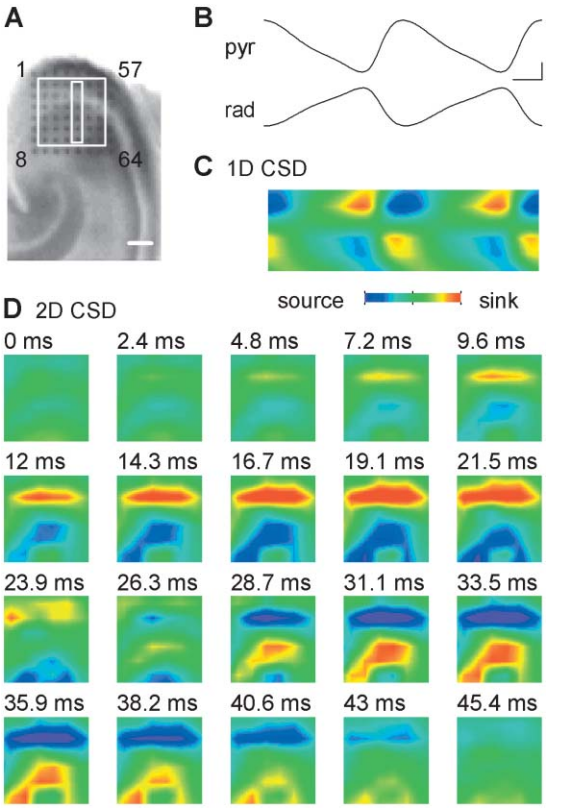

Figure 2. Spatial Pattern of Current Sinks and Sources during Fast Network Oscillations

(A) Multielectrode arrays were used to calculate 1D and 2D CSD profiles across CA3 for carbachol-induced fast network oscillations. The white rectangle marks the column of six electrodes used for 1D CSD profiles. The large white box marks the area of 36 electrodes included in the 2D CSD profiles. Electrode numbers are provided for reference. Scale bar, 200 μm.

(B) Examples of peak-to-peak cycle averages from the stratum pyramidale (#35) and distal stratum radiatum (#38), which were used to construct CSD profiles. Scale bars, 20 μV and 10 ms.

(C) Linearly interpolated 1D CSD profile from the column of electrodes shown in (A), temporally aligned with peak-to-peak cycle averages in (B). The 1D CSD profile displays alternating current sink (red) and source (blue) pairs in the stratum pyramidale and stratum radiatum.

(D) 2D CSD profile for all 36 electrodes marked in (A), sampled every ~2.4 ms. The alternating current sink/source pairs in the stratum pyramidale and stratum radiatum were evident across the extent of CA3. Color coding for sinks (red) and sources (blue) on same scale as for (C).

membrane voltage changes that varied significantly across the CA3b somatodendritic axis [RM ANOVA, $F_{(1.9, 46.1)} = 13.2$, $p < 0.001$]. These changes were most prominent in the stratum pyramidale (pyramidale versus distal radiatum; $\Delta F/F = 6.2 \pm 1.0$ versus $3.8 \pm 0.6 \times 10^{-5}$; $p < 0.001$; see Figure 3Bi). The maximum rate of increase in fractional fluorescence in the stratum pyramidale preceded that in the stratum radiatum by 0.5 ± 0.1 radians (28.6 ± 6.6 degrees; 4.0 ± 0.9 ms) (statistical analysis performed on delays relative to peak field potential in distal radiatum; $p < 0.001$; see Figure 3Bii). The maximum negative change in the optical signal occurred in the stratum pyramidale (0.6 ± 0.1 radians,

dc_71_10

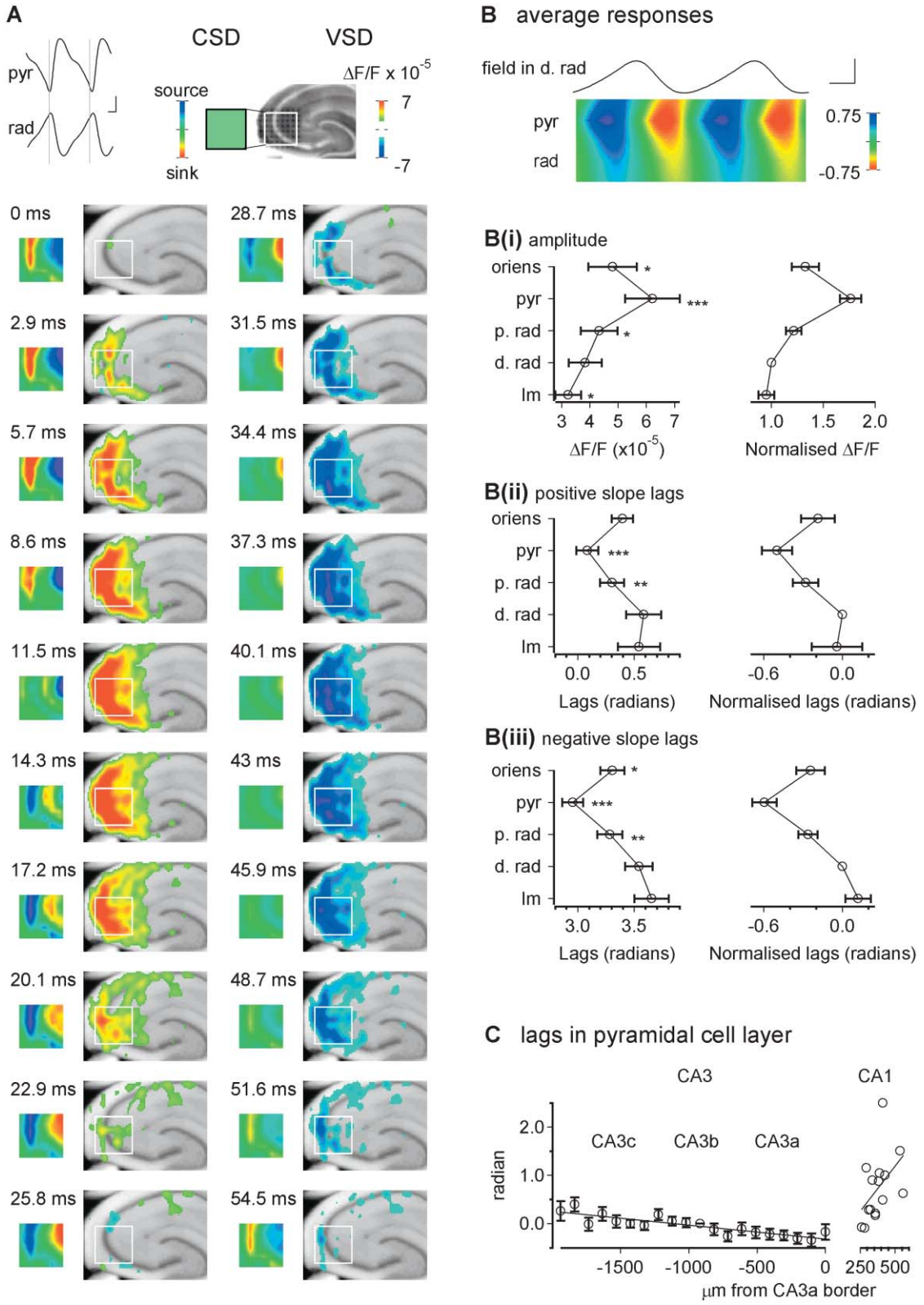

Figure 3. Voltage-Sensitive Dye Imaging of the Active Current Sinks and Sources Underlying Fast Network Oscillations

(A) VSD imaging using 200 μM Di-4-ANEPPS. Carbachol-induced oscillations were simultaneously recorded with multielectrode arrays. Examples of peak-to-peak cycle averages from the stratum pyramidale (pyr) and stratum radiatum (rad) are shown. For presentation, the 2D CSD profile from the inner 36 electrodes was displaced to the left, and pseudocolor images of the VSD signal were superposed on the image of the slice. The panel shows the 2D CSD profile sampled every ~2.9 ms. In the stratum pyramidale, current sinks (red) were followed by a

34.0 ± 5.3 degrees; 4.8 ± 0.8 ms) prior to that in the distal stratum radiatum ($p < 0.001$; see Figure 3Biii). Thus, the current sinks and sources in the stratum pyramidale appeared to represent the active events driving fast network oscillations, producing predominantly passive return currents in the stratum radiatum.

The changes in membrane voltage during fast network oscillations, revealed by imaging with voltage-sensitive dyes, were almost synchronous across the CA3 pyramidal cell layer (Figure 3A). Quantitatively, however, there were small, but significant, phase differences between the different CA3 subsegments. The time of the maximum negative slope in the optical signal was sampled for 20 equidistant points along the pyramidal cell layer of CA3 in each slice. This phase varied significantly across the CA3 stratum pyramidale [RM ANOVA, $F_{(8.3, 132.4)} = 4.34$, $p < 0.001$], showing a significant linear increase from CA3a to CA3c [RM ANOVA, $F_{(1, 16)} = 13.3$, $p < 0.01$] (Figure 3C). The average delay between the most extreme points in CA3a and CA3c was 0.6 radians (31.9 degrees; 4.5 ms) over a distance of approximately 2 mm. This result represents an average feature of the oscillation and does not suggest that the oscillation is exclusively generated in CA3a, as in some slices, rather than lagging, the CA3b/CA3c led the CA3a. Moreover, when the CA3a and CA3c were isolated by a physical cut, both subareas independently generated fast network oscillations (data not shown). The limited dimensions of the multielectrode probes precluded a detailed analysis of the fast network oscillations using field potentials. Nevertheless, in slices in which oscillations in the pyramidal cell layer could be recorded in the CA3a/CA3c relative to a central point in CA3b, there was a trend for the oscillations to be delayed in CA3c relative to CA3a (±200–600 μm from CA3b), consistent with the VSD data, but this delay did not reach statistical significance ($n = 10$, $r = 0.41$, $p = 0.07$). In contrast, there was a prominent delay in the optical signal in the CA1 relative to the CA3 (see Figure 3A). For slices in which the CA1 was present in the imaging window, there was a significant correlation between distance into CA1 and the delay in the optical signal ($n = 16$, $r = 0.52$, $p < 0.05$), with an average delay relative to the signal in CA3b of 0.4 radians (21.4 degrees; 4.3 ms) per 100 μm (Figure 3C). This is an order of magnitude greater than the mean delay of approximately 0.03 radians (1.6 degrees; 0.23 ms) per 100 μm observed within CA3. These data are consistent with propagation of the fast network oscillations along the Schaffer collaterals from CA3 into CA1, consistent with the properties of intrahippocampal gamma oscillations recorded in vivo (Csicsvari et al., 2003).

It was perhaps unexpected that no active current sinks/sources were observed in the stratum radiatum during fast network oscillations. To confirm that VSD imaging could detect a synaptically driven change of membrane potential in the dendritic membrane, we recorded the response of the CA3 network to extracellular stimulation in the stratum radiatum. This produced a transient sink in the CA3 stratum pyramidale, most likely due to antidromic conduction of action potentials into pyramidal cell somata, followed by a predominant sink/source pair in the stratum radiatum/stratum pyramidale due to local dendritic synaptic excitation (Figures 4Ai–4Ci). Indeed, VSD imaging showed that the current sink produced in the stratum radiatum by extracellular stimulation was followed by dendritic depolarization, as expected (Figure 4Di). In contrast, the current sink in the stratum radiatum during fast network oscillations was followed by membrane hyperpolarization in both the stratum pyramidale and stratum radiatum (Figures 4Aii–4Dii), suggesting that the extracellularly recorded sinks in the stratum radiatum during fast network oscillations are passive and predominantly reflect perisomatic inhibition. This result emphasizes the advantage of combining CSD analysis with other techniques to interpret CSD profiles (Bragin et al., 1995; Csicsvari et al., 2003).

Pyramidal Neurons Fire Phase Locked to Fast Network Oscillations

Both CSD and VSD profiles of the hippocampus predominantly reflect the electrical events occurring in pyramidal neurons, suggesting that carbachol-induced fast network oscillations involve rhythmic polarizations of pyramidal cell somata. To confirm the presence of these cellular oscillations, whole-cell current clamp recordings were made from CA3 pyramidal neurons, in combination with multielectrode recordings of the field potential. Eight out of ten pyramidal neurons recorded showed significant phase locking of action potential fir-

depolarization (red), and current sources (blue) were followed by hyperpolarization (blue). The membrane voltage changes spread into the dendrites, but there was no apparent membrane polarization associated directly with the current sinks/sources in the distal stratum radiatum. (B) Averages of VSD signals across slices in the stratum oriens (oriens), stratum pyramidale (pyr), proximal and distal stratum radiatum (p. rad and d. rad, respectively), and stratum lacunosum-moleculare (lm). The signals were normalized to those recorded in the distal stratum radiatum. The bilinearly interpolated, average, normalized VSD signal is presented, with the average peak-to-peak field oscillation in the distal stratum radiatum shown for reference. (Bi) The largest amplitude VSD signal was consistently observed in the stratum pyramidale, with the amplitude gradually decreasing with distance into the dendritic layers. (Bii) Maximum slopes of the VSD signal measured relative to the peak electrophysiological signal in the distal stratum radiatum. The maximum increase in the VSD signal in the stratum pyramidale occurred very shortly after the peak distal stratum radiatum field potential and after a delay in the dendritic layers. The VSD signal in the stratum lacunosum-moleculare sometimes occurred prior to that in the distal stratum radiatum, but was highly variable even after normalization. (Biii) Maximum negative slope of the VSD signal also occurred initially in the stratum pyramidale and later in the dendritic layers, but the signal in the stratum lacunosum-moleculare was more consistent with passive spread of the membrane potential changes. ($n = 25$; *$p < 0.05$; **$p < 0.01$; ***$p < 0.001$ in comparison with distal stratum radiatum; RM ANOVA, followed by within-subjects contrasts).

(C) Delay in the maximum negative slope of the VSD signal normalized to the delay at a central point in CA3b. On average, there was a significant linear delay in the VSD signal from CA3a to CA3c, and a linear fit is plotted with a lag of 0.6 radians across approximately 2 mm. Where possible, the delays in the VSD signals in the CA1 relative to the same signal in CA3b were also measured, showing a linearly increasing lag of 0.4 radians per 100 μm. For each slice, the delays were measured at equidistant points around the CA3, and the average distance between these points is given.

dc_71_10

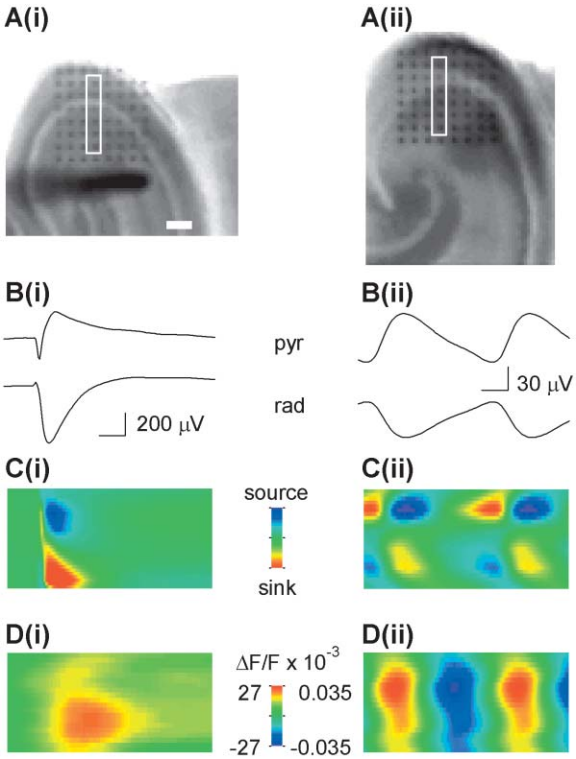

Figure 4. Comparison of the Active Sinks and Sources in CA3 Produced by Antidromic Activation and Fast Network Oscillations

(A) Multielectrode arrays were used to record field potentials in CA3 for (Ai) antidromic stimulation of the Schaffer collateral pathway and (Aii) carbachol-induced fast network oscillations. Scale bar, 200 μm. The white boxes show the electrodes used to construct 1D CSD profiles and the regions used for VSD images.

(B)(Bi) Sample averages of 16 responses evoked by bipolar stimulation (stimulation strength, 4 V) from the stratum pyramidale (pyr) and distal stratum radiatum (rad). Stimulation artifacts are removed for clarity. (Bii) Peak-to-peak cycle averages for the fast network oscillation for the stratum pyramidale and distal stratum radiatum. Horizontal scale bar, 10 ms.

(C) 1D CSD profiles were constructed for both (Ci) evoked responses and (Cii) fast network oscillations. The CSD profiles were aligned on the time of the maximum current sink (red) in the stratum radiatum, and the graphs in (B) and (D) aligned accordingly.

(D)(Di) The evoked sink in the distal stratum radiatum, accompanied by a source in the stratum pyramidale, produced a predominant depolarization in the dendritic layers. (Dii) A similar sink/source pair appearing during fast network oscillations was accompanied by a hyperpolarization of the pyramidal cell layer. The active current is the sink in the stratum radiatum for stimulation and the source in the stratum pyramidale for cholinergically induced fast network oscillations.

ing to the ongoing fast network oscillation (Rayleigh test, $p < 0.05$; spikelets were not observed). These phase locked pyramidal cells showed an average firing rate of 0.57 ± 0.18 Hz (coefficient of variation in interspike interval [CV_{ISI}] = 1.04 ± 0.17; n = 8), with a population mean phase of 5.9 [5.6, 0.1] radians (338.9 [321.6, 3.2] degrees) (second-order circular mean [95% confidence limits]) relative to the positive peak of the field oscillation in the distal stratum radiatum (Figure 5). The maximum discharge probability occurred later in the fast network oscillation, at a mean phase of 0.0 [6.0, 0.2] radians (358.2 [343.8, 12.7] degrees) (circular mean of the mode [95% confidence limits]). Such a skewed distribution of firing probability is consistent with the firing rate of the pyramidal cell population increasing as the current sink in the stratum pyramidale develops and promptly shutting off as the current source is initiated (see Figures 5D and 5F). To explore the membrane polarizations underlying these discharge probabilities, cycle averages of the pyramidal membrane potentials were constructed, excluding periods containing action potentials and the following two cycles (Figures 5D and 5E). The membrane potential was found to closely follow the field oscillation in the stratum pyramidale, with a mean delay in the peak membrane potential of 0.3 radians (14.6 degrees) (Figure 5G). Thus, both the discharge probabilities and membrane potential oscillations of CA3 pyramidal neurons are consistent with the network events suggested by the combination of CSD and VSD analysis.

Perisomatic-Targeting Interneurons Fire after Pyramidal Neurons during Fast Network Oscillations

The most likely explanation for the active source in the stratum pyramidale during fast network oscillations, accompanied by hyperpolarization of pyramidal cells and a rapid curtailment of their discharge rate, is rhythmic perisomatic inhibition. To test this hypothesis more directly, extracellular unit recordings were obtained from perisomatic-targeting interneurons in the CA3, which were subsequently intracellularly labeled for post hoc anatomical identification (Figure 6A). Five out of six perisomatic-targeting interneurons recorded participated in fast network oscillations, as evidenced by significant phase locking of action potential firing (Rayleigh test, $p < 0.05$). These interneurons fired at an average rate of 8.2 ± 2.6 Hz (CV_{ISI} = 0.72 ± 0.07; n = 5). The perisomatic-targeting interneurons fired at a significantly later phase in the oscillation than did the pyramidal neurons, with a mean phase of 0.6 [0.0, 1.7] radians (34.0 [2.4, 97.1] degrees) (two-sample Hotelling test; $F_{2,10} = 44.5$, $p < 0.001$ compared with phase-locked pyramidal cells) and a mean phase of maximum discharge probability at 0.5 [0.2, 0.9] radians (30.1 [11.4, 48.8] degrees) (Watson-Williams test; $F_{1,11} = 10.3$, $p < 0.01$ compared with phase locked pyramidal cells) (Figures 6B–6E). For a fast network oscillation at 20 Hz, these phase delays between the firing of pyramidal neurons and perisomatic-targeting interneurons correspond to time delays of 7.7 ms and 4.4 ms for the average mean and mode discharge phases, respectively. These values would be consistent with monosynaptic excitation of perisomatic inhibitory cells by pyramidal neurons.

Fast Synaptic Excitation and Inhibition Are Both Necessary for Oscillogenesis

All of these results indicate a major role for chemical synaptic transmission in cholinergically induced gamma activity. We therefore proceeded with a pharmacological dissection of the synaptic currents involved. Bath application of AMPA (α-amino-3-hydroxy-5-methyl-4-isoxazolepropionic acid) receptor-selective antagonist GYKI 53655 (10–25 μM) (Tarnawa et al., 1993; Bleakman et al., 1996) completely blocked carbachol-induced oscillations (power in the 10–45 Hz band; 174.9 ± 35.8 versus

dc_71_10

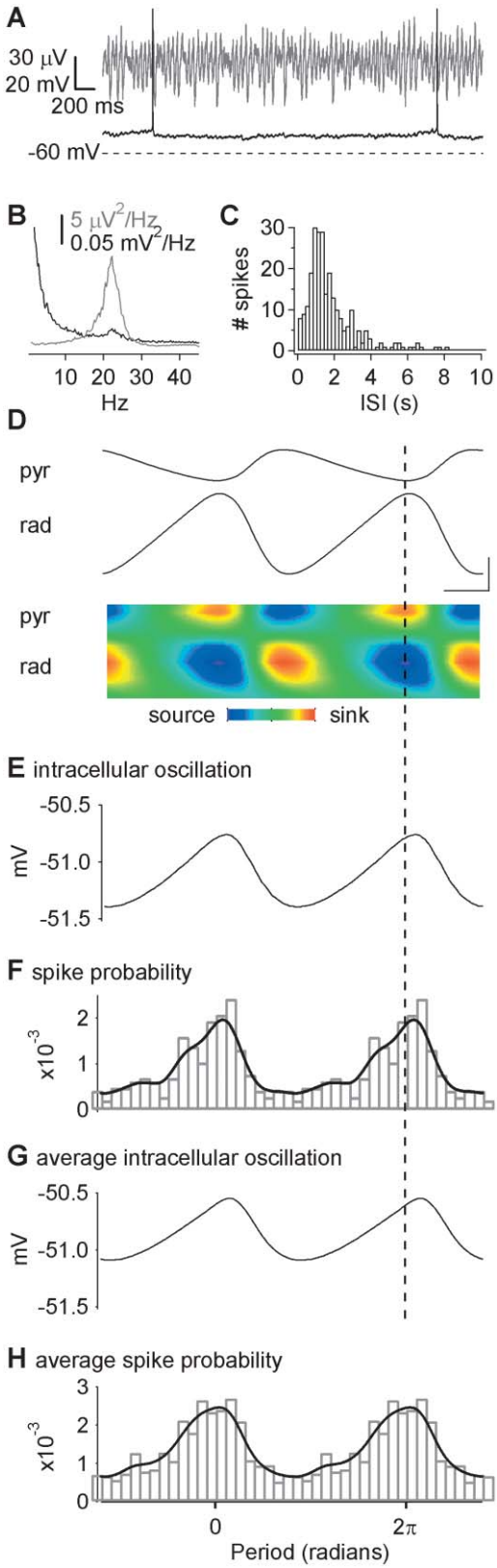

Figure 5. Pyramidal Cell Discharge and Intracellular Oscillations during Fast Network Oscillations

Multielectrode arrays were used to record field potentials in CA3 during carbachol-induced fast network oscillations, with simultaneous recording in whole-cell current-clamp from identified CA3 pyramidal cells. (A) Typical activity recorded from a CA3 pyramidal neuron (black trace) during carbachol-induced oscillations, showing low-frequency single action potential firing. The intracellular recording is aligned with the field potential recorded in the distal stratum radiatum (gray trace). Action potentials are truncated at +30 mV. (B) Power spectral density of the intracellular oscillation of the recorded pyramidal neuron (black) and the field oscillation in the distal stratum radiatum (gray), both showing peaks at ~20 Hz. (C) Interspike interval histogram for the recorded pyramidal neuron. (D) Peak-to-peak cycle averages of the field recordings from the stratum pyramidale (pyr) and distal stratum radiatum (rad) during the carbachol-induced fast network oscillation shown in (A), with the 1D CSD profile below. The vertical dashed line shows the time of the peak sink in the stratum pyramidale. Scale bars, 10 μV and 10 ms. (E) Cycle average of the membrane potential of a pyramidal cell recorded during the network oscillation shown in (A), with the exclusion of periods containing spikes or spike afterhyperpolarizations. The membrane potential peaked after the maximum sink in the stratum pyramidale, with a delay of 0.3 radians. (F) Spike probability histogram for the pyramidal cell, with the estimated probability density function superimposed. The profile of pyramidal cell discharge was skewed, with a mean phase of 6.1 radians relative to the peak signal recorded in the distal stratum radiatum. The peak discharge probability at 0.1 radians, measured from the estimated probability density function, coincided with the peak in the intracellular membrane potential oscillation in the absence of firing shown in (E). (G) The average intracellular membrane oscillation for the eight out of ten pyramidal cells that showed significant phase coupling to the fast network oscillations. Confidence limits have been omitted for clarity. (H) The average spike probability histogram and estimated probability density function for phase-coupled pyramidal cells (n = 8).

5.4 ± 2.5 μV^2; paired two-sample t test on log power; $p < 0.001$, n = 8), while the NMDA (*N*-methyl-D-aspartate) receptor antagonist D-AP5 (50 μM) had no significant effect (285.1 ± 113.1 versus 214.6 ± 70.9 μV^2; n = 4). The $GABA_A$ (γ-aminobutyric acid) receptor antagonist gabazine (200 nM) blocked carbachol-induced oscillations (57.8 ± 13.2 versus 3.8 ± 1.0 μV^2; $p < 0.01$, n = 4) and induced ripple-associated epileptiform events at higher concentrations (see Supplemental Figure S2) [http://www.neuron.org/cgi/content/full/45/1/105/DC1/]). The $GABA_B$ receptor antagonist CGP 52432 (5 μM) had no significant effect (215.6 ± 62.4 versus 209.0 ± 53.8 μV^2; n = 4). Therefore, consistent with previous reports, carbachol-induced oscillations appear to be dependent upon fast GABAergic inhibition and AMPA receptor-mediated excitation (Fisahn et al., 1998).

Fast Synaptic Transmission in the Stratum Radiatum Is Not Required for Oscillogenesis

The apical dendrites of pyramidal neurons receive recurrent excitation and feedback inhibition, so how do these dendritic currents contribute to oscillogenesis and the generation of the field potential? This question was addressed through local blockade of synaptic transmission in the strata radiatum and lacunosum-moleculare. The efficacy of local antagonist application was assessed by the effects on responses to extracellular stimulation in the stratum radiatum. Local application of 12.5 mM GYKI 53655 reduced the negative peak of the fEPSP across the stratum radiatum by 95% ± 2%, yet subsequent bath application of 25 μM carbachol still induced fast network oscillations (16.1 ± 0.9 Hz; n = 3; Figure 7A). Further perisomatic application of GYKI 53655 blocked

dc_71_10

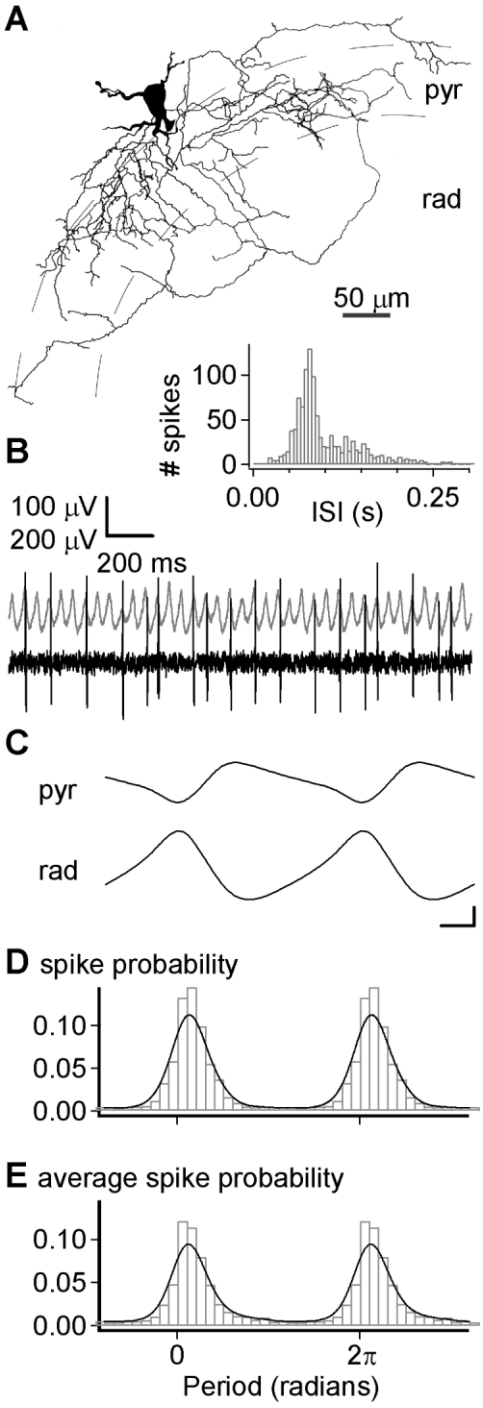

Figure 6. Discharge Probabilities of Perisomatic-Targeting Interneurons Relative to Fast Network Oscillations

Single-unit activity from visually identified interneurons in CA3 were recorded simultaneously with multielectrode recordings of the fast network oscillations. The interneurons were subsequently labeled for morphological identification, and only those showing axon arborization in the perisomatic regions of CA3 pyramidal neurons were included in the analysis. (A) Reconstruction of a perisomatic-targeting interneuron in the CA3, recorded during carbachol-induced fast network oscillations. Dashed gray lines represent the borders of the stratum pyramidale (pyr). rad, stratum radiatum. Scale bar, 50 μm. (B) Unit recording from interneuron shown in (A) (high-pass filtered at 200 Hz), aligned with field recording from the distal stratum radiatum. (Inset) Interspike interval histogram. (C) Peak-to-peak cycle averages for the field recordings from the stratum pyramidale (pyr) and distal stratum radiatum (rad) during the fast network oscillation in which cell (A) was recorded. Scale bars, 20 μV and 10 ms. (D) Spike probability histogram for the perisomatic-targeting interneuron shown in (A), with superimposed estimated probability density function. (E) The average spike probability histogram and estimated probability density function for phase-coupled perisomatic-targeting interneurons (n = 5).

these oscillations (power in the 10–45 Hz band; 160.5 ± 141.7 versus 1.5 ± 0.4 μV^2; paired two-sample t test on log power; $p < 0.05$, n = 3). Local application of 100 μM gabazine in the stratum radiatum increased the negative peak of the fEPSP by 33% ± 6% (n = 5), which appeared to represent near-maximum blockade of local phasic inhibition; additional application of carbachol induced fast network oscillations in 3 out of 5 slices (19.5 ± 2.8 Hz; Figure 7A) and large-amplitude (~3 Hz) epileptiform discharges in the other two slices. The fast network oscillations were blocked by further perisomatic application of gabazine (77.2 ± 25.6 versus 4.9 ± 1.7 μV^2; $p < 0.05$, n = 3) (Figure 7A).

These results suggest that synaptic inputs to the apical dendrites of pyramidal neurons are not necessary for oscillogenesis. Indeed, local application of 1 mM tetrodotoxin (TTX), which reduced the negative peak of the fEPSP by 97% ± 1%, did not prevent the subsequent induction of network oscillations (12.5 ± 2.7 Hz; power area in 5–45 Hz band, 51.2 ± 14.5 μV^2; n = 3; Figure 7A). However, these oscillations appeared to have slightly different properties from those recorded under control conditions, and, to further investigate such effects, TTX was applied in the strata radiatum and lacunosum-moleculare after oscillations had been induced. It was found that local application of TTX significantly reduced the oscillation frequency (16.1 ± 1.9 versus 10.5 ± 1.4 Hz; paired two-sample t test; $p < 0.05$, n = 5) and changed the waveform (Figures 7B and 7C; see Supplemental Figure S3 for details [http://www.neuron.org/cgi/content/full/45/1/105/DC1/]), but the oscillations remained associated with alternating sink and source pairs in the stratum pyramidale and distal stratum radiatum (Figure 7D). In one experiment, it was confirmed that additional perisomatic application of TTX abolished all oscillatory activity. Therefore, currents in the stratum radiatum/lacunosum-moleculare appear to elaborate the principal oscillatory events at perisomatic sites.

Fast Synaptic Excitation of Both Pyramidal Neurons and Interneurons Is Necessary for Beta-Gamma Frequency Rhythmic Inhibition

Finally, in order to examine the precise function of fast synaptic excitation in oscillogenesis, we recorded from individual pyramidal cells and perisomatic-targeting interneurons during the application of a selective AMPA receptor antagonist, GYKI 53655. This treatment blocked carbachol-induced oscillations (as shown earlier) and was accompanied by a hyperpolarization of pyramidal cells below action potential threshold (12.5 μM GYKI 53655; membrane potential, −59.6 ± 3.1 versus −67.2 ± 1.8 mV; firing rate, 0.42 ± 0.20 versus 0 Hz; n = 4;

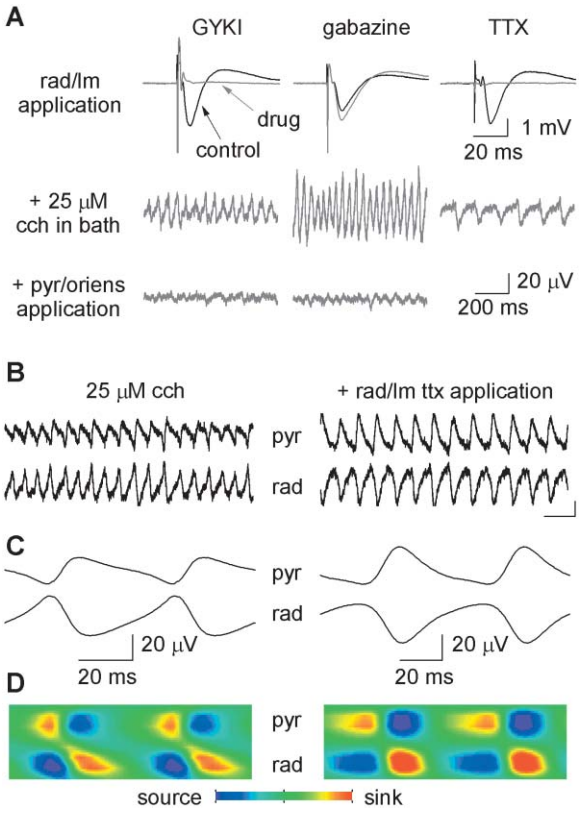

Figure 7. Synaptic Transmission in the Strata Radiatum and Lacunosum-Moleculare Is Not Required for Oscillogenesis

(A) Multielectrode arrays were used to record field potentials across the CA3, with representative traces from single electrodes in the stratum radiatum displayed. Initially, responses to antidromic stimulation of the Schaffer collateral pathway were recorded to monitor the effects of local pressure ejection in the strata radiatum and lacunosum-moleculare of the AMPA receptor-selective antagonist GYKI 53655 (GYKI, 12.5 mM), the $GABA_A$ receptor antagonist gabazine (100 μM), or tetrodotoxin (TTX, 1 mM). For GYKI and TTX experiments, application continued until the fEPSP disappeared, while gabazine was applied until the negative peak of the fEPSP increased by ~30%. Subsequent bath application of 25 μM carbachol (CCh) was still able to induce network oscillations. Further local application of GYKI and gabazine in the strata pyramidale and oriens abolished the oscillations.

(B) The effects of local application of TTX (1 mM) in the strata radiatum and lacunosum-moleculare on previously established carbachol-induced fast network oscillations recorded in the stratum pyramidale (pyr) and distal stratum radiatum (rad), showing a reduction in oscillation frequency and a change in waveform. Scale bars, 20 μV and 100 ms.

(C) Peak-to-peak cycle averages for the oscillations recorded in the stratum pyramidale and distal stratum radiatum.

(D) The 1D CSD profiles for carbachol-induced oscillations before and after local application of TTX in the strata radiatum and lacunosum-moleculare displayed alternating current sink (red) and source (blue) pairs in the stratum pyramidale and stratum radiatum.

Figure 8A). This suggests that AMPA receptor-mediated excitation contributes to the depolarization of pyramidal cells, but does not resolve the role of such fast excitation in network synchronization. As blocking AMPA receptors shifts the membrane potential of pyramidal cells toward the reversal potential for $GABA_A$ receptors, it is conceivable that a network of interneurons could still fire synchronously, but elicit reduced synaptic currents, thus rendering this oscillation undetectable in the field potential. To evaluate the effect of GYKI 53655 on synchronized inhibition, we recorded excitatory and inhibitory postsynaptic currents (EPSCs and IPSCs) in CA3 pyramidal cells held in whole-cell voltage clamp at −70 mV and 0 mV, respectively. We found that, in addition to completely blocking the fast network oscillations recorded in the field potential (power in the 10–45 Hz band; 227.6 ± 58.2 versus 2.5 ± 1.5 μV^2; paired two-sample t test on log power; $p < 0.01$, $n = 4$), 10–25 μM GYKI 53655 blocked both EPSCs (131.1 ± 66.8 versus 2.5 ± 0.6 pA^2; $p < 0.01$, $n = 4$) and rhythmic IPSCs (520.9 ± 200.7 versus 26.8 ± 10.8 pA^2; $p < 0.01$, $n = 4$) (Figures 8B–8D). Therefore, fast synaptic excitation appears to be necessary for interneuronal synchronization.

To test whether such AMPA receptor-mediated excitation is also required for the recruitment of inhibition, extracellular unit recordings were obtained from five anatomically identified perisomatic-targeting interneurons. Application of 10–25 μM GYKI 53655 had no significant effect on firing rate (8.8 ± 1.1 versus 7.3 ± 1.2 Hz; paired t test, $n = 5$) (Figure 8E), demonstrating that these interneurons can fire independently of fast synaptic excitation. However, the initial degree of phase coupling appeared to be positively correlated with the extent to which AMPA receptor-mediated excitation determined this interneuronal firing pattern, as measured by the effect of GYKI 53655 on both the ISI mean ($n = 5$, $r = 0.66$, not significant) and ISI mode ($n = 5$, $r = 0.65$, not significant) (Figures 8F–8H). These results support the proposition that cholinergically induced fast network oscillations are dependent upon fast synaptic excitation to both maintain the excitability of pyramidal neurons and synchronize the firing of perisomatic-targeting GABAergic interneurons.

Discussion

Our principal findings are that (1) cholinergically induced fast network oscillations in the hippocampus in vitro are associated with alternating current sink and source pairs in the CA3 stratum pyramidale and stratum radiatum, which resemble those observed during intrahippocampal gamma oscillations in vivo, (2) the active current sinks and sources are localized in the stratum pyramidale, as revealed by voltage-sensitive dye imaging, local blockade of synaptic transmission, and intracellular recordings from CA3 pyramidal cells, (3) these oscillations are driven by rhythmic hyperpolarizing GABAergic inputs to pyramidal cells from perisomatic-targeting interneurons, and (4) the synchronization of the perisomatic-targeting interneurons and, thus, the generation of fast network oscillations are dependent on AMPA receptor-mediated fast recurrent excitation from pyramidal cells.

Both 1D and 2D CSD analysis revealed that cholinergically induced fast network oscillations in the CA3 are associated with alternating current sink and source pairs in the strata pyramidale and radiatum (Figure 2), which is similar to the sink/source distribution observed during intrahippocampal gamma oscillations in the behaving rat (Bragin et al., 1995; Csicsvari et al., 2003). Indeed, this

dc_71_10

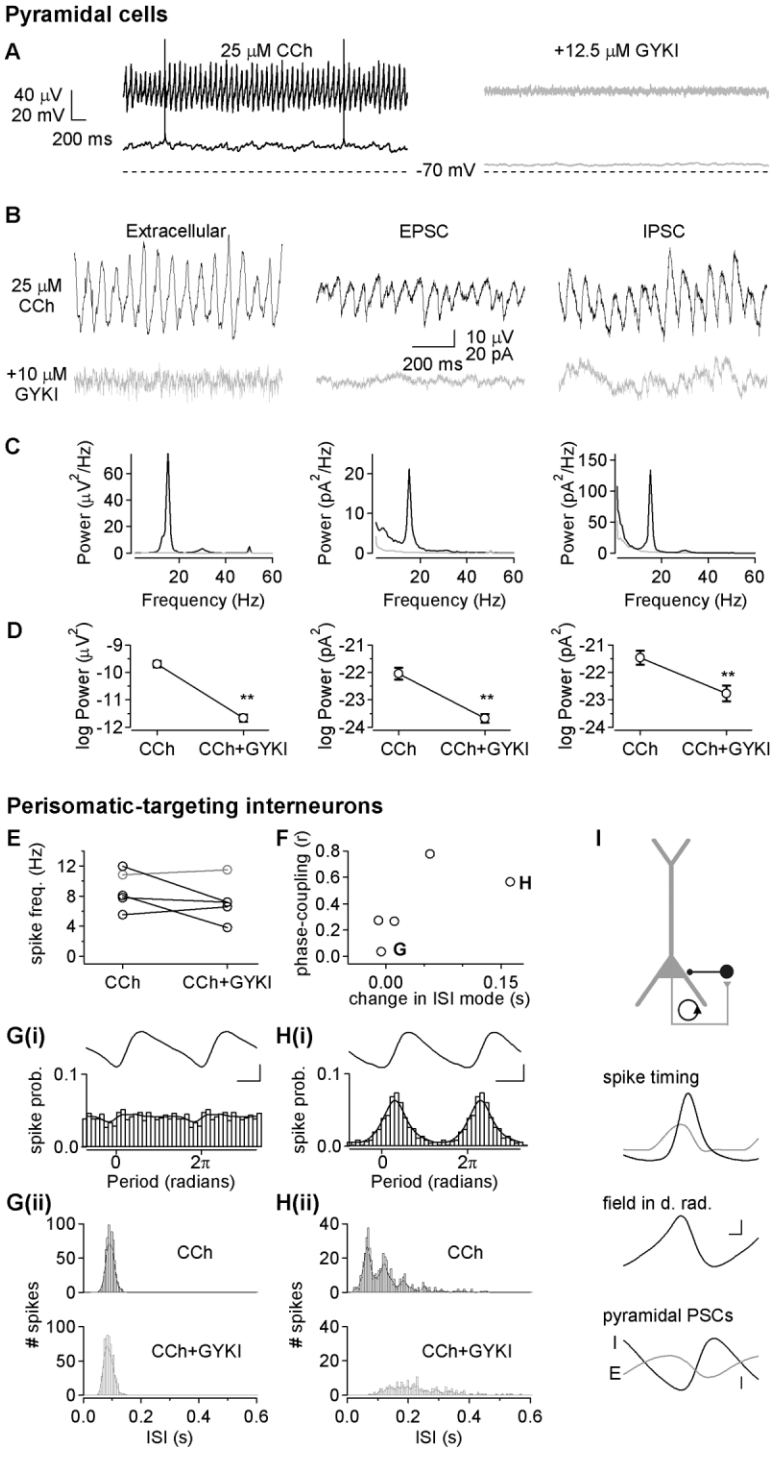

Figure 8. Carbachol-Induced Oscillations Are Dependent on Fast Synaptic Transmission

(A) Whole-cell current-clamp from CA3 pyramidal cells was performed simultaneously with multielectrode recordings of the fast network oscillation. Application of the AMPA receptor-selective antagonist GYKI 53655 (GYKI) blocked the extracellular field oscillations and produced a hyperpolarization of pyramidal neurons below action potential threshold (n = 4). Action potentials are truncated at +20 mV.

(B) In separate experiments, synaptic currents recorded in whole-cell voltage-clamp from CA3 pyramidal neurons at holding potentials of −70 mV (EPSC) and 0 mV (IPSC) were monitored simultaneously with multielectrode recordings of the fast network oscillation. Extracellular field oscillations (example from the distal stratum radiatum of CA3) and both rhythmic EPSCs and IPSCs were blocked by GYKI 53655.

(C) Power spectral density plots for the recordings from field, EPSCs, and IPSCs in the presence of 25 μM carbachol (black lines). In some cases there was also a low-frequency peak in the power spectral density of the EPSC recording. Following the application of GYKI 53655, the oscillatory components of both field potential and synaptic currents disappeared (gray lines).

(D) Logarithm of the power in the 10–45 Hz range plotted for the statistical analysis of the average effects of GYKI 53655 (10–25 μM) on the fast network oscillations induced by 25 μM carbachol (CCh). (n = 4, **$p < 0.01$; paired two-sample t test.)

(E) Application of 10–25 μM GYKI 53655 had no significant effect on the firing rate of anatomically identified perisomatic-targeting interneurons (n = 5, $p > 0.05$; paired two-sample t test; black markers). The cell depicted in gray was not significantly phase coupled (Rayleigh test, $p > 0.05$).

(F) The phase coupling of the perisomatic-targeting interneurons to the network oscillation, as measured by the vector length (r), was positively correlated with the subsequent effect of 10–25 μM GYKI 53655 on the ISI mode. Cells analyzed in more detail in panels (G) and (H) are labeled.

(G)(Gi) Peak-to-peak cycle averages for the field recordings from the stratum pyramidale during the fast network oscillation in which the non-phase-coupled perisomatic-targeting interneuron was recorded. Below is the spike probability histogram, with superimposed estimated probability density function. Scale bars, 40 μV and 20 ms. (Gii) Interspike interval histogram before (black) and after (gray) GYKI 53655 application, showing that the firing of this non-phase-coupled perisomatic-targetinginterneuron was not controlled by AMPA receptor-mediated excitation.

(H) Same analysis as in panel (G) for a perisomatic-targeting interneuron that was strongly phase-coupled, showing that fast excitation contributes to driving the firing of some interneurons, in addition to its role in synchronization. Scale bars, 40 μV and 20 ms.

(I) Synaptic feedback model for the generation of fast network oscillations in vitro, involving primarily CA3 pyramidal neurons (gray) and perisomatic-targeting interneurons (black). Below the cartoon are the average estimated probability density functions for the spiking of pyramidal cells (gray) and interneurons (black). To facilitate comparison, the functions have been normalized to an area of 1 prior to averaging. The cycle average of the oscillations in the distal stratum radiatum (d. rad.) is shown below (experiments in [B]–[D]) (scale bars, 10 μV and π/8 radians). The bottom figure depicts the corresponding average inhibitory (I) and excitatory (E) postsynaptic currents (PSCs) recorded in pyramidal neurons during fast network oscillations. (n = 4; scale bar, 10 pA.)

in vitro model shares many physiological characteristics with hippocampal gamma oscillations in vivo. In particular, pyramidal neurons fire at low frequencies (<5 Hz), phase locked to the current sink in stratum pyramidale (Figure 5) (Penttonen et al., 1998; Csicsvari et al., 2003); the pyramidal neurons receive rhythmic inhibition (Penttonen et al., 1998) (Figure 6); and perisomatic-targeting interneurons in the CA3 are capable of firing on almost every cycle of the oscillation, but discharge at a significantly later phase than do CA3 pyramidal cells (see Figures 5, 6, and 8I) (Csicsvari et al., 2003). Furthermore, in both cases the oscillation appears to be generated in CA3 and propagate to CA1 (Figure 3C) (Fisahn et al., 1998; Csicsvari et al., 2003).

The advantage of using an in vitro model of hippocampal gamma oscillations was that we could use a combination of different techniques to examine more directly the cellular and network mechanisms underlying "current" and "rhythm" generation, i.e., the cellular currents that generate the oscillation in the extracellular field potential and the mechanism by which such activity is synchronized. First, a comparison of 1D and 2D CSD analyses showed only subtle differences between them in the magnitude of the currents, temporal relations, and the precise localization of phase reversal (Figure 2 and Supplemental Figure S1 [http://www.neuron.org/cgi/content/full/45/1/105/DC1/]), justifying the use of 1D CSD for fast oscillations in vivo. Second, VSD imaging (Grinvald et al., 1982; Tominaga et al., 2002) was employed to identify the active sinks and sources during fast network oscillations. The dye signal has been shown earlier to reflect predominantly the membrane polarizations of pyramidal neurons (Tominaga et al., 2000). This signal occurred first and with the largest amplitude in the pyramidal cell layer, suggesting a perisomatic origin of sinks and sources (Figure 3). This result was supported by intracellular recordings from CA3 pyramidal neurons (Figure 5) and the fact that blocking synaptic transmission in the strata radiatum and lacunosum-moleculare did not prevent oscillogenesis (Figure 7). Together, these results demonstrate that cholinergically induced fast oscillations in the field potential primarily reflect rhythmic currents at the level of pyramidal cell somata and perisomatic membrane, rather than distal dendritic excitation or inhibition.

Although pyramidal cells receive rhythmic excitation (Figure 8B), an active current sink was not detected in the stratum radiatum (Figures 3, 4, and 7), probably because recurrent excitation has a relatively small amplitude and/or targets both the apical and basal dendrites. In fact, it has been reported that the majority of boutons from pyramidal cells in CA3 are found in the stratum oriens (Sik et al., 1993). Thus, it is likely that much of the synaptic excitation occurs in the basal dendrites. This recurrent excitation is important for the depolarization of pyramidal neurons (Figure 8A) in conjunction with intrinsic tonic conductances (Fisahn et al., 2002), which might explain why carbachol-induced fast network oscillations are generated in the CA3 and not in the CA1 (Figure 3; Fisahn et al., 1998).

Evidence from both in vitro and in vivo studies supports the hypothesis that fast network oscillations are driven by perisomatic inhibition (Figure 6) (Whittington et al., 1995; Fisahn et al., 1998; Penttonen et al., 1998; Traub et al., 2000; Csicsvari et al., 2003), but does not resolve the question of how these interneurons would be synchronized. In this study, we showed that an AMPA receptor-selective antagonist (10–25 μM GYKI 53655) blocked both the field oscillation and rhythmic inhibitory currents on pyramidal neurons (Figure 8), suggesting that interneuronal synchronization is mediated by fast recurrent excitation. Therefore, cholinergically induced fast network oscillations in the CA3 appear to be generated by a synaptic feedback circuit between pyramidal cells and perisomatic-targeting interneurons (Figure 8I), consistent with the model originally suggested for prepyriform cortex by Freeman (1968).

Studying the mechanisms of hippocampal gamma oscillations in a cholinergic model appears relevant, since the dense cholinergic projection to the hippocampus, originating from the medial septum/diagonal band of Broca, is thought to play a permissive role in the generation of hippocampal network oscillations (Leung, 1985; but see Lee et al., 1994). Nonetheless, fast network oscillations in the hippocampus in vitro can be induced by a variety of paradigms (for review, see Whittington and Traub, 2003), which might recruit additional mechanisms contributing to network synchronization, such as interneuronal (Whittington et al., 1995) or axo-axonal coupling (Traub et al., 2001, 2003a, 2003b; Fischer, 2004) via gap junctions. Gap junction blockers, such as carbenoxolone and octanol, block gamma frequency oscillations in vitro (Traub et al., 2000), but these drugs may have other effects that can inhibit network activity via different mechanisms (Rouach et al., 2003; Fischer, 2004; Vessey et al., 2004). Indeed, mice deficient in connexin36, the predominant neuronal gap junction protein in the brain (Rash et al., 2000), continue to display gamma oscillations both in vitro (Hormuzdi et al., 2001) and in vivo (Buhl et al., 2003), although the power of these oscillations is substantially reduced. Chemical synaptic interactions are sufficient for fast synchronization in network models of leaky integrate-and-fire neurons with physiologically realistic firing rates (Brunel and Wang, 2003), and, overall, the CA3 synaptic feedback model appears to explain satisfactorily the generation of both cholinergically induced fast network oscillations in vitro (Figure 8) (Fisahn et al., 1998) and intrahippocampal gamma oscillations in vivo (Csicsvari et al., 2003). Gap junction coupling might play a more fundamental role in the generation of gamma oscillations in other subregions of the hippocampus (Traub et al., 2003a).

Elucidating the mechanisms underlying current and rhythm generation of intrahippocampal gamma oscillations is necessary in order to understand both how individual cell types process the collective network input and also identify the functional processes that this rhythm could support. With its predominantly perisomatic location, the source of hippocampal gamma oscillations appears to control primarily the output of hippocampal pyramidal neurons. Such a mechanism might permit the dendritic integration of inputs that are not phase coupled to the intrahippocampal oscillation. Furthermore, since gamma frequency rhythmic inhibition appears to be synchronized by the firing of the pyramidal neurons themselves, hippocampal gamma oscillations could enable the serial activation and disbandment of

dc_71_10

neuronal assemblies and thus support the encoding and retrieval of memory sequences.

Experimental Procedures

Slice Preparation and Electrophysiology

Detailed methods are provided in the Supplemental Data (http://www.neuron.org/cgi/content/full/45/1/105/DC1/). Briefly, horizontal hippocampal slices (400 μm) were prepared from P12–P18 Wistar rats and maintained in an interface chamber, between humidified carbogen gas (95% O_2/5% CO_2) and artificial cerebrospinal fluid (ACSF) containing 126 mM NaCl, 3 mM KCl, 1.25 mM NaH_2PO_4, 2 mM $MgSO_4$, 2 mM $CaCl_2$, 26 mM $NaHCO_3$, and 10 mM glucose (pH 7.2–7.4). Slices were left to recover at room temperature for at least 1 hr. For recordings, slices were mounted on 8 × 8 arrays of planar microelectrodes (electrode size, 20 μm × 20 μm; interpolar distance, 100 μm; Panasonic MED-P2105; Tensor Biosciences, Irvine, CA), maintained in a submerged condition at room temperature, and superfused with ACSF, bubbled with carbogen, at 3–6 ml/min^{-1}. Electrical stimuli (0.02 ms square pulse) were delivered through a concentric bipolar electrode (FHC, Bowdoinham, ME) controlled via a stimulation isolation unit (Digitimer, Welwyn Garden City, UK). Spontaneous and evoked field potentials from all 64 recording electrodes were acquired simultaneously at 2–5 kHz, using the Panasonic MED64 system (Tensor Biosciences).

For voltage-sensitive dye imaging, each slice was stained for 25 min with VSD solution, containing 200 μM Di-4-ANEPPS (Molecular Probes) in 2.7% ethanol, 0.13% Cremaphor EL (Sigma), 50% fetal bovine serum (Sigma), and 50% ACSF. Optical signals were recorded using a MiCAM01 CCD camera (BrainVision; SciMedia Ltd., Tokyo, Japan), with a spatial resolution of approximately 22 × 22 μm and an acquisition rate of 200–500 Hz.

Whole-cell current-clamp recordings from CA3 pyramidal neurons were performed with glass pipettes, pulled from standard borosilicate glass, containing: 110 mM potassium gluconate, 40 mM HEPES, 4 mM NaCl, 2 mM ATP-Mg, 0.3 mM GTP, and 5 mg/ml^{-1} biocytin (pH 7.2–7.3; osmolarity, 290–300 mosmol/l^{-1}). For whole-cell voltage-clamp recordings, potassium gluconate was replaced with equimolar cesium gluconate. Single-unit recordings from interneurons were made with patch pipettes filled with ACSF and were performed to avoid altering the intracellular milieu, which affects action potential timing in interneurons (N.H., unpublished data). Current-clamp and single-unit recordings were made with an Axoclamp-2B amplifier in bridge mode, while voltage-clamp recordings were made with an Axopatch-1D amplifier. Following intracellular recording, the slices were fixed in 4% paraformaldehyde in 0.1 M phosphate buffer (PB; pH 7.4). Biocytin-filled cells were visualized following standard procedures.

Data Analysis

CSD analysis was performed on the peak-to-peak average cycles using previously described methods (Shimono et al., 2000). CSDs are shown using an inverted color scale, with warm colors corresponding to sinks (i.e., neuronal membrane inward currents). For analysis of the optical signal, the peak-to-peak average of fractional change in fluorescence over time was passed through a 5 × 5 × 5 point averaging filter. Depolarization produces a reduction in fluorescence; thus, to allow depolarization to be represented by positive values, the polarity of the fluorescence signal was inverted.

The spike timing in single cells was analyzed relative to the ongoing field oscillation, and cells not significantly coupled to the network were excluded from further analysis (Rayleigh test, $p < 0.05$). The modal phase was determined from the estimated probability density functions. For comparisons between cell classes, the population mean mode was quantified as a first-order circular statistic (Watson-Williams test), and the population mean of the mean phases was quantified as a second-order circular statistic (Hotelling test) (Batschelet, 1981; Zar, 1999).

All data are presented as means ± SEM, except where stated. Paired Student's t tests, repeated measures analysis of variance (RM ANOVA), and Pearson correlation coefficients were calculated in SPSS. Circular statistics were programmed in Igor.

Drugs and Chemicals

GYKI 53655 was a gift from IVAX Drug Research Institute, Ltd. (Budapest, Hungary). All other drugs and chemicals were obtained from Sigma-Aldrich (Poole, Dorset, UK) and Tocris (Bristol, UK). Local application of antagonists in ACSF was achieved by pressure ejection through a patch pipette (50–200 ms; 10 psi; 30–60 applications per hippocampal subregion), using a Picospritzer II (General Valve Corporation).

Acknowledgments

The authors are grateful to Ms. Charmaine Nelson for help with histological processing. The research was supported by the Biotechnology and Biological Sciences Research Council (UK). Additional financial support from Matsushita Co., Ltd. (Japan), Alpha Med Sciences Co., Ltd. (Japan), and Pfizer, Inc. (USA) is gratefully acknowledged. N.H. was a grantee of the NATO Science Fellowship.

Received: April 30, 2004
Revised: August 5, 2004
Accepted: November 17, 2004
Published: January 5, 2005

References

Batschelet, E. (1981). Circular statistics in biology (London: Academic Press).

Bleakman, D., Ballyk, B.A., Schoepp, D.D., Palmer, A.J., Bath, C.P., Sharpe, E.F., Woolley, M.L., Bufton, H.R., Kamboj, R.K., Tarnawa, I., and Lodge, D. (1996). Activity of 2,3-benzodiazepines at native rat and recombinant human glutamate receptors in vitro: stereospecificity and selectivity profiles. Neuropharmacology *35*, 1689–1702.

Bragin, A., Jando, G., Nadasdy, Z., Hetke, J., Wise, K., and Buzsaki, G. (1995). Gamma (40–100 Hz) oscillation in the hippocampus of the behaving rat. J. Neurosci. *15*, 47–60.

Brunel, N., and Wang, X. (2003). What determines the frequency of fast network oscillations with irregular neural discharges? I. Synaptic dynamics and excitation-inhibition balance. J. Neurophysiol. *90*, 415–430.

Buhl, D.L., Harris, K.D., Hormuzdi, S.G., Monyer, H., and Buzsaki, G. (2003). Selective impairment of hippocampal gamma oscillations in connexin-36 knock-out mouse in vivo. J. Neurosci. *23*, 1013–1018.

Buzsaki, G. (2002). Theta oscillations in the hippocampus. Neuron *33*, 325–340.

Buzsaki, G., Buhl, D.L., Harris, K.D., Csicsvari, J., Czeh, B., and Morozov, A. (2003). Hippocampal network patterns of activity in the mouse. Neuroscience *116*, 201–211.

Csicsvari, J., Jamieson, B., Wise, K.D., and Buzsaki, G. (2003). Mechanisms of gamma oscillations in the hippocampus of the behaving rat. Neuron *37*, 311–322.

Dickinson, R., Awaiz, S., Whittington, M.A., Lieb, W.R., and Franks, N.P. (2003). The effects of general anaesthetics on carbachol-evoked gamma oscillations in the rat hippocampus in vitro. Neuropharmacology *44*, 864–872.

Fellous, J.M., and Sejnowski, T.J. (2000). Cholinergic induction of oscillations in the hippocampal slice in the slow (0.5–2 Hz), theta (5–12 Hz), and gamma (35–70 Hz) bands. Hippocampus *10*, 187–197.

Fisahn, A., Pike, F.G., Buhl, E.H., and Paulsen, O. (1998). Cholinergic induction of network oscillations at 40 Hz in the hippocampus in vitro. Nature *394*, 186–189.

Fisahn, A., Yamada, M., Duttaroy, A., Gan, J.W., Deng, C.X., McBain, C.J., and Wess, J. (2002). Muscarinic induction of hippocampal gamma oscillations requires coupling of the M1 receptor to two mixed cation currents. Neuron *33*, 615–624.

Fischer, Y. (2004). The hippocampal intrinsic network oscillator. J. Physiol. *554*, 156–174.

Freeman, W.J. (1968). Relations between unit activity and evoked potentials in prepyriform cortex of cats. J. Neurophysiol. *31*, 337–348.

dc_71_10

Fries, P., Neuenschwander, S., Engel, A.K., Goebel, R., and Singer, W. (2001). Rapid feature selective neuronal synchronization through correlated latency shifting. Nat. Neurosci. *4*, 194–200.

Grinvald, A., Manker, A., and Segal, M. (1982). Visualization of the spread of electrical activity in rat hippocampal slices by voltage-sensitive optical probes. J. Physiol. *333*, 269–291.

Hasselmo, M.E., Wyble, B.P., and Wallenstein, G.V. (1996). Encoding and retrieval of episodic memories: role of cholinergic and GABAergic modulation in the hippocampus. Hippocampus *6*, 693–708.

Holsheimer, J. (1987). Electrical conductivity of the hippocampal CA1 layers and application to current-source-density analysis. Exp. Brain Res. *67*, 402–410.

Hormuzdi, S.G., Pais, I., LeBeau, F.E., Towers, S.K., Rozov, A., Buhl, E.H., Whittington, M.A., and Monyer, H. (2001). Impaired electrical signaling disrupts gamma frequency oscillations in connexin 36-deficient mice. Neuron *31*, 487–495.

Jensen, O., and Lisman, J.E. (1996). Theta/gamma networks with slow NMDA channels learn sequences and encode episodic memory: role of NMDA channels in recall. Learn. Mem. *3*, 264–278.

Lee, M.G., Chrobak, J.J., Sik, A., Wiley, R.G., and Buzsaki, G. (1994). Hippocampal theta activity following selective lesion of the septal cholinergic system. Neuroscience *62*, 1033–1047.

Leung, L.W. (1985). Spectral analysis of hippocampal EEG in the freely moving rat: effects of centrally active drugs and relations to evoked potentials. Electroencephalogr. Clin. Neurophysiol. *60*, 65–77.

Lisman, J.E., and Idiart, M.A. (1995). Storage of 7 +/− 2 short-term memories in oscillatory subcycles. Science *267*, 1512–1515.

Llinas, R., Ribary, U., Contreras, D., and Pedroarena, C. (1998). The neuronal basis for consciousness. Philos. Trans. R. Soc. Lond. B Biol. Sci. *353*, 1841–1849.

Mitzdorf, U. (1985). Current source-density method and application in cat cerebral cortex: investigation of evoked potentials and EEG phenomena. Physiol. Rev. *65*, 37–100.

Oka, H., Shimono, K., Ogawa, R., Sugihara, H., and Taketani, M. (1999). A new planar multielectrode array for extracellular recording: application to hippocampal acute slice. J. Neurosci. Methods *93*, 61–67.

Penttonen, M., Kamondi, A., Acsady, L., and Buzsaki, G. (1998). Gamma frequency oscillation in the hippocampus of the rat: intracellular analysis in vivo. Eur. J. Neurosci. *10*, 718–728.

Rash, J.E., Staines, W.A., Yasumura, T., Patel, D., Furman, C.S., Stelmack, G.L., and Nagy, J.I. (2000). Immunogold evidence that neuronal gap junctions in adult rat brain and spinal cord contain connexin-36 but not connexin-32 or connexin-43. Proc. Natl. Acad. Sci. USA *97*, 7573–7578.

Rouach, N., Segal, M., Koulakoff, A., Giaume, C., and Avignone, E. (2003). Carbenoxolone blockade of neuronal network activity in culture is not mediated by an action on gap junctions. J. Physiol. *553*, 729–745.

Shimono, K., Brucher, F., Granger, R., Lynch, G., and Taketani, M. (2000). Origins and distribution of cholinergically induced beta rhythms in hippocampal slices. J. Neurosci. *20*, 8462–8473.

Sik, A., Tamamaki, N., and Freund, T.F. (1993). Complete axon arborization of a single CA3 pyramidal cell in the rat hippocampus, and its relationship with postsynaptic parvalbumin-containing interneurons. Eur. J. Neurosci. *5*, 1719–1728.

Singer, W. (1993). Synchronization of cortical activity and its putative role in information processing and learning. Annu. Rev. Physiol. *55*, 349–374.

Tarnawa, I., Berzsenyi, P., Andrási, F., Botka, P., Hámori, T., Ling, I., and Körösi, J. (1993). Structure-activity relationships of 2,3-benzodiazepine compounds with glutamate antagonist action. Bioorg. Med. Chem. *3*, 99–104.

Tominaga, T., Tominaga, Y., Yamada, H., Matsumoto, G., and Ichikawa, M. (2000). Quantification of optical signals with electrophysiological signals in neural activities of Di-4-ANEPPS stained rat hippocampal slices. J. Neurosci. Methods *102*, 11–23.

Tominaga, T., Tominaga, Y., and Ichikawa, M. (2002). Optical imaging of long-lasting depolarization on burst stimulation in area CA1 of rat hippocampal slices. J. Neurophysiol. *88*, 1523–1532.

Torrence, C., and Compo, G. (1998). A practical guide to wavelet analysis. Bull. Am. Meteorol. Soc. *79*, 61–78.

Traub, R.D., Bibbig, A., Fisahn, A., LeBeau, F.E., Whittington, M.A., and Buhl, E.H. (2000). A model of gamma-frequency network oscillations induced in the rat CA3 region by carbachol in vitro. Eur. J. Neurosci. *12*, 4093–4106.

Traub, R.D., Kopell, N., Bibbig, A., Buhl, E.H., LeBeau, F.E., and Whittington, M.A. (2001). Gap junctions between interneuron dendrites can enhance synchrony of gamma oscillations in distributed networks. J. Neurosci. *21*, 9478–9486.

Traub, R.D., Cunningham, M.O., Gloveli, T., LeBeau, F.E., Bibbig, A., Buhl, E.H., and Whittington, M.A. (2003a). GABA-enhanced collective behavior in neuronal axons underlies persistent gamma-frequency oscillations. Proc. Natl. Acad. Sci. USA *100*, 11047–11052.

Traub, R.D., Pais, I., Bibbig, A., LeBeau, F.E., Buhl, E.H., Hormuzdi, S.G., Monyer, H., and Whittington, M.A. (2003b). Contrasting roles of axonal (pyramidal cell) and dendritic (interneuron) electrical coupling in the generation of neuronal network oscillations. Proc. Natl. Acad. Sci. USA *100*, 1370–1374.

Vessey, J.P., Lalonde, M.R., Mizan, H.A., Welch, N.C., Kelly, M.E., and Barnes, S. (2004). Carbenoxolone inhibition of voltage-gated Ca channels and synaptic transmission in the retina. J. Neurophysiol. *92*, 1252–1256.

Whittington, M.A., and Traub, R.D. (2003). Interneuron diversity series: inhibitory interneurons and network oscillations in vitro. Trends Neurosci. *26*, 676–682.

Whittington, M.A., Traub, R.D., and Jefferys, J.G. (1995). Synchronized oscillations in interneuron networks driven by metabotropic glutamate receptor activation. Nature *373*, 612–615.

Zar, J.H. (1999). Biostatistical analysis, 4th ed (Upper Saddle River, N.J.: Prentice Hall).

dc_71_10

9. számú melléklet

Behavioral/Systems/Cognitive

Synaptic Currents in Anatomically Identified CA3 Neurons during Hippocampal Gamma Oscillations *In Vitro*

Iris Oren,[1] Edward O. Mann,[1] Ole Paulsen,[1] and Norbert Hájos[2]

[1]Department of Physiology, Anatomy, and Genetics, University of Oxford, Oxford OX1 3PT, United Kingdom, and [2]Department of Cellular and Network Neurobiology, Institute of Experimental Medicine, Hungarian Academy of Sciences, H-1450 Budapest, Hungary

Gamma-frequency oscillations are prominent during active network states in the hippocampus. An intrahippocampal gamma generator has been identified in the CA3 region. To better understand the synaptic mechanisms involved in gamma oscillogenesis, we recorded action potentials and synaptic currents in distinct types of anatomically identified CA3 neurons during carbachol-induced (20–25 μM) gamma oscillations in rat hippocampal slices. We wanted to compare and contrast the relationship between excitatory and inhibitory postsynaptic currents in pyramidal cells and perisomatic-targeting interneurons, cell types implicated in gamma oscillogenesis, as well as in other interneuron subtypes, and to relate synaptic currents to the firing properties of the cells. We found that phasic synaptic input differed between cell classes. Most strikingly, the dominant phasic input to pyramidal neurons was inhibitory, whereas phase-coupled perisomatic-targeting interneurons often received a strong phasic excitatory input. Differences in synaptic input could account for some of the differences in firing rate, action potential phase precision, and mean action potential phase angle, both between individual cells and between cell types. There was a strong positive correlation between the ratio of phasic synaptic excitation to inhibition and firing rate over all neurons and between the phase precision of excitation and action potentials in interneurons. Moreover, mean action potential phase angle correlated with the phase of the peak of the net-estimated synaptic reversal potential in all phase-coupled neurons. The data support a recurrent mechanism of gamma oscillations, whereby spike timing is controlled primarily by inhibition in pyramidal cells and by excitation in interneurons.

Key words: **gamma oscillation; interneuron; synaptic; cholinergic; hippocampus; rat**

Introduction

Gamma-frequency oscillations (30–100 Hz) are prevalent in active cortical networks. Although such network oscillations have been studied extensively *in vivo*, neither their underlying mechanisms nor functions are well understood (Paulsen and Sejnowski, 2006). In the hippocampal formation, gamma oscillations are often seen during theta activity (4–7 Hz), which occurs during exploratory behavior and rapid eye movement sleep (Buzsaki et al., 1983; Bragin et al., 1995; Csicsvari et al., 2003). Hippocampal gamma oscillations can also occur independently of theta oscillations (Penttonen et al., 1998; Csicsvari et al., 2003) and may be an inherent property of the local network.

In vitro models of gamma oscillations have provided some insights into the mechanisms of gamma oscillogenesis in the hippocampus. Analysis of carbachol (CCh)-induced gamma oscillations in hippocampal slices has identified an intrinsic gamma generator in area CA3 (Fisahn et al., 1998), which also appears to operate *in vivo* (Csicsvari et al., 2003). The CA3 network architecture is highly recurrent (Amaral et al., 1990): pyramidal cells (PCs) innervate PCs and interneurons, which in turn synapse onto PCs and other interneurons, making recurrent feedback inhibition a strong candidate mechanism for the generation of gamma oscillations in CA3. A PC–interneuron recurrent model of CCh-induced oscillations is attractive because the same mechanism is suggested by the spike order of PCs and interneurons during theta-related gamma oscillations *in vivo* (Csicsvari et al., 2003), and theta activity itself is believed to depend on septal cholinergic input (Stewart and Fox, 1990). Other gamma models implicate an independent interneuronal network as the primary rhythm generator (Whittington et al., 1995; Whittington and Traub, 2003; Bacci and Huguenard, 2006; Vida et al., 2006).

To better understand the synaptic mechanisms involved in gamma oscillogenesis and to distinguish between these two models, the present study aimed to record synaptic currents in anatomically identified neurons during cholinergically induced gamma oscillations. If CCh-induced oscillations are generated by a recurrent mechanism, interneurons would be expected to receive a dominant phasic excitatory drive and PCs would be expected to receive a dominant phasic inhibitory input, whereas if oscillations result from an interneuronal network, the dominant phasic input to both PCs and interneurons should be inhibitory. We therefore wanted to compare and contrast the relationship between excitatory and inhibitory synaptic currents in PCs and

Received April 12, 2006; revised July 6, 2006; accepted Aug. 15, 2006.

This work was supported by The Wellcome Trust, the Biotechnology and Biological Sciences Research Council, the British Council, the Alzheimer's Research Trust, and Országos Tudományos Kutatási Alapprogramok Grant T049517. N.H. was awarded the Bolyai János Scholarship. We are grateful for the generous support of Prof. Tamás F. Freund. We also thank János Pálhalmi for contributions during the early stages of this work and Katalin Lengyel for excellent technical assistance.

Correspondence should be addressed to Dr. Ole Paulsen, Department of Physiology, Anatomy and Genetics, University of Oxford, Sherrington Building, Parks Road, Oxford OX1 3PT, UK. E-mail: ole.paulsen@physiol.ox.ac.uk.

DOI:10.1523/JNEUROSCI.1580-06.2006

 0270-6474/06/269923-12$15.00/0

interneurons, focusing on PCs and perisomatic-targeting interneurons, cell types that have been suggested to underlie gamma oscillogenesis in the recurrent model (Fisahn et al., 1998; Gloveli et al., 2005a,b; Mann et al., 2005a,b). Furthermore, we wanted to relate the synaptic input to the firing properties of individual cells, which have been shown to differ between cell classes (Hájos et al., 2004). We found that synaptic input differed between cell classes and that differences in synaptic input could account for some of the differences in both the firing rate and phase coupling. Our results are consistent with a recurrent model for CCh-induced gamma oscillations in CA3.

Materials and Methods

Slice preparation. Experiments were conducted in accordance with the United Kingdom Animals (Scientific Procedures) Act (1986), the Hungarian Act of Animal Care and Experimentation (1998, XXVIII, section 243/1998), and the guidelines of the institutional ethical codes. Wistar rats (postnatal day 13–20) were deeply anesthetized with isoflurane and decapitated, and the brain was removed and placed in ice-cold cutting solution containing the following (in mM): 252 sucrose, 2.5 KCl, 26 $NaHCO_3$, 0.5 $CaCl_2$, 5 $MgCl_2$, 1.25 NaH_2PO_4, and 10 glucose. The cutting solution had been bubbled with 95% O_2/5% CO_2 (carbogen gas) for at least 30 min before use. Horizontal slices (350–400 μm thick) were cut and trimmed of most extrahippocampal areas. The slices were stored in interface conditions with artificial CSF (ACSF) containing the following (in mM): 126 NaCl, 3 KCl, 1.25 NaH_2PO_4, 2 $MgSO_4$, 2 $CaCl_2$, 26 $NaHCO_3$; and 10 glucose for at least 60 min before being transferred individually to the recording chamber.

Electrophysiological recordings. The recordings were conducted in a submerged-type recording chamber maintained at 29–33°C. Carbogen-bubbled ACSF was superfused at a flow rate of 3.5–5.5 ml/min. Oscillations were induced by bath application of 20–25 μM CCh (Sigma-Aldrich, St. Louis, MO). Patch pipettes (≈4–8 MΩ) filled with ACSF were used to record field oscillations and action potentials extracellularly. The field pipette was placed in the stratum pyramidale of the CA3 region, whereas a second pipette was used to detect action potentials from individual neurons identified using differential interference contrast microscopy (Axioskop; Zeiss, Jena, Germany). Action potentials were recorded for ~60 s. The pipette was then withdrawn from the slice, and the cell was patched with a new pipette filled with intracellular solution containing the following: 138 mM K-gluconate, 3 mM CsCl, 10 mM phosphocreatine, 4 mM ATP, 0.4 mM GTP, 10 mM HEPES, 0.2 mM QX-314 [*N*-(2,6-dimethylphenylcarbamoylmethyl)-triethylammonium bromide], and 3 mg/ml biocytin. Seal resistance before whole-cell access was ≥1 GΩ. Whole-cell series resistance was in the range of 5–15 MΩ. All data were recorded with a Multiclamp 700A amplifier (Molecular Devices, Foster City, CA). During voltage-clamp recordings, series resistance, compensation was applied as necessary using the built-in series resistance compensation of the amplifier (12–17 kHz, 40–75%). Voltage measurements were not corrected for liquid–liquid junction potential. To record EPSCs and avoid interference from inhibitory events, cells were voltage clamped at a nominal holding potential of the estimated reversal potential for IPSCs (−65 to −60 mV of the uncorrected potential). Similarly, IPSCs were recorded at a nominal holding potential of the estimated EPSC reversal potential (0–20 mV of the uncorrected potential). Both field and unit recordings were low-pass filtered at 2 kHz using the built-in Bessel filter of the amplifier. Data were digitized at 5 kHz with either a PCI-6042E board (National Instruments, Austin, TX) and EVAN 1.3 software (courtesy of Prof. I Mody, University of California, Los Angeles, CA) or an ITC-16 board (Instrutech, Port Washington, NY) and Igor software (Wavemetrics, Lake Oswego, OR). All data were analyzed off-line using Igor Pro 5.01.

Event detection and analysis. The field recording was further filtered using a digital, bidirectional, phase-conserving, low-pass filter at 1 kHz. Extracellular unit recordings were digitally, bidirectionally high-pass filtered at 40 Hz to isolate the spikes. Whole-cell recordings of postsynaptic currents (PSCs) were digitally, bidirectionally high-pass filtered at 1 Hz to filter out slow fluctuations in holding current. *Post hoc* digital filtering was done using Igor DSP filters (ftp://ftp.wavemetrics.net/IgorPro/User_Contributions/DSPFilters.ipf.zip).

To measure the power of the field oscillation, power spectral density analysis was performed on recordings of ~60 s, using standard Igor Pro procedures. Time windows of ~1.5 s with 50% overlap were multiplied by a Hanning window to minimize end-effects before the fast Fourier transform was performed. Gamma power was taken as the area under the power spectral density curve between 20 and 40 Hz.

To examine phase coupling, event times were converted into phase with respect to the background field oscillation using wavelet analysis (Torrence and Compo, 1998; Le Van Quyen et al., 2001). The Morlet wavelet transform of the field recording was examined between 10 and 45 Hz with scales chosen to reflect the equivalent Fourier frequency (see Fig. 1*C–E*) (Torrence and Compo, 1998). For each time point, the maximum of the wavelet transform magnitude was found, and the corresponding frequency was identified. The phase of the time point was defined in terms of this dominant frequency (Fig. 1*D*,*E*). Phase was defined such that $-\pi$ was associated with the minimum of the oscillation, and a full cycle ran from $-\pi$ to π (see Fig. 1*F*). To validate the wavelet technique, a peak-to-peak linear mapping phase analysis of action potentials was also used. A significant positive correlation was found between action potential phase as determined by the two methods ($r = 0.83$; $p < 0.01$; $n = 35$; angular–angular correlation; data not shown).

Phasic charge transfer was calculated as the mean of the integral from a baseline value over each cycle with the baseline defined as follows: (1) an overall initial baseline level estimate was obtained by computing the cycle-averaged event for the entire recording (see below). The maximum (for EPSCs) or minimum (for IPSCs) of this average event was taken as the initial baseline estimate. (2) For each 0.2 s epoch, the mean of all current values exceeding this initial baseline estimate was calculated. This mean was used as the baseline for the epoch. (3) If no current value was found to exceed the initial baseline estimate during the epoch, the baseline estimate would increment negatively for EPSCs and positively for IPSCs until such current values were found. This was repeated for all epochs of the entire recording (see Fig. 2*B*,*C*). Event times for PSCs were defined as time of peak current per cycle of the oscillation, and these were converted to wavelet phases as described.

The cycle-averaged field and cycle-averaged events (see Figs. 1*G*, 3*B*) were obtained by summing recordings over cycles between $-\pi$ and π and dividing by the number of cycles. Cycles were scaled to span 2π radians. This phase is referred to as the cycle-averaged phase to distinguish it from the phase as defined by wavelet analysis.

The net apparent reversal potential (E_{syn}^{rev}) was estimated by first converting the cycle-averaged PSCs to excitatory (g_e) and inhibitory (g_i) conductances using the following equation:

$$g_{e/i} = \frac{I_{e/i}}{(V_h - E_{e/i}^{rev})}, \quad (1)$$

where $I_{e/i}$ is the phasic excitatory/inhibitory current, V_h is the holding potential, and $E_{e/i}^{rev}$ is the estimated reversal potential for the conductance of interest. The conductances were used to estimate the membrane potential of zero synaptic current (E_{syn}^{rev}) by solving the following equation:

$$I_{syn} = g_e(E_{syn}^{rev} - E_e^{rev}) + g_i(E_{syn}^{rev} - E_i^{rev}) = 0 \quad (2)$$

$$\Rightarrow E_{syn}^{rev} = \frac{I_{syn} + g_e E_e^{rev} + g_i E_i^{rev}}{g_e + g_i}.$$

Event times for action potentials were defined as the time of crossing a voltage threshold set by visual inspection, and the event phase was taken as the wavelet phase of the dominant frequency at this event time. Analysis was done both by using all spikes per cycle and only the first spike per cycle. A significant positive correlation for phase-coupling variables (see below, Statistics) was found between values obtained with the two methods (action potential coupling strength: $r = 0.99$, $p < 0.01$, $n = 43$, Pearson's correlation; mean action potential phase: $r = 0.99$, $p < 0.01$, $n = 35$, angular–angular correlation; data not shown). The results reported here use all events detected.

To evaluate spike-timing precision, spike times (Δt_i) were defined as

the time difference between the preceding minimum of the smoothed field oscillation and the time of threshold crossing. If $\Delta t_I \geq T_i/2$, where T_i is the cycle period, then Δt_i was taken as the negative time difference from the subsequent minimum. T_i was calculated as the time between two consecutive minima in the field oscillation (see Fig. 4*A*). To enable comparison between the SDs for spike times ($\sigma_{\Delta t}$) and the corresponding SD for phase (σ_ϕ), $\sigma_{\Delta t}$ was normalized by the cycle period as follows:

$$\sigma_t^{norm} = \frac{\sigma_{\Delta t}}{\bar{T}}, \tag{3}$$

where $\bar{T}$ is the mean oscillation period. This quantity is comparable to the normalized SD of phase:

$$\sigma_\phi^{norm} = \frac{\sigma_\phi}{2\pi}, \tag{4}$$

where σ_ϕ is taken as the circular SD (see below, Statistics).

In some slices, phase-coupling strength of action potentials varied over time with the oscillation power such that phase-coupling strength decreased with decreasing oscillation magnitude (data not shown). Therefore, a reduced data set was obtained for the analysis of the relationships between synaptic events and firing properties. Cells for which the wavelet magnitude of the field oscillation changed by >2 SDs between spike train and PSC recordings were excluded from the reduced data set. Results are stated for both the full and reduced data set where applicable.

Statistics. Coefficients of variation of the magnitude and frequency of the field oscillation (CV_{mag} and CV_{freq}, respectively) were calculated from the SD of the maximum magnitude and the SD of the corresponding dominant frequency of the wavelet transform for each time point over the entire recording.

Circular statistics were used to determine the phase coupling of events. The phase of each event was represented by a unit vector pointing in the direction of the phase angle. The individual vectors were summed vectorally over the time epoch in question to give a resultant vector, $\vec{R}$. The direction of the resultant vector, ϕ, was used as the mean event phase for the epoch. The normalized length of $\vec{R}$, $r = |\vec{R}|/n$, where n is the number of events, served as a measure of the strength of the phase coupling. If the events are perfectly phase coupled, $r = 1$. If events are random, the vectors will cancel, and $r \rightarrow 0$.

To determine the significance of the phase coupling, the Rayleigh probability of $\vec{R}$ was calculated using the following:

$$p = e^{-z} \times \left(1 + \frac{2Z - Z^2}{4n} - \frac{24Z - 132Z^2 + 76Z^3 - 9Z^4}{288n^2}\right), \tag{5}$$

where n is the number of spikes, and $Z = n\,r^2$ (Fisher, 1993).

Before testing equality of means of linear variables, the Levene statistic was evaluated to test homogeneity of variances. ANOVA was used to compare means between homogenous distributions ($p > 0.05$, Levene statistic), and the more robust Welch statistic was used for nonhomogenous distributions. The Bonferroni *post hoc* test was performed to find significant differences between distributions with equal variance. The Games-Howell *post hoc* test was performed to find significant differences between distributions with unequal variances. The multi-sample Watson-Williams test (Zar, 1999) was used to test equality of means of angular variables. The tests used in each case are specified in the text.

Before correlation tests for linear variables, the normality of a distribution was tested by the Kolmogorov–Smirnov test. To correlate variables from normal distributions ($p > 0.05$, Kolmogorov–Smirnov test), the Pearson's correlation coefficient was used. For variables from nonnormal distributions, the more robust Spearman's rank correlation coefficient was used.

To correlate angular–angular variables, the following parametric angular–angular correlation coefficient was used:

$$r = \frac{\sum_{i=1}^{n-1}\sum_{j=i+1}^{n} \sin(a_i - a_j)\sin(b_i - b_j)}{\sqrt{\sum_{i=1}^{n-1}\sum_{j=i+1}^{n} \sin^2(a_i - a_j) \sum_{i=1}^{n-1}\sum_{j=i+1}^{n} \sin^2(b_i - b_j)}}, \tag{6}$$

where the ith pair of data are denoted as a_i, b_i. The confidence interval was determined by a jackknifing procedure (Zar, 1999). All correlation coefficients are quoted as r, and tests used are specified in the text.

The circular SD was taken as follows:

$$\sigma = \sqrt{-2 \ln r}, \tag{7}$$

where r is the phase-coupling strength (Zar, 1999). Values are given as mean ± SEM, unless stated otherwise.

Anatomical identification. After intracellular recording and biocytin filling, the slice was fixed in 4% paraformaldehyde in 0.1 M phosphate buffer (PB), pH 7.4, for at least 30 min, followed by washout with PB several times and incubation in cryoprotecting solution (30% sucrose in 0.01 M PB) for 2 h. Slices were then freeze-thawed three times above liquid nitrogen and treated with 1% H_2O_2 in PB for 15 min to reduce endogenous peroxidase activity. Filled cells were visualized using avidin-biotinylated horseradish peroxidase complex reaction (Vector Laboratories, Burlingame, CA) with nickel-intensified 3,3′-diaminobenzidine (Sigma-Aldrich, St. Louis, MO) as chromogen giving a dark reaction product. After dehydration and embedding in Durcupan (Sigma-Aldrich), neurons were identified based on their dendritic and axonal arborization, and representative cells were reconstructed with the aid of a drawing tube using a 40× objective (see Fig. 2).

Results

Fast network oscillations were induced in the CA3 region of horizontal hippocampal slices by bath application of CCh (20–25 μM). The network oscillations were monitored by recording the field potential using an ACSF-filled micropipette placed in the stratum pyramidale. Action potentials of individual neurons were recorded extracellularly from visually selected neurons using a second ACSF-filled pipette. This second pipette was then withdrawn, and the EPSCs and IPSCs were recorded in whole-cell voltage-clamp mode with a pipette containing intracellular solution. Biocytin in the intracellular solution was used for *post hoc* anatomical identification of recorded cells. Of 74 neurons, 43 cells were successfully recovered and anatomically identified based on their dendritic and axonal arborization. Only anatomically identified neurons were included in the following analysis. Data reported excludes outliers (defined as >3 SDs from the mean of the measure of interest for each cell type). Two cells were excluded from additional analysis on this basis.

CCh-induced fast network oscillations

To characterize the field oscillations, extracellular recordings of ~1 min (Fig. 1*A*) were acquired and used to obtain a power spectrum (Fig. 1*B*). Calculation of the power spectral density function revealed a peak in the beta–gamma frequency range with a mean peak frequency over all recordings of 28.1 ± 0.6 Hz (f_{PSD}) and mean gamma power of 1782.9 ± 418.7 μV^2 ($n = 43$). Wavelet analysis using a Morlet wavelet basis (Fig. 1*C*) was used to extract the magnitude and phase of different frequency components (10–45 Hz) of the field oscillation (Fig. 1*D–F*). Both the maximum field wavelet magnitude and the corresponding dominant wavelet frequency fluctuated over time (CV_{mag} = 24.4 ± 1.1%; CV_{freq} = 14.1 ± 1.2%; see Materials and Methods). Inspec-

tion of Figure 1, *A* and *D*, suggests that the fluctuations in the oscillation magnitude might be rhythmical. Indeed, in 28 of the 43 recordings, a power spectrum analysis of the maximum wavelet magnitude over time revealed a low frequency peak (2.8 ± 1.6 Hz; $n = 28$; data not shown).

To further validate that wavelet analysis provided an appropriate definition of phase, the cycle-averaged field potential was calculated (Fig. 1*G*) (see Materials and Methods). This had a regular form, providing qualitative support for the method. Moreover, the frequency corresponding to the period of these cycle-averaged events (29.6 ± 0.7 Hz; $n = 43$) was similar to and correlated with f_{PSD} ($r = 0.95$; $p < 0.01$, Pearson's correlation; $n = 43$).

Comparison of synaptic input in different cell types

To understand the synaptic mechanisms underlying gamma oscillations, PSCs were recorded from PCs (Fig. 2*Ai*) ($n = 17$) and perisomatic-targeting interneurons (basket and axo-axonic cells; $n = 9$) (Fig. 2*Aii*). Recordings were also obtained from dendritic-targeting interneurons [$n = 7$, comprising OLM cells, interneurons with a dendritic tree in the stratum oriens projecting to the stratum lacunosum moleculare ($n = 3$), and radiatum cells/radiatum-lacunosum-moleculare cells ($n = 4$)] (Fig. 2*Aiii*) and interneuron-selective interneurons [as defined by Hájos et al. (2004); $n = 7$] (Fig. 2*Aiv*) for comparison. Cells were voltage clamped at the estimated inhibitory and excitatory reversal potentials to record EPSCs and IPSCs, respectively (Fig. 2*B*,*C*) (see Materials and Methods). This information could reveal differences in the dominant input to cells and thus suggest a functional network architecture underlying gamma oscillations. Hereafter, any reference to excitation or inhibition refers to phasic excitation or phasic inhibition.

If phasic excitation drives cell firing, differences in the excitatory input to the cells may lead to differences in the recruitment of the various subpopulations of neurons. Phasic excitatory charge transfer (Q_e) differed significantly between cell types (Fig. 2*D*) ($p < 0.01$, Welch statistic; $n = 40$). Q_e was smallest in PCs ($Q_e = 0.56 \pm 0.063$ pC; $n = 17$) and was, on average, largest in perisomatic-targeting interneurons ($Q_e = 3.1 \pm 0.91$ pC, $n = 9$; dendritic-targeting interneurons: $Q_e = 0.94 \pm 0.267$ pC, $n = 7$; interneuron-selective interneurons: $Q_e = 2.2 \pm 0.42$ pC, $n = 7$).

The balance of excitation and inhibition was investigated by comparison of the

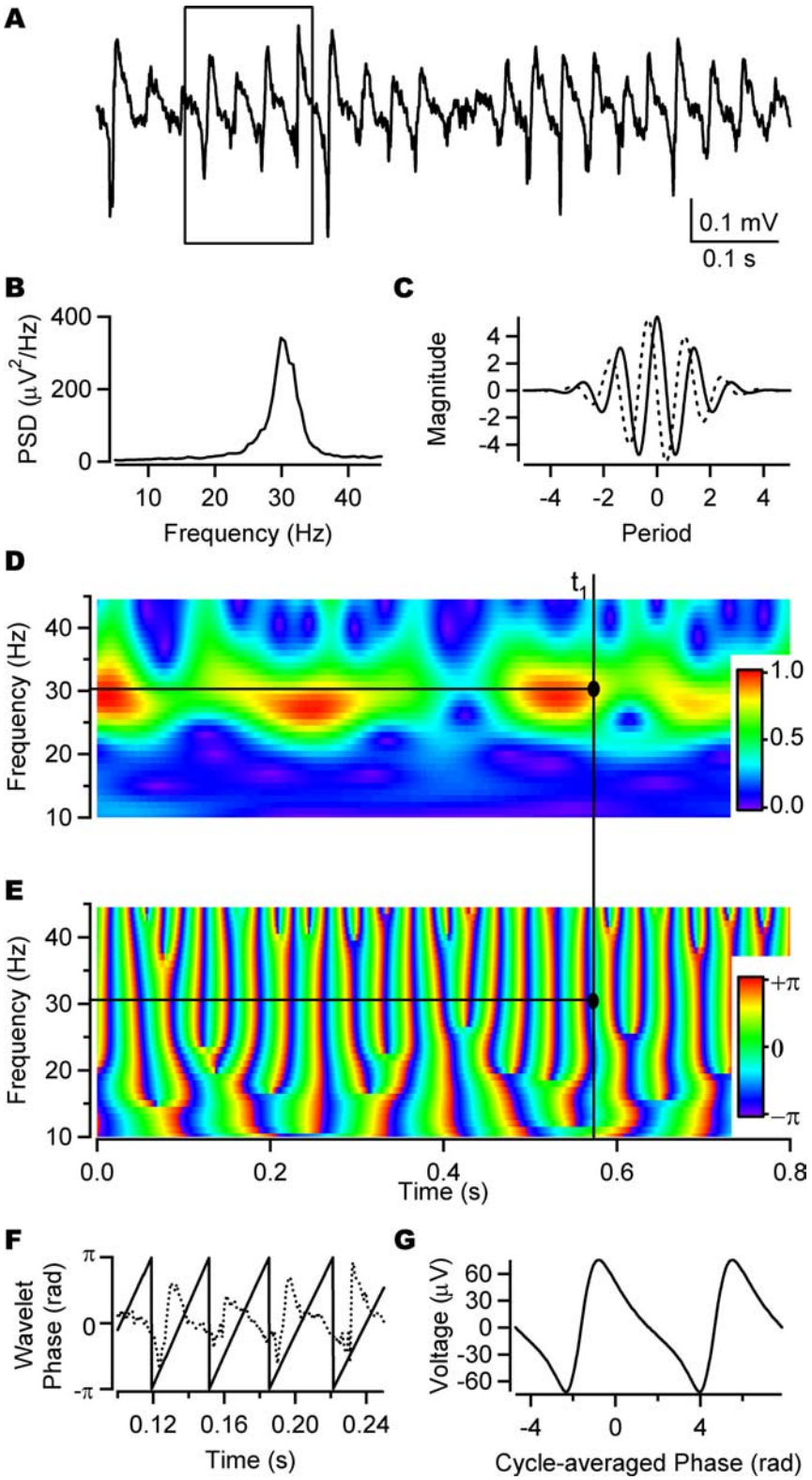

Figure 1. Wavelet analysis of CCh-induced field oscillation. ***A***, Field oscillation recorded extracellularly from the stratum pyramidale of the CA3 region after bath application of 20 μM CCh. ***B***, Power spectral density function of the trace in ***A*** showing gamma-frequency peak. ***C***, Real component (solid) and imaginary component (dotted) of Morlet wavelet basis. ***D***, Normalized magnitude component of wavelet transform of the trace in ***A***. ***E***, Phase component of wavelet transform of the trace in ***A***. ***D*** and ***E*** show how the phase of the gamma oscillation is defined for an arbitrary time, t_1. The dominant frequency at t_1 is defined as the frequency of the maximum magnitude at time t_1 (here ~30 Hz). The oscillation phase is then determined for the dominant frequency at time t_1. The time scale is the same for ***A***, ***D***, and ***E***. ***F***, Expansion of the boxed area in ***A*** showing phase for all time points as defined by the dominant frequency of the wavelet transform as shown in ***D*** and ***E***. ***G***, Cycle average of the field oscillation in ***A***, with the start of each cycle defined by the wavelet phase.

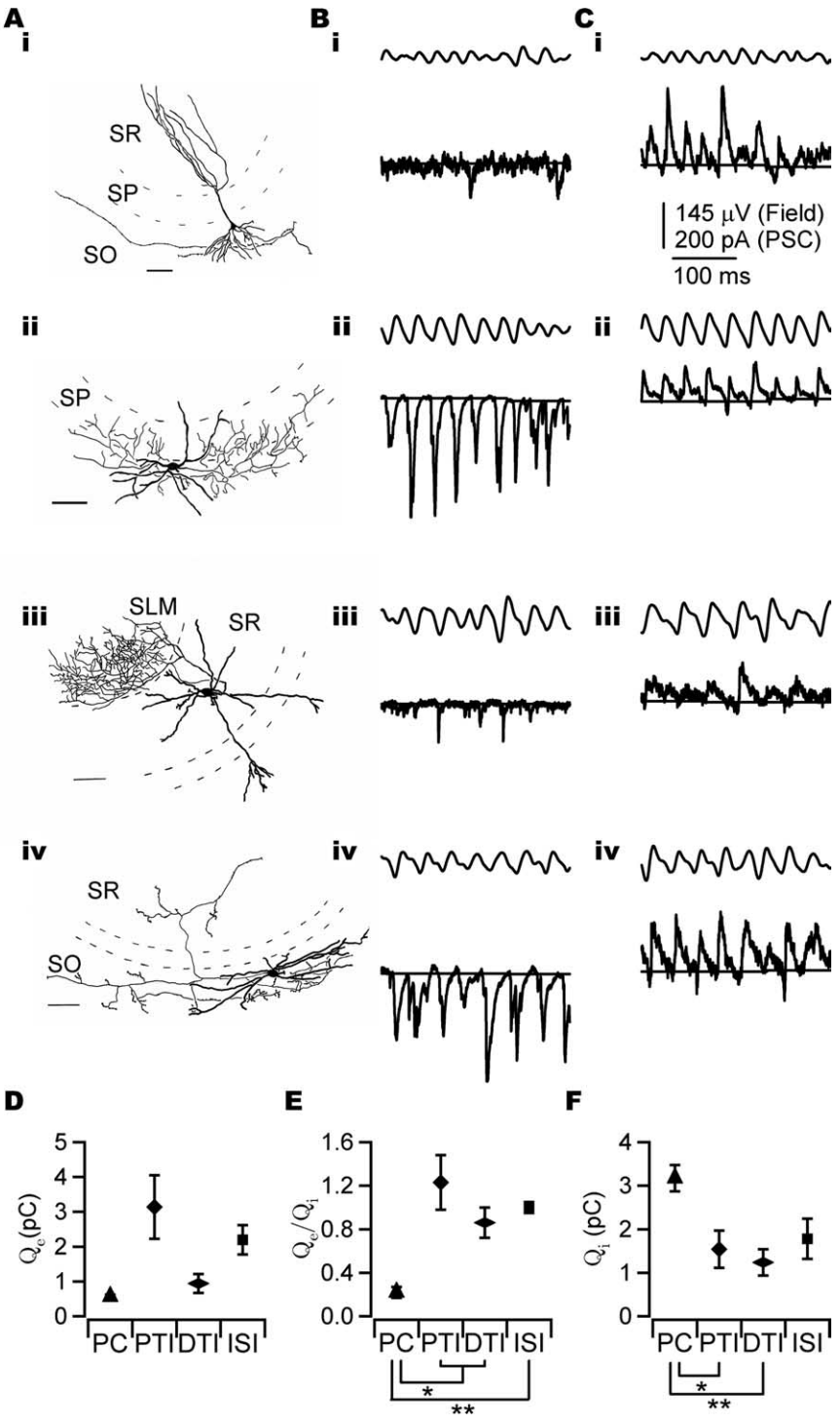

Figure 2. Phasic charge transfer of EPSCs and IPSCs during CCh-induced oscillations. ***A***, Camera lucida drawing of a PC (***i***), perisomatic-targeting interneuron (a putative axo-axonic cell; ***ii***), dendritic-targeting interneuron (radiatum-lacunosum moleculare cell; ***iii***), and interneuron-selective interneuron (***iv***). SR, Stratum radiatum; SP, stratum pyramidale; SO, stratum oriens; SLM, stratum lacunosum-moleculare. ***B***, Bidirectional bandpass-filtered field potential (10–45 Hz; top trace) and EPSCs (bottom trace) recorded from the soma of the cells illustrated in ***A***, at a holding potential of −60 mV. ***C***, Bidirectional bandpass-filtered field potential (10–45 Hz; top trace) and IPSCs (bottom trace) recorded from the same cells at 0 mV (***i***), +20 mV (***ii***), and +10 mV (***iii***, ***iv***). The horizontal solid line is the calculated baseline used for phasic charge estimation (see Materials and Methods). ***D***, The phasic excitatory charge (Q_e) differed significantly between cell classes ($p < 0.01$). PCs, $n = 17$; perisomatic-targeting interneurons, $n = 9$; dendritic-targeting interneurons, $n = 7$; interneuron-selective interneurons, $n = 7$. ***E***, Phasic excitatory to inhibitory charge ratio (Q_e/Q_i) in different cell classes. Q_e/Q_i was smaller in PCs than in all classes of interneuron. PCs, $n = 17$; perisomatic-targeting interneurons, $n = 7$; dendritic-targeting interneurons, $n = 7$; interneuron-selective interneurons, $n = 4$. ***F***, PCs received a significantly larger phasic inhibitory charge (Q_i) than perisomatic-targeting interneurons and dendritic-targeting interneurons. The number of cells is as in ***E***. Error bars indicate SEM. *$p < 0.05$; **$p < 0.01$. Scale bars, 100 μm. PTI, Perisomatic-targeting interneuron; DTI, dendritic-targeting interneuron; ISI, interneuron-selective interneuron.

ratio of phasic excitatory to inhibitory charge (Q_e/Q_i) between cell types. Phasic inhibition exceeded phasic excitation in all PCs ($Q_e/Q_i = 0.23 \pm 0.049$; $n = 17$), whereas the dominant input to interneurons was often excitatory with perisomatic-targeting interneurons showing the largest excitation to inhibition ratio ($Q_e/Q_i = 1.2 \pm 0.25$, $n = 7$; dendritic-targeting interneurons: $Q_e/Q_i = 0.86 \pm 0.14$, $n = 7$; interneuron-selective interneurons: $Q_e/Q_i = 1.0 \pm 0.05$, $n = 4$) (Fig. 2*E*). The difference in Q_e/Q_i between PCs and interneuron classes was significant (Fig. 2*E*) ($p < 0.01$, Welch statistic and ANOVA with *post hoc* Games-Howell test; $n = 35$).

Although the significant difference in Q_e/Q_i between PCs and interneurons could result from a larger phasic excitatory input to interneurons, a larger phasic inhibitory input to PCs could also contribute to this difference. Comparison of Q_i between cell types revealed a significantly larger Q_i in PCs ($Q_i = 3.2 \pm 0.30$ pC; $n = 17$) than in interneurons (Fig. 2*F*) ($n = 35$; $p < 0.01$, ANOVA; perisomatic-targeting interneurons: $Q_i = 1.5 \pm 0.43$ pC, $n = 7$; dendritic-targeting interneurons: $Q_i = 1.2 \pm 0.30$ pC, $n = 7$; interneuron-selective interneurons: $Q_i = 1.8 \pm 0.46$ pC, $n = 4$). Interestingly, Q_i was found to correlate with field magnitude ($r = 0.58$; $p < 0.01$, Pearson's correlation; $n = 35$) (see supplemental Fig. 1, available at www.jneurosci.org as supplemental material), and this might account for some of the observed difference in Q_i between cell type ($p < 0.05$, ANOVA with field magnitude as covariate; $n = 35$; partial $\eta^2_{\text{celltype}} = 0.25$; partial $\eta^2_{\text{fieldmag}} = 0.16$). A correlation between charge and field magnitude was not seen for excitatory charge ($r = -0.21$; $p = 0.80$, Spearman's correlation; $n = 40$) (see supplemental Fig. 1, available at www.jneurosci.org as supplemental material). The data support the conclusion that both excitatory and inhibitory inputs differ between cell types.

The majority of cells received significantly phase-coupled ($p < 0.05$, Rayleigh probability) excitatory and inhibitory synaptic input as measured by the phase of the peak current recorded in each cycle (40 of 40 and 36 of 37, respectively). The coupling strength of the peak of the EPSC (r_e) did not differ significantly between cell types (Fig. 3*Ai*) ($p = 0.27$, ANOVA; $n = 40$), whereas the coupling strength of inhibitory inputs (r_i) was significantly larger in PCs ($r_i = 0.83 \pm 0.024$; $n = 17$) than in interneurons (Fig. 3*Aii*) ($p < 0.01$, Welch statistic; $n = 37$; perisomatic-targeting

interneurons: $r_i = 0.63 \pm 0.074$, $n = 9$; dendritic-targeting interneurons: $r_i = 0.46 \pm 0.122$, $n = 7$; interneuron-selective interneurons: $r_i = 0.57 \pm 0.059$, $n = 4$).

In all cells, the phase of the peak of the cycle-averaged EPSC preceded the peak of the cycle-averaged IPSC (Fig. 3*B*). To capture the temporal interaction between inhibitory and excitatory synaptic conductances, the effective synaptic conductance was estimated by calculation of the net apparent synaptic reversal potential E_{syn}^{rev} (see Materials and Methods). The shape of the E_{syn}^{rev} curve differed between PCs and interneurons (Fig. 3*C*), with the half-width (measured in radians) of the peak of the E_{syn}^{rev} curve being significantly narrower in PCs (half-width of 0.79 ± 0.157; $n = 17$) than in interneurons (Fig. 3*D*) ($p < 0.01$, ANOVA with Bonferroni *post hoc* test; $n = 35$; perisomatic-targeting interneurons: half-width of 2.6 ± 0.32, $n = 7$; dendritic-targeting interneurons: half-width of 2.6 ± 0.25, $n = 7$; interneuron-selective interneurons: half-width of 2.7 ± 0.23, $n = 4$), primarily as a result of the dominant inhibitory input received by PCs.

Firing properties of anatomically identified neurons during fast network oscillations

To characterize the firing properties of the cells, action potentials were recorded extracellularly for ~1 min (Fig. 4*A*) before whole-cell recording with another pipette (see Materials and Methods for details). The firing properties of the cells were quantified using three parameters: mean firing rate, action potential coupling strength (r_{AP}), and mean action potential phase (ϕ_{AP}; see Materials and Methods).

Firing rate

PCs fired at a significantly lower rate (6.0 ± 0.82 Hz; $n = 17$) than interneurons (Fig. 4*B*) ($p < 0.01$, Welch statistic and ANOVA with Games-Howell *post hoc* test; $n = 42$), whereas perisomatic-targeting (rate, 19 ± 2.3 Hz; $n = 10$) and interneuron-selective (rate, 21 ± 3.2 Hz; $n = 8$) interneurons fired at slightly higher rates than dendritic-targeting interneurons (rate, 16 ± 2.8 Hz; $n = 7$), in agreement with previous results (Hájos et al., 2004).

Phase versus time

The timing of action potentials after synaptic excitation may be the result of the intrinsic properties of the neuron, recurrent inhibitory synaptic input from the network, or both. If intrinsic properties play a dominant role in governing spike timing, then the absolute spike time after

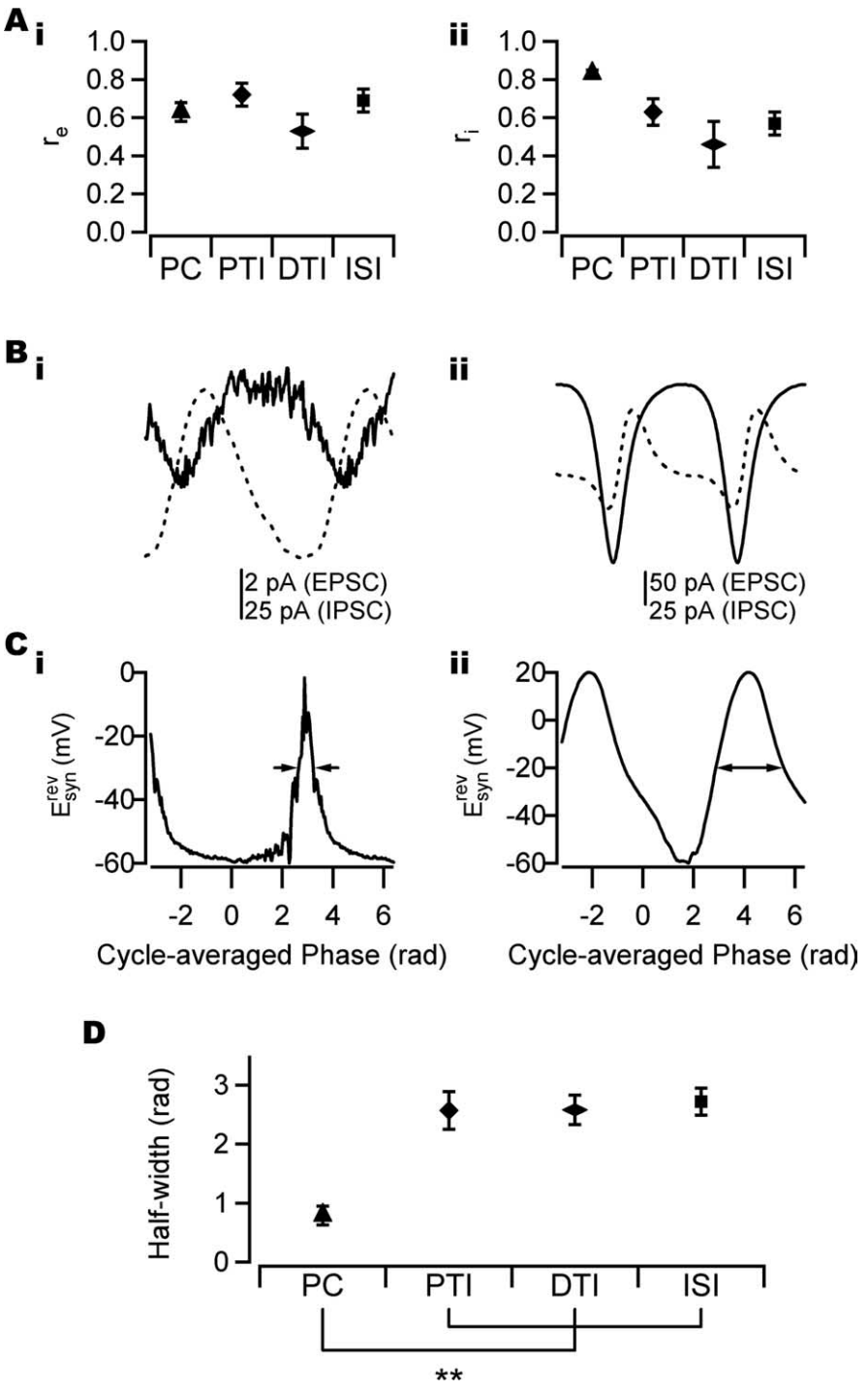

Figure 3. PSC phase-coupling strength and synaptic reversal potential during CCh-induced oscillations. ***A***, Coupling strength of PSCs as measured by the phase of the peak time in different cell types. ***i***, No significant difference was seen in EPSC coupling strength (r_e) between cell types. PCs, $n = 17$; perisomatic-targeting interneurons, $n = 9$; dendritic-targeting interneurons, $n = 7$; interneuron-selective interneurons, $n = 7$. ***ii***, A significant difference in IPSC coupling strength (r_i) was found between cell types ($p < 0.01$). PCs, $n = 17$; perisomatic-targeting interneurons, $n = 9$; dendritic-targeting interneurons, $n = 7$; interneuron-selective interneurons, $n = 4$. ***B***, Cycle-averaged PSCs in PC (***i***) and perisomatic-targeting interneuron (***ii***). Solid line, EPSC; dotted line, IPSC. The same cells as in Figure 2, *Ai* and *Aii*, are shown. Note the different scales in ***i*** and ***ii***. ***C***, Net apparent synaptic reversal potential (E_{syn}^{rev}) for cells in ***B***. For details of calculation, see Materials and Methods. Arrows indicate half-width of E_{syn}^{rev}. ***D***, Half-width of E_{syn}^{rev} in different cell classes. The difference in half-width of E_{syn}^{rev} between PCs and interneurons was significant ($^{**}p < 0.01$). PCs, $n = 17$; perisomatic-targeting interneurons, $n = 7$; dendritic-targeting interneurons, $n = 7$; interneuron-selective interneuron, $n = 4$. Error bars indicate SEM. PTI, Perisomatic-targeting interneuron; DTI, dendritic-targeting interneuron; ISI, interneuron-selective interneuron.

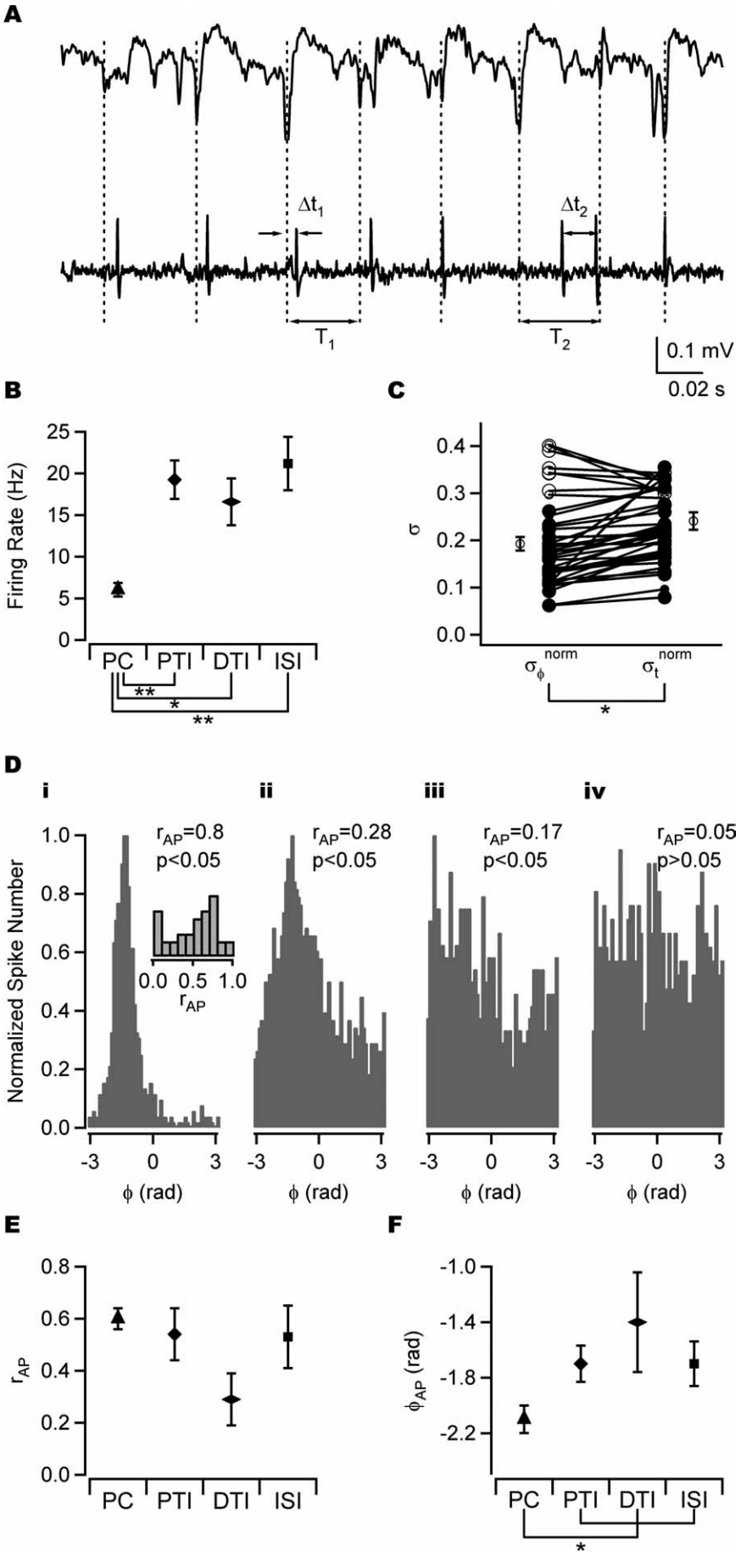

the arrival of the excitatory synaptic input should remain constant independent of the oscillation frequency. Alternatively, spike timing might be more tightly controlled by both the excitatory and inhibitory synaptic input. The field oscillation emerges from the total network activity, and therefore if spike timing is predominantly controlled by both the excitatory and inhibitory synaptic input, variability in spike phase relative to the field oscillation should be smaller than variability in absolute time. This provided the motivation to compare spike-timing precision in terms of absolute time and phase. If the oscillation frequency remains constant, the two measures should give comparable results. However, if the frequency varies over the recording, the results will differ. The SD of spike times relative to the field oscillation (σ_t^{norm}) and the SD of the spike phases (σ_ϕ^{norm}; see Materials and Methods) were used to evaluate precision (Mainen and Sejnowski, 1995). Overall, σ_ϕ^{norm} was significantly smaller than σ_t^{norm} (Fig. 4*C*) ($p < 0.05$, paired-samples t test; $n = 42$), indicating that both excitatory and inhibitory synaptic inputs are important in the control of spike timing of CA3 neurons. However, $\sigma_t^{norm} > \sigma_\phi^{norm}$ in cells that were weakly phase coupled (r_{AP}<0.2; see below, Action potential phase-coupling strength).

←

Figure 4. Firing properties of distinct types of neuron during CCh-induced oscillations. ***A***, Simultaneous extracellular recordings of field potential (top trace) and spike train (bottom trace) from an anatomically identified perisomatic-targeting interneuron. ΔT_i, Relative spike times used for time analysis of precision; T_i, cycle periods used for time analysis of precision (see Materials and Methods). ***B***, Firing rate in different cell classes. PCs ($n = 17$) fired at significantly lower rates than perisomatic-targeting interneurons ($n = 10$), interneuron-selective interneurons ($n = 8$), and dendritic-targeting interneurons ($n = 7$). ***C***, Comparison of phase and time precision as quantified by the SD of phase normalized by 2π (σ_ϕ^{norm}) and SD of time relative to oscillation minimum normalized by the mean oscillation period (σ_t^{norm}). σ_ϕ^{norm} was significantly smaller than σ_t^{norm}. ***D***, Spike-phase histograms normalized by the maximum bin count of strongly phase-coupled cells (***i***, ***ii***), weakly phase-coupled cell (***iii***), and non-phase-coupled cell (***iv***). Inset, Histogram of action potential phase-coupling strength (r_{AP}) over all cells showing a bimodal distribution with minimum around $r_{AP} = 0.2$, the cutoff value between strong and weak phase coupling. ***E***, Average r_{AP} in different cell types. The number of cells is as in ***B***. ***F***, Firing phase (ϕ_{AP}) of strongly phase-coupled cells in different cell types. PCs fired significantly earlier than all classes of interneurons. PCs, $n = 17$; perisomatic-targeting interneurons, $n = 8$; dendritic-targeting interneurons, $n = 3$; interneuron-selective interneurons, $n = 6$. Error bars indicate SEM. $^*p < 0.05$; $^{**}p < 0.01$. PTI, Perisomatic-targeting interneuron; DTI, dendritic-targeting interneuron; ISI, interneuron-selective interneuron.

Action potential phase-coupling strength

Thirty-eight of the 42 cells were significantly phase coupled ($p < 0.05$, Rayleigh probability). The degree of phase coupling varied between significantly phase-coupled cells. The distribution of r_{AP} appeared bimodal with a minimum around $r_{AP} = 0.2$ (Fig. 4*D*, inset). This was set as the cutoff value to classify cells as strongly or weakly phase coupled. Inspection of the spike-phase histograms confirmed this as an appropriate choice (Fig. 4*D*) [see also Hájos et al. (2004), their Fig. 7*C*]. The phase histogram of strongly phase-coupled cells ($r_{AP} > 0.2$) exhibited a clear peak in the phase histogram, whereas the phase histograms of weakly phase-coupled cells did not. The majority of PCs, perisomatic-targeting, and interneuron-selective interneurons were strongly phase coupled ($r_{AP} > 0.2$; 17 of 17, 8 of 10, and 6 of 8, respectively), whereas this was the case for only 3 of the 7 dendritic-targeting interneurons (Fig. 4*D*). It has been reported that the precision of phase coupling is lower in PCs than in the majority of interneurons (Hájos et al., 2004). Consistent with this, r_{AP} of PCs tended to be smaller than that of strongly coupled perisomatic-targeting interneurons (0.60 ± 0.04, $n = 17$ vs 0.66 ± 0.08, $n = 8$). Action potential phase-coupling strength was, on average, weakest in dendritic-targeting interneurons, consistent with previous findings (Hájos et al., 2004). The difference in r_{AP} between cell types failed to reach statistical significance (Fig. 4E) ($p = 0.1$, Welch statistic; $n = 42$).

Mean action potential phase angle

Strongly phase-coupled PCs fired near the minimum of the field oscillation ($\phi_{AP} = -2.1 \pm 0.09$; $n = 17$; phase measured in radians), whereas strongly phase-coupled interneurons tended to fire later in the cycle. This difference was significant (Fig. 4*F*) ($p < 0.01$, Watson-Williams test; $n = 34$). Phase-coupled dendritic-targeting interneurons tended to fire later in the cycle ($\phi_{AP} = -1.4 \pm 0.36$; $n = 3$) than perisomatic-targeting ($\phi_{AP} = -1.7 \pm 0.13$; $n = 8$) and interneuron-selective ($\phi_{AP} = -1.7 \pm 0.16$; $n = 6$) interneurons, but this was not statistically significant (Fig. 4*F*) ($p = 0.20$ and $p = 0.34$, respectively, Watson-Williams test). These findings are consistent with the findings of Hájos et al. (2004).

Thus, different cell types display different firing properties during CCh-induced oscillations with respect to firing rate, action potential coupling strength, and mean action potential phase angle.

Synaptic input and firing properties during fast network oscillations

The relationship between synaptic input from the network and firing properties was investigated next in terms of the three parameters discussed, namely firing rate, action potential phase-coupling strength, and mean action potential phase angle.

Synaptic input and firing rate

If phasic excitatory input drives cells to fire, the firing rate would be expected to vary with the magnitude of the excitatory input. Hence, the relationship between Q_e and spike rate was investigated. Over all cells, a significant positive correlation was found between rate and excitatory charge (Fig. 5*A*) (full set: $r = 0.51$, $p < 0.01$, $n = 39$; reduced set: $r = 0.61$, $p < 0.01$, $n = 31$; Spearman's correlation; see Materials and Methods). We have shown that perisomatic-targeting and interneuron-selective interneurons fire at a higher rate than PCs and dendritic-targeting cells (Fig. 4*B*). If the firing rate is controlled by excitatory synaptic input, perhaps differences in the amount of excitation received by different cell classes could account for differences in the firing rate.

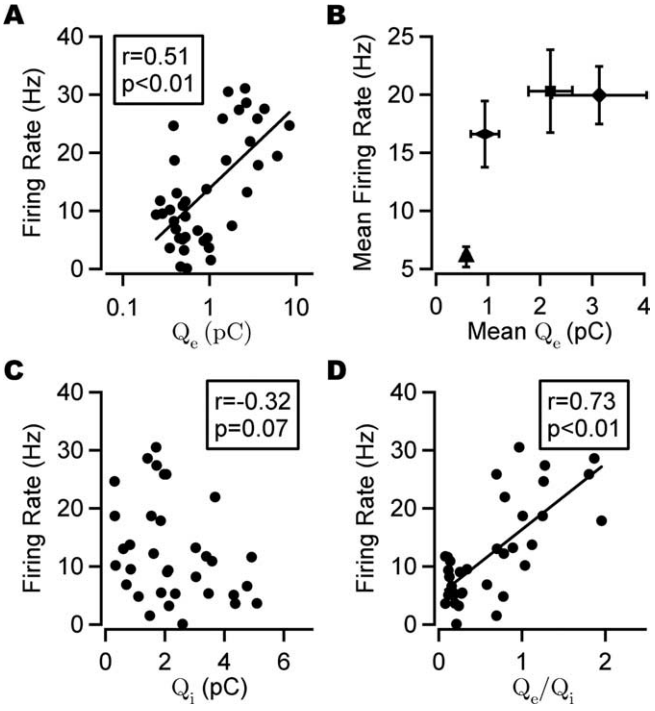

Figure 5. Firing rate and phasic synaptic charge transfer. ***A***, Firing rate plotted against phasic excitatory charge transfer (Q_e) for individual cells. Overall, a significant correlation (Spearman's correlation) was found between the firing rate and Q_e (shown here on a log scale). A least-square fit line is shown. ***B***, Relationship between the firing rate and Q_e in different cell classes. Both the mean firing rate and Q_e were higher, on average, in perisomatic-targeting interneurons ($n = 9$) and interneuron-selective interneurons ($n = 7$) compared with PCs ($n = 16$) and dendritic-targeting interneurons ($n = 7$). The same key as in Figure 2 is shown. Error bars indicate SEM. ***C***, Firing rate plotted against phasic inhibitory charge (Q_i) for individual cells. No significant correlation was found between the firing rate and Q_i in the complete data set (Pearson's correlation). ***D***, Firing rate plotted against charge ratio (Q_e/Q_i). A significant positive correlation was found between the firing rate and Q_e/Q_i (Pearson's correlation). A least-square fit line is shown.

Indeed, cell types with high firing rates received, on average, more excitation than cell types with low firing rates (Figs. 2*D*, 5*B*).

If inhibition suppresses firing, a negative correlation would be expected between Q_i and the firing rate. This relationship was seen in the reduced data set but failed to reach statistical significance in the full data set (Fig. 5*C*) (reduced set: $r = -0.40$, $p < 0.05$, $n = 27$; full set: $r = -0.32$, $p = 0.07$, $n = 34$; Pearson's correlation). A stronger correlation was found between the firing rate and Q_e/Q_i (Fig. 5*D*) (full set: $r = 0.73$, $p < 0.01$, $n = 34$; reduced set: $r = 0.79$, $p < 0.01$, $n = 27$; Pearson's correlation).

Synaptic input and action potential phase-coupling strength

Whereas phase coupling is a robust phenomenon in a large proportion of CA3 neurons, the strength of the phase coupling differed between cells. Could differences in synaptic input account for this variation? We have shown that cell classes differ with respect to the dominant input received from the network (Fig. 2*D*). Because cell classes also differ in their intrinsic properties, this led to the question of whether cell classes process synaptic input differently. To investigate this, the relationship between Q_e/Q_i and r_{AP} was assessed for each cell type studied. All PCs received a dominant inhibition and showed strong phase coupling. In perisomatic-targeting interneurons, Q_e/Q_i differed between strongly and weakly phase-coupled cells. In this cell group, the dominant input in strongly phase-coupled neurons tended to be excitatory or the inputs were approximately equal such that,

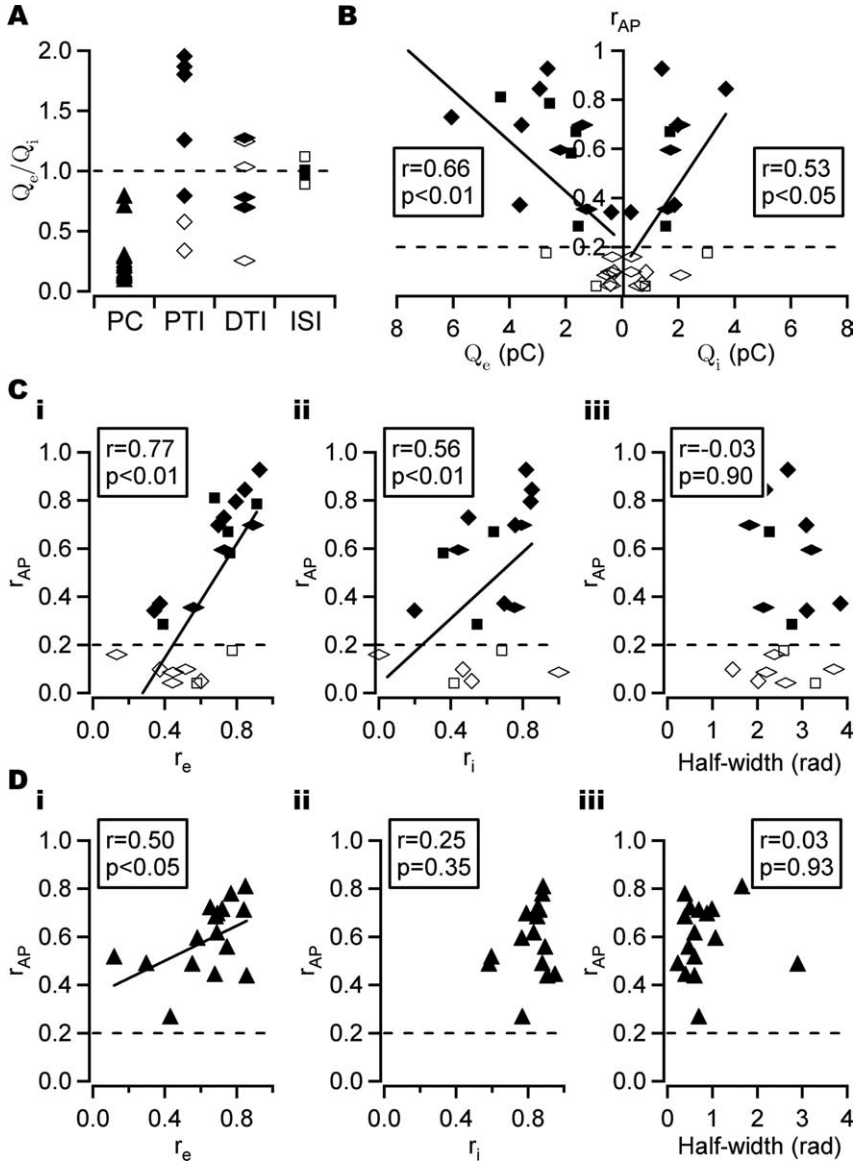

Figure 6. Action potential phase-coupling strength and synaptic input. ***A***, Phasic excitatory/inhibitory charge ratio (Q_e/Q_i) in different cell classes. Coupling strength in perisomatic-targeting interneurons differed between strongly and weakly coupled cells, with strongly phase-coupled cells showing, on average, $Q_e/Q_i > 1$, whereas weakly phase-coupled cells received a dominant phasic inhibition ($Q_e/Q_i < 1$). This relationship did not hold for other cell types. The dashed line shows $Q_e/Q_i = 1$. Filled symbols, Strongly phase-coupled cells; open symbols, weakly/non-phase-coupled cells. PTI, Perisomatic-targeting interneuron; DTI, dendritic-targeting interneuron; ISI, interneuron-selective interneuron. The same symbol key applies to all panels. ***B***, Action potential phase-coupling strength (r_{AP}) and phasic excitatory charge (Q_e) and phasic inhibitory charge (Q_i) in interneurons. Significant correlations were found between phasic charge transfer and r_{AP} (Pearson's correlation). ***C***, r_{AP} and peak EPSC coupling strength (r_e; ***i***), peak IPSC coupling strength (r_i; ***ii***), and half-width of E_{syn}^{rev} (***iii***) in interneurons. A significant positive correlation was found between r_{AP} and the coupling strength of both EPSC and IPSC peaks. No significant correlation was found between r_{AP} and the half-width of E_{syn}^{rev} (Pearson's correlation). ***D***, As in ***C***, but in PCs. A correlation was seen between r_{AP} and r_e in PCs, whereas no such correlation was seen for either r_i or the half-width (Pearson's correlation). The dashed line in ***B–D*** shows $r_{AP} = 0.2$, the cutoff value used to distinguish between strongly and weakly phase-coupled cells. A least-squares fit line is shown for significant correlations.

on average, $Q_e/Q_i > 1$, whereas weakly phase-coupled cells received a dominant inhibitory input ($Q_e/Q_i < 1$). This relationship was not observed in other cell types. Dendritic-targeting interneurons showed a broad range of Q_e/Q_i and variable r_{AP}, whereas the ratio of excitation to inhibition in interneuron-selective interneurons was approximately equal, with Q_e/Q_i values closer to 1 independent of the value of r_{AP} (Fig. 6*A*).

If the ratio of excitation to inhibition cannot fully explain the coupling strength of the cell, it may be that the total synaptic input is more important. Indeed, it was found that strongly phase-coupled perisomatic-targeting interneurons received, on average, a larger synaptic drive (both inhibitory and excitatory) than weakly phase-coupled cells. This result extended to the other interneuron classes studied, in which a significant correlation was found between Q_e and r_{AP} and between Q_i and r_{AP} in the full data set (Fig. 6*B*) (full set: $r = 0.66$, $p < 0.01$, $n = 23$, and $r = 0.53$, $p < 0.05$, $n = 18$, respectively; reduced set: $r = 0.67$, $p < 0.01$, $n = 19$, and $r = 0.3$, $p = 0.27$, $n = 15$, respectively; Pearson's correlation).

If synaptic input controls spike timing, the phase-coupling strength of the synaptic input would be expected to contribute toward the strength of action potential phase coupling. Indeed, in interneurons, a positive correlation was found between r_{AP} and r_e (Fig. 6*Ci*) (full set: $r = 0.77$, $p < 0.01$, $n = 23$; reduced set: $r = 0.73$, $p < 0.01$, $n = 19$; Pearson's correlation), and a weaker correlation was found between r_{AP} and r_i (Fig. 6*Cii*) (full set: $r = 0.56$, $p < 0.01$, $n = 21$; reduced set: $r = 0.47$, $p = 0.057$, $n = 17$; Pearson's correlation), suggesting that it is predominantly the timing precision of excitatory input that controls spike-timing precision in interneurons. In PCs, the correlation between r_{AP} and r_e was weaker than in interneurons (Fig. 6*Di*) (full set: $r = 0.50$, $p < 0.05$, $n = 16$; reduced set: $r = 0.37$, $p = 0.23$, $n = 12$; Pearson's correlation), whereas no significant correlation was found between r_{AP} and r_i (Fig. 6*Dii*) (full set: $r = 0.25$, $p = 0.35$, $n = 16$; reduced set: $r = 0.14$, $p = 0.66$, $n = 12$; Pearson's correlation).

Because cells receive excitatory and inhibitory inputs concomitantly, the temporal interaction of excitation and inhibition may also contribute toward the action potential coupling strength. If the net resultant synaptic input alone controls spike time, then the width of the peak of E_{syn}^{rev} should give a time window for action potential firing. A correlation analysis of the half-width of E_{syn}^{rev} and r_{AP} revealed no such relationship in interneurons (Fig. 6*Ciii*) (full set: $r = -0.03$, $p = 0.90$, $n = 18$; reduced set: $r = -0.29$, $p = 0.30$, $n = 15$; Pearson's correlation) or PCs (Fig. 6*Diii*) (full set: $r = 0.03$, $p = 0.93$, $n = 16$; reduced set: $r = 0.03$, $p = 0.93$, $n = 12$; Pearson's correlation).

We conclude that both the precision and strength of synaptic input contribute toward controlling r_{AP} in interneurons.

Synaptic input and mean action potential phase angle

We have shown that different classes of cell preferentially fire at different phases of the gamma oscillation. Could differences in

the timing of the synaptic input account for the differences in mean action potential phase angle? The relationship between ϕ_{AP} and synaptic input was investigated next. ϕ_{AP} in strongly phase-coupled cells was found to either follow (10 of 26) or precede (16 of 26) the peak of the cycle-averaged EPSC and always preceded the peak of the cycle-averaged IPSC (Fig. 7*A*). When the effects of excitation and inhibition were combined through the estimation of E_{syn}^{rev}, it was found that the peak of E_{syn}^{rev} (ϕ_{syn}) preceded ϕ_{AP} in the vast majority of strongly phase-coupled cells (24 of 26). In PCs, ϕ_{syn} reflected the phase of least inhibition, whereas in phase-coupled perisomatic-targeting interneurons and other interneurons receiving a large excitatory input, it was associated with the peak of the excitation (Fig. 7*B*).

If the timing of excitatory input controls spike timing in all cells, it might be expected that excitation arrives earlier in PCs than in interneurons, because they fire at earlier phases. However, the phase of peak excitation was significantly later in phase-coupled PCs ($\phi_E = -1.1 \pm 0.08$; $n = 16$) than in phase-coupled interneurons (Fig. 7*C*) (full set: $p < 0.01$; perisomatic-targeting interneurons: $\phi_E = -1.8 \pm 0.25$, $n = 7$; dendritic-targeting interneurons: $\phi_E = -1.7 \pm 0.04$, $n = 3$; interneuron-selective interneurons: $\phi_E = -1.5 \pm 0.15$, $n = 5$; reduced set: $p < 0.01$, Watson-Williams test; $n = 26$). This suggests that it is not excitation alone that governs precise action potential timing. Indeed, when the effect of excitation and inhibition were combined, ϕ_{syn} was found to be significantly earlier in phase-coupled PCs ($\phi_{syn} = -2.7 \pm 0.09$; $n = 16$) than in phase-coupled interneurons (Fig. 7*D*) (full set: $p < 0.01$; perisomatic-targeting interneurons: $\phi_{syn} = -2.2 \pm 0.20$, $n = 5$; dendritic-targeting interneurons: $\phi_{syn} = -1.7 \pm 0.05$, $n = 3$; interneuron-selective interneurons: $\phi_{syn} = -2.1 \pm 0.86$, $n = 2$; reduced set: $p < 0.01$, Watson-Williams test; $n = 20$), resulting in a significant correlation between ϕ_{syn} and ϕ_{AP} over all cells (Fig. 7*E*) (full set: $r = 0.46$, $p < 0.01$, $n = 26$; reduced set: $r = 0.61$, $p < 0.01$, $n = 20$; angular–angular correlation).

In conclusion, we have shown that differences in synaptic input are important in controlling the distinct firing properties of neurons during gamma oscillations.

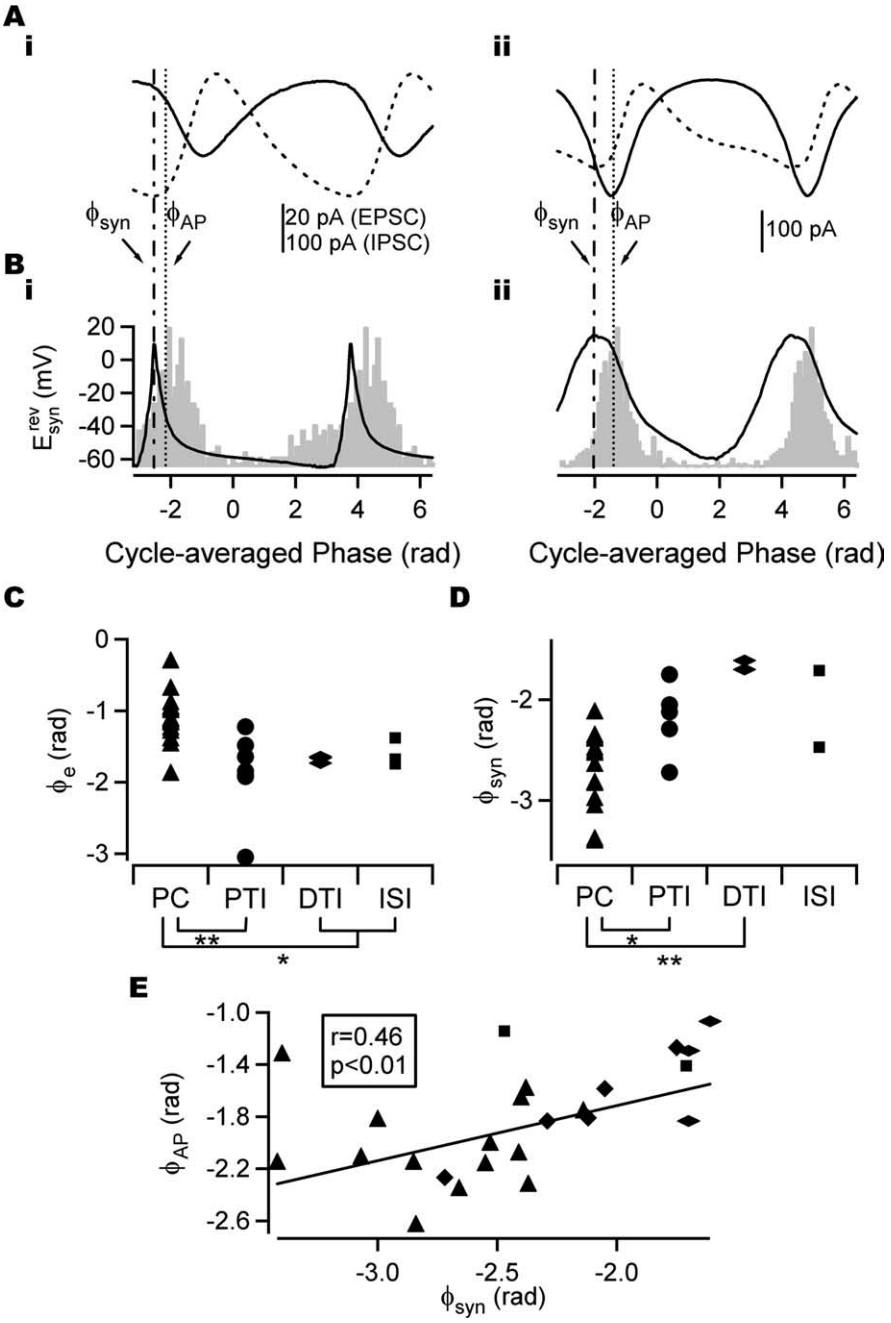

Figure 7. Mean action potential phase and synaptic input in strongly phase-coupled cells. ***A***, Cycle-averaged EPSC (solid trace) and IPSC (dashed trace) with a mean firing phase (ϕ_{AP}) shown as a dotted line in a PC (***i***) and perisomatic-targeting interneuron (***ii***). ϕ_{AP} either slightly led or lagged the (negative) peak of the cycle-averaged EPSC but was always earlier than the (positive) peak of cycle-averaged IPSC in phase-coupled cells. ***B***, E_{syn}^{rev} (solid line) and spike-phase histogram (gray) for the same cells as shown in ***A***. The peak of E_{syn}^{rev} (ϕ_{syn}; dashed-dotted line) preceded ϕ_{AP} in the majority of phase-coupled cells. Note that ϕ_{AP} does not necessarily coincide with the peak of the spike-phase histogram. ***C***, Phase of peak excitation (ϕ_e) in different cell types. The phase of peak excitation arrived significantly later in PCs than in perisomatic-targeting interneurons, dendritic-targeting interneurons, and interneuron-selective interneurons. ***D***, ϕ_{syn} in different cell types. ϕ_{syn} occurred significantly earlier in PCs than in perisomatic-targeting interneurons and dendritic-targeting interneurons. ***E***, ϕ_{AP} and ϕ_{syn} plotted for individual strongly phase-coupled cells. A significant positive correlation was found (angular–angular correlation). A least-squares fit line is shown. The same key as in ***C*** and ***D*** is shown. $^*p < 0.05$; $^{**}p < 0.01$. PTI, Perisomatic-targeting interneuron; DTI, dendritic-targeting interneuron; ISI, interneuron-selective interneuron.

Discussion

It has been reported previously that different subclasses of CA3 neurons differ in their firing properties during cholinergically induced oscillations (McMahon et al., 1998; Hájos et al., 2004). The present study investigated PSCs in anatomically identified CA3 neurons during CCh-induced network oscillations and related the PSCs to the firing properties of the cells. Our main findings were as follows: (1) synaptic input differed between cell classes during cholinergically induced gamma oscillation; and (2)

features of synaptic input could be used to predict firing properties, namely firing rate and spike timing (quantified by phase-coupling strength and mean phase angle).

Variability in CCh-induced field oscillation

Wavelet analysis revealed a rhythmicity in the magnitude of the field oscillation in approximately half of the recordings. This could arise from the interference of oscillators, oscillating at similar, but unequal frequencies, or, alternatively, from slow membrane potential oscillations. Cunningham et al. (2003) suggested that I_h-dependent membrane potential oscillations of stellate cells can produce a theta-frequency modulation of gamma oscillations in the entorhinal cortex. Theta-frequency membrane potential oscillations have been recorded in hippocampal PCs (Leung and Yim, 1991), raising the possibility that a similar mechanism may generate the low frequency modulation seen here. These possibilities were not explored further.

Different synaptic input in distinct cell classes and local network architecture

Cell classes differed in their dominant synaptic input. Inhibitory synaptic currents exceeded excitatory synaptic currents in all PCs, whereas excitation was, on average, stronger and often dominated over inhibition in phase-coupled perisomatic-targeting interneurons. In fact, these phase-coupled neurons received the largest excitatory input of all cell types. In line with these results, anatomical investigations have revealed that perisomatic-targeting interneurons containing the calcium binding protein parvalbumin received the largest number of excitatory synapses among all inhibitory cells (Gulyas et al., 1999).

Based on current source density analysis and spike-time measurement, it has been suggested that hippocampal gamma oscillations arise from the disynaptic interaction of excitatory PCs and inhibitory perisomatic-targeting interneurons (Mann et al., 2005a,b). Our data provide the first direct evidence of the synaptic currents in these neuronal populations (Fig. 2) and is consistent with a recurrent inhibitory model of gamma oscillations (Freeman, 1968). This model is supported by four of our findings: (1) the relative spike times of PCs and interneurons (Fig. 4); (2) the relative timing of excitatory and inhibitory events (Fig. 3*B*); (3) the differences in excitatory and inhibitory charge in different cell types (Fig. 2); and (4) the differences in coupling strength of the IPSC peak in different cell types. The fact that r_i was larger in PCs than in interneurons (Fig. 3*A*) is in agreement with a recurrent model of gamma oscillogenesis in which a strongly phase-coupled interneuron population provides a perisomatic source of inhibition to PCs, whereas interneurons receive inhibition from numerous subpopulations of interneurons with varied phase coupling. Interestingly, Mann et al. (2005b) observed that the current source was not confined to the soma and axon initial segment but extended to the proximal dendritic region. In our sample, we have recorded from two inhibitory neurons that arborize in the proximal dendritic region (data not included), that showed phase coupling, and received a large excitatory current, comparable to perisomatic-targeting interneurons, suggesting that this population might also be actively involved in oscillogenesis.

Synaptic input controls spike output

Although differences in synaptic input exist between cell classes, it appears that the cell classes also differ in their responses to similar synaptic input (Fig. 6*A*). This raises the question of the importance of synaptic input versus the intrinsic properties of a cell in the control of firing properties during gamma oscillations.

Firing rate

It was found that PCs fire at a significantly lower rate than interneurons. Although intrinsic conductances, such as the one underlying I_h, can contribute to setting a firing rate preference (Maccaferri and McBain, 1996; Pike et al., 2000, Hu et al., 2002), differences in synaptic input could also account for differences in the firing rate. Indeed, over all cells, a stronger positive correlation was found between the firing rate and Q_e/Q_i than between the firing rate and Q_e, suggesting that both phasic excitation and inhibition contribute toward controlling the firing rate. Furthermore, cell types with high firing rates received larger phasic excitatory synaptic input than cell types with lower firing rates, supporting the conclusion that although intrinsic properties set a firing rate preference, synaptic input also clearly contributes to the differences in firing rates of different cell types.

Spike-timing precision

The ability of neurons to fire action potentials reliably and precisely has been shown for artificially generated input (Mainen and Sejnowski, 1995; Hunter et al., 1998; Fellous et al., 2001; Haas and White, 2002). The CCh model allows for a measure of precision under more physiological conditions. A precise spike output could be the result of intrinsic membrane properties, net synaptic input, or an interaction between the two. The SD of the spike phase distribution was smaller than the equivalent measure for absolute spike time in strongly phase-coupled cells. The opposite relationship was seen in weakly phase-coupled cells. This suggests that synaptic input provides a considerable contribution to the control of spike timing in strongly phase-coupled neurons.

Action potential phase-coupling strength

We found that all interneuron types, including dendritic-targeting interneurons, fire phase coupled to the oscillation when they receive sufficiently strong excitatory synaptic input (Fig. 6*B*). Moreover, perisomatic-targeting interneurons receiving a dominant excitation were strongly phase coupled, whereas those with $Q_e/Q_i < 1$ tended not to be. However, the relationship of Q_e/Q_i to r_{AP} seen in perisomatic-targeting interneurons was not observed in other cell types. The apparent lack of relationship between phasic charge ratio and r_{AP} in dendritic-targeting and interneuron-selective interneurons could be attributable to the relatively small number of neurons sampled, or to the fact that these cells were treated as two populations when, in fact, they are composed of several distinct subpopulations (radiatum and OLM, and IS-1, IS-2, and IS-3, respectively) (Freund and Buzsaki, 1996). Differences in intrinsic properties might also contribute toward the observed differences between cell types in the relationship between Q_e/Q_i and r_{AP}.

In interneurons, a positive correlation was found between the phase-coupling strength of synaptic current and action potentials, suggesting that a more precise input leads to a more precise output. Moreover, the correlation was stronger for excitatory inputs, corroborating the conclusion that interneuron spike phase precision is primarily controlled by PCs. In PCs, no strong correlation was found between the precision of the peak phase of synaptic input and r_{AP}, suggesting that other factors control the precise time of action potential generation in this cell class.

If the net synaptic input sets the time window for action potential firing, and because PCs had a narrow E_{syn}^{rev} peak compared with interneurons, it might be expected that the coupling of PC firing to the oscillation be stronger than interneuron phase coupling, because PCs had a narrow E_{syn}^{rev} peak compared with interneurons. However, this was not the case, because phase coupling of PCs was weaker than that of phase-coupled interneurons, in

line with previous findings (Hájos et al., 2004). Consistent with these findings, Fricker and Miles (2000) demonstrated that most CA1 interneurons fire more precisely in response to excitatory input than do PCs. They attributed this difference to differences in intrinsic properties between these cell types. Similarly, differences in intrinsic properties, as well as differences in the somatodendritic distribution of synaptic inputs, might account for some of the differences in spike phase precision observed here. Future experiments will be needed to dissociate the relative contributions of synaptic input and intrinsic properties toward spike output.

Mean action potential phase angle

Action potentials occurred, on average, earlier in PCs than in interneurons, yet the peak of synaptic excitation occurred later in PCs. However, ϕ_{syn}, which approximates the time when phasic excitation is most dominant relative to phasic inhibition, occurred significantly earlier in PCs than in interneurons, suggesting that both excitation and inhibition are important in the control of spike timing. In PCs, ϕ_{syn} occurred when inhibition is at a minimum, whereas in perisomatic-targeting interneurons, the main target of PCs, ϕ_{syn} occurred near the peak of the excitation. Hence, during gamma oscillations, PC spike time is controlled by inhibition, whereas excitation is important in the control of perisomatic-targeting interneuron spike timing. It has been reported, however, that the average firing rate of PCs *in vivo* is significantly lower than that observed here (Csicsvari et al., 2003). Thus, even with a higher recurrent connectivity in the intact brain, Q_e might be overestimated in our study, and PC control of perisomatic-targeting interneuron spike timing may be complemented by other mechanisms *in vivo*, such as interneuronal gap junctions (Traub et al., 2001).

In conclusion, our findings support a model of cholinergically induced gamma oscillations mediated by an interaction of PCs and perisomatic-targeting interneurons. The results highlight the importance of synaptic input in the control of firing in both PCs and interneurons. These results shed light on the mechanism underlying hippocampal gamma oscillations *in vitro*. A thorough understanding of the mechanism of *in vitro* oscillogenesis may provide a first step toward understanding the mechanism and function of these oscillations in the intact brain.

References

Amaral DG, Ishizuka N, Claiborne B (1990) Neurons, numbers and the hippocampal network. Prog Brain Res 83:1–11.

Bacci A, Huguenard JR (2006) Enhancement of spike-timing precision by autaptic transmission in neocortical inhibitory interneurons. Neuron 49:119–130.

Bragin A, Jando G, Nadasdy Z, Hetke J, Wise K, Buzsaki G (1995) Gamma (40–100 Hz) oscillation in the hippocampus of the behaving rat. J Neurosci 15:47–60.

Buzsaki G, Leung LW, Vanderwolf CH (1983) Cellular bases of hippocampal EEG in the behaving rat. Brain Res 287:139–171.

Csicsvari J, Jamieson B, Wise KD, Buzsaki G (2003) Mechanisms of gamma oscillations in the hippocampus of the behaving rat. Neuron 37:311–322.

Cunningham MO, Davies CH, Buhl EH, Kopell N, Whittington MA (2003) Gamma oscillations induced by kainate receptor activation in the entorhinal cortex *in vitro*. J Neurosci 23:9761–9769.

Fellous JM, Houweling AR, Modi RH, Rao RP, Tiesinga PH, Sejnowski TJ (2001) Frequency dependence of spike timing reliability in cortical pyramidal cells and interneurons. J Neurophysiol 85:1782–1787.

Fisahn A, Pike FG, Buhl EH, Paulsen O (1998) Cholinergic induction of network oscillations at 40 Hz in the hippocampus in vitro. Nature 394:186–189.

Fisher NI (1993) Statistical analysis of circular data. Cambridge, UK: Cambridge UP.

Freeman WJ (1968) Relations between unit activity and evoked potentials in prepyriform cortex of cats. J Neurophysiol 31:337–348.

Freund TF, Buzsaki G (1996) Interneurons of the hippocampus. Hippocampus 6:347–470.

Fricker D, Miles R (2000) EPSP amplification and the precision of spike timing in hippocampal neurons. Neuron 28:559–569.

Gloveli T, Dugladze T, Saha S, Monyer H, Heinemann U, Traub RD, Whittington MA, Buhl EH (2005a) Differential involvement of oriens/pyramidale interneurones in hippocampal network oscillations *in vitro*. J Physiol (Lond) 562:131–147.

Gloveli T, Dugladze T, Rotstein HG, Traub RD, Monyer H, Heinemann U, Whittington MA, Kopell NJ (2005b) Orthogonal arrangement of rhythm-generating microcircuits in the hippocampus. Proc Natl Acad Sci USA 102:13295–13300.

Gulyas AI, Megias M, Emri Z, Freund TF (1999) Total number and ratio of excitatory and inhibitory synapses converging onto single interneurons of different types in the CA1 area of the rat hippocampus. J Neurosci 19:10082–10097.

Haas JS, White JA (2002) Frequency selectivity of layer II stellate cells in the medial entorhinal cortex. J Neurophysiol 88:2422–2429.

Hájos N, Pálhalmi J, Mann EO, Nemeth B, Paulsen O, Freund TF (2004) Spike timing of distinct types of GABAergic interneuron during hippocampal gamma oscillations *in vitro*. J Neurosci 24:9127–9137.

Hu H, Vervaeke K, Storm JF (2002) Two forms of electrical resonance at theta frequencies, generated by M-current, h-current and persistent Na+ current in rat hippocampal pyramidal cells. J Physiol (Lond) 545:783–805.

Hunter JD, Milton JG, Thomas PJ, Cowan JD (1998) Resonance effect for neural spike time reliability. J Neurophysiol 80:1427–1438.

Leung LW, Yim CY (1991) Intrinsic membrane potential oscillations in hippocampal neurons *in vitro*. Brain Res 553:261–274.

Le Van Quyen M, Foucher J, Lachaux J, Rodriguez E, Lutz A, Martinerie J, Varela FJ (2001) Comparison of Hilbert transform and wavelet methods for the analysis of neuronal synchrony. J Neurosci Methods 111:83–98.

Maccaferri G, McBain CJ (1996) The hyperpolarization-activated current (Ih) and its contribution to pacemaker activity in rat CA1 hippocampal stratum oriens-alveus interneurones. J Physiol (Lond) 497:119–130.

Mainen ZF, Sejnowski TJ (1995) Reliability of spike timing in neocortical neurons. Science 268:1503–1506.

Mann EO, Radcliffe CA, Paulsen O (2005a) Hippocampal gamma-frequency oscillations: from interneurones to pyramidal cells, and back. J Physiol (Lond) 562:55–63.

Mann EO, Suckling JM, Hájos N, Greenfield SA, Paulsen O (2005b) Perisomatic feedback inhibition underlies cholinergically induced fast network oscillations in the rat hippocampus *in vitro*. Neuron 45:105–117.

McMahon LL, Williams JH, Kauer JA (1998) Functionally distinct groups of interneurons identified during rhythmic carbachol oscillations in hippocampus *in vitro*. J Neurosci 18:5640–5651.

Paulsen O, Sejnowski TJ (2006) From invertebrate olfaction to human cognition: emergent computational functions of synchronized oscillatory activity. J Neurosci 26:1661–1662.

Penttonen M, Kamondi A, Acsady L, Buzsaki G (1998) Gamma frequency oscillation in the hippocampus of the rat: intracellular analysis *in vivo*. Eur J Neurosci 10:718–728.

Pike FG, Goddard RS, Suckling JM, Ganter P, Kasthuri N, Paulsen O (2000) Distinct frequency preferences of different types of rat hippocampal neurones in response to oscillatory input currents. J Physiol (Lond) 529:205–213.

Stewart M, Fox SE (1990) Do septal neurons pace the hippocampal theta rhythm? Trends Neurosci 13:163–168.

Torrence C, Compo GP (1998) A practical guide to wavelet analysis. Bull Am Meteorol Soc 79:61–78.

Traub RD, Kopell N, Bibbig A, Buhl EH, LeBeau FE, Whittington MA (2001) Gap junctions between interneuron dendrites can enhance synchrony of gamma oscillations in distributed networks. J Neurosci 21:9478–9486.

Vida I, Bartos M, Jonas P (2006) Shunting inhibition improves robustness of gamma oscillations in hippocampal interneuron networks by homogenizing firing rates. Neuron 49:107–117.

Whittington MA, Traub RD (2003) Interneuron diversity series: inhibitory interneurons and network oscillations *in vitro*. Trends Neurosci 26:676–682.

Whittington MA, Traub RD, Jefferys JG (1995) Synchronized oscillations in interneuron networks driven by metabotropic glutamate receptor activation. Nature 373:612–615.

Zar JH (1999) Biostatistical analysis. Upper Saddle River, NJ: Prentice Hall.

dc_71_10

10. számú melléklet

The Journal of Neuroscience, September 19, 2007 • 27(38):10211–10222 • 10211

Cellular/Molecular

Involvement of Nitric Oxide in Depolarization-Induced Suppression of Inhibition in Hippocampal Pyramidal Cells during Activation of Cholinergic Receptors

Judit K. Makara,[1] István Katona,[1] Gábor Nyíri,[1] Beáta Németh,[1] Catherine Ledent,[2] Masahiko Watanabe,[3] Jan de Vente,[4] Tamás F. Freund,[1] and Norbert Hájos[1]

[1]Department of Cellular and Network Neurobiology, Institute of Experimental Medicine, Hungarian Academy of Sciences, H-1083 Budapest, Hungary, [2]Institut de Recherche Interdisciplinaire en Biologie Humaine et Moleculaire, Universite Libre de Bruxelles, 1070 Brussels, Belgium, [3]Department of Anatomy, Hokkaido University School of Medicine, Sapporo 060-8638, Japan, and [4]European Graduate School of Neuroscience, Department of Psychiatry and Neuropsychology, Division of Cellular Neuroscience, Maastricht University, 6200 MD Maastricht, The Netherlands

Several types of neurons are able to regulate their synaptic inputs via releasing retrograde signal molecules, such as endocannabinoids or nitric oxide (NO). Here we show that, during activation of cholinergic receptors, retrograde signaling by NO controls CB_1 cannabinoid receptor (CB_1R)-dependent depolarization-induced suppression of inhibition (DSI). Spontaneously occurring IPSCs were recorded in CA1 pyramidal neurons in the presence of carbachol, and DSI was induced by a 1-s-long depolarization step. We found that, in addition to the inhibition of CB_1Rs, blocking the NO signaling pathway at various points also disrupted DSI. Inhibitors of NO synthase (NOS) or NO-sensitive guanylyl cyclase (NO-sGC) diminished DSI, whereas a cGMP analog or an NO donor inhibited IPSCs and partially occluded DSI in a CB_1R-dependent manner. Furthermore, an NO scavenger applied extracellularly or postsynaptically also decreased DSI, whereas L-arginine, the precursor for NO, prolonged it. DSI of electrically evoked IPSCs was also blocked by an inhibitor of NOS in the presence, but not in the absence, of carbachol. In line with our electrophysiological data, double immunohistochemical staining revealed an NO-donor-induced cGMP accumulation in CB_1R-positive axon terminals. Using electron microscopy, we demonstrated the postsynaptic localization of neuronal NOS at symmetrical synapses formed by CB_1R-positive axon terminals on pyramidal cell bodies, whereas NO-sGC was found in the presynaptic terminals. These electrophysiological and anatomical results in the hippocampus suggest that NO is involved in depolarization-induced CB_1R-mediated suppression of IPSCs as a retrograde signal molecule and that operation of this cascade is conditional on cholinergic receptor activation.

Key words: **synaptic plasticity; hippocampus; GABA; CB_1 receptor; cGMP; retrograde**

Introduction

Retrograde signaling in synaptic communication regulates information flow in neuronal networks by altering the neurotransmitter release from presynaptic axon terminals in response to activation of a postsynaptic neuron. Several chemically distinct molecules mediating retrograde signaling have been proposed, for instance, classical neurotransmitters (e.g., glutamate and GABA), peptides (e.g., BDNF and dynorphin), gaseous molecules [e.g., nitric oxide (NO) and carbon monoxide], or lipids (e.g., arachidonic acid and endocannabinoids) (Tao and Poo, 2001; Alger, 2002). One of the best studied forms of retrograde signaling is the short-term depression of GABA release induced by depolarization of the postsynaptic neuron. This phenomenon, called depolarization-induced suppression of inhibition (DSI) was first described in the cerebellum (Llano et al., 1991) and the hippocampus (Pitler and Alger, 1992) and was later discovered in other brain areas (for review, see Chevaleyre et al., 2006). In DSI, the postsynaptic rise of Ca^{2+} concentration and the subsequent activation of presynaptically localized CB_1 cannabinoid receptors (CB_1R) are essential (Di Marzo et al., 1998; Lenz and Alger, 1999; Freund et al., 2003; Isokawa and Alger, 2006). According to the currently accepted model, depolarization of the postsynaptic cell is thought to lead to the release of endocannabinoids, which activates presynaptic CB_1Rs, which, in turn, suppresses GABA release from those axon terminals (Kreitzer and Regehr, 2001; Ohno-Shosaku et al., 2001; Wilson and Nicoll, 2001).

However, a rise of Ca^{2+} concentration during depolarization

Received Dec. 22, 2006; revised July 18, 2007; accepted July 22, 2007.

This work was supported by the Howard Hughes Medical Institute, European Union Grant LSHM-CT-2004-005166, National Research and Development Programs Grant 1A/002/2004, Hungarian Scientific Research Fund Grants T46820 and F046407, Hungarian Medical Research Council Grant 474/2003, and National Institutes of Health (NIH) Grant NS30549. N.H. is the recipient of a Wellcome Trust International Senior Research Fellowship. I.K. is a grantee of the Bolyai János Scholarship. We thank Eszter Szabadits and Csaba Cserép for their essential contribution to the anatomical experiments and observations. We thank Drs. György Buzsáki, István Mody, Roger Nicoll, Péter Somogyi, Thomas Klausberger, and Zoltán Nusser for advice and comments on a previous version of this manuscript and Dr. Zsolt Borhegyi for help with confocal microscopy. We also thank Dr. Ken Mackie (supported by NIH Grant DA11322) for the rabbit anti-CB_1R antibody. The excellent technical assistance of Katalin Lengyel, Emőke Simon, Katalin Iványi, Gabriella Urbán, and Győző Goda is also gratefully acknowledged.

Correspondence should be addressed to Dr. Norbert Hájos, Department of Cellular and Network Neurobiology, Institute of Experimental Medicine, Hungarian Academy of Sciences, Budapest H-1450, Hungary. E-mail: hajos@koki.hu.

DOI:10.1523/JNEUROSCI.2104-07.2007

 0270-6474/07/2710211-12$15.00/0

may influence several signaling cascades in addition to the endocannabinoid system. One example is NO, a well known intercellular signaling molecule (Medina and Izquierdo, 1995; Prast and Philippu, 2001). NO can be synthesized by neurons in a Ca^{2+}-dependent manner (Prast and Philippu, 2001) from L-arginine by NO synthases (NOS), which enzymes are present in hippocampal pyramidal cells (Wendland et al., 1994; Burette et al., 2002), and their activities could be significantly enhanced during the activation of acetylcholine receptors (Arnal et al., 1999; Christopoulos and El-Fakahany, 1999). Stimulation of NO-sensitive guanylyl cyclase (NO-sGC) is one of the main effector targets of NO, resulting in elevation of cGMP concentration. Because NO is a gaseous molecule that freely crosses membranes, it has been implicated as a retrograde messenger, e.g., in long-term potentiation in the hippocampus (O'Dell et al., 1991; Medina and Izquierdo, 1995; Prast and Philippu, 2001) (but see Cummings et al., 1994).

The aim of the present study was to investigate the contribution of NO signaling to DSI. We recorded action potential-dependent IPSCs in CA1 pyramidal cells while synaptic activity was enhanced by the cholinergic receptor agonist carbachol. Pharmacological manipulation of the NO signaling pathway at various points was used to examine its interference with DSI. We also tested the involvement of NO signaling in DSI of electrically evoked IPSCs. Moreover, immunohistochemical double staining was performed to investigate the NO donor-induced elevation of cGMP in CB_1R-expressing boutons and the localization of neuronal NOS and NO-sGC at symmetrical synapses formed by CB_1R-immunopositive axon terminals.

Materials and Methods

Slice preparation and electrophysiology. Experiments were performed according to the guidelines of the institutional ethical code and the Hungarian Act of Animal Care and Experimentation (1998; XXVIII, section 243/1998.). Animals were deeply anesthetized with isoflurane and decapitated, and the brain was removed and placed in ice-cold cutting solution containing the following (in mM): 252 sucrose, 2.5 KCl, 1.25 NaH_2PO_4, 5 $MgCl_2$, 0.5 $CaCl_2$, 26 $NaHCO_3$, and 10 glucose. The cutting solution had been bubbled with 95% O_2/5% CO_2 (carbogen gas). Horizontal slices of the hippocampus (350–400 μm thick) were prepared from male Wistar rats (14–19 d old) or 300-μm-thick sections from the hippocampus of littermate wild-type (CD1) or CB_1R knock-out mice [22–41 d old of both sexes (Ledent et al., 1999)] using a Leica (Nussloch, Germany) VT1000S vibratome. Slices were incubated for 1 h in artificial CSF (ACSF) (in mM: 126 NaCl, 2.5 KCl, 1.25 NaH_2PO_4, 2 $MgCl_2$, 2 $CaCl_2$, 26 $NaHCO_3$, and 10 glucose) at room temperature in interface conditions and then transferred to a submerged type of recording chamber that was optimized for laminar flow. The flow rate was 3–4 ml/min, ensuring better oxygenization and more stable recordings (N. Hájos, unpublished observations). Whole-cell recordings were performed at 24–26°C under visual guidance using a Zeiss (Jena, Germany) Axioskop. Patch electrodes had resistances of 3–6 MΩ when filled with the intrapipette solution containing the following (in mM): 80 CsCl, 60 Cs-gluconate, 1 $MgCl_2$, 2 Mg-ATP, 3 NaCl, 10 HEPES, and 5 QX-314 [2(triethylamino)-*N*-(2,6-dimethylphenyl) acetamine], pH 7.3 (290 mOsm). The pipette solution contained 0.1–0.3% biocytin in a subset of the experiments, and *post hoc* morphological identification of recorded cells using immunoperoxidase reaction confirmed that these were all pyramidal cells (n = 73). All experiments were performed on at least two independent preparations.

Spontaneous IPSCs (sIPSCs) were measured in ACSF containing the following (in mM): 126 NaCl, 2.5 KCl, 26 $NaHCO_3$, 2 $CaCl_2$, 2 $MgCl_2$, 1.25 NaH_2PO_4, 10 glucose, 2 kynurenic acid, and 0.005 carbachol (equilibrated with 5% CO_2–95% O_2 gas). Access resistance (between 5 and 20 MΩ, compensated 65–75%) was frequently monitored and did not change substantially (±25%) during the analyzed period. Signals were recorded with an Axopatch 200B or Multiclamp 700A amplifier (Molecular Devices, Foster City, CA), filtered at 2 kHz, digitized at 6–10 kHz with a PCI-6024E board (National Instruments, Austin, TX), and off-line analyzed using the EVAN software (http://www.thotec.com/evan). Cells were held at −60 mV, and DSI was elicited usually every 100–130 s by step depolarizations to 0 mV for 1 s. After automatic event detection, integrated charge transfer of sIPSCs was determined. For calculation of DSI, the average charge of sIPSCs was measured during 10 s before depolarization ($charge_{ctr}$) and during 5 s after depolarization ($charge_{depol}$), discarding the first second after the voltage step, which includes the latency period of DSI (Wilson et al., 2001). The magnitude of DSI is expressed as $DSI = 100 \times (1 - charge_{depol}/charge_{ctr})$, i.e., the percentage reduction of charge transfer. DSI was calculated from the averaged results of two to four DSIs under control and two to three DSIs under drug-treated conditions. In experiments in which drug effects were measured in the same cells, we analyzed cells only when DSI in the control period was at least 30% (±15% maximum SD) on average and exhibited at least >3 pA (pC for 1 s) basal charge transfer. In experiments in which differently treated groups were compared (see Figs. 1*E*,*F* and 4, and experiments with intracellular inhibitors), all measured cells receiving sufficient action potential-dependent inhibitory input (>3 pA) were included in the analysis regardless of their ability to express DSI. In these cases, control and drug-treated slices from the same brains were selected randomly. Basal charge transfer was usually measured for 10 s preceding depolarization except for Figure 4*A*–*D*, in which charge was measured for 30 s. There was no correlation between control basal charge and DSI ($p > 0.5$) (supplemental Fig. 1, available at www.jneurosci.org as supplemental material). The recovery time course of DSI was fitted with single-exponential decay. When different intrapipette solutions were compared, we routinely applied weak positive pressure after breaking into whole-cell configuration to improve equilibrium of the pipette solution in the cytoplasm, and DSIs were measured between 5 and 15 min after break-in.

Drugs were applied for 5–15 min. We noticed that bath application of L-arginine for >10–15 min significantly reduced sIPSC charge; therefore, in these experiments, those periods were compared with the control, in which the charge was not significantly decreased.

Miniature IPSCs (mIPSCs) were measured after the addition of 0.5 μM tetrodotoxin (TTX) to the extracellular solution used for measurement of sIPSCs. Only those cells were tested for mIPSCs that expressed DSI of spontaneous IPSCs before application of TTX.

Evoked IPSCs were triggered every 3 s (0.33 Hz) with silver wires inserted in an ACSF-containing theta electrode, which was placed to the border of strata radiatum and pyramidale (within ~50–100 μm from the recorded cell). Current impulses of 0.1 ms and 10–50 μA were used in all experiments, aiming to activate a single presynaptic axon. In this case, the mean amplitude of IPSCs showed a clear step without additional changes with increasing stimulus intensity (Hájos et al., 2000). The extracellular solution was the same as for sIPSCs, except for carbachol concentration, which was either 0 or 5 μM. DSI was calculated as $DSI = 100 \times (1 - amplitude_{depol}/amplitude_{ctr})$, where $amplitude_{ctr}$ is the average of the last 10 events before depolarization, and $amplitude_{depol}$ is the average of the first three events after depolarization. Note that the value of DSI can be positive or negative (representing a decrease or increase, respectively, of amplitude after depolarization). To give a measure of DSI, two to four DSIs of evoked IPSCs were averaged under each conditions. Because the variance in the magnitude of DSI was smaller than for DSI of sIPSCs, we analyzed cells in which DSI in the control period was at least 20% on average.

For measurement of Ca^{2+} currents, the ACSF described above was complemented with 30 mM tetraethylammonium (TEA)-Cl (instead of 30 mM NaCl) to reduce K^+ currents and 50 μM picrotoxin to inhibit all synaptic activity. Pipette solution contained the following (in mM): 110 CsCl, 30 TEA-Cl, 1 $CaCl_2$, 10 EGTA, 1 $MgCl_2$, 4 ATP, 3 NaCl, and 10 HEPES, pH 7.3 (300 mOsm). Voltage-gated Ca^{2+} currents were evoked every 15 s by a 500-ms-long depolarizing step from −60 to 0 mV. Currents were normalized as Cd^{2+}-sensitive current component (measured at the end of the experiments by adding 200 μM Cd^{2+}) and corrected for rundown.

In the experiments with the NO donor, slices prepared from 14- to 32-d-old rats were first preincubated with a broad-spectrum inhibitor of phosphodiesterases 3-isobuthyl-1-methylxanthine (IBMX) (1 mM) for 15–30 min, followed by the application of the NO donor sodium nitroprusside (SNP) for 10 min. For immunohistochemical studies, incubations were performed both at room temperature as well as at 34–35°C.

Immunohistochemistry. After incubation, rat hippocampal slices were fixed for 2 h in freshly prepared ice-cold 4% paraformaldehyde dissolved in 0.1 M phosphate buffer (PB). During this step and throughout the staining procedure, the sections were continuously rinsed in a free-floating manner. The slices were then washed in PB for 10 min, pasted onto wax plates, and resectioned into 50 μm thin sections using a Leica VT1000S vibratome. The sections were first washed four times for 15 min in PB and then twice for 20 min in 0.05 M Tris-buffered saline (TBS) containing 0.3% Triton X-100 (TBST; Sigma, St. Louis, MO). Blocking was performed in 10% normal donkey serum (Vector Laboratories, Burlingame, CA) dissolved in TBST for 45 min. Incubation with primary antibodies was performed at 4°C for 48 h. As primary antibody, sheep anti-cGMP (1:4000) was used in combination with either rabbit anti-CB_1R (1:2000) or rabbit anti-parvalbumin (PV) (1:2000; Sigma), all dissolved in TBS. The specificity and an estimate of the detection limit of the anti-formaldehyde-fixed cGMP antisera have been described previously (Tanaka et al., 1997). The specificity of the anti-CB_1R antibody was proved in CB_1R knock-out animals (Hájos et al., 2000). After primary antibody incubation, the sections were washed extensively in TBS and then incubated for 2 h in a mixture of the following secondary antisera: Alexa Fluor 488 donkey anti-sheep and Alexa Fluor 594 donkey anti-rabbit (Invitrogen, Carlsbad, CA), both diluted 1:200 in TBS. Afterward, the sections were washed three times for 15 min in TBS, then mounted onto glass slides, covered in Vectashield (Vector Laboratories), and sealed the coverslips with nail polish. Immunofluorescence staining was analyzed with an Olympus Optical (Tokyo, Japan) FluoView300 confocal laser scanning microscope using a sequential scanning mode. The ratio of labeled terminals was not different in slices treated at room temperature or 34–35°C; therefore, data were pooled.

Quantification of immunostaining. Altogether, 1800 axon terminals were analyzed to establish the presence or absence of NO donor-induced or NO-independent cGMP immunoreactivity in either CB_1R-containing or PV-positive axon terminals in three animals. Quantification of cGMP immunostaining was performed by an observer blind to the type of pretreatment. Images were taken from three slices from each animal from each the four experimental paradigms. Randomly selected areas in the CA1 pyramidal layer were photographed at 60× magnification separately, for either CB_1R/cGMP or PV/cGMP immunoreactivity. Images were then analyzed using Adobe Photoshop 8.0 (Adobe Systems, San Jose, CA). First, 50 CB_1R- or PV-immunoreactive axon terminals were selected and numbered in the image randomly, the corresponding image with the cGMP immunoreactivity was copied onto the first image, and the presence or absence of immunocytochemically detectable amount of cGMP was determined for each numbered bouton. The quantity of NO donor-induced increase in cGMP immunoreactivity may depend on several factors, such as the specificity of the inhibitor for cGMP-degrading phosphodiesterases, the concentration of NO donor (van Staveren et al., 2005), its penetration into the 400-μm-thick slices, and the success of immediate fixation, whereas penetration of primary antibodies for CB_1R or PV may also vary. Therefore, in our analysis, we compared the ratio of cGMP-positive CB_1R- and PV-immunoreactive axon terminals between NO donor-treated and untreated slices, which were derived from the same animal and were processed in parallel. Note also that absence of cGMP immunoreactivity does not rule out the presence of cGMP in immunohistochemically undetectable amounts in some other terminals. Thus, data obtained using this method always represent the minimal estimation of axon terminals, in which NO donor-dependent cGMP induction occurs.

Preembedding immunogold and immunoperoxidase reactions. Six adult male Wistar rats (Charles River, Budapest, Hungary) were anesthetized with an intraperitoneal injection of an anesthetic mixture (containing 2.5% ketamine, 0.5% xylazine hydrochloride, 0.25% promethazine hydrochloride, 0.0025% benzetonium chloride, and 0.002% hydrochinone) used at 0.2 ml/100 g body weight. Animals were perfused through the heart with 0.9% NaCl saline. Then, in the experiments localizing neuronal NOS (nNOS), it was followed by fixative perfusion containing 1% paraformaldehyde in 0.1 M PB, pH 7.4, for 60 min. In the experiments localizing NO-sGC at the electron microscopic level, rats were perfused first for 2 min with a fixative containing 4% paraformaldehyde in Na-acetate buffer, pH 6.0, and then with a fixative containing 4% paraformaldehyde in Borax buffer, pH 8.5, for 40 min. Fixative perfusions were followed by perfusion with 0.1 M PB for 10 min, and then the brains were removed from the skulls. Blocks from the dorsal hippocampus were dissected and sectioned on a vibratome at 60 μm thickness, followed by washing in 0.1 M PB, and then they were incubated in 10 and 30% sucrose for cryoprotection and freeze thawed over liquid nitrogen several times. After repeated washes in 0.1 M PB, the sections were processed for immunostaining.

First, sections were incubated in 1% human serum albumin (HSA) (Sigma) diluted in TBS. In case of the experiments with nNOS, this was followed by a 48 h incubation in solutions of primary antibodies raised against neuronal NOS (rabbit polyclonal antibody, 1:500; Zymed Laboratories, San Francisco, CA), with or without CB_1R antibody (goat polyclonal antibody, 1:2000). The specificity of this antibody developed against CB_1R was proven in CB_1R knock-out animals. In the experiments with NO-sGC, sections were incubated in solutions of primary antibodies raised against α_1 subunit of NO-sGC (rabbit polyclonal antibody, 1:1000; Sigma), with the CB_1R antibody. After repeated washes in TBS, sections were treated with blocking solution (Gel-BS) containing 0.5% cold water fish skin gelatin (GE Healthcare, Little Chalfont, UK) and 0.5% HSA in TBS for 1 h. In the experiments with nNOS, this was followed by 24 h incubation with 0.8 nm gold-conjugated anti-rabbit antibody (donkey polyclonal antibody, 1:80; Aurion, Wageningem, The Netherlands), whereas in the experiments with NO-sGC α_1 subunit, this was followed by incubation with 0.8 nm gold-conjugated anti-goat antibody (donkey polyclonal antibody, 1:80; Aurion) to recognize CB_1R, and it was diluted in Gel-BS. After intensive washes in TBS, the sections were treated with 2% glutaraldehyde in PB for 15 min, to fix the gold particles into the tissue. This was followed by washes in PB and in enhancement conditioning solution (ECS) (Aurion). After this, sections were incubated in silver enhancement solution for electron microscopy (SE-EM; Aurion) for 60 min at room temperature. This was followed by wash in ECS and repeated washes in PB. Then sections in the experiments with nNOS were incubated in biotinylated anti-goat (horse polyclonal antibody, 1:200; Vector Laboratories) for 24 h, whereas sections in the experiments with NO-sGC were incubated in biotinylated anti-rabbit (biotin-SP-conjugated AffiniPure donkey polyclonal antibody, 1:200; Jackson ImmunoResearch, West Grove, PA), followed by incubation in Elite ABC (1:300; Vector Laboratories) diluted in TBS for 3 h. The immunoperoxidase reaction was developed using 3,3 diaminobenzidine (Sigma) as chromogen. All sections were treated with OsO_4 in PB on ice followed by dehydration in ascending alcohol series and propylene oxide and were embedded in Durcupan. During dehydration, the sections were treated with 1% uranyl acetate in 70% ethanol for 30 min. Finally, sections were reembedded and investigated by electron microscope.

Materials and data analysis. N_ω-Nitro-L-arginine methyl ester (L-NAME), N_ω-nitro-D-arginine methyl ester (D-NAME), L-arginine, SNP, 8-Br-cGMP, and tetrodotoxin (Alomone Labs, Jerusalem, Israel) were dissolved in distilled water. 7-Nitroindazole (7-NI), 1*H*-[1,2,4]oxadiazolo[4,3-a]quinoxalin-1-one (ODQ), 2-(4-carboxyphenyl)-4,4,5,5-tetramethylimidazoline-1-oxyl-3-oxide (CPTIO), AF-DX116 (11-[[2-[(diethylamino)methyl]-1-piperidinyl]acetyl]-5, 11-dihydro-6*H*-pyrido-[2,3-b][1,4]benzodiazepin-6-one) (Tocris Bioscience, Bristol, UK), IBMX, SR141716A [*N*-piperidino-5-(4-chlorophenyl)-1-(2,4-dichlorophenyl)-4-methyl-3-pyrazole carboxamide] (National Institute on Drug Abuse drug supply service), and AM251 [*N*-1-(2,4-dichlorophenyl)-5-(4-iodophenyl)-4-methyl-*N*-1-piperidinyl-1*H*-pyrazole-3-carboxamide] (Tocris Bioscience) were dissolved in DMSO. WIN 55,212-2 [*R*-(+)-(2,3-dihydro-5-methyl-3-[(4-morpholinyl)methyl]pyrol[1,2,3-de]-1,4-benzoxazin-6-yl)-(1-naphthalenyl) methanone monomethanesulfonate] was dissolved in 0.1N HCl. Drugs were prepared as stock solutions and diluted at least by

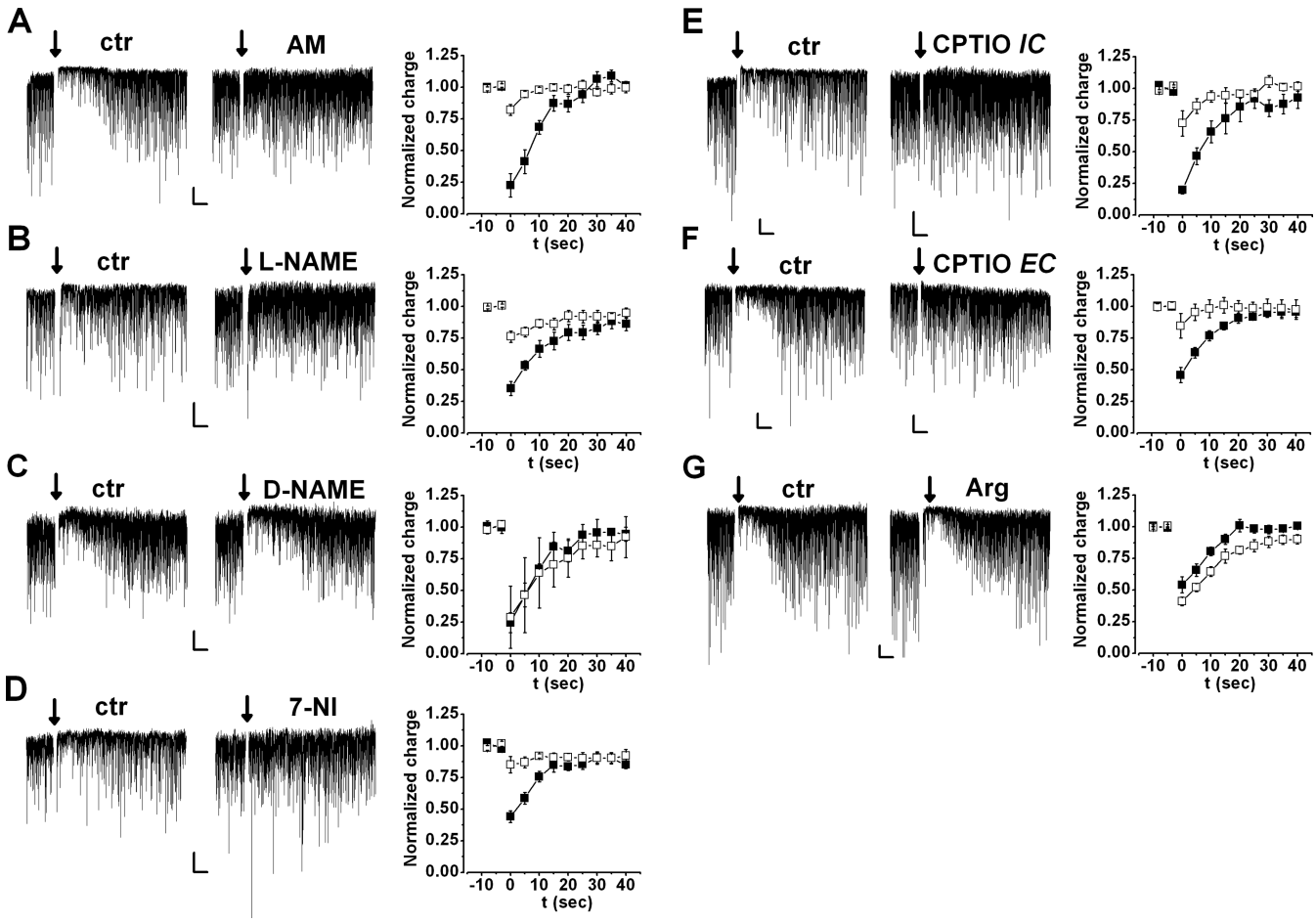

Figure 1. Postsynaptically produced NO is involved in DSI. Spontaneous IPSCs (downward deflections from the baseline) showed transient reduction after a depolarizing step (arrow) in control (ctr) conditions (left; DSI); this alteration was compared after drug applications (middle). ***A–D***, Left and Middle, Representative recordings of pyramidal cells before (left) and during (middle) application of 2 μM AM251 (CB_1R antagonist; ***A***), 100 μM L-NAME (NOS antagonist; ***B***), 100 μM D-NAME (inactive analog of L-NAME; ***C***), and 100 μM 7-NI (NOS inhibitor; ***D***) for 5–10 min. Right, Magnitude and kinetics of DSI under control conditions (filled squares) and during application (open squares) of 2 μM AM251 or SR141716A (pooled, $n = 6$) (***A***), 100 μM L-NAME ($n = 8$) (***B***), 100 μM D-NAME ($n = 4$) (***C***), or 100 μM 7-NI ($n = 7$) (***D***). Charge was normalized to the control period before depolarization. ***E***, DSI in two representative cells recorded using intrapipette solution containing only vehicle (0.1% DMSO; left) or 1 mM CPTIO (NO scavenger; middle). Right, Summary of DSI measured with pipettes containing DMSO (filled squares; $n = 7$) or CPTIO (open squares; $n = 7$). ***F***, DSI in two cells pretreated for 30 – 40 min with 0.1% DMSO (left) or 500 μM extracellular CPTIO (middle). Right, Summary of DSI measured in DMSO (filled squares; $n = 15$) or in CPTIO (open squares; $n = 9$). ***G***, Left and Middle, Representative recordings of pyramidal cells before (left) and during (middle) application of 0.2–1 mM L-arginine (NO precursor). Right, Magnitude and kinetics of DSI under control conditions (filled squares) and during application of L-arginine ($n = 6$). Except D-NAME, all drugs significantly altered DSI. Calibration: 50 pA, 5 s.

1:1000. All drugs were obtained from Sigma-Aldrich (St. Louis, MO), unless otherwise stated.

For statistical analysis of electrophysiological data, the Wilcoxon's matched pairs test (for dependent samples), the Mann–Whitney *U* test (for independent samples), or the Kolmogorov–Smirnov test (for mIPSC distributions) was used. Fluorescent immunohistochemical results were analyzed using two-way repeated-measures ANOVA with Tukey's *post hoc* test (Statistica 6.0; StatSoft, Tulsa, OK). $p < 0.05$ was considered significant. Data are presented as mean ± SEM, unless otherwise indicated.

Results

We recorded sIPSCs enhanced by bath application of 5 μM carbachol in CA1 pyramidal cells, using whole-cell patch-clamp technique. Under these conditions, synaptic currents had fast rise times (10–90% rise time, 1.21 ± 0.13 ms; calculated from events measured in 10 randomly selected cells), suggesting that they primarily originated from the perisomatic region (Maccaferri et al., 2000). As shown previously, a form of retrograde signaling triggered by depolarization of the postsynaptic neuron (a phenomenon called depolarization-induced suppression of inhibition, or DSI) can be reliably studied, when cholinergic receptors are activated (Pitler and Alger, 1992). Consistent with previous data (Pitler and Alger, 1992; Wilson and Nicoll, 2001), depolarization of CA1 pyramidal cells from −60 to 0 mV for 1 s temporarily reduced charge transfer by sIPSCs (Fig. 1). The magnitude of DSI was independent of basal IPSC charge (supplemental Fig. 1, available at www.jneurosci.org as supplemental material). In line with previous descriptions (Wilson and Nicoll, 2001), DSI of sIPSCs was dependent on the activation of CB_1Rs, because the CB_1R antagonists SR141716A or AM251 (2 μM for both) significantly reduced DSI from 77.7 ± 9.2 to 18.1 ± 4.3% (pooled, $n = 6$; $p < 0.05$) (Fig. 1*A*), and it was absent in CB_1R knock-out mice (knock-out, 7.9 ± 2.6%, $n = 6$; wild-type littermates, 52.3 ± 8.6%, $n = 6$; $p < 0.01$).

Blockers of nitric oxide synthesis or application of NO scavengers inhibit DSI

To test the involvement of NO in DSI, we first applied inhibitors of the NOS enzymes. Bath application of the nonspecific NOS inhibitor L-NAME (100 μM) for 5–10 min reduced the magni-

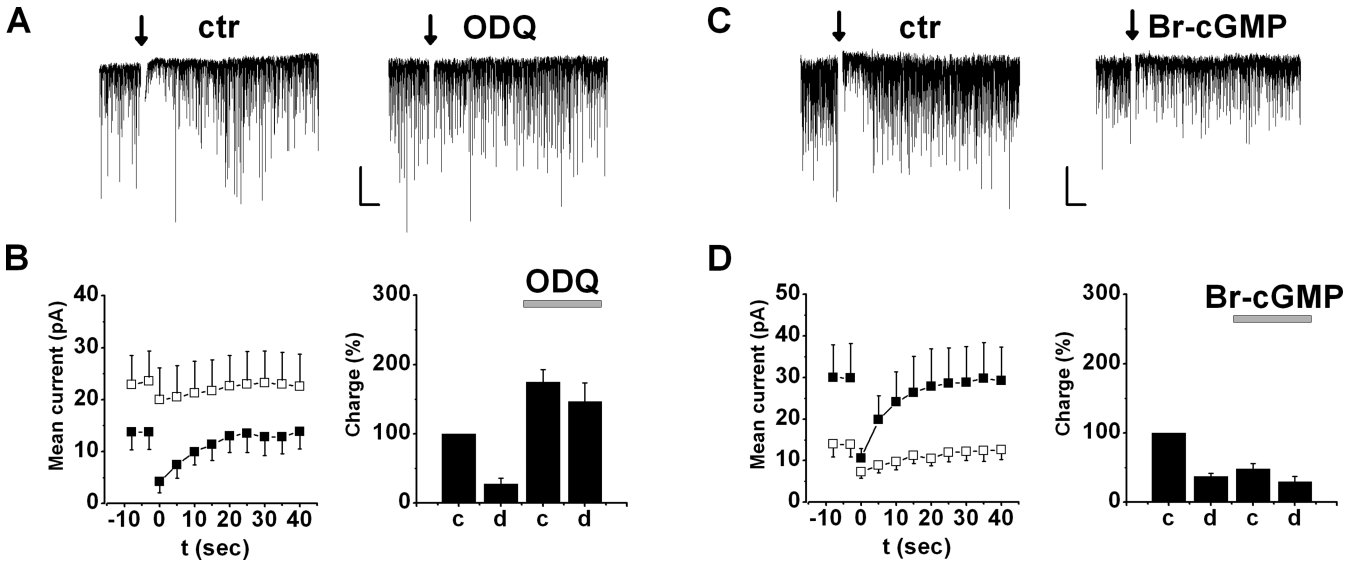

Figure 2. cGMP production by NO-sGC is involved in DSI. ***A***, Representative experiment of DSI in a cell before (left) and during (right) application of the NO-sGC inhibitor ODQ (10 μM). ***B***, Left, Mean current and DSI under control conditions (filled squares) and in ODQ (open squares). Mean current was calculated as the sum of sIPSCs charge in every second. Right, sIPSC charge transfer before (c) and after (d) depolarization under control conditions and after addition of ODQ ($n = 7$). Charge was normalized to the average value before depolarization under control conditions. ***C***, Representative DSI before (left) and during (right) application of 100 μM 8-Br-cGMP. ***D***, Effect of 8-Br-cGMP on DSI and charge transfer ($n = 8$; see ***B***). Calibration: 100 pA, 5 s. ctr, Control.

tude of DSI from 64.7 ± 5.5 to 24.0 ± 4.7% ($n = 8$; $p < 0.05$) (Fig. 1*B*) (see also a complete representative recording in supplemental Fig. 2, available at www.jneurosci.org as supplemental material), whereas the inactive analog D-NAME (100 μM) did not affect DSI (control, 75.6 ± 7.8%; D-NAME, 71.2 ± 12.3%; $n = 4$; $p > 0.6$) (Fig. 1*C*). Similar to L-NAME, another NOS blocker, 7-NI (100 μM), also reduced DSI from 56.1 ± 4.6 to 15.1 ± 6.4% ($n = 7$; $p < 0.05$) (Fig. 1*D*). Thus, under our recording conditions, blockers of NO synthase inhibited DSI as efficiently as blockers of CB_1Rs.

To determine whether the source of NO was the postsynaptic pyramidal cell, we added L-NAME (200 μM) to the intrapipette solution and compared DSI of cells from the same preparations using either control (vehicle-containing) or L-NAME-containing pipettes. Although DSI was detected in all control cells (64.1 ± 6.0%; $n = 9$), DSI was variable but on average significantly reduced in L-NAME-treated cells (34.0 ± 10.5%; $n = 8$; $p < 0.05$). However, L-NAME is membrane permeable; therefore, it cannot be ruled out that it exerted its effect not only in the pyramidal cell but also in the neighboring cellular compartments. Therefore, we also tested the NO scavenger CPTIO, which is considered to be membrane impermeable (Ko and Kelly, 1999). Although control cells (measured with pipette solution containing the vehicle DMSO only) exhibited robust DSI (80.2 ± 3.1%; $n = 7$), DSI was significantly reduced in cells treated with 1 mM intracellular CPTIO (27.5 ± 9.9%; $n = 7$; $p < 0.01$) (Fig. 1*E*). These results indicate that the postsynaptic presence of NO is necessary for DSI. To assess whether NO may act as an intercellular messenger in DSI, we tested whether extracellular application of CPTIO also affects the phenomenon. In cells pretreated for 30–40 min with 500 μM extracellular CPTIO, DSI was inhibited compared with control cells that were pretreated with vehicle only (DSI in 0.1% DMSO, 54.3 ± 6.1%, $n = 15$; DSI in 500 μM CPTIO, 15.4 ± 9.7%, $n = 9$; $p < 0.01$) (Fig. 1*F*). NOS enzymes use L-arginine as a substrate for NO production (Palmer et al., 1988). Thus, exogenously applied L-arginine could potentiate NO production by NOS, which might enhance DSI. Indeed, after 5-min-long application of 0.2–1 mM L-arginine, the decay time of DSI was significantly prolonged to 140.3 ± 18.9% of control (control τ, 13.3 ± 2.2 s vs L-arginine τ, 17.2 ± 1.7 s; $n = 6$; $p < 0.05$), and its magnitude was also enhanced (control, 45.8 ± 6.2%; L-arginine, 58.9 ± 3.3%; $n = 6$; $p < 0.05$) (Fig. 1*G*).

In conclusion, these results suggest that, during DSI of sIPSCs in the presence of carbachol, NO could be released postsynaptically and diffuse through the extracellular space to reach its (presumably) presynaptic target.

NO affects DSI via GC–cGMP pathways

The main effector molecule of NO is NO-sGC, which converts GTP to cGMP. To examine whether activation of NO-sGC mediates the effect of NO on DSI, we tested a specific NO-sGC blocker, ODQ. Similar to NOS inhibitors, bath application of ODQ (10 μM) for 5–10 min reduced DSI from 72.0 ± 8.2 to 18.8 ± 10.9% ($n = 7$; $p < 0.05$) (Fig. 2*A*,*B*). Moreover, ODQ significantly increased basal charge transfer to 174.7 ± 17.7% of control ($p < 0.05$) (Fig. 2*B*) (see Fig. 4*E*), suggesting that tonic activation of NO-sGC suppresses sIPSCs under control conditions. In contrast, when ODQ was included in the intrapipette solution, the magnitude of DSI (DSI in 0.05% DMSO, 47.3 ± 5.1%, $n = 10$; DSI in 10 μM ODQ, 40.3 ± 5.1, $n = 11$; $p > 0.3$) or the charge transfer (control in 0.05% DMSO, 14.4 ± 2.1 pA, $n = 10$; in 10 μM ODQ, 17.6 ± 2.1 pA, $n = 11$; $p > 0.2$) did not differ significantly even after 10–15 min of recordings. Subsequent bath application of ODQ in the same cells for 5–7 min could still inhibit DSI (DSI with intrapipette ODQ, 37.4 ± 4.8%; DSI after bath application of ODQ, 14.4 ± 9.2%, $n = 4$; $p < 0.05$). These data imply that, under these conditions, NO activates NO-sGC in the presynaptic axon terminals rather than in the postsynaptic pyramidal cells.

Additional evidence for the involvement of NO-sGC activation in DSI was provided by bath application of the membrane-permeable cGMP analog 8-Br-cGMP (100 μM) for 5–10 min, which decreased sIPSC charge transfer to 48.2 ± 7.7% of control ($n = 8$; $p < 0.05$) (Fig. 2*C*,*D*) (see also Fig. 4*E*) and partially occluded DSI (control DSI, 63.2 ± 4.8%; in 8-Br-cGMP, 42.5 ± 8.5%; $n = 8$; $p < 0.05$) (Fig. 2*C*,*D*).

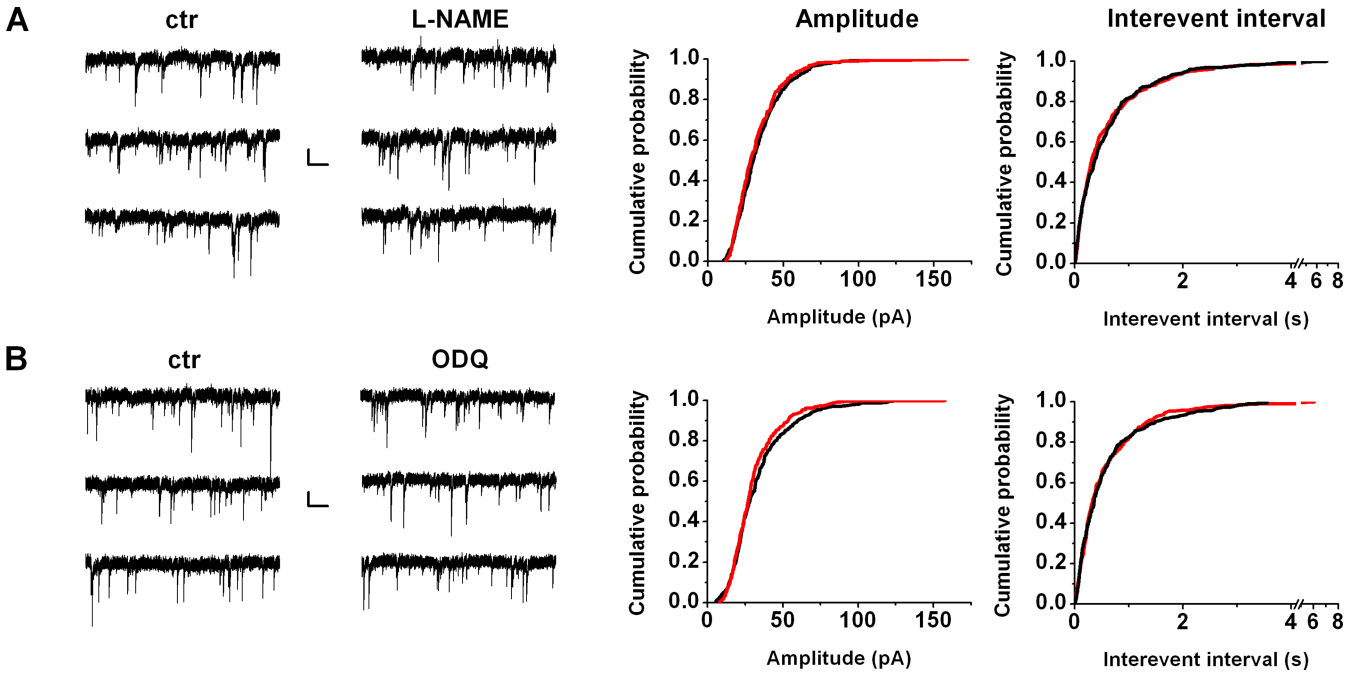

Figure 3. Effect of NO signaling modulators on miniature IPSCs. After cells were positively tested for DSI of spontaneous IPSCs, 0.5 μM TTX was applied to inhibit sIPSCs and uncover mIPSCs. After obtaining mIPSC baseline, L-NAME (100 μM, $n = 6$; ***A***) or ODQ (10 μM, $n = 6$; ***B***) was applied for 5–8 min. Left panels show representative recordings from individual cells (3 traces consecutive in time) before and after drug application. Amplitude (middle panels) and interevent interval (right panels) cumulative probabilities were compared on 60 randomly selected mIPSCs from every cell both under control (ctr) conditions and after drug application, using Kolmogorov–Smirnov statistics showing no significant effect. Calibration: 20 pA, 0.5 s.

Application of ODQ significantly increased basal charge transfer, suggesting that a basal activity of NO-sGC might influence sIPSCs under our conditions. In addition to ODQ, L-NAME also caused a smaller but significant increase in charge transfer (136.7 ± 16.9%; $p < 0.05$). Other drugs, although some of them also tended to increase charge transfer, did not cause significant alteration in sIPSC charge (AM251 or SR141716A, 170.8 ± 75.3, $p > 0.7$; 7-NI, 162.9 ± 34.8%, $p > 0.05$). Theoretically, enhanced GABA release from other, CB_1R-lacking axon terminals might mask the reduction of sIPSCs from DSI-sensitive boutons after depolarization, and, therefore, inhibition of DSI with drugs that enhance charge transfer might be indirect. To test this possibility, we used a muscarinic acetylcholine receptor type 2 (M_2R) antagonist to specifically enhance GABA release from axon terminals expressing M_2R that innervate the perisomatic region of pyramidal cells and are distinct from CB_1R bearing axon endings (Hájos et al., 1998; Freund et al., 2003; Fukudome et al., 2004). Because we recorded sIPSCs in the presence of carbachol, a general agonist of acetylcholine receptors, M_2Rs were likely to be constitutively activated under our recording conditions. Thus, application of a selective antagonist of M_2Rs should specifically augment GABA release from those axon terminals that do not express CB_1Rs. In 6 of 10 experiments, bath application of 0.1–0.2 μM AF-DX116, an M_2R antagonist, enhanced charge transfer. The increase of basal IPSC charge in these six cells was 164.9 ± 8.9% of control ($p < 0.05$), yet the magnitude of DSI only slightly changed (control, 55.5 ± 4.9%; AF-DX116, 43.9 ± 3.8; $n = 6$; $p > 0.1$) (supplemental Fig. 3, available at www.jneurosci.org as supplemental material). These data show that IPSC enhancement from cannabinoid-insensitive axon terminals cannot explain the significant reduction of DSI, when charge transfer increases after application of various drugs.

To exclude the possibility that drugs used to inhibit NO signaling influenced postsynaptic $GABA_A$ receptors directly, we measured miniature IPSCs in the presence of 0.5 μM tetrodotoxin. Amplitude and frequency of mIPSCs were not affected by L-NAME or ODQ (Fig. 3), implying that mainly action potential-dependent GABA release and not postsynaptic GABA sensitivity was affected by these drugs. Furthermore, we also confirmed that the inhibitory effect of NOS and NO-sGC blockers on DSI was not the result of postsynaptic reduction of Ca^{2+} influx, because charge transfer carried by voltage-gated Ca^{2+} channels was not influenced by 100 μM L-NAME (103.3 ± 4.1% of control; $n = 4$; $p > 0.7$) or 10 μM ODQ (94.1 ± 6.7% of control; $n = 4$; $p > 0.2$).

CB_1R activation is downstream of NO signaling in DSI

A plausible explanation of the above results is that, in response to the depolarization-evoked Ca^{2+} signal, NO is released postsynaptically, diffuses to the presynaptic terminal, and increases cGMP synthesis via NO-sGC activation, which leads to suppression of GABA release by a mechanism that involves CB_1Rs. To test the involvement of CB_1Rs in the effects of the NO signaling pathway, we first compared the effect of 100 μM 8-Br-cGMP on spontaneous IPSCs between cells from control slices and from slices pretreated with AM251 (2 μM) for 15–20 min. Because AM251 eliminated DSI (5.1 ± 2.9%, $n = 15$; DSI in control slices, 55.2 ± 5.9%, $n = 15$; $p < 0.001$), we analyzed the effect of 8-Br-cGMP on basal charge transfer. Whereas in control cells 8-Br-cGMP strongly decreased charge transfer to 50.3 ± 8.5% of control ($n = 7$) (Fig. 4*A*,*E*), in AM251-pretreated cells, the charge transfer measured after application of 8-Br-cGMP was not changed on average (101.3 ± 22.0%; $n = 7$) (Fig. 4*C*,*E*). The effect of 8-Br-cGMP differed significantly between control and AM251-pretreated cells ($p < 0.01$). In additional experiments, we tested the effect of inhibition of NO-sGC on spontaneous IPSCs in the absence and presence of AM251. Application of ODQ (10 μM) increased sIPSC charge to 157.8 ± 17.1% of control ($n = 8$) (Fig. 4*B*,*E*), whereas in cells from slices pretreated

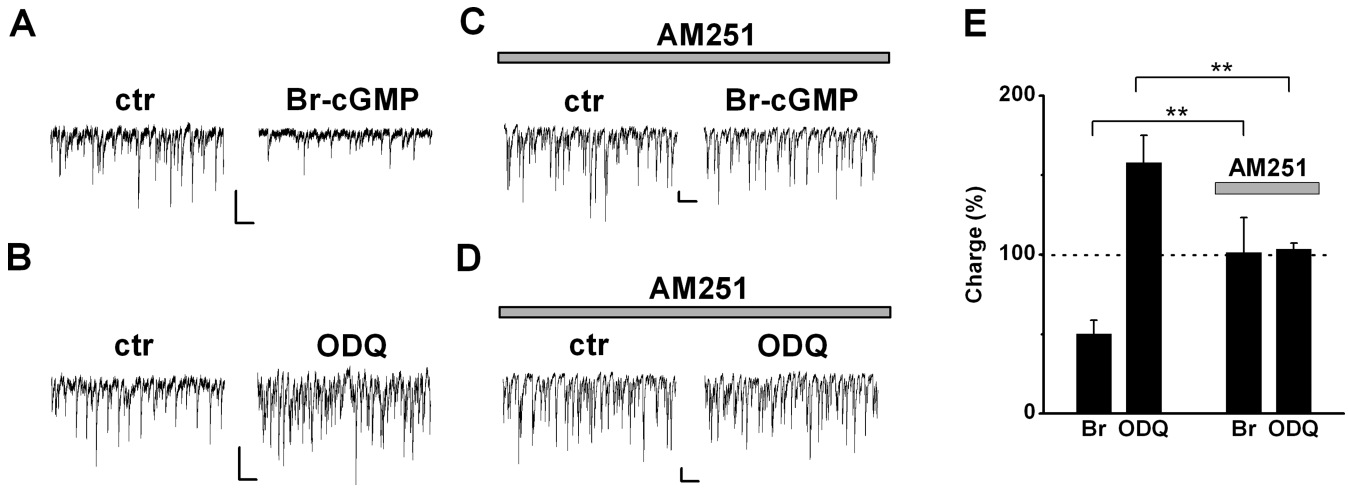

Figure 4. CB_1R function is a prerequisite for modulation of DSI by Br-cGMP and ODQ. ***A***, ***B***, Effect of 100 μM 8-Br-cGMP (***A***) and 10 μM ODQ (***B***) on sIPSCs in control (ctr) cells. ***C***, ***D***, Effect of 100 μM 8-Br-cGMP (***C***) and 10 μM ODQ (***D***) on sIPSCs in cells pretreated with 2 μM AM251 for >15 min. ***E***, Summary of the effect of 100 μM 8-Br-cGMP and 10 μM ODQ on sIPSC charge, in control and in AM251-pretreated cells ($n = 7$ and 7 for 8-Br-cGMP; $n = 8$ and 8 for ODQ). Values are expressed as percentage of control before perfusion of the drugs. Note that changes in sIPSC charge may reflect both amplitude and frequency alteration. Calibration: 100 pA, 500 ms. $^{**}p < 0.01$.

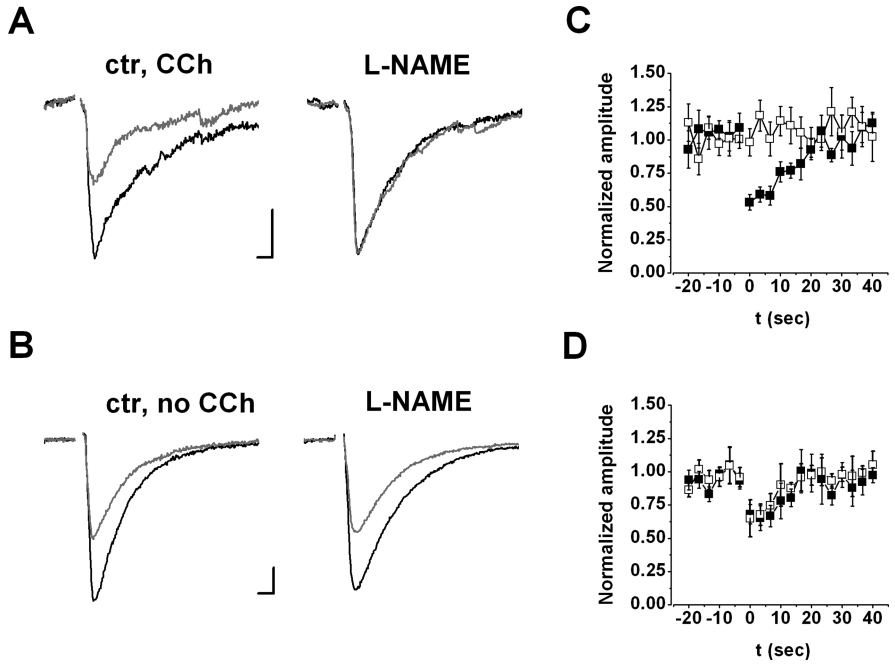

Figure 5. Involvement of NO in DSI of evoked IPSCs with (***A***, ***C***) or without (***B***, ***D***) carbachol (CCh). ***A***, ***B***, Left and Middle, Representative recordings of pyramidal cells before (left) and during (middle) application of 100 μM L-NAME (NOS inhibitor). IPSCs (black) evoked by minimal stimulation of fibers in the close vicinity of cell bodies showed transient reduction after a depolarizing step (gray) under control conditions (ctr) (left; DSI). DSI was absent after drug application (***A***, middle) in the presence of carbachol, but it was unaltered (***B***, middle) in recordings without carbachol. Traces are averages of three and three consecutive events before and after depolarization, respectively. Stimulus artifacts were removed. Calibration: 50 pA, 5 s. Right, Magnitude and kinetics of DSI under control conditions (filled squares) and during application (open squares) of 100 μM L-NAME in the presence (***C***; $n = 7$) or in the absence (***D***; $n = 5$) of carbachol. Amplitude was normalized to the control period before depolarization.

with AM251, the charge transfer remained unchanged by application of ODQ (103.6 ± 3.8%; $n = 8$) (Fig. 4*D*,*E*), although in some cases increased appearance of small-amplitude IPSCs, which did not affect total charge substantially, could still be observed. Again, the effect of ODQ was significantly different between control and AM251-pretreated cells ($p < 0.01$). In summary, these data suggest that the NO signaling cascade acts either upstream of CB1Rs or at a target that is dependent on CB_1R function.

To further test this hypothesis, we asked whether, on the contrary, impairment of NO signaling would influence the effect of cannabinoid agonists on sIPSCs and DSI. We compared the effect of the CB_1R agonist WIN 55,212-2 between control cells and cells that were pretreated with the NO-sGC inhibitor ODQ (10 μM) for >10 min. As described before (Fig. 2), ODQ treatment strongly inhibited DSI (9.0 ± 5.8%; $n = 12$) compared with control cells (51.8 ± 6.5%; $n = 13$; $p < 0.001$). However, application of WIN 55,212-2 (2 μM) for 10 min decreased sIPSC charge similarly in the two cell groups (control, to 74.5 ± 10.1%, $n = 7$; ODQ-pretreated, to 68.2 ± 3.7%, $n = 6$; $p > 0.3$). Thus, results of this experiment exclude the possibility that inhibition of NO-sGC signaling decreased DSI by impairing the effect of CB_1R activation on GABA release.

Contribution of NO signaling to DSI of electrically evoked IPSCs

All data presented so far clearly show that, in the presence of carbachol, NO plays an important role in DSI of spontaneously occurring IPSCs. However, any change in the DSI of sIPSCs on interfering NO signaling could be attributable to the alteration in GABA release at the presynaptic site, to the modification of firing properties of inhibitory neurons, or both. To investigate whether NO could indeed control GABA release from the axon terminals, we evoked IPSCs by minimal electrical stimulation of fibers in the close vicinity of cell bodies (Hájos et al., 2000) and tested their DSI sensitivity. In the presence of carbachol, 10 of 45 evoked IPSCs showed clearly detectable DSI (i.e., larger than a 20% re-

duction in the amplitude after 1-s-long depolarization in a given cell). After recording a control period, the effect of L-NAME (100 μM) was successfully tested in seven cells. Without changing the basal amplitude (103.4 ± 20.4% of control; $p > 0.5$; $n = 7$), the NOS inhibitor abolished DSI (control DSI, 43.2 ± 2.9%; in L-NAME, −5.7 ± 6.3%; $p < 0.05$; $n = 7$) (Fig. 5*A*,*C*). These results undoubtedly indicate that DSI of evoked IPSCs is also dependent on NO when cholinergic receptors are activated and also suggest that the NO-cGMP signaling cascade exerts its effect directly on the axons of CB_1R-positive interneurons.

Because DSI of evoked IPSCs is routinely studied in the absence of carbachol, we investigated whether NO is involved under these circumstances as well. In 5 of 21 cells, a substantial DSI of evoked IPSCs was observed (control, 33.4 ± 3.8%; $n = 5$). In contrast to the results measured in the presence of carbachol, bath application of 100 μM L-NAME did not alter DSI in the absence of the cholinergic agonist (control, 33.4 ± 3.8%; in L-NAME, 30.9 ± 4.4%; $n = 5$; $p > 0.5$) (Fig. 5*B*,*D*). These data suggest that, without activation of cholinergic receptors, retrograde signaling at GABAergic synapses does not involve NO.

NO donor-induced cGMP production in CB_1R-expressing boutons

In cortical networks, at least two major GABAergic interneuron populations with separate physiological functions control the output of pyramidal neurons (Freund, 2003). Axon terminals of these interneuron populations can be visualized by immunostaining for either CB_1Rs [and cholecystokinin (CCK)] or parvalbumin (Katona et al., 1999; Hájos et al., 2000). It has been established that only GABAergic synapses formed by CB_1R-containing axon terminals can undergo DSI (Ohno-Shosaku et al., 2001; Wilson et al., 2001). Thus, we hypothesized that NO signaling should preferentially induce cGMP production in axon terminals expressing CB_1Rs. Indeed, after incubation of hippocampal slices in the presence of the NO donor SNP (0.1–0.2 mM) and the phosphodiesterase blocker IBMX (1 mM) in standard carbachol-containing ACSF, cGMP immunoreactivity appeared in 67.0 ± 1.0% of CB_1R-containing axon terminals (Fig. 6*A*–*C*), which represents a ninefold increase relative to basal conditions in the presence of IBMX only (7.3 ± 1.2%) (Fig. 6*G*) (supplemental Fig. 4*A*–*C*, available at www.jneurosci.org as supplemental material). In contrast, SNP treatment did not increase the level of cGMP immunoreactivity in parvalbumin-positive boutons (basal, 19.3 ± 4.8%; SNP-treated, 18.0 ± 3.8%) (Fig. 6*D*–*F*). Thus, cGMP formation on NO donor-induced sGC activity is proved to be present in axon terminals, which contain CB_1Rs. In line with the anatomical results, application of SNP (100 μM) in IBMX-pretreated slices partially occluded DSI of sIPSCs (DSI in IBMX only, 42.7 ± 7.1%; DSI in SNP, 21.7 ± 11.8%; $n = 9$; $p < 0.05$) (Fig. 6*H*). It is also important to note that no enhancement or appearance of cGMP immunoreactivity during application of SNP has been observed in the somata of pyramidal cells (Fig. 6*B*,*E*).

Molecular and anatomical basis of NO signaling at synapses formed by CB_1R-immunopositive axon terminals

Finally, we asked whether nNOS, which has been shown to be present in the postsynaptic densities at glutamatergic synapses (Burette et al., 2002), could also be located at GABAergic synapses. Using immunogold labeling in mildly fixed hippocampal tissue, nNOS labeling could be found not only in dendritic spines at excitatory synapses in the CA1 region (data not shown) but also at symmetrical synapses on pyramidal cell somata (Fig. 7*A*–

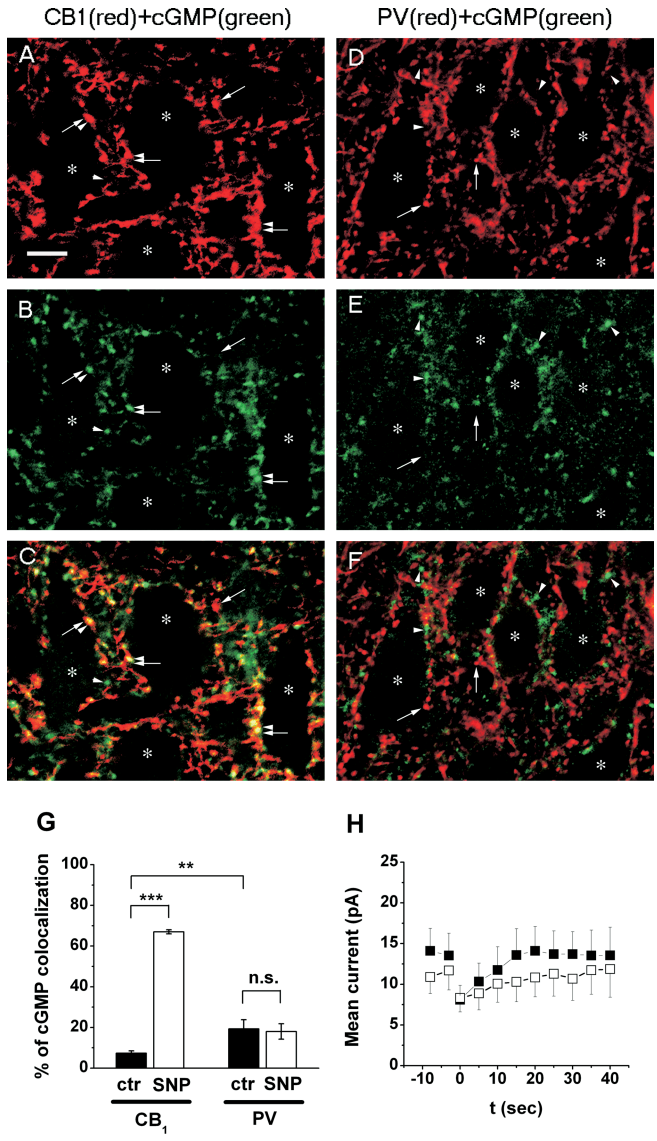

Figure 6. NO donor-induced cGMP immunoreactivity is enhanced in CB_1 cannabinoid receptor-containing axon terminals after IBMX treatment. ***A***, ***B***, Immunostaining for CB_1R (***A***) and cGMP (***B***) visualizes a dense meshwork of axons in the stratum pyramidale of the CA1 subfield, which forms characteristic pericellular arrays of boutons around immunonegative cell bodies of pyramidal neurons (depicted by asterisks). ***C***, Overlay of the two images reveals that the majority of these axon terminals contain both CB_1R and cGMP. ***D***, ***E***, In contrast, boutons of the other basket cell population visualized by immunostaining for PV (***D***) do not contain NO donor (SNP)-induced cGMP immunoreactivity (***E***). ***F***, In the overlaid image, red parvalbumin-positive boutons and green cGMP-positive axon terminals are located in a primarily complementary position. Double-positive boutons are labeled by the combination of arrow and arrowhead throughout the images, whereas single-positive CB_1R- and PV- or cGMP-immunoreactive boutons are marked by single arrows or arrowheads, respectively. Asterisks label double-immunonegative pyramidal cell bodies. Scale bar, 10 μm. ***G***, Summary of the ratio of cGMP-containing boutons of all perisomatic axon terminals positive for either CB_1R or PV. cGMP immunoreactivity appears in 67% of CB_1R-positive axon terminals after activation of NO-sGC by SNP. In contrast, SNP treatment does not change the ratio of cGMP immunostaining in PV-positive boutons. $^{**}p < 0.01$, $^{***}p < 0.001$; ctr, Control; n.s., not significant. ***H***, Mean current and DSI in the presence of 1 mM IBMX only (control, filled squares) and after application of 100 μM SNP (open squares; $n = 9$).

C). The labeling was specifically associated with the symmetrical synaptic active zones on pyramidal cell bodies and avoided extrasynaptic membranes. Some labeling was also found in the cytoplasm of the pyramidal cells around the endoplasmic reticulum (Fig. 7*C/b*). Next, we specifically tested whether nNOS is present

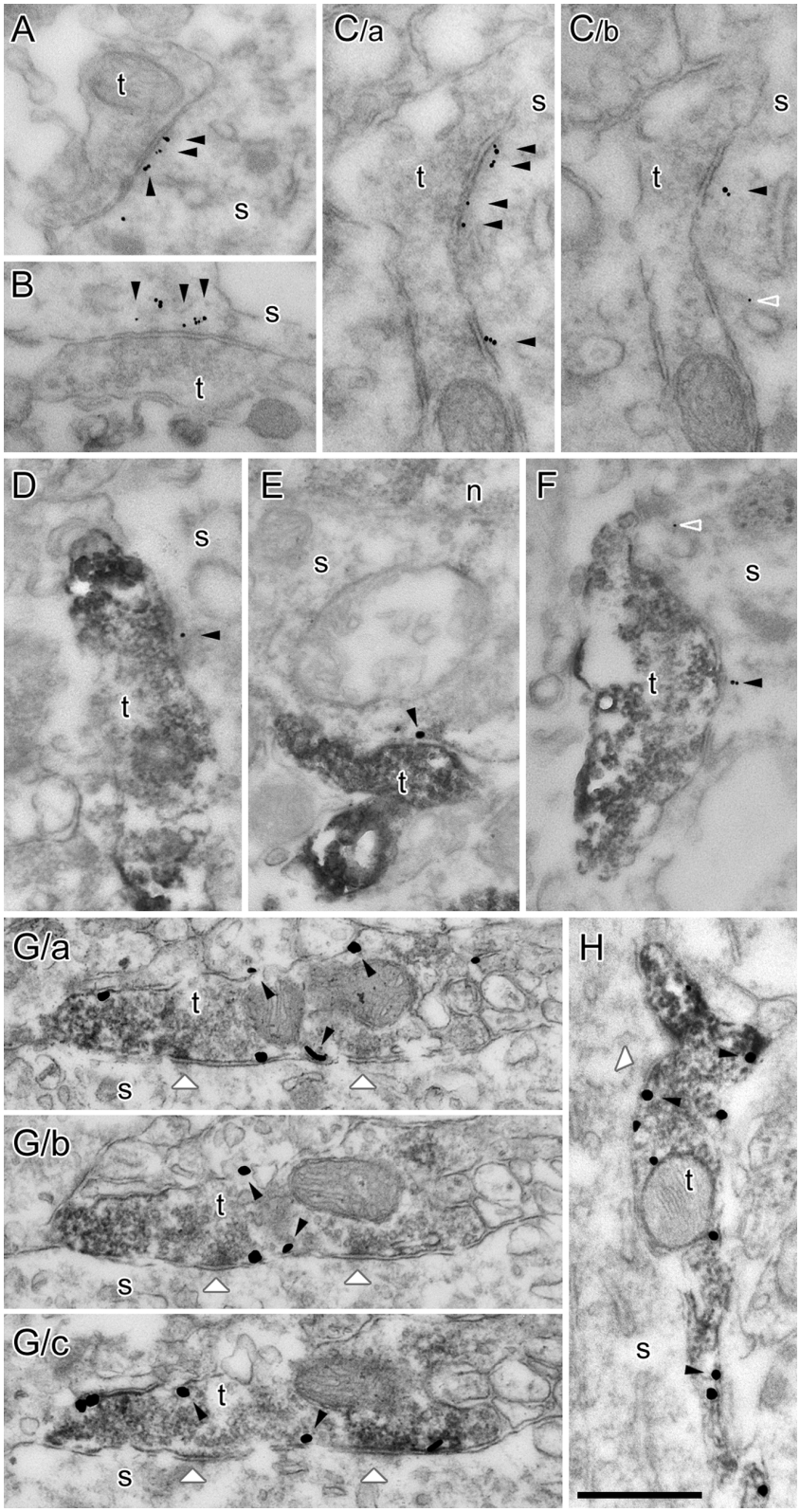

Figure 7. Neuronal NOS labeling is present postsynaptically at CB_1R-positive axon terminals, which terminals also show immunopositivity for NO-sGC. ***A–C***, Electron micrographs from immunogold labeling experiments in hippocampal CA1 area of the rat brain. Gold particles show that postsynaptic nNOS labeling (arrowheads) is closely associated with the synapses established by three terminals (t) on pyramidal cell somata (***C/a*** and ***C/b*** are serial sections of the same terminal). ***D–F***, Electron micrographs from immunogold–immunoperoxidase double-labeling experiments. CB_1R labeling is shown with dark DAB precipitation in the terminals (t) that establish symmetrical synapses on pyramidal cell somata (s). Gold particles show nNOS labeling postsynaptically (arrowheads) or occasionally in the cytoplasm around endoplasmic reticulum membranes (open arrowhead in ***C/b*** and ***F***). The smaller numbers of gold particles is attributable to technical limitations of the double-labeling method. ***G***, ***H***, Electron micrographs show the colocalization of CB_1R and NO-sGC in axon terminals contacting CA1 pyramidal cells (***G/a–G/c*** are serial sections of the same terminal). NO-sGC labeling is shown with dark DAB precipitation in the terminals (t) that establish symmetrical synapses (white arrowheads) on pyramidal cell somata (s). CB_1Rs are labeled with silver-intensified gold particles (some of them are labeled with black arrowheads). n, Nucleus. Scale bar, 500 nm.

at those GABAergic synapses that express CB_1Rs. Experiments using immunogold–immunoperoxidase double staining revealed that nNOS labeling was indeed localized to the postsynaptic membranes of symmetrical synapses formed by CB_1R-positive axon terminals (Fig. 7*D–F*). If NO is a retrograde signaling molecule in DSI, then its receptor, NO-sGC, should be present in these presynaptic terminals. In fact, using double immunostainings, α_1 subunits of NO-sGC were unequivocally found in CB_1R-expressing axon endings (Fig. 7*G*,*H*). These anatomical data provide the structural basis of NO-mediated retrograde signaling in CB_1R-dependent DSI.

Discussion

In this study, we investigated the role of nitric oxide in short-term retrograde regulation of GABAergic synaptic transmission. We found that inhibition of NOS and NO-sGC enzymes diminished DSI at cholinergically enhanced spontaneously active inhibitory inputs of CA1 pyramidal cells, whereas a cGMP analog mimicked and partially occluded DSI in a CB_1R-dependent manner. Moreover, increasing NO levels by L-arginine enhanced DSI. In the presence, but not in the absence, of carbachol, DSI of evoked IPSCs was eliminated by an NOS inhibitor. We also found that an NO donor, which partially occluded DSI, increased the level of cGMP preferentially in CB_1R-positive axon terminals, providing an anatomical link between the two signaling systems. In addition, electron microscopic investigation revealed that neuronal NOS was postsynaptically located at symmetrical synapses formed by CB_1R-immunopositive axon terminals. Importantly, in these presynaptic terminals, the presence of NO-sGC immunopositivity was also demonstrated. We propose that, in the presence of cholinergic receptor agonists, activation of NO signaling by depolarization-induced Ca^{2+} transients is involved in a form of CB_1R-dependent DSI in the presence of cholinergic receptor agonists.

Several lines of evidence support the involvement of CB_1Rs and the retrograde action of endocannabinoids in hippocampal DSI (Ohno-Shosaku et al., 2001; Wilson and Nicoll, 2001). Cannabinoid analogs reduce GABA release measured with either electrophysiological (Hájos et al., 2000; Ohno-Shosaku et al., 2001; Wilson and Nicoll, 2001) or biochemical (Katona et al., 1999) tech-

niques and partially occlude DSI (Wilson and Nicoll, 2001), whereas pharmacological suppression or genetic deletion of CB_1Rs abolishes DSI (Ohno-Shosaku et al., 2001; Varma et al., 2001; Wilson et al., 2001). Endogenous cannabinoids can be produced by neurons in a Ca^{2+}-dependent manner (Di Marzo et al., 1998; Freund et al., 2003). Although the enzyme responsible for endocannabinoid production at inhibitory synapses has not yet been identified, CB_1Rs are expressed at a very high density on presynaptic terminals of CCK-positive interneurons (Nyiri et al., 2005). Finally, inhibition of endocannabinoid degradation by cyclooxygenase-2 (Kim and Alger, 2004) or by monoacylglycerol lipase inhibitors (Makara et al., 2005; Hashimotodani et al., 2007) prolongs DSI.

Although endocannabinoids are currently the most widely accepted retrograde signal molecules, other modulators of synaptic activity have also been considered previously (Medina and Izquierdo, 1995; Alger, 2002). However, according to the literature, only some of these molecules, e.g., adenosine or glutamate (Pitler and Alger, 1994; Morishita et al., 1998), have been investigated in hippocampal DSI. The rapidly diffusing NO is ideally suited for intercellular signaling and has been implicated as retrograde messenger in hippocampal long-term potentiation (O'Dell et al., 1991; Prast and Philippu, 2001). Several arguments, presented in this study or reported previously, support the idea that NO may also modulate DSI as a retrograde messenger, generated in the postsynaptic cell and acting at the presynaptic terminal. The nNOS enzyme is activated by Ca^{2+} (Schmidt et al., 1992), and it is reasonable to assume that the large postsynaptic Ca^{2+} signal evoked by the DSI paradigm (Isokawa and Alger, 2006) is sufficient to stimulate NO production. In support of NO as a retrograde signal molecule, previous data showed that nNOS could be found at the postsynaptic densities of glutamatergic synapses (Wendland et al., 1994; Burette et al., 2002), and presynaptic localization of NO-sGC in glutamatergic afferents terminating on CA1 pyramidal cells has also been described (Burette et al., 2002). We provide anatomical evidence that postsynaptic nNOS and presynaptic NO-sGC are expressed also at inhibitory synapses and that axon terminals forming such inhibitory synapses are equipped with CB_1Rs. Moreover, we found that, after inhibiting the activity of phosphodiesterases with IBMX, an NO donor could evoke cGMP production in CB_1R-positive axon terminals. Beside the anatomical evidence, we also show that inhibition of NOS or scavenging NO intracellularly in pyramidal cells decreases DSI, suggesting that NO is generated by the postsynaptic pyramidal cells. Conversely, blocking NO-sGC inhibits DSI only when applied extracellularly but not postsynaptically. Supporting the idea that NO should diffuse in the extracellular space to reach its target, extracellular application of a membrane-impermeable NO scavenger substantially reduced DSI. This is concordant with our immunocytochemical results, which show cGMP accumulation in CB_1R-expressing axon terminals but not in the postsynaptic pyramidal cells. These observations suggest that NO could trigger cGMP synthesis on the presynaptic rather than the postsynaptic side of synapses formed by cannabinoid-sensitive axon terminals and strongly support a role for NO in modulating the function of GABAergic synapses as a retrograde messenger. Importantly, the effect of ODQ and 8-Br-cGMP on sIPSCs was inhibited by pretreatment with the CB_1R antagonist AM251, whereas the effect of the CB_1R agonist WIN 55,212-2 was not influenced by pretreatment with the NO-sGC antagonist ODQ. These experiments point to a functional interaction between the two cascades instead of a simple parallel effect on GABA release and suggest that cGMP exerted its effect either upstream of CB_1R activation or at a target that is crucially dependent on CB_1Rs. Although the above results strongly support the idea that the observed effects of NO on DSI were mediated at the presynaptic terminals, a postsynaptic site of effect, e.g., an enhancement of endocannabinoid production by NO, cannot be ruled out. The $\alpha 2/\beta 1$ subunit composition of NO-sGC is expressed by pyramidal cells, but the protein has been reported to be predominantly presynaptic in glutamatergic synapses (Burette et al., 2002), whereas the $\alpha 1$ subunit of NO-sGC (either protein or mRNA) is not detectable in postsynaptic pyramidal cells (Szabadits et al., 2007). Although low levels of sGC may be present also in pyramidal cell bodies, their activation by NO donors did not result in a detectable increase in cGMP levels. The highly diffusible nature of NO and the lack of membrane-impermeable inhibitors of NOS and sGC also complicate the interpretation of pharmacological experiments, conducted in the tightly packed structure of presynaptic and postsynaptic compartments in the slice. For example, although the extracellular NO scavenger inhibited DSI, this effect might have been the result of "sinking" fast diffusible NO molecules from the postsynaptic cell. It should be noted that a putative postsynaptic action of NO does not rule out a simultaneous presynaptic effect, which is favored by the evidence we presented. Additional experiments are required to pinpoint the precise site of action of NO as a signaling molecule in DSI.

Importantly, we have shown that NO represents a crucial component of the signaling machinery in DSI only when cholinergic receptors are activated. Activation of acetylcholine receptors is critical for the detection of DSI of spontaneous, action potential-dependent IPSCs, because DSI of these currents is rarely observed in the absence of a cholinergic agonist (Martin and Alger, 1999). Carbachol increases firing of DSI-susceptible interneurons (Martin and Alger, 1999; Martin et al., 2001) and favors GABA release from CB_1R-positive axon terminals but inhibits release from PV-containing boutons likely via activation of presynaptically located M_2Rs (Hájos et al., 1998; Fukudome et al., 2004; present study). Moreover, postsynaptic activation of type 1 and 3 muscarinic acetylcholine receptors (Martin and Alger, 1999; Kim et al., 2002; Ohno-Shosaku et al., 2003; Edwards et al., 2006) were shown to enhance DSI in slices, although the explanation for their precise mode of action is still lacking (Edwards et al., 2006). Based on our data with evoked IPSCs, in which L-NAME inhibited DSI only in the presence of carbachol, we propose that activation of cholinergic receptors is essential for the induction of the NO signaling cascade. This induction mechanism is well established in the vascular system, in which activation of muscarinic acetylcholine receptors has long been known to enhance the activity of endothelial NOS (Furchgott and Vanhoutte, 1989; Arnal et al., 1999). Neuronal NOS can also be activated by muscarinic receptors, either by Ca^{2+} mobilization or via Ca^{2+}-independent pathways (Christopoulos and El-Fakahany, 1999), and stimulatory effect of cholinergic agonists on NO and cGMP production in the brain has been observed (de Vente, 2004). Such cholinergic augmentation of DSI by NO could take place *in vivo* under conditions when tissue concentration of acetylcholine is high, e.g., during exploratory activity (Marrosu et al., 1995).

In summary, the physiological and anatomical results presented in this study strongly suggest that NO as a retrograde signal molecule cooperates with endocannabinoids to control GABA release from CB_1R-expressing axon terminals in an activity-dependent manner, when cholinergic receptors are activated. *In vivo*, CB_1R-expressing interneurons could play a role in

the temporal coordination of pyramidal cell ensembles necessary for normal hippocampal function (Klausberger et al., 2005; Robbe et al., 2006). Convergence of distinct, state-dependent physiological stimuli simultaneously activating NO and endocannabinoid signaling in a select population of pyramidal neurons may change their entrainment by inhibition as well as the precise timing of their action potentials that is critical for temporal coding. Thus, a fast, activity-dependent and target-selective retrograde signaling achieved by the cooperation of NO and endocannabinoids may shed new light on the regulation of neuronal activity patterns associated with information coding and transfer (Freund et al., 2003), as well as with pathophysiological states such as anxiety (Haller et al., 2002) and epilepsy (Chen et al., 2003).

References

Alger BE (2002) Retrograde signaling in the regulation of synaptic transmission: focus on endocannabinoids. Prog Neurobiol 68:247–286.

Arnal JF, Dinh-Xuan AT, Pueyo M, Darblade B, Rami J (1999) Endothelium-derived nitric oxide and vascular physiology and pathology. Cell Mol Life Sci 55:1078–1087.

Burette A, Zabel U, Weinberg RJ, Schmidt HH, Valtschanoff JG (2002) Synaptic localization of nitric oxide synthase and soluble guanylyl cyclase in the hippocampus. J Neurosci 22:8961–8970.

Chen K, Ratzliff A, Hilgenberg L, Gulyas A, Freund TF, Smith M, Dinh TP, Piomelli D, Mackie K, Soltesz I (2003) Long-term plasticity of endocannabinoid signaling induced by developmental febrile seizures. Neuron 39:599–611.

Chevaleyre V, Takahashi KA, Castillo PE (2006) Endocannabinoid-mediated synaptic plasticity in the CNS. Annu Rev Neurosci 29:37–75.

Christopoulos A, El-Fakahany EE (1999) The generation of nitric oxide by G protein-coupled receptors. Life Sci 64:1–15.

Cummings JA, Nicola SM, Malenka RC (1994) Induction in the rat hippocampus of long-term potentiation (LTP) and long-term depression (LTD) in the presence of a nitric oxide synthase inhibitor. Neurosci Lett 176:110–114.

de Vente J (2004) cGMP: a second messenger for acetylcholine in the brain? Neurochem Int 45:799–812.

Di Marzo V, Melck D, Bisogno T, De Petrocellis L (1998) Endocannabinoids: endogenous cannabinoid receptor ligands with neuromodulatory action. Trends Neurosci 21:521–528.

Edwards DA, Kim J, Alger BE (2006) Multiple mechanisms of endocannabinoid response initiation in hippocampus. J Neurophysiol 95:67–75.

Freund TF (2003) Interneuron diversity series: rhythm and mood in perisomatic inhibition. Trends Neurosci 26:489–495.

Freund TF, Katona I, Piomelli D (2003) Role of endogenous cannabinoids in synaptic signaling. Physiol Rev 83:1017–1066.

Fukudome Y, Ohno-Shosaku T, Matsui M, Omori Y, Fukaya M, Tsubokawa H, Taketo MM, Watanabe M. Manabe T, Kano M (2004) Two distinct classes of muscarinic action on hippocampal inhibitory synapses: M2-mediated direct suppression and M1/M3-mediated indirect suppression through endocannabinoid signaling. Eur J Neurosci 19:2682–2692.

Furchgott RF, Vanhoutte PM (1989) Endothelium-derived relaxing and contracting factors. FASEB J 3:2007–2018.

Hájos N, Papp EC, Acsady L, Levey AI, Freund TF (1998) Distinct interneuron types express m2 muscarinic receptor immunoreactivity on their dendrites or axon terminals in the hippocampus. Neuroscience 82:355–376.

Hájos N, Katona I, Naiem SS, Mackie K, Ledent C, Mody I, Freund TF (2000) Cannabinoids inhibit hippocampal GABAergic transmission and network oscillations. Eur J Neurosci 12:3239–3249.

Haller J, Bakos N, Szirmay M, Ledent C, Freund TF (2002) The effects of genetic and pharmacological blockade of the CB1 cannabinoid receptor on anxiety. Eur J Neurosci 16:1395–1398.

Hashimotodani Y, Ohno-Shosaku T, Kano M (2007) Presynaptic monoacylglycerol lipase activity determines basal endocannabinoid tone and terminates retrograde endocannabinoid signaling in the hippocampus. J Neurosci 27:1211–1219.

Isokawa M, Alger BE (2006) Ryanodine receptor regulates endogenous cannabinoid mobilization in the hippocampus. J Neurophysiol 95:3001–3011.

Katona I, Sperlagh B, Sik A, Kofalvi A, Vizi ES, Mackie K, Freund TF (1999) Presynaptically located CB1 cannabinoid receptors regulate GABA release from axon terminals of specific hippocampal interneurons. J Neurosci 19:4544–4558.

Kim J, Alger BE (2004) Inhibition of cyclooxygenase-2 potentiates retrograde endocannabinoid effects in hippocampus. Nat Neurosci 7:697–698.

Kim J, Isokawa M, Ledent C, Alger BE (2002) Activation of muscarinic acetylcholine receptors enhances the release of endogenous cannabinoids in the hippocampus. J Neurosci 22:10182–10191.

Klausberger T, Marton LF, O'Neill J, Huck JH, Dalezios Y, Fuentealba P, Suen WY, Papp E, Kaneko T, Watanabe M, Csicsvari J, Somogyi P (2005) Complementary roles of cholecystokinin- and parvalbumin-expressing GABAergic neurons in hippocampal network oscillations. J Neurosci 25:9782–9793.

Ko GY, Kelly PT (1999) Nitric oxide acts as a postsynaptic signaling molecule in calcium/calmodulin-induced synaptic potentiation in hippocampal CA1 pyramidal neurons. J Neurosci 19:6784–6794.

Kreitzer AC, Regehr WG (2001) Cerebellar depolarization-induced suppression of inhibition is mediated by endogenous cannabinoids. J Neurosci 21:RC174(1–5).

Ledent C, Valverde O, Cossu G, Petitet F, Aubert JF, Beslot F, Bohme GA, Imperato A, Pedrazzini T, Roques BP, Vassart G, Fratta W, Parmentier M (1999) Unresponsiveness to cannabinoids and reduced addictive effects of opiates in CB1 receptor knockout mice. Science 283:401–404.

Lenz RA, Alger BE (1999) Calcium dependence of depolarization-induced suppression of inhibition in rat hippocampal CA1 pyramidal neurons. J Physiol (Lond) 521:147–157.

Llano I, Leresche N, Marty A (1991) Calcium entry increases the sensitivity of cerebellar Purkinje cells to applied GABA and decreases inhibitory synaptic currents. Neuron 6:565–574.

Maccaferri G, Roberts JD, Szucs P, Cottingham CA, Somogyi P (2000) Cell surface domain specific postsynaptic currents evoked by identified GABAergic neurones in rat hippocampus in vitro. J Physiol (Lond) 524:91–116.

Makara JK, Mor M, Fegley D, Szabo SI, Kathuria S, Astarita G, Duranti A, Tontini A, Tarzia G, Rivara S, Freund TF, Piomelli D (2005) Selective inhibition of 2-AG hydrolysis enhances endocannabinoid signaling in hippocampus. Nat Neurosci 8:1139–1141.

Marrosu F, Portas C, Mascia MS, Casu MA, Fa M, Giagheddu M, Imperato A, Gessa GL (1995) Microdialysis measurement of cortical and hippocampal acetylcholine release during sleep-wake cycle in freely moving cats. Brain Res 671:329–332.

Martin LA, Alger BE (1999) Muscarinic facilitation of the occurrence of depolarization-induced suppression of inhibition in rat hippocampus. Neuroscience 92:61–71.

Martin LA, Wei DS, Alger BE (2001) Heterogeneous susceptibility of GABA(A) receptor-mediated IPSCs to depolarization-induced suppression of inhibition in rat hippocampus. J Physiol (Lond) 532:685–700.

Medina JH, Izquierdo I (1995) Retrograde messengers, long-term potentiation and memory. Brain Res Brain Res Rev 21:185–194.

Morishita W, Kirov SA, Alger BE (1998) Evidence for metabotropic glutamate receptor activation in the induction of depolarization-induced suppression of inhibition in hippocampal CA1. J Neurosci 18:4870–4882.

Nyiri G, Cserep C, Szabadits E, Mackie K, Freund TF (2005) CB1 cannabinoid receptors are enriched in the perisynaptic annulus and on preterminal segments of hippocampal GABAergic axons. Neuroscience 136:811–822.

O'Dell TJ, Hawkins RD, Kandel ER, Arancio O (1991) Tests of the roles of two diffusible substances in long-term potentiation: evidence for nitric oxide as a possible early retrograde messenger. Proc Natl Acad Sci USA 88:11285–11289.

Ohno-Shosaku T, Maejima T, Kano M (2001) Endogenous cannabinoids mediate retrograde signals from depolarized postsynaptic neurons to presynaptic terminals. Neuron 29:729–738.

Ohno-Shosaku T, Matsui M, Fukudome Y, Shosaku J, Tsubokawa H, Taketo MM, Manabe T, Kano M (2003) Postsynaptic M1 and M3 receptors are responsible for the muscarinic enhancement of retrograde endocannabinoid signalling in the hippocampus. Eur J Neurosci 18:109–116.

Palmer RM, Ashton DS, Moncada S (1988) Vascular endothelial cells synthesize nitric oxide from L-arginine. Nature 333:664–666.

Pitler TA, Alger BE (1992) Postsynaptic spike firing reduces synaptic

$GABA_A$ responses in hippocampal pyramidal cells. J Neurosci 12:4122–4132.

Pitler TA, Alger BE (1994) Depolarization-induced suppression of GABAergic inhibition in rat hippocampal pyramidal cells: G protein involvement in a presynaptic mechanism. Neuron 13:1447–1455.

Prast H, Philippu A (2001) Nitric oxide as modulator of neuronal function. Prog Neurobiol 64:51–68.

Robbe D, Montgomery SM, Thome A, Rueda-Orozco PE, McNaughton BL, Buzsaki G (2006) Cannabinoids reveal importance of spike timing coordination in hippocampal function. Nat Neurosci 9:1526–1533.

Schmidt HH, Pollock JS, Nakane M, Forstermann U, Murad F (1992) Ca^{2+}/calmodulin-regulated nitric oxide synthases. Cell Calcium 13:427–434.

Szabadits E, Cserep C, Ludanyi A, Katona I, Gracia-Llanes J, Freund TF, Nyiri G (2007) Hippocampal GABAergic synapses possess the molecular machinery for retrograde nitric oxide signaling. J Neurosci 27: 8101–8111.

Tanaka J, Markerink-van Ittersum M, Steinbusch HW, de Vente J (1997) Nitric oxide-mediated cGMP synthesis in oligodendrocytes in the developing rat brain. Glia 19:286–297.

Tao HW, Poo M (2001) Retrograde signaling at central synapses. Proc Natl Acad Sci USA 98:11009–11015.

van Staveren WC, Markerink-van Ittersum M, Steinbusch HW, Behrends S, de Vente J (2005) Localization and characterization of cGMP-immunoreactive structures in rat brain slices after NO-dependent and NO-independent stimulation of soluble guanylyl cyclase. Brain Res 1036:77–89.

Varma N, Carlson GC, Ledent C, Alger BE (2001) Metabotropic glutamate receptors drive the endocannabinoid system in hippocampus. J Neurosci 21:RC188(1–5).

Wendland B, Schweizer FE, Ryan TA, Nakane M, Murad F, Scheller RH, Tsien RW (1994) Existence of nitric oxide synthase in rat hippocampal pyramidal cells. Proc Natl Acad Sci USA 91:2151–2155.

Wilson RI, Nicoll RA (2001) Endogenous cannabinoids mediate retrograde signalling at hippocampal synapses. Nature 410:588–592.

Wilson RI, Kunos G, Nicoll RA (2001) Presynaptic specificity of endocannabinoid signaling in the hippocampus. Neuron 31:453–462.

dc_71_10

11. számú melléklet

dc_71_10

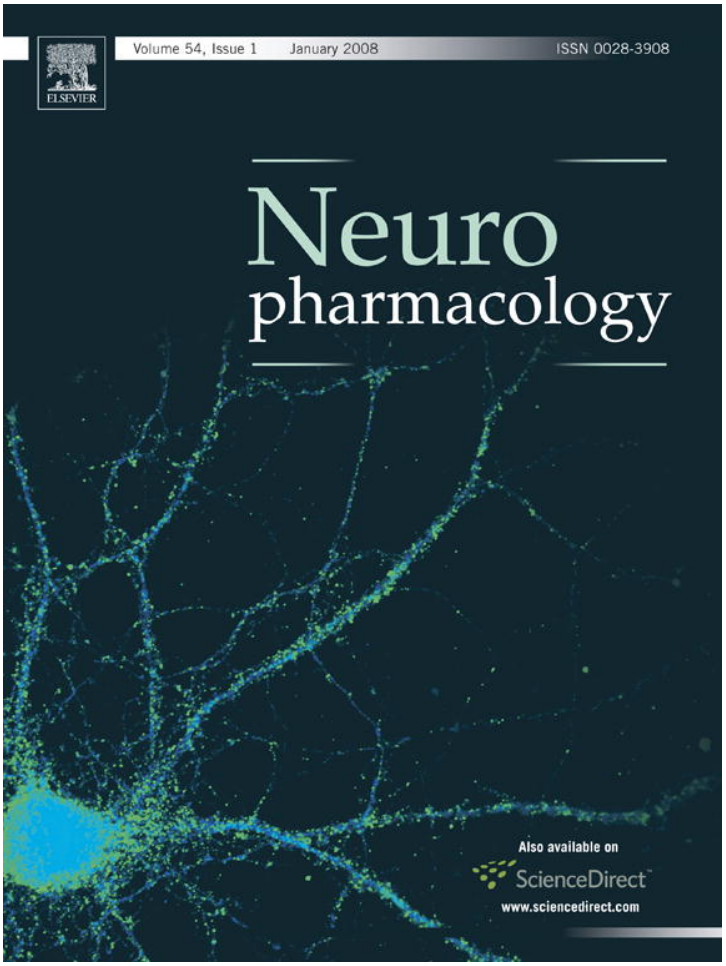

dc_71_10

Available online at www.sciencedirect.com
ScienceDirect

Neuropharmacology 54 (2008) 51–57

NEURO PHARMACOLOGY

www.elsevier.com/locate/neuropharm

CB_1 receptor-dependent and -independent inhibition of excitatory postsynaptic currents in the hippocampus by WIN 55,212-2

Beáta Németh [a], Catherine Ledent [b], Tamás F. Freund [a], Norbert Hájos [a,*]

[a] *Institute of Experimental Medicine, Hungarian Academy of Sciences, Szigony u. 43, Budapest H-1450, Hungary*
[b] *Institut de Recherche Interdisciplinaire en Biologie Humaine et Moleculaire, Universite Libre de Bruxelles, 1070 Brussels, Belgium*

Received 26 March 2007; received in revised form 27 June 2007; accepted 4 July 2007

Abstract

We investigated the effect of a synthetic cannabinoid, WIN 55,212-2 on excitatory postsynaptic currents (EPSCs) evoked by stimulation of Schaffer collaterals in CA1 pyramidal cells. Bath application of WIN 55,212-2 reduced the amplitude of EPSCs in dose-dependent manner tested between 0.01 nM and 30 μM. In rats and mice, this cannabinoid ligand inhibited excitatory synapses in two steps at the nM and μM concentrations. When the function of CB_1 cannabinoid receptors (CB_1R) was impaired, either by the application of a CB_1R antagonist AM251, or by using CB_1R knockout mice, WIN 55,212-2 in μM concentrations could still significantly reduced the amplitude of EPSCs. WIN 55,212-2 likely affected the efficacy of excitatory transmission only at presynaptic sites, since both at low and high doses the paired pulse ratio of EPSC amplitude was significantly increased. The inactive enantiomer, WIN 55,212-3, mimicked the effect of WIN 55,212-2 applied in high doses. In further experiments we found that the CB_1R-independent effect of 10 μM WIN 55,212-2 at glutamatergic synapses was fully abolished, when slices were pre-treated with ω-conotoxin GVIA, but not with ω-agatoxin IVA.

These data suggest that, in the hippocampus, WIN 55,212-2 reduces glutamate release from Schaffer collaterals solely via CB_1Rs in the nM concentration range, whereas in μM concentrations, WIN 55,212-2 suppresses excitatory transmission, in addition to activation of CB_1Rs, by directly blocking N-type voltage-gated Ca^{2+} channels independent of CB_1Rs.

Keywords: Brain slices; Glutamate; Transmitter release; Hippocampus; Pyramidal cell; Cannabinoids

1. Introduction

The type 1 cannabinoid receptors (CB_1Rs) have been shown to control the release of different neurotransmitters, but the mechanisms underlying the regulation of synaptic communication could substantially vary between brain regions (Freund et al., 2003). Pharmacological results, suggesting a presynaptic locus of action of cannabinoid receptor ligands, have been fully supported by immunohistochemical data. Several studies demonstrated at the electron microscopic level that CB_1Rs decorated both inhibitory and excitatory axon terminals (Katona et al., 1999, 2006; Kawamura et al., 2006). In addition, recent high-resolution quantitative studies established that CB_1Rs were found all around the axon membrane, but were enriched in the perisynaptic annulus and on preterminal segments, whereas immunolabelling was weaker in the synaptic active zone (Nyiri et al., 2005; Kawamura et al., 2006). This subcellular distribution of CB_1Rs might imply an action on several regulatory mechanisms of transmitter release, including the control of Ca^{2+} entry via voltage-dependent Ca^{2+} channels (primarily by receptors located in the perisynaptic annulus), the reduction of axonal conduction (by receptors present on the preterminal segments), or a direct action on exocytosis (Wilson et al., 2001; Diana and Marty, 2003).

In spite of the direct anatomical evidence, several pharmacological observations suggest that some synthetic

* Corresponding author. Tel.: +36 1 2109 400/387; fax: +36 1 210 9412.
E-mail address: hajos@koki.hu (N. Hájos).

0028-3908/$ - see front matter © 2007 Elsevier Ltd. All rights reserved.
doi:10.1016/j.neuropharm.2007.07.003

cannabinoid agonists (mainly WIN 55,212-2) could also have a CB_1R-independent action on synaptic glutamate release. This possibility has been fuelled primarily by experiments using CB_1R knockout mice. Our laboratory was the first to show that, in the absence of CB_1Rs, WIN 55,212-2 was still able to reduce excitatory, but not inhibitory postsynaptic currents in CA1 pyramidal neurons (Hájos et al., 2001). Moreover, WIN 55,212-2 was more potent in suppressing GABAergic than glutamatergic transmission (Hoffman and Lupica, 2000; Ohno-Shosaku et al., 2002; Hájos and Freund, 2002), providing further support for the possible presence of CB_1R-independent binding site at excitatory synapses. Importantly, AM251, a CB_1R antagonist prevented the reduction of synaptic inhibition after application of WIN 55,212-2, whereas glutamatergic transmission could still be suppressed by about 50% in the presence of AM251 (Hájos and Freund, 2002). In contrast to the above findings showing that hippocampal glutamatergic synapses were effectively regulated independent of CB_1Rs, electrophysiological data from other groups suggested that CB_1Rs were solely responsible for the cannabinoid modulation of excitatory synaptic transmission in the hippocampus (Ohno-Shosaku et al., 2002; Domenici et al., 2006; Takahashi and Castillo, 2006).

To shed light on the reasons behind the contradictory findings regarding the involvement of CB_1R-dependent vs. -independent mechanisms in the regulation of hippocampal excitatory synapses, we re-examined the effect of WIN 55,212-2 on monosynaptically evoked excitatory postsynaptic currents (EPSCs) in CA1 pyramidal cells. All these experiments were performed in a modified submerged recording conditions (Hájos et al., 2005).

2. Methods

Experiments were carried out according to the guidelines of the institutional ethical code and the Hungarian Act of Animal Care and Experimentation (1998. XXVIII. section 243/1998.). Male Wistar rats (14–18 days old), as well as wild type and CB_1R knockout mice (15–25 days old, CD1 strain) were used. The animals were deeply anaesthetized with isoflurane followed by decapitation. After opening the skull, the brain was quickly removed and immersed into ice-cold cutting solution containing (in mM: sucrose 252; KCl 2.5; $NaHCO_3$ 26; $CaCl_2$ 0.5; $MgCl_2$ 5; NaH_2PO_4 1.25; glucose 10). The solution had been bubbled with 95% O_2/5% CO_2 (carbogen gas) for at least 30 min before use. Thick horizontal slices (350 μm from mice and 400 μm from rats) were prepared using a Leica VT1000S Vibratome. The CA3 region was removed to prevent epileptic burst firings. The slices were stored in an interface type chamber containing ACSF (in mM: 126 NaCl, 2.5 KCl, 26 $NaHCO_3$, 2 $CaCl_2$, 2 $MgCl_2$, 1.25 NaH_2PO_4, and 10 glucose) at room temperature for at least 1 h before recording. After the initial incubation period, slices were transferred individually into a submerged type recording chamber.

Whole-cell patch-clamp recordings were obtained at 30–32 °C from CA1 pyramidal cells visualized by infrared DIC videomicroscopy (Zeiss Axioscope, Germany). Patch electrodes were pulled from borosilicate glass capillaries with an inner filament (1.5 mm O.D.; 1.12 mm I.D., Hilgenberg, Germany) using a Sutter P-87 puller. Electrodes (~3–6 MΩ) were filled with a solution containing (in mM) 80 CsCl, 60 Cs-gluconate, 3 NaCl, 1 $MgCl_2$, 10 HEPES, 2 Mg-ATP, and 5 QX-314 (pH 7.2–7.3 adjusted with CsOH; osmolarity 275–290 mOsm). Excitatory postsynaptic currents (EPSCs) were recorded at a holding potential of −65 mV. Slices were perfused with ACSF containing 70–100 μM picrotoxin to block inhibitory neurotransmission. The solution was bubbled with carbogen gas at room temperature and perfused at a flow rate of 3–4.5 ml/min in a slice chamber optimized for laminar flow to ensure the stability of the amplitude of evoked currents and a better oxygenation of submerged slices (Hájos et al., 2005). To evoke EPSCs, the stimulating electrode was placed in the stratum radiatum of CA1. Pairs of electrical stimuli separated by 50 ms were delivered via a theta glass pipette (Sutter Instrument Company, Novato, CA) filled with ACSF at 0.1 Hz using a Supertech timer and isolator (Supertech LTD, Pécs, Hungary, http://www.superte.ch). Access resistances (between 4 and 18 MΩ, compensated 65–70%) were frequently monitored and remained constant (±20%) during the period of analysis. Signals were recorded with a Multiclamp 700A (Molecular Devices, Sunnyvale, CA), filtered at 2 kHz, digitized at 6 kHz (National Instruments PCI-6024E A/D board, Austin, TX), and analyzed off-line with the EVAN program (courtesy of Prof. I. Mody, UCLA, CA).

The drug was perfused in a given concentration until the maximal effect was reached. The time needed for maximal inhibition was usually 6–8 min. To avoid the possible effect of a changing pH, we added the same amount of HCl to the control solution. The concentration response relationship for WIN 55,212-2 was obtained as follows: control EPSC amplitudes in a 2–3 min time window were compared to those measured after 10 min drug application for the same period of time. Only those experiments were included that had stable amplitudes at least for 10 min before drug application. After each experiment, the tubing made of Teflon was washed with ethanol for 10 min and with ACSF for 15 min. Each data point represents the mean ± SEM of the maximal inhibition of the evoked EPSCs ($n = 3–7$). EC_{50} values were estimated by fitting a curve to the points of the dose response plots obtained in rats or wild type mice using the equation of $f(x) = a/(1 + \exp(-(x - c)/b)) + (100 - a)/(1 + \exp(-(x - e)/d))$, where '$c$' and '$e$' give the values for high and low affinity binding sites, respectively. The data points obtained in the presence of AM251 or in CB1 knockout mice were fitted by the equation of $f(x) = a/(1 + \exp(-(x - c)/b))$, where '$c$' gives the value of EC_{50}. The curve fitting was done using Origin 7.5 (OriginLab Corporation, MA). The paired pulse ratio was calculated from the mean amplitude of the second EPSCs divided by the mean amplitude of the first EPSCs. The paired pulse ratio after drug treatment was compared with the control using Wilcoxon matched pairs test in Statistica 6.1 (Statsoft, Inc., Tulsa, OK). Data are presented as mean ± SEM.

Picrotoxin, WIN 55,212-2 and WIN 55,212-3 were purchased from Sigma-Aldrich, AM251 was obtained from Tocris, while ω-conotoxin GVIA and ω-agatonix IVA from Alomone Labs. For all experiments, WIN-55,212-2 was dissolved in 0.1N HCl giving a 20 mM stock solution stored at 4 °C. AM251 was dissolved in DMSO (100 mM) and stored at −20 °C. WIN 55,212-3 dissolved in DMSO (100 mM) was stored at 4 °C. From these stock solutions, the final dilution of drugs was done in ACSF containing picrotoxin under constant stirring and the prepared solution was bath applied. In control solutions, the vehicle was diluted in the same concentration as in the solutions containing drugs. Bovine serum albumin (BSA) was added in a concentration of 0.1 mg/ml to the solutions used for experiments with WIN 55,212-3.

3. Results

The effects of the cannabinoid agonist WIN 55,212-2 on EPSCs evoked by focal stimulation of Schaffer collaterals were measured in hippocampal CA1 pyramidal cells. First we performed concentration response analyses for the inhibitory effects of WIN 55,212-2 on evoked EPSC in rat slices (Fig. 1a). WIN 55,212-2 bath applied between the concentrations of 0.1 nM and 30 μM suppressed the amplitude of EPSCs in two steps. The apparent EC_{50} values from the fitted curve were 2.91 nM and 3.77 μM (Fig. 1c). Then we investigated the WIN 55,212-2-sensitivity of EPSCs, when AM251, a CB_1R specific antagonist was added to the bath solution in the concentration of 2 μM. In spite of the presence of AM251, the cannabinoid agonist could still reduce the amplitude of evoked currents, but only in the μM range (Fig. 1a). The estimated EC_{50} value for this effect was 1.69 μM (Fig. 1c).

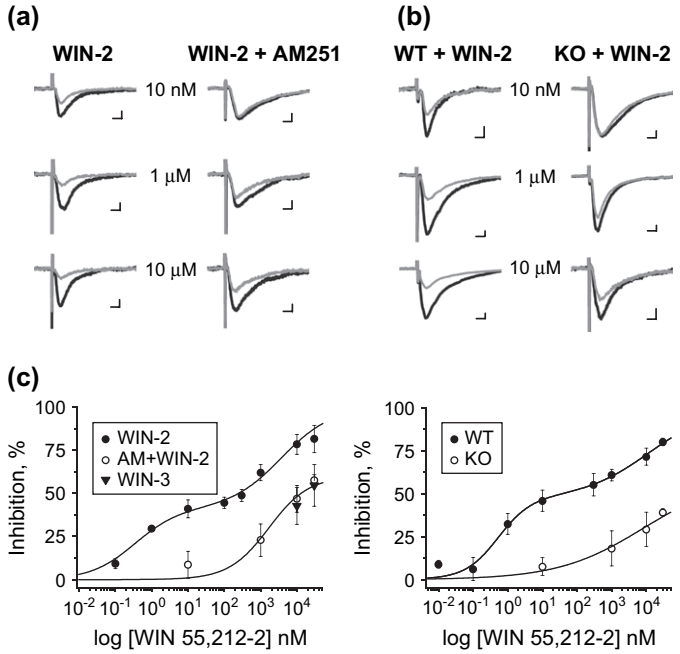

Fig. 1. The suppression of excitatory postsynaptic currents by WIN 55,212-2 via CB_1R-dependent and independent mechanisms in rats and mice. **a**, In rat slices, representative averaged records of 6–12 consecutive events taken before (black) and after 10 min of WIN 55,212-2 application (gray) in the absence or presence of 2 μM AM251 are superimposed. **b**, Averaged recordings of 8–12 consecutive EPSCs taken before (black) and after application of WIN 55,212-2 (WIN-2; gray) in wild type mice (WT) or in CB_1R knockouts (KO). The concentration of the CB_1R agonist is indicated for each example. Scale bars are 25 pA and 5 ms. **c**, Concentration-response relationship of WIN 55,212-2 in the inhibition of evoked EPSCs recorded in CA1 pyramidal cells in rats (left panel) and mice (right panel). The agonist inhibited the amplitude of events in two steps in rats and wild type mice, whereas only high doses of WIN 55,212-2 reduced synaptic currents in the presence of AM251 or in CB_1R knockout mice. Data obtained after application of the inactive enantiomer WIN 55,212-3 (WIN-3) are also included on the left graph.

In the next set of experiments, we examined the concentration response relationship for the WIN 55,212-2-induced reduction of evoked EPSCs in mouse slices (Fig. 1b). The sensitivity of synaptic currents for WIN 55,212-2 was tested between the concentrations of 0.01 nM and 30 μM. Similar to that observed in rat slices, the cannabinoid agonist also decreased the amplitude of EPSCs in two steps. The EC_{50} values estimated by fitting a curve to the points of the dose response plot were 1.91 nM and 12.1 μM (Fig. 1c). To reveal whether WIN 55,212-2 could still suppress excitatory transmission in CB_1R-independent manner in mice, we examined the effect of the cannabinoid agonist in CB_1R knockout animals. As shown in Fig. 1b, WIN 55,212-2 effectively reduced the amplitude of EPSCs, but only in the μM range. The apparent EC_{50} value estimated from the curve fitting was 8.32 μM (Fig. 1c).

These results obtained both in rats and mice suggest that WIN 55,212-2 in nM concentrations inhibits excitatory synaptic transmission exclusively via CB_1Rs, whereas in μM concentrations it has a mixed CB_1R-dependent and -independent effect on glutamatergic transmission at Schaffer collateral synapses.

By a comparison of the paired-pulse ratios of evoked EPSCs, we next investigated whether the CB_1R-independent action of WIN 55,212-2 is presynaptic, i.e. whether it is inhibiting glutamate release similar to that seen earlier for CB_1Rs. We first examined the effect of 10 nM WIN 55,212-2 on the paired-pulse ratio in rats and wild type mice. After drug application, the ratio significantly increased to $132.5 \pm 9.4\%$ of control in rats and to $129.5 \pm 14.2\%$ of control and mice (Fig. 2; $n = 5$ each, $p < 0.05$, Wilcoxon test). These data are in line with both electrophysiological and anatomical results, suggesting a presynaptic locus of CB_1R-dependent action. To check that the changes in the paired-pulse ratio were due to the activation of CB_1Rs, we contrasted these values before and after the application of 10 nM WIN 55,212-2 in the presence of AM251. As expected, the paired-pulse ratio was not altered ($98.4 \pm 6.1\%$, $n = 6$; $p > 0.1$, Wilcoxon test; Figs. 2a,c). Next we compared the paired-pulse ratio before and after the application of 30 μM WIN 55,212-2. The ratio of evoked currents was significantly increased to $145.1 \pm 5.3\%$ of control in rat slices ($n = 5$; $p < 0.05$, Wilcoxon test) and to $141.3 \pm 11.8\%$ in slices from wild type mice ($n = 7$; $p < 0.05$, Wilcoxon test). To reveal that the CB_1R-independent action of WIN 55,212-2 also modifies transmitter release, we investigated the paired-pulse ratio after application of 30 μM WIN 55,212-2, while 2 μM AM251 was included in the bath. The ratio of the amplitude of evoked EPSCs still significantly increased, to $136.4 \pm 8.4\%$ of control (Figs. 2a,c; $n = 7$, $p < 0.05$, Wilcoxon test). Similar to these results, 30 μM WIN 55,212-2 also raised the paired pulse ratio to $121.1 \pm 2.9\%$ of control in CB_1R knockout mice (Figs. 2b,c; $n = 6$, $p < 0.05$, Wilcoxon test). Thus, the CB_1R-independent effect of WIN 55,212-2 also appears to be presynaptic, reducing glutamate release from Schaffer collateral terminals.

As reported earlier (Shen and Thayer, 1998), WIN 55,212-2 in μM concentrations could directly alter Ca^{2+} currents independent of CB_1Rs, an effect that could be mimicked by its inactive enantiomer WIN 55,212-3. To test whether at glutamatergic axon terminals a similar mechanism would be responsible for the reduction of EPSC amplitude, WIN 55,212-3 was bath applied in two different concentrations to rat slices. This inactive enantiomer significantly suppressed the amplitude of evoked EPSCs by $42.8 \pm 10.7\%$ ($n = 5$) and $54.7 \pm 12.1\%$ ($n = 3$) in 10 μM and 30 μM concentrations, respectively (Fig. 1c). These effects were indistinguishable from those values, which were obtained in the presence of AM251 after application of 10 μM ($46.9 \pm 7.8\%$; $n = 5$) or 30 μM ($59.6 \pm 3.2\%$; $n = 4$) WIN 55,212-2 ($p > 0.1$, Mann–Whitney U-test). These results suggest that the CB_1R-independent action of WIN 55,212-2 on glutamatergic transmission might be due to the direct inhibition of Ca^{2+} entry into the presynaptic boutons.

To get deeper insight into the mechanisms underlying the CB_1R-independent effects of WIN 55,212-2, we specifically examined the involvement of voltage-gated Ca^{2+} channels in this process. Rat slices were pre-incubated either in 250 nM ω-agatoxin IVA (a specific blocker of P/Q-type Ca^{2+} channels) or in 250 nM ω-conotoxin GVIA (a specific inhibitor of N-type Ca^{2+} channels) at least for an hour. After placing the pre-treated slices in the recording chamber, we bath

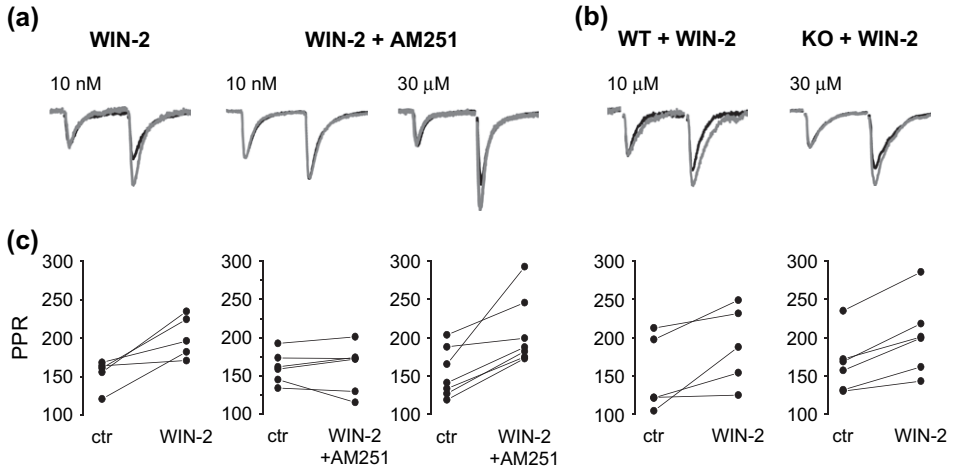

Fig. 2. Both CB_1R-dependent and -independent effects of WIN 55,212-2 enhance the paired-pulse facilitation of evoked EPSCs. **a**, In rat slices, the paired-pulse ratio was similarly increased after application of WIN 55,212-2 (WIN-2) in low concentrations or in high concentrations, when 2 μM AM251 was present in the bath, as seen on the scaled representative averages of 10–12 consecutive events before (black) and after (gray) the drug treatments. However, the paired pulse ratio remained unchanged, when WIN 55,212-2 in 10 nM concentration was co-applied with AM 251. **b**, Averaged recordings of consecutive EPSCs taken before (black) and after application of WIN 55,212-2 (gray) in wild type mice (WT) or in CB_1R knockouts (KO) were scaled to indicate the enhancement of the paired-pulse ratio. The stimulus artefacts were removed from the traces. **c**, The paired-pulse ratios (PPR) calculated from each recordings in control conditions (ctr) and after drug application are presented for corresponding experiments.

applied 10 μM WIN 55,212-2 in the presence of 2 μM AM251. In slices pre-treated with ω-agatoxin IVA, the amplitude of EPSCs was reduced by 39.7 ± 8.3% ($n = 4$, $p < 0.05$, Wilcoxon test; Fig. 3a), whereas there was no change in the synaptic currents after application of WIN 55,212-2 in slices pre-incubated with ω-conotoxin GVIA (95.8 ± 3.2% of control, $n = 6$, $p > 0.1$, Wilcoxon test; Fig. 3b). The results of these experiments suggest that the CB_1R-independent action of WIN 55,212-2 at glutamatergic synapses is mediated via inhibition of N-type Ca^{2+} channels.

4. Discussion

Our data presented here demonstrate that excitatory synapses of Schaffer collaterals in CA1 pyramidal cells are inhibited by WIN 55,212-2 both via CB_1R-dependent and independent mechanisms. In low nM concentrations, this cannabinoid ligand solely acts as a CB_1R agonist reducing glutamate release. In contrast, WIN 55,212-2 in the μM range suppresses glutamatergic synaptic transmission via activation of CB_1Rs as well as inhibiting N-type Ca^{2+} channels independent of CB_1Rs.

Shen et al., (1996) were the first to show that excitatory transmission in the hippocampus could be reduced by WIN 55,212-2, a finding that has been strengthened later by several other laboratories (Misner and Sullivan, 1999; Al-Hayani and Davies, 2000; Hájos and Freund, 2002; Ohno-Shosaku et al., 2002; Hoffman et al., 2003). Similarly to that observed in the hippocampus, WIN 55,212-2 was also shown to suppress excitatory synapses in other brain regions, including the cerebellum (Levenes et al., 1998; Takahashi and Linden, 2000), neocortex (Domenici et al., 2006), basolateral amygdala (Azad et al., 2003; Domenici et al., 2006), or striatum (Gerdeman and Lovinger, 2001; Huang et al., 2001). In earlier studies, the lack of immunostaining for CB_1Rs at excitatory terminals (Katona et al., 1999; Hájos et al., 2000), taken together with experiments showing that WIN 55,212-2 could significantly reduce glutamate release in CB_1R knockouts (Hájos et al., 2001; Kofalvi et al., 2003), fuelled the concept that distinct cannabinoid receptors control synaptic excitation and inhibition. This interpretation was supported by the unequivocal demonstration of high densities of CB_1Rs on GABAergic axons, while adjacent glutamatergic terminals remained negative (Katona et al., 1999; Hájos et al., 2000; Nyiri et al., 2005), as well as by the complete disappearance of cannabinoid sensitivity of IPSCs in CB_1R knockouts (Hájos et al., 2000, 2001; Varma et al., 2001; Wilson et al., 2001). Moreover, Hájos and Freund (2002) showed that AM251 could fully antagonise the effect of WIN 55,212-2 at GABAergic, but not at glutamatergic synapses, further strengthening the existence of a novel cannabinoid-sensitive binding site at hippocampal excitatory synapses. Recently this concept was substantially challenged both by anatomical and electrophysiological experiments, including studies from our own laboratory. First, using a different type of antibody, CB_1Rs were convincingly shown to be present on glutamatergic terminals, although in much smaller quantities than on GABAergic axons (Katona et al., 2006; Kawamura et al., 2006). Specificity of the staining has been confirmed in CB_1R knockout tissue. Second, excitatory transmission was found to be insensitive to the application of WIN 55,212-2 in distinct strains of transgenic mice lacking CB_1Rs (Ohno-Shosaku et al., 2002; Domenici et al., 2006; Takahashi and Castillo, 2006). The discrepancy between earlier and recent data might be resolved by the present findings suggesting that at low nM concentrations WIN 55,212-2 specifically activates CB_1Rs, whereas in the μM range the agonist could further reduce glutamate release via direct inhibition

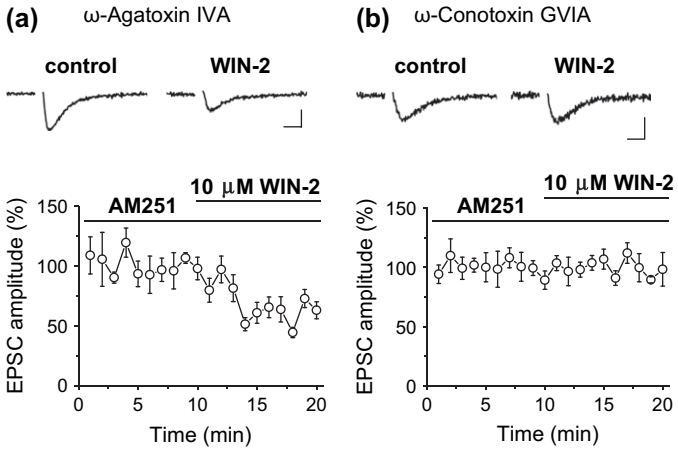

Fig. 3. CB_1R-independent effect of WIN 55,212-2 at excitatory synapses is mediated via inhibition of N-type Ca^{2+} channels. Rat slices were pre-treated with 250 nM ω-agatoxin IVA or with ω-conotoxin GVIA at least for an hour before the experiments. To block CB_1Rs, 2 μM AM251 was included in the solution. **a**, In slices pre-incubated with ω-agatoxin IVA, 10 μM WIN 55,212-2 effectively reduced the amplitude of evoked EPSCs as shown on the averaged recordings of 8–10 consecutive events before (right) and after (left) drug application. The bottom graph calculated from 4 experiments indicates that wash-in of 10 μM WIN 55,212-2 significantly suppressed the EPSC amplitude. **b**, In contrast, when 10 μM WIN 55,212-2 was applied onto slices that were pre-incubated in ω-conotoxin GVIA, no change in the amplitude of EPSC was observed. Averaged traces before (right) and after (left) drug application are shown. The stimulus artefacts were removed from the traces. Scale bars are 20 pA and 5 ms. The bottom plot obtained from 6 experiments shows that WIN 55,212-2 could not alter the glutamatergic transmission, indicating that, independent of CB_1Rs, N-type voltage-gated Ca^{2+} channels are required for presynaptic inhibition by this cannabinoid compound applied in high doses.

of presynaptic Ca^{2+} entry independent of CB_1Rs (present study; Shen and Thayer, 1998; Kofalvi et al., 2007). This difference in the specificity of WIN 55,212-2 as a function of its concentration can be noticed already in studies reported by the Kano laboratory. WIN 55,212-2 in 100 nM caused a large reduction in the amplitude of EPSCs in wild type mice, but in CB_1R knockouts less then 5% suppression was found (Ohno-Shosaku et al., 2002). However, in 2 μM concentration, WIN 55,212-2 inhibited excitatory transmission by about 20% in CB_1R knockout mice, an effect that was unaltered in the presence of CB_1R antagonists (Kawamura et al., 2006). Further support to the hypothesis that WIN 55,212-2 in μM concentrations can reduce excitatory transmission via CB_1R-independent mechanisms come from the work of Hoffman et al. (2005), where the authors showed that in the presence of AM251, 3 μM WIN 55,212-2 significantly (appr. by 40%) reduced excitation. This view, however, is not supported by two recent studies using CB_1R knockout animals, in which 5 μM WIN 55,212-2 was found to be completely ineffective at excitatory synapses (Domenici et al., 2006; Takahashi and Castillo, 2006). The explanation for these negative findings remains to be investigated.

Another finding of the present study that deserves discussion is that the effective concentration of WIN 55,212-2 that significantly inhibited the amplitude of synaptic events in slice preparations was 100 fold lower than it was earlier reported by several laboratories using similar recording circumstances (Takahashi and Linden, 2000; Robbe et al., 2001; Hájos and Freund, 2002; Hoffman et al., 2005). Compared to earlier studies, we changed some conditions that could account for the distinct efficacy of WIN 55,212-2, which allowed clearly separating CB_1R-dependent and independent effects. The preparation and storage of slices, as well as the flow rate of the solution during recordings was modified: slices were cut in a sucrose containing solution and stored in an interface-type chamber before recordings, and a higher flow rate was used in the recording chamber, ensuring a better oxygenation of the tissue (Hájos et al., 2005). Under these circumstances, the amplitude of evoked synaptic currents became more stable, and, more importantly, the efficacy of WIN 55,212-2 to suppress excitatory synapses was comparable with those measured in cell cultures (Ohno-Shosaku et al., 2002) or binding assays (Felder et al., 1995).

Several studies in different brain regions suggested that the CB_1R-independent effect of WIN 55,212-2 might significantly alter synaptic communication among neurons (Hájos et al., 2001; Pistis et al., 2004; Kofalvi et al., 2005; Matyas et al., 2006), presumably through a direct blockade of Ca^{2+} entry at the presynaptic terminals (Shen and Thayer, 1998; Kofalvi et al., 2007). In the present study, we provided evidence that the CB_1R-independent effect of WIN 55,212-2 at glutamatergic synapses was mediated by inhibiting N-type Ca^{2+} channels.

The question arises whether WIN 55,212-2 in high doses could also alter GABAergic transmission independent of CB_1Rs, since GABA release from CB_1R-expressing axon terminals is known to depend on N-type Ca^{2+} channel activation (Wilson et al., 2001). Indeed, we found that in CB_1R knockout mice 10 μM WIN 55,212-2 substantially reduced the amplitude of IPSCs to $62.8 \pm 20.5\%$ of control ($n = 4$). In contrast, when CB_1R function was intact, both low and high doses of WIN 55,212-2 led to a comparable reduction of IPSC amplitudes (in 3 nM: $47.9 \pm 15.4\%$ of control, $n = 4$; in 10 μM: $45.2 \pm 19.7\%$ of control, $n = 4$), similar to results obtained earlier (Hájos and Freund, 2002). The reason why WIN 55,212-2 in 10 μM concentration did not result in an

additional suppression of inhibitory events in the presence of functional CB_1Rs may be explained by the fact that CB_1R-dependent inhibition of GABAergic currents is entirely due to blocking N-type Ca^{2+} channels, which occludes the CB_1R -independent action of WIN 55,212-2 directly on the same Ca^{2+} channels. Testing this hypothesis, and other novel aspects of cannabinoid modulation of GABAergic transmission is the subject of another line of investigations in our laboratory.

The question arises whether at glutamatergic synapses, under some experimental conditions, endocannabinoids can reduce the efficacy of neurotransmission via CB_1R-dependent and -independent mechanisms, similar to high concentrations of WIN 55,212-2, which can modify Ca^{2+} entry directly. Some results indeed imply that endocannabinoids could directly inhibit different types of voltage-gated Ca^{2+} channels independent of CB_1Rs (Chemin et al., 2001; Fisyunov et al., 2006), yet other data suggest that endocannabinoids released upon depolarization of a postsynaptic neuron (or exogenously applied) are unable to suppress excitatory transmission in CB_1R knockout mice (Ohno-Shosaku et al., 2002; Straiker and Mackie, 2005, but see Rouach and Nicoll, 2003). Nevertheless, the importance of identifying a CB_1R-independent binding site for WIN 55,212-2 as N-type Ca^{2+} channels at excitatory terminals lies in resolving some contradictions in pharmacological and behavioural studies that emerged partly due to the use of WIN 55,212-2 in widely varying concentrations (see a thorough discussion of this issue in Haller et al., 2007).

Acknowledgements

This work was supported by the Howard Hughes Medical Institute, by EU (LSHM-CT-2004-005166), NKFP 1A/002/2004, OTKA Hungary (T46820), and NIH (NS30549). N.H. is the recipient of a Wellcome Trust International Senior Research Fellowship. We thank Dr. István Katona for advice and comments on the manuscript, and Dr. Szabolcs Káli for help with curve fitting. The excellent technical assistance of Katalin Lengyel, Emőke Simon and Katalin Iványi is also gratefully acknowledged.

References

Al-Hayani, A., Davies, S.N., 2000. Cannabinoid receptor mediated inhibition of excitatory synaptic transmission in the rat hippocampal slice is developmentally regulated. British Journal of Pharmacology 131, 663–665.

Azad, S.C., Eder, M., Marsicano, G., Lutz, B., Zieglgansberger, W., Rammes, G., 2003. Activation Of The Cannabinoid Receptor Type 1 Decreases Glutamatergic And Gabaergic Synaptic Transmission In The Lateral Amygdala Of The Mouse. In: Learning & Memory, vol. 10. Cold Spring Harbor, NY, pp. 116–128.

Chemin, J., Monteil, A., Perez-Reyes, E., Nargeot, J., Lory, P., 2001. Direct inhibition of T-type calcium channels by the endogenous cannabinoid anandamide. EMBO Journal 20, 7033–7040.

Diana, M.A., Marty, A., 2003. Characterization of depolarization-induced suppression of inhibition using paired interneuron—Purkinje cell recordings. Journal of Neuroscience 23, 5906–5918.

Domenici, M.R., Azad, S.C., Marsicano, G., Schierloh, A., Wotjak, C.T., Dodt, H.U., Zieglgansberger, W., Lutz, B., Rammes, G., 2006. Cannabinoid receptor type 1 located on presynaptic terminals of principal neurons in the forebrain controls glutamatergic synaptic transmission. Journal of Neuroscience 26, 5794–5799.

Felder, C.C., Joyce, K.E., Briley, E.M., Mansouri, J., Mackie, K., Blond, O., Lai, Y., Ma, A.L., Mitchell, R.L., 1995. Comparison of the pharmacology and signal transduction of the human cannabinoid CB1 and CB2 receptors. Molecular Pharmacology 48, 443–450.

Fisyunov, A., Tsintsadze, V., Min, R., Burnashev, N., Lozovaya, N., 2006. Cannabinoids modulate the P-type high-voltage-activated calcium currents in purkinje neurons. Journal of Neurophysiology 96, 1267–1277.

Freund, T.F., Katona, I., Piomelli, D., 2003. The role of endogenous cannabinoids in synaptic signaling. Physiological Reviews 83, 1017–1066.

Gerdeman, G., Lovinger, D.M., 2001. CB1 cannabinoid receptor inhibits synaptic release of glutamate in rat dorsolateral striatum. Journal of Neurophysiology 85, 468–471.

Hájos, N., Freund, T.F., 2002. Pharmacological separation of cannabinoid sensitive receptors on hippocampal excitatory and inhibitory fibers. Neuropharmacology 43, 503–510.

Hájos, N., Katona, I., Naiem, S.S., MacKie, K., Ledent, C., Mody, I., Freund, T.F., 2000. Cannabinoids inhibit hippocampal GABAergic transmission and network oscillations. European Journal of Neuroscience 12, 3239–3249.

Hájos, N., Ledent, C., Freund, T.F., 2001. Novel cannabinoid-sensitive receptor mediates inhibition of glutamatergic synaptic transmission in the hippocampus. Neuroscience 106, 1–4.

Hájos, N., Mann, E.O., Freund, T.F., Paulsen, O., 2005. Oxygen content of extracellular solution determines the stability of network oscillations in submerged hippocampal slices. 35th Society for Neuroscience Meeting, 275.18.

Haller, J., Mátyás, F., Soproni, K., Varga, B., Barsy, B., Németh, B., Mikics, É., Freund, T.F., Hájos, N., 2007. Correlated species differences in the effects of cannabinoid ligands on anxiety and on GABAergic/glutamatergic synaptic transmission. European Journal of Neuroscience 25, 2445–2456.

Hoffman, A.F., Lupica, C.R., 2000. Mechanisms of cannabinoid inhibition of GABA(A) synaptic transmission in the hippocampus. Journal of Neuroscience 20, 2470–2479.

Hoffman, A.F., Riegel, A.C., Lupica, C.R., 2003. Functional localization of cannabinoid receptors and endogenous cannabinoid production in distinct neuron populations of the hippocampus. European Journal of Neuroscience 18, 524–534.

Hoffman, A.F., Macgill, A.M., Smith, D., Oz, M., Lupica, C.R., 2005. Species and strain differences in the expression of a novel glutamate-modulating cannabinoid receptor in the rodent hippocampus. European Journal of Neuroscience 22, 2387–2391.

Huang, C.C., Lo, S.W., Hsu, K.S., 2001. Presynaptic mechanisms underlying cannabinoid inhibition of excitatory synaptic transmission in rat striatal neurons. Journal of Physiology 532, 731–748.

Katona, I., Sperlagh, B., Sik, A., Kafalvi, A., Vizi, E.S., Mackie, K., Freund, T.F., 1999. Presynaptically located CB1 cannabinoid receptors regulate GABA release from axon terminals of specific hippocampal interneurons. Journal of Neuroscience 19, 4544–4558.

Katona, I., Urban, G.M., Wallace, M., Ledent, C., Jung, K.M., Piomelli, D., Mackie, K., Freund, T.F., 2006. Molecular composition of the endocannabinoid system at glutamatergic synapses. Journal of Neuroscience 26, 5628–5637.

Kawamura, Y., Fukaya, M., Maejima, T., Yoshida, T., Miura, E., Watanabe, M., Ohno-Shosaku, T., Kano, M., 2006. The CB1 cannabinoid receptor is the major cannabinoid receptor at excitatory presynaptic sites in the hippocampus and cerebellum. Journal of Neuroscience 26, 2991–3001.

Kofalvi, A., Vizi, E.S., Ledent, C., Sperlagh, B., 2003. Cannabinoids inhibit the release of [3H]glutamate from rodent hippocampal synaptosomes via a novel CB1 receptor-independent action. European Journal of Neuroscience 18, 1973–1978.

Kofalvi, A., Rodrigues, R.J., Ledent, C., Mackie, K., Vizi, E.S., Cunha, R.A., Sperlágh, B., 2005. Involvement of cannabinoid receptors in the regulation

of neurotransmitter release in the rodent striatum: a combined immunochemical and pharmacological analysis. Journal of Neuroscience 25, 2874–2884.

Kofalvi, A., Pereira, F.M., Rebola, N., Rodrigues, R.J., Oliveira, C.R., Cunha, R.A., 2007. Anandamide and NADA bi-directionally modulate presynaptic Ca^{2+} levels and transmitter release in the hippocampus. British Journal of Pharmacology 151, 551–563.

Levenes, C., Daniel, H., Soubrie, P., Crepel, F., 1998. Cannabinoids decrease excitatory synaptic transmission and impair long-term depression in rat cerebellar Purkinje cells. Journal of Physiology 510, 867–879.

Matyas, F., Yanovsky, Y., Mackie, K., Kelsch, W., Misgeld, U., Freund, T.F., 2006. Subcellular localization of type 1 cannabinoid receptors in the rat basal ganglia. Neuroscience 137, 337–361.

Misner, D.L., Sullivan, J.M., 1999. Mechanism of cannabinoid effects on long-term potentiation and depression in hippocampal CA1 neurons. Journal of Neuroscience 19, 6795–6805.

Nyiri, G., Cserep, C., Szabadits, E., Mackie, K., Freund, T.F., 2005. CB1 cannabinoid receptors are enriched in the perisynaptic annulus and on preterminal segments of hippocampal GABAergic axons. Neuroscience 136, 811–822.

Ohno-Shosaku, T., Tsubokawa, H., Mizushima, I., Yoneda, N., Zimmer, A., Kano, M., 2002. Presynaptic cannabinoid sensitivity is a major determinant of depolarization-induced retrograde suppression at hippocampal synapses. Journal of Neuroscience 22, 3864–3872.

Pistis, M., Perra, S., Pillolla, G., Melis, M., Gessa, G.L., Muntoni, A.L., 2004. Cannabinoids modulate neuronal firing in the rat basolateral amygdala: evidence for CB1- and non-CB1-mediated actions. Neuropharmacology 46, 115–125.

Robbe, D., Alonso, G., Duchamp, F., Bockaert, J., Manzoni, O.J., 2001. Localization and mechanisms of action of cannabinoid receptors at the glutamatergic synapses of the mouse nucleus accumbens. Journal of Neuroscience 21, 109–116.

Rouach, N., Nicoll, R.A., 2003. Endocannabinoids contribute to short-term but not long-term mGluR-induced depression in the hippocampus. European Journal of Neuroscience 18, 1017–1020.

Shen, M., Thayer, S.A., 1998. The cannabinoid agonist Win 55,212-2 inhibits calcium channels by receptor-mediated and direct pathways in cultured rat hippocampal neurons. Brain Research 783, 77–84.

Shen, M., Piser, T.M., Seybold, V.S., Thayer, S.A., 1996. Cannabinoid receptor agonists inhibit glutamatergic synaptic transmission in rat hippocampal cultures. Journal of Neuroscience 16, 4322–4334.

Straiker, A., Mackie, K., 2005. Depolarization-induced suppression of excitation in murine autaptic hippocampal neurones. Journal of Physiology 569, 501–517.

Takahashi, K.A., Castillo, P.E., 2006. The CB1 cannabinoid receptor mediates glutamatergic synaptic suppression in the hippocampus. Neuroscience 139, 795–802.

Takahashi, K.A., Linden, D.J., 2000. Cannabinoid receptor modulation of synapses received by cerebellar Purkinje cells. Journal of Neurophysiology 83, 1167–1180.

Varma, N., Carlson, G.C., Ledent, C., Alger, B.E., 2001. Metabotropic glutamate receptors drive the endocannabinoid system in hippocampus. Journal of Neuroscience 4, 4.

Wilson, R.I., Kunos, G., Nicoll, R.A., 2001. Presynaptic specificity of endocannabinoid signaling in the hippocampus. Neuron 31, 453–462.

dc_71_10

12. számú melléklet

EJN fens EUROPEAN JOURNAL OF NEUROSCIENCE
dc_71_10
European Journal of Neuroscience, Vol. 29, pp. 319–327, 2009 doi:10.1111/j.1460-9568.2008.06577.x

SYNAPTIC MECHANISMS

TECHNICAL SPOTLIGHT
Maintaining network activity in submerged hippocampal slices: importance of oxygen supply

Norbert Hájos,[1,*] Tommas J. Ellender,[2,*] Rita Zemankovics,[1] Edward O. Mann,[2] Richard Exley,[2] Stephanie J. Cragg,[2] Tamás F. Freund[1] and Ole Paulsen[2]
[1]Department of Cellular and Network Neurobiology, Institute of Experimental Medicine, Hungarian Academy of Sciences, Szigony u. 43, 1083 Budapest, Hungary
[2]Department of Physiology, Anatomy and Genetics, University of Oxford, Oxford, UK

Keywords: GABAergic interneuron, gamma oscillation, hippocampus, *in vitro*, rodent, sharp wave–ripple oscillation

Abstract

Studies in brain slices have provided a wealth of data on the basic features of neurons and synapses. In the intact brain, these properties may be strongly influenced by ongoing network activity. Although physiologically realistic patterns of network activity have been successfully induced in brain slices maintained in interface-type recording chambers, they have been harder to obtain in submerged-type chambers, which offer significant experimental advantages, including fast exchange of pharmacological agents, visually guided patch-clamp recordings, and imaging techniques. Here, we investigated conditions for the emergence of network oscillations in submerged slices prepared from the hippocampus of rats and mice. We found that the local oxygen level is critical for generation and propagation of both spontaneously occurring sharp wave–ripple oscillations and cholinergically induced fast oscillations. We suggest three ways to improve the oxygen supply to slices under submerged conditions: (i) optimizing chamber design for laminar flow of superfusion fluid; (ii) increasing the flow rate of superfusion fluid; and (iii) superfusing both surfaces of the slice. These improvements to the recording conditions enable detailed studies of neurons under more realistic conditions of network activity, which are essential for a better understanding of neuronal network operation.

Introduction

Much insight into the cellular basis of brain function stems from experiments conducted in acute brain slices *in vitro* (Yamamoto & McIlwain, 1966; Skrede & Westgaard, 1971). However, there are notable differences between brain slices and the intact brain in both the amount and patterns of activity, especially in relation to the rhythmic synchronous neuronal events as reflected in the electroencephalogram (Steriade, 2001). Studies of neurons and synapses under more realistic conditions would benefit from *in vitro* preparations retaining local network activity. Recently, by altering the ionic composition of the superfusion media, or by the addition of pharmacological agents, attempts have been made to capture naturalistic network activity in brain slice preparations. This has been particularly successful in interface-type slice chambers, in which brain slices are held at the interface between artificial cerebrospinal fluid (ACSF) and humidified gas (e.g. Fisahn *et al.*, 1998; Sanchez-Vives & McCormick, 2000; Kubota *et al.*, 2003; Maier *et al.*, 2003). Maintaining physiologically relevant network activity in submerged slices has proven much harder, but, if successful, would offer important experimental advantages over interface conditions, including faster exchange of pharmacological agents, visually guided patch-clamp recordings and advanced imaging techniques. Previously, synchronous network activity in submerged slices has been recorded only transiently (McMahon *et al.*, 1998; Kawaguchi, 2001; Gloveli *et al.*, 2005). Recently, however, sustained network oscillations were successfully recorded in submerged hippocampal slices at increased flow rates of superfusion solution (Hájos *et al.*, 2004; Mann *et al.*, 2005; Wu *et al.*, 2005).

Here, we explored conditions conducive to the emergence of sharp wave–ripple oscillations and fast oscillations in submerged hippocampal slices. We found that the local oxygen level in the superfusion fluid is a critical factor for the generation and propagation of network activity. In addition, we describe ways to improve oxygen supply to submerged brain slices, including the use of a new type of slice chamber with dual-surface superfusion.

Materials and methods

All experiments were carried out in accordance with the UK Animals (Scientific Procedures) Act (1986) and the Hungarian Act of Animal Care and Experimentation (1998, XXVIII, section 243/1998), and with the guidelines of the institutional ethical code. Male Wistar rats (postnatal day 14–20; Harlan UK, Bicester, UK, or Charles River Hungary, Budapest) or CD1 mice (postnatal day 16–18; Charles River,

Correspondence: Dr N. Hájos, as above.
E-mail: hajos@koki.hu

*N.H. and T.J.E. contributed equally to this work.

Received 29 February 2008, revised 8 November 2008, accepted 13 November 2008

Hungary, Budapest) were deeply anaesthetized with isoflurane and decapitated. Following decapitation, the brain was quickly removed into ice-cold cutting solution. Transverse hippocampal slices 400–450 μm in thickness were prepared using a Leica VT1000S microtome (Leica, Nussloch, Germany), and kept in an interface-type holding chamber at room temperature for at least 60 min before recording in standard or modified ACSF. The standard ACSF was composed of 126 mM NaCl, 2.5 mM KCl, 1.25 mM NaH_2PO_4, 2 mM $MgCl_2$, 2 mM $CaCl_2$, 26 mM $NaHCO_3$, and 10 mM glucose, prepared with ultrapure water and bubbled with 95% O_2/5% CO_2 (carbogen gas), pH 7.2–7.4. All experiments were performed using rat hippocampal slices, except the investigation of the propagation of network activities from CA3 to CA1, which was performed in slices prepared from mice. Recordings were made in either an 'Oslo'-style interface chamber or in commercially available submerged-type slice chambers (Luigs & Neumann, Ratingen, Germany, and MED64 probes, Alpha MED Sciences, Osaka, Japan). In preliminary experiments, we found that persistent oscillations in these conventional submerged-type slice chambers were only achieved with a flow rate exceeding 10 mL/min, similar to previous observations of hippocampal network activity (Wu *et al.*, 2005). Adding a dye to the superfusion fluid to visualize the flow, we noticed that the solution tended to flow along the edges of these chambers. The chamber design was therefore modified in either of two ways. First, in order to reduce the volume of the chamber and direct the superfusion fluid over the slice, an inert plastic insert was used (Fig. 1A and B). These plastic inserts were used in all experiments in which the effect of flow rate on generation of network oscillations was investigated. The second modification allowed a double superfusion system to be used (Supertech Ltd, Pecs, Hungary; http://www.super-tech.eu). In this design, the slices were placed on a mesh glued between two plastic rings with a thickness of 2 mm. Two separate fluid inlets allowed ACSF to flow separately above and below the slice (Fig. 1C–F). This second design was only used to study the propagation of network activity from CA3 to CA1.

Measurement of oxygen saturation in the superfusate

The local oxygen saturation of the ACSF was measured 50–100 μm vertically above the CA3 region of the slice with an optode (tip diameter ~50 μm; Microx TX3, PreSens GmbH, Germany). Vertical adjustment of the optode between 50 and 100 μm above the slice did not cause any substantial change in measured values at a given flow rate. The sensor was calibrated as follows: 2–3 mM sodium sulfite (Na_2SO_3) was used to eliminate dissolved oxygen from non-bubbled

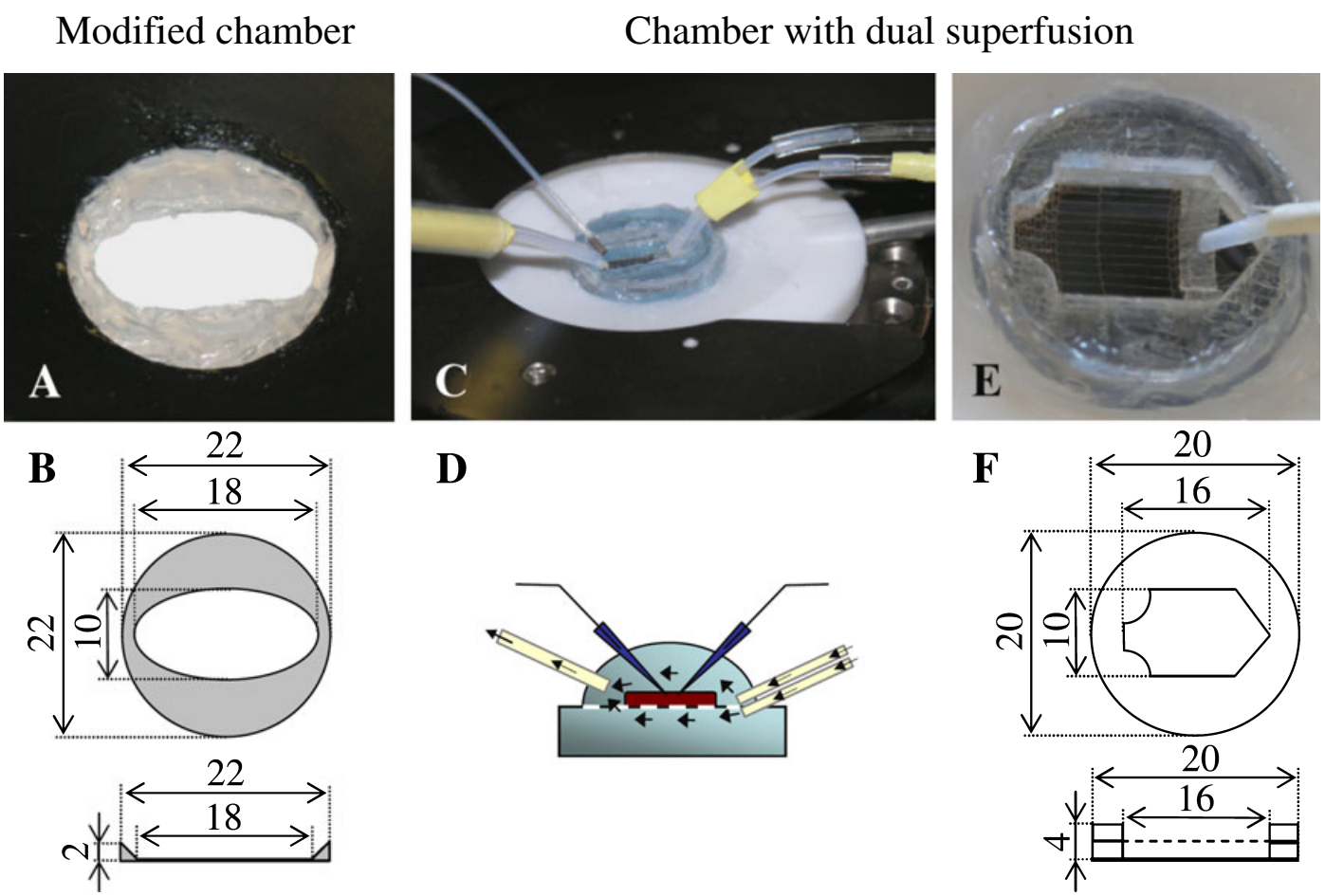

FIG. 1. Modified submerged slice chambers with single and dual superfusion. (A) Commercially available standard submerged slice chamber modified with an inert plastic insert to optimize the flow of artificial cerebrospinal fluid (ACSF) across the slice. (B) Scaled drawings of the top view and the cross-section of the chamber insert (in mm). (C) Low magnification of a submerged slice chamber with two fluid inlets and one outlet. (D) Schematic diagram of the flow in the dual superfusion chamber. (E) Picture taken at higher magnification of a chamber insert developed for dual superfusion. In this design, the slices were placed on a mesh glued between two plastic rings with a thickness of 2 mm. Two separate fluid inlets allowed ACSF to flow separately above and below the slice. (F) Scaled drawing (in mm) of the insert shown in E.

ACSF, to give 0% oxygen, and 95% oxygen was achieved in ACSF by bubbling for 1 h with 95% O_2/5% CO_2. Thus, the maximal P_{O_2} in ACSF at room temperature was estimated to be ~720 Torr. In a subset of experiments, ACSF bubbled with a mixture of 95% N_2/5% CO_2 was used to change the oxygen level in the chamber while retaining a constant flow rate.

Measurement of oxygen saturation within the slice tissue

Oxygen was measured within submerged hippocampal slices using fast-scan cyclic voltammetry at carbon-fibre microelectrodes (fibre diameter 7 μm, tip length 20–30 μm, fabricated in-house) and a Millar voltammeter (J. Millar, Barts & the London School of Medicine and Dentistry, UK), using methods similar to those described previously for the detection of other electroactive biological substances, e.g. dopamine (Cragg & Greenfield, 1997; Cragg, 2003; Exley *et al.*, 2008). For the detection of oxygen specifically, the applied voltage was a triphasic waveform scanning from 0.0 to +0.8 V to −1.4 V and back to 0.0 V (vs. Ag/AgCl), as described previously (Venton *et al.*, 2003), with a scan rate of 880 V/s and a sampling frequency of 8 Hz. The peak reduction current for oxygen was detected between −1.3 and −1.4 V. The bath temperature was 32 °C. Currents due to oxygen were determined after subtraction of the background current that results from the charging of the electrode as well as exposure to the brain tissue environment. Currents were normalized to the current observed in solution at a flow rate of 6 mL/min, which was subsequently set to 80% saturation as measured with the optode at this perfusion speed.

Measurements were made outside of the tissue (50–100 μm above the surface) as well as 50 and 150 μm below the upper surface of the slice in the CA3 pyramidal cell layer. Perfusion speeds were 6, 3 or 1.8 mL/min. For a given flow rate and electrode depth, a steady-state background measurement was first obtained in oxygen-free ACSF (bubbled with 95% N_2/5% CO_2); oxygen-saturated buffer (bubbled with 95% O_2/5% CO_2) was then applied, and the increase in detected oxygen was recorded. The slice was thoroughly superfused with oxygen-free ACSF between each change in flow rate or change in electrode placement.

Sharp wave–ripple oscillations

Slicing of rat hippocampus was performed in cutting solution containing 124 mM NaCl, 3 mM KCl, 1.25 mM KH_2PO_4, 5 mM $MgSO_4$, 3.4 mM $CaCl_2$, 26 mM $NaHCO_3$, and 10 mM glucose, pH 7.2–7.4, bubbled with carbogen gas. Storage and recording were done in modified ACSF containing 124 mM NaCl, 3 mM KCl, 1.25 mM KH_2PO_4, 1 mM $MgSO_4$, 3 mM $CaCl_2$, 26 mM $NaHCO_3$, and 10 mM glucose. Slices were mounted on planar 8 × 8 microelectrode arrays (electrode size, 50 × 50 μm; interpolar distance, 150 μm; Panasonic MED-P2105, Alpha MED Sciences), and maintained in a submerged condition at 32 °C, superfused with modified ACSF at 1.2–6 mL/min. Spontaneous field potentials from all 64 recording electrodes were acquired at 5 kHz, using the Panasonic MED64 system (Alpha MED Sciences).

Data were analysed off-line using IGOR Pro (Wavemetrics, Lake Oswego, OR, USA). Continuous MED64 recordings were divided into 10-s segments. Each segment was analysed for the incidence and amplitude of sharp waves. For sharp wave detection, recordings were filtered between 0.1 and 20 Hz, and sharp waves were detected as voltage fluctuations of more than two standard deviations above the baseline value, with a duration of more than 40 ms.

Cholinergically induced oscillations and unit recordings

Cutting solution for preparing slices from rat or mouse hippocampus contained 252 mM sucrose, 2.5 mM KCl, 26 mM $NaHCO_3$, 1 mM $CaCl_2$, 5 mM $MgCl_2$, 1.25 mM NaH_2PO_4, and 10 mM glucose, bubbled with carbogen gas. Standard ACSF was used for storage and recording. Oscillations were induced by bath application of 20 μM carbachol, and acquired at room temperature unless otherwise stated, using the MED64 planar multielectrode array system or a patch pipette containing ACSF. Spiking activity of individual cells was monitored extracellularly using a patch pipette filled with ACSF (Hájos *et al.*, 2004). Power spectra were estimated from 10-s traces with the Welch method using 1-s-wide time windows with 50% overlap. Oscillatory power between 10 and 20 Hz for measurements at room temperature was calculated with a Morlet wavelet. Spike rates were binned into 1-s time windows and averaged.

Statistical analyses

Statistical analyses were performed using Origin 7.5 software (OriginLab Corporation, Northampton, MA, USA). Data are presented as mean ± SD, unless otherwise indicated. Datasets were compared by independent or paired Student's *t*-test, as appropriate in each case. Pearson's product–moment correlation coefficient was used to estimate correlations between variables.

Results

To compare network activity in submerged and interface conditions, we started by recording spontaneous sharp wave–ripples and cholinergically induced network oscillations in the CA3 region of hippocampal slices. Whereas these oscillations were reliably seen in interface slices, as previously reported (Fisahn *et al.*, 1998; Kubota *et al.*, 2003), no such activity persisted in submerged slices using standard flow rates (1.8–2.4 mL/min) either in the chamber standard or the modified submerged chamber (Figs 1A and B, and 2A). As the metabolic demand may be greater during ongoing network activity (Huchzermeyer *et al.*, 2008), we searched for submerged conditions with improved metabolic supply to allow the recording of network activities similar to those observed in interface chambers and the intact brain. We found that increasing the flow rate (5.2 mL/min) of the superfusion fluid in a recording chamber modified with an inert plastic insert to optimize laminar flow across the slice (Fig. 1A and B) allowed us to record both spontaneous sharp wave–ripples (Fig. 2Ai) and cholinergically induced fast oscillations (Fig. 2Aii), network activities that are known to be generated intrinsically within CA3 of the hippocampus *in vivo* (Buzsaki, 1986; Csicsvari *et al.*, 2003). These network activities were only rarely seen in CA1, even at high superfusion rates. CA1 sharp wave–ripples were seen in one out of five slices, whereas CA1 fast oscillations were seen in two out of nine slices. However, using the dual superfusion chamber, even with a flow rate of 3–3.5 mL/min for each channel (Fig. 1C–F), we readily observed in CA1 both spontaneous sharp wave–ripples propagated from the CA3 local network (six out of nine slices; Fig. 2Bi) and prominent cholinergically induced oscillations (six out of eight slices) (Fig. 2Bii).

Superfusion rate correlates with local oxygen saturation

We hypothesized that an important difference between low and high flow rates could be variation in the oxygen saturation of the

superfusion solution in the recording chamber, which would influence the metabolic state of the slice. To test this idea, we first measured the oxygen saturation in the ACSF immediately above the slice while the flow rate was altered (Fig. 3A). The oxygen saturation changed almost linearly with flow rate ($R = 0.913$, $P < 0.01$, Pearson's correlation, $n = 5$ slices; Fig. 3B). To exclude the possibility that the oxygen probe could be sensitive to changes in flow rate by itself, we superfused ACSF equilibrated with air using different flow rates. Changes in flow rate did not affect the oxygen measurement (Fig. 3C). As the oxygen saturation within the tissue differs from that of the superfusate (Foster *et al.*, 2005), we also measured the oxygen saturation above the slice and within the slice at depths of 50 μm and 150 μm using carbon-fibre voltammetry at flow rates of 6, 3 and 1.8 mL/min ($n = 5$ slices; Fig. 3D). Measurement of oxygen level immediately above the tissue showed a reduction in oxygen saturation from 79 ± 11% at 6 mL/min to 36 ± 6% and 35 ± 4% at 3 mL/min and 1.8 mL/min, respectively. Oxygen saturation decreased steeply between 50 and 150 μm inside the tissue. At 150 μm depth within the slice, there were slightly hyperoxic conditions (26 ± 11%) at 6 mL/min, whereas hypoxic conditions (10 ± 3% and 6 ± 2%) were seen at 3 and 1.8 mL/min.

Importance of oxygen supply for the maintenance of sharp wave–ripple oscillations

To investigate the relationship between flow rate, oxygen saturation and sharp wave–ripple activity, we monitored both oxygen saturation and the incidence and amplitude of sharp waves while altering the flow rate (Fig. 4A). Reducing the superfusion rate from 6 to 1.2 mL/min caused a rapid reduction in the incidence of sharp wave–ripples, and there was a strong correlation between the incidence of sharp wave–ripples and the measured oxygen saturation ($R = 0.92$, $P < 0.01$, Pearson's correlation, $n = 4$ slices; Fig. 4A and B). To test whether oxygen saturation was a causal factor, we repeated the experiment at a constant high flow rate and altered the oxygen content of the superfusion solution by bubbling it with 95% N_2/5% CO_2. Again, we observed a rapid decrease in oxygen saturation of the ACSF, accompanied by a reduction in the incidence of sharp wave–ripples ($n = 4$ slices; Fig. 4C and D). These data suggest that the spontaneous emergence of sharp wave–ripples in hippocampal slices critically depends on sufficient oxygen supply.

Importance of oxygen supply for the maintenance of cholinergically induced fast network oscillations

Next, we investigated whether the requirement of oxygen supply also holds for cholinergically induced fast network oscillations. Reducing the superfusion rate from 6 to 1.2 mL/min caused a rapid reduction in the power of fast oscillations, a change that could be reversed by increasing the flow rate (Fig. 5Ai–iv). Similarly, reducing the oxygen content of the superfusion solution by bubbling it with 95% N_2/5%

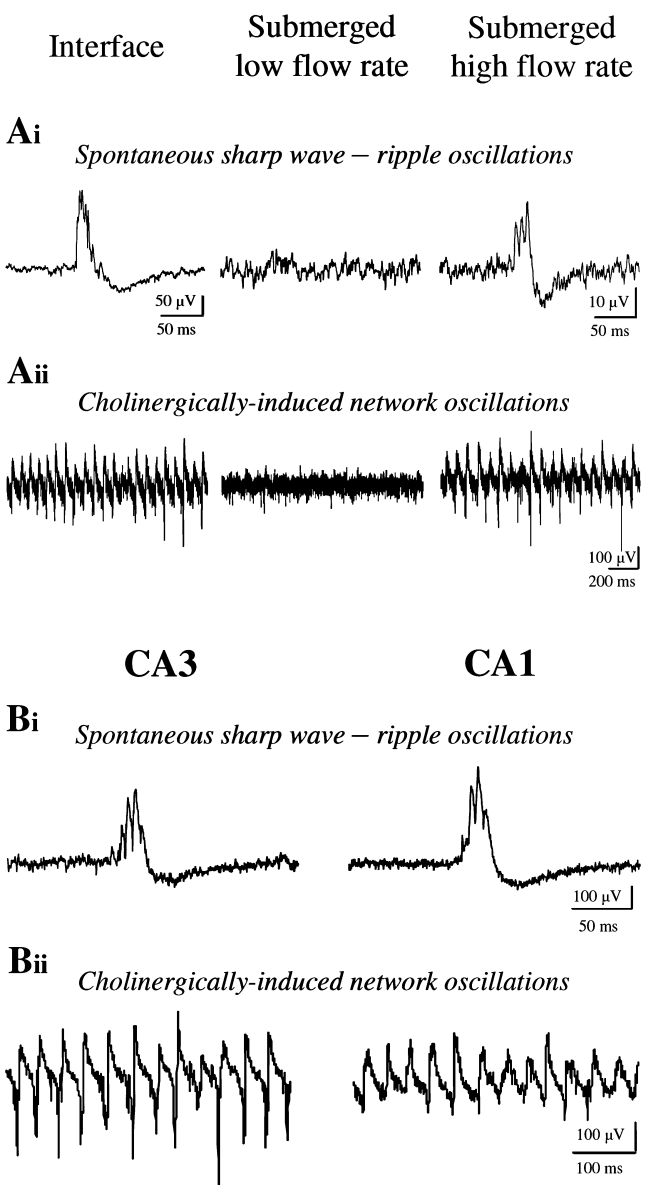

FIG. 2. Generation and propagation of network events in submerged slice chambers. (A) Comparison of network activity recorded from hippocampal slices in an 'Oslo'-style interface chamber and a modified submerged slice chamber with standard superfusion at low and high flow rates. (i) Spontaneous network activity recorded in an interface chamber (left), a submerged slice chamber at a low flow rate of 1.9 mL/min (middle), and a high flow rate of 5.2 mL/min (right). Note sharp wave–ripple activity in the interface chamber and only at a high flow rate in the submerged slice chamber. (ii) Cholinergically induced network activity in an interface chamber (left), and in a submerged slice chamber at a low flow rate (middle) and at a high flow rate (right). Note network oscillations in the interface chamber and only at a high flow rate in the submerged slice chamber. These recordings were made extracellularly in the pyramidal cell layer of CA3 of transverse hippocampal slices prepared from postnatal day 14–20 Wistar rats. Spontaneous sharp wave–ripple activity was recorded in slightly modified ACSF (see Materials and methods). After induction of fast network oscillations by bath application of 20 μM carbachol in standard ACSF, recordings were taken after 15 min. Sharp wave–ripple events were digitally bandpass filtered between 0.1 and 500 Hz; fast network oscillations were low-pass filtered at 2 or 5 kHz. (B) Propagation of network events in a modified submerged slice chamber with dual superfusion. Sample traces of sharp wave–ripples (i) and cholinergically induced fast network oscillations (ii) recorded simultaneously in CA3 and CA1 of mouse hippocampal slices. These recordings were made in standard ACSF with a flow rate of 3–3.5 mL/min for each channel at 30–32 °C. The incidence and the peak amplitude of spontaneous sharp wave–ripples were comparable in both hippocampal regions (CA3, 1.3 ± 0.8 Hz and 418 ± 100 μV; CA1, 1.2 ± 0.9 Hz and 350 ± 118 μV; $n = 6$; $P > 0.1$, independent Student's t-test). In the case of fast oscillations, the frequency of the network activity was not different (CA3, 30.4 ± 2.2 Hz; CA1, 30.8 ± 2.1 Hz; $n = 6$; $P > 0.1$, independent Student's t-test), whereas the mean peak power was significantly smaller in CA1 than in CA3 (CA3, 275 ± 120 μV^2/Hz; CA1, 41 ± 17 μV^2/Hz; $n = 6$; $P < 0.05$, independent Student's t-test).

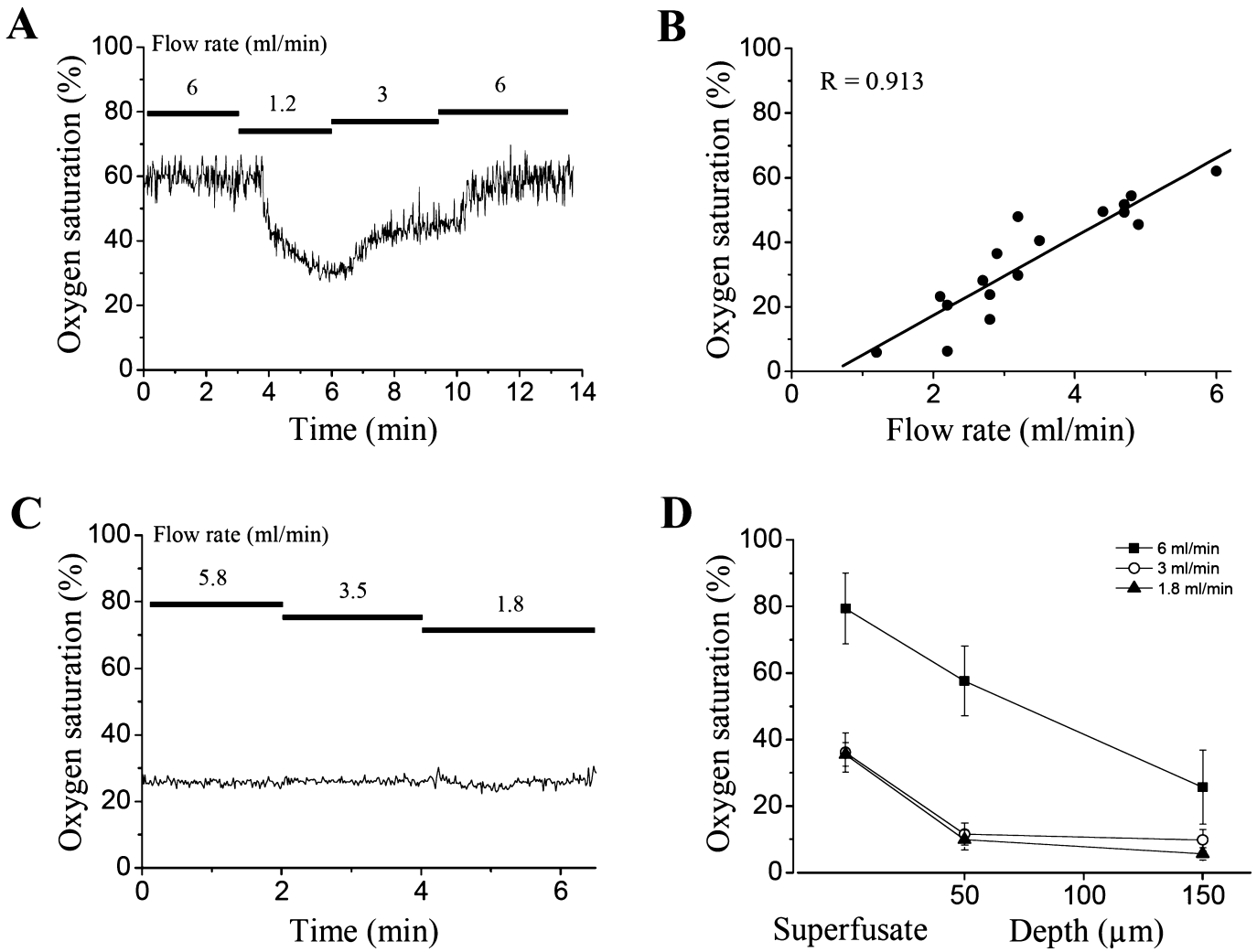

FIG. 3. Relationship between flow rate and oxygen saturation in a modified submerged slice chamber. (A) The effect of flow rate on oxygen saturation measured 50–100 μm above CA3 of a submerged hippocampal slice. (B) Oxygen saturation as a function of flow rate measured at room temperature (n = 5 slices; two to three data points per slice). Polyethylene tubing with substantial permeability for O_2 was used in these experiments. (C) The oxygen measurement was not sensitive to changes in the flow rate of non-bubbled solution. (D) Oxygen saturation as measured using carbon-fibre voltammetry 50–100 μm above, and 50 μm and 150 μm below, the upper surface of the slice at flow rates of 6, 3 and 1.8 mL/min. Similarly to the optode measurements, a reduction in oxygen saturation was observed in the perfusate at 3 and 1.8 mL/min, respectively. At 50 μm depth within the tissue, at perfusion speeds of 6, 3 and 1.8 mL/min, oxygen saturation was reduced to 58 ± 10%, 12 ± 3% and 10 ± 3%, respectively. At 150 μm, this was reduced further to 26 ± 11%, 10 ± 3% and 6 ± 2%, respectively (mean ± SEM). Tygon tubing with low permeability for O_2 was used in this experiment.

CO_2 led to a rapid decrease in oxygen saturation of the ACSF and caused a parallel reduction in the power of fast network oscillations. There was a strong linear correlation between the power of network oscillations and the measured oxygen saturation in the chamber, both when modified by flow rate (R = 0.855, P < 0.01, Pearson's correlation, n = 8; Fig. 5B), and when modified by 95% N_2/5% CO_2 (R = 0.923, P < 0.01, Pearson's correlation, n = 8; Fig. 5C). These data show that not only the spontaneous emergence of network activity, but also pharmacologically induced oscillations, require sufficient oxygen supply.

Importance of oxygen supply for the maintenance of GABAergic inhibition during cholinergically induced fast network oscillations

Finally, in order to understand the underlying mechanisms of the oxygen demand, we investigated the effects of changing the flow rate on individual cells in the network. We have previously shown that carbachol-induced oscillations depend on GABAergic inhibition (Fisahn *et al.*, 1998; Pálhalmi *et al.*, 2004). We therefore investigated whether changes in flow rate also alter GABAergic inhibition. We recorded the spiking activity of visually identified inhibitory interneurons in the stratum oriens of CA3 (Fig. 6A). In control conditions, 46% (13/28) of tested cells fired action potentials at low flow rates (1.8–2.4 mL/min), whereas 66% (19/29) were active at high flow rates (4.1–5.8 mL/min). The average firing rate of the active neurons was 1.5 ± 1.0 Hz (n = 13) and 2.3 ± 2.8 Hz (n = 19) at low and high flow rates, respectively, which did not differ significantly (P > 0.1, independent Student's t-test).

At low flow rates, carbachol induced a transient increase in the firing rate of both spontaneously active (from 9.1 ± 3.2 Hz to 15.8 ± 3.9 Hz; n = 3, P < 0.01, paired Student's t-test) and originally non-spiking (from 0 to 15.1 ± 4.3 Hz, n = 4, P < 0.01, paired Student's t-test) neurons associated with fast oscillatory activity (Fig. 6B), but the oscillations disappeared rapidly and the firing rate

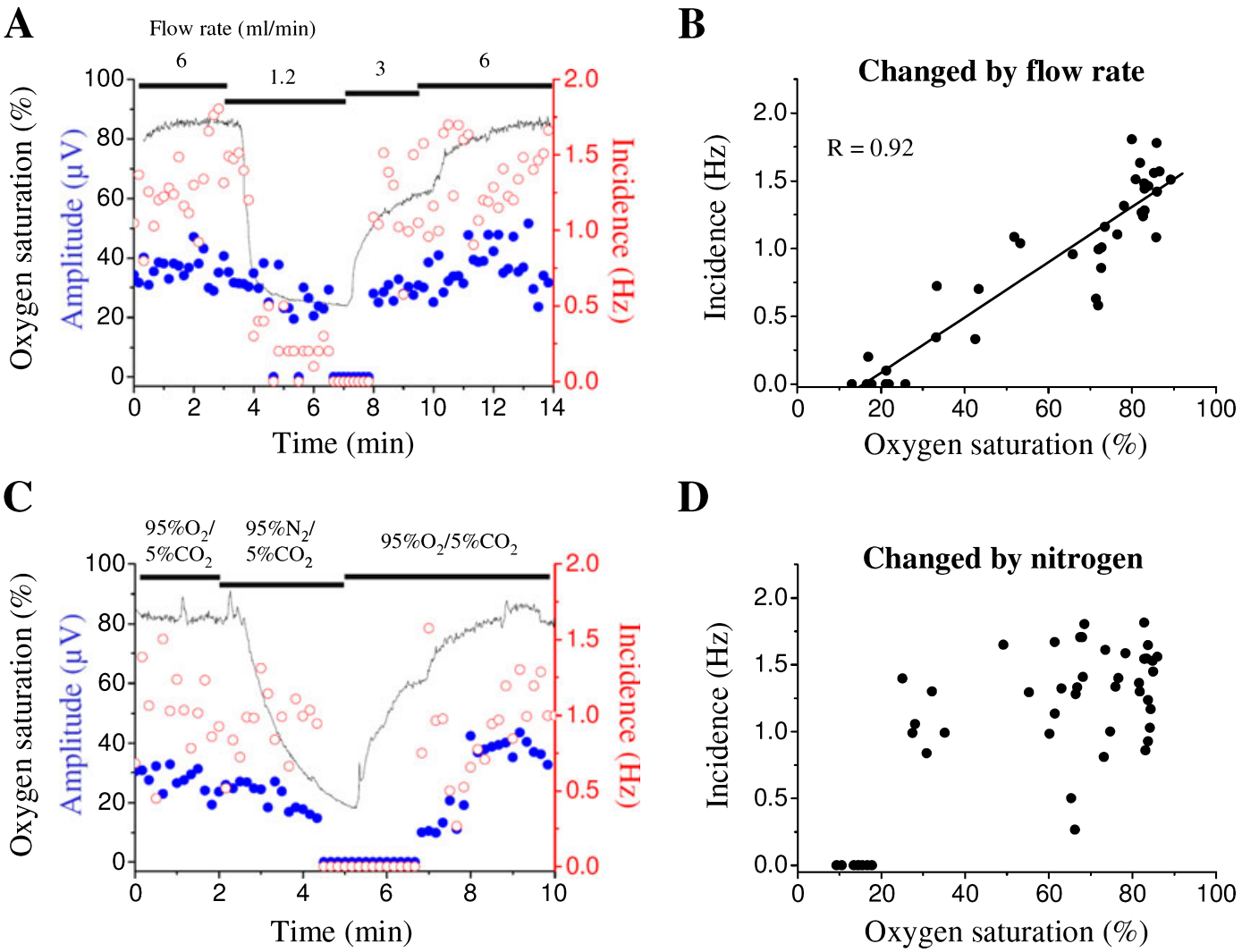

FIG. 4. Importance of oxygen levels for maintenance of spontaneous sharp wave–ripples. (A) Effect of flow rate on oxygen saturation and incidence of sharp wave–ripples recorded with a planar 8 × 8 microelectrode array. Black trace, oxygen saturation (%) during experiment; open circles, incidence of sharp wave–ripples (Hz); filled circles, amplitude of sharp wave–ripples (μV). Note the reduction of the incidence of sharp wave–ripples with lower oxygen saturation. The incidences were 1.1 ± 0.1 Hz, 1.3 ± 0.1 Hz and 0.4 ± 0.14 Hz (mean ± SEM) at flow rates of 6, 3 and 1.2 mL/min, respectively. The incidence at 1.2 mL/min was significantly lower than that at either 6 or 3 mL/min (both $P < 0.01$, paired Student's *t*-test, $n = 4$ slices). The corresponding amplitudes were 28.0 ± 7.4 μV, 27.0 ± 8.2 μV and 23.3 ± 6.3 μV, respectively ($P > 0.1$, paired Student's *t*-test, $n = 4$ slices). (B) Plot of incidence of sharp wave–ripples against oxygen saturation modified by reduced flow rate ($n = 4$ slices; five or six data points per slice). Least-squares line fit superimposed. (C) Superfusion of the slice with artificial cerbrospinal fluid bubbled with 95% N_2/5% CO_2 abolishes sharp wave–ripples. Black trace, oxygen saturation (%) during the experiment; open circles, incidence of sharp wave–ripples (Hz); filled circles, amplitude of sharp wave–ripples (μV). The incidences were 1.3 ± 0.1 and 0.3 ± 0.2 Hz (mean ± SEM; $P < 0.01$, paired Student's *t*-test, $n = 4$ slices) with 95% O_2/5% CO_2 and 95% N_2/5% CO_2, respectively. The corresponding amplitudes were 17.5 ± 3.1 μV and 16.3 ± 2.4 μV ($P > 0.1$, paired Student's *t*-test, $n = 4$ slices). (D) Plot of incidence of sharp wave–ripples against oxygen saturation modified by bubbling with 95% N_2/5% CO_2 ($n = 4$ slices; five or six data points per slice). Tygon tubing with low permeability for O_2 was used in these experiments.

decreased again within 20 min in the continued presence of carbachol (for spontaneously active cells, 10.2 ± 3.8 Hz, $P > 0.1$, and for originally non-spiking neurons, 6.3 ± 4.1 Hz, $P < 0.05$, as compared to control using paired Student's *t*-test; Fig. 6B). In contrast, at high flow rates, an increased firing rate persisted for tens of minutes during superfusion of carbachol-containing solution in both spontaneously active neurons (from 4.2 ± 2.5 Hz to 12.9 ± 4.1 Hz, $n = 4$, $P < 0.01$, paired Student's *t*-test; and remained after 16 min at 13.4 ± 3.5 Hz, $n = 4$, $P < 0.01$, as compared to control using paired Student's *t*-test) and originally non-spiking neurons (from 0 to 6.1 ± 3.1 Hz, $P < 0.01$, paired Student's *t*-test; and remained after 16 min at 8.8 ± 4.3 Hz, $P < 0.01$, as compared to control using paired Student's *t*-test), associated with persistent fast network oscillations (Fig. 6A and B; see also Figure 1 in Hájos *et al.*, 2004). Thus, increasing the flow rate enhances the firing of interneurons and enables the maintenance of persistent synchronous network activities in slice preparations.

Discussion

The main findings of the present study are as follows: (i) high laminar flow rate (4.1–6.0 mL/min) enables stable spontaneous and pharmacologically induced network activity in submerged hippocampal slices; (ii) this network activity is enabled by the increased oxygen

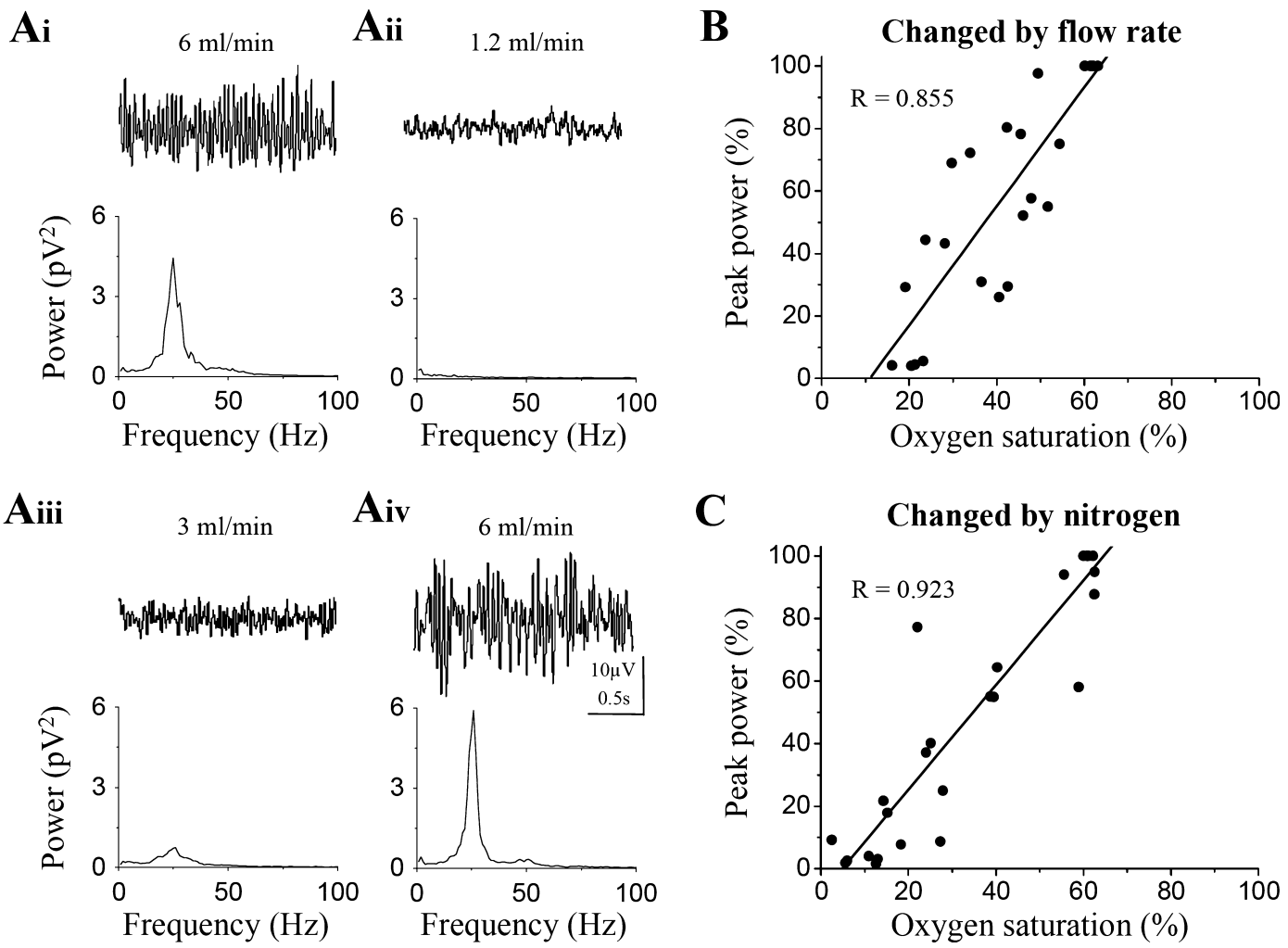

FIG. 5. Importance of oxygen levels for the maintenance of cholinergically induced fast network oscillations. (Ai–iv) Temporal sequence of representative traces of rhythmic activity at different flow rates and their corresponding power spectra showing the sensitivity of network activity to oxygen levels. Oscillations were detected using a planar 8 × 8 microelectrode array. Peak power: 4.1 ± 1.8 pV^2/Hz at 6 mL/min; and 0.02 ± 0.1 pV^2/Hz at 1.2 mL/min ($P < 0.01$, paired Student's *t*-test, $n = 8$). On return to a 6 mL/min flow rate, peak power returned to the control levels (4.8 ± 2.5 pV^2/Hz; $P > 0.1$, paired Student's *t*-test, $n = 5$). (B) Relationship between the oxygen saturation of artificial cerbrospinal fluid changed by flow rate and the power of the oscillation ($n = 8$ slices; two or three data points per slice). Least-squares line fit superimposed. (C) Relationship between the power of oscillations and the oxygen saturation changed by bubbling of 95% N_2/5% CO_2 at a constant flow rate of 5.4 mL/min ($n = 8$ slices; two or three data points per slice). Least-squares line fit superimposed. The power of the oscillations was normalized to the maximum value observed at 6 mL/min. Polyethylene tubing with substantial permeability for O_2 was used in these experiments.

supply provided by a higher flow rate in the modified submerged chamber; and (iii) interneurons can maintain their firing rate during cholinergic activation only with the higher flow rate.

The high sensitivity of hippocampal network activity to oxygen tension is consistent with other recent studies (Wu *et al.*, 2005; Huchzermeyer *et al.*, 2008). Earlier investigations into the cellular mechanisms underlying network oscillations have been hampered by the transient nature of the induced activity in submerged conditions (McMahon *et al.*, 1998; Kawaguchi, 2001; Gloveli *et al.*, 2005) as compared to interface conditions (e.g. Whittington *et al.*, 1995; Fisahn *et al.*, 1998; Sanchez-Vives & McCormick, 2000; Kubota *et al.*, 2003). We suggest that higher superfusion flow rate could ameliorate this problem.

In addition to the flow rate, the oxygen supply to the slice under submerged conditions will depend on several other factors, including the type of tubing used and the configuration of the slice chamber. Short tubing with minimal oxygen permeability (e.g. Tygon or Teflon) helps to maintain high oxygen levels (note the difference in the initial values of oxygen saturation using polyethylene and Tygon tubing in Figs 3A and 4A, respectively). We could reduce the flow rate and still observe oscillations by reducing the volume of the chamber and help to create laminar flow by using a custom-made inert plastic insert (Fig. 1A and B). Propagation of network oscillations from CA3 to CA1 was supported by superfusing the slice from both surfaces (Fig. 1C–F). Thus, the flow rate needed to ensure sufficient oxygen supply at a given recording condition could vary with several other technical factors.

The recognition that oxygen levels might be insufficient to support some energy-consuming neuronal functions in submerged slices at low flow rates, such as interneuronal firing activity during network oscillations, raises the question of whether baseline neuronal properties might also be significantly influenced by low flow rates. Reassuringly, a recent study showed that evoked local field potential responses could remain unaltered despite significantly reduced power

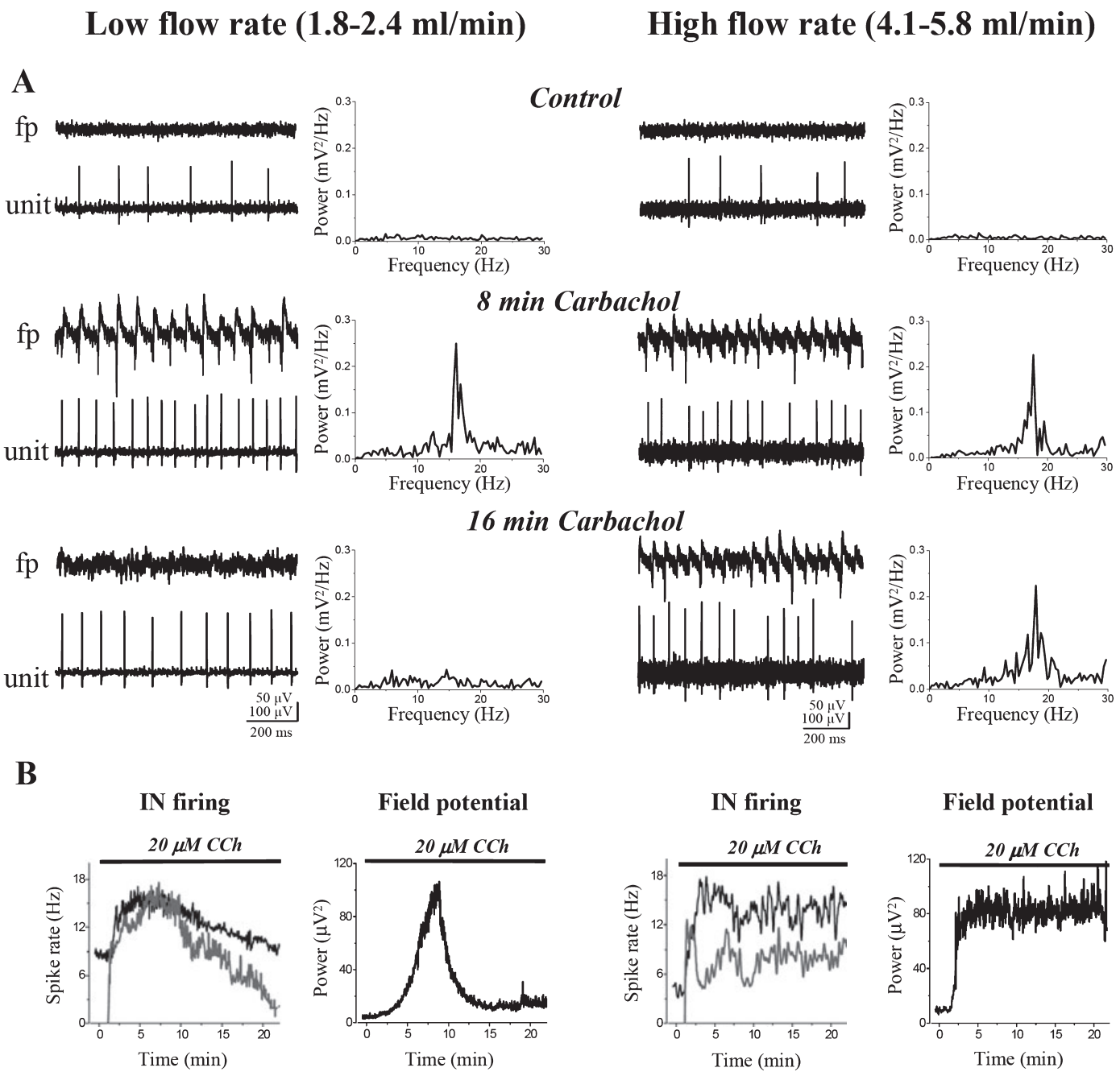

FIG. 6. Dependence of the cholinergically enhanced interneuronal (IN) firing and network oscillation on the flow rate. (A) Concurrent recording of field potential (fp) with power spectrum and spiking activity of individual neurons in the stratum oriens (unit) of the hippocampal CA3 at different times after bath application of the cholinergic receptor agonist carbachol (CCh) (20 μM) at low (left) and high flow rates (right) in submerged rat slices. (B) Oscillatory power (10–22 Hz), spiking frequency (black, cells with spontaneous activity before application of carbachol; grey, neurons firing only in the presence of carbachol) plotted over time after the start of carbachol application during low (left) and high flow rate (right). Carbachol induced only transient oscillatory activity [peak frequency, 17.2 ± 0.4 Hz at room temperature; peak power, control, 3.9 ± 2.1 μV^2/Hz (n = 7); in drug (8 min), 98.1 ± 29.1 μV^2/Hz ($P < 0.01$, paired Student's t-test); in drug (16 min), 17.6 ± 12.5 μV^2/Hz ($P > 0.1$, as compared to control using paired Student's t-test)] in parallel with a transient increase of interneuronal firing during low flow rates. In contrast, both oscillations [peak frequency, 17.9 ± 0.6 Hz; peak power, control, 9.9 ± 4.1 μV^2 (n = 7); in drug (8 min), 83.5 ± 25.4 μV^2 ($P < 0.01$, paired Student's t-test); in drug (16 min), 80.6 ± 19.9 μV^2 ($P < 0.01$, as compared to control using paired Student's t-test)] and increased firing activity were persistent in the presence of carbachol at high flow rates.

of cholinergically induced gamma oscillations with reduced oxygen levels (Huchzermeyer *et al.*, 2008).

Although our results suggest that a relatively high oxygen level in the superfusion solution is necessary to maintain network activity in slices, one should be aware that hyperoxygenation of tissue could alter several parameters of neuronal operation and even induce acute cell death (Mulkey *et al.*, 2001; Pomper *et al.*, 2001). Thus, a number of studies have shown that the use of carbogen gas can increase oxygen tension within a slice to levels substantially higher (200–500 Torr) than have been measured in the intact brain (10–34 Torr) (Jiang *et al.*, 1991; Mulkey *et al.*, 2001). In our experiments, at 6 mL/min flow rate, oxygen tension was slightly elevated at 150 μm depth relative to

air. One reason for the necessity of a higher oxygen tension *in vitro* might be the longer diffusion distances in the absence of blood circulation. Differences between slices and the intact brain in oxygen availability during neuronal activity have been discussed in detail in a recent review (Turner *et al.*, 2007).

Conclusion

We conclude that naturalistic network activity can be studied under submerged conditions when a sufficient oxygen supply is maintained by a high flow rate of superfusion fluid. The exact flow rate required depends on several technical factors that are unique to each experimental setup. We suggest that measurement of oxygen could be a useful tool with which to optimize the experimental conditions, although several other factors might contribute, including P_{CO_2} and pH (e.g. Stenkamp *et al.*, 2001).

Acknowledgements

This work was supported by the British Council, the Hungarian Medical Council (ETT 47/2003), the Hungarian Scientific Research Fund (OTKA T049517), and a Collaborative Research Initiative Grant from The Wellcome Trust. N. Hájos was sponsored by a NATO Scientific Fellowship. T. J. Ellender was supported by an OXION Wellcome Trust-funded 4-year DPhil studentship. We are very grateful to K. Buckler for the loan of instruments for oxygen measurements, and to V. Varga for help with data analysis. N. Hájos is an inventor on a patent application.

Abbreviations

ACSF, artificial cerebrospinal fluid.

References

Buzsaki, G. (1986) Hippocampal sharp waves: their origin and significance. *Brain Res.*, **398**, 242–252.

Cragg, S.J. (2003) Variable dopamine release probability and short-term plasticity between functional domains of the primate striatum. *J. Neurosci.*, **23**, 4378–4385.

Cragg, S.J. & Greenfield, S.A. (1997) Differential autoreceptor control of somatodendritic and axon terminal dopamine release in substantia nigra, ventral tegmental area, and striatum. *J. Neurosci.*, **23**, 4378–4385.

Csicsvari, J., Jamieson, B., Wise, K.D. & Buzsaki, G. (2003) Mechanisms of gamma oscillations in the hippocampus of the behaving rat. *Neuron*, **37**, 311–322.

Exley, R., Clements, M.A., Hartung, H., McIntosh, J.M. & Cragg, S.J. (2008) α6-containing nicotinic acetylcholine receptors dominate the nicotine control of dopamine neurotransmission in nucleus accumbens. *Neuropsychopharmacology*, **33**, 2158–2166.

Fisahn, A., Pike, F.G., Buhl, E. & Paulsen, O. (1998) Cholinergic induction of network oscillations at 40 Hz in the hippocampus in vitro. *Nature*, **394**, 186–189.

Foster, K.A., Beaver, C.J. & Turner, D.A. (2005) Interaction between tissue oxygen tension and NADH imaging during synaptic stimulation and hypoxia in rat hippocampal slices. *Neuroscience*, **132**, 645–657.

Gloveli, T., Dugladze, T., Saha, S., Monyer, H., Heinemann, U., Traub, R.D., Whittington, M.A. & Buhl, E.H. (2005) Differential involvement of oriens/pyramidale interneurones in hippocampal network oscillations in vitro. *J. Physiol.*, **562**, 131–147.

Hájos, N., Pálhalmi, J., Mann, E.O., Németh, B., Paulsen, O. & Freund, T.F. (2004) Spike timing of distinct types of GABAergic interneuron during hippocampal gamma oscillations in vitro. *J. Neurosci.*, **24**, 9127–9137.

Huchzermeyer, C., Albus, K., Gabriel, H.-J., Otahal, J., Taubenberger, N., Heinemann, U., Kovacs, R. & Kann, O. (2008) Gamma oscillations and spontaneous network activity in the hippocampus are highly sensitive to decreases in pO_2 and concomitant changes in mitochondrial redox state. *J. Neurosci.*, **28**, 1153–1162.

Jiang, C., Agulian, S. & Haddad, G.G. (1991) O_2 tension in adult and neonatal brain slices under several experimental conditions. *Brain Res.*, **568**, 159–164.

Kawaguchi, Y. (2001) Distinct firing patterns of neuronal subtypes in cortical synchronized activities. *J. Neurosci.*, **21**, 7261–7272.

Kubota, D., Colgin, L.L., Casale, M., Brucher, F.A. & Lynch, G. (2003) Endogenous waves in hippocampal slices. *J. Neurohysiol.*, **89**, 81–89.

Maier, N., Nimmrich, V. & Draguhn, A. (2003) Cellular and network mechanisms underlying spontaneous sharp wave–ripple complexes in mouse hippocampal slices. *J. Physiol.*, **550**, 873–887.

Mann, E.O., Suckling, J.M., Hájos, N., Greenfield, S.A. & Paulsen, O. (2005) Perisomatic feedback inhibition underlies cholinergically induced fast network oscillations in the rat hippocampus in vitro. *Neuron*, **45**, 105–117.

McMahon, L.L., Williams, J.H. & Kauer, J.A. (1998) Functionally distinct groups of interneurons identified during rhythmic carbachol oscillations in hippocampus in vitro. *J. Neurosci.*, **18**, 5640–5651.

Mulkey, D.K., Henderson, R.A. III, Olson, J.E., Putnam, R.W. & Dean, J.B. (2001) Oxygen measurements in brain stem slices exposed to normobaric hyperoxia and hyperbaric oxygen. *J. Appl. Physiol.*, **90**, 1887–1899.

Pálhalmi, J., Paulsen, O., Freund, T.F. & Hájos, N. (2004) Distinct properties of carbachol- and DHPG-induced network oscillations in hippocampal slices. *Neuropharmacology*, **47**, 381–389.

Pomper, J.K., Graulich, J., Kovacs, R., Hoffmann, U., Gabriel, S. & Heinemann, U. (2001) High oxygen tension leads to acute cell death in organotypic hippocampal slice cultures. *Brain Res.*, **126**, 109–116.

Sanchez-Vives, M.V. & McCormick, D.A. (2000) Cellular and network mechanisms of rhythmic recurrent activity in neocortex. *Nat. Neurosci.*, **3**, 1027–1034.

Skrede, K.K. & Westgaard, R.H. (1971) The transverse hippocampal slice: a well-defined cortical structure maintained in vitro. *Brain Res.*, **35**, 589–593.

Stenkamp, K., Palva, J.M., Uusisaari, M., Schuchmann, S., Schmitz, D., Heinemann, U. & Kaila, K. (2001) Enhanced temporal stability of cholinergic hippocampal gamma oscillations following respiratory alkalosis in vitro. *J. Neurophysiol.*, **85**, 2063–2069.

Steriade, M. (2001) *The Intact and Sliced Brain*. MIT Press, Cambridge, MA.

Turner, D.A., Foster, K.A., Galeffi, F. & Somjen, G.G. (2007) Differences in O_2 availability resolve the apparent discrepancies in metabolic intrinsic optical signals in vivo and in vitro. *Trends Neurosci.*, **30**, 390–398.

Venton, B.J., Michael, D.J. & Wightman, R.M. (2003) Correlation of local changes in extracellular oxygen and pH that accompany dopaminergic terminal activity in the rat caudate-putamen. *J. Neurochem.*, **84**, 373–381.

Whittington, M.A., Traub, R.D. & Jeffreys, J.G.R. (1995) Synchronized oscillations in interneurons driven by metabotropic glutamate receptor activation. *Nature*, **373**, 612–615.

Wu, C., Luk, W.P., Gillis, J., Skinner, F. & Zhang, L. (2005) Size does matter: generation of intrinsic network rhythms in thick mouse hippocampal slices. *J. Neurophysiol.*, **93**, 2302–2317.

Yamamoto, C. & McIlwain, H. (1966) Potentials evoked in vitro in preparations from the mammalian brain. *Nature*, **210**, 1055–1056.

dc_71_10

13. számú melléklet

Journal of Neuroscience Methods 183 (2009) 107–113

Contents lists available at ScienceDirect

Journal of Neuroscience Methods

journal homepage: www.elsevier.com/locate/jneumeth

Invited review

Establishing a physiological environment for visualized *in vitro* brain slice recordings by increasing oxygen supply and modifying aCSF content

Norbert Hájos[a,*], Istvan Mody[b,**]

[a] *Department of Cellular and Network Neurobiology, Institute of Experimental Medicine, Hungarian Academy of Sciences, Szigony u. 43, 1083 Budapest, Hungary*
[b] *Department of Neurology, David Geffen School of Medicine, University of California, Los Angeles, CA 90095, USA*

ARTICLE INFO

Article history:
Accepted 3 June 2009

Keywords:
Oscillation
Sharp wave–ripple activity
GABA
Interneuron
Hippocampus
Neurotransmitter

ABSTRACT

Our insights into the basic characteristics of neuronal function were significantly advanced by combining the *in vitro* slice technique with the visualization of neurons and their processes. The visualization through water immersion objectives requires keeping slices submerged in recording chambers where delivering artificial cerebro-spinal fluid (aCSF) at flow rates of 2–3 ml/min results in a limited oxygen supply [Hájos N, Ellender TJ, Zemankovics R, Mann EO, Exley R, Cragg SJ, et al. Maintaining network activity in submerged hippocampal slices: importance of oxygen supply. Eur J Neurosci 2009;29:319–27]. Here we review two methods aimed at providing sufficient oxygen levels to neurons in submerged slices to enable high energy consuming processes such as elevated firing rates or network oscillations. The use of these methods may also influence the outcome of other electrophysiological experiments in submerged slices including the study of intercellular signaling pathways. In addition, we also emphasize the importance of various aCSF constituents used in *in vitro* experiments.

Contents

Ideally, the different aspects of neuronal function should be investigated in the intact brain. However, this aim is difficult to achieve owing to several technical limitations. To overcome some of these problems, acute tissue slices prepared from live brain were introduced to investigate the intra- and extracellular neuronal signaling (Andersen et al., 1977; Schwartzkroin and Andersen, 1975; Skrede and Westgaard, 1971; Yamamoto and McIlwain, 1966). These *in vitro* studies significantly advanced our understanding of the basic principles of information processing in the central nervous system (CNS). Naturally, the maintenance of living cells in tissue slices and keeping them in conditions resembling those found in the intact brain is of paramount importance.

The first chambers developed to study the cellular basis of brain function using tissue slices were of the interface type (Skrede and Westgaard, 1971; Yamamoto and McIlwain, 1966). In interface type chambers (more frequently called the “Oslo” or “Haas” type brain slice chambers) (Haas et al., 1979; Dingledine, 1984; Reid et al., 1988; Steriade, 2001), slices are held on a nylon mesh at the interface between artificial cerebro-spinal fluid (aCSF) and humidified gas (the mixture of 95% O_2/5% CO_2), providing adequate conditions for the maintenance of functional living cells and their microcircuits in several hundred-μm-thick brain slices for many hours. In such

* Corresponding author. Tel.: +36 1 2109400x387; fax: +36 1 2109412.
** Corresponding author at: UCLA Neurology, NRB1 Rm. 575D, 635 Charles E. Young Drive South, Los Angeles, CA 90095-7335, USA. Tel.: +1 310 206 4481; fax: +1 310 825 0033.
E-mail addresses: hajos@koki.hu (N. Hájos), mody@ucla.edu (I. Mody).

0165-0270/$ – see front matter © 2009 Published by Elsevier B.V.
doi:10.1016/j.jneumeth.2009.06.005

chambers the nutrient supply from the oxygenated aCSF reaches the slices from the bottom, while a significant portion of the 95% O_2/5% CO_2 mixture also diffuses though a thin (50–200 μm) layer of aCSF that covers the slices. The flow rate of aCSF is usually kept low, around 1 ml/min, which means that the full effects of hydrophobic drugs will require at least 30 min of perfusion, to allow for the drug to reach the slice and for its slow diffusion into the tissue (e.g. Thomson et al., 2000). This produces a substantial challenge for the experimenter if a stable control period, a drug effect followed by a washout need to be obtained. But the major disadvantage of the interface type slice chamber is the lack of possibility for high-resolution visualization of the cells and their fine processes.

The technical innovation that combined the electrophysiological recordings and the visualization of cells in slices came in 1989 in thin slices with the use of water immersion objectives (Edwards et al., 1989; Sakmann et al., 1989; Stuart et al., 1993). To visualize the neurons and their fine processes, brain slices are typically placed on a thin transparent plate made of glass or plastic, and are superfused with aCSF, i.e., slices are submerged in the extracellular solution. In submerged slice chambers, brain slices are supplied with gas and nutrients solely through the aCSF using typical flow rates of 2–3 ml/min. This relatively higher flow rate and the submerged nature of the slices allows for the faster exchange of pharmacological agents. Although submerged slice chambers vary a great deal in their shape and the material used for their construction, in every type of submerged chamber slices are superfused only at one of their surface while resting on the other. Under these conditions, concentration gradients for oxygen, nutrients and various chemicals contained in the aCSF develop by default in the slices, which can dramatically affect the experimental results. Not surprisingly, some results obtained in slices maintained in interface type chambers better resembled findings observed in the intact brain, and could not be reproduced in experiments using submerged brain slices. Most differences were observed in experiments where maintaining high levels of neuronal activity was essential (e.g. during network oscillations) (McMahon et al., 1998; Gloveli et al., 2005; Hájos et al., 2009) and in studies of neuronal oxygen deprivations (Croning and Haddad, 1998). These initial observations implied that the oxygen supplies to tissues maintained in interface and submerged slice chambers were considerably different.

1. Should the oxygen supply of submerged brain slices be altered?

In the intact brain the vascular system delivers oxygen in a highly controlled manner wherever and whenever is necessary (Vanzetta and Grinvald, 1999; Vanzetta et al., 2005). In contrast, in brain slices where the vascular system is not functional, the oxygen supply of neurons is limited by the diffusion from the tissue environment (Pomper et al., 2001). Thus, *in vivo* the oxygen supply is modified on demand depending on the local neuronal activity, whereas *in vitro* the experimenter sets a constant oxygen concentration that is difficult to change. Although the results of some electrophysiological investigations obtained in slices are not significantly affected by the amount of oxygen supplied (e.g. evoked potentials; Huchzermeyer et al., 2008), other neuronal functions critically depend on high energy consumption, and accordingly on the amount of oxygen supply. For instance, gamma (30–100 Hz) oscillations, synchronous network activities that emerge from the rhythmic discharges of large neuronal ensembles (Csicsvari et al., 2003; Mann et al., 2005), consume a significant amount of energy (Huchzermeyer et al., 2008). Such oscillations, however, could only be recorded transiently in submerged slices using flow rates of 2–3 ml/min (McMahon et al., 1998; Gloveli et al., 2005; Hájos et al., 2009). These findings imply that the oxygen supply to slices maintained in submerged recording conditions is inferior compared to the conditions of interface chambers and those of the intact brain (Reid et al., 1988). Differences between slices and the intact brain in oxygen availability during neuronal function have been discussed in detail in a recent review (Turner et al., 2007).

In this paper we show that not only network oscillations depend on oxygen concentration supplied to the submerged slices, but other critical experiments might also be affected by the recoding conditions. First, we will present some technical solutions to help increase the oxygen supply of submerged slices.

2. Improving the oxygen supply of submerged brain slices

There are at least two methods to improve the oxygen supply of slices maintained in a submerged chamber. First, if slices are being superfused only at one surface, the volume of the submerged chamber should be reduced as much as possible and the flow rate of superfused aCSF should be considerably increased. Second, if the slices can be placed on a mesh with some distance from the supporting plate, the aCSF may be superfused individually at both surfaces of the submerged slices.

We have found that by increasing the flow rate of the aCSF to 3–6 ml/min and reducing the volume of the chamber to 0.5 ml, network oscillations could be readily maintained in hippocampal slices (Hájos et al., 2004; Mann et al., 2005; Oren et al., 2006). In preliminary experiments we found that persistent oscillations in conventional slice chambers designed for visualized patch clamp recordings with volumes of 1–2 ml could only be achieved by increasing the flow rate to >10 ml/min. This is reminiscent of previous observations that persistent network activities in the hippocampal CA3 region (Wu et al., 2005) and spinal cord preparations (Wilson et al., 2003) could only be maintained when using flow rates of 15 ml/min and 22 ml/min, respectively. Thus, the flow rate of the aCSF is a key element in determining the oxygen concentration delivered to the slices. Consequently, higher flow rates can sustain the higher oxygen demand required for synchronous discharges of extensive neuronal ensembles leading to larger oscillatory activities in field potentials. Our recent measurements fully support this assumption (Hájos et al., 2009). Clearly, more oxygen can be delivered by increasing the flow rate, but increasing the rate of slice perfusion has its own technical limitations (e.g. the shape and the volume of the slice chamber, the length and the material of tubing used for perfusion, etc.) (Hájos et al., 2009). The higher perfusion speed may reduce the available time for the diffusion of oxygen through the increased surface of the liquid introduced by the water immersion objective.

A major drawback of a high flow rate however, is the resulting mechanical instability of the slices, particularly when slice stability is critical for lasting electrophysiological recordings and optical imaging of fine processes. To overcome, or at least to considerably reduce, the problem of slice instability at high flow rates, a dual-superfusion slice chamber may be used, where the slices are placed on a mesh and both surfaces of the slices are individually superfused with aCSF. In this type of slice chamber the mechanical stability of the slices is greatly improved, and the one-sided chemical gradients are significantly reduced, which improves the recording conditions even at relatively low flow rates of 2–3 ml/min (Fig. 1). For more technical details see Hájos et al. (2009).

3. Network activity in submerged hippocampal slices

In the intact brain network oscillations, considered to be typical features of neuronal processing, are rhythmic activities generated by the precisely timed discharge of large neuronal populations (Buzsáki, 2006). Oscillations with similar characteristics to those found *in vivo* can be routinely recorded in brain slices maintained in an interface type recording chamber (Whittington et al.,

dc_71_10

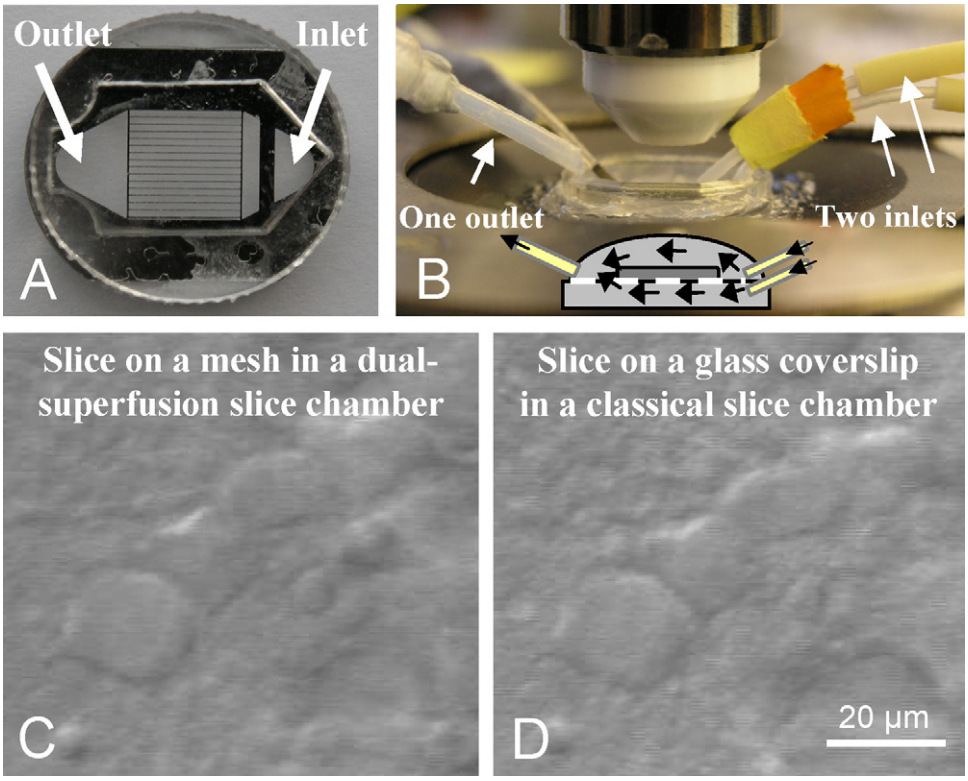

Fig. 1. Dual-superfusion slice chamber. (A), Picture of a chamber insert developed for dual-superfusion. The slices are placed on a mesh glued between two plastic rings of a thickness of 2 mm. Solution is separately perfused below and above the slice through two inlets (B). The flow rates and temperatures of the two solutions should be equal to ensure similar conditions at both slice surfaces. Inset in B represents the schematic drawing of the fluid stream in the dual-superfusion slice chamber. Images taken with a CCD camera of the same hippocampal neurons in slices placed on a mesh in a dual-superfusion slice chamber (C), or, for comparison, on a glass coverslip in a classical submerged slice chamber (D). The visibility of neurons and their processes is not compromised in the dual-superfusion slice chamber.

1995; Fisahn et al., 1998; Hájos et al., 2000; Hughes et al., 2004; Lorincz et al., 2008; Maier et al., 2003; Pálhalmi et al., 2004). Yet, network activities in submerged slices are extremely difficult to obtain unless the necessary oxygen supply is provided by elevating the flow rate or by keeping the slices in a dual-superfusion slice chamber. For instance, sharp wave/ripple oscillations known to occur spontaneously in CA3 hippocampal networks *in vivo* (Buzsáki, 2006) and in slices kept in interface type slice chambers (Maier et al., 2003; Buzsáki, 2006) have been readily recorded under these modified submerged conditions (Fig. 2A and B) (Spampanato and Mody, 2007; Hájos et al., 2009). In addition, maintaining pharmacologically induced gamma (30–100 Hz) oscillations in hippocampal slices for extended periods of time (>30 min) also heavily depend on the recording conditions. In submerged chambers with low flow rates, gamma oscillations could be recorded only transiently, whereas at high flow rates these oscillations were maintained just like in recordings in a dual-superfusion slice chamber at lower flow rates (Fig. 2C and D) (Hájos et al., 2004; Hájos et al., 2009). Since pharmacologically induced gamma oscillations could be induced only transiently in submerged slices at low flow rates, yet they were maintained for long periods of time in submerged slices at high flow rates (Hájos et al., 2004; Mann et al., 2005; Oren et al., 2006), in slices kept in interface conditions (Fisahn et al., 1998; Pálhalmi et al., 2004), and in the intact brain (Sakatani et al., 2008), these findings are consistent with the idea that impaired slice oxygen levels might indeed be a limiting factor for network activities in submerged brain slices at low flow rates.

4. Single cell synaptic activity in submerged slices

In addition to synchronous network events the discharge probability of individual neurons is also affected by oxygen supply in submerged slices. In the absence of any additional pharmacological agents in the aCSF, the frequency of spontaneous inhibitory postsynaptic currents (sIPSCs) recorded in hippocampal slices submerged in a chamber with single superfusion, is significantly higher at high flow rates compared to low flow rates (Fig. 3). There is no difference in the peak conductance of the sIPSCs between the two conditions indicating that more oxygen delivered to slices is vital for the spontaneous firing of hippocampal interneurons in submerged slices. Similarly to the enhanced synaptic inhibition, the oxygen supply can also affect excitatory synaptic transmission. Both the amplitude and the frequency of spontaneous excitatory synaptic potentials (sEPSPs) recorded in CA1 hippocampal interneurons have been found to be significantly larger in slices kept in dual-superfusion chamber compared to those slices, which were placed in a classical chamber with single superfusion at flow rate of 2–3 ml/min (G. Katona, A. Kaszás, G. Turi, B. Rózsa, unpublished observation). The elevated synaptic activity due to the higher oxygen supply might be common in all cortical structures. For instance, in neocortical submerged slices using a flow rate of >8 ml/min, the frequency of spontaneous synaptic currents (both sEPSCs and sIPSCs) has been found to be around 40 Hz recorded in pyramidal cells or in interneurons (Spampanato et al., 2008), values that are substantially higher than those obtained at lower flow rates (~5–8 Hz, Bandrowski et al., 2003; Yang et al., 2007). These data collectively indicate that the discharge probability of both inhibitory interneurons and pyramidal cells in submerged slices can be varied with oxygen levels. Indeed, it has been observed that more dissolved oxygen in aCSF depolarized the membrane potential and caused a parallel increase in the membrane resistance of CA3 pyramidal neurons (Bingmann et al., 1984), changes that could contribute to the excitability of neurons.

With the improved spontaneous activity of neurons at rest by elevated oxygen supply, the modulation of neuronal firing by var-

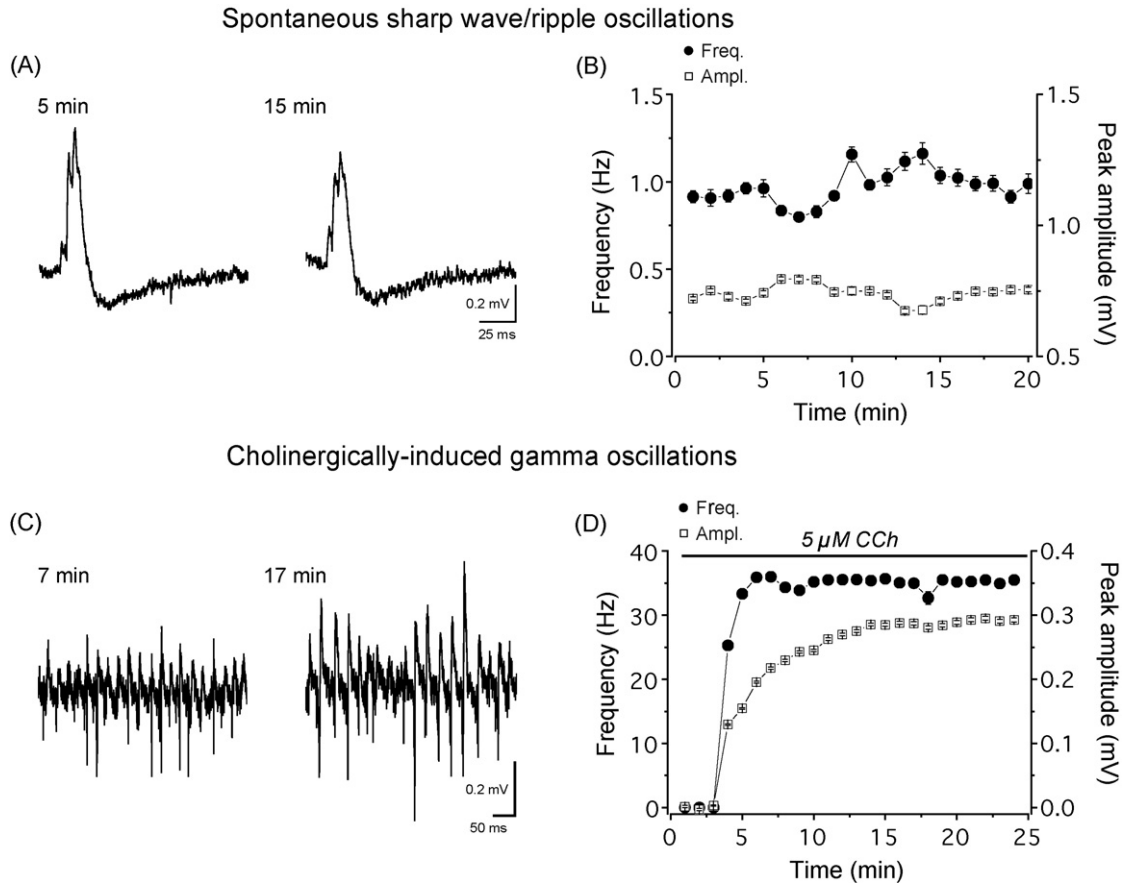

Fig. 2. Network oscillations in the CA3 region of mouse hippocampal slices maintained in a dual-superfusion chamber. (A), Sharp wave/ripple oscillations (sample traces taken from the indicated time points) could be readily detected under these recording conditions. (B), the stability of sharp wave/ripple oscillations is shown, where the frequency of their occurrence and their peak amplitudes are plotted as a function of time. (C), Cholinergically induced gamma oscillations could be easily induced in this type of slice chamber using carbachol (CCh) at concentrations as low as 1–5 μM. The raw traces of oscillations were taken from the indicated time points from the plot in (C). (D), Development and stabilization of cholinergically induced gamma oscillations during the wash-in of 5 μM CCh (indicated by horizontal bar) in a plot of the frequency and the peak amplitudes of oscillations as a function of time. In both cases, the network oscillations were recorded in aCSF containing 2 mM Ca^{2+} and 2 mM Mg^{2+} at 32–34 °C. The flow rate was 2–3 ml/min for each channel. Oscillations were recorded with a patch pipette filled with aCSF, placed in the stratum pyramidale. Data are mean ± SEM.

ious pharmacological agents might also be altered in submerged chambers when tissue oxygen supply is enhanced. It is well known that in hippocampal slices kept in interface type chambers cholinergic receptor activation (e.g. by carbachol) dramatically increases the spiking activity of inhibitory interneurons. As a consequence, the $GABA_A$ receptor-mediated synaptic events recorded in principal cells are enhanced for periods lasting tens of minutes (Pitler and Alger, 1992). A similar lasting increase in synaptic inhibition cannot be observed in submerged slices, unless the recoding conditions are changed. At low flow rates, bath application of carbachol only transiently increases both the amplitude and the frequency of sIPSCs recorded in pyramidal cells of CA3 hippocampal region. In contrast, the carbachol-induced enhancement of synaptic inhibition persists during the whole duration of the perfusion of this cholinergic agonist (Fig. 4) indicating that the high oxygen supply is necessary for the sustained firing of interneurons induced by carbachol.

5. Effects of the oxygen supply on intercellular signaling in submerged slices

As shown above, network oscillations, basal and drug-induced firing rates are all affected by the oxygen supply to submerged slices. Therefore, it is reasonable to assume that other critical neuronal events such retrograde signaling at synapses might also be affected by the oxygen levels reaching the slices maintained in submerged conditions. We have recently shown that in the presence of carbachol, nitric oxide and endocannabinoids are critically involved in a form of short-term plasticity at hippocampal GABAergic synapses, the depolarization-induced suppression of inhibition (DSI) (Makara et al., 2007). After comparing the properties of DSI at different flow rates in the presence of carbachol, DSI was more consistently observed in CA1 pyramidal cells at high flow rates (5–6 ml/min; 8/10 DSI) than at low flow rates (2–3 ml/min; 6/19 DSI). Moreover, the magnitude of DSI was also significantly different (at high flow rates: 47.1 ± 13.6%, $n = 8$; at low flow rates: 34.3 ± 6.1%, $n = 6$; $p < 0.05$, Student's t-test; N. Hájos, unpublished observations). Since the production of nitric oxide by nitric oxide synthase is affected by the oxygen concentration (Nathan and Xie, 1994), at low oxygen levels caused by low flow rates, the synthesis of nitric oxide might be diminished. Consequently, both the occurrence and the magnitude of DSI would be limited by the oxygen concentration available to the neurons.

To this point, we emphasized the necessity of increasing the oxygen supply of neurons in submerged slices that could help studies of neuronal events under conditions more approaching those *in vivo*. However, the possibility of hyper-oxygenation, which could significantly affect several parameters of neuronal function and may even cause acute cell death (Mulkey et al., 2001; Pomper et al., 2001), should be considered. In the ranges of the flow rates and oxygenation used in our experiments, we have not observed any cell death or neuronal activity that was not also observed *in vivo*. Nevertheless, an optimal range of oxygen supply may need to vary during various recording conditions, and possible unwanted effects of too high oxygen concentrations should also be taken into account.

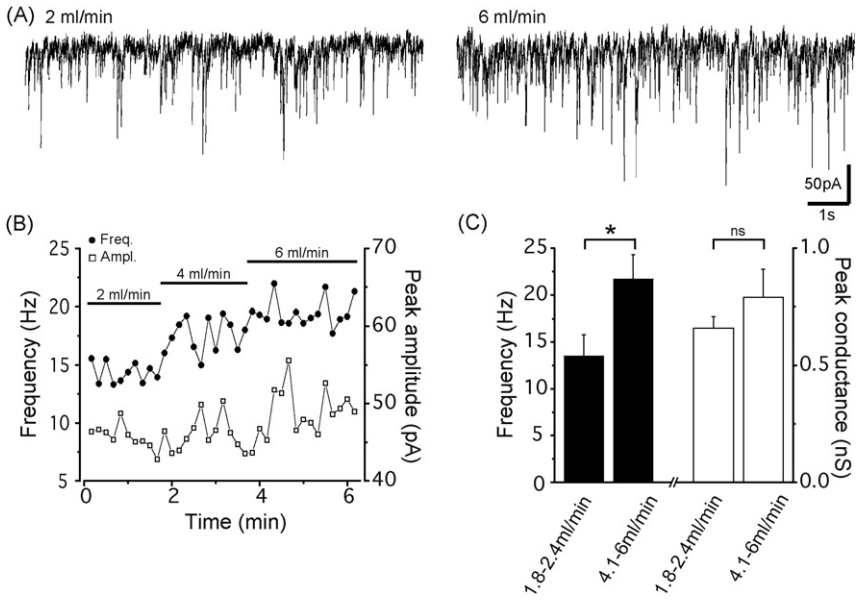

Fig. 3. The flow rate determines the spontaneous activity of interneurons as monitored by recording spontaneous inhibitory postsynaptic currents (sIPSCs) in a principal cell. (A), Raw IPSC recordings in a CA3 pyramidal cell using different flow rates. Hippocampal slices prepared from P16–20 rats were maintained in a classical submerged type recording chamber with single superfusion. sIPSCs were recorded by the whole-cell patch-clamp technique in the presence of the ionotropic glutamate receptor blocker kynurenic acid (3 mM) at a holding potential of −65 mV. (B), Plot of the effects of the flow rate on the frequency and the peak amplitudes of IPSCs from the same experiment. (C), At high flow rates, the frequency of sIPSCs recorded in CA3 pyramidal cells was significantly higher (21.7 ± 2.6 Hz, $n = 9$) compared to those recorded at low flow rates (13.5 ± 2.3 Hz, $n = 11$, $p < 0.05$, Student's t-test), whereas the average peak conductances of the sIPSCs were similar (low flow rate: 0.66 ± 0.05 nS, $n = 9$; high flow rate: 0.79 ± 0.12 nS, $n = 11$, $p > 0.1$, Student's t-test).

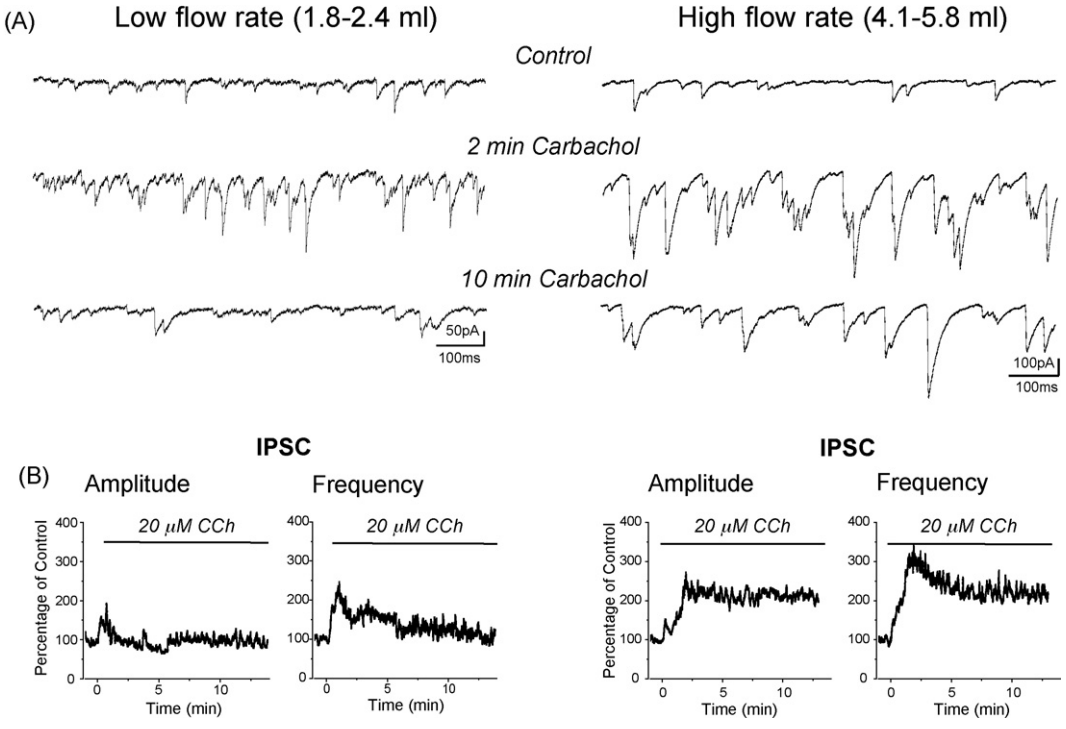

Fig. 4. The duration of the cholinergically enhanced inhibitory transmission critically depends on the flow rate in a single superfusion submerged type chamber. (A), Recording of IPSCs before and after carbachol application at low and high flow rates. Measurements were done in rat CA3 pyramidal cells as described in the legend of Fig. 3. (B), Plot of the amplitudes and frequencies of sIPSCs as a function of time at low and high flow rates. The times of the carbachol (CCh) applications are indicated by horizontal bars. Carbachol induced only a transient increase in sIPSC amplitude and frequency at low flow rates. In contrast, increased synaptic inhibition persisted in the presence of carbachol at high flow rates. The values calculated from 5 experiments for both conditions were normalized to control conditions (i.e., before carbachol application).

Table 1
Summary of *in vitro* physiological effects of some CSF components that are not routinely included in aCSF.

CSF components	In CSF (μM)	Preparation	Effects	References
GABA	1–5	Hippocampal slices	Maintaining tonic currents	Glykys and Mody (2006)
Glutamine	400–800	Hypothalamic slice Hippocampal slices	Increased spontaneous firing Necessary for synaptic function in >4 h, but not in <4 h slices	Nishimura et al. (1995) Kam and Nicoll (2007), An et al. (2008)
Ascorbic acid	500	Forebrain slices Hippocampal slices	Volume regulation Free radical scavenger	Brahma et al. (2000) Monje et al. (2000)
Taurine	1–10	Hippocampal slices	Volume regulation Maintained K+ content Higher ATP concentrations in slices	Kreisman and Olson (2003)
Lactate	800–2000	Hippocampal slices	Energy supply	Fowler (1993), Schurr et al. (1997); but see Yamane et al. (2000)
Serotonin	1–2	Hippocampal slices	Endogenous release of serotonin from fibers by a 5-HT releaser fenfluramine	Wojtowicz et al. (2009)

6. Notes on the composition of the aCSF to better approximate physiological conditions

The ionic composition of aCSF used by different laboratories is generally similar with small differences in K^+, Ca^{2+} and Mg^{2+} concentrations (Reid et al., 1988). These ions are typically added at higher concentrations to the aCSF than they are found in the regular CSF (Di Terlizzi and Platt, 2006). There is also a notable difference between aCSF and CSF in their glucose concentrations. In the CSF, glucose reaches concentration between 1.5 and 5 mM (McNay and Sherwin, 2004), whereas its concentration is kept at 10–25 mM in the aCSF. A difference in glucose availability was shown to affect distinct neuronal functions in slices including network events (Cunningham et al., 2006). Thus, when comparing results from different laboratories it is best to keep in mind that even subtle differences in some of the basic components of the aCSF might impact the outcome of the experiments (Reid et al., 1988).

What about other key ingredients of the natural CSF which are routinely excluded from the aCSF? For instance, neurotransmitter molecules in concentrations sufficient to act through various ionotropic and/or metabotropic receptors are consistently found in the normal CSF (Nyitrai et al., 2006). Neurotransmitter concentrations found in the normal CSF are sufficient to activate tonic conductances in distinct types of neurons by activating high affinity extrasynaptic receptors (Glykys and Mody, 2007). Such molecules are not customarily added to the aCSF, although the activated conductances significantly affect neuronal excitability and network oscillations in slice preparations (Glykys et al., 2008). Since the $GABA_A$ receptor-mediated tonic conductance was shown to depend even on the storage conditions of the slices (Glykys and Mody, 2006), it can be assumed that the amount of GABA in slices will considerably vary depending on the slice preparation and maintenance procedures used in various laboratories. Such discrepancies might be ameliorated by adding GABA to the aCSF to yield a final free GABA concentration of 200–500 nM, similar to that found in the normal CSF (Nyitrai et al., 2006). In addition to GABA, glutamate, acetylcholine, and many other known neuroactive molecules are also present in the normal CSF, some of them such as glutamine in mM concentrations (Lerma et al., 1986). Clearly, the concentrations of neuroactive compounds are not steady in the CSF, but are continuously changing as a function of brain activity. For instance, there are dramatic differences in the concentrations of acetylcholine and serotonin during slow wave sleep compared to that found in the CSF of awake animals (Westerink, 1995). Therefore, an argument could be made to use a variety of aCSF with different concentrations of neuroactive compounds to study the equivalent conditions of various brain states *in vitro*.

Neuromodulators like taurine, D-serine, ascorbate, etc. contained in the normal CSF could also significantly impact neuronal signaling if included in the aCSF. Of these compounds, ascorbic acid, an effective controller of free radical levels in the brain and a modulator of cellular excitability and synaptic communication (Rebec and Pierce, 1994), is used more and more often as an additive (1–3 mM) to the aCSF particularly during slice cutting procedure, but rarely in the aCSF used for recordings. In the rat brain CSF the concentration of ascorbic acid is around 0.5 mM, but neurons and glia can accumulate it by Na^+-dependent transporters (SVCT1 and SVCT2) up to 10 mM and 1 mM, respectively (Rice, 2000). In brain slices the concentration of ascorbate drops to 20% of control levels even after a brief incubation time with ascorbate-free media (Rice, 2000), a reduction that might be prevented by adding ~0.3 mM ascorbic acid to aCSF. It is reasonable to assume that ascorbic acid is but one of the compounds washed out from slices maintained *in vitro* (see e.g. Kapetanovic et al., 1993), that could significantly affect the experimental results (Table 1.). Therefore, we strongly feel that in order for slice preparations to better resemble the physiological environment of neurons in the intact brain, several compounds should be included in the aCSF. This approach together with ensuring a better oxygen supply to the slices should help the study of the behavior of neurons and their networks as it takes place in the intact brain.

7. Concluding remarks

In this review we emphasize the necessity of adequate oxygen supply to submerged slices that might impact the outcome of diverse electrophysiological experiments. Two methods are provided for improving the oxygen supply to submerged slices without significant disturbance of the visualization and recording. We also draw attention to the discrepancy between the components of normal CSF and those of the aCSF used for preparing and maintaining brain slices. We propose including some of the normal CSF constituents in the aCSF and appeal to form a consensus among interested neuroscientists.

Acknowledgments

This work was supported by the Wellcome Trust and the Hungarian Scientific Research Fund (OTKA T049517) to NH and NIH Grant NS30549 to IM.

References

An JH, Su Y, Radman T, Bikson M. Effects of glucose and glutamine concentration in the formulation of the artificial cerebrospinal fluid (ACSF). Brain Res 2008;1218:77–86.
Andersen P, Sundberg SH, Sveen O, Wigström H. Specific long-lasting potentiation of synaptic transmission in hippocampal slices. Nature 1977;266:737–9.
Bandrowski AE, Huguenard JR, Prince DA. Baseline glutamate levels affect group I and II mGluRs in layer V pyramidal neurons of rat sensorimotor cortex. J Neurophysiol 2003;89:1308–16.

Bingmann D, Kolde G, Lipinski HG. Relations between PO2 and neuronal activity in hippocampal slices. Advances in experimental medicine and biology 1984;169:215–26.

Brahma B, Forman RE, Stewart EE, Nicholson C, Rice ME. Ascorbate inhibits edema in brain slices. J Neurochem 2000;74:1263–70.

Buzsáki G. Rhythms of the brain. Oxford University Press; 2006.

Croning MD, Haddad GG. Comparison of brain slice chamber designs for investigations of oxygen deprivation in vitro. J Neurosci Methods 1998;81:103–11.

Csicsvari J, Jamieson B, Wise KD, Buzsaki G. Mechanisms of gamma oscillations in the hippocampus of the behaving rat. Neuron 2003;37:311–22.

Cunningham MO, Pervouchine DD, Racca C, Kopell NJ, Davies CH, Jones RS, et al. Neuronal metabolism governs cortical network response state. Proc Natl Acad Sci USA 2006;103:5597–601.

Dingledine R. Brain slices. Springer; 1984.

Di Terlizzi R, Platt S. The function, composition and analysis of cerebrospinal fluid in companion animals. Part I. Function and composition. Vet J 2006;172:422–31.

Edwards FA, Konnerth A, Sakmann B, Takahashi T. A thin slice preparation for patch clamp recordings from neurones of the mammalian central nervous system. Pflugers Arch 1989;414:600–12.

Fisahn A, Pike FG, Buhl E, Paulsen O. Cholinergic induction of network oscillations at 40 Hz in the hippocampus in vitro. Nature 1998;394:186–9.

Fowler JC. Glucose deprivation results in a lactate preventable increase in adenosine and depression of synaptic transmission in rat hippocampal slices. J Neurochem 1993;60:572–6.

Gloveli T, Dugladze T, Saha S, Monyer H, Heinemann U, Traub RD, et al. Differential involvement of oriens/pyramidale interneurones in hippocampal network oscillations in vitro. J Physiol 2005;562:131–47.

Glykys J, Mann EO, Mody I. Which GABA(A) receptor subunits are necessary for tonic inhibition in the hippocampus? J Neurosci 2008;28:1421–6.

Glykys J, Mody I. Activation of GABAA receptors: views from outside the synaptic cleft. Neuron 2007;56:763–70.

Glykys J, Mody I. Hippocampal network hyperactivity after selective reduction of tonic inhibition in GABA A receptor alpha5 subunit-deficient mice. J Neurophysiol 2006;95:2796–807.

Haas HL, Schaerer B, Vosmansky M. A simple perfusion chamber for the study of nervous tissue slices in vitro. J Neurosci Methods 1979;1:323–5.

Hájos N, Ellender TJ, Zemankovics R, Mann EO, Exley R, Cragg SJ, et al. Maintaining network activity in submerged hippocampal slices: importance of oxygen supply. Eur J Neurosci 2009;29:319–27.

Hájos N, Katona I, Naiem SS, MacKie K, Ledent C, Mody I, et al. Cannabinoids inhibit hippocampal GABAergic transmission and network oscillations. Eur J Neurosci 2000;12:3239–49.

Hájos N, Palhalmi J, Mann EO, Nemeth B, Paulsen O, Freund TF. Spike timing of distinct types of GABAergic interneuron during hippocampal gamma oscillations in vitro. J Neurosci 2004;24:9127–37.

Huchzermeyer C, Albus K, Gabriel HJ, Otahal J, Taubenberger N, Heinemann U, et al. Gamma oscillations and spontaneous network activity in the hippocampus are highly sensitive to decreases in pO2 and concomitant changes in mitochondrial redox state. J Neurosci 2008;28:1153–62.

Hughes SW, Lorincz M, Cope DW, Blethyn KL, Kekesi KA, Parri HR, et al. Synchronized oscillations at alpha and theta frequencies in the lateral geniculate nucleus. Neuron 2004;42:253–68.

Kam K, Nicoll R. Excitatory synaptic transmission persists independently of the glutamate–glutamine cycle. J Neurosci 2007;27:9192–200.

Kapetanovic IM, Yonekawa WD, Kupferberg HJ. Time-related loss of glutamine from hippocampal slices and concomitant changes in neurotransmitter amino acids. J Neurochem 1993;61:865–72.

Kreisman NR, Olson JE. Taurine enhances volume regulation in hippocampal slices swollen osmotically. Neuroscience 2003;120:635–42.

Lerma J, Herranz AS, Herreras O, Abraira V, Martin del Rio R. In vivo determination of extracellular concentration of amino acids in the rat hippocampus. A method based on brain dialysis and computerized analysis. Brain Res 1986;384:145–55.

Lorincz ML, Crunelli V, Hughes SW. Cellular dynamics of cholinergically induced alpha (8–13 Hz) rhythms in sensory thalamic nuclei in vitro. J Neurosci 2008;28:660–71.

Maier N, Nimmrich V, Draguhn A. Cellular and network mechanisms underlying spontaneous sharp wave–ripple complexes in mouse hippocampal slices. J Physiol 2003;550:873–87.

Makara JK, Katona I, Nyiri G, Nemeth B, Ledent C, Watanabe M, et al. Involvement of nitric oxide in depolarization-induced suppression of inhibition in hippocampal pyramidal cells during activation of cholinergic receptors. The J Neurosci 2007;27:10211–22.

Mann EO, Suckling JM, Hájos N, Greenfield SA, Paulsen O. Perisomatic feedback inhibition underlies cholinergically induced fast network oscillations in the rat hippocampus in vitro. Neuron 2005;45:105–17.

McMahon LL, Williams JH, Kauer JA. Functionally distinct groups of interneurons identified during rhythmic carbachol oscillations in hippocampus in vitro. J Neurosci 1998;18:5640–51.

McNay EC, Sherwin RS. From artificial cerebro-spinal fluid (aCSF) to artificial extracellular fluid (aECF): microdialysis perfusate composition effects on in vivo brain ECF glucose measurements. J Neurosci Methods 2004;132:35–43.

Monje ML, Chatten-Brown J, Hye SE, Raley-Susman KM. Free radicals are involved in the damage to protein synthesis after anoxia/aglycemia and NMDA exposure. Brain Res 2000;857:172–82.

Mulkey DK, Henderson 3rd RA, Olson JE, Putnam RW, Dean JB. Oxygen measurements in brain stem slices exposed to normobaric hyperoxia and hyperbaric oxygen. J Appl Physiol 2001;90:1887–99.

Nathan C, Xie QW. Regulation of biosynthesis of nitric oxide. J Biochem 1994;269:13725–8.

Nishimura F, Nishihara M, Mori M, Torii K, Takahashi M. Excitability of neurons in the ventromedial nucleus in rat hypothalamic slices: modulation by amino acids at cerebrospinal fluid levels. Brain Res 1995;691:217–22.

Nyitrai G, Kekesi KA, Juhasz G. Extracellular level of GABA and Glu: in vivo microdialysis-HPLC measurements. Curr Top Med Chem 2006;6:935–40.

Oren I, Mann EO, Paulsen O, Hajos N. Synaptic currents in anatomically identified CA3 neurons during hippocampal gamma oscillations in vitro. J Neurosci 2006;26:9923–34.

Pálhalmi J, Paulsen O, Freund TF, Hájos N. Distinct properties of carbachol- and DHPG-induced network oscillations in hippocampal slices. Neuropharmacology 2004;47:381–9.

Pitler TA, Alger BE. Cholinergic excitation of GABAergic interneurons in the rat hippocampal slice. J Physiol 1992;450:127–42.

Pomper JK, Graulich J, Kovacs R, Hoffmann U, Gabriel S, Heinemann U. High oxygen tension leads to acute cell death in organotypic hippocampal slice cultures. Brain Res 2001;126:109–16.

Rebec GV, Pierce RC. A vitamin as neuromodulator: ascorbate release into the extracellular fluid of the brain regulates dopaminergic and glutamatergic transmission. Prog Neurobiol 1994;43:537–65.

Reid KH, Edmonds Jr HL, Schurr A, Tseng MT, West CA. Pitfalls in the use of brain slices. Prog Neurobiol 1988;31:1–18.

Rice ME. Ascorbate regulation and its neuroprotective role in the brain. Trends Neurosci 2000;23:209–16.

Sakatani S, Seto-Ohshima A, Shinohara Y, Yamamoto Y, Yamamoto H, Itohara S, et al. Neural-activity-dependent release of S100B from astrocytes enhances kainate-induced gamma oscillations in vivo. J Neurosci 2008;28:10928–36.

Sakmann B, Edwards F, Konnerth A, Takahashi T. Patch clamp techniques used for studying synaptic transmission in slices of mammalian brain. J Exp Physiol 1989;74:1107–18.

Schurr A, Payne RS, Miller JJ, Rigor BM. Brain lactate, not glucose, fuels the recovery of synaptic function from hypoxia upon reoxygenation: an in vitro study. Brain Res 1997;744:105–11.

Schwartzkroin PA, Andersen P. Glutamic acid sensitivity of dendrites in hippocampal slices in vitro. Adv Neurol 1975;12:45–51.

Skrede KK, Westgaard RH. The transverse hippocampal slice: a well-defined cortical structure maintained in vitro. Brain Res 1971;35:589–93.

Spampanato J, Gu X, Yang XW, Mody I. Progressive synaptic pathology of motor cortical neurons in a BAC transgenic mouse model of Huntington's disease. Neuroscience 2008;157:606–20.

Spampanato J, Mody I. Spike timing of lacunosom-moleculare targeting interneurons and CA3 pyramidal cells during high-frequency network oscillations in vitro. J Neurophysiol 2007;98:96–104.

Steriade M. The intact and sliced brain. MIT Press 2001.

Stuart GJ, Dodt HU, Sakmann B. Patch-clamp recordings from the soma and dendrites of neurons in brain slices using infrared video microscopy. Pflugers Arch 1993;423:511–8.

Thomson AM, Bannister AP, Hughes DI, Pawelzik H. Differential sensitivity to Zolpidem of IPSPs activated by morphologically identified CA1 interneurons in slices of rat hippocampus. Eur J Neurosci 2000;12:425–36.

Turner DA, Foster KA, Galeffi F, Somjen GG. Differences in O(2) availability resolve the apparent discrepancies in metabolic intrinsic optical signals in vivo and in vitro. Trends Neurosci 2007;30:390–8.

Vanzetta I, Grinvald A. Increased cortical oxidative metabolism due to sensory stimulation: implications for functional brain imaging. Science 1999;286:1555–8.

Vanzetta I, Hildesheim R, Grinvald A. Compartment-resolved imaging of activity-dependent dynamics of cortical blood volume and oximetry. J Neurosci 2005;25:2233–44.

Westerink BH. Brain microdialysis and its application for the study of animal behaviour. Behav Brain Res 1995;70:103–24.

Whittington MA, Traub RD, Jeffreys JGR. Synchronized oscillations in interneurons driven by metabotropic glutamate receptor activation. Nature 1995;373:612–5.

Wilson RJ, Chersa T, Whelan PJ. Tissue PO2 and the effects of hypoxia on the generation of locomotor-like activity in the in vitro spinal cord of the neonatal mouse. Neuroscience 2003;117:183–96.

Wojtowicz AM, van den Boom L, Chakrabarty A, Maggio N, Haq RU, Behrens CJ, et al. Monoamines block kainate- and carbachol-induced gamma-oscillations but augment stimulus-induced gamma-oscillations in rat hippocampus in vitro. Hippocampus 2009;19:273–88.

Wu C, Luk WP, Gillis J, Skinner F, Zhang L. Size does matter: generation of intrinsic network rhythms in thick mouse hippocampal slices. J Neurophysiol 2005;93:2302–17.

Yamamoto C, McIlwain H. Potentials evoked in vitro in preparations from the mammalian brain. Nature 1966;210:1055–6.

Yamane K, Yokono K, Okada Y. Anaerobic glycolysis is crucial for the maintenance of neural activity in guinea pig hippocampal slices. J Neurosci Methods 2000;103:163–71.

Yang J, Wetterstrand C, Jones RS. Felbamate but not phenytoin or gabapentin reduces glutamate release by blocking presynaptic NMDA receptors in the entorhinal cortex. Epilepsy Res 2007;77:157–64.

dc_71_10

14. számú melléklet

Neural Networks 22 (2009) 1113–1119

Contents lists available at ScienceDirect

Neural Networks

journal homepage: www.elsevier.com/locate/neunet

2009 Special Issue

Network mechanisms of gamma oscillations in the CA3 region of the hippocampus

Norbert Hájos [a,*], Ole Paulsen [b,**]

[a] Department of Cellular and Network Neurobiology, Institute of Experimental Medicine, Hungarian Academy of Sciences, Budapest, Hungary
[b] Department of Physiology, Anatomy and Genetics, University of Oxford, Oxford OX1 3PT, UK

ARTICLE INFO

Article history:
Received 30 March 2009
Received in revised form 22 June 2009
Accepted 14 July 2009

Keywords:
Gamma oscillation
GABA
Inhibition
Interneuron
Hippocampus

ABSTRACT

Neural networks of the brain display multiple patterns of oscillatory activity. Some of these rhythms are generated intrinsically within the local network, and can therefore be studied in isolated preparations. Here we discuss local-circuit mechanisms involved in hippocampal CA3 gamma oscillations, one of the best understood locally generated network patterns in the mammalian brain. Perisomatic inhibitory cells are crucial players in gamma oscillogenesis. They provide prominent rhythmic inhibition to CA3 pyramidal cells and are themselves synchronized primarily by excitatory synaptic inputs derived from the local collaterals of CA3 pyramidal cells. The recruitment of this recurrent excitatory–inhibitory feedback loop during hippocampal gamma oscillations suggests that local gamma oscillations not only control *when*, but also *how many* and *which* pyramidal cells will fire during each gamma cycle.

Oscillatory activity in the gamma-frequency band (30–70 Hz) occurs in many regions of the awake brain and is associated with several cognitive functions including sensory processes (Gray, 1994; Singer, 1993), selective attention (Fries, Reynolds, Rorie, & Desimone, 2001), and memory (Fell et al., 2001). During exploratory behaviour, prominent gamma oscillations are seen nested in the theta rhythm in the rodent hippocampus (Bragin et al., 1995; Chrobak & Buzsáki, 1998; Csicsvari, Jamieson, Wise, & Buzsáki, 2003; Fell et al., 2001; Leung, 1979), where they have been suggested to contribute to encoding and retrieval of memory (Bauer, Paz, & Paré, 2007; Hasselmo, Wyble, & Wallenstein, 1996; Montgomery & Buzsáki, 2007; Varela, Lachaux, Rodriguez, & Martinerie, 2001). To gain deeper insight into the function of these network oscillations in neuronal signal processing, the underlying cellular mechanisms need to be uncovered. *In vivo* studies have revealed that gamma oscillations can emerge locally in some cortical regions and propagate to neighboring areas (Bragin et al., 1995; Csicsvari et al., 2003; König, Engel, & Singer, 1995). These oscillations were found to be generated spontaneously only in those neuronal networks in which the recurrent excitatory collateral system among principal cells is significant, including the neocortex, the CA3 region of the hippocampus, and the basolateral amygdala (Bragin et al., 1995; Collins, Pelletier, & Paré, 2001; König et al., 1995). In brain areas lacking local recurrent connections among excitatory cells, such as the dentate gyrus and the CA1 region of the hippocampus, gamma oscillations appear to depend on extrinsic rhythmic inputs (Bragin et al., 1995; Csicsvari et al., 2003). This is not because these areas are intrinsically unable to maintain rhythmic activity, since under certain experimental conditions gamma oscillations could be recorded in isolated neuronal networks from the dentate gyrus or the CA1 region *in vitro* (Poschel, Draguhn, & Heinemann, 2002; Towers et al., 2002; Whittington, Traub, & Jefferys, 1995; for review see Bartos, Vida, & Jonas, 2007), but *in vivo*, such rhythmic activity appears to emerge spontaneously only in neuronal networks with substantially interconnected excitatory cells. The capability of cortical areas to generate gamma oscillations intrinsically allows us to study the basic cellular mechanisms in isolated neuronal networks, for example in acute brain slice preparations. Indeed, several *in vitro* models of gamma oscillations were established in slices from the rodent hippocampus (Fisahn, Pike, Buhl, & Paulsen, 1998; Fischer, Wittner, Freund, & Gähwiler, 2002; Hájos et al., 2000; LeBeau, Towers, Traub, Whittington, & Buhl, 2002; Pálhalmi, Paulsen, Freund, & Hájos, 2004; Whittington et al., 1995), entorhinal cortex (Cunningham, Davies, Buhl, Kopell, & Whittington, 2003), amygdala (Sinfield & Collins, 2006) as well as neocortex (Buhl,

* Corresponding address: Institute of Experimental Medicine, Hungarian Academy of Sciences, Szigony u. 43, 1083 Budapest, Hungary. Tel.: +36 1 2109400x367; fax: +36 1 2109412.
** Corresponding address: Department of Physiology, Anatomy and Genetics, University of Oxford, Parks Road, Oxford OX1 3PT, UK. Tel.: +44 1865 272535; fax: +44 1865 272469.
E-mail addresses: hajos@koki.hu (N. Hájos), ole.paulsen@dpag.ox.ac.uk (O. Paulsen).

0893-6080/$ – see front matter © 2009 Elsevier Ltd. All rights reserved.
doi:10.1016/j.neunet.2009.07.024

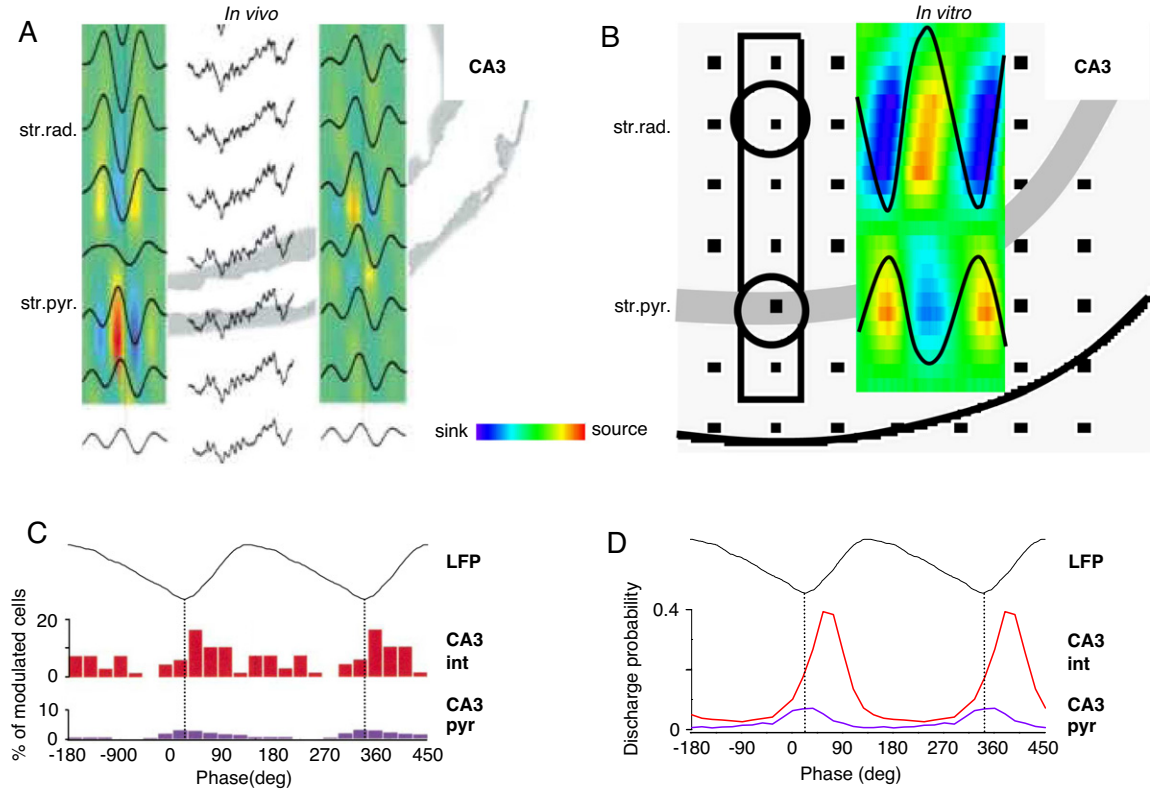

Fig. 1. Comparison of gamma oscillations in the CA3 region of the hippocampus recorded in the behaving rat (*in vivo*) with those induced in rat hippocampal slices by activation of cholinergic receptors (*in vitro*). (A, B). In both cases, the field potential reversal is seen between the pyramidal cell layer (str. pyr.) and the apical dendritic layer of pyramidal cells (str. rad.), and the current source density profiles look similar. In the intact brain, oscillations were recorded with a silicon probe implanted in the hippocampus. In the slices, network activities were detected using a 64-channel multielectrode array. The current source density analysis was performed on signals recorded from the electrodes outlined by the rectangle, while the circles label two recording sites from which the averaged field potentials were calculated (B). (C, D). In addition to the marked similarities of local voltage deflections and current flow during gamma oscillations, the spike phase of CA3 pyramidal cells (pyr) and GABAergic interneurons (int) was also equivalent *in vivo* (C) and *in vitro* (D), as in both cases, the firing of principal cells at the negative peak of local field potentials (LFP) was followed by the discharge of local inhibitory neurons. Panels A and C are reproduced from Csicsvari et al. (2003), while B and D are modified from Hájos et al. (2004).

Tamás, & Fisahn, 1998; Compte et al., 2008, Yamawaki, Stanford, Hall, & Woodhall, 2008). All these studies, first performed in interface recording chambers, showed that the rhythmic discharge of local inhibitory cells is pivotal for the emergence of oscillatory activities in the local field potential. In some models, phasic excitation was also crucial for oscillogenesis (Fisahn et al., 1998; Mann, Suckling, Hájos, Greenfield, & Paulsen, 2005). The detailed investigation of the mechanisms underlying gamma oscillations was further assisted by the establishment of conditions under which oscillations could be studied in submerged slices, which offer a number of experimental advantages, including the possibility to use imaging techniques and visualize individual neurons (Gloveli et al., 2005; Hájos et al., 2009, 2004). To date, most of these studies have focused on oscillogenesis in the CA3 region of the hippocampus, where the input–output features of different types of neurons during gamma oscillations in slices have been investigated in detail (Hájos et al., 2004; Mann, Suckling et al., 2005; Oren, Mann, Paulsen, & Hájos, 2006). Before we discuss these studies, let us first compare the properties of gamma oscillations in CA3 recorded in behaving animals with those induced pharmacologically in slice preparations.

1. Comparison of network oscillations in vitro and in vivo

A prerequisite for studying physiologically relevant mechanisms of oscillatory activity *in vitro* is that the oscillations share some properties with oscillatory activity occurring in the same structures *in vivo*. One of the best studied *in vitro* models of gamma oscillations is the cholinergic induction of fast oscillations in the CA3 of hippocampal slices (Fisahn et al., 1998). This oscillatory activity is intended to mimic *in vivo* gamma oscillations recorded during exploratory behaviour, when acetylcholine levels are reported to be high (Marrosu et al., 1995). *In vivo* data are consistent with the intrinsic generation of gamma oscillations in the CA3 network (Bragin et al., 1995; Csicsvari et al., 2003). The activity appears to be controlled by feed-forward inhibition from the dentate gyrus both in awake and anesthetized animals (Bragin et al., 1995; Csicsvari et al., 2003). Therefore, it is not surprising that field oscillations emerge when hippocampal slices are treated with cholinergic receptor agonists, such as carbachol, which elevate the excitability of CA3 pyramidal neurons and reduce the activity of dentate granule cells (Müller & Misgeld, 1986; Nabekura, Ebihara, & Akaike, 1993), decreasing the potential impact of feed-forward inhibition from the dentate gyrus.

Several basic features of gamma oscillations induced in the CA3 of hippocampal slices are comparable with the properties of gamma oscillations recorded in behaving animals (Fig. 1). Firstly, the phase of the local field potential reverses between the cell body layer of CA3 pyramidal cells (stratum pyramidale) and their apical dendritic regions (stratum radiatum), with the minimal amplitude found in the stratum lucidum (Fig. 1(A), (B)). Secondly, current source density profiles are very similar *in vivo* and *in vitro* (Fig. 1(A), (B)). Thirdly, the discharge probability of CA3 pyramidal cells is highest at the negative peaks of gamma oscillations recorded in the cell body layer, and is followed by the firing of CA3 inhibitory neurons with a delay consistent with monosynaptic excitation both *in vivo* and *in vitro* (Fig. 1(C), (D)). These similarities strengthen the suggestion that cholinergically-induced fast network oscillations *in vitro* are a good model of

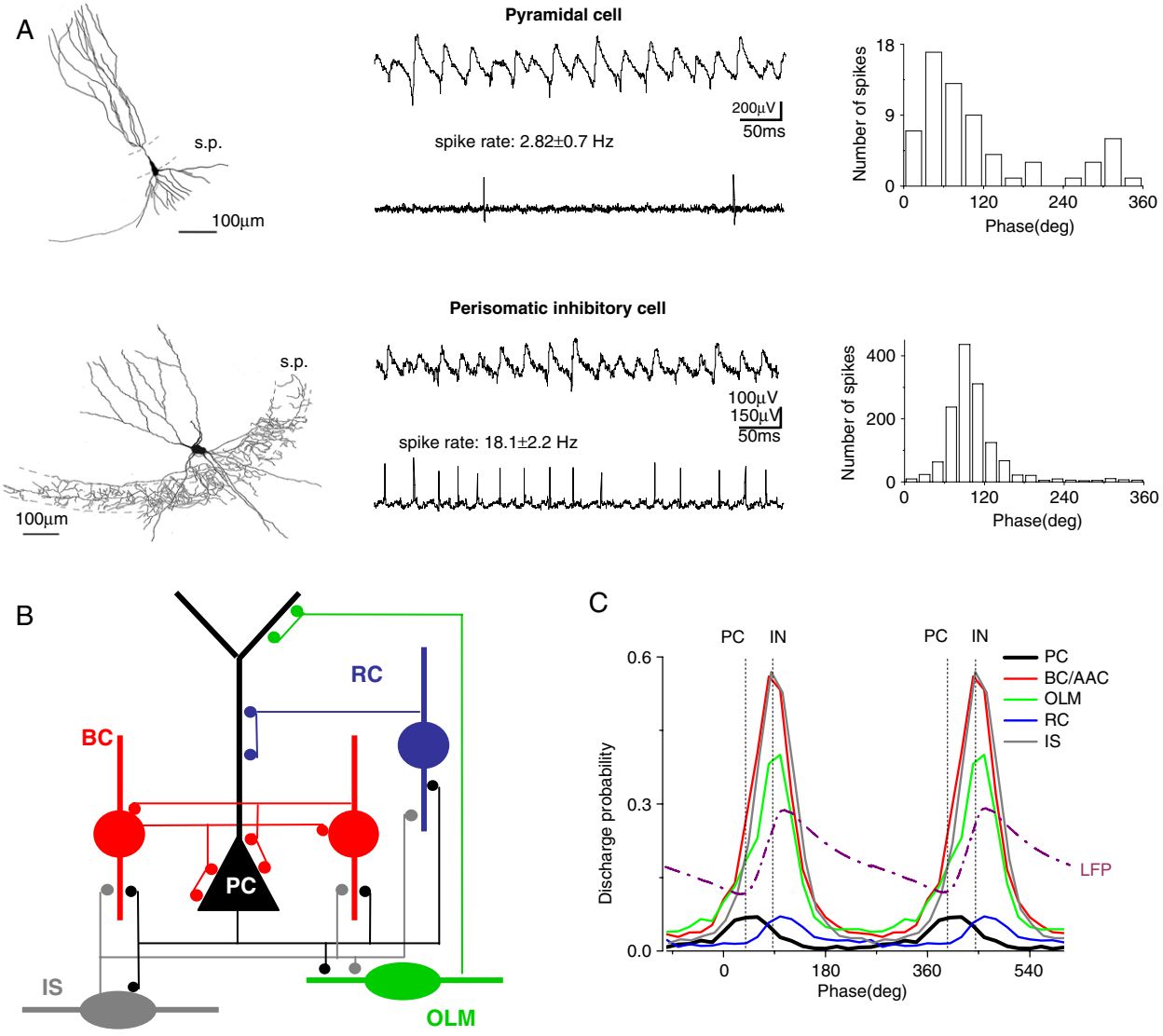

Fig. 2. Distinct output features of CA3 neurons during gamma oscillations *in vitro*. (A). Two examples of anatomically-identified cells and their firing properties with the corresponding spike phase histograms during cholinergically-induced gamma oscillations. Pyramidal cells fired at low rate and earlier within a gamma cycle compared to the more active inhibitory neurons. (B). Schematic diagram of the CA3 hippocampal circuitry. (C). Averaged phase histograms of phase-coupled cell types during gamma oscillations. In all cases, gamma-modulated firing of inhibitory cells (IN) followed the discharge of pyramidal cells (PC). BC, basket cell; AAC, axo-axonic cell; OLM, interneurons in the stratum oriens projecting to the stratum lacunosum-moleculare; RC, interneurons with both dendritic and axonal arborizations restricted to the stratum radiatum; IS, cells with horizontal dendritic tree with morphological appearance resembling interneuron-selective interneurons; LFP, local field potential; s.p. stratum pyramidale. Adapted from Hájos et al. (2004).

behaviorally relevant gamma oscillations, and justify studying the underlying mechanisms in hippocampal slices.

2. CA3 network architecture

What is the functional connectivity within the CA3 neuronal network? As all cortical structures, the hippocampus contains both excitatory principal neurons and inhibitory local-circuit interneurons. The former cell type is thought to process, store and retrieve information (Marr, 1971; Rolls & Treves, 1994), whereas the latter provides local spatial and temporal control of these principal cells and are critically important for the synchronization of rhythmic activity (Buzsáki & Chrobak, 1995; Mann & Paulsen, 2007; Paulsen & Moser, 1998). In addition to excitatory afferents from the dentate gyrus and the entorhinal cortex, pyramidal cells in the CA3 region receive synaptic excitation from other CA3 pyramidal neurons and give rise to axon collaterals terminating in both the ipsi and contralateral CA3 as well as both ipsi and contralateral CA1. In both regions, the excitation is mediated predominantly via single synaptic contacts (Sorra & Harris, 1993). In addition to each other, pyramidal cells also innervate local GABAergic interneurons, via connections that are also formed typically by single synapses (Gulyás et al., 1993b; Sik, Tamamaki, & Freund, 1993; Wittner, Henze, Zaborszky, & Buzsáki, 2006). Whereas principal neurons are rather uniform within each area of the hippocampus, a large morphological and functional heterogeneity is characteristic of GABAergic interneurons (Freund & Buzsáki, 1996). Functionally, three main GABAergic cell classes were suggested to coexist in cortical networks (Fig. 2(B)). *Perisomatic inhibitory neurons* can effectively control the firing of principal cells (Buhl, Halasy, & Somogyi, 1994; Cobb, Buhl, Halasy, Paulsen, & Somogyi, 1995; Gulyás, Hájos, & Freund, 1996). *Dendritic targeting inhibitory cells* are in a position to regulate synaptic input and dendritic Ca^{2+} signaling (Gulyás & Freund, 1996; Miles, Tóth, Gulyás, Hájos, & Freund, 1996; Tsubokawa & Ross, 1996). *GABAergic cells specifically*

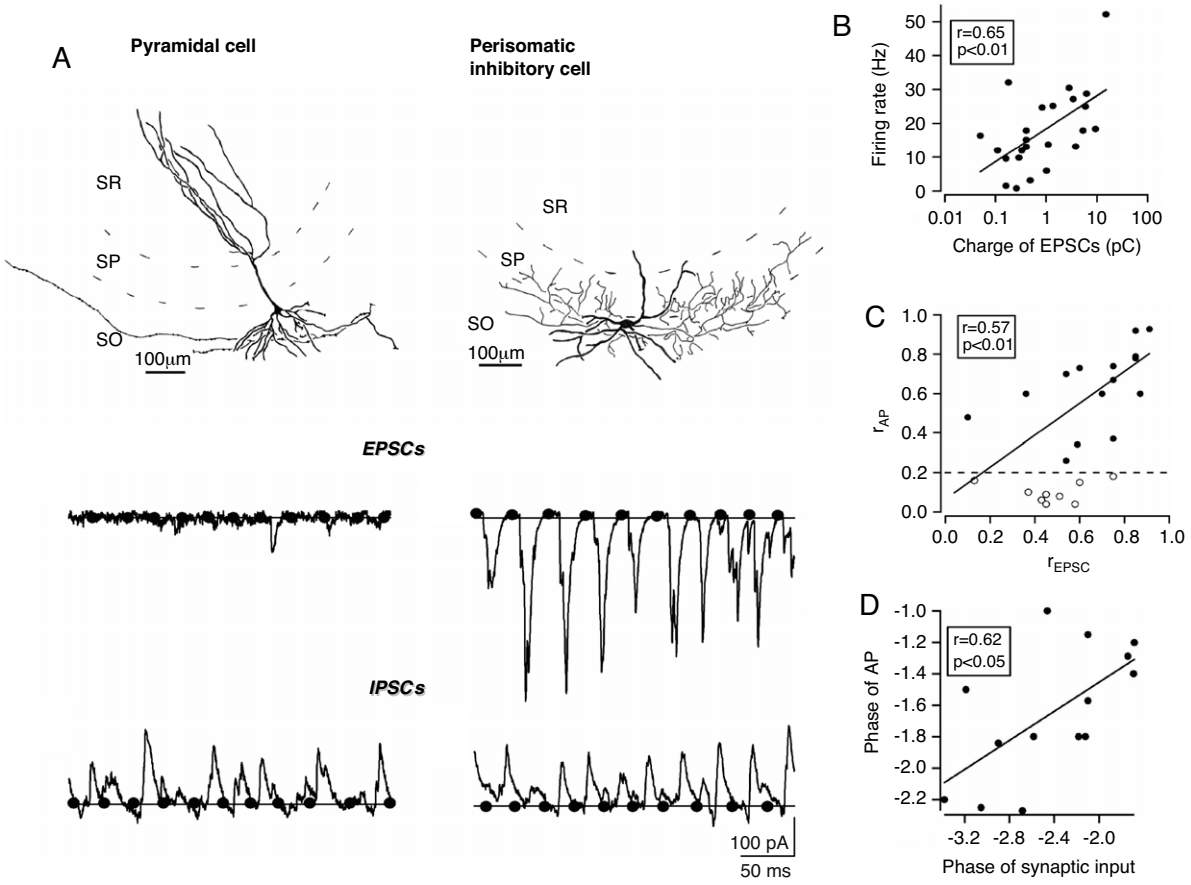

Fig. 3. Distinct synaptic inputs of CA3 neurons during gamma oscillations *in vitro*. (A). Two examples of anatomically-identified cells and their excitatory and inhibitory synaptic currents during gamma oscillations. Excitatory and inhibitory postsynaptic currents (EPSCs and IPSCs) were detected at holding potentials of −65 mV and 0 mV, respectively. While IPSCs had similar properties in all cell types, EPSCs were markedly smaller in CA3 pyramidal cells compared to those recorded in inhibitory cells. (B). Firing rate of all neurons was found to correlate with the amount of synaptic excitation within an oscillation cycle. (C). The strength of the phase-coupling of action potentials (r_{AP}) was correlated with the strength of the phase-coupling of excitatory synaptic inputs (r_{EPSC}) in interneurons. Filled symbols, strongly phase-coupled cells; open symbols, weakly or non-phase-coupled cells. (D). The phase of action potential discharge of strongly phase-coupled cells depended on the phase of the net resultant synaptic input. Phase is given in radians. For more details see Oren et al. (2006).

innervating other inhibitory interneurons can play a substantial role in the synchronization of the activity of large neuronal ensembles locally or in brain regions they project to (Gulyás et al., 1996; Gulyás, Hájos, Katona, & Freund, 2003). All inhibitory cell types innervate their targets via multiple contacts (Biro, Holderith, & Nusser, 2006; Buhl et al., 1994; Gulyás & Freund, 1996; Gulyás, Miles, Hájos, & Freund, 1993a; Miles et al., 1996). Since the synaptic input of basket and axo-axonic cells (i.e. perisomatic inhibitory interneurons) can synchronize the firing of postsynaptic pyramidal cells (Cobb et al., 1995), these cell types are likely to play key roles in rhythm generation. It might be of interest that basket cells innervate their pyramidal cell targets via 2–3 synaptic contacts on average in the CA3 region (Biro et al., 2006; Miles et al., 1996), via 10–12 boutons in the CA1 region (Buhl et al., 1994) and via 5–6 contacts in the dentate gyrus (Kraushaar & Jonas, 2000), suggesting that the convergence of perisomatic input received by the principal cells might not be uniform in every cortical structure. The details of the synaptic connectivity among hippocampal interneurons in CA3 are not available. However, data obtained in the CA1 subfield suggest that basket cells are mutually interconnected via multiple synapses (Cobb et al., 1997; Karson, Tang, Milner, & Alger, 2009; Klausberger, Roberts, & Somogyi, 2002).

In short, excitatory and inhibitory synaptic transmission in the CA3 subfield is mediated via single and multiple anatomical contacts, respectively. From the functionally diverse group of interneurons, it is likely that perisomatic inhibitory cells are the key elements of the CA3 neuronal network that contribute to fast rhythm generation.

3. Firing patterns of distinct types of neurons during gamma oscillations

A first step towards understanding the network mechanisms of gamma oscillations is to elucidate the behavior of anatomically distinct neuron types during this network activity. The parallel recording of firing of individual neurons with the recording of local field oscillations revealed that pyramidal cells tend to fire at around 2–4 Hz during gamma oscillations, both *in vitro* (Fisahn et al., 1998; Gloveli et al., 2005; Hájos et al., 2004) and *in vivo* (Senior, Huxter, Allen, O'Neill, & Csicsvari, 2008) (Fig. 2(A)). Most types of inhibitory neuron are more active than pyramidal cells both *in vitro* and *in vivo* (Csicsvari et al., 2003; Gloveli et al., 2005; Hájos et al., 2004; Tukker, Fuentealba, Hartwich, Somogyi, & Klausberger, 2007) (Fig. 2(A)). The perisomatic inhibitory cells (including basket and axo-axonic cells), GABAergic cells with long projections (including trilaminar and/or interneuron-specific interneurons) and bistratified cells were found to fire action potentials on almost every gamma cycle in hippocampal slices (Hájos et al., 2004). The discharge of other types of interneuron that target the dendritic regions of CA3 pyramidal cells (O-LM and radiatum cells) typically skipped two–three cycles (Gloveli et al., 2005; Hájos et al., 2004). With some exceptions, mainly among

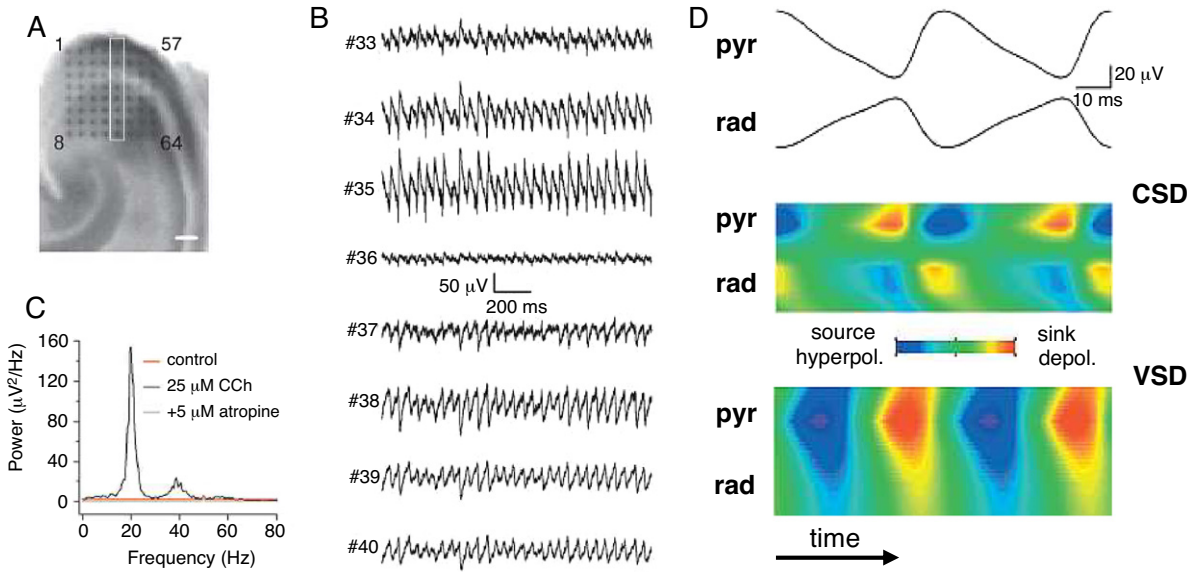

Fig. 4. Perisomatic inhibition generates fast network oscillations in the CA3 region of hippocampal slices. (A). A hippocampal slice mounted on a 64-channel multielectrode array. The white box indicates the column of electrodes used to detect local field potentials shown in B. Scale bar is 200 μm. (B). Bath application of carbachol (25 μM CCh) induced oscillations in the field potentials across the different layers of CA3, with reversal of the polarity of the field oscillation in the stratum lucidum (#36). (C). The power spectral density of the oscillations recorded in the stratum pyramidale (#35) showed a peak at 20 Hz, with an harmonic at 40 Hz in the presence of CCh. No rhythmicity was detected before CCh application or in the presence of the muscarinic receptor antagonist atropine. (D). Peak-to-peak cycle averages of the local field potentials from the stratum pyramidale (pyr) and distal stratum radiatum (rad) during CCh-induced fast oscillations, with current source density (CSD) profile and averages of voltage sensitive dye (VSD) signals below, indicating that the active current source is mainly restricted to the pyramidal cell layer. Thus interneurons innervating the perisomatic region of principal cells play a pivotal role in oscillogenesis. Modified from Mann, Suckling et al. (2005).

interneurons located in the stratum radiatum, the firing of both excitatory and inhibitory cells was phase-coupled to the gamma oscillations (Fig. 2(C)).

4. Synaptic mechanisms of network oscillations

What determines the discharge pattern of individual neurons within a cell group and among the cell types during gamma oscillations? An analysis of synaptic inputs correlated with the firing characteristics of neurons might give an answer to this question. Analysis of excitatory and inhibitory synaptic currents (EPSCs and IPSCs) revealed that inhibitory cells tend to receive larger EPSCs than pyramidal cells, whereas IPSCs were found to be more pronounced in pyramidal cells compared to those seen in inhibitory cells (Fig. 3(A); Oren et al., 2006). Inhibitory synaptic input in CA3 pyramidal cells dominated over the phasic excitation, whereas excitatory synaptic conductance was about the same or larger than the phasic inhibitory conductance in GABAergic cells. Compared to the extracellularly monitored spiking activity, in all cells, the firing frequency was found to be correlated with the synaptic excitatory charge received per cycle (Fig. 3(B); see also Fig. 5(B) in Oren et al. (2006)). The phase of the action potential discharge was controlled by the timing of both excitation and inhibition (Fig. 3(D); Oren et al., 2006). The strength of the phase-coupling of action potential discharge in GABAergic cells was correlated to the strength of the phase-coupling of both phasic excitation and inhibition, whereas in pyramidal cells the strength of the action potential phase-coupling correlated only weakly or was not correlated with the strength of phase-coupling of synaptic input (Fig. 3(C); Oren et al., 2006). These data are consistent with a recent study demonstrating that strong gamma-modulated excitation of pyramidal neurons is inconsistent with spike patterns recorded during neocortical gamma oscillations (Morita, Kalra, Aihara, & Robinson, 2008). The importance of synaptic excitation of interneurons is further emphasized by recent experimental evidence showing that selective reduction of phasic excitation, but not inhibition, on fast-spiking basket and axo-axonic cells disrupts gamma oscillations (Fuchs et al., 2007; Wulff et al., 2009). In line with these findings, a modelling study suggested that phasic excitation of interneurons within an excitatory–inhibitory feedback loop is sufficient to explain the emergence of gamma oscillations when pyramidal neurons are tonically excited (Mann, Radcliffe, & Paulsen, 2005). Indeed, carbachol is able to tonically drive action potentials in CA3 pyramidal cells (Müller & Misgeld, 1986), providing a physiological basis for these modeling results.

The differences in synaptic inputs are important in determining the distinct spiking behavior of neurons during gamma oscillations. However, many distinct cell types take part in the network activity, and the question arises as to which of these cell types are the most important for the generation of gamma oscillations. To answer this question, one needs to clarify the spatial distribution of active currents during oscillations, where active sources would indicate synaptic inhibition. Experimentally, this aim was achieved by a combination of current source density analysis with the monitoring of membrane potential changes using voltage sensitive dyes during oscillatory activities. It was found that currents restricted mainly to the perisomatic region of pyramidal cells were the active sources in carbachol-induced network oscillations (Fig. 4; Mann, Suckling et al., 2005). Thus, the rhythmic activity of perisomatic inhibitory cells is likely to play a pivotal role in the generation of gamma oscillations in the CA3 region of the hippocampus.

5. Computational implications

Whilst there is agreement that gamma oscillations can emerge locally, two distinct models have been proposed for the generation of gamma-frequency hippocampal oscillations. One posits that interneurons form a network that generates a network oscillation independent of pyramidal neurons (Whittington et al., 1995), the other requires feedback interaction between pyramidal neurons and perisomatic targeting interneurons (Fisahn et al., 1998; Mann, Suckling et al., 2005).

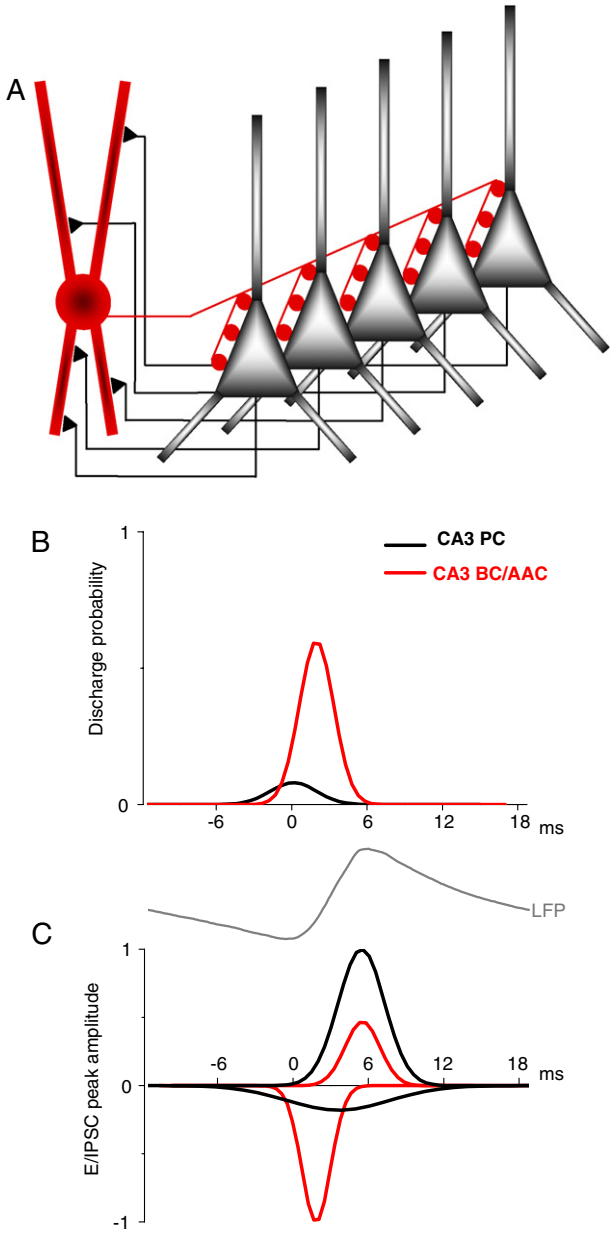

Fig. 5. (A). Schematic diagram of minimal neuronal network needed for generation of intrinsic gamma oscillations in the CA3 hippocampal circuitry. (B). Time sequence of firing of CA3 pyramidal cells (CA3 PC) and perisomatic inhibitory cells (BC/AAC, basket and axo-axonic cells) during an oscillatory cycle. LFP, local field potential. (C). Time sequence of the relative peak amplitude distributions of EPSCs (downward) and IPSCs (upward) during an oscillatory cycle. Population discharge of CA3 pyramidal cells drives the firing of perisomatic inhibitory cells, which subsequently temporarily silence the pyramidal cell population. When inhibition fades, pyramidal cell activity reaches the threshold for discharge of perisomatic inhibitory cells again, initiating the next cycle of gamma oscillations.

In both of these models the rhythmic activity of interneurons synchronizes spiking in pyramidal cells. The computational implications of such synchronization have been reviewed extensively (Bartos et al., 2007; Whittington, Traub, Kopell, Ermentrout, & Buhl, 2000). The second model, however, in addition to controlling *when* principal cells fire, also affords control of *which* cells fire, how many and in what order (Mann, Radcliffe et al., 2005). A specific computational rule for how the network selects which neurons fire during gamma oscillations driven by a feedback mechanism was recently suggested (de Almeida, Idiart, & Lisman, 2009).

6. Conclusion and further directions

The establishing of physiologically relevant *in vitro* models of gamma oscillations in slice preparations has enabled detailed studies of the network mechanisms involved. These studies revealed that perisomatic inhibitory cells are crucial in oscillogenesis, and that their firing activity is synchronized primarily by excitatory synaptic inputs derived from the local collaterals of pyramidal cells (Fig. 5). When these perisomatic inhibitory cells discharge synchronously, pyramidal cell activity will be temporarily suppressed by strong synaptic inhibition. After the effect of inhibition fades, the population discharge of pyramidal cells would again take place, and a new gamma cycle is initiated. Other interneuron types that receive phasic excitation during gamma oscillations were also found to discharge in a phase-coupled manner, yet they do not appear to contribute directly to local oscillogenesis. These GABAergic cells might play a role in controlling Ca^{2+} spike generation in the dendrites (dendritic targeting inhibitory cells) and in the propagation of gamma rhythm to other hippocampal subfields (interneuron-selective GABAergic cells).

There are several questions that remain to be answered. For instance, what is the mechanism of synchronous population discharge by pyramidal cell ensembles that drives the perisomatic inhibitory cell firing, and how synchronous need it be to activate the inhibitory cells? Which type(s) of perisomatic inhibitory cells are necessary for oscillogenesis, and how many of these inhibitory cells must contribute to generate gamma oscillations? Further studies are needed to address these questions, and the answers will help us to better understand the functional role of gamma oscillations in cortical structures.

Acknowledgments

This work was supported by the Wellcome Trust. The authors acknowledge individual support from the Hungarian Scientific Research Fund (OTKA T049517) to N.H. and the Biotechnology and Biological Sciences Research Council, U.K. to O.P.

References

Bartos, M., Vida, I., & Jonas, P. (2007). Synaptic mechanisms of synchronized gamma oscillations in inhibitory interneuron networks. *Nature Reviews Neuroscience*, *8*, 45–56.

Bauer, E. P., Paz, R., & Paré, D. (2007). Gamma oscillations coordinate amygdalo-rhinal interactions during learning. *Journal of Neuroscience*, *27*, 9369–9379.

Biro, A. A., Holderith, N. B., & Nusser, Z. (2006). Release probability-dependent scaling of the postsynaptic responses at single hippocampal GABAergic synapses. *Journal of Neuroscience*, *26*, 12487–12496.

Bragin, A., Jando, G., Nadasdy, Z., Hetke, J., Wise, K., & Buzsáki, G. (1995). Gamma (40–100 Hz) oscillation in the hippocampus of the behaving rat. *Journal of Neuroscience*, *15*, 47–60.

Buhl, E. H., Halasy, K., & Somogyi, P. (1994). Diverse sources of hippocampal unitary inhibitory postsynaptic potentials and the number of synaptic release sites. *Nature*, *368*, 823–828.

Buhl, E. H., Tamás, G., & Fisahn, A. (1998). Cholinergic activation and tonic excitation induce persistent gamma oscillations in mouse somatosensory cortex in vitro. *Journal of Physiology*, *513*, 117–126.

Buzsáki, G., & Chrobak, J. J. (1995). Temporal structure in spatially organized neuronal ensembles: a role for interneuronal networks. *Current Opinion in Neurobiology*, *5*, 504–510.

Chrobak, J. J., & Buzsáki, G. (1998). Gamma oscillations in the entorhinal cortex of the freely behaving rat. *Journal of Neuroscience*, *18*, 388–398.

Cobb, S. R., Buhl, E. H., Halasy, K., Paulsen, O., & Somogyi, P. (1995). Synchronization of neuronal activity in hippocampus by individual GABAergic interneurons. *Nature*, *378*, 75–78.

Cobb, S. R., Halasy, K., Vida, I., Nyiri, G., Tamás, G., Buhl, E. H., et al. (1997). Synaptic effects of identified interneurons innervating both interneurons and pyramidal cells in the rat hippocampus. *Neuroscience*, *79*, 629–648.

Collins, D. R., Pelletier, J. G., & Paré, D. (2001). Slow and fast (gamma) neuronal oscillations in the perirhinal cortex and lateral amygdala. *Journal of Neurophysiology*, *85*, 1661–1672.

Compte, A., Reig, R., Descalzo, V. F., Harvey, M. A., Puccini, G. D., & Sanchez-Vives, M. V. (2008). Spontaneous high-frequency (10–80 Hz) oscillations during up states in the cerebral cortex in vitro. *Journal of Neuroscience*, *28*, 13828–13844.

Csicsvari, J., Jamieson, B., Wise, K. D., & Buzsáki, G. (2003). Mechanisms of gamma oscillations in the hippocampus of the behaving rat. *Neuron*, *37*, 311–322.
Cunningham, M. O., Davies, C. H., Buhl, E. H., Kopell, N., & Whittington, M. A. (2003). Gamma oscillations induced by kainate receptor activation in the entorhinal cortex in vitro. *Journal of Neuroscience*, *23*, 9761–9769.
de Almeida, L., Idiart, M., & Lisman, J. E. (2009). A second function of gamma frequency oscillations: An *E*%-max winner-take-all mechanism selects which cells fire. *Journal of Neuroscience*, *29*, 7497–7503.
Fell, J., Klaver, P., Lehnertz, K., Grunwald, T., Schaller, C., Elger, C. E., et al. (2001). Human memory formation is accompanied by rhinal-hippocampal coupling and decoupling. *Nature Neuroscience*, *4*, 1259–1264.
Fisahn, A., Pike, F. G., Buhl, E., & Paulsen, O. (1998). Cholinergic induction of network oscillations at 40 Hz in the hippocampus in vitro. *Nature*, *394*, 186–189.
Fischer, Y., Wittner, L., Freund, T. F., & Gähwiler, B. H. (2002). Simultaneous activation of gamma and theta network oscillations in rat hippocampal slice cultures. *Journal of Physiology*, *539*, 857–868.
Freund, T. F., & Buzsáki, G. (1996). Interneurons of the hippocampus. *Hippocampus*, *6*, 345–470.
Fries, P., Reynolds, J. H., Rorie, A. E., & Desimone, R. (2001). Modulation of oscillatory neuronal synchronization by selective visual attention. *Science*, *291*, 1560–1563.
Fuchs, E. C., Zivkovic, A. R., Cunningham, M. O., Middleton, S., Lebeau, F. E., Bannerman, D. M., et al. (2007). Recruitment of parvalbumin-positive interneurons determines hippocampal function and associated behavior. *Neuron*, *53*, 591–604.
Gloveli, T., Dugladze, T., Saha, S., Monyer, H., Heinemann, U., Traub, R. D., et al. (2005). Differential involvement of oriens/pyramidale interneurones in hippocampal network oscillations in vitro. *Journal of Physiology*, *562*, 131–147.
Gray, C. M. (1994). Synchronous oscillations in neuronal systems: mechanisms and functions. *Journal of Computational Neuroscience*, *1*, 11–38.
Gulyás, A. I., & Freund, T. F. (1996). Pyramidal cell dendrites are the primary targets of calbindin D28k- immunoreactive interneurons in the hippocampus. *Hippocampus*, *6*, 525–534.
Gulyás, A. I., Hájos, N., & Freund, T. F. (1996). Interneurons containing calretinin are specialized to control other interneurons in the rat hippocampus. *Journal of Neuroscience*, *16*, 3397–3411.
Gulyás, A. I., Hájos, N., Katona, I., & Freund, T. F. (2003). Interneurons are the local targets of hippocampal inhibitory cells which project to the medial septum. *European Journal of Neuroscience*, *17*, 1861–1872.
Gulyás, A. I., Miles, R., Hájos, N., & Freund, T. F. (1993a). Precision and variability in postsynaptic target selection of inhibitory cells in the hippocampal CA3 region. *European Journal of Neuroscience*, *5*, 1729–1751.
Gulyás, A. I., Miles, R., Sik, A., Tóth, K., Tamamaki, N., & Freund, T. F. (1993b). Hippocampal pyramidal cells excite inhibitory neurons through a single release site. *Nature*, *366*, 683–687.
Hájos, N., Ellender, T. J., Zemankovics, R., Mann, E. O., Exley, R., Cragg, S. J., et al. (2009). Maintaining network activity in submerged hippocampal slices: importance of oxygen supply. *European Journal of Neuroscience*, *29*, 319–327.
Hájos, N., Katona, I., Naiem, S. S., MacKie, K., Ledent, C., Mody, I., et al. (2000). Cannabinoids inhibit hippocampal GABAergic transmission and network oscillations. *European Journal of Neuroscience*, *12*, 3239–3249.
Hájos, N., Pálhalmi, J., Mann, E. O., Németh, B., Paulsen, O., & Freund, T. F. (2004). Spike timing of distinct types of GABAergic interneuron during hippocampal gamma oscillations in vitro. *Journal of Neuroscience*, *24*, 9127–9137.
Hasselmo, M. E., Wyble, B. P., & Wallenstein, G. V. (1996). Encoding and retrieval of episodic memories: Role of cholinergic and GABAergic modulation in the hippocampus. *Hippocampus*, *6*, 693–708.
Karson, M. A., Tang, A. H., Milner, T. A., & Alger, B. E. (2009). Synaptic cross talk between perisomatic-targeting interneuron classes expressing cholecystokinin and parvalbumin in hippocampus. *Journal of Neuroscience*, *29*, 4140–4154.
Klausberger, T., Roberts, J. D., & Somogyi, P. (2002). Cell type- and input-specific differences in the number and subtypes of synaptic $GABA_A$ receptors in the hippocampus. *Journal of Neuroscience*, *22*, 2513–2521.
König, P., Engel, A. K., & Singer, W. (1995). Relation between oscillatory activity and long-range synchronization in cat visual cortex. *Proceedings of National Academy of Sciences USA*, *92*, 290–294.
Kraushaar, U., & Jonas, P. (2000). Efficacy and stability of quantal GABA release at a hippocampal interneuron–principal neuron synapse. *Journal of Neuroscience*, *20*, 5594–5607.
LeBeau, F. E., Towers, S. K., Traub, R. D., Whittington, M. A., & Buhl, E. H. (2002). Fast network oscillations induced by potassium transients in the rat hippocampus in vitro. *Journal of Physiology*, *542*, 167–179.
Leung, S. W. (1979). Potentials evoked by alvear tract in hippocampal CA1 region of rats. II. Spatial field analysis. *Journal of Neurophysiology*, *42*, 1571–1589.
Mann, E. O., & Paulsen, O. (2007). Role of GABAergic inhibition in hippocampal network oscillations. *Trends in Neurosciences*, *20*, 343–349.
Mann, E. O., Radcliffe, C. A., & Paulsen, O. (2005). Hippocampal gamma-frequency oscillations: From interneurones to pyramidal cells, and back. *Journal of Physiology*, *562*, 55–63.
Mann, E. O., Suckling, J. M., Hájos, N., Greenfield, S. A., & Paulsen, O. (2005). Perisomatic feedback inhibition underlies cholinergically induced fast network oscillations in the rat hippocampus in vitro. *Neuron*, *45*, 105–117.
Marr, D. (1971). Simple memory: A theory for archicortex. *Philosophical Transactions of Royal Society of London Series B Biological Sciences*, *262*, 23–81.
Marrosu, F., Portas, C., Mascia, M. S., Casu, M. A., Fa, M., Giagheddu, M., et al. (1995). Microdialysis measurement of cortical and hippocampal acetylcholine release during sleep–wake cycle in freely moving cats. *Brain Research*, *671*, 329–332.
Miles, R., Tóth, K., Gulyás, A. I., Hájos, N., & Freund, T. F. (1996). Differences between somatic and dendritic inhibition in the hippocampus. *Neuron*, *16*, 815–823.
Montgomery, S. M., & Buzsáki, G. (2007). Gamma oscillations dynamically couple hippocampal CA3 and CA1 regions during memory task performance. *Proceedings of National Academy of Sciences USA*, *104*, 14495–14500.
Morita, K., Kalra, R., Aihara, K., & Robinson, H. P. (2008). Recurrent synaptic input and the timing of gamma-frequency-modulated firing of pyramidal cells during neocortical "UP" states. *Journal of Neuroscience*, *28*, 1871–1881.
Müller, W., & Misgeld, U. (1986). Slow cholinergic excitation of guinea pig hippocampal neurons is mediated by two muscarinic receptor subtypes. *Neuroscience Letters*, *67*, 107–112.
Nabekura, J., Ebihara, S., & Akaike, N. (1993). Muscarinic receptor activation of potassium channels in rat dentate gyrus neurons. *Journal of Neurophysiology*, *70*, 1544–1552.
Oren, I., Mann, E. O., Paulsen, O., & Hájos, N. (2006). Synaptic currents in anatomically identified CA3 neurons during hippocampal gamma oscillations in vitro. *Journal of Neuroscience*, *26*, 9923–9934.
Pálhalmi, J., Paulsen, O., Freund, T. F., & Hájos, N. (2004). Distinct properties of carbachol- and DHPG-induced network oscillations in hippocampal slices. *Neuropharmacology*, *47*, 381–389.
Paulsen, O., & Moser, E. I. (1998). A model of hippocampal memory encoding and retrieval: GABAergic control of synaptic plasticity. *Trends in Neurosciences*, *21*, 273–278.
Poschel, B., Draguhn, A., & Heinemann, U. (2002). Glutamate-induced gamma oscillations in the dentate gyrus of rat hippocampal slices. *Brain Research*, *938*, 22–28.
Rolls, E. T., & Treves, A. (1994). Neural networks in the brain involved in memory and recall. *Progress in Brain Research*, *102*, 335–341.
Senior, T. J., Huxter, J. R., Allen, K., O'Neill, J., & Csicsvari, J. (2008). Gamma oscillatory firing reveals distinct populations of pyramidal cells in the CA1 region of the hippocampus. *Journal of Neuroscience*, *28*, 2274–2286.
Sik, A., Tamamaki, N., & Freund, T. F. (1993). Complete axon arborization of a single CA3 pyramidal cell in the rat hippocampus, and its relationship with postsynaptic parvalbumin-containing interneurons. *European Journal of Neuroscience*, *5*, 1719–1728.
Sinfield, J. L., & Collins, D. R. (2006). Induction of synchronous oscillatory activity in the rat lateral amygdala in vitro is dependent on gap junction activity. *European Journal of Neuroscience*, *24*, 3091–3095.
Singer, W. (1993). Synchronization of cortical activity and its putative role in information processing and learning. *Annual Reviews in Physiology*, *55*, 349–374.
Sorra, K. E., & Harris, K. M. (1993). Occurrence and 3-dimensional structure of multiple synapses between individual radiatum axons and their target pyramidal cells in hippocampal area-CA1. *Journal of Neuroscience*, *13*, 3736–3748.
Towers, S. K., LeBeau, F. E., Gloveli, T., Traub, R. D., Whittington, M. A., & Buhl, E. H. (2002). Fast network oscillations in the rat dentate gyrus in vitro. *Journal of Neurophysiology*, *87*, 1165–1168.
Tsubokawa, H., & Ross, W. N. (1996). IPSPs modulate spike backpropagation and associated [Ca2+]i changes in the dendrites of hippocampal CA1 pyramidal neurons. *Journal of Neurophysiology*, *76*, 2896–2906.
Tukker, J. J., Fuentealba, P., Hartwich, K., Somogyi, P., & Klausberger, T. (2007). Cell type-specific tuning of hippocampal interneuron firing during gamma oscillations in vivo. *Journal of Neuroscience*, *27*, 8184–8189.
Varela, F., Lachaux, J. P., Rodriguez, E., & Martinerie, J. (2001). The brainweb: Phase synchronization and large-scale integration. *Nature Reviews Neuroscience*, *2*, 229–239.
Whittington, M. A., Traub, R. D., & Jefferys, J. G. (1995). Synchronized oscillations in interneuron networks driven by metabotropic glutamate receptor activation. *Nature*, *373*, 612–615.
Whittington, M. A., Traub, R. D., Kopell, N., Ermentrout, B., & Buhl, E. H. (2000). Inhibition-based rhythms: Experimental and mathematical observations on network dynamics. *International Journal of Psychopharmacology*, *38*, 315–336.
Wittner, L., Henze, D. A., Zaborszky, L., & Buzsáki, G. (2006). Hippocampal CA3 pyramidal cells selectively innervate aspiny interneurons. *European Journal of Neuroscience*, *24*, 1286–1298.
Wulff, P., Ponomarenko, A. A., Bartos, M., Korotkova, T. M., Fuchs, E. C., Bahner, F., et al. (2009). Hippocampal theta rhythm and its coupling with gamma oscillations require fast inhibition onto parvalbumin-positive interneurons. *Proceedings of National Academy of Sciences USA*, *106*, 3561–3566.
Yamawaki, N., Stanford, I. M., Hall, S. D., & Woodhall, G. L. (2008). Pharmacologically induced and stimulus evoked rhythmic neuronal oscillatory activity in the primary motor cortex in vitro. *Neuroscience*, *151*, 386–395.

dc_71_10

15. számú melléklet

Identification of the current generator underlying cholinergically induced gamma frequency field potential oscillations in the hippocampal CA3 region

Iris Oren[1,2], Norbert Hájos[3] and Ole Paulsen[1]

[1] Department of Physiology, Anatomy and Genetics, University of Oxford, Oxford OX1 3PT, UK
[2] Department of Clinical and Experimental Epilepsy, Institute of Neurology, University College London, London WC1N 3BG, UK
[3] Department of Cellular and Network Neurobiology, Institute of Experimental Medicine, Hungarian Academy of Sciences, Budapest H-1450, Hungary

Gamma frequency oscillations (30–100 Hz) are prominent in the hippocampal EEG signal during active network states. An intrahippocampal gamma generator has been identified in the CA3 region. To understand the mechanism of oscillation generation, both the rhythm and the current generators must be identified. While earlier work has elucidated mechanisms of rhythm generation, little attention has been given to identifying the CA3 gamma current generator. Here, we aimed to identify a current generator underlying cholinergically induced gamma frequency oscillations *in vitro*. To this end, we analysed the instantaneous fluctuations in the wavelet amplitude of the field potential oscillation recorded in the stratum pyramidale, and concomitantly recorded action potentials and synaptic input in individual, anatomically identified neurons. The data revealed that perisomatic inhibitory currents in pyramidal cells generated the majority of the field potential. Pyramidal cell action currents also contributed to the field. In contrast, we found no evidence that excitatory currents contribute significantly to the field oscillations in this model. The moment-by-moment analysis of the dynamics of the field potential presented here provides insight into the distinct contributions of synaptic and action currents to the EEG signal and sheds light on the changing balance of excitation and inhibition during cholinergically induced gamma frequency oscillations.

(Received 28 August 2009; accepted after revision 5 January 2010; first published online 5 January 2010)
Corresponding author O. Paulsen: Physiological Laboratory, Department of Physiology, Development and Neuroscience, University of Cambridge, Downing Street, Cambridge CB2 3EG, UK. Email: op210@cam.ac.uk

Abbreviations CCh, carbachol; LFP, local field potential.

Introduction

Network oscillations are ubiquitous phenomena in the brain, reflected in field potential recordings, including the human EEG. The regular structure of the hippocampus has provided neuroscientists with a model system in which to study the origin of local field potential (LFP) oscillations. The development of *in vitro* models of hippocampal network oscillations (Whittington *et al.* 1995; Fisahn *et al.* 1998; Traub *et al.* 2000; LeBeau *et al.* 2002) has provided reduced systems which can be used to investigate the mechanisms underlying the generation of these oscillations. The induction of gamma frequency network oscillations (30–100 Hz, hereafter referred to as 'gamma oscillations') in CA3 by bath application of the cholinergic receptor agonist, carbachol (CCh), is one such model which resembles hippocampal gamma oscillations recorded *in vivo* (Csicsvari *et al.* 2003; Hájos & Paulsen, 2009).

To understand LFP oscillations, two generators must be accounted for: the rhythm and the current generator (Buzsáki, 2002). The term 'rhythm generator' refers to the cellular and/or network mechanisms that control the rhythmicity of the oscillation. Thus, the rhythm generator controls the frequency of the oscillation. In contrast, the 'current generator' refers to the membrane currents that underlie the LFP and thus will account for the amplitude of the oscillation.

Cholinergically induced gamma oscillations require both excitatory, AMPA receptor-mediated, and inhibitory, $GABA_A$ receptor-mediated, synaptic transmission (Fisahn *et al.* 1998; Mann *et al.* 2005*b*). Previous studies of these oscillations have implicated both excitatory and inhibitory synaptic conductances in the rhythm

 DOI: 10.1113/jphysiol.2009.180851

generation. Pyramidal cell firing tends to precede that of interneurons (Hájos *et al.* 2004; Oren *et al.* 2006), which receive a large excitatory input. In contrast, inhibitory currents dominate the synaptic input on pyramidal cell somata (Oren *et al.* 2006). Moreover, it was found that prolonging the IPSC decay time constant reduces the oscillation frequency (Fisahn *et al.* 1998), suggesting that the inhibitory synaptic currents are involved in setting the oscillation frequency. These findings are consistent with a recurrent feedback loop between pyramidal cells and inhibitory interneurons (Freeman, 1968) underlying cholinergically induced gamma oscillations in the hippocampal CA3 region (Fisahn *et al.* 1998; Traub *et al.* 2000; Mann *et al.* 2005*a*; Hájos & Paulsen, 2009).

The present study aimed to identify the current generator underlying cholinergically induced gamma oscillations. Fluctuations in both the amplitude and frequency of the oscillations have been reported both *in vitro* and *in vivo* (Mann *et al.* 2005*b*; Oren *et al.* 2006; Atallah & Scanziani, 2009). To shed light on the nature of the current generator, we analysed these moment-by-moment fluctuations of oscillatory activity. This was done by relating the instantaneous LFP oscillation recorded extracellularly in the stratum pyramidale to simultaneously recorded firing and synaptic activity in individual anatomically identified neurons. Our results suggest that inhibitory synaptic currents at pyramidal cell somata account for the majority of the current underlying the LFP oscillation. In addition, action potential repolarization currents also contribute to the recorded potential. Surprisingly, we found no evidence that excitatory synaptic currents provide a major contribution to the field potential oscillation in this model.

Methods

Ethical approval

All experiments were conducted in accordance with the UK Animals (Scientific Procedures) Act (1986) and the Hungarian Act of Animal Care and Experimentation (1998. XXVIII. section 243/1998), and with the guidelines of the institutional ethical codes. The experiments comply with the policies and regulations as required by *The Journal of Physiology* (Drummond, 2009).

Experimental protocols

The analysis presented here was performed on the same data set as presented in Oren *et al.* (2006). A total of 27 Wistar rats (postnatal day 13–20) were used in the experiments. Briefly, animals were anaesthetized using isoflurane, and decapitated. Horizontal slices, 350–400 μm thick, were recorded in a submerged-type recording chamber at $31 \pm 2^{\circ}$C in high flow rate conditions (3.5–5.5 ml min^{-1}; Hájos *et al.* 2009). The artificial cerebrospinal fluid (ACSF) contained (in mM): NaCl 126; KCl 2.5 or 3; NaH_2PO_4 1.25; $MgSO_4$ 2; $CaCl_2$ 2; $NaHCO_3$ 26; glucose 10. Oscillations were induced by bath application of 20–25 μM carbachol (CCh, Sigma-Aldrich). Patch pipettes (4–8 MΩ) filled with ACSF were used to record field oscillations in the stratum pyramidale of the CA3 region and action potentials extracellularly from individual neurons in all layers, selected using differential interference contrast microscopy. Labelling of cells and recording of synaptic currents were carried out with a second pipette filled with a solution containing (in mM): potassium gluconate 138; CsCl 3; phosphocreatine 10; ATP 4; GTP 0.4; Hepes 10; QX 314 0.2; biocytin 3 mg ml^{-1}. Whole-cell series resistance was in the range of 5–15 MΩ. All data were recorded with a Multiclamp 700A amplifier (Axon Instruments, Union City, CA, USA). During voltage-clamp recordings, series resistance compensation was applied as necessary using the built-in series resistance compensation of the amplifier (12–17 kHz, 40–75%). Voltage measurements were not corrected for liquid–liquid junction potential. EPSCs were recorded at a nominal holding potential of −65 to −60 mV (IPSC reversal potential), whereas IPSCs were recorded at a nominal holding potential of 0–20 mV positive to the uncorrected potential (EPSC reversal potential). Both field and single-cell recordings were low-pass filtered at 2 kHz using the built-in Bessel filter of the amplifier and digitized at 5 kHz. All data were analysed off-line using IGOR Pro 5.01. *Post hoc* anatomical cell identification was performed as described earlier (Hájos *et al.* 2004; Oren *et al.* 2006).

Pyramidal cell action potentials used in the analysis presented in Fig. 6 were recorded in current clamp. Intracellular solution for current clamp recordings contained (in mM): potassium gluconate 110; NaCl 4; Hepes 40; ATP 2; GTP 0.3; biocytin 5 mg ml^{-1}; pH 7.3–7.4. Osmolarity, 290–300 mosmol l^{-1}.

Event detection and analysis

The field recording was further filtered using a digital, bidirectional, phase-conserving, low-pass filter at 1 kHz. Extracellular unit recordings were digitally, bidirectionally high-pass filtered at 40 Hz to isolate the spikes. Whole-cell recordings of PSCs were digitally, bidirectionally, high-pass filtered at 1 Hz to filter out slow fluctuations in holding current. *Post hoc* digital filtering was done using IGOR DSP filters (ftp://ftp.wavemetrics.net/IgorPro/User_Contributions/).

Power spectral density analysis was performed on 30–60 s epochs, using standard IGOR Pro procedures: Time windows of approximately 1.5 s with 50% overlap were multiplied by a Hanning window to minimize end-effects before a fast Fourier transform was performed.

Wavelet analysis was used to quantify the instantaneous oscillation amplitude (Torrence & Compo, 1998; Le Van Quyen *et al.* 2001). The Morlet wavelet transform of the field recording was examined between 10 and 45 Hz with scales chosen to reflect the equivalent Fourier frequency (Fig. 1*B*; Torrence & Compo, 1998). For each time point, the maximum of the wavelet transform amplitude was found, and the corresponding frequency identified. The phase at that time point was defined in terms of this dominant frequency, and this phase was used to evaluate action potential phases. Phase was defined such that $-\pi$ was associated with the minimum of the oscillation, and a full cycle ran from $-\pi$ to π (see Fig. 1 in this paper, and Fig. 1 of Oren *et al.* 2006).

To investigate the relationship between the instantaneous wavelet amplitude and the spike probability, the difference in wavelet amplitude between cycles with and without action potentials (Δ_{amp}) was calculated, such that,

$$\Delta_{\mathrm{amp}} = \mathrm{amp}_1 - \mathrm{amp}_0$$

where amp_i is the mean wavelet amplitude for cycles with (1) and without (0) action potentials. To compare Δ_{amp} between cells, the normalized Δ_{amp}, ($\Delta_{\mathrm{amp}}^{\mathrm{norm}}$) was calculated as follows:

$$\Delta_{\mathrm{amp}}^{\mathrm{norm}} = 2\Delta_{\mathrm{amp}}/(\mathrm{amp}_1 + \mathrm{amp}_0)$$

To investigate the relationship between the instantaneous wavelet amplitude and action potential phase-coupling strength, action potential phases were binned according to wavelet amplitude, in bins of 50 wavelet amplitude units. The phase-coupling strength was quantified using circular statistics. Briefly, action potential phases were represented as unit vectors and summed. The normalized resultant vector, r_{AP}, provided a measure of the phase-coupling strength for each bin. Only bins with significant phase-coupling (Rayleigh significance $P < 0.05$) were used in the calculation of the correlation of r_{AP} and oscillation wavelet amplitude. Similarly, the phase-coupling strength of time-binned action potentials was calculated to investigate the slow fluctuations in phase-coupling strength with time. Action potentials were binned using a bin size of 5 s.

To investigate the relationship between fluctuations in the LFP wavelet amplitude and the amplitude of the synaptic current, the synaptic current amplitude was estimated as the envelope of the maximal phasic current per cycle. The cross-covariance (xr) between the maximal synaptic current and the wavelet amplitude for the simultaneously recorded LFP oscillation was then evaluated for 5 s-long windows. Consecutive windows were shifted by 1 s. The cross-covariance was normalized by the square-root of the product of the maximum auto-covariances of the variables. To detect significant peaks in the cross-covariance, the central peak value was compared to the cross-covariance that would be expected from a random signal of the same mean amplitude and variance (resampling without replacement from the current envelope). The standard deviation (S.D.) of this cross-covariance was evaluated, and this procedure was repeated twenty times, and the mean S.D. calculated. The threshold for detection of a significant peak was set at 1.96 S.D. This analysis was carried out on the initial 5 s time window of each recording. The detection threshold was fairly constant over all recordings (threshold $= (8.4 \pm 0.1) \times 10^{-3}$, $n = 74$).

To estimate the contribution of the action currents to the LFP oscillation, the mean pyramidal cell spike probability was used. This mean spike probability was computed by representing the action potential phase for each pyramidal cell as a fraction of the cycle length. These fractions were then mapped onto a cycle of 40 ms duration and the spike distribution calculated. The distribution for each cell was normalized by the total number of cycles in the recording. The distributions for 13 pyramidal cells were then averaged and yielded the distribution shown in Fig. 6. To compare cycles with and without population spikes, cycles were categorized by threshold value crossings. Two separate threshold values were set for cycles with and without population spikes. Thresholds were set by visual inspection of the 1 Hz high-pass-filtered recording (Fig. 6). Setting two threshold values ensured that only cycles with or without a definite population spike were included.

Statistical analysis

ANOVA and the t test were used when comparing between groups for non-circular homogeneously distributed data ($P > 0.05$ for the Levene statistic), otherwise the Welch statistic was used. Circular statistics were used when appropriate (Zar, 1999). Other tests were used as specified in the text. Values are given as mean ± standard error of the mean, unless otherwise stated.

Results

Fast network oscillations were induced in the CA3 region of horizontal hippocampal slices by bath application of CCh (20–25 μM; Fig. 1*A*; power spectral density peak frequency 28.1 ± 0.6 Hz, $n = 43$; Oren *et al.* 2006). Changes in the oscillation amplitude were quantified by the amplitude of the wavelet transform (hereafter referred to as the 'wavelet amplitude'), which was found to fluctuate over time (Fig. 1*B*). We wanted to relate the instantaneous, cycle-to-cycle variations in neuronal activity to the fluctuations in the ongoing LFP oscillation. This analysis was done in several parts. We first related the

firing of the cells to the ongoing oscillation by (a) relating the instantaneous spike probability (firing rate) to the field, and (b) relating the instantaneous phase-coupling strength (spike timing) to the field. We then carried out a similar analysis of the synaptic currents relative to the field oscillation, namely, (c) relating the instantaneous synaptic current amplitude to the field, and (d) relating the instantaneous synaptic current timing to the field. Lastly, we examined the contribution of pyramidal cell action currents to the LFP oscillation. Our analysis focused on the activity recorded in pyramidal cells and perisomatic-targeting interneurons as these cell types have been previously implicated in hippocampal oscillogenesis (Mann *et al.* 2005*b*; Oren *et al.* 2006).

LFP oscillations and instantaneous spike probability

The relationship between the instantaneous oscillation wavelet amplitude and the firing rate was investigated by examining the action potential trains and the wavelet amplitude of the ongoing LFP oscillation (Fig. 2*A*). Figure 2*Aia* shows the action potential train of a pyramidal cell and the wavelet amplitude of the simultaneously recorded LFP oscillation. The likelihood of the cell firing appears to be independent of the instantaneous wavelet amplitude. However, the variation in the firing rate of the perisomatic-targeting interneuron shown in Fig. 2*Aib* seems to be related to the instantaneous wavelet amplitude such that the spike probability is higher during epochs when the wavelet amplitude is large. In addition to this GABAergic cell type, the dendritic-targeting interneurons (Fig. 2*Aic*) and interneuron-selective interneurons (Fig. 2*Aid*) were also examined. For the detailed anatomical description and identification of these interneuronal subtypes see Oren *et al.* (2006).

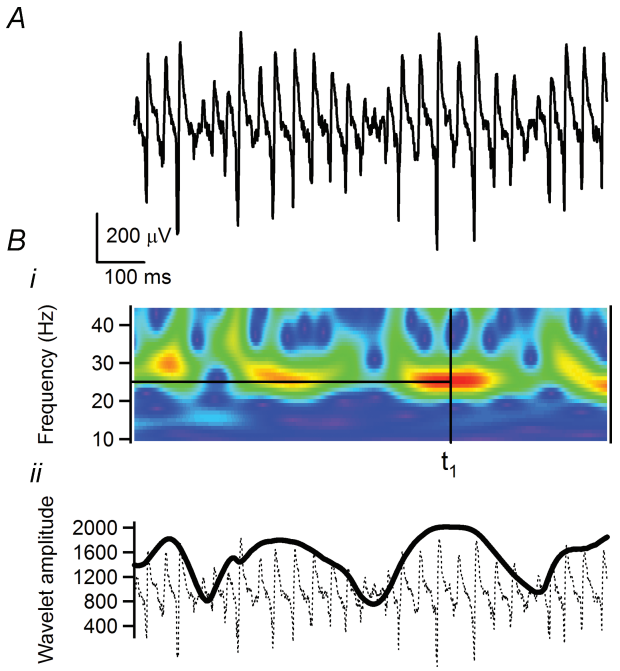

Figure 1. Wavelet amplitude fluctuations of cholinergically induced LFP oscillation
A, extracellularly recorded LFP oscillations induced by bath application of carbachol (20 μM). *B*, wavelet analysis of LFP oscillation: *i*, amplitude component of wavelet transform of the oscillation shown in *A*. The oscillation wavelet amplitude at any time point was quantified by the maximal wavelet amplitude, shown here for time t_1 to correspond to the wavelet amplitude of the 25 Hz component. See also Oren *et al.* (2006); *ii*, continuous line shows the maximum wavelet amplitude for each time point of LFP oscillation (dotted line).

Quantifying these results by comparing the average wavelet amplitude per cycle between cycles with and without action potentials yielded no significant difference for the firing data of the pyramidal cell (Fig. 2*Aiia*, $P = 0.85$, ANOVA), while a significant difference in wavelet amplitude was found between cycles with and without action potentials for the perisomatic-targeting interneuron (Fig. 2*Aiib*, $P < 0.05$, Welch statistic with *post hoc* Games-Howell test).

These results extended to the majority of cells of the respective cell classes such that the average wavelet amplitude per cycle and number of action potentials per cycle appeared unrelated in the majority of pyramidal cells (13 of 17), while in the majority of perisomatic-targeting interneurons (8 of 10), the wavelet amplitude was significantly larger in cycles with one action potential than in cycles with zero action potentials. The wavelet amplitude for cycles with more than one action potential was variable (data not shown). Hence the likelihood of perisomatic-targeting interneurons firing an action potential co-varied positively with the wavelet amplitude of the ongoing gamma cycle, while no such relationship was seen in the majority of pyramidal cells.

To quantify this relationship and to allow for comparison between cells, Δ_{amp} was normalized by the average of the wavelet amplitude in the cycles of interest (Δ_{amp}^{norm}; see Methods). In interneurons, Δ_{amp}^{norm} was significantly greater than zero ($P < 0.01$, $n = 25$, one-sample t test), while in pyramidal cells, Δ_{amp}^{norm} was not significantly different from zero ($P = 0.85$, $n = 17$, one-sample t test). The difference in Δ_{amp}^{norm} between cell types was statistically significant (Fig. 2*B*; $P < 0.05$, $n = 42$, Welch statistic). This difference did not result from differences in the modulation depth of the oscillation as there was no significant correlation between Δ_{amp}^{norm} and the area under the power spectral density of the instantaneous wavelet amplitude (data not shown; $r = -0.21$, $P = 0.18$, $n = 42$, Spearman's correlation).

It is possible that the spike probability is related not only to the oscillation wavelet amplitude of the ongoing gamma cycle, as seen in interneurons, but also, and perhaps more strongly, to the oscillation wavelet amplitude during neighbouring cycles. To investigate the

relationship between spike probability and the wavelet amplitude as a function of time, spike-triggered averages of the wavelet amplitude curve were evaluated for 200 ms windows centred on the action potential (Fig. 2*C*). The time of the maximum in the spike-triggered average of the wavelet amplitude (T_{max}) tended to occur at time windows longer than the time corresponding to approximately one oscillation cycle, 50 ms, in the majority of pyramidal cells (12 of 17; $T_{max} = -41 \pm 17$ ms, $n = 17$; Fig. 2*C*), corroborating the lack of a strong relation between instantaneous pyramidal cell firing rate and the wavelet amplitude during the immediate oscillation cycle. In contrast, the firing of perisomatic-targeting interneurons tended to precede T_{max} by < 50 ms ($T_{max} = 21 \pm 2$ ms, $n = 10$; Fig. 2*C*). The spike-triggered averages of the wavelet amplitude for other interneuron subclasses resembled those of perisomatic-targeting interneurons (dendritic-targeting interneurons: $T_{max} = 7.6 \pm 24.1$ ms, $n = 7$; interneuron-selective interneurons: $T_{max} = 12 \pm 22$ ms, $n = 8$; Fig. 2*Cii*). Thus

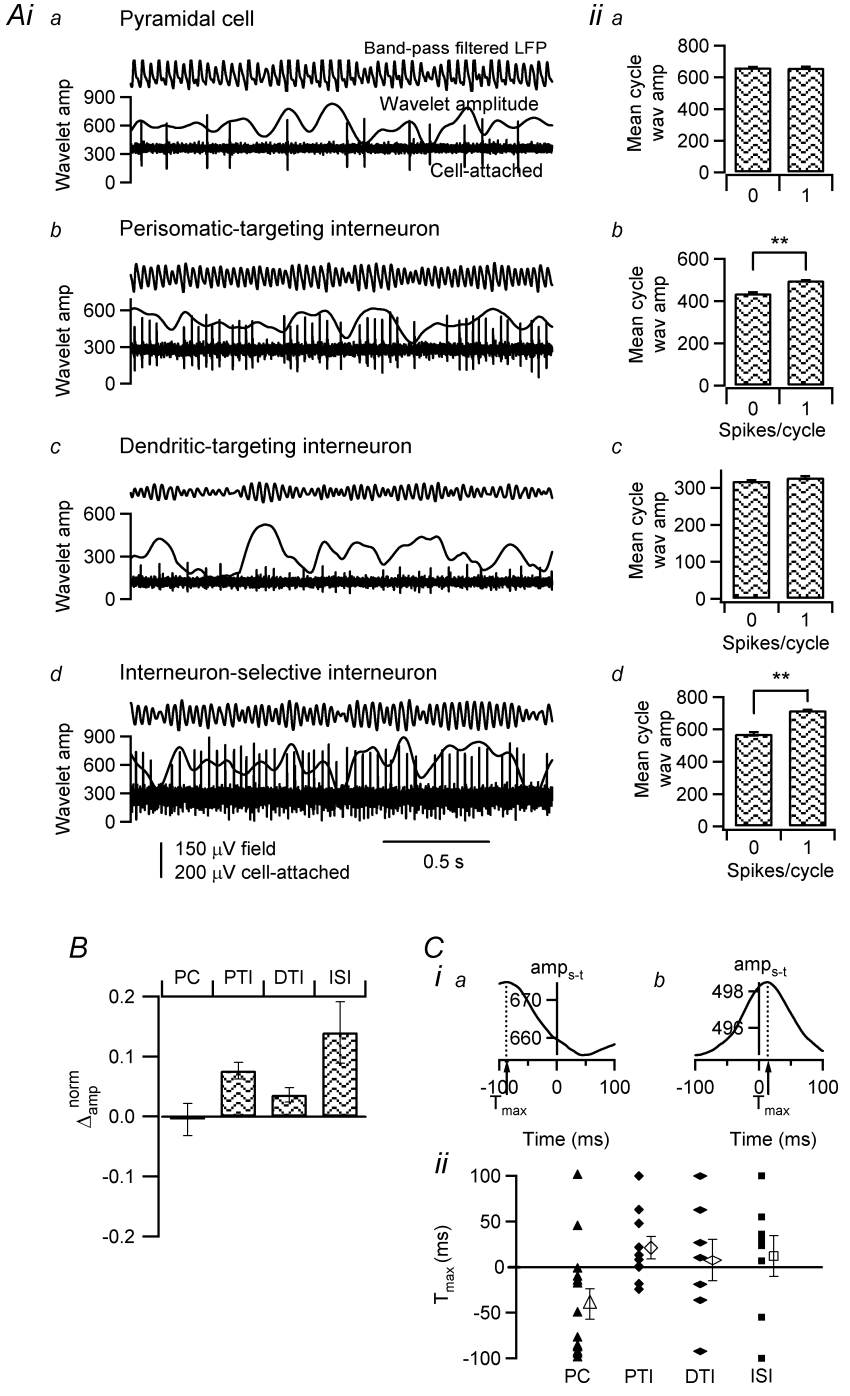

Figure 2. LFP oscillation and instantaneous spike probability
A, wavelet amplitude and number of action potentials. *Ai*, wavelet amplitude and action potential firing in pyramidal cell (PC, *a*), perisomatic-targeting interneuron (PTI, *b*), dendritic-targeting interneuron (DTI, *c*) and interneuron-selective interneuron (ISI, *d*). Upper trace: bandpass filtered (10–45 Hz) extracellular LFP recording. Middle trace: wavelet amplitude. Lower trace: high-pass filtered (40 Hz), simultaneously acquired cell-attached recording. *Aii*, mean wavelet amplitude per gamma cycle binned according to the number of action potentials per cycle for cells shown in *Ai*. *B*, normalized difference in mean wavelet amplitude between cycles with one and zero action potentials (Δ_{amp}^{norm}) in different cell types (PC, $n = 17$; PTI, $n = 10$; DTI, $n = 7$; ISI, $n = 8$). *Ci*, spike-triggered averages of wavelet amplitude ($amp_{s\text{-}t}$ for 200 ms windows centred on action potentials in PC (*a*) and PTI (*b*)). Same cells as in *A*. Dotted line indicates the time of the maximum of the spike-triggered average (T_{max}). *Cii*, T_{max} in different cell types. Filled symbols, individual cells; open symbols, means for each cell type; $^{**}P < 0.01$.

increases in oscillation wavelet amplitude occur shortly after interneuronal firing, while pyramidal cell firing lags the increased oscillation wavelet amplitude by time windows greater than one cycle.

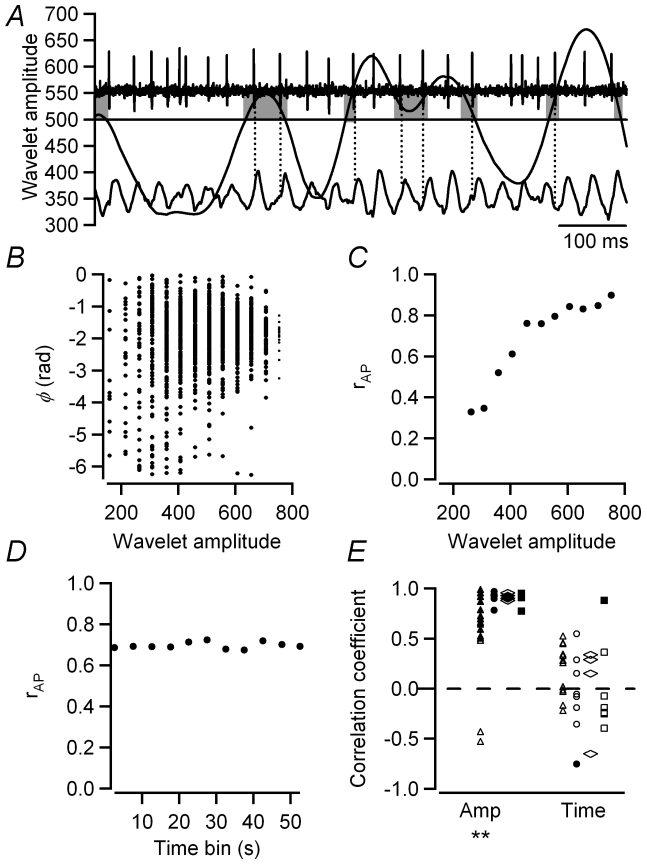

Figure 3. LFP oscillation and instantaneous phase-coupling strength

A, illustration of method of binning action potential phase by wavelet amplitude. The wavelet amplitude (middle trace) was divided into bins of 50 units. Oscillation epochs corresponding to a single wavelet amplitude bin are shown in grey. The phase of all action potentials occurring in a particular bin was evaluated with respect to the ongoing LFP oscillation (lower trace and dotted vertical lines), and the phase-coupling strength of all action potentials in a single bin evaluated using circular statistics. Upper trace: cell-attached recording from perisomatic-targeting interneuron. Lower trace: bandpass filtered (10–45 Hz) LFP recording. *B*, phase rasterplot of action potentials recorded from the perisomatic-targeting interneuron shown in *A*, binned into wavelet amplitude bins of 50 units. *C*, action potential phase-coupling strength (r_{AP}; see Methods) calculated for each bin and plotted against wavelet amplitude for the rasterplot shown in *A*. A significant positive correlation was found between r_{AP} and wavelet amplitude ($r = 0.92$, $P < 0.01$, Pearson's correlation). *D*, action potential phase was binned according to time in 5 s time bins and the r_{AP} calculated for each time bin. No significant correlation was found between r_{AP} and time ($r = 0.15$, $P = 0.65$, Pearson's correlation). *E*, correlation coefficients for wavelet amplitude-based and time-based binning of action potential phase for all cells. Filled/open symbols, significant/non-significant correlation coefficients; cell type symbol key as in Fig. 2*C*. Dashed line indicates a correlation coefficient of zero. $^{**}P < 0.01$, one-sample *t* test.

LFP oscillations and instantaneous spike timing

Earlier work has shown that the firing of cells can be coupled to particular phases of the ongoing gamma oscillation (Hájos *et al.* 2004; Gloveli *et al.* 2005; Mann *et al.* 2005*b*; Oren *et al.* 2006; Tukker *et al.* 2007). Both the degree of phase-coupling and the preferred firing phase have been found to differ between cell types. These earlier works have investigated spike timing as a mean measure over the entire recording epoch. However, it might be that the degree of phase-coupling is related to the wavelet amplitude of the oscillation. This led us to examine the variations in phase-coupling strength (r_{AP}; see Methods) with oscillation wavelet amplitude.

To quantify the instantaneous phase-coupling strength, action potential phases were binned according to wavelet amplitude and the phase-coupling strength calculated for each bin (Fig. 3*A* and *B*; see Methods). In the majority of cells, the strength of phase-coupling, r_{AP}, showed a strong, positive correlation to the wavelet amplitude of the ongoing oscillation (Fig. 3*C* and *E*, $P < 0.01$, $n = 34$, one-sample *t* test)

It is possible that the variation in r_{AP} is not related to the variations in the oscillation wavelet amplitude, but an underlying slow variation in action potential phase-coupling strength with time. To address this issue, an equivalent analysis was performed by binning phase according to time (see Methods). No significant correlation was found between r_{AP} and recording time in the majority of cells (Fig. 3*D* and *E*; $r = 0.08 \pm 0.06$, $P = 0.16$, $n = 35$, one-sample *t* test). Hence we concluded that while there was no consistent time trend in the phase-coupling strength of the activity of cells, the action potential phase-coupling strength did co-vary with the wavelet amplitude of the ongoing LFP oscillation.

LFP oscillations and instantaneous synaptic current amplitude

To help elucidate the contribution of synaptic currents to the LFP oscillation, the relationship between fluctuations in synaptic currents and the field oscillation wavelet amplitude was investigated within individual cells. To do this, the values of the peak current per cycle were extracted and used to estimate the envelope of the maximal current (Fig. 4; see Methods). This envelope provided a continuous measure of the phasic current amplitude and was used to calculate the cross-covariance with the wavelet amplitude of the ongoing field oscillation (Fig. 4*B* and *E*). This analysis was carried out for both the excitatory and inhibitory synaptic currents.

The majority of cells (33 of 40) exhibited a significant peak in the cross-covariance between the excitatory current amplitude and the wavelet amplitude. The strength of the covariance, as measured by the peak

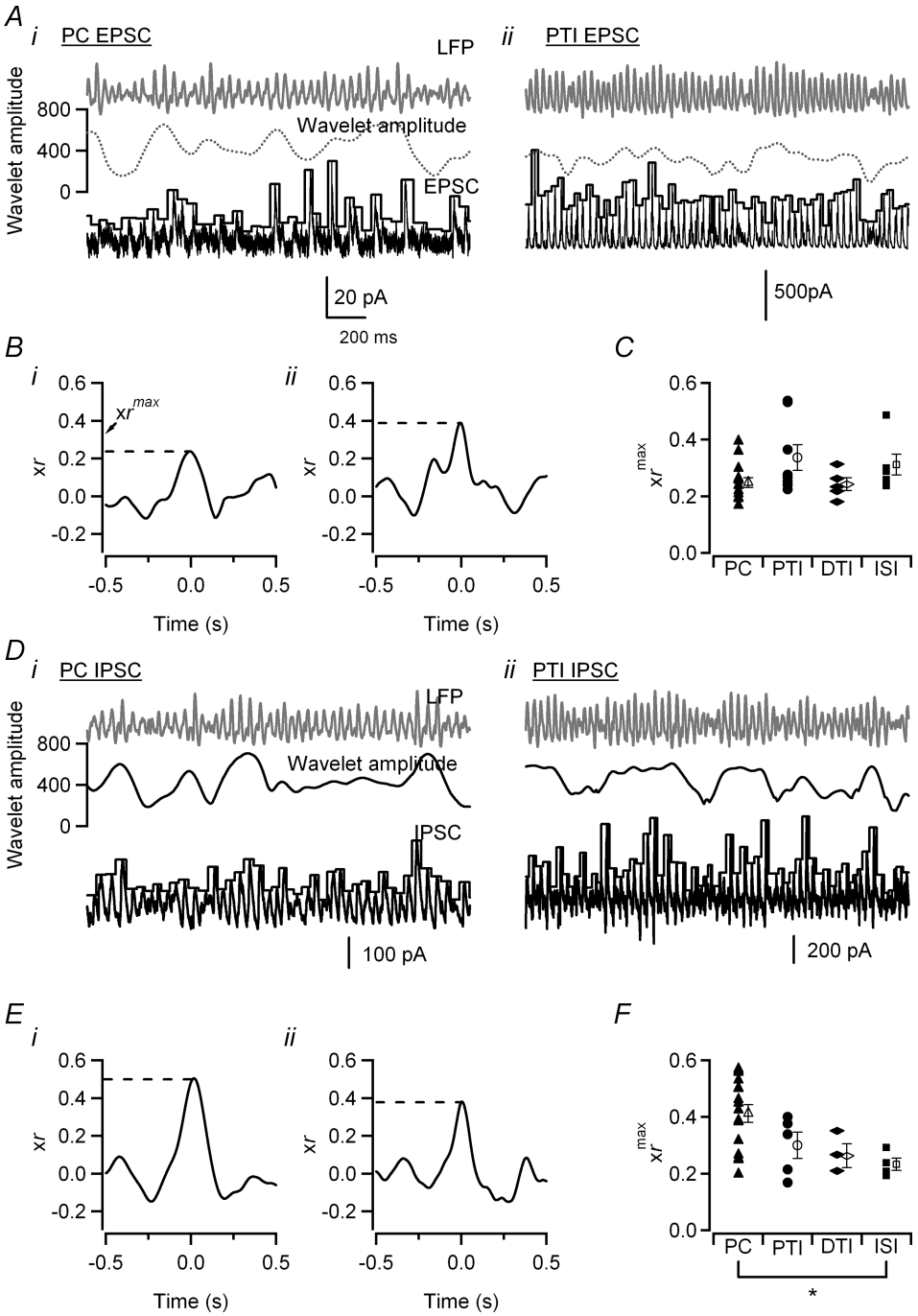

Figure 4. LFP oscillation and instantaneous current amplitude

A, excitatory current amplitude and LFP wavelet amplitude fluctuations within cells. Simultaneously recorded LFP (grey upper trace, bandpass filtered 10–45 Hz) and inverted EPSC recording (lower trace) from pyramidal cell (PC, *i*) and perisomatic-targeting interneuron (PTI, *ii*). The dotted line shows the oscillation wavelet amplitude, and the black cityscape shows the maximal current of the EPSC in each cycle. *B*, normalized cross-covariance (x*r*) of current amplitude envelope and wavelet amplitude for cells in *A*. *C*, comparison between cell types of maximal value xr^{max} of significant central cross-covariance peaks. No significant difference in the value of xr^{max} was found between cell types. Filled symbols, individual cells; open symbols, means; DTI, dendritic-targeting interneurons; ISI, interneuron-selective interneuron. *D–F*, equivalent analysis of inhibitory currents as in panels *A–C*. The value of xr^{max} differed significantly between cell types. $^{*}P < 0.05$.

value (of significant peaks) of the cross-covariance (xr^{max}), did not differ significantly between cell types for cells with significant peaks ($P = 0.10$, $n = 33$, ANOVA; Fig. 4*C*; pyramidal cells $xr^{max} = 0.25 \pm 0.02$, $n = 14$ of 17; perisomatic-targeting interneurons $xr^{max} = 0.34 \pm 0.05$, $n = 8$ of 9; interneuron-selective interneurons $xr^{max} = 0.31 \pm 0.04$, $n = 6$ of 7; dendritic-targeting interneurons $xr^{max} = 0.24 \pm 0.02$, $n = 5$ of 7).

Equivalent analysis of the IPSC amplitude and wavelet amplitude revealed a significant peak in the cross-covariance in 29 of 34 recordings. In recordings that showed a significant peak in the cross-covariance function, the covariance was on average stronger in pyramidal cells ($xr^{max} = 0.41 \pm 0.03$, $n = 16$ of 17) than in interneurons (perisomatic-targeting interneurons $xr^{max} = 0.30 \pm 0.05$, $n = 5$ of 7; dendritic-targeting interneurons $xr^{max} = 0.26 \pm 0.03$, $n = 4$ of 6; interneuron-selective interneurons $xr^{max} = 0.23 \pm 0.02$, $n = 4$ of 4). The difference in the xr^{max} between IPSC amplitude and wavelet amplitude between cell types was statistically significant (Fig. 4*F*; $P < 0.05$, $n = 27$, ANOVA with Bonferroni *post hoc* test). Hence it appears that the amplitude of both the excitatory and inhibitory currents co-vary with the oscillation wavelet amplitude. However, the cross-covariance was strongest between the amplitudes of the LFP oscillation and the inhibitory currents recorded in pyramidal cells.

LFP oscillations and instantaneous synaptic current timing

Since the timing of action potentials differs between cell types (Hájos *et al.* 2004; Oren *et al.* 2006), and CA3 neuronal populations show target selectivity (Freund & Buzsáki, 1996), the timing of PSCs would also be expected to differ between cell types. We next investigated the timing of excitatory and inhibitory synaptic currents in relation to the ongoing LFP oscillation in different cell types.

Inspection of the bandpass-filtered (10–45 Hz) synaptic currents and LFP recordings (Fig. 5) revealed a difference between the timing of excitatory and inhibitory synaptic currents. While the bandpass-filtered excitatory current oscillation slightly led the LFP oscillation, the inhibitory currents and LFP oscillation were highly synchronized. These temporal relationships were quantified by computing the cross-covariance of the bandpass-filtered recordings. Central peaks were found in the cross-covariance functions of excitatory and inhibitory currents in all cells analysed.

The absolute value of the maximum cross-covariance peak gives an indication of the correlation strength of the synaptic events. No differences were found in the peak value of the cross-covariance between the EPSCs and LFP between cell types (xr^{max}; Fig. 5*C*; $P = 0.26$, $n = 40$, ANOVA; pyramidal cell EPSCs $xr^{max} = 0.65 \pm 0.05$, $n = 17$; perisomatic-targeting interneuron $xr^{max} = 0.78 \pm 0.07$, $n = 9$; dendritic-targeting interneuron $xr^{max} = 0.61 \pm 0.10$, $n = 7$; interneuron-selective interneuron $xr^{max} = 0.77 \pm 0.06$, $n = 7$). In contrast, significant differences in the peak values of the cross-covariance between the IPSCs and LFP were found between cell types (Fig. 5*C*; $P < 0.05$, $n = 34$, Welch statistic), and was on average strongest in pyramidal cells (pyramidal cell IPSCs $xr^{max} = 0.88 \pm 0.03$, $n = 17$; perisomatic-targeting interneuron $xr^{max} = 0.70 \pm 0.08$, $n = 7$; dendritic-targeting interneuron $xr^{max} = 0.52 \pm 0.13$, $n = 6$; interneuron-selective interneuron $xr^{max} = 0.65 \pm 0.07$, $n = 4$).

The time of the cross-covariance peak between the EPSCs and LFP oscillations (minimum peak) was positive (mean $T(xr^{max}) = 6.6 \pm 0.6$ ms; $P < 0.01$, $n = 40$, one-sample t test). The central (maximum) peak in the cross-covariance between the inhibitory current and LFP oscillation was not significantly different from zero ($T(xr^{max}) = 0.0 \pm 0.5$ ms; $P > 0.99$, $n = 34$, one-sample t test). Differences in $T(xr^{max})$ were found between cell types for the cross-covariance function both between the EPSCs and LFP, and between the IPSCs and LFP (Fig. 5*D*; $P < 0.05$, $n = 40$ and $P < 0.01$, $n = 34$, ANOVA with Bonferroni *post hoc* test. EPSCs $T(xr^{max})$: pyramidal cell $T(xr^{max}) = 4.9 \pm 0.5$ ms, $n = 17$; perisomatic-targeting interneuron $T(xr^{max}) = 8.3 \pm 0.8$ ms, $n = 9$; dendritic-targeting interneuron $T(xr^{max}) = 7.7 \pm 1.0$ ms, $n = 7$; interneuron-selective interneuron $T(xr^{max}) = 7.3 \pm 1.4$ ms, $n = 7$. IPSCs $T(xr^{max})$: pyramidal cell $T(xr^{max}) = 0.03 \pm 0.01$ ms, $n = 17$; perisomatic-targeting interneuron $T(xr^{max}) = -0.01 \pm 0.03$ ms, $n = 7$; dendritic-targeting interneuron $T(xr^{max}) = -0.10 \pm 0.06$ ms, $n = 6$; interneuron-selective interneuron $T(xr^{max}) = -0.01 \pm 0.01$ ms, $n = 4$). The differences in $T(xr^{max})$ between excitatory and inhibitory currents were significant after accounting for cell type ($P < 0.01$, $n = 74$, ANOVA with cell type as covariate). Furthermore, differences in oscillation frequency between recordings could not account for the observed differences in $T(xr^{max})$ as an analysis of the frequency-normalized cross-covariance functions yielded equivalent results (data not shown). Hence the data show that while excitatory events slightly led the maximum of the bandpass-filtered field oscillation, the inhibitory currents were strongly synchronized with the LFP oscillation, with the strongest correlation being seen in the pyramidal cell IPSC recordings.

LFP oscillations and action currents

We have shown that the LFP oscillation is strongly correlated with both the inhibitory synaptic currents in

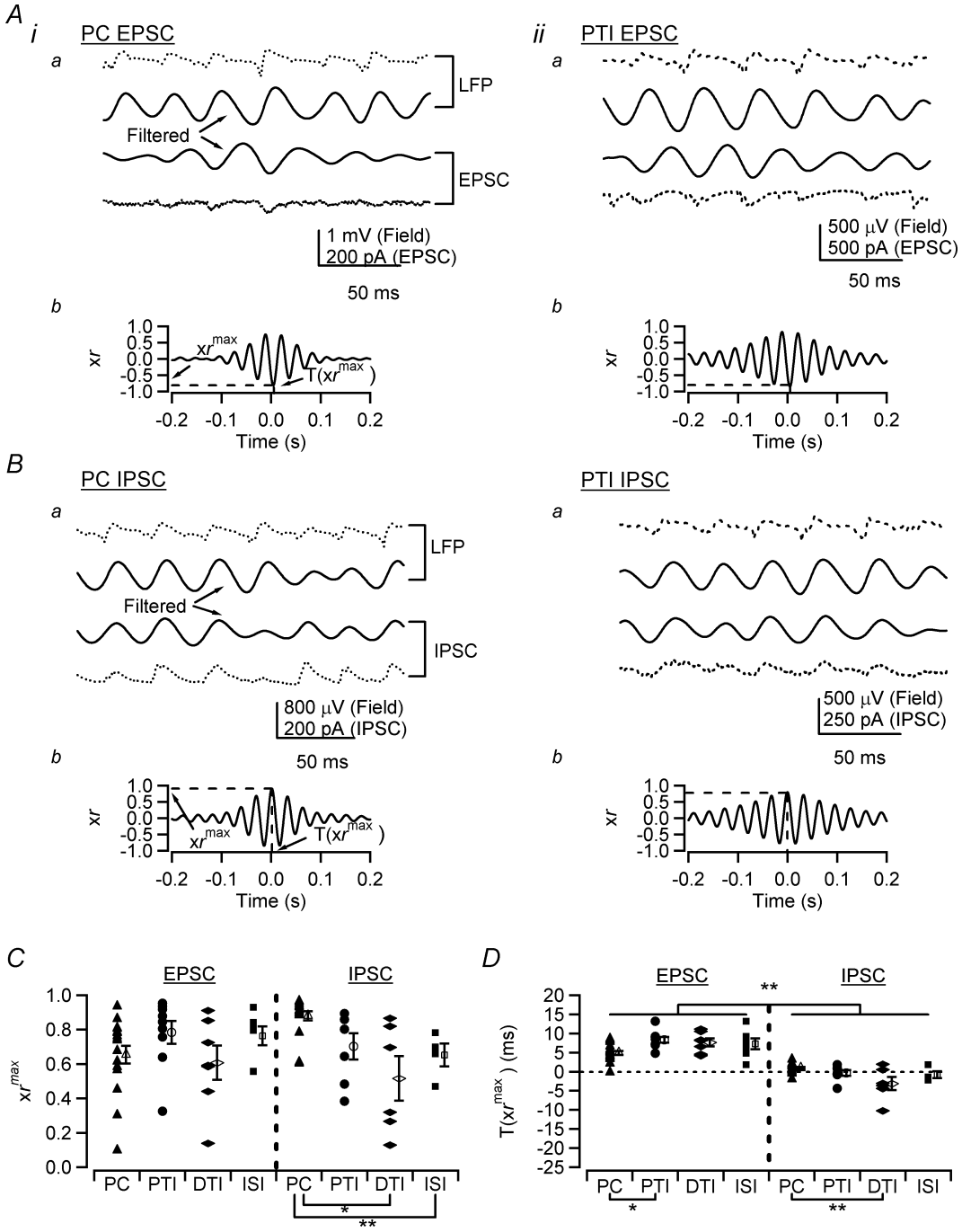

Figure 5. Instantaneous synaptic currents and LFP oscillation
Aia, LFP oscillation and bi-directionally bandpass filtered (10–45 Hz) LFP (upper two traces) and EPSCs and bi-directionally bandpass filtered (10–45 Hz) EPSCs recorded in pyramidal cell (PC, lower two traces). *Aib*, cross-covariance (x*r*) of bandpass-filtered EPSC and LFP. *Aii*, as in *i*, but EPSCs recorded in perisomatic-targeting interneurons (PTI). *B*, as in *A*, but for IPSC recordings. *C*, comparison between cell types of maximal value of central cross-covariance peaks (xr^{max}). No significant difference in xr^{max} was found between cell types for the EPSC–LFP cross-covariance, while xr^{max} for IPSCs was significantly larger in PCs. *D*, comparison of the PSC–LFP cross-covariance peak time ($T(xr^{max})$) for EPSCs and IPSCs between cell types. $T(xr^{max})$ differed significantly between EPSCs and IPSCs as well as between cell types. Dashed line indicates $T(xr^{max}) = 0$; DTI, dendritic-targeting interneurons; ISI, interneuron-selective interneurons; $^*P < 0.05$; $^{**}P < 0.01$.

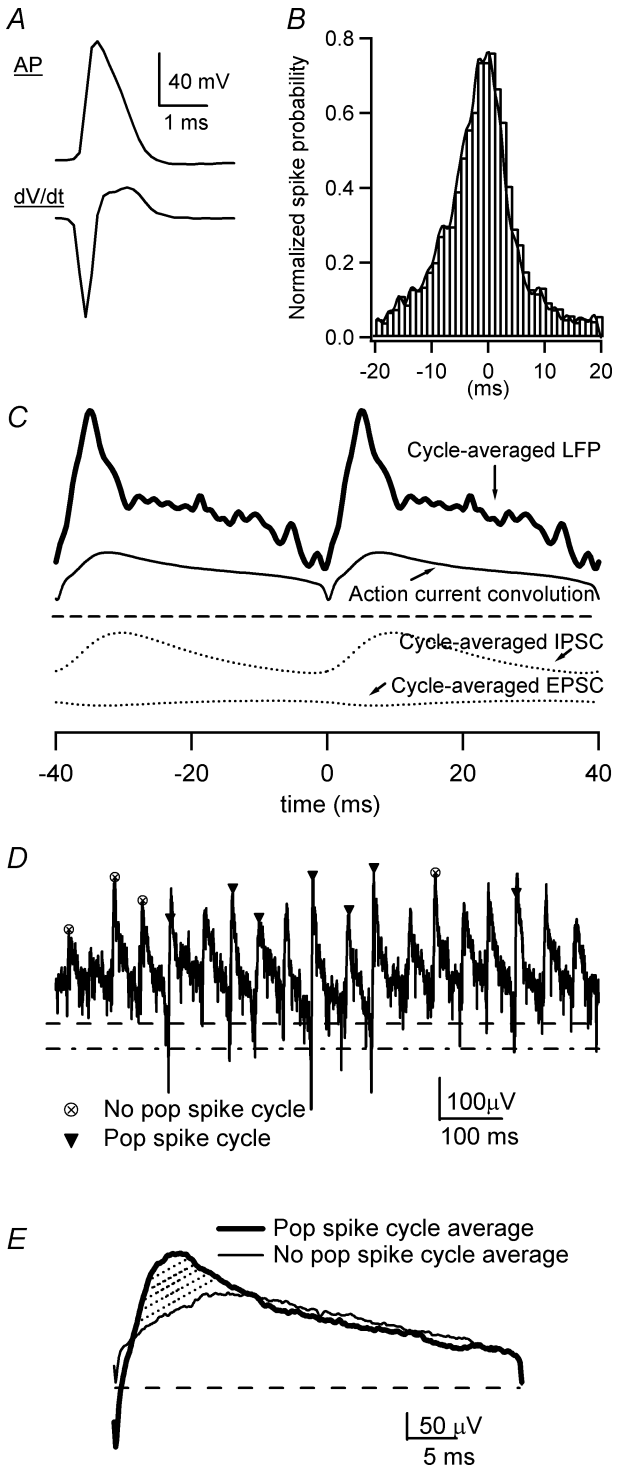

Figure 6. Action current contribution to LFP oscillation
A, single action potential (AP, upper trace) recorded in whole-cell current-clamp configuration from a CA3 pyramidal cell in drug-free ACSF in response to a step depolarization. The time derivative (lower trace) was used to approximate the waveform of the action current. *B*, average normalized spike time probabilities for 13 pyramidal cells during carbachol-induced oscillations, and mapped onto a 40 ms cycle. Spike time histograms for each cell were normalized to the peak value, and the normalized histograms averaged over cells. *C*, continuous thick trace: convolution of action potential d*V*/d*t* (*A*, lower) and average normalized spike time probability (*B*); continuous thin trace: cycle-averaged CCh-induced oscillation showing relative phase of population action current. Below the dashed line, the cycle-averaged IPSC (dotted trace upper) and EPSC (dotted trace lower) recorded in an individual pyramidal cell during CCh-induced oscillations are shown (averaged between cycle minima). *D*, to extract the action current-mediated contribution to the LFP, cycles with and without population spikes were identified by a user-defined threshold detection (dashed lines). Peaks of identified cycles with and without population spikes are shown. *E*, cycles with and without population spikes were cycle averaged separately between cycle minima to reveal the action current-mediated component of the LFP. Area of the action current-mediated component (filled area) was compared to area of the average cycle with no population spike (area in between horizontal dashed and 'No pop spike cycle average' plot, see Results).

pyramidal cells and the firing of perisomatic-targeting interneurons, while the correlation of the LFP with the excitatory synaptic currents is weaker. Hence, we conclude that IPSCs in pyramidal cells, evoked by the firing of perisomatic-targeting interneurons, contribute to the current generator of CA3 gamma oscillations. However, action potential-associated currents might also contribute to the LFP oscillation. This issue was investigated next.

To ascertain whether action currents could contribute to the observed LFP oscillation we estimated the waveform of the current that would be recorded in stratum pyramidale generated by a population of pyramidal cells firing phase-locked to the oscillation. To a first approximation, the membrane current underlying an action potential is proportional to the first time derivative of the voltage (Johnston & Wu, 1995). Hence, we approximated the waveform of the action current by differentiating the voltage change of a single somatically recorded action potential in response to a constant current depolarization (Fig. 6*A*; action potentials recorded in whole-cell current-clamp configuration). Both the time course and ratio of inward to outward currents of this differential were in agreement with earlier computational models of action currents in pyramidal cells (Gold *et al.* 2006; Milstein & Koch, 2008).

The waveform of the current generated by a population of pyramidal cells was estimated by convolving the waveform of the action current and the mean normalized spike probability distribution from 13 pyramidal cells during CCh-induced oscillations (Fig. 6*B*). As can be seen from Fig. 6*C*, the time course of this population action current bears resemblance to the LFP oscillation. The early positive-going peak results from the action potential repolarization currents. The analysis was repeated for the time derivative of the action potential recorded from three different pyramidal cells, and resulted in equivalent population action currents (data not shown). Hence, the time course of the population action current suggests

that the action potential-associated currents could indeed contribute to the gamma current generator.

Population spikes, resulting from synchronized pyramidal cell action potential firing (Andersen *et al.* 1971), are seen in a proportion of cycles during CCh-induced gamma oscillations (Fig. 6*D*). To estimate the contribution of the action currents to the LFP oscillation, we averaged cycles with and without population spikes separately (Fig. 6*E*). While the late phase of the cycle-averages overlapped, an early component was evident in the averages of cycles with population spikes ($n = 5$ recordings of 60 s duration). The area of this action current-mediated component was $9.4 \pm 1.5\%$ ($n = 5$) of the area of the cycle-averaged oscillation without population spikes.

Discussion

Inhibitory current source of LFP

Cortical EEG potentials are generated by the summed electric dipole moments created by currents flowing across the membranes of spatially aligned neurons (Schaul, 1998; Niedermeyer & Lopes da Silva, 2004; Nunez & Srinivasan, 2006). It is generally assumed that synaptic currents are the predominant active sinks and sources underlying the LFP (Niedermeyer & Lopes da Silva, 2004), but the relative contributions of excitatory and inhibitory synaptic currents to the field events have not been previously studied. Here, we analysed the instantaneous fluctuations in the LFP and single cell activity to identify the synaptic events underlying the gamma current generator. Four results emerging from this analysis indicate that inhibitory but not excitatory currents in the principal cell layer are the predominant current source underlying cholinergically induced LFP oscillations *in vitro*. (1) Within a given cycle, the firing probability of perisomatic-targeting interneurons tended to increase prior to increases in LFP wavelet amplitude. In contrast, the firing probability of pyramidal cells and the LFP wavelet amplitude appeared unrelated. (2) There was a strong cross-covariance between the pyramidal cell inhibitory synaptic current amplitude and LFP oscillation wavelet amplitude. (3) The cross-covariance between the LFP and synaptic currents was strongest for IPSCs recorded in pyramidal cells. (4) IPSCs in pyramidal cells were highly synchronized with the LFP. The conclusion that an inhibitory current source is a major contributor to the field is further supported by the striking similarity between the waveforms of the pyramidal cell IPSCs and the LFP (Figs 5*Ba* and 6*C*), and the identification of a perisomatic current source during hippocampal gamma frequency oscillations (Csicsvari *et al.* 2003; Mann *et al.* 2005*b*).

Our conclusion is consistent with the recent observation that the firing of a single hippocampal basket cell can generate a detectable LFP signal in the stratum pyramidale (Glickfeld *et al.* 2009). Hence, the gamma-modulated activity of a population of basket cells (Hájos *et al.* 2004; Oren *et al.* 2006) may contribute to the gamma-frequency LFP. In further support of this conclusion, physiological gamma-modulated firing of principal neurons in somatosensory cortex was shown to require strongly gamma-modulated inhibitory conductances but not recurrent excitatory conductances (Morita *et al.* 2008).

While we did not differentiate between classes of perisomatic-targeting interneurons, it has been shown that parvalbumin (PV) and cholecystokinin (CCK)-expressing basket cells are recruited differentially during hippocampal network oscillations (Klausberger *et al.* 2005; Tukker *et al.* 2007). PV-positive basket cells tend to fire at higher rates than CCK-positive basket cells (Tukker *et al.* 2007). Since the perisomatic-targeting interneurons reported here tended to follow the gamma rhythm (see Oren *et al.* 2006), we suggest that the sample was largely composed of PV-positive cells. However, this cannot be safely concluded without immunohistochemical analysis.

It is possible that space-clamp errors might have contaminated our voltage-clamp data and led to an underestimation of the glutamatergic currents which arrive distally. These effects could be confounded by the large perisomatic inhibitory conductances which will reduce the effectiveness of a somatic voltage clamp. However, since the poorly clamped conductances are located in the distal dendritic regions and the active current source of the LFP is located in the proximal perisomatic region (Mann *et al.* 2005*b*), space-clamp errors would not alter our main conclusion that inhibitory currents in principal cells act as the primary current generator underlying cholinergically induced gamma oscillations *in vitro*.

Action current contribution to LFP

In addition to synaptic currents, action currents in spatially aligned principal cells may contribute to the LFP. Here, we quantitatively estimated the contribution of action currents in pyramidal cells to the LFP recorded *in vitro*. The contribution of the action current to the LFP was dominated by the active current source of the repolarization conductances as opposed to the fast inward current sinks. Convolution of these slow action potential-associated currents with the broadly synchronized firing of spatially aligned pyramidal cells provides a contribution to the LFP in a proportion of cycles, and suggests that action currents may be responsible for a small ($< 10\%$) but significant contribution to the LFP.

Our analysis of the action currents' contribution to the LFP was based on a comparison of cycles with and without population spikes, and thus implicitly assumed that the only feature that differs between these two categories of cycles is the action potential-associated currents. An additional possible contribution to the positive wave following the population spike is the recruitment of a different subpopulation of interneurons whose activation leads to an early component of the pyramidal cell IPSC. However, the time course of the convolution of the approximated action currents with pyramidal cell spike timing distribution (Fig. 6*A*–*C*) is consistent with our conclusion that repolarization currents act as a source contributing to the early component of the LFP.

Excitatory–inhibitory balance during gamma oscillations

The amplitude of both excitatory and inhibitory currents co-varied with the LFP oscillation wavelet amplitude. Atallah & Scanziani (2009) have recently suggested that excitation and inhibition fluctuate in balance during hippocampal gamma oscillations. Our phasic current data are in agreement with their findings, such that both the EPSC and IPSC amplitude covaried with the LFP wavelet amplitude, although we found that the cross-covariance with wavelet amplitude was on average stronger for the IPSC amplitude than for the EPSC amplitude. However, our action potential data revealed that while interneuron firing probability was increased during periods of large oscillation wavelet amplitude, pyramidal cell firing probability (and resulting excitatory drive) was less well correlated to the LFP wavelet amplitude. At first the two results might appear contradictory. However, it should be borne in mind that an increased phasic current can be the result of increased firing rate as well as increased synchrony. Our data suggest that the apparent fluctuations in excitatory current were not the result of increased pyramidal cell firing, but instead reflected a transition from asynchronous ('tonic') to synchronous ('phasic') pyramidal cell firing. It seems likely that the increased phasic excitation during periods of large LFP was thus primarily the result of increased synchrony. Hence, while the phasic PSCs appear to fluctuate in balance as reported by Atallah and Scanziani, the balance of excitation and inhibition in the CA3 network in fact fluctuates, such that epochs with a large oscillation wavelet amplitude are associated with larger increases in inhibitory over excitatory drive. A supralinear increase in inhibition with increasing excitation has been shown in recurrent networks in other cortical regions (Kapfer *et al.* 2007; Silberberg & Markram, 2007). Such increases in inhibition over excitation could serve to keep the network within a band of excitatory and inhibitory drives. Changes in the balance between excitation and inhibition could result in epochs in which the network is differentially prone to undergo plastic changes (Paulsen & Moser, 1998) or could be involved in gating incoming synaptic input (Salinas & Sejnowski, 2001).

Our finding that epochs of large oscillation wavelet amplitude are associated with increased spike timing precision in all cell types (Fig. 3) is in agreement with reports of hippocampal gamma oscillations recorded *in vivo* (Tukker *et al.* 2007). These results suggest that epochs in which inhibition is strong are associated with highly synchronous activity. Earlier work has demonstrated that pyramidal cell firing phase is primarily controlled by inhibition (Oren *et al.* 2006), Thus, epochs of large LFP wavelet amplitude (i.e. large inhibitory current) would be associated with highly synchronous pyramidal cell activity which could result in a population spike. The population spike would in turn provide an additional current source to the oscillation as discussed earlier. The synchronicity of activity is likely to have computational importance in signal integration and plasticity (Sejnowski & Paulsen, 2006).

In conclusion, this work has quantified the contributions of the somatic currents underlying cholinergically induced LFP oscillations *in vitro*. Since gamma oscillations *in vivo* share many features with the cholinergically induced *in vitro* model (Csicsvari *et al.* 2003; Hentschke *et al.* 2007; Hájos & Paulsen, 2009), it is possible that the same current generators contribute to the LFP oscillations *in vivo*, and similar mechanisms might contribute to the EEG signal in other brain regions.

References

Andersen P, Bliss TV & Skrede KK (1971). Unit analysis of hippocampal population spikes. *Exp Brain Res* **13**, 208–221.

Atallah BV & Scanziani M (2009). Instantaneous modulation of gamma oscillation frequency by balancing excitation with inhibition. *Neuron* **62**, 566–577.

Buzsáki G (2002). Theta oscillations in the hippocampus. *Neuron* **33**, 325–340.

Csicsvari J, Jamieson B, Wise KD & Buzsáki G (2003). Mechanisms of gamma oscillations in the hippocampus of the behaving rat. *Neuron* **37**, 311–322.

Drummond GB (2009) Reporting ethical matters in *The Journal of Physiology*: standards and advice. *J Physiol* **587**, 713–719.

Fisahn A, Pike FG, Buhl EH & Paulsen O (1998). Cholinergic induction of network oscillations at 40 Hz in the hippocampus *in vitro*. *Nature* **394**, 186–189.

Freeman WJ (1968). Relations between unit activity and evoked potentials in the prepyriform cortex of cats. *J Neurophysiol* **31**, 337–348.

Freund TF & Buzsáki G (1996). Interneurons of the hippocampus. *Hippocampus* **6**, 347–470.

Glickfeld LL, Roberts JD, Somogyi P & Scanziani M (2009). Interneurons hyperpolarize pyramidal cells along the entire somatodendritic axis. *Nat Neurosci* **12**, 21–23.

Gloveli T, Dugladze T, Saha S, Monyer H, Heinemann U, Traub RD, Whittington MA & Buhl EH (2005). Differential involvement of oriens/pyramidale interneurones in hippocampal network oscillations *in vitro*. *J Physiol* **562**, 131–147.

Gold C, Henze DA, Koch C & Buzsáki G (2006). On the origin of the extracellular action potential waveform: A modelling study. *J Neurophysiol* **95**, 3113–3128.

Hájos N, Ellender TJ, Zemankovics R, Mann EO, Exley R, Cragg SJ, Freund TF & Paulsen O (2009). Maintaining network activity in submerged hippocampal slices: importance of oxygen supply. *Eur J Neurosci* **29**, 319–327.

Hájos N, Pálhalmi J, Mann EO, Németh B, Paulsen O & Freund TF (2004). Spike timing of distinct types of GABAergic interneuron during hippocampal gamma oscillations *in vitro*. *J Neurosci* **24**, 9127–9137.

Hájos N & Paulsen O (2009). Network mechanisms of gamma oscillations in the CA3 region of the hippocampus. *Neural Netw* **22**, 1113–1119.

Hentschke H, Perkins MG, Pearce RA & Banks MI (2007). Muscarinic blockade weakens interaction of gamma with theta rhythms in mouse hippocampus. *Eur J Neurosci* **26**, 1642–1656.

Johnston D & Wu SM (1995). *Foundations of Cellular Neurophysiology*. Massachusetts Institute of Technology, Cambridge, Massachusetts.

Kapfer C, Glickfeld LL, Atallah BV & Scanziani M (2007). Supralinear increase of recurrent inhibition during sparse activity in the somatosensory cortex. *Nat Neurosci* **10**, 743–753.

Klausberger T, Marton LF, O'Neill J, Huck JH, Dalezios Y, Fuentealba P, Suen WY, Papp E, Kaneko T, Watanabe M, Csicsvari J & Somogyi P (2005). Complementary roles of cholecystokinin- and parvalbumin-expressing GABAergic neurons in hippocampal network oscillations. *J Neurosci* **25**, 9782–9793.

LeBeau FE, Towers SK, Traub RD, Whittington MA & Buhl EH (2002). Fast network oscillations induced by potassium transients in the rat hippocampus *in vitro*. *J Physiol* **542**, 167–179.

Le Van Quyen M, Foucher J, Lachaux J, Rodriguez E, Lutz A, Martinerie J & Varela FJ (2001). Comparison of Hilbert transform and wavelet methods for the analysis of neuronal synchrony. *J Neurosci Methods* **111**, 83–98.

Mann EO, Radcliffe CA & Paulsen O (2005*a*). Hippocampal gamma-frequency oscillations: from interneurones to pyramidal cells, and back. *J Physiol* **562**, 55–63.

Mann EO, Suckling JM, Hájos N, Greenfield SA & Paulsen O (2005*b*). Perisomatic feedback inhibition underlies cholinergically induced fast network oscillations in the rat hippocampus in vitro. *Neuron* **45**, 105–117.

Milstein JN & Koch C (2008). Dynamic moment analysis of the extracellular electric field of a biologically realistic spiking neuron. *Neural Comput* **20**, 2070–2084.

Morita K, Kalra R, Aihara K & Robinson HP (2008). Recurrent synaptic input and the timing of gamma-frequency-modulated firing of pyramidal cells during neocortical 'UP' states. *J Neurosci* **28**, 1871–1881.

Niedermeyer E & Lopes da Silva FH (2004). *Electroencephalography: Basic Principles, Clinical Applications, and Related Fields*. Lippincott Williams & Wilkins, Philadelphia.

Nunez PL & Srinivasan R (2006). *Electric Fields of the Brain*. Oxford University Press, New York.

Oren I, Mann EO, Paulsen O & Hájos N (2006). Synaptic currents in anatomically identified CA3 neurons during hippocampal gamma oscillations in vitro. *J Neurosci* **26**, 9923–9934.

Paulsen O & Moser EI (1998). A model of hippocampal memory encoding and retrieval: GABAergic control of synaptic plasticity. *Trends Neurosci* **21**, 273–278.

Salinas E & Sejnowski TJ (2001). Correlated neuronal activity and the flow of neural information. *Nat Rev Neurosci* **2**, 539–550.

Schaul N (1998). The fundamental neural mechanisms of electroencephalography. *Electroencephalogr Clin Neurophysiol* **106**, 101–107.

Sejnowski TJ & Paulsen O (2006). Network oscillations: emerging computational principles. *J Neurosci* **26**, 1673–1676.

Silberberg G & Markram H (2007). Disynaptic inhibition between neocortical pyramidal cells mediated by Martinotti cells. *Neuron* **53**, 735–746.

Torrence C & Compo GP (1998). A practical guide to wavelet analysis. *Bulletin of the American Meteorological Society* **79**, 61–78.

Traub RD, Bibbig A, Fisahn A, LeBeau FEN, Whittington MA & Buhl EH (2000). A model of gamma-frequency network oscillations induced in the rat CA3 region by carbachol in vitro. *Eur J Neurosci* **12**, 4093–4106.

Tukker JJ, Fuentealba P, Hartwich K, Somogyi P & Klausberger T (2007). Cell type-specific tuning of hippocampal interneuron firing during gamma oscillations *in vivo*. *J Neurosci* **27**, 8184–8189.

Whittington MA, Traub RD & Jefferys JG (1995). Synchronized oscillations in interneuron networks driven by metabotropic glutamate receptor activation. *Nature* **373**, 612–615.

Zar JH (1999). *Biostatistical Analysis*. Prentice Hall, Upper Saddle River, NJ, USA.

Author contributions

All authors contributed to the conception and design of the experiments. I.O. and N.H. conducted the experiments. I.O. analysed the data. I.O. and O.P. drafted the manuscript. All authors participated in the interpretation of the data, revised the article and approved the final version for publication. Experiments were conducted in the Department of Physiology, Anatomy and Genetics, Oxford University, UK and the Department of Cellular and Network Neurobiology, Institute of Experimental Medicine, Hungarian Academy of Sciences, Budapest, Hungary.

Acknowledgements

This work was supported by The Wellcome Trust, the Biotechnology and Biological Sciences Research Council, the British Council, the Alzheimer's Research Trust, and Országos Tudományos Kutatási Alapprogramok Grant T049517.

dc_71_10

16. számú melléklet

Differences in subthreshold resonance of hippocampal pyramidal cells and interneurons: the role of h-current and passive membrane characteristics

Rita Zemankovics[1], Szabolcs Káli[1,2], Ole Paulsen[3,4], Tamás F. Freund[1,5] and Norbert Hájos[1]

[1] *Department of Cellular and Network Neurobiology, Institute of Experimental Medicine, Hungarian Academy of Sciences, Budapest, Hungary*
[2] *Infobionic and Neurobiological Plasticity Research Group, Hungarian Academy of Sciences–Péter Pázmány Catholic University–Semmelweis University, Budapest, Hungary*
[3] *Department of Physiology, Anatomy and Genetics, University of Oxford, Oxford, UK*
[4] *Department of Physiology, Development and Neuroscience, University of Cambridge, Cambridge, UK*
[5] *Faculty of Information Technology, Péter Pázmány Catholic University, Budapest, Hungary*

The intrinsic properties of distinct types of neuron play important roles in cortical network dynamics. One crucial determinant of neuronal behaviour is the cell's response to rhythmic subthreshold input, characterised by the input impedance, which can be determined by measuring the amplitude and phase of the membrane potential response to sinusoidal currents as a function of input frequency. In this study, we determined the impedance profiles of anatomically identified neurons in the CA1 region of the rat hippocampus (pyramidal cells as well as interneurons located in the stratum oriens, including OLM cells, fast-spiking perisomatic region-targeting interneurons and cells with axonal arbour in strata oriens and radiatum). The basic features of the impedance profiles, as well as the passive membrane characteristics and the properties of the sag in the voltage response to negative current steps, were cell-type specific. With the exception of fast-spiking interneurons, all cell types showed subthreshold resonance, albeit with distinct features. The HCN channel blocker ZD7288 (10 μM) eliminated the resonance and changed the shape of the impedance curves, indicating the involvement of the hyperpolarisation-activated cation current I_h. Whole-cell voltage-clamp recordings uncovered differences in the voltage-dependent activation and kinetics of I_h between different cell types. Biophysical modelling demonstrated that the cell-type specificity of the impedance profiles can be largely explained by the properties of I_h in combination with the passive membrane characteristics. We conclude that differences in I_h and passive membrane properties result in a cell-type-specific response to inputs at given frequencies, and may explain, at least in part, the differential involvement of distinct types of neuron in various network oscillations.

(Received 11 December 2009; accepted after revision 20 April 2010; first published online 26 April 2010)
Corresponding author N. Hájos: Department of Cellular and Network Neurobiology, Institute of Experimental Medicine, Hungarian Academy of Sciences, Szigony u. 43, Budapest, 1083 Hungary. Email: hajos@koki.hu

Abbreviations BIC, Bayesian information criterion; FFT, fast Fourier transform; FS PTI, fast spiking perisomatic region-targeting interneuron; HCN channel, hyperpolarisation-activated cyclic nucleotide-gated channel; I_h, h-current; MP, membrane potential; OLM, oriens-lacunosum-moleculare; O-R, oriens-radiatum; PC, pyramidal cell.

Introduction

Information processing in neural networks depends on the behaviour of individual neurons, which is governed by both intrinsic membrane properties and synaptic inputs. Intrinsic membrane properties arise from the interaction of passive membrane properties and active conductances, i.e. the operation of voltage-gated ion channels. These built-in membrane characteristics of a cell shape the amplitude and the temporal dynamics of the neuronal response, influence the integration of synaptic inputs, and contribute to controlling the precise timing of the action potential output (Magee, 1998; Magee, 1999; Richardson *et al.* 2003; McLelland & Paulsen, 2009). Moreover, the presence of active conductances can endow neurons with the capability of producing

 DOI: 10.1113/jphysiol.2009.185975

intrinsic membrane potential oscillations and resonance at different frequencies (Hutcheon & Yarom, 2000). These frequency tuning properties enable the cells to respond preferentially to inputs at certain frequencies (Pike *et al.* 2000), and they can influence the precise spike timing of the cell relative to the ongoing network activity (Lengyel *et al.* 2005; Kwag & Paulsen, 2009; McLelland & Paulsen, 2009). As a net effect these features of the cells may play a significant role in setting network dynamics (Hutcheon & Yarom, 2000).

In the hippocampus pyramidal cells are known to express subthreshold resonance at frequencies within the theta range (4–7 Hz) (Leung & Yu, 1998; Pike *et al.* 2000; Hu *et al.* 2002; Narayanan & Johnston, 2007), which might contribute to their membrane potential oscillations *in vivo* (Ylinen *et al.* 1995; Kamondi *et al.* 1998) as well as to their discharge properties (Pike *et al.* 2000). Recent studies have revealed that subthreshold resonance in pyramidal cells is predominantly mediated by the hyperpolarisation-activated cyclic nucleotide-gated channels (HCN channels), which generate a non-selective cation current – termed I_h (Hu *et al.* 2002). In addition to having a key role in producing resonance in distinct types of neurons and its vital function in pacemaker activities as well as in network oscillations (Kocsis & Li, 2004), this conductance has been suggested to contribute to synaptic waveform normalization (Magee, 1999) and even to learning processes (Nolan *et al.* 2003).

In addition to pyramidal cells, cortical neuronal networks contain morphologically and functionally diverse populations of inhibitory interneurons (Freund & Buzsáki, 1996; Klausberger & Somogyi, 2008). It has been shown that some hippocampal interneurons also tend to show frequency tuning properties (Gloveli *et al.* 2005; Lawrence *et al.* 2006) and can also resonate at certain frequencies (Pike *et al.* 2000). However, it is still unclear which GABAergic cell types show resonance at which frequencies, and what cellular mechanisms are involved.

To understand how neuronal networks operate, detailed knowledge of the intrinsic properties of the cells that are embedded in them would appear necessary, serving as a basis for realistic modelling. Therefore, we investigated the impedance profiles of distinct types of anatomically identified neurons in the CA1 region of rat hippocampal slices. We focused on the dissimilarities in the voltage response of the cells to sinusoidal current inputs and wanted to determine the role of I_h in producing these differences. Experimental data and computational modelling indicated that impedance characteristics are cell-type dependent, and that the impedance profiles of the cells were predominantly determined by the kinetic properties of I_h in combination with the passive membrane properties of the neurons.

Methods

Slice preparation

Animals were kept and used according to the regulations of the European Community's Council Directive of 24 November 1986 (86/609/EEC), and experimental procedures were reviewed and approved by the Animal Welfare Committee of the Institute of Experimental Medicine. Altogether 52 animals were used in this study and all the experiments comply with the policies and regulations of *The Journal of Physiology* given by Drummond (2009). Male Wistar rats (postnatal day 14–26) were decapitated under deep isoflurane anaesthesia, and their brains were removed into ice cold cutting solution (containing in mM: 252 sucrose, 2.5 KCl, 26 $NaHCO_3$, 0.5 $CaCl_2$, 5 $MgCl_2$, 1.25 NaH_2PO_4, 10 glucose, saturated with 95% O_2–5% CO_2). Horizontal hippocampal slices (400 μm) were cut using a vibrating blade microtome (Leica VT1000S). The slices were kept in an interface chamber containing artificial cerebrospinal fluid (ACSF) at room temperature for at least 1 h before use. The ACSF had the following composition (in mM): 126 NaCl, 2.5 KCl, 26 $NaHCO_3$, 2 $CaCl_2$, 2 $MgCl_2$, 1.25 NaH_2PO_4, 10 glucose, saturated with 95% O_2–5% CO_2. During the recordings the slices were kept submerged in a chamber perfused with ACSF at a flow rate of 3–4 ml min^{-1}. All recordings were made at 34–37°C.

Electrophysiological recordings and data analysis

Whole-cell patch-clamp experiments were performed under visual guidance using a Versascope (E. Marton Electronics, Canoga Park, CA, USA) or an infrared differential interference contrast microscope (Olympus BX61WI). Electrodes were pulled from borosilicate glass capillaries (Hilgenberg, Malsfeld, Germany). Pipette resistances were 3–5 MΩ when filled with the intrapipette solution. The intrapipette solution contained (in mM): 125 potassium gluconate, 6 KCl, 4 NaCl, 10 Hepes, 10 disodium creatine phosphate, 4 Mg-ATP, 0.3 Tris-GTP (pH 7.38; 284–290 mosmol l^{-1}). Biocytin at 5 mg ml^{-1} was added to the pipette solution for later morphological identification of the recorded cells. Recordings were made using an Axopatch 200B or a Multiclamp 700B amplifier (Molecular Devices, Sunnyvale, CA, USA). Data were digitised using a PCI-MIO-16-4E board (National Instruments, Austin, TX, USA). Traces were filtered at 2 kHz and digitised at 8 kHz in the current-clamp experiments and 6 kHz in the voltage-clamp experiments. Data for current-clamp experiments were acquired and analysed with Igor Pro 4.0 software (WaveMetrics, Inc., Lake Oswego, OR, USA). For voltage-clamp experiments data acquisition was carried out using the EVAN program (courtesy of Prof. I. Mody; UCLA, CA, USA) or Stimulog

software (courtesy of Prof. Z. Nusser; Institute of Experimental Medicine, Hungarian Academy of Sciences, Budapest, Hungary), and analysed with Origin 7.0 software (OriginLab Corp. Northamton, MA, USA).

The extracellular solution for current-clamp experiments was ACSF as described above. In all voltage-clamp experiments 50–100 μM picrotoxin and 2–3 mM kynurenic acid (Sigma-Aldrich, St Louis, MO, USA) were added to abolish synaptic events, and 0.5 μM TTX (Alomone Labs, Jerusalem, Israel) was added to block voltage-dependent Na^+ channels. Blocking the h-current was accomplished by adding 10 μM ZD7288 (4-ethylphenylamino-1,2-dimethyl-6-methylaminopyrimidinium chloride, Tocris Bioscience Ltd, Bristol, UK) to the bath solution. In voltage-clamp experiments, series resistance was compensated and was between 5 and 15 MΩ. Only cells with stable resting membrane potential and overshooting action potentials with stable amplitude were included in the study. Resting membrane potential was measured in bridge mode ($I = 0$) immediately after obtaining whole-cell access. Reported values for membrane potential were not corrected for the liquid junction potential.

From perisomatic region-targeting interneurons only those cells were included in this study which could be identified unequivocally as fast-spiking interneurons based on their action potential phenotype. These cells were characterised by a fast-decaying afterhyperpolarisation (AHP) measured at 25% of the AHP amplitude (less than 3.2 ms) and by the small width of action potentials determined at half peak amplitude of the first and the last action potentials of the train (less than 0.5 ms; for 800 ms, 0.2 nA pulses) (Han, 1994; Pawelzik *et al.* 2002; Lien & Jonas, 2003). To validate that the classification is not sensitive to this particular choice of parameters, we also did principal component analysis on 20 different parameters related to the action potential phenotype and firing pattern of these cells, and, by choosing an appropriate threshold value for the first principal component, obtained identical results.

The basic physiological characteristics of the cells were determined from the voltage responses to a series of hyperpolarising and depolarising square current pulses of 800 ms duration and amplitudes between −200 and 200 pA, at 20 pA intervals from a holding potential of −60 mV. To estimate the membrane time constant and the total membrane capacitance at −60 mV, single exponential functions with a common decay time constant were fitted simultaneously to the voltage responses to the five smallest amplitude hyperpolarising current steps (−20 to −100 pA) between 5 and 37.5 ms after the onset of the pulse. The median value of the membrane capacitance estimated from these fits was used. In order to estimate the input resistance of the cell, double exponential functions were fitted to the voltage traces during the current step, and the minimum and steady-state voltage values were determined (this procedure also allowed us to characterise the voltage sag; see below). Estimated steady-state voltage responses were then plotted against current amplitude for the five smallest amplitude hyperpolarising current steps (−20 to −100 pA), and the input resistance at −60 mV was estimated from the slope of the linear regression through these points (Fig. 2*A*).

In many cells, a voltage sag was observed in response to a hyperpolarising current pulse. We characterised this voltage sag by fitting the difference of two exponential functions to the membrane potential during the pulse (see above). The sag responses were described quite accurately by this class of function; our choice of functional description was further motivated by the fact that the response of a simple model of I_h-containing neurons (the linearised I_h model, described below) can be calculated analytically, and also predicts a sag shaped as a difference of exponential functions. Fitting a continuous function to the data allowed us to robustly estimate the relative sag amplitude, defined as the ratio of two differences in membrane potential: the difference between the minimum voltage during the sag and the steady-state voltage later in the pulse, and the difference between the steady-state voltage and the membrane potential measured immediately after the beginning of the step (see Fig. 2*B*). We also determined the peak delay, defined as the time of the negative peak of the membrane potential relative to the beginning of the current pulse. Both the relative sag amplitude and the peak delay were calculated for the five largest amplitudes of the negative current steps (−120 to −200 pA), and their median values were used to characterise the sag in each cell.

Characterisation of neuronal impedance profiles and resonance properties

To determine the impedance profile and subthreshold resonance properties of each cell, 3 s-long sinusoidal currents were injected into the cells with a peak-to-peak amplitude of 120 pA at fixed frequencies (0.5, 1, 2, 3, 4, 5, 6, 7, 8, 9, 10, 15, 20, 40 Hz). This amplitude represented the optimal trade-off between linearity (which requires a small input) and signal-to-noise ratio (which is better for large signals). Since the neuronal impedance is in general voltage dependent, measurements were repeated at different subthreshold membrane potentials (−60, −70, −80, and in some cases at −90 mV). These baseline potentials were manually adjusted by direct current (DC) injection through the recording electrode. The complex impedance value (Z) at a given frequency (f) was determined by calculating the fast Fourier transform (FFT) of the voltage response and dividing the FFT component corresponding to the input frequency by the equivalent FFT component

of the input current. We found that 3 s-long sinusoidal currents allowed us to estimate both the amplitude and the phase of the voltage response at a high level of precision, even for the lowest reported frequencies (see Supplemental Material).

The magnitude of the impedance was plotted against input frequency to give the impedance magnitude profile. In order to facilitate the comparison of multiple impedance magnitude profiles, we characterised the impedance magnitude curves by four summary statistics. First, we measured the impedance value at the lowest input frequency (0.5 Hz), $Z_{(0.5\ \mathrm{Hz})}$. Cutoff frequency (f_{cutoff}) was defined as the input frequency at which the magnitude of the impedance first dipped below $\frac{1}{\sqrt{2}} \cdot Z_{(0.5\ \mathrm{Hz})}$ (this definition returns the classic cutoff frequency $\frac{1}{2\pi RC}$ for a passive linear cell, where $R \approx Z_{(0.5\ \mathrm{Hz})}$). Since many of our cells displayed a clear peak in the impedance magnitude profile at some nonzero frequency, we also defined the resonance magnitude (Q) as the impedance magnitude at the resonance peak (maximal impedance value) divided by the impedance magnitude at the lowest input frequency (0.5 Hz), i.e. $Q = Z_{\max}/Z_{(0.5\ \mathrm{Hz})}$ (Hutcheon *et al.* 1996*b*). Finally, the frequency of maximal impedance ($f_{\max}$) was determined as the frequency at which the maximum impedance magnitude value was detected. In those cells that showed no peak in their impedance profile ($Q = 1$), $f_{\max}$ is equal to 0.5 Hz.

The phase of the impedance (which equals the difference between the phases of the voltage and current oscillations) was also determined and plotted as a function of frequency to define the phase profile of the neuron. Since positive values of this quantity (i.e. the response leading the input) indicate a membrane with non-linear properties with potential computational significance (see Results and Discussion), following Narayanan & Johnston (2008) we defined Φ_{L} as the area under the positive part of the phase profile. This is a robust measure of the resonance properties of the membrane. Finally, we combined the magnitude and phase of the impedance to obtain the complex-valued impedance of the neuron. A plot of the complex impedance for all frequencies (i.e. a plot of the imaginary part of the impedance against the real part as frequency varies, known as a Nyquist plot) is a useful indicator of the basic properties of a system, and is widely used in engineering applications.

Characterisation of I_{h} in different cell types

In order to determine the properties of I_{h}, 800 ms-long voltage-clamp steps were given in −10 mV increments up to −120 mV from a holding potential of −40 mV. Since I_{h} has quite slow activation kinetics, rather long voltage steps are needed to activate the current fully at a given membrane potential. However, most of the interneurons proved to be sensitive to prolonged hyperpolarising pulses, and therefore we adjusted our protocol to have the shortest possible voltage step that still enabled us to measure the current. Nevertheless, we note that the shortness of the steps, in combination with the voltage-dependent kinetics of I_{h}, may cause some negative shift (up to a few mV) of the estimated activation curves.

I_{h} was obtained by subtracting the current traces before and after the application of 10 μM ZD7288, a specific blocker of HCN channels (Harris & Constanti, 1995). This current difference trace during the voltage step was used to determine the time constant(s) of I_{h} activation as well as the steady-state current, while the tail current recorded immediately after the end of the step was used to estimate the steady-state activation function. To determine the time constant(s) of I_{h} activation, either a single- or a double-exponential model was fitted to the difference current recorded from 20 ms after the beginning of the voltage step to the end of the step. The steady-state current was determined concurrently for all step potentials by fitting exponential functions with a common time constant to the current traces during the late phase (last 500 ms) of the voltage step. The I_{h} activation curve was calculated by fitting single exponential functions to the tail current between 2 and 20 ms after the end of the voltage step (the first 2 ms were excluded to ignore fast transients), and extrapolating back to the end of the step to determine the instantaneous tail current. We then plotted the tail current as a function of the step potential, and fitted a sigmoidal function:

$$I(V) = \frac{I_{\max}}{1 + \exp\left(-\left(V - V_{1/2}\right)/m\right)} \qquad (1)$$

where $I_{\max}$ is the asymptotic maximum of the sigmoid, $V_{1/2}$ is the potential of half-maximal I_{h} activation, and $\frac{1}{4m}$ is the slope of the activation function at $V_{1/2}$. The measured tail current values at each voltage were then divided by $I_{\max}$ to arrive at the activation function for each cell.

The I_{h} reversal potential for each cell type was calculated for a subset of our cells from the open-channel I–V relationship, which was obtained by the following protocol: I_{h} was activated with an 800 ms-long pulse to −120 mV and this was followed by steps to different test potentials (from −110 to −40 mV in +10 mV increments). The instantaneous I–V plot was constructed from the tail current amplitudes measured at each test potential in the same way as described above, and a straight line was fitted through the data points. The reversal potential of I_{h} was defined as the voltage at which the fitted line crossed the V axis.

Once the I_h reversal potential was known, the maximal conductance of I_h in each cell could be determined from the steady-state I–V relationship. Assuming a sigmoidal form for the activation function, the steady-state current can be written as:

$$I_{ss} = \bar{g}_h \frac{1}{1 + \exp\left(-\left(V - V_{1/2}\right)/m\right)} \left(V - E_h\right) \quad (2)$$

where $\bar{g}_h$ is the maximal I_h conductance, and E_h is the I_h reversal potential. Three parameters of this function ($\bar{g}_h$, $V_{1/2}$ and m) were optimised to fit the measured I–V relationship, resulting in an estimate of the maximal conductance value for each cell.

Statistical analyses

Since, in many cases, data were not normally distributed (according to a Lilliefors test), non-parametric statistical tests were used whenever possible. We employed Wilcoxon's signed rank test to compare medians from two groups. When comparing more than two groups, a Kruskal–Wallis test was used, often followed by *post hoc* comparisons based on average ranks using Tukey–Kramer critical values to account for multiple comparisons. However, in a few cases for which no appropriate non-parametric test has been established (such as in a three-way design, or a two-way design combining between- and within-subject factors), conventional parametric tests (such as ANOVA) were used. Summary statistics are also displayed in a form appropriate for non-Gaussian distributions, including box plots, which indicate the median of the data as well as its interquartile range, with whiskers showing the full range of the data, and extreme outliers (data points outside 2.5 times the interquartile range) marked by crosses outside the whiskers. The notch around the median value indicates a robust estimate of the confidence of the median, such that non-overlapping notches for two groups mean that the two medians are significantly different at the 5% level.

Comparisons of the goodness of fit between models with a different number of free parameters were performed using the Bayesian information criterion (BIC) (Bishop, 2006). The BIC attempts to compensate for the fact that better fits are more easily achieved with more complex models by penalising models according to the number of free parameters. For each model we calculate the quantity:

$$\mathrm{BIC} = n \ln\left(\frac{\mathrm{RSS}}{n}\right) + k \ln\left(n\right) \quad (3)$$

where RSS is the residual sum of squares for the model, n is the number of data points, and k is the number of free parameters. Then, out of two or more models of the same data set, the best model is the one for which the quantity defined by eqn (3) is the smallest.

Anatomical identification of the cells

The methods for anatomical identification have been described in detail in Gulyás *et al.* (1993). Briefly, the recorded cells were filled with biocytin during the recording. After the recording the slices were fixed in 4% paraformaldehyde in 0.1 M phosphate buffer (PB; pH 7.4) for at least 1 h, followed by washout with PB several times and incubation in 30% sucrose in 0.01 M PB for at least 2 h. Then slices were freeze-thawed three times above liquid nitrogen and treated with 1% H_2O_2 in PB for 15 min to reduce the endogenous peroxidase activity. Recorded cells were visualised using avidin-biotinylated horseradish peroxidase complex reaction (Vector Laboratories Inc., Burlingame, CA, USA) with nickel-intensified 3,3′-diaminobenzidine as chromogen giving a dark reaction product. After dehydration and embedding in Durcupan, representative neurons were reconstructed using a drawing tube.

Computational model

In an attempt to capture quantitatively the experimentally measured impedance profiles of single hippocampal neurons, single-compartment models of varying complexity were constructed and their parameters were optimised. The simplest model, which will be referred to as the passive model, contained only the membrane capacitance and a (voltage-independent) leak conductance. The temporal evolution of the membrane potential (V_m) in this model cell can be described by the following equation:

$$C\frac{\mathrm{d}V_m}{\mathrm{d}t} = g_l\left(E_l - V_m\right) + I_i \quad (4)$$

where C is the total capacitance of the neuron, g_l is the leak conductance, E_l is the reversal potential of the leak current, and I_i is the external current injection.

The second model (called the I_h model) also contained, in addition to the membrane capacitance and the leak conductance, a voltage-gated hyperpolarisation-activated conductance, which was described by a Hodgkin–Huxley-type formalism with a single gating variable, and whose parameters matched the properties of I_h in different cell types as determined in our experiments. This model is defined by the following set of equations:

$$C\frac{\mathrm{d}V_m}{\mathrm{d}t} = g_l\left(E_l - V_m\right) + \bar{g}_h m_h\left(E_h - V_m\right) + I_i \quad (5)$$

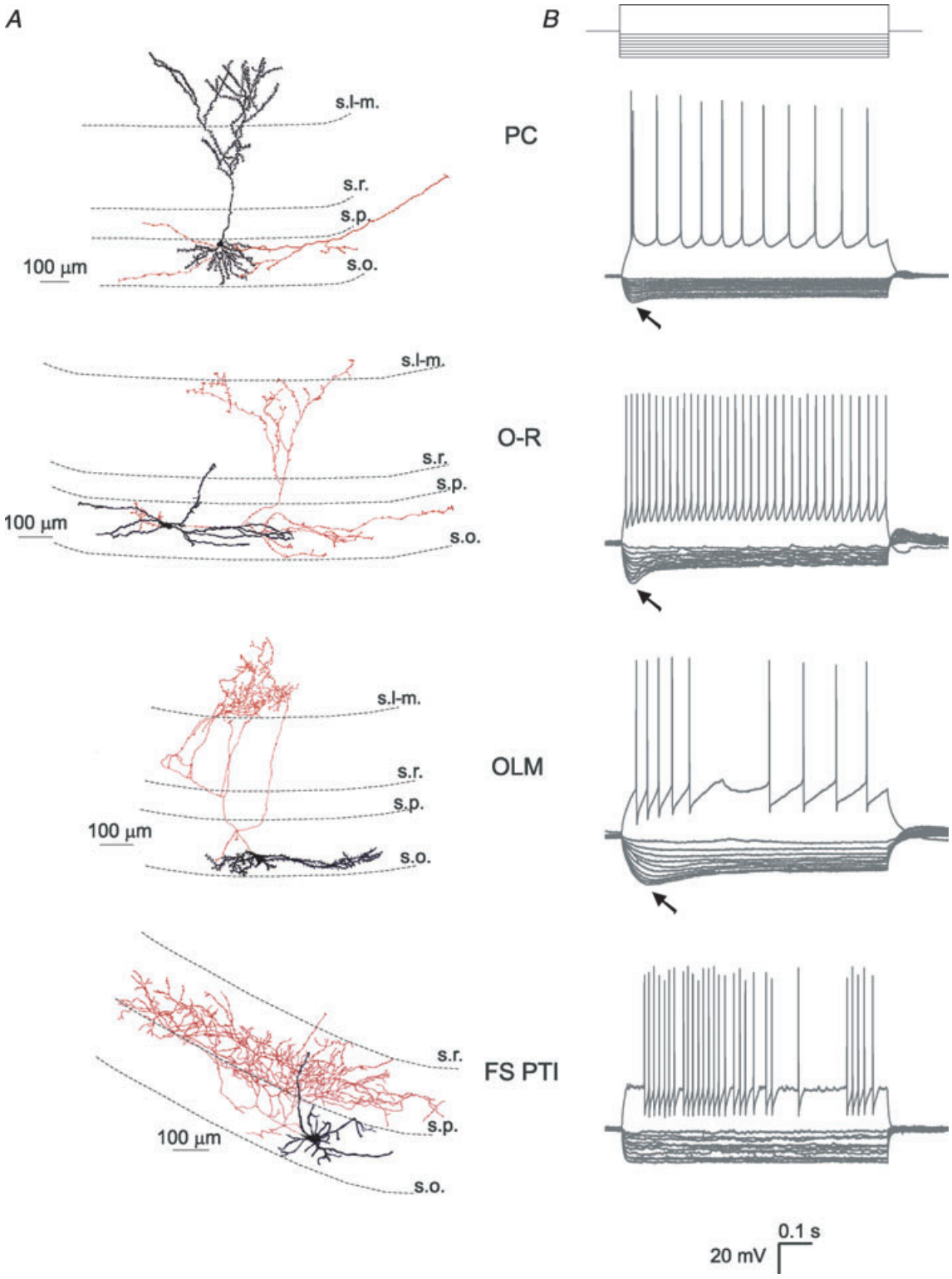

Figure 1. Light microscopic reconstructions and voltage responses to current steps of the investigated cell types recorded in the stratum oriens of hippocampal CA1 region
A, example artistic renderings of light microscopic reconstructions of a pyramidal cell (PC), an oriens-radiatum cell (O-R), an oriens-lacunosum-moleculare cell (OLM), and a fast spiking perisomatic region-targeting interneuron (FS PTI). Dendrites are represented in black and axons in red. Dendritic spines are enhanced for visibility. *B*, voltage responses to depolarising (200 pA) and hyperpolarising current steps (from −20 to −200 pA in increments of

Table 1. Passive membrane properties and sag characteristics of the investigated cell types

	PC ($n = 19$)	O-R ($n = 11$)	OLM ($n = 12$)	FS PTI ($n = 7$)
Input resistance (MΩ)	101 (91–131)	144 (116–199)	197 (169–211)	117 (112–219)
Membrane capacitance (pF)	155 (121–195)	97 (84–110)	181 (136–255)	106 (91–132)
Membrane time constant (ms)	16.6 (13.4–19.6)	18.5 (15.4–25.5)	37.7 (31.9–46.9)	8.7 (8.3–16.2)
Passive cutoff frequency (Hz)	9.6 (8.1–11.9)	8.6 (6.2–10.3)	4.2 (3.4–5.0)	18.4 (10.6–19.3)
Relative sag amplitude	0.175 (0.160–0.216)	0.687 (0.560–0.695)	0.445 (0.382–0.644)	0.074 (0.021–0.138)
Peak delay (ms)	44.7 (39.9–49.2)	36.8 (32.0–60.2)	92.3 (69.5–107.0)	74.0 (67.6–80.4)*

Data are presented as the median with interquartile range in parentheses. *$n = 2$ (only cells with a relative sag amplitude >0.1)

and

$$\frac{\mathrm{d}m_\mathrm{h}}{\mathrm{d}t} = \frac{m_\infty^{(h)}(V_\mathrm{m}) - m_\mathrm{h}}{\tau_\mathrm{h}(V_\mathrm{m})} \tag{6}$$

where $\bar{g}_\mathrm{h}$ is the maximal conductance of I_h, m_h is the gating variable for the activation of I_h, E_h is the I_h reversal potential, while $m_\infty^{(h)}(V_\mathrm{m})$ is the steady-state value and $\tau_\mathrm{h}(V_\mathrm{m})$ is the time constant for changes in m_h as a function of V_m.

For both of the above models, the impedance profile (the amplitude and phase of the voltage response to small-amplitude sinusoidal current injection as a function of input frequency) could be determined analytically by linearising all the defining equations in the vicinity of a given baseline potential. The explicit formulae derived in this manner allowed us to explore how the various parameters affect impedance, and vastly simplified the task of finding the optimal set of parameters to fit experimental data. Linearisation involved neglecting terms of second and higher order in the difference between the current membrane potential and the baseline potential in both the membrane voltage equation and the expressions for steady state activation of conductances, and neglecting the voltage dependence of the time constant of all voltage-gated conductances. The rationale for and further details of this procedure may be found in Hutcheon *et al.* (1994). For the passive model, this approach is exact (since the model is linear to begin with), and results in the following expression for the impedance of the membrane:

$$Z = \frac{1}{g_\mathrm{l} + i\omega C} \tag{7}$$

where $\omega = 2\pi f$, and f is the frequency of the oscillating input. Taking the absolute value of the complex impedance reproduces the well-known expression $|Z| = (g_\mathrm{l}^2 + \omega^2 C^2)^{-1/2}$ for the impedance magnitude.

In the I_h model, linearisation involved approximating the steady-state activation of I_h as $m_\infty^{(h)}(V_\mathrm{m}) \approx m_\infty^{(h)}(V_0) + b(V_\mathrm{m} - V_0)$ (where V_0 is the membrane potential in the absence of the oscillating input, b is the slope of the function $m_\infty^{(h)}(V_\mathrm{m})$ at V_0), and taking a voltage-independent value for τ_h. This allowed us to assume that, in response to a sinusoidal current injection, both V_m and m_h have a sinusoidal time dependence at the input frequency, and the amplitude and phase of these oscillations (relative to the input current) can be determined from eqns (5) and (6), producing the following formula for the (complex) impedance of the I_h model:

$$Z = \frac{1}{g_\mathrm{l} + i\omega C + \bar{g}_\mathrm{h} m_\infty^{(h)}(V_0) + \frac{\bar{g}_\mathrm{h} b(V_0 - E_\mathrm{h})}{1 + i\omega\tau_\mathrm{h}}} \tag{8}$$

Results

Using the whole-cell patch-clamp method, we recorded from hippocampal neurons located in the stratum oriens or pyramidale of the CA1 region. During the recording the cells were filled with biocytin and morphologically identified *post hoc* on the basis of their dendritic and axonal arborisation. In addition to pyramidal cells (PCs, $n = 27$, Fig. 1*A*), three interneuron types were recognized. Those interneurons that could not be unambiguously classified as belonging to any one of these categories were excluded from the present study.

One group of interneurons had cell bodies and smooth or sparsely spiny horizontal dendrites restricted to the stratum oriens. Their axon, which predominantly originated from the soma, ramified sparsely in strata radiatum and oriens and carried en passant and often drumstick-like boutons, which were distributed irregularly along them (Fig. 1*A*). Some of the axon collaterals could be followed to the subiculum or to the

20 pA). A sag (marked with arrows) indicating the presence of I_h can be seen in PCs, O-R cells and OLM cells. FS PTIs had a small or no sag. s.l-m., stratum lacunosum-moleculare; s.r., stratum radiatum; s.p., stratum pyramidale; s.o., stratum oriens.

CA3 region. The overall appearance of their axon cloud was spread out longitudinally compared to the other two interneuron types (see below). These neurons resembled a class of cells that were earlier characterised by Gulyás *et al.* (2003), Hájos *et al.* (2004) and Goldin *et al.* (2007) in slice preparations, and by Jinno *et al.* (2007) in intact brain. Although these neurons may represent a heterogeneous population of inhibitory cells including local interneurons as well as GABAergic cells with long-range projections (such as backprojecting cells, oriens retrohippocampal

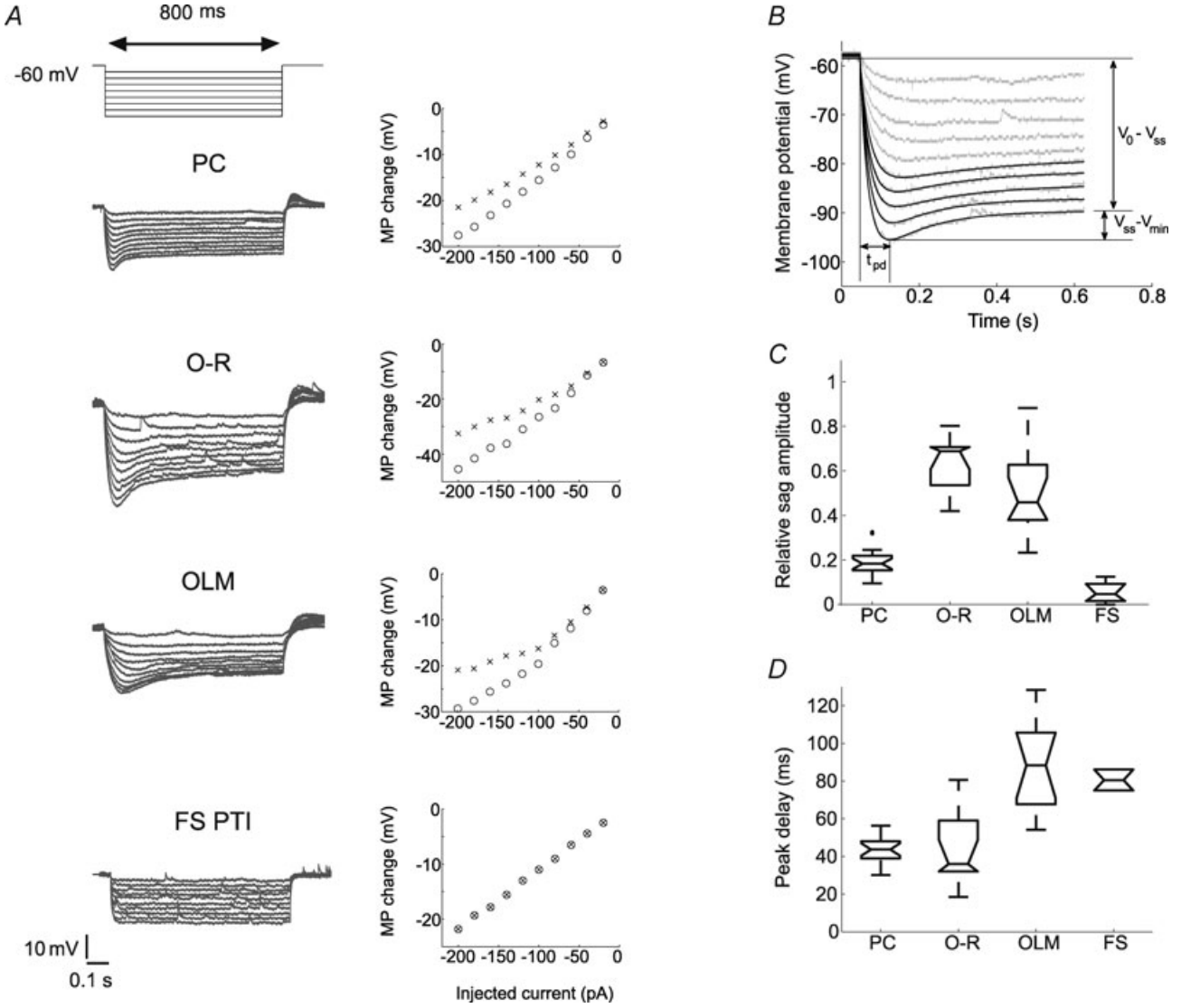

Figure 2. Properties of the sag in the investigated cell types
A, representative voltage responses of the investigated cell types to hyperpolarising current pulses (800 ms long steps from −20 to −200 pA, at 20 pA intervals from a holding potential of −60 mV), and the corresponding *I–V* plots of the peak (open circles) and the steady state membrane potential (MP) changes of the same cells (crosses). *B*, sag parameters were determined from the voltage response of the cell to the five largest amplitudes of the negative current steps (from −120 pA to −200 pA, in 20 pA steps). Relative sag amplitude is the ratio of the difference between the steady state voltage at the end of the pulse and the minimum voltage during the sag ($V_{ss} - V_{min}$), and the difference between the holding potential and the steady-state voltage ($V_o - V_{ss}$). The holding potential was approximately −60 mV in each cell. The peak delay (t_{pd}) was defined as the time of the negative peak of the membrane potential relative to the beginning of the current pulse. *C* and *D*, relative sag amplitudes and peak delays in the different cell types. Note that PCs ($n = 19$) displayed small but rather fast sag, O-R cells ($n = 11$) had a large and fast sag, while OLM cells ($n = 12$) usually showed a rather large but relatively slow sag. Two out of seven FS PTIs also showed a sag but it was rather small and could be observed only at membrane potentials negative to −90 mV.

Table 2. Properties of the impedance curves

	PC			O-R			OLM			FS PTI		
	−80	−70	−60	−80	−70	−60	−80	−70	−60	−80	−70	−60
Z	53	59	68	99	117	129	105	130	147	79	83	66
(0.5 Hz)	(43–66)	(51–80)	(60–92)	(60–128)	(76–172)	(80–154)	(98–117)	(111–148)	(135–153)	(60–93)	(69–102)	(61–105)
(MΩ)												
Q	1.17	1.22	1.14	1.10	1.12	1.05	1.10	1.05	1.04	1.02	1.01	1.00
	(1.08–1.28)	(1.14–1.32)	(1.11–1.17)	(1.04–1.35)	(1.04–1.26)	(1.04–1.24)	(1.00–1.17)	(1.00–1.15)	(1.02–1.12)	(1.00–1.04)	(1.00–1.03)	(1.00–1.02)
f_{cutoff}	18.5	16.6	13.3	14.0	11.3	9.4	7.9	6.2	4.9	18.3	14.7	20.6
(Hz)	(17.2–21.5)	(14.2–19.0)	(10.3–15.8)	(9.4–28.2)	(6.9–16.2)	(6.6–18.7)	(6.8–12.1)	(4.5–9.0)	(3.8–7.1)	(12.6–22.2)	(11.2–19.4)	(11.1–23.1)
f_{max}	5.0	6.0	5.0	2.0	2.5	2.0	1.0	1.0	1.0	1.0	0.8	1.0
(Hz)	(5.0–5.3)	(4.0–6.0)	(3.5–5.0)	(2.0–4.0)	(1.5–4.0)	(2.0–4.0)	(0.5–2.3)	(0.5–2.0)	(1.0–1.8)	(0.5–1.0)	(0.5–3.0)	(0.5–2.5)
Φ_L	0.09	0.06	0.00	0.21	0.13	0.01	0.06	0.00	0.00	0.00	0.00	0.00
(rad Hz)	(0.05–0.18)	(0.05–0.11)	(0.00–0.03)	(0.07–0.40)	(0.00–0.39)	(0.00–0.20)	(0.00–0.20)	(0.00–0.10)	(0.00–0.05)	(0.00–0.01)	(0.00–0.00)	(0.00–0.02)

Data are presented as the median with interquartile range in parentheses.

projection cells, or double projection cells based on the review of Maccaferri, 2005 and Klausberger & Somogyi, 2008), their physiological features were rather comparable; therefore the data obtained in neurons with this type of morphology were pooled under the name of oriens–radiatum (O-R) cells ($n = 24$). This name only refers to the fact that the axon collaterals of these neurons were restricted to the strata oriens and radiatum in hippocampal slices, and may not correspond to a functional category.

Another group of interneurons also had both the cell body and dendritic tree in the stratum oriens, but their horizontally running dendrites were often densely decorated with long spines. Their axon frequently originated from a proximal dendrite, and after ramification the main axon without boutons could be followed into the stratum lacunosum-moleculare. In this layer the axon ramified extensively bearing heavily packed varicosities. Some axon collaterals with boutons were also observed in the stratum oriens. These neurons were identified as oriens–lacunosum-moleculare (OLM) cells ($n = 26$) (Fig. 1*A*; McBain *et al.* 1994).

The somata of the third group of interneurons were also found in the stratum oriens, sometimes in the close vicinity of the stratum pyramidale. Their aspiny or sparsely spiny dendritic tree had either horizontal or vertical orientation, and the axonal arbour was predominantly located in the stratum pyramidale (Fig. 1*A*). Thus, these interneurons belonged to the perisomatic region-targeting inhibitory cells, which comprise both basket cells and axo-axonic cells (Freund & Buzsáki, 1996). Since the light microscopic examination of these interneurons did not allow us to unequivocally distinguish them from each other, data from all perisomatic region-targeting interneurons were pooled. Moreover, only those neurons were included in the following physiological comparison that could be classified as fast spiking cells based on the properties of their action potentials evoked by 800 ms long, 0.2 nA current pulses ($n = 7$). Therefore, we refer to them as fast-spiking perisomatic region-targeting interneurons (FS PTIs).

Basic electrophysiological characteristics

We first determined the apparent passive membrane properties (i.e. input resistance and time constant) of the neuronal classes included in our study by injecting small-amplitude hyperpolarising current steps (see Methods). Both input resistance and membrane time constant varied significantly among the different cell types (Kruskal–Wallis (KW) test, $P < 0.001$). Multiple *post hoc* comparisons (see Methods) indicated that OLM cells ($n = 12$) had a significantly higher input resistance than PCs ($P < 0.01$, $n = 19$) and FS PTIs ($P < 0.05$, $n = 7$) (Table 1). OLM cells also had a significantly slower membrane time constant at rest than any other cell type studied (OLM *vs.* PC: $P < 0.001$; OLM *vs.* O-R: $P < 0.05$; OLM *vs.* FS PTI: $P < 0.001$) (Table 1). In order to facilitate later comparisons with models that directly include capacitance as a parameter, we also estimated the membrane capacitance from the small-amplitude transient responses. Capacitance varied significantly between cell types (KW test, $P < 0.01$); in particular, OLM cells had a significantly larger capacitance than O-R cells ($n = 11$) and FS PTIs (both $P < 0.05$) (Table 1). The resting membrane potentials were estimated to be -62.4 ± 2.4 mV for PCs ($n = 21$), -55.4 ± 9.5 mV for O-R cells ($n = 17$), -55.7 ± 6.5 mV for OLM cells ($n = 19$) and -50.4 ± 8.1 mV for FS PTIs ($n = 7$) (data presented here as means ± S.D.).

Distinct features of depolarising *sag* in hippocampal neuron types

We observed a sag in the voltage response of PCs, O-R cells and OLM cells to negative current steps of suitable magnitudes (Figs 1*B* and 2*A*). In these cells a rebound depolarising hump could also be detected after the offset of the current step and in a few interneurons some rebound spikes could be observed as well (in 5 out of 17 O-R cells and in 4 out of 19 OLM cells). Both the sag and rebound depolarisation were eliminated by bath application of the specific I_h blocker, ZD7288

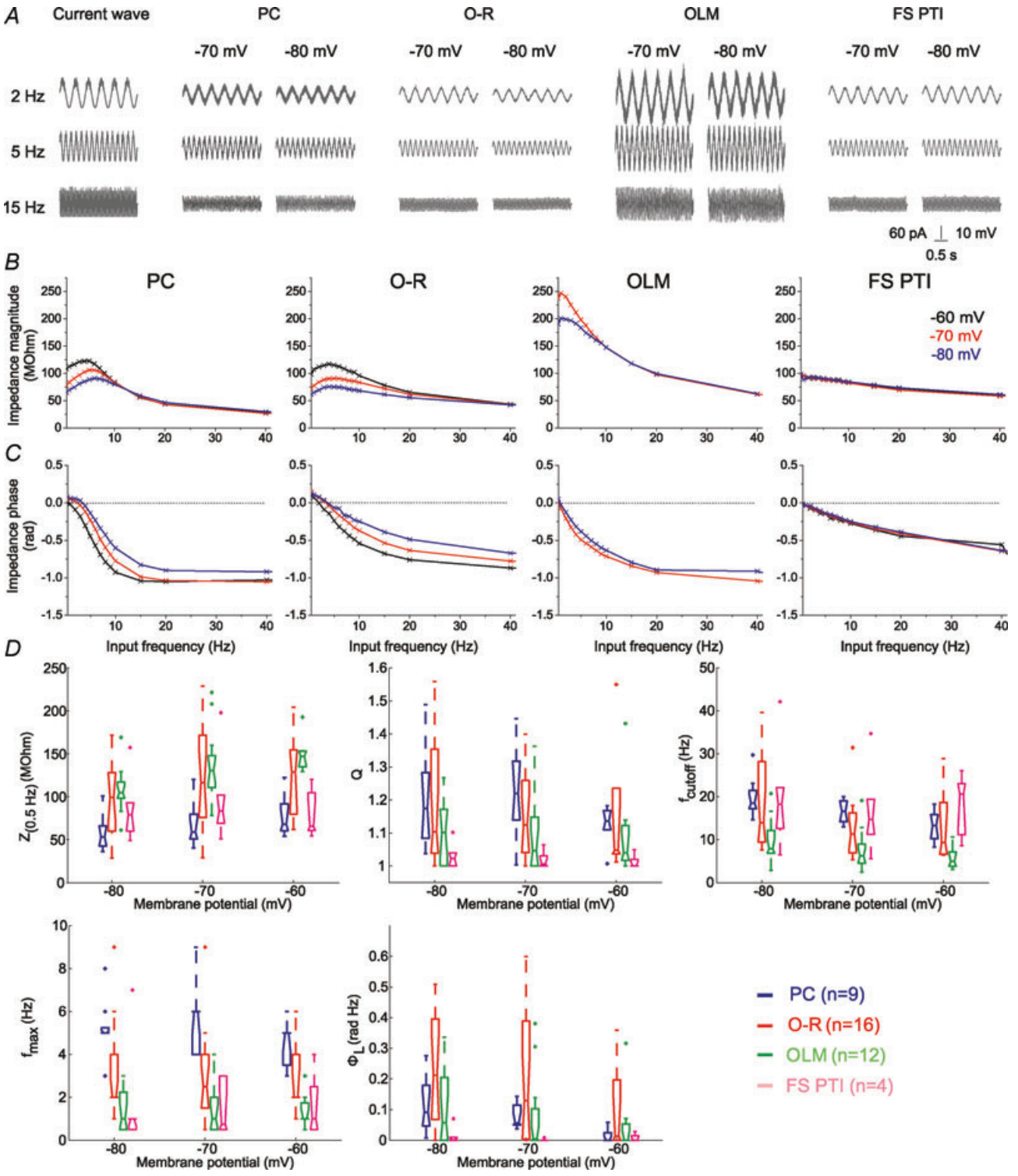

Figure 3. Characterisation of the impedance profile in the different cell types
A, voltage responses of sample cells of the investigated cell types to 3 s-long sinusoidal current inputs at 2, 5 and 15 Hz at a holding potential of −70 and −80 mV. *B*, the impedance magnitude–frequency relationship of the same cells as in *A* at different membrane potentials. PCs and O-R cells showed a clear resonance peak in the theta frequency range. Most of the OLM cells also showed resonance, although it was less apparent and occurred at lower frequencies. Fast spiking interneurons (FS PTIs) showed no subthreshold resonance. *C*, the impedance phase profile of the different cell types at the investigated potentials. Note that the amplitude and frequency extent of positive phase values increased with membrane hyperpolarisation in PCs, O-R cells and OLM cells. Colours identify corresponding membrane potentials. *D*, five parameters were used to quantitatively characterise the properties of

Table 3. Passive membrane properties and sag amplitude after the application of ZD7288

	PC ($n = 7$)	O-R ($n = 8$)	OLM ($n = 6$)	FS PTI ($n = 5$)
Input resistance (MΩ)	125 (112–159)	211 (186–235)	233 (182–245)	119 (109–190)
Membrane capacitance (pF)	220 (199–256)	160 (104–190)	208 (149–275)	135 (111–219)
Membrane time constant (ms)	25.3 (19.3–27.9)	23.5 (20.0–30.8)	26.0 (23.7–33.0)	8.9 (7.5–20.0)
Passive cutoff frequency (Hz)	6.3 (5.7–8.3)	6.8 (5.2–8.0)	6.1 (4.8–6.7)	17.9 (8.5–21.4)
Relative sag amplitude	0.066 (0.050–0.084)	0.099 (0.036–0.155)	0.076 (0.004–0.086)	0.0 (0.0–0.029)

Data are presented as median with interquartile range in parentheses.

(10 μM; data not shown). The properties of the sag varied substantially between the cell types (Fig. 2*C*,*D*). In particular, the cell types differed significantly in the relative sag amplitude ($P < 0.001$, KW test), and *post hoc* multiple comparisons indicated that O-R cells and OLM cells had a significantly larger relative sag amplitude than PCs (O-R *vs.* PC: $P < 0.001$; OLM *vs.* PC: $P < 0.01$) and FS PTIs (both $P < 0.001$) (Fig. 2*C*). The time taken to reach the negative peak amplitude of membrane potential during the current step (i.e. peak delay) also varied significantly between cell types ($P < 0.001$, KW test). OLM cells, in particular, had a significantly slower sag than PCs and O-R cells (both $P < 0.001$, *post hoc* multiple comparisons as detailed above) (Fig. 2*D*).

Qualitatively, PCs ($n = 18$ out of 19) displayed a small but rather fast sag, O-R cells ($n = 11$) had the largest and fastest sag, while OLM cells ($n = 12$) usually showed a large but relatively slow sag. In 2 out of 7 fast-spiking cells some I_h-mediated sag could be observed, but even in these particular neurons the sag was rather small and tended to appear only at very negative potentials (more negative than −90 mV).

These data suggest that, in addition to passive membrane characteristics, the properties of some active conductances such as the non-selective cation conductance mediating I_h, might be different between these cell types.

The impedance profiles and resonance properties of four types of hippocampal neuron

The differences in sag characteristics among cell types suggest that the I_h-dependent resonance could also be dissimilar. In order to characterise the subthreshold impedance profiles and possible resonance properties of the cells, a 3 s-long sinusoidal current was injected into the cells at different membrane potentials negative to the firing threshold (Fig. 3). Impedance magnitude and phase curves were characterised by five summary statistics (Table 2): impedance at 0.5 Hz ($Z_{(0.5\ \mathrm{Hz})}$; this quantity can also be used as an estimate of the input resistance of the cell, which, by definition, is the same as the impedance magnitude at 0 Hz), cutoff frequency (f_{cutoff}), resonance magnitude (Q), the frequency of maximal impedance (f_{max}) and total inductive phase (Φ_L), as described in Methods. These quantities were then compared statistically between the different cell types and experimental conditions.

We found that cell type had a significant effect on all five of the derived statistics: $Z_{(0.5\ \mathrm{Hz})}$, f_{cutoff}, Q, f_{max} and Φ_L ($P < 0.001$ in each case, KW test; Fig. 3*B*–*D*). Multiple comparisons indicated that PCs had a significantly smaller $Z_{(0.5\ \mathrm{Hz})}$ than OLM cells and O-R cells (both $P < 0.001$) and FS PTIs also had a smaller $Z_{(0.5\ \mathrm{Hz})}$ than OLM cells ($P < 0.01$); f_{cutoff} was significantly lower in OLM cells than in any other cell type studied (all $P < 0.001$); Q was significantly larger in PCs, O-R cells and OLM cells than in FS PTIs ($P < 0.001$ for PCs and O-R cells, and $P < 0.05$ for OLM cells) and it was significantly larger in PCs than in OLM cells ($P < 0.01$); PCs had a significantly higher f_{max} than any other cell type (all $P < 0.001$), and f_{max} was also significantly higher in O-R cells than in OLM cells ($P < 0.01$) and FS PTIs ($P < 0.01$). Φ_L was significantly smaller in FS PTIs than in O-R cells ($P < 0.001$) and in PCs ($P < 0.05$) (Fig. 3*D*). In addition, the shape of the impedance profiles changed with variations in baseline membrane potential (Fig. 3). In particular, a two-way analysis of variance (ANOVA) using cell type as between-subject factor and membrane potential as within-subject factor showed that three of the summary statistics varied significantly with membrane potential ($Z_{(0.5\ \mathrm{Hz})}$: $P < 0.001$; f_{cutoff}: $P < 0.001$; Φ_L: $P < 0.05$).

the impedance curves. $Z_{(0.5\ \mathrm{Hz})}$ is the impedance value at the lowest input frequency (0.5 Hz). The Q value ($Z_{\mathrm{max}}/Z_{(0.5\ \mathrm{Hz})}$) was used to quantify the magnitude of the resonance. f_{max} means the input frequency at which the maximal impedance value was detected. Cutoff frequency (f_{cutoff}) is the input frequency where the magnitude of the impedance first dipped below $\frac{1}{\sqrt{2}} \cdot Z_{(0.5\ \mathrm{Hz})}$. Φ_L is the total inductive phase defined as the area under the positive segment of the impedance phase profile. PCs are shown in blue, O-R cells in red, OLM cells in green and FS PTIs in magenta. (See also Table 2.)

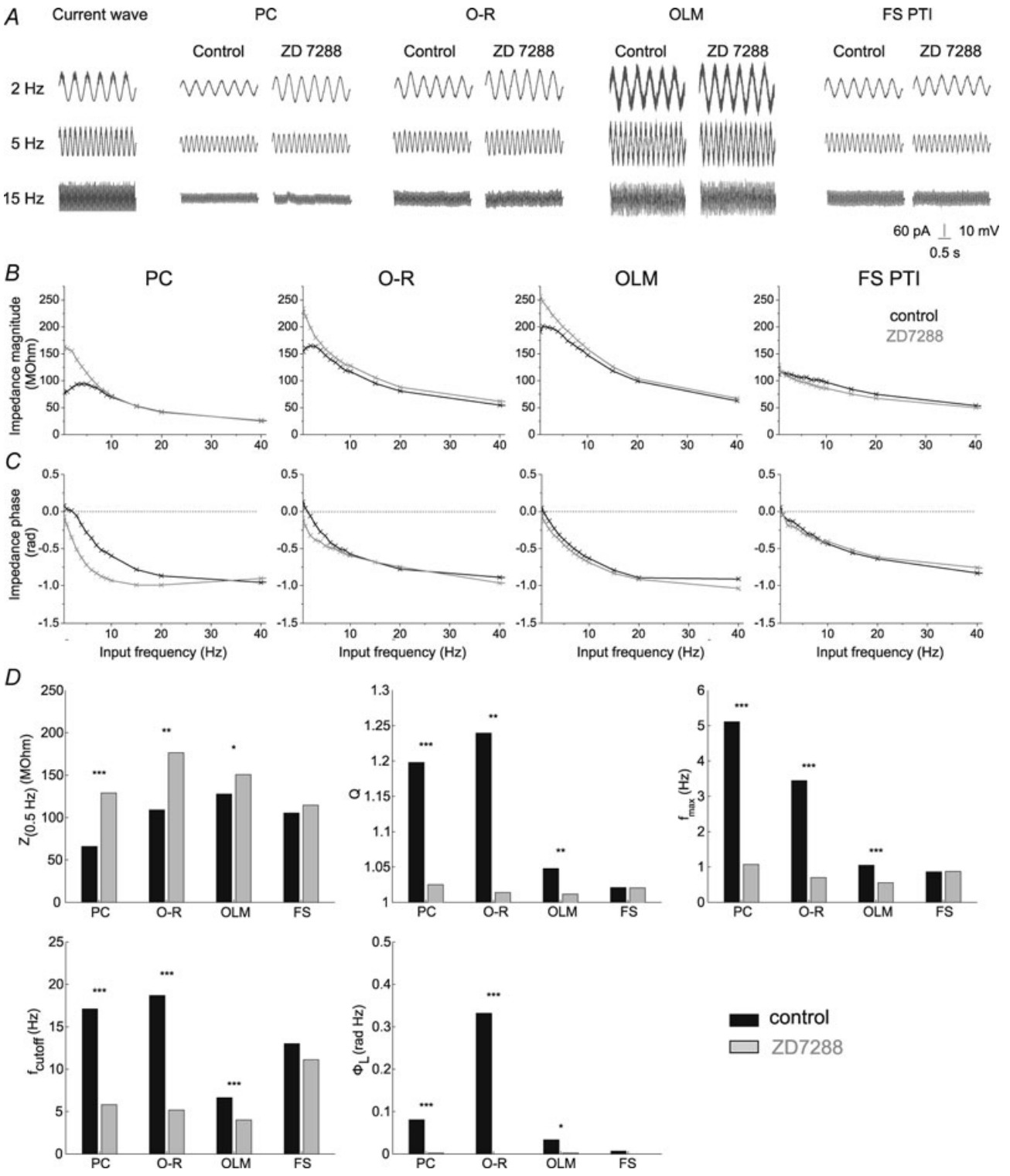

Figure 4. The effect of blocking I_h on the impedance profile of the investigated cell types
A, voltage responses of representative cells of the investigated cell types to 3 s long sinusoidal current inputs at 2, 5 and 15 Hz at a holding potential of −80 mV under control conditions and in the presence of the I_h-blocker ZD7288 (10 μM). *B* and *C*, the magnitude and phase of the impedance as a function of input frequency of the same cells measured at −80 mV in control conditions (black) and in the presence of 10 μM ZD7288 (grey). Note that after blocking I_h both the magnitude and the phase profiles changed substantially in PCs, O-R cells and OLM cells; however, ZD7288 had no apparent effect on the shape of the impedance profiles in FS PTIs. *D*, statistical comparison of the five investigated parameters in the different cell types under control

To separate cells with a monotonically decreasing impedance profile from those with resonance, resonating cells were defined as cells with a Q value greater than 1.05 at any of the investigated membrane potentials. We found that all PCs showed resonance ($n = 9$), indicated as a clear peak in the impedance curve. Resonance was most prominent at hyperpolarised potentials (at -70 and -80 mV), but was also apparent (though weaker) at depolarised potentials (Fig. 3*B* and *D*). The f_{max} values fell into the theta range (4–6 Hz) (Fig. 3*D*). Almost all O-R cells also exhibited resonance ($n = 15$ out of 16), although a rather large variance could be seen in Q values; f_{max} was between 2 and 6 Hz. Ten out of 15 OLM cells also showed resonance, but the resonance frequency fell in the range of 1–3 Hz. An obvious resonance peak could be observed in only 1 out of 7 FS PTIs at the investigated membrane potentials (Fig. 3*B* and *D*).

In line with the prediction based on the sag characteristics, both the impedance profiles and the resonance properties were found to vary substantially between the cell types. Therefore, we next investigated the contribution of I_h to their impedance profiles.

The involvement of I_h in impedance profiles and resonance

I_h is an active conductance, which was shown to be essential for the emergence of resonance behaviour in some neurons (Hutcheon *et al.* 1996*b*; Lüthi & McCormick, 1998; Hu *et al.* 2002; Narayanan & Johnston, 2007). In our experiments only those cells that showed an I_h-dependent sag showed subthreshold resonance. Furthermore, the application of 10 μM ZD7288, a blocker of HCN channels, strongly reduced or eliminated the sag in all cell types ($P < 0.001$ overall, and $P < 0.05$ in each individual cell type except FS PTIs). ZD7288 also had a moderate effect on passive membrane properties at -60 mV, increasing both the input resistance ($P < 0.05$ overall) and the apparent membrane capacitance ($P < 0.001$ overall) (Table 3). Therefore, the effect of ZD7288 on the impedance profile was tested in each of the investigated cell types. A three-way ANOVA, with cell type as a between-subject factor, and membrane potential and ZD7288 treatment as within-subject factors, indicated that ZD7288 had a significant effect on all five of our summary measures ($Z_{(0.5\ Hz)}$, f_{cutoff}, Q, f_{max}, and Φ_L; Fig. 4). In particular, the blockade of HCN channels significantly increased $Z_{(0.5\ Hz)}$ in PCs ($n = 9$, $P < 0.001$), O-R cells ($n = 6$, $P < 0.01$) and OLM cells ($n = 7$, $P < 0.01$) and significantly decreased f_{cutoff} in the same three cell types (PCs: $P < 0.001$; O-R cells: $P < 0.01$; OLM cells: $P < 0.001$). Most importantly, ZD7288 completely abolished the resonance, resulting in a significant reduction in the Q value in PCs ($P < 0.001$), O-R cells ($P < 0.01$) and in OLM cells ($P < 0.05$) (Fig. 4). The elimination of resonance by ZD7288 was also evident in the change in f_{max}, which was significant in PCs ($P < 0.001$), O-R cells ($P < 0.01$) and in OLM cells ($P < 0.01$), and in Φ_L, which was significantly reduced in the same three cell types (PCs: $P < 0.001$; O-R cells: $P < 0.01$; OLM cells: $P < 0.05$). However, ZD7288 had no effect on the shape of the impedance profile (as characterised by these five quantities) at any of the investigated membrane potentials in FS PTIs ($n = 4$) (Fig. 4).

These results suggest that I_h is essential for subthreshold resonance in pyramidal cells, O-R cells and OLM cells, and that it contributes substantially to the shape of the impedance profile even in some cells without a clear resonance, e.g. in some of the OLM cells. We also found that the shape of the impedance profile varied substantially between different cell types. Therefore, we set out to investigate whether the observed differences in the impedance curves among cell types might be due to distinct properties of I_h.

The properties of I_h in the different cell types

To examine the differences in the properties of I_h between the cell types (excluding FS PTIs since their impedance curve was not substantially affected by ZD7288 application), whole-cell voltage-clamp experiments were performed (Fig. 5*A*). First, the voltage-dependent activation of I_h was measured based on the instantaneous tail current at the end of 800 ms steps to different potentials (see Methods). We found that I_h was significantly more activated in PCs than in interneurons at all potentials between -60 and -100 mV; there was no significant difference between O-R cells and OLM cells at any membrane potential (Fig. 5*B*). Based on sigmoidal fits to activation values, the potential of half-maximal I_h activation ($V_{1/2}$) was -82.9 ± 4.9 mV in pyramidal cells ($n = 6$), -97.3 ± 4.7 mV in O-R cells ($n = 7$) and -97.7 ± 5.0 mV in OLM cells ($n = 7$, Fig. 5*B*). The slope of the activation function was similar in all cell types: the parameter m was -12.4 ± 1.9 mV in PCs,

conditions and in the presence of 10 μM ZD7288. Since ZD7288 had a similar effect at all investigated membrane potentials, data measured at different potentials were pooled in this figure. Note that ZD7288 significantly changed all properties of the impedance curves in cell types expressing a sag, but had no significant effect in FS PTIs. $^*P < 0.05$; $^{**}P < 0.01$; $^{***}P < 0.001$. (See also Table 3.)

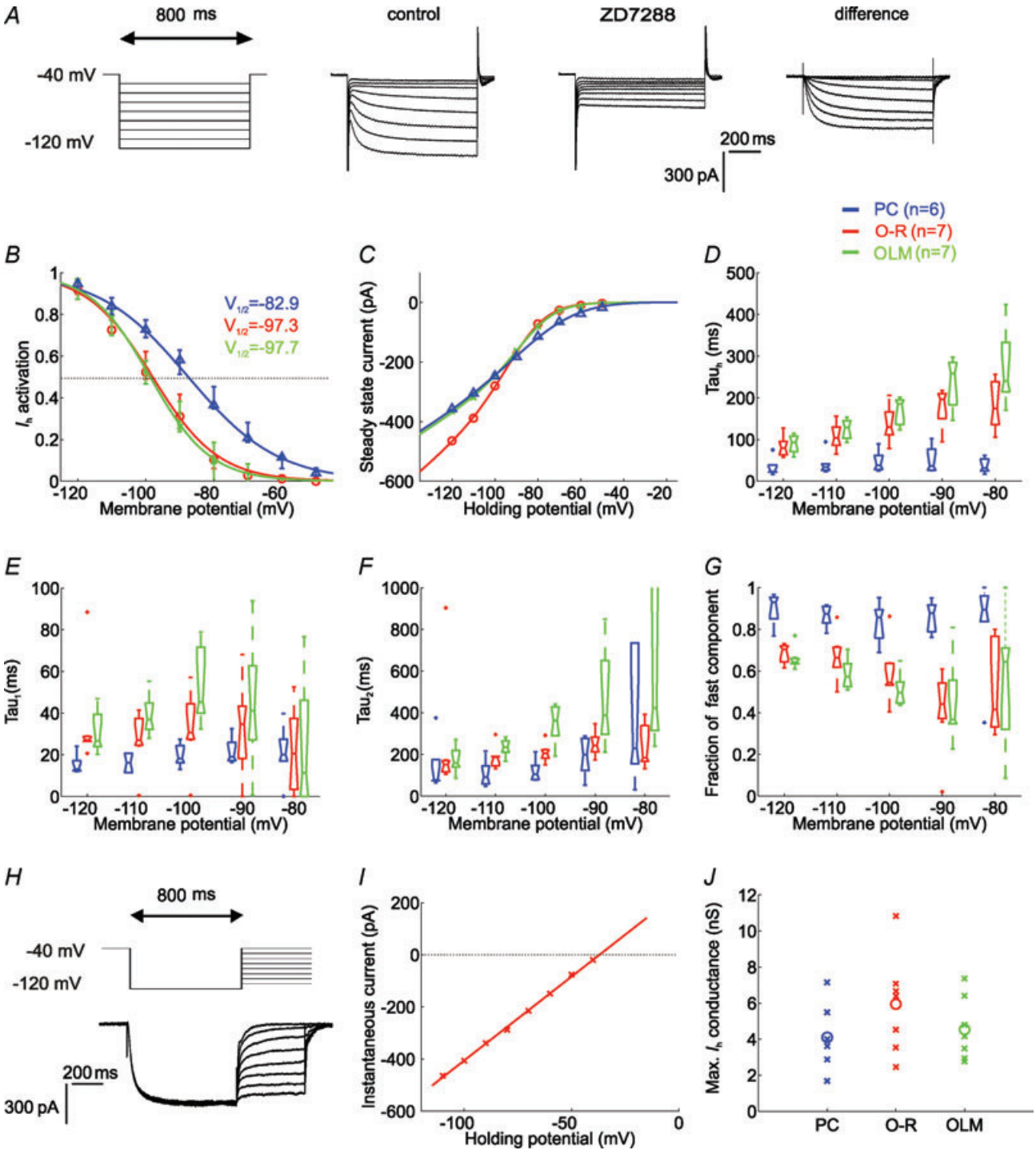

Figure 5. The properties of I_h in the different cell types
A, I_h was elicited by 800 ms-long hyperpolarising voltage steps from a holding potential of −40 mV to the range of −50 to −120 mV, in 10 mV steps. Current traces recorded before and after the application of 10 μM ZD7288. The ZD7288-sensitive current was obtained by digital subtraction. *B*, the activation curves of I_h in the investigated cell types, calculated from tail current amplitudes. *C*, the current–voltage (*I–V*) relation of I_h in the different cell types obtained by plotting steady-state currents. Note that at physiologically relevant potentials (positive to −90 mV), a significantly larger amplitude of I_h was activated in PCs than in interneurons. *D*, the activation kinetics (Tau_h) of I_h plotted against membrane potential for PCs, O-R cells and OLM cells obtained from single exponential fits. The time course of activation was generally more rapid in PCs than in interneurons over the entire voltage range. *E* and *F*, two components of the activation kinetics could be clearly identified with double exponential fits in all cell types. Fast (Tau_1, E) and slow time constant (Tau_2, F) of I_h activation as a function of voltage for PCs, O-R cells and OLM cells. In

-10.2 ± 2.7 mV in O-R cells and -8.9 ± 4.0 mV in OLM cells. No significant difference was found in the I_h reversal potential – measured using the instantaneous *I–V* plot, see Methods – between the different cell types (-33.0 ± 13.4 mV in PCs ($n = 3$), -38.8 ± 2.9 mV in O-R cells ($n = 4$), and -37.0 ± 5.9 mV in OLM cells ($n = 4$)). Therefore, reversal potential values from all cells were pooled and averaged to arrive at a single figure (-36.6 mV) that was used in all subsequent calculations and models (Fig. 5*H* and *I*). Next, we determined the maximal I_h conductance in each cell based on the steady-state current (Fig. 5*C*). We found no significant difference between the cell types, and a substantial variation within any given class (4.1 ± 1.9 nS in PCs, 5.9 ± 2.8 nS in O-R cells, and 4.6 ± 1.8 nS in OLM cells (data presented here as means $\pm$ S.D.) (Fig. 5*J*).

Finally, we analysed the kinetics of I_h by fitting either single or double exponential functions to the time course of I_h activation at different membrane potentials. Although the time course could be described fairly accurately using a single exponential function (Fig. 5*D*), a better fit was seen when a double exponential function was used, and the two components could be clearly identified in essentially all cells, with little variation within a given cell type (Fig. 5*E*,*F*). The single exponential fit indicated that activation of I_h was significantly faster at all membrane potentials between -80 and -120 mV in PCs than in O-R cells ($P < 0.001$ between -80 mV and -100 mV, and $P < 0.01$ at -110 and -120 mV) and OLM cells ($P < 0.001$ at all voltages in this range). The double exponential fit clearly identified a fast (time constant, 20–50 ms) and a slower (100–500 ms) component of I_h activation in all cell types. Both components tended to be slower in interneurons than in PCs, a difference that reached significance at some (more hyperpolarised) membrane potentials. However, the most substantial difference was in the relative weight of the two components: the activation of I_h was dominated by the fast component at all membrane potentials in PCs, while the two components contributed almost equally in interneurons (Fig. 5*G*). No significant difference was seen in the kinetics of I_h activation between O-R cells and OLM cells. The activation kinetics were found to be voltage dependent in all cell types investigated, approximated either with single or double exponential functions (Fig. 5*D–F*).

In summary, differences in the properties of I_h – specifically, the voltage dependence of steady-state activation and the kinetics of activation – between PCs and the two classes of interneuron with subthreshold resonance suggest that PCs and investigated interneuron types may express distinct subunit compositions of HCN channels, and that this may account for some of the differences in the impedance profiles between different cell types. On the other hand, the lack of any such difference in I_h characteristics between O-R cells and OLM cells, two cell types with distinct impedance profiles, indicates that factors other than the magnitude and kinetic properties of I_h are responsible for the observed variation in their impedance properties.

Computational model

To provide a quantitative account of the observed differences in the impedance profiles and resonance properties between the different cell types, we fitted the impedance profiles of single-compartment, conductance-based model neurons to those measured experimentally. The simpler model contained a membrane capacitance and a leak conductance, while the more complex model also included a voltage-gated conductance (see Methods for details). The main advantage of using models of such moderate complexity is that the impedance profile could be computed analytically by linearising the defining equations around an arbitrary baseline potential (see Methods). The relatively small number of parameters in these models also allowed us to determine, using standard non-linear optimisation algorithms, the optimal set of parameters to fit a particular set of impedance profiles (see below).

We determined and compared the best fits to individual impedance profiles using the passive model and the linearised I_h model; examples of the fits for each cell type are shown in Fig. 6*A–C* (where amplitude, phase, and

each cell type the fast time constant was about 5–8 times more rapid than the slow time constant of activation at a given potential. *G*, the fraction of the fast exponential component (Tau_1) as a function of voltage. Note that in PCs the fraction of Tau_1 was predominant over the entire voltage range, while in interneurons the fast component becomes predominant only at hyperpolarised potentials (below -100 mV) but even at -120 mV it represents only 70% of the total current amplitude. *H*, to determine the reversal potential of the current, I_h was fully activated with a voltage pulse to -120 mV and this was followed by steps to different test potentials (from -110 mV to -40 mV in 10 mV increments). *I*, the open-channel *I–V* plot was constructed from the tail current amplitudes measured at each test potential and the reversal potential of I_h was extrapolated from these plots. *J*, the estimated maximal conductance values of I_h for each cell of the different cell types (crosses). Circles indicate median values. There was no significant difference in the maximal conductance of I_h between the investigated cell types. In all plots PCs are shown in blue, O-R cells in red and OLM cells in green.

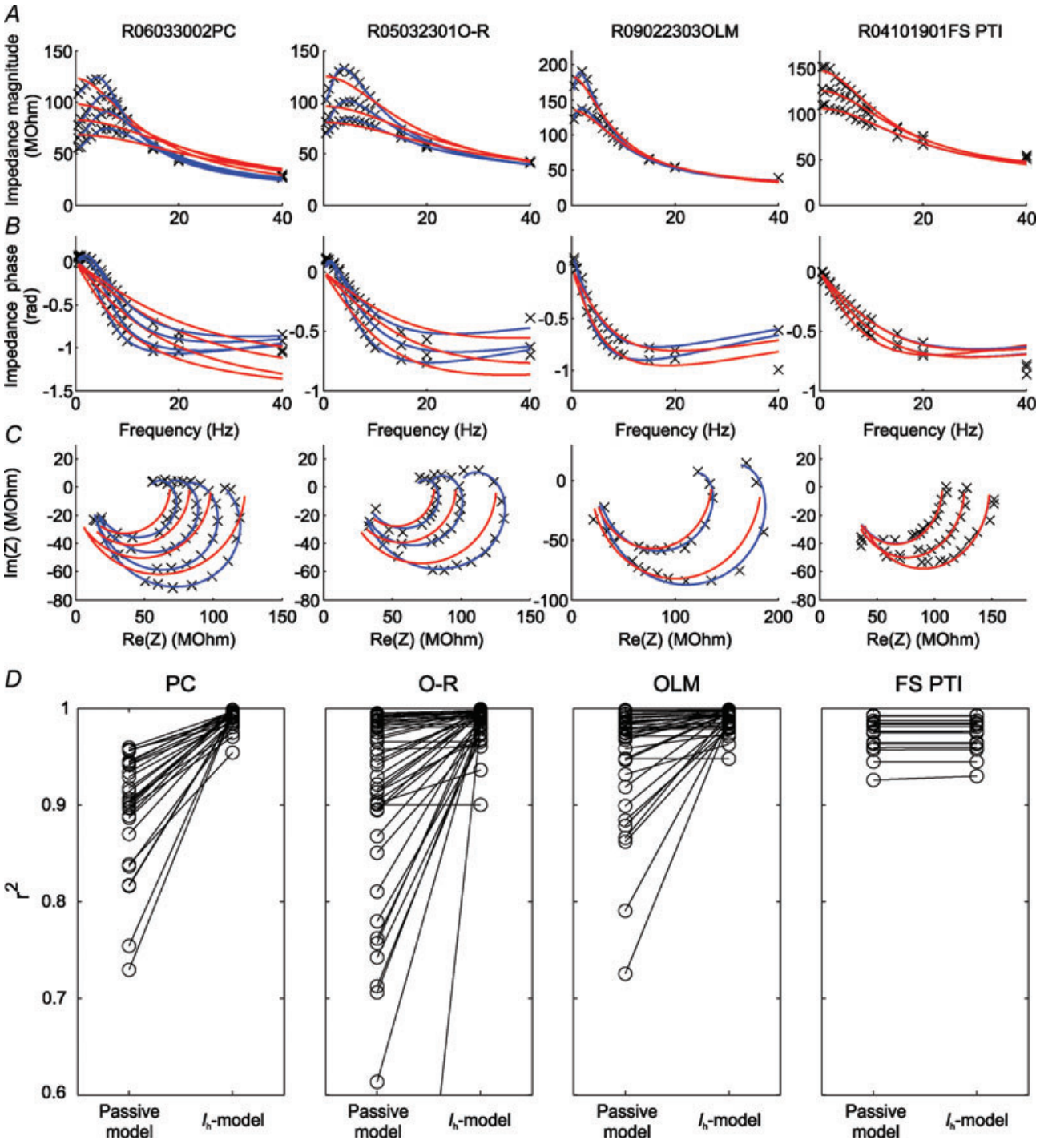

Figure 6. Comparison of fits using a passive and an active model (I_h model) in various hippocampal cell types

A–C, examples of the impedance profiles (measured at multiple membrane potentials in each cell) for a single cell of each type in the study are indicated by the crosses; the red lines show best fits to each individual curve based on a passive (three-parameter) cell model; the blue lines are best fits based on the (effectively five-parameter) I_h model (see Methods for details). *A* displays the absolute value (magnitude) of the impedance and *B* the phase of the impedance as a function of input frequency, while in *C* the complex impedance values (as defined by the magnitude and the phase) are plotted in the complex plane (in this plot, known as a Nyquist plot, frequency is not explicitly represented). *D*, comparison of fit quality between the passive and the I_h model as measured by the r-square statistic for all impedance profiles recorded under control conditions.

complex impedance are displayed separately). The passive model has only three free parameters (the input resistance, the total capacitance of the cell, and an additive serial resistance), while the linearised I_h model has five effective free parameters. (It has a total of seven parameters: the capacitance, the leak conductance, the maximal I_h conductance, the value of the activation variable at the baseline potential, the derivative of the activation variable with respect to voltage at the baseline potential, the time constant of the activation of I_h, and the series resistance, but these quantities appear only in certain combinations in the expression for the impedance, eqn (8), which reduces the number of actual free parameters to five.) We used the Bayesian information criterion (BIC, which takes into account the number of free parameters, see Methods) to compare the quality of the best fit in the two models (Fig. 6*D*). We found that the I_h model described the control impedance curves of PCs, O-R cells and OLM cells better than the passive model (median $r^2 = 0.991$ *vs.* 0.904 in PCs; $r^2 = 0.992$ *vs.* 0.949 in O-R cells; $r^2 = 0.993$ *vs.* 0.978 in OLM cells), and the value of the BIC was lower for the I_h model in these cell types, indicating that the I_h model is better even when we take into account the difference in the number of free parameters. On the other hand, the two models were about equally good at describing single control curves in FS PTIs (median $r^2 = 0.976$ for both models), and the BIC in this case favoured the passive model. In contrast, for the impedance curves measured in the presence of ZD7288, the I_h model did not perform significantly better than the passive model for any cell type (median $r^2 = 0.992$ for both models in PCs; $r^2 = 0.983$ for both models in O-R cells; $r^2 = 0.977$ *vs.* 0.976 in OLM cells; $r^2 = 0.955$ *vs.* 0.954 in FS PTIs); in fact, the simpler passive model was found to be better in all cell types according to the BIC. These results suggest that I_h makes an essential contribution to the shape of the impedance profile in PCs, O-R cells and OLM cells, converting a basically passive impedance curve into one that is more adequately described by assuming voltage-dependent mechanisms.

Next, we wanted to determine whether the presence of I_h in itself (in combination with appropriate passive characteristics) is sufficient to explain the observed impedance profiles of hippocampal neurons. We also wished to understand to what extent the observed differences in impedance curves between the different cell types could be due to differences in the properties of I_h itself, as described in the previous section. Thus, for each individual neuron, we simultaneously fitted all the available impedance curves (measured under control conditions at different baseline membrane potentials) using the linearised I_h model, with the properties of I_h (the value and the slope of the steady-state activation and the time constant, all at the appropriate membrane potentials) set according to our voltage-clamp data for the given cell type, and only four free parameters (capacitance, leak conductance and maximal I_h conductance of the neuron, and an additional series resistance) to fit for each cell. This is a much more heavily constrained fit than the ones considered above (which had 3–5 free parameters for every impedance curve, and thus up to 20 for each cell); here, the four fitted parameters are assumed to be the same at all membrane potentials in a given cell, and we constrain the voltage-gated conductance to have the cell-type-specific characteristics that we measured for I_h. Typical examples of the fit attained in different cell types are shown in Fig. 7*A*–*C* in the form of frequency–amplitude, frequency–phase, and complex (Nyquist) plots. The quality of the fit was fairly good in all cell types (median $r^2 = 0.941$ in PCs; $r^2 = 0.931$ in O-R cells; $r^2 = 0.959$ OLM cells), especially considering the small number of free parameters, indicating that I_h (in combination with passive membrane properties) is the main determinant of the subthreshold impedance profile in these cells. Importantly, the range of parameters determined through the fitting procedure (in particular, the total capacitance and the maximal I_h conductance) was in good agreement with the values measured in the experimental current-clamp and voltage-clamp protocols (Fig. 7*D*; cf. Fig. 2 and Fig. 5). Notably, our resonance fits predicted a significantly larger membrane capacitance in the OLM cell population than in the population of O-R cells ($P < 0.01$; Wilcoxon rank sum test), while there was no significant difference in the maximal conductance of I_h between the two cell types. Both of these conclusions are in agreement with our experimental measurements, and suggest that the observed differences between the impedance profiles of OLM cells and O-R cells are primarily due to a difference in passive properties rather than a difference in the kinetics or magnitude of a voltage-gated conductance (i.e. I_h).

Finally, some systematic deviations of the data from the fitted curves were also evident. These were quantified by computing for the fitted curves the five summary statistics we had defined for the characterisation of impedance profiles, and comparing them with the same statistics computed from the actual data (Fig. 7*E*). We found that the I_h model was able to capture the overall shape of the impedance profiles as measured by the input resistance and the cutoff frequency quite accurately. On the other hand, the degree of resonance (as measured by Q and Φ_{total}) and the resonant frequency were less well predicted. In particular, the fits consistently predicted a larger degree of resonance (a higher Q value) in interneurons (but not in PCs) than the value determined directly from the data. Thus, the single-compartment I_h model provides a fairly good but still incomplete account of the impedance profiles of the neurons in our study, and factors not included in this model (such as dendritic morphology, the subcellular localization of I_h, or additional voltage-gated conductances)

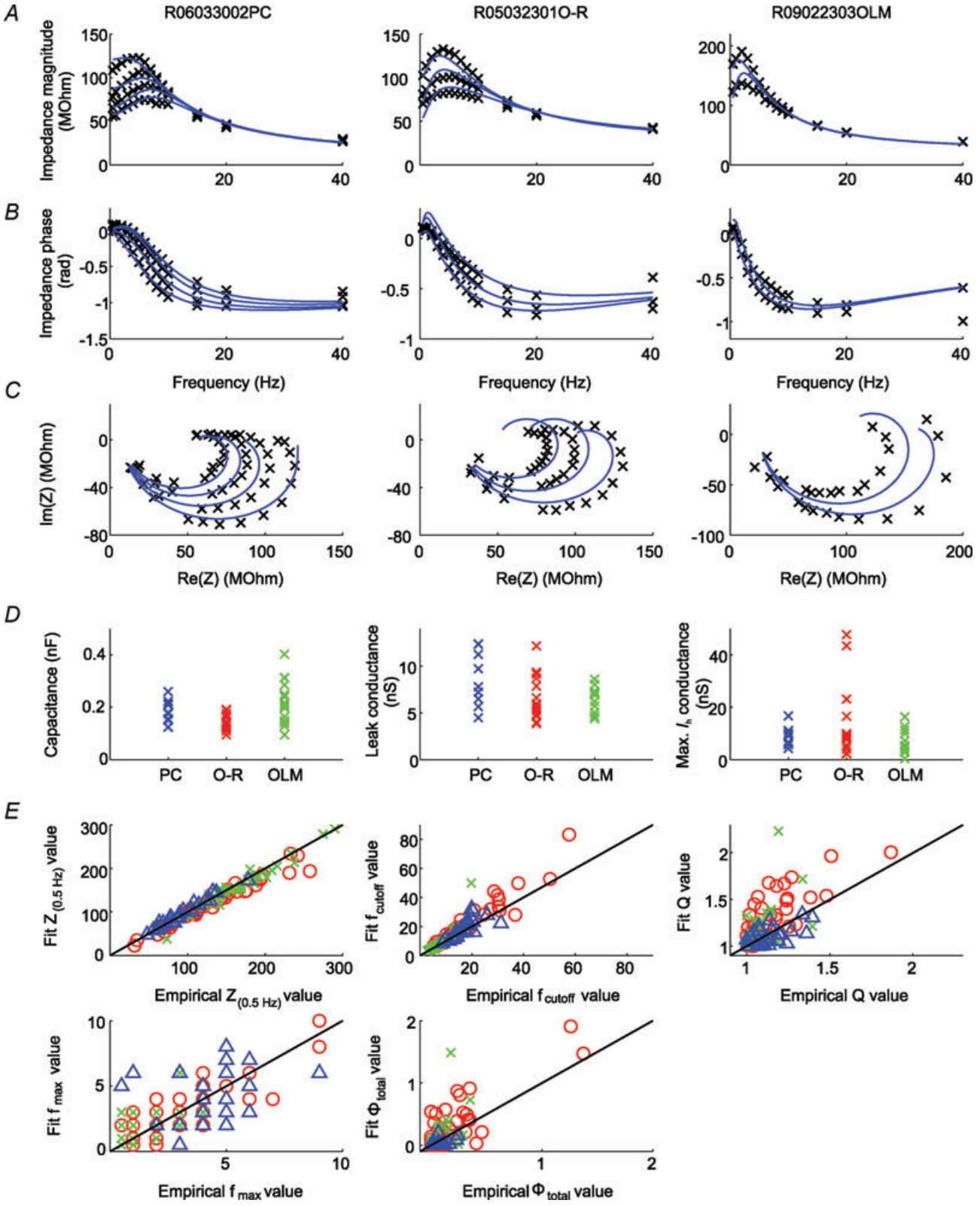

Figure 7
A–C, examples of model fits to experimentally measured impedance curves when the characteristics of I_h (voltage of half-activation, slope at half-activation, time constant) were fixed to their empirically determined values (as appropriate for each cell type), and only the capacitance, the leak conductance, and the maximal I_h conductance (as well as an additional series resistance) were allowed to vary. The types of plots in *A–C* are similar to those in

might also contribute to the measured impedance characteristics.

Discussion

Our results show that the impedance profiles of neurons calculated from their voltage responses to sinusoidal current inputs differ in pyramidal cells and different classes of interneurons investigated in the CA1 region of the hippocampus. Using electrophysiological measurements combined with computational modelling we could demonstrate that these differences arise primarily from differences in the activation properties of I_h, but the passive membrane properties of the cells also made significant contributions.

We found, in agreement with previous results, that the subthreshold resonance at theta frequencies in PCs is dependent on I_h (Hutcheon *et al.* 1996*b*; Pape & Driesang, 1998; Dickson *et al.* 2000; Hu *et al.* 2002; Fransén *et al.* 2004; Narayanan & Johnston, 2007). In addition to the I_h-mediated resonance, a so called M-resonance, produced by a depolarisation-activated potassium current below the firing threshold has also been described in PCs (Hu *et al.* 2002, 2009; Peters *et al.* 2005). According to their findings this type of resonance occurs at about −60 mV, whereas the I_h-mediated resonance they observed was only seen below −70 mV. The apparent lack of M-resonance in our experiments can be explained by the fact that we observed I_h-mediated resonance at −60 mV, suggesting that M-resonance might only be seen at more depolarised potentials, and possibly only above spike threshold under our conditions.

We found that horizontal interneurons of the stratum oriens were not uniform in their impedance properties. Although both O-R and OLM cells showed some frequency preference due to active membrane conductances, because of their high capacitance and low cutoff frequency the low-pass filter properties still dominated in OLM cells. Our results verify the earlier observations by Pike *et al.* (2000), in which some interneurons in the stratum oriens were shown to display resonance, and extend it by showing that not all oriens interneurons have the same high-pass characteristics. The finding that O-R cells and OLM cells have distinct impedance properties raises the possibility that similar synaptic input received by these two cell types (Blasco-Ibanez & Freund, 1995) may result in different discharge patterns during specific network events, such as theta and gamma rhythms or sharp-wave-associated ripple oscillations (Klausberger *et al.* 2003; Gloveli *et al.* 2005; Lawrence *et al.* 2006; Goldin *et al.* 2007; Jinno *et al.* 2007).

Previous studies (Aponte *et al.* 2006) and our observation that some FS PTIs (2 out of 7) expressed a minor sag indicate that I_h could also be present in this cell type. However, I_h does not seem to have any effect on the impedance profile of these cells at the investigated potentials. Whereas I_h-mediated subthreshold resonance was negligible in FS PTIs (present study, Hutcheon *et al.* 1996*b*), these cells exhibited obvious resonance at gamma frequencies in a study by Pike *et al.* (2000). This type of resonance is mediated by activation of persistent voltage-dependent sodium channels, opening at membrane potentials positive to −60 mV. Thus, under our conditions this form of resonance would not be expected, since we obtained recordings only at or negative to −60 mV. However, it is apparent already at these subthreshold membrane potentials that their fast membrane time constant and correspondingly high cutoff frequency would allow these cells to be capable of transmitting high frequency inputs.

Although ZD7288 is a widely used inhibitor of I_h (Harris & Constanti, 1995; Gasparini & DiFrancesco, 1997), it should be noted that ZD7288 may have unspecific effects on synaptic transmission (Chevaleyre & Castillo, 2002). However, these non-specific effects of ZD7288 were observed only after long application of the drug in rather high concentrations (∼50 μM). Thus, it seems unlikely that our results were influenced in any major way by unspecific effects of ZD7288.

Since subthreshold resonance seemed to be related to the occurrence of the membrane potential sag, which also showed significant differences among the investigated cell types, our initial supposition was that distinct resonance properties could arise from the differences in I_h properties among the different cell types. Our data revealed no significant differences between the absolute amounts of I_h-mediated conductance in the investigated cell types. However, as the observed differences in apparent membrane capacitance probably reflect differences in membrane surface area, the conductance density could still differ substantially. Although it was not possible to directly determine the conductance density from our measurements, we can estimate the cell-type dependence of this quantity by looking at the ratio

Fig. 6. *D*, values of the capacitance, the leak conductance, and the maximal I_h conductance as determined by the best fit to the measured impedance curves for each cell (with values from the three I_h-containing cell types shown separately for comparison). *E*, empirically determined summary statistics (i.e. $Z_{(0.5\ Hz)}$, f_{cutoff}, Q, f_{max}, and Φ_L) *versus* the values of the same statistics predicted by the best-fitting I_h model (with fixed I_h characteristics). Pyramidal cells are indicated by blue triangles, O-R cells by red circles, and OLM cells by green crosses.

of the measured absolute conductance and the average membrane capacitance (as estimated from current clamp experiments) in the different cell types. This comparison suggests that differences in I_h conductance density may indeed be substantial, with O-R cells having an approximately two-fold higher density than PCs and OLM cells, which may explain the stronger resonance observed in O-R cells.

Our experiments also revealed that a significantly larger amount of I_h was activated in PCs than in interneurons at physiologically relevant potentials (above −90 mV), where the resonance properties were investigated. PCs are known to express HCN channels mainly on their distal dendrites (Magee, 1998; Lörincz *et al.* 2002); therefore the differences in I_h activation might be explained by space clamp limitations. However, analysis of the activation kinetics of I_h in the distinct cell types precluded this interpretation, as more distal localization would imply slower apparent kinetics, which is opposite to our findings.

We found a clear difference in the kinetics of I_h between PCs and interneurons. Not only the time course of activation but also the relative proportion of components with a slow and a fast time constant and its change with the membrane potential were different in PCs and interneurons (Fig. 5*G*). It has been shown that the activation kinetics of HCN channels are predominantly determined by the relative contribution of HCN channel isoforms to the composition of homomeric or heteromeric channels (Santoro *et al.* 2000); therefore, one possible explanation for these differences in the activation characteristics of I_h in hippocampal neurons is different subunit compositions of HCN channels. Indeed, both immunohistochemical (Brewster *et al.* 2002; Notomi & Shigemoto, 2004) and *in situ* mRNA hybridisation studies (Santoro *et al.* 2000; Bender *et al.* 2001; Brewster *et al.* 2007) suggest that while PCs express mainly HCN1 and HCN2 in their distal dendrites, the proportion of HCN2 and HCN4 (subunits which contribute to slower activation kinetics of I_h; Franz *et al.* 2000; Santoro *et al.* 2000; Ishii *et al.* 2001) is much larger in the stratum oriens, suggesting that they are likely to be expressed in interneurons. Of course we cannot exclude the possibility that various elements of the neuronal membrane, such as putative auxiliary subunits, scaffolding proteins or cytoskeletal proteins (Wahl-Schott & Biel, 2009) interact with the HCN channels and may also influence the properties of I_h in the distinct hippocampal neurons.

In summary, the different cell types in our study were distinct both in terms of the observed properties of I_h and in terms of their passive membrane properties. The effects of various neuronal properties on the impedance profile could be predicted by the I_h model, by first using average (median) parameter values (as determined in our various experiments) for measured cell types, and then varying parameters either individually or in combination to observe the changes in the shape of the impedance curve (Fig. 8). The consequences of several manipulations are highlighted by these examples. First, changes in the half-activation voltage, which may occur in response to neuromodulatory influences (e.g. Maccaferri & McBain, 1996), essentially convert each impedance curve into one that could be measured in the original cell at a membrane potential shifted by the equivalent amount to the change in $V_{1/2}$ (but in the opposite direction). Second, alterations in the time constant of I_h profoundly affect the shape of the impedance curve, and especially the degree and frequency of resonance. Third, changes in the passive membrane resistance (the reciprocal of the leak conductance) can also have a pronounced effect on all aspects of the impedance profile, partly by changing the weight of voltage-gated conductances relative to the voltage-independent leak conductance. Fourth, the membrane capacitance affected mainly the cutoff frequency (as expected), but also played a role in shaping the resonance peak. A final important point is that no single parameter was found to be dominant in determining the differences in the characteristics of the impedance profiles of distinct cell types; concurrent changes in several parameters were required to convert one type of impedance curve into another type, as demonstrated by the last two examples in Fig. 8.

Our computational model strengthened the idea that I_h is the major determinant of the impedance characteristics at subthreshold membrane potentials in hippocampal neurons. However, our result that in stratum oriens interneurons a smaller degree of resonance was observed than that predicted from the model suggests that some other conductances might also be active at these membrane potentials in these particular cell types and dampen the effect of I_h on the impedance profile. The inward rectifier K^+ current might be a good candidate for this effect, as suggested by both theoretical and experimental studies by Hutcheon *et al.* (1996*a*,*b*) in neocortical neurons.

Physiological relevance

Several studies have shown that I_h substantially promotes firing when the fluctuation in the membrane potential can activate a sufficient number of HCN channels (Manseau *et al.* 2008). Importantly, if such fluctuation occurs simultaneously in several PCs even after the activation of a single perisomatic inhibitory cell (Cobb *et al.* 1995), then a large number of principal neurons could discharge action potentials synchronously, contributing to rhythm generation at theta frequencies. Thus, activation of I_h near or below the spike threshold might indeed be important for oscillatory activities (Kocsis & Li, 2004). This has been directly demonstrated in hippocampal slices, where blocking of I_h diminished the synchronous firing of

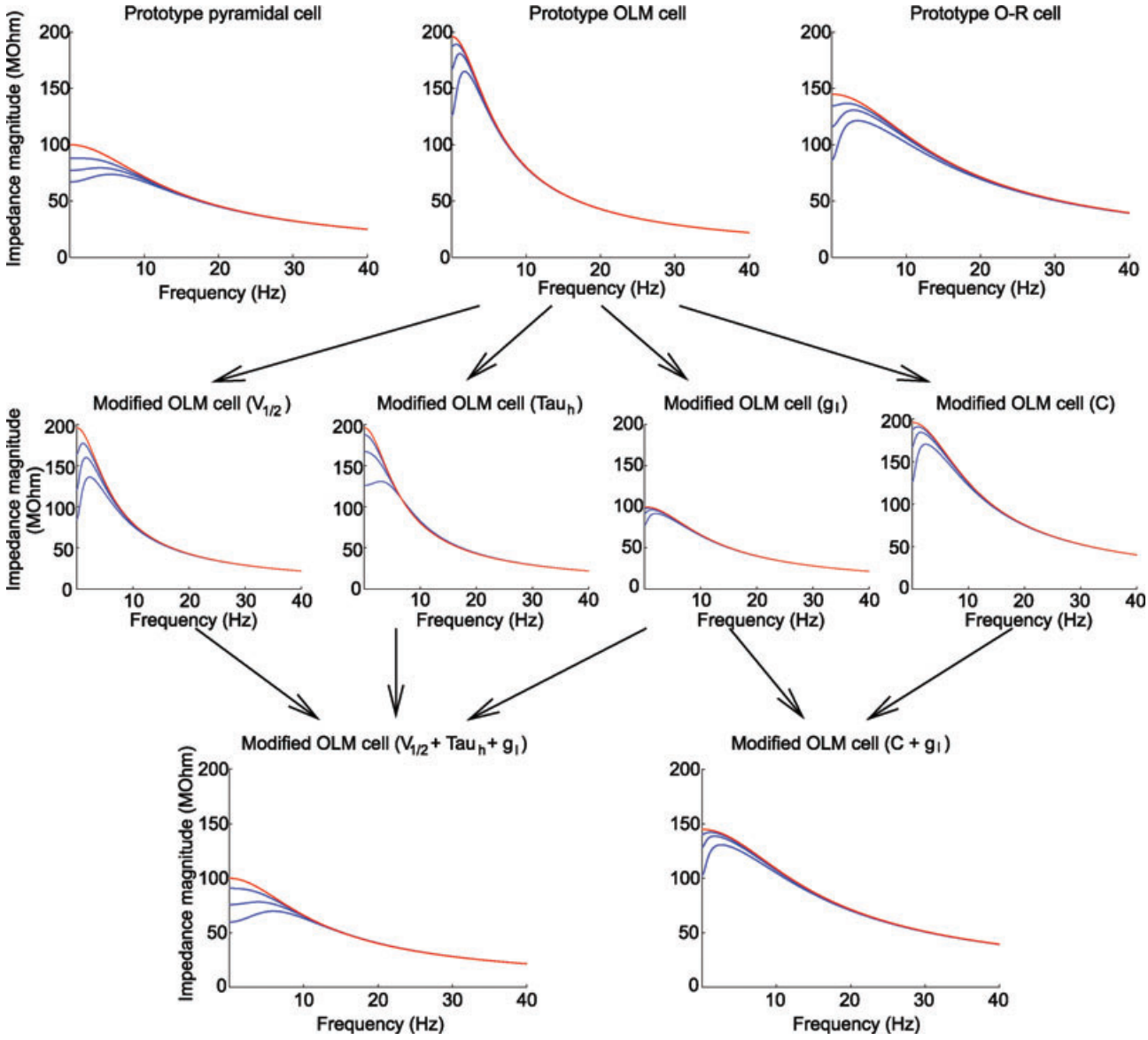

Figure 8. The effects of various cell parameters on the shape of the impedance magnitude curve
Panels in the top row show theoretically constructed impedance curves at multiple membrane potentials for the three I_h-containing cell types based on the I_h model (blue lines) using cell-type-specific median values of all parameters (g_l, C, $\bar{g}_h$, $V_{1/2}$, m, and Tau_h (V_m)) measured using current steps (Table 1) and in voltage-clamp experiments (Fig. 5).To simulate the effects of the I_h-blocker ZD7288, impedance curves were constructed using the same parameters, but with I_h set to zero (red lines). The middle row displays four theoretical examples where one of the parameters of the OLM cell model has been modified. In the first example, $V_{1/2}$ was increased by 14 mV (to −83 mV, the value characteristic of PCs) to shift the I_h activation curve to the right; in the second, Tau_h was adjusted (at all membrane potentials) to values measured for PCs, making the activation of I_h substantially faster; in the third, g_l was increased by approximately a factor of 2, thereby reducing R_{in} to a value typical of PCs; and in the fourth, C was reduced by approximately a factor of 2 to a value characterising O-R neurons. In the bottom left plot, three of these manipulations were applied simultaneously (as indicated by the arrows), resulting in impedance magnitude curves which are remarkably similar to the PC curves in the top row, despite the remaining differences in C, $\bar{g}_h$, and m. Similarly, two types of manipulation in the middle row were combined to yield the impedance curve in the bottom right, which resembles the O-R cell profile in the top row (note that the actual value of g_l in bottom right plot was different from its value in the bottom left plot, and also from the value used in the third plot in the middle row). In each plot, the blue lines represent impedance curves at three different membrane potentials (from top to bottom: −60, −70 and −80 mV) in the full I_h model, while the red curve represents a passive version of the model with $\bar{g}_h$ set to 0.

pyramidal cells at theta frequencies (Cobb *et al.* 2003). Our voltage-clamp data support these results, since a substantial proportion of HCN channels in pyramidal cells was activated at the resting membrane potential. In contrast, a much lower proportion of HCN channels would be open at resting membrane potential in OLM cells and O-R cells, which is in line with the findings that interneurons in the stratum oriens exhibited less obvious membrane potential oscillations at theta frequencies (Chapman & Lacaille, 1999).

The activation curve of I_h can be profoundly shifted by cyclic nucleotides, which are regulated by G-protein coupled receptor activation (Chen *et al.* 2001); therefore, subcortical neurotransmitter systems acting on these receptors could significantly affect the opening of HCN channels. Thus, theta frequency membrane potential oscillations as well as the impedance of the interneurons that express HCN channels can be modulated in a state-dependent manner (Fig. 8; Maccaferri & McBain, 1996; Gasparini & DiFrancesco, 1999; Placantonakis *et al.* 2000; Bickmeyer *et al.* 2002; Rosenkranz & Johnston, 2006), controlling their recruitment into network activity.

I_h has been shown to influence the occurrence of dendritic spikes (Tsay *et al.* 2007) and the amplitude of EPSPs (George *et al.* 2009) by interacting with other voltage-gated ion channels, such as N- or T-type Ca^{2+} channels or the so-called M-current mediated by voltage-gated K^+ channels. Therefore the observation that I_h is activated at more hyperpolarised potentials in oriens interneurons than in pyramidal cells might also be important in understanding the differences in dendritic signal-processing mechanisms of these cells.

While several studies have measured the impedance amplitude in various cell types, much less has been known about the phase of the impedance. We determined and compared the impedance phase profiles of four types of hippocampal neuron. In the three 'resonant' cell types in our study, positive as well as negative phase shifts could be seen depending on the frequency. Since I_h works effectively as an inductive element in the membrane, it can produce a significant positive phase shift in the voltage response of the cell to an oscillatory input. Both theoretical and experimental studies suggest that this feature of I_h might be important in many processes including control of spike timing (Lengyel *et al.* 2005; Kwag & Paulsen, 2009) and synaptic plasticity (Narayanan & Johnston, 2007, 2008). Specifically, during oscillations, the phase of the impedance quantifies the phase shift of the cell's membrane potential oscillation relative to the phase of its rhythmic current input. A positive phase shift is especially interesting, since it leads to an apparent paradox whereby the cell's response seems to lead the corresponding change in its input – although this holds in a rigorous sense only for regular sinusoidal oscillations. The fact that distinct classes of hippocampal cells show well-defined, cell-type-specific impedance amplitude and phase-response characteristics may indicate a crucial role of these cellular properties in the complex dynamics involved in information processing in the central nervous system.

References

Aponte Y, Lien CC, Reisinger E & Jonas P (2006). Hyperpolarization-activated cation channels in fast-spiking interneurons of rat hippocampus. *J Physiol* **574**, 229–243.

Bender RA, Brewster A, Santoro B, Ludwig A, Hofmann F, Biel M & Baram TZ (2001). Differential and age-dependent expression of hyperpolarization-activated, cyclic nucleotide-gated cation channel isoforms 1–4 suggests evolving roles in the developing rat hippocampus. *Neuroscience* **106**, 689–698.

Bickmeyer U, Heine M, Manzke T & Richter DW (2002). Differential modulation of I_h by 5-HT receptors in mouse CA1 hippocampal neurons. *Eur J Neurosci* **16**, 209–218.

Bishop CM (2006). *Pattern Recognition and Machine Learning*. Springer, Singapore.

Blasco-Ibanez JM & Freund TF (1995). Synaptic input of horizontal interneurons in stratum oriens of the hippocampal CA1 subfield: structural basis of feed-back activation. *Eur J Neurosci* **7**, 2170–2180.

Brewster A, Bender RA, Chen Y, Dube C, Eghbal-Ahmadi M & Baram TZ (2002). Developmental febrile seizures modulate hippocampal gene expression of hyperpolarization-activated channels in an isoform- and cell-specific manner. *J Neurosci* **22**, 4591–4599.

Brewster AL, Chen Y, Bender RA, Yeh A, Shigemoto R & Baram TZ (2007). Quantitative analysis and subcellular distribution of mRNA and protein expression of the hyperpolarization-activated cyclic nucleotide-gated channels throughout development in rat hippocampus. *Cereb Cortex* **17**, 702–712.

Chapman CA & Lacaille JC (1999). Intrinsic theta-frequency membrane potential oscillations in hippocampal CA1 interneurons of stratum lacunosum-moleculare. *J Neurophysiol* **81**, 1296–1307.

Chen S, Wang J & Siegelbaum SA (2001). Properties of hyperpolarization-activated pacemaker current defined by coassembly of HCN1 and HCN2 subunits and basal modulation by cyclic nucleotide. *J Gen Physiol* **117**, 491–504.

Chevaleyre V & Castillo PE (2002). Assessing the role of Ih channels in synaptic transmission and mossy fibre LTP. *Proc Natl Acad Sci U S A* **99**, 9538–9543.

Cobb SR, Buhl EH, Halasy K, Paulsen O & Somogyi P (1995). Synchronization of neuronal activity in hippocampus by individual GABAergic interneurons. *Nature* **378**, 75–78.

Cobb SR, Larkman PM, Bulters DO, Oliver L, Gill CH & Davies CH (2003). Activation of I_h is necessary for patterning of mGluR and mAChR induced network activity in the hippocampal CA3 region. *Neuropharmacology* **44**, 293–303.

Dickson CT, Magistretti J, Shalinsky MH, Fransén E, Hasselmo ME & Alonso A (2000). Properties and role of I_h in the pacing of subthreshold oscillations in entorhinal cortex layer II neurons. *J Neurophysiol* **83**, 2562–2579.

Drummond GB (2009). Reporting ethical matters in *The Journal of Physiology*: standards and advice. *J Physiol* **587**, 713–719.

Fransén E, Alonso AA, Dickson CT, Magistretti J & Hasselmo ME (2004). Ionic mechanisms in the generation of subthreshold oscillations and action potential clustering in entorhinal layer II stellate neurons. *Hippocampus* **14**, 368–384.

Franz O, Liss B, Neu A & Roeper J (2000). Single-cell mRNA expression of *HCN1* correlates with a fast gating phenotype of hyperpolarization-activated cyclic nucleotide-gated ion channels (I_h) in central neurons. *Eur J Neurosci* **12**, 2685–2693.

Freund TF & Buzsáki G (1996). Interneurons of the hippocampus. *Hippocampus* **6**, 345–470.

Gasparini S & DiFrancesco D (1997). Action of the hyperpolarization-activated current (I_h) blocker ZD 7288 in hippocampal CA1 neurons. *Pflugers Arch* **435**, 99–106.

Gasparini S & DiFrancesco D (1999). Action of serotonin on the hyperpolarization-activated cation current (I_h) in rat CA1 hippocampal neurons. *Eur J Neurosci* **11**, 3093–3100.

George MS, Abbott LF & Siegelbaum SA (2009). HCN hyperpolarization-activated cation channels inhibit EPSPs by interactions with M-type K^+ channels. *Nat Neurosci* **12**, 577–584.

Gloveli T, Dugladze T, Saha S, Monyer H, Heinemann U, Traub RD, Whittington MA & Buhl EH (2005). Differential involvement of oriens/pyramidale interneurones in hippocampal network oscillations in vitro. *J Physiol* **562**, 131–147.

Goldin M, Epsztein J, Jorquera I, Represa A, Ben-Ari Y, Crepel V & Cossart R (2007). Synaptic kainate receptors tune oriens-lacunosum moleculare interneurons to operate at theta frequency. *J Neurosci* **27**, 9560–9572.

Gulyás AI, Miles R, Hájos N & Freund TF (1993). Precision and variability in postsynaptic target selection of inhibitory cells in the hippocampal CA3 region. *Eur J Neurosci* **5**, 1729–1751.

Gulyás AI, Hájos N, Katona I & Freund TF (2003). Interneurons are the local targets of hippocampal inhibitory cells which project to the medial septum. *Eur J Neurosci* **17**, 1861–1872.

Hájos N, Pálhalmi J, Mann EO, Németh B, Paulsen O & Freund TF (2004). Spike timing of distinct types of GABAergic interneuron during hippocampal gamma oscillations in vitro. *J Neurosci* **24**, 9127–9137.

Han ZS (1994). Electrophysiological and morphological differentiation of chandelier and basket cells in the rat hippocampal formation: a study combining intracellular recording and intracellular staining with biocytin. *Neurosci Res* **19**, 101–110.

Harris NC & Constanti A (1995). Mechanism of block by ZD 7288 of the hyperpolarization-activated inward rectifying current in guinea pig substantia nigra neurons in vitro. *J Neurophysiol* **74**, 2366–2378.

Hu H, Vervaeke K & Storm JF (2002). Two forms of electrical resonance at theta frequencies, generated by M-current, h-current and persistent Na^+-current in rat hippocampal pyramidal cells. *J Physiol* **545**, 783–805.

Hu H, Vervaeke K, Graham LJ & Storm JF (2009). Complementary theta resonance filtering by two spatially segregated mechanisms in CA1 hippocampal pyramidal neurons. *J Neurosci* **29**, 14472–14483.

Hutcheon B, Miura RM, Yarom Y & Puil E (1994). Low-threshold calcium current and resonance in thalamic neurons: a model of frequency preference. *J Neurophysiol* **71**, 583–594.

Hutcheon B, Miura RM & Puil E (1996*a*). Models of subthreshold membrane resonance in neocortical neurons. *J Neurophysiol* **76**, 698–714.

Hutcheon B, Miura RM & Puil E (1996*b*). Subthreshold membrane resonance in neocortical neurons. *J Neurophysiol* **76**, 683–697.

Hutcheon B & Yarom Y (2000). Resonance, oscillation and the intrinsic frequency preferences of neurons. *Trends Neurosci* **23**, 216–222.

Ishii TM, Takano M & Ohmori H (2001). Determinants of activation kinetics in mammalian hyperpolarization-activated cation channels. *J Physiol* **537**, 93–100.

Jinno S, Klausberger T, Marton LF, Dalezios Y, Roberts JD, Fuentealba P, Bushong EA, Henze D, Buzsáki G & Somogyi P (2007). Neuronal diversity in GABAergic long-range projections from the hippocampus. *J Neurosci* **27**, 8790–8804.

Kamondi A, Acsády L, Wang XJ & Buzsáki G (1998). Theta oscillations in somata and dendrites of hippocampal pyramidal cells in vivo: activity-dependent phase-precession of action potentials. *Hippocampus* **8**, 244–261.

Klausberger T, Magill PJ, Marton LF, Roberts JD, Cobden PM, Buzsaki G & Somogyi P (2003). Brain-state- and cell-type-specific firing of hippocampal interneurons in vivo. *Nature* **421**, 844–848.

Klausberger T & Somogyi P (2008). Neuronal diversity and temporal dynamics: the unity of hippocampal circuit operations. *Science* **321**, 53–57.

Kocsis B & Li S (2004). In vivo contribution of h-channels in the septal pacemaker to theta rhythm generation. *Eur J Neurosci* **20**, 2149–2158.

Kwag J & Paulsen O (2009). The timing of external input controls the sign of plasticity at local synapses. *Nat Neurosci* **12**, 1219–1221.

Lawrence JJ, Grinspan ZM, Statland JM & McBain CJ (2006). Muscarinic receptor activation tunes mouse stratum oriens interneurones to amplify spike reliability. *J Physiol* **571**, 555–562.

Lengyel M, Kwag J, Paulsen O & Dayan P (2005). Matching storage and recall: hippocampal spike timing-dependent plasticity and phase response curves. *Nat Neurosci* **8**, 1677–1683.

Leung LS & Yu HW (1998). Theta-frequency resonance in hippocampal CA1 neurons in vitro demonstrated by sinusoidal current injection. *J Neurophysiol* **79**, 1592–1596.

Lien CC & Jonas P (2003). Kv3 potassium conductance is necessary and kinetically optimized for high-frequency action potential generation in hippocampal interneurons. *J Neurosci* **23**, 2058–2068.

Lörincz A, Notomi T, Tamás G, Shigemoto R & Nusser Z (2002). Polarized and compartment-dependent distribution of HCN1 in pyramidal cell dendrites. *Nat Neurosci* **5**, 1185–1193.

Lüthi A & McCormick DA (1998). H-current: properties of a neuronal and network pacemaker. *Neuron* **21**, 9–12.

Maccaferri G & McBain CJ (1996). The hyperpolarization-activated current (I_h) and its contribution to pacemaker activity in rat CA1 hippocampal stratum oriens-alveus interneurones. *J Physiol* **497**, 119–130.

Maccaferri G (2005). Stratum oriens horizontal interneurone diversity and hippocampal network dynamics. *J Physiol* **562**, 73–80.

Magee JC (1998). Dendritic hyperpolarization-activated currents modify the integrative properties of hippocampal CA1 pyramidal neurons. *J Neurosci* **18**, 7613–7624.

Magee JC (1999). Dendritic I_h normalizes temporal summation in hippocampal CA1 neurons. *Nat Neurosci* **2**, 508–514.

Manseau F, Goutagny R, Danik M & Williams S (2008). The hippocamposeptal pathway generates rhythmic firing of GABAergic neurons in the medial septum and diagonal bands: an investigation using a complete septohippocampal preparation in vitro. *J Neurosci* **28**, 4096–4107.

McBain CJ, DiChiara TJ & Kauer JA (1994). Activation of metabotropic glutamate receptors differentially affects two classes of hippocampal interneurons and potentiates excitatory synaptic transmission. *J Neurosci* **14**, 4433–4445.

McLelland D & Paulsen O (2009). Neuronal oscillations and the rate-to-phase transform: mechanism, model and mutual information. *J Physiol* **587**, 769–785.

Narayanan R & Johnston D (2007). Long-term potentiation in rat hippocampal neurons is accompanied by spatially widespread changes in intrinsic oscillatory dynamics and excitability. *Neuron* **56**, 1061–1075.

Narayanan R & Johnston D (2008). The h channel mediates location dependence and plasticity of intrinsic phase response in rat hippocampal neurons. *J Neurosci* **28**, 5846–5860.

Nolan MF, Malleret G, Lee KH, Gibbs E, Dudman JT, Santoro B, Yin D, Thompson RF, Siegelbaum SA, Kandel ER & Morozov A (2003). The hyperpolarization-activated HCN1 channel is important for motor learning and neuronal integration by cerebellar Purkinje cells. *Cell* **115**, 551–564.

Notomi T & Shigemoto R (2004). Immunohistochemical localization of I_h channel subunits, HCN1–4, in the rat brain. *J Comp Neurol* **471**, 241–276.

Pape HC & Driesang RB (1998). Ionic mechanisms of intrinsic oscillations in neurons of the basolateral amygdaloid complex. *J Neurophysiol* **79**, 217–226.

Pawelzik H, Hughes DI & Thomson AM (2002). Physiological and morphological diversity of immunocytochemically defined parvalbumin- and cholecystokinin-positive interneurones in CA1 of the adult rat hippocampus. *J Comp Neurol* **443**, 346–367.

Peters HC, Hu H, Pongs O, Storm JF & Isbrandt D (2005). Conditional transgenic suppression of M channels in mouse brain reveals functions in neuronal excitability, resonance and behaviour. *Nat Neurosci* **8**, 51–60.

Pike FG, Goddard RS, Suckling JM, Ganter P, Kasthuri N & Paulsen O (2000). Distinct frequency preferences of different types of rat hippocampal neurones in response to oscillatory input currents. *J Physiol* **529**, 205–213.

Placantonakis DG, Schwarz C & Welsh JP (2000). Serotonin suppresses subthreshold and suprathreshold oscillatory activity of rat inferior olivary neurones in vitro. *J Physiol* **524**, 833–851.

Richardson MJ, Brunel N & Hakim V (2003). From subthreshold to firing-rate resonance. *J Neurophysiol* **89**, 2538–2554.

Rosenkranz JA & Johnston D (2006). Dopaminergic regulation of neuronal excitability through modulation of I_h in layer V entorhinal cortex. *J Neurosci* **26**, 3229–3244.

Santoro B, Chen S, Lüthi A, Pavlidis P, Shumyatsky GP, Tibbs GR & Siegelbaum SA (2000). Molecular and functional heterogeneity of hyperpolarization-activated pacemaker channels in the mouse CNS. *J Neurosci* **20**, 5264–5275.

Tsay D, Dudman JT & Siegelbaum SA (2007). HCN1 channels constrain synaptically evoked Ca^{2+} spikes in distal dendrites of CA1 pyramidal neurons. *Neuron* **56**, 1076–1089.

Wahl-Schott C & Biel M (2009). HCN channels: structure, cellular regulation and physiological function. *Cell Mol Life Sci* **66**, 470–494.

Ylinen A, Soltész I, Bragin A, Penttonen M, Sík A & Buzsáki G (1995). Intracellular correlates of hippocampal theta rhythm in identified pyramidal cells, granule cells, and basket cells. *Hippocampus* **5**, 78–90.

Author contributions

R.Z., S.K., O.P. and N.H. contributed to the conception and design of the experiments. R.Z. conducted the electrophysiological experiments. S.K. performed the modelling part of the study. R.Z. and S.K. analysed the data. R.Z., S.K., O.P., T.F.F. and N.H. participated in the interpretation of the data. All authors drafted the manuscript and approved the final version for publication. Experiments were conducted in the Department of Cellular and Network Neurobiology, Institute of Experimental Medicine, Hungarian Academy of Sciences, Budapest, Hungary.

Acknowledgements

We thank Ms Katalin Lengyel and Erzsébet Gregori for their excellent technical assistance. This work was supported by the Hungarian Scientific Research Fund (OTKA T049517, OTKA K60927, NKTH-OTKA CNK 77793), the Wellcome Trust, the BBSRC, and the British Council.

dc_71_10

17. számú melléklet

EJN fens
EUROPEAN JOURNAL OF NEUROSCIENCE
dc_71_10
European Journal of Neuroscience, Vol. 31, pp. 2234–2246, 2010 doi:10.1111/j.1460-9568.2010.07292.x

Distinct synaptic properties of perisomatic inhibitory cell types and their different modulation by cholinergic receptor activation in the CA3 region of the mouse hippocampus

Gergely G. Szabó,[1] Noémi Holderith,[1] Attila I. Gulyás,[2] Tamás F. Freund[2] and Norbert Hájos[1]
[1]Laboratory of Network Neurophysiology, Institute of Experimental Medicine, Hungarian Academy of Sciences, H-1083 Budapest, Hungary
[2]Laboratory of Cerebral Cortex Research, Institute of Experimental Medicine, Hungarian Academy of Sciences, Budapest, Hungary

Keywords: GABA, inhibition, interneuron, IPSC, synchronization

Abstract

Perisomatic inhibition originates from three types of GABAergic interneurons in cortical structures, including parvalbumin-containing fast-spiking basket cells (FSBCs) and axo-axonic cells (AACs), as well as cholecystokinin-expressing regular-spiking basket cells (RSBCs). These interneurons may have significant impact in various cognitive processes, and are subjects of cholinergic modulation. However, it is largely unknown how cholinergic receptor activation modulates the function of perisomatic inhibitory cells. Therefore, we performed paired recordings from anatomically identified perisomatic interneurons and pyramidal cells in the CA3 region of the mouse hippocampus. We determined the basic properties of unitary inhibitory postsynaptic currents (uIPSCs) and found that they differed among cell types, e.g. GABA released from axon endings of AACs evoked uIPSCs with the largest amplitude and with the longest decay measured at room temperature. RSBCs could also release GABA asynchronously, the magnitude of the release increasing with the discharge frequency of the presynaptic interneuron. Cholinergic receptor activation by carbachol significantly decreased the uIPSC amplitude in all three types of cell pairs, but to different extents. M2-type muscarinic receptors were responsible for the reduction in uIPSC amplitudes in FSBC– and AAC–pyramidal cell pairs, while an antagonist of CB_1 cannabinoid receptors recovered the suppression in RSBC–pyramidal cell pairs. In addition, carbachol suppressed or even eliminated the short-term depression of uIPSCs in FSBC– and AAC–pyramidal cell pairs in a frequency-dependent manner. These findings suggest that not only are the basic synaptic properties of perisomatic inhibitory cells distinct, but acetylcholine can differentially control the impact of perisomatic inhibition from different sources.

Introduction

Although in cortical structures only every fifth neuron is GABAergic (Somogyi *et al.*, 1998), these neurons significantly influence information processing in neuronal networks (Miles *et al.*, 1996; Pouille & Scanziani, 2004). GABAergic cells express distinct sets of proteins and give rise to characteristic dendritic and axonal arbours, leading to functional diversity (Freund & Buzsaki, 1996; Klausberger & Somogyi, 2008). Based on target preference, cortical GABAergic cells with local axonal projections can be divided into two major categories: cells innervating predominantly either the perisomatic membranes or the dendrites of principal neurons (Buhl *et al.*, 1994; Miles *et al.*, 1996); this study does not address the latter category. The perisomatic region is defined as the domain of the plasma membrane which includes the proximal dendrites, the cell body and the axon initial segment (AIS; Freund & Buzsaki, 1996). This region is targeted by three types of inhibitory neurons in cortical areas, namely by the parvalbumin (PV)-expressing fast-spiking basket cells (FSBCs) and axo-axonic cells (AACs) as well as by the cholecystokinin (CCK)-containing regular-spiking basket cells (RSBCs). The basket cells innervate the somata and proximal dendrites (Blackstad & Flood, 1963) whereas the AACs target the AISs of pyramidal neurons (Somogyi, 1977).

Perisomatic inhibitory cells can effectively control the generation of sodium-dependent action potentials, and thereby determine the output of principal cells (Cobb *et al.*, 1995; Miles *et al.*, 1996; Szabadics *et al.*, 2006). As different types of perisomatic inhibitory cells have been found to be distinctly recruited during local network operation (Glickfeld & Scanziani, 2006), and their behaviour is also dissimilar during various oscillatory activities (Klausberger *et al.*, 2003, 2005), these GABAergic cells probably accomplish distinct functions in information processing.

Acetylcholine can substantially regulate the function of perisomatic inhibitory cells by affecting their membrane properties or by modulating their GABA release (Lawrence, 2008), and thus altering network dynamics (Hasselmo, 2006). While CCK- but not PV-containing interneurons in the neocortex can be depolarized by cholinergic receptor activation (Kawaguchi & Kubota, 1997), GABA release from both cell types is depressed by cholinergic receptor agonists, although by different mechanisms (Fukudome *et al.*, 2004). AACs have not been distinguished from basket cells in these studies

Correspondence: Dr Norbert Hájos, as above.
E-mail: hajos@koki.hu

Received 15 February 2010, revised 16 April 2010, accepted 23 April 2010

so it is unknown how their GABA release is affected by acetylcholine.

As the three perisomatic inhibitory cell types have similar dendritic and axonal arborizations, they cannot be unequivocally identified at the light-microscopic level. Usually PV-containing interneurons are separated from CCK-expressing GABAergic cells based on their neurochemically different characters and/or their physiological properties (Kawaguchi & Kubota, 1997; Pawelzik *et al.*, 2002; Hefft & Jonas, 2005), but the distinction between FSBCs and AACs was only possible by analyzing their targets using electron microscopy (Gulyas *et al.*, 1993). In this study, we identified AACs at the light-microscopic level by double-staining to visualize their targets, i.e. the AISs. Using whole-cell recordings, we examined the basic properties of unitary inhibitory postsynaptic currents (uIPSCs) in perisomatic inhibitory interneuron–pyramidal cell pairs and the short-term plasticity of these connections. In addition, we investigated the effect of cholinergic receptor activation on the properties and dynamics of uIPSCs.

Materials and methods

Experimental animals and slice preparation

All experiments were carried out in accordance with the Hungarian Act of Animal Care and Experimentation (1998, XXVIII, section 243/1998), and with the guidelines of the institutional ethical code. Transgenic mice expressing enhanced green fluorescent protein (eGFP) controlled by glutamate decarboxylase 65 (GAD65) promoter (Lopez-Benedito *et al.*, 2004) or PV promoter (Meyer *et al.*, 2002) were used. Mice (postnatal days 15–23) were deeply anaesthetized with isoflurane and decapitated. The brain was quickly removed and placed into ice-cold cutting solution containing (in mM): sucrose, 252; KCl, 2.5; NaH_2PO_4, 1.25; $MgCl_2$, 5; $CaCl_2$, 0.5; $NaHCO_3$, 26; and glucose, 10. The cutting solution was bubbled with 95% O_2 and 5% CO_2 (carbogen gas) for at least half an hour before use. Horizontal hippocampal slices (200–300 μm thick) were prepared using a Leica VT 1000S or a VT1200S microtome (Leica, Nussloch, Germany), and kept in an interface-type holding chamber at room temperature for at least 60 min before recording in standard ACSF with the composition (in mM) NaCl, 126; KCl, 2.5; NaH_2PO_4, 1.25; $MgCl_2$, 2; $CaCl_2$, 2; $NaHCO_3$, 26; and glucose, 10. Solutions were prepared with ultra pure water and bubbled with carbogen gas.

Paired recordings

Slices were transferred to a submersion type of recording chamber. To reduce the occurrence of spontaneous synaptic events, the flow rate was 2–3 mL/min. Experiments were performed at room temperature under visual guidance using an Olympus microscope (BX61WI; Olympus Corp., Tokyo, Japan). Fluorescence of eGFP-containing cells was excited by a monochromator at 488 nm wavelength or by standard epifluorescence using a UV lamp, and the resulting fluorescence visualized with a CCD camera (TILL photonics, Gräfelfing, Germany, or Hamamatsu Photonics, Japan). Whole-cell patch-clamp recordings were made using a Multiclamp 700B amplifier (Molecular Devices), filtered at 2 kHz, digitized at 5 kHz with a PCI-6024E board (National Instruments, Austin, TX, USA), recorded with in-house data acquisition and stimulus software (Stimulog, courtesy of Professor Zoltán Nusser, Institute of Experimental Medicine, Hungarian Academy of Sciences) and analyzed off-line using the EVAN software (courtesy of Professor István Mody, UCLA, CA). Patch pipettes were pulled from borosilicate glass tubing with resistances of 3–6 MΩ. The intracellular solution used for the presynaptic cell contained (in mM) K-gluconate, 110; NaCl, 4; Mg-ATP, 2; HEPES, 40; and GTP, 0.3; with 0.2% biocytin; adjusted to pH 7.3 using KOH and with an osmolarity of 290 mOsm/L. The intrapipette solution used for the postsynaptic cell contained (in mM) CsCl, 80; Cs-gluconate, 60; $MgCl_2$, 1; Mg-ATP, 2; NaCl, 3; HEPES, 10; and QX-314 [2(triethylamino)- *N*-(2,6-dimethylphenyl) acetamine], 5; adjusted to pH 7.3 with CsOH, and with an osmolarity of 295 mOsm/L. Presynaptic interneurons were held in current-clamp mode around a membrane potential of −65 mV, and stimulated by brief current pulses (1.5 ms, 1–2 nA). Pyramidal cells were clamped at a holding potential of −65 mV. Series resistance was frequently monitored and compensated between 65–75%, and cells that changed > 25% during recording were discarded from further analysis. For the analysis of the kinetic properties of uIPSCs we used only those recordings where series resistance changed by ≤ 10% (Fig. 7, Table 2). In experiments with carbachol, 5 μM NBQX was occasionally added to the bath solution to reduce the high background synaptic activity.

Post hoc anatomical identification of interneurons

After recording, slices were fixed in 4% paraformaldehyde in 0.1 M phosphate buffer (PB; pH 7.4) for at least 60 min, followed by washout with PB several times, cryoprotected in 20% sucrose and repeatedly freeze–thawed (for details see Gulyas *et al.*, 1993). Biocytin was visualized using avidin-biotinylated horseradish peroxidase complex reaction (ABC; Vector Laboratories, Burlingame, CA, USA) with nickel-intensified 3,3-diaminobenzidine as a chromogen. After dehydration and embedding in Durcupan (Fluka), neurons were identified based on their dendritic and axonal arborization and some representative cells were reconstructed with the aid of a drawing tube using a 40× objective.

Identification of FSBCs and AACs using double immunofluorescent labelling

After recordings, the slices were fixed as above, washed, cryoprotected, embedded in agar (1%) and re-sectioned at 60 μm thickness. Every third section was processed for electron microscopy where biocytin was visualized as above. The sections were then treated in 1% OsO_4, followed by 1% uranyl acetate, dehydrated in a graded series of ethanol, and embedded in epoxy resin (Durcupan; Fluka). Ultrathin sections of 60 nm thickness were cut for electron microscopy, and the postsynaptic targets of 5–10 boutons of each examined cells were identified. The remaining sections were processed for fluorescent double immunolabelling. They were treated with 0.2 mg/mL pepsin (Cat. No.: S3002; Dako) in 0.2 M HCl at 37°C for 5 min and were washed in 0.1 M PB similar to the procedure developed by Watanabe *et al.* (1998). Sections were blocked in normal goat serum (NGS; 10%) made up in Tris-buffered saline (TBS, pH = 7.4) followed by incubations in mouse anti-Ankyrin-G (1 : 100; Santa Cruz Biotechnology) diluted in TBS containing 2% NGS and 0.3% Triton X-100. Following several washes in TBS, Cy3-conjugated goat antimouse (1 : 500; Jackson) was used to visualize the immunoreaction, while Alexa488-conjugated streptavidin (1 : 500; Invitrogen) to visualize the biocytin. Sections were then mounted on slides in Vectashield (Vector Laboratories). Images were taken using an AxioImager Z1 axioscope (Carl Zeiss MicroImaging GmbH, Germany).

Data analysis and materials

The kinetic properties of uIPSCs were investigated on averaged events that were calculated with excluding the transmission failures. The latency of synaptic transmission was calculated by subtracting the time of the action potential peaks from the start of the postsynaptic currents. This latter value was estimated by subtracting the rise time from the peak time of events calculated from the time of the action potential peaks. Calculation of asynchronous release was achieved by the comparison of the average charge (area under the curve) of all currents in a 100-ms-long time window before and after the action potential trains. Fitting of single exponential functions on the decaying phases of averaged uIPSCs and statistical analyses were performed using Origin 8.0 software (OriginLab Corporation, Northampton, MA, USA). As most data in this work did not have a Gaussian distribution according to the Shapiro–Wilk's *W* test or the Kolmogorov–Smirnov test, nonparametric statistics were used. Multiple groups of data were compared using the nonparametric Kruskal–Wallis ANOVA test completed with comparison of samples as pairs with the Mann–Whitney *U*-test. For dependent samples the Wilcoxon signed-ranks test was used. $P < 0.05$ was considered a significant difference. Data are presented as mean ± SEM.

All chemicals and drugs were purchased from Sigma Aldrich (St Louis, MO, USA), except AM251 and AF/DX 116, which were obtained from Tocris (Bristol, UK).

Results

Identification of different types of perisomatic interneurons

To investigate the synaptic properties of the three types of perisomatic inhibitory neurons in the CA3 region of the hippocampus, it was indispensable to unequivocally separate them from each other. RSBCs were sampled in *in vitro* slices prepared from transgenic mice in which eGFP expression was under the control of the GAD65 promoter. As in this mouse line PV-containing interneurons do not express eGFP at all in the hippocampus (Lopez-Benedito *et al.*, 2004), we used another transgenic mouse to specifically target the FSBCs and AACs. In this mouse line the bacterial artificial chromosome technique was used to drive the expression of eGFP selectively in PV-containing cells (Meyer *et al.*, 2002), providing a tool to obtain recordings from hippocampal FSBCs and AACs (Katsumaru *et al.*, 1988).

All the recorded interneurons were tested for firing characteristics and filled with biocytin to allow *post hoc* visualization of their morphology (Fig. 1A and B). Only those neurons identified in this study as RSBCs sampled from GAD65-eGFP mice, which had an axonal arbour predominantly in the stratum pyramidale surrounding somata, and had typical regular firing, were used ($n = 17$; Daw *et al.*, 2009). To distinguish FSBCs and AACs after recordings obtained in slices from PV-eGFP mice, double immunofluorescent staining was performed to visualize the biocytin-filled axon collaterals together with the AISs of neurons, which were labelled with an antibody developed against ankyrin-G. This scaffolding protein is present in high concentrations in the AIS of neurons, where it anchors several proteins, including voltage-gated sodium channels (Nav1.2 and 1.6; Jenkins & Bennett, 2001), so it is appropriate to visualize AISs at the light microscopic level (Boiko *et al.*, 2007). We observed two clearly distinguishable patterns of labelling in the double-stained materials. There were cells with biocytin-filled axons that only rarely approached ankyrin-G-stained profiles ($n = 23$, Fig. 1C), whereas other cells had axon collaterals forming close appositions with ankyrin-G-labelled segments, often in a climbing fiber-like manner ($n = 26$, Fig. 1E). To confirm that intracellularly-labelled boutons avoiding ankyrin-G-immunoreactive elements derived from basket cells, as suggested by the morphology, electron microscopic examination was performed. In all cases tested, we found that axon terminals of these neurons formed symmetrical synapses on the somata or proximal dendrites of CA3 pyramidal cells ($n = 5$; Fig. 1D), therefore these interneurons were confirmed to be basket cells. In those cases in which biocytin-filled boutons surrounded ankyrin-G-immunopositive segments, electron microscopic studies confirmed that axon terminals formed synaptic contacts on the AIS of pyramidal cells ($n = 5$; Fig. 1F); as a result, we identified these interneurons as AACs. In PV-eGFP mice, we also recorded four bistratified cells and one oriens–lacunosum moleculare cell, which was not unexpected as previous data indicated that these GABAergic cell types could express PV at low levels (Klausberger & Somogyi, 2008). These neurons were excluded from this study.

Hence, using anatomical methods, we identified all the three types of perisomatic inhibitory interneurons whose synaptic outputs have been investigated.

Basic synaptic properties of connections between perisomatic inhibitory cells and postsynaptic pyramidal neurons

In the first set of experiments we investigated the basic properties of synapses formed by the three types of perisomatic inhibitory cells on their pyramidal cell targets. To this end, uIPSCs were recorded from synaptically coupled perisomatic inhibitory cell–pyramidal neuron pairs in the CA3 region. We compared the peak amplitude (including failures), potency (excluding failures), 10–90% rise time and T50 values (i.e. the width of currents at the half of the peak amplitude) of uIPSCs. In addition, the synaptic latency of transmission (i.e. the time between the action potential peak and the beginning of the postsynaptic current) and the probability of transmission failure were also calculated (Fig. 2; Table 1). The analysis showed that the three groups are different regarding peak amplitude ($H_{2,50} = 22.36$; $P < 0.0001$), synaptic potency ($H_{2,50} = 18.8$; $P < 0.0001$), probability of failures ($H_{2,50} = 20.83$; $P < 0.0001$), T50 value ($H_{2,48} = 18.2$; $P = 0.0001$) and latency ($H_{2,49} = 14.23$; $P = 0.0008$) whereas 10–90% rise time values belonging to the three groups did not differ significantly from each other ($H_{2,49} = 4.15$; $P = 0.12$). Further statistical investigations revealed that in AAC–pyramidal cell pairs synaptic currents had the largest peak amplitude and potency, as did T50 values of postsynaptic currents; these parameters significantly differed from the values of the other two groups (Fig. 2; Table 1). Moreover, synaptic transmission of RSBCs was found to have a higher probability of failures and longer latency than either FSBCs or AACs (Fig. 2; Table 1). These results indicate that the synaptic output of the individual AACs could have the largest potential to influence the activity of pyramidal neurons in the CA3 region of the hippocampus.

Carbachol, an ACh receptor agonist, reduced the amplitudes of uIPSCs to different extents depending on the presynaptic cell type

Hippocampal circuits are extensively supplied by cholinergic fibers arriving from the medial septum (Wenk *et al.*, 1975; Wainer *et al.*, 1985). To investigate the effect of cholinergic receptor activation on the perisomatic inhibition, we obtained paired recordings during pharmacological activation of ACh receptors by bath application of

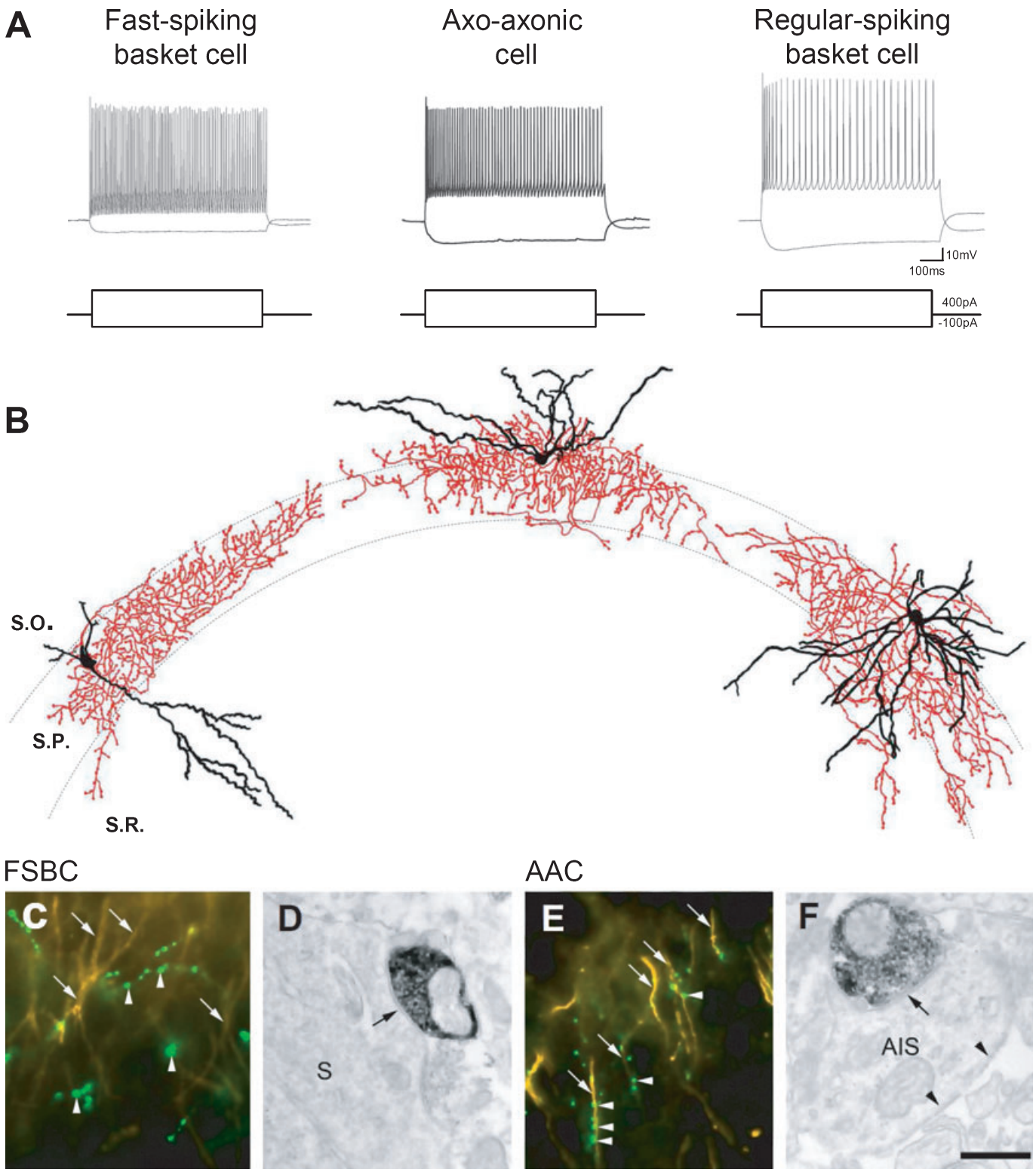

FIG. 1. Electrophysiological and morphological properties of the three types of perisomatic inhibitory interneurons in the CA3 region of the mouse hippocampus. (A) Firing characteristics of three representative cells in response to depolarizing and hyperpolarizing current steps of 400 pA and −100 pA, respectively. (B) Camera lucida reconstructions of representative biocytin-loaded neurons. Left, fast-spiking basket cell (FSBC); middle, axo-axonic cell (AAC); right, regular-spiking basket cell (RSBC). Cell bodies and dendrites of interneurons are shown in black and axon clouds in red. (C) Double immunofluorescent labelling for biocytin (green; arrowheads point to labelled terminals) and for ankyrin-G (yellow; arrowheads point to labelled AISs) shows no close appositions of biocytin-filled boutons with AISs. (D) An electron micrograph of a peroxidase-labelled axon terminal of the same cell as in C illustrates that this bouton formed symmetrical synapses (arrow) on CA3 pyramidal cell soma(s), a characteristic of basket cells. (E) Double immunofluorescent labelling as in C shows tight appositions of biocytin-labelled boutons (green; arrowheads) and ankyrin-G-labelled AISs (yellow; arrows), suggesting that this neuron is an AAC. (F) An electron micrograph of a peroxidase-labelled axon ending of the same cell as in E confirms that this interneuron formed synapses (arrow) on AISs of CA3 pyramidal cells, indicating that the recorded neuron was an AAC. Arrowheads show undercoating, characteristic of AISs. Scale bar in F, 100 μm (B), 15 μm (C and E) and 0.5 μm (D and F).

FIG. 2. Basic properties of synaptic communication between perisomatic inhibitory interneurons and pyramidal cells. (A) Ten superimposed uIPSCs (thin lines) evoked by single presynaptic action potentials in representative FSBC–, AAC– and RSBC–pyramidal cell pairs. Averages of uIPSCs are indicated by thick black lines. (B) Comparison of the peak amplitude, the synaptic potency, the 10–90% rise time, the failure probability, the half-decay (T50) and the latency obtained in the three types of perisomatic inhibitory interneurons and pyramidal cell pairs. Bars show the averages and short lines show the mean values for individual cell pairs. Asterisks indicate significant differences (see Table 1).

TABLE 1. Summary of uIPSC properties

	FSBC			AAC			RSBC		
Parameter	Data	*P*-value*	*n*	Data	*P*-value†	*n*	Data	*P*-value‡	*n*
Peak amplitude (pA)	274.9 ± 84.7	0.004	17	463.3 ± 61.8	< 0.0001	18	107.1 ± 13.9	0.049	15
Potency (pA)	288.4 ± 84.3	0.006	17	475.5 ± 63.8	< 0.0001	18	133.0 ± 16.2	0.08	15
Rise time (10–90%, ms)	1.2 ± 0.1	0.36	17	1.1 ± 0.1	0.05	18	1.8 ± 0.3	0.23	14
T50 (ms)	7.3 ± 0.6	0.0002	17	11.0 ± 0.6	0.0005	17	7.4 ± 0.5	0.74	14
Probability of failure	0.056 ± 0.025	0.06	17	0.016 ± 0.011	< 0.0001	18	0.168 ± 0.029	0.002	15
Latency (ms)	1.5 ± 0.1	0.31	17	1.7 ± 0.1	0.008	18	2.3 ± 0.2	0.0002	14

P-values represent the results of the statistical comparison of *FSBC vs. AAC, †AAC vs. RSBC and ‡RSBC vs. FSBC using the Mann–Whitney *U*-test. AAC, axo-axonic cell; FSBC, fast-spiking basket cell; RSBC, regular-spiking basket cell; uIPSC, unitary IPSC.

carbachol (2–5 μM). First we examined the postsynaptic effect of carbachol in the different types of perisomatic inhibitory cells. The analysis revealed that cholinergic receptor activation similarly changed the membrane potential of all types of perisomatic inhibitory cells ($H_{2,26} = 4.81$; $P = 0.09$). Carbachol depolarized FSBCs by 6.1 ± 1.3 mV ($n = 8$), AACs by 3.6 ± 2.0 mV ($n = 11$) and RSBCs by 6.3 ± 1.1 mV ($n = 7$). Next, we investigated the presynaptic effect of carbachol by looking into the properties of uIPSCs. In these sets of experiments transmission failures were included in the average uIPSCs. Carbachol caused a robust decrease in uIPSC amplitudes in all three types of cell pairs. In FSBC–pyramidal cell pairs and in AAC–pyramidal cell pairs, the synaptic currents were reduced to 29.9 ± 2.5% ($n = 16$, $P < 0.0001$, Fig. 3) and 27.1 ± 2.8% of control amplitude ($n = 16$, $P < 0.0001$, Fig. 3), respectively. In contrast, carbachol caused an almost total suppression of neurotransmission in RSBC–pyramidal cell pairs, reducing the amplitude to 6.0 ± 3.4% of control ($n = 13$, $P < 0.0001$). Accordingly, the magnitude of the reduction in the amplitude caused by carbachol proved to be dissimilar among different types of cell pairs ($H_{2,45} = 19.98$; $P < 0.0001$). Whereas the magnitude of the suppression in FSBC– and AAC–pyramidal cell pairs was similar ($P = 0.44$), both differed significantly from the results obtained in RSBC–pyramidal cell pairs ($P = 0.0001$). Next, we investigated the nature of receptors involved in the reduction in uIPSCs. In slices prepared from PV-eGFP mice, a muscarinic receptor antagonist AF/DX 116, which prefers M2-type receptors, was tested. In FSBC–pyramidal cell pairs, CCh decreased the amplitudes of uIPSCs to 28.3 ± 3.6% of control ($n = 6$, $P = 0.03$), an effect that was restored by the antagonist to 95.6 ± 19.7% of control ($n = 6$, $P = 0.31$). Similarly, in AAC–pyramidal cell pairs the amplitudes were reduced to 30.2 ± 4.0% of control by CCh ($n = 8$, $P = 0.008$), a decrease that could be reversed with AF/DX 116–101.6 ± 12.4% of control ($n = 8$, $P = 0.38$). As shown earlier, carbachol may trigger the synthesis of endocannabinoids via M1/M3 muscarinic receptors; these endocannabinoid signalling molecules could reduce GABA release from RSBC terminals by activating CB_1 cannabinoid receptors (Fukudome *et al.*, 2004; Neu *et al.*, 2007). Therefore, we tested whether the suppression of release at these synapses can be reversed by antagonizing CB_1 receptor function. In RSBC–pyramidal cell pairs, the amplitude of uIPSCs was reduced to 2.9 ± 0.7% of control ($n = 6$, $P = 0.03$); this was completely reversed by the co-application of a CB_1 receptor antagonist AM251 (104.6 ± 39.2% of control, $n = 6$, $P = 0.84$; Fig. 3).

These data demonstrate that carbachol effectively decreases the GABA release from perisomatic inhibitory cells to a different extent via different mechanisms, suggesting that the network dynamics could be substantially affected by cholinergic septal input and also via controlling the contribution of distinct cell types to perisomatic inhibition.

Carbachol reduces the short-term depression at FSBC– and AAC–pyramidal cell synapses in a frequency-dependent manner

In the next set of experiments we studied the short-term changes of uIPSC amplitudes evoked by action potential trains with distinct frequencies and sought to determine the effect of carbachol on the dynamics of synapses. To this end, uIPSCs were recorded in response to 10 action potentials evoked at frequencies of 1, 5, 10, 15 and 30 Hz. An example of these experiments is presented in Fig. 4, where the discharges of presynaptic interneurons were elicited at 30 Hz. Synaptic currents in FSBC– and AAC–pyramidal cell pairs showed powerful depression during the trains (Fig. 4A), whereas the uIPSC amplitudes in this RSBC–pyramidal cell pair was facilitating and depressing (Fig. 4A). In contrast to FSBC– and AAC–pyramidal cell pairs, in which the typical depression of uIPSC amplitudes increased with the firing frequency of interneurons (Fig. 5), we observed that the dynamics of RSBC–pyramidal cell synapses were very heterogeneous regarding the short-term plasticity. These synapses showed depression, facilitation or facilitation–depression, which gave on average no change in the uIPSC amplitude at all tested frequencies (an example is shown for 30 Hz in Fig. 4C).

After performing the recordings in control conditions, carbachol was bath-applied. As expected in RSBC–pyramidal cell pairs, GABA release suffered almost full block upon cholinergic receptor activation, thus no further investigations of short-term changes of IPSCs could be performed. In the case of PV-containing interneuron–pyramidal cell pairs, the magnitude of the depression notably decreased as a result of carbachol treatment (Fig. 4B). We found that carbachol altered the synaptic depression in a frequency-dependent manner. In the case of FSBC–pyramidal cell pairs the extent of the depression decreased significantly at 30 Hz ($P = 0.01$; $n = 14$) and tended to decrease at the other tested frequencies ($P = 0.05$ at 15 Hz, $P = 0.21$ at 10 Hz, $P = 0.58$ at 5 Hz and $P = 0.05$ at 1 Hz), whereas at AAC–pyramidal cell connections the synaptic depression was reduced or even eliminated at all tested frequencies ($P = 0.0003$ at 30 Hz, $P = 0.0002$ at 15 Hz, $P = 0.017$ at 10 Hz, $P = 0.015$ at 5 Hz and $P = 0.001$ at 1 Hz; $n = 17$; Fig. 5).

These data suggest that cholinergic receptor activation not only changes the magnitude of perisomatic inhibition originated from FSBCs and AACs but also effectively regulates its short-term plasticity in a frequency-dependent manner.

Asynchronous GABA release from RSBC terminals showed frequency dependence

Previous studies reported that CCK-containing basket cells in the dentate gyrus or in the CA1 hippocampal region were capable of

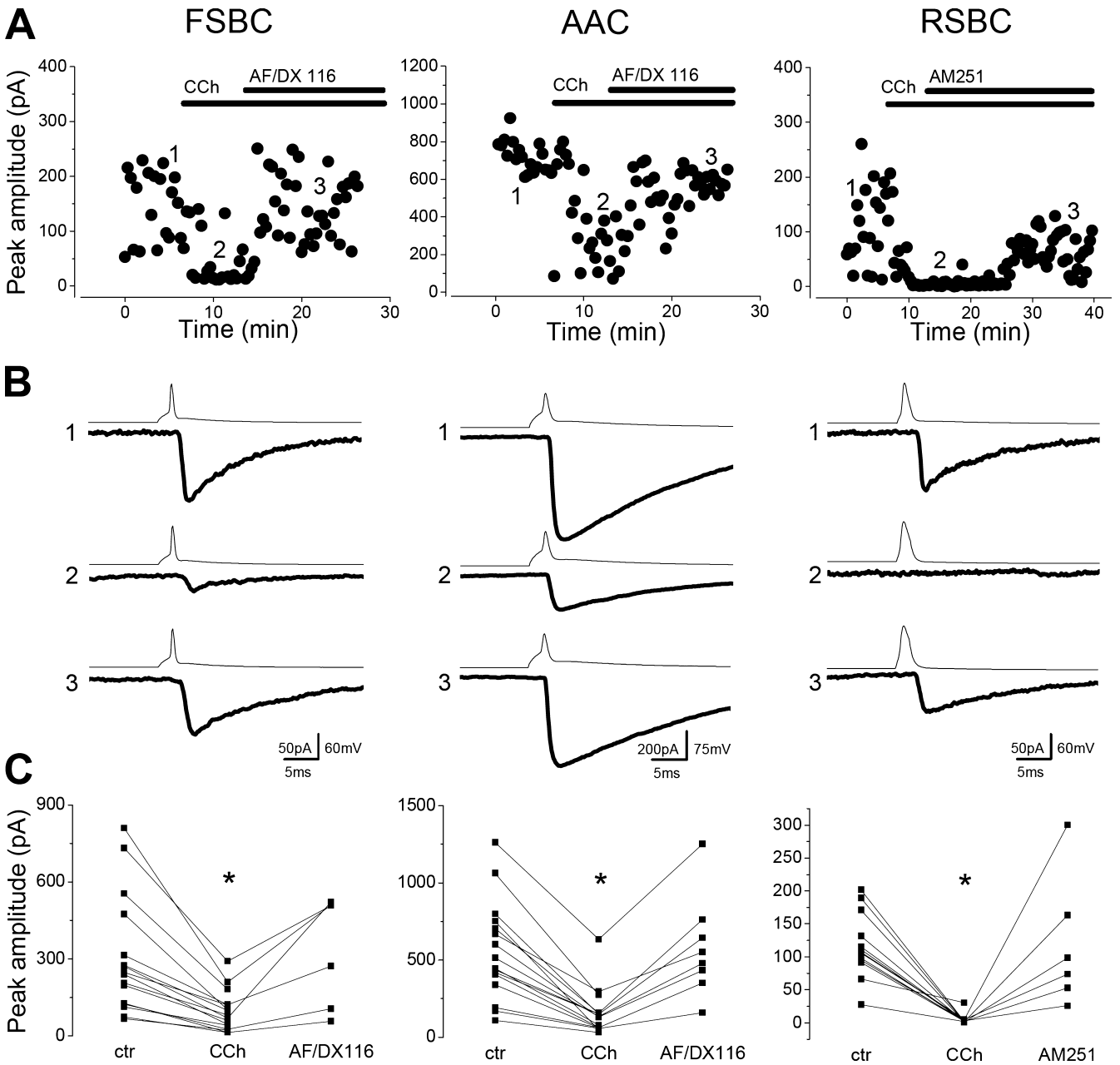

FIG. 3. Cell-type-specific suppression of uIPSC amplitudes by the ACh receptor agonist carbachol. (A) Representative experiments obtained in FSBC–, AAC– and RSBC–pyramidal cell pairs. In each case, bath application of 5 μM carbachol suppressed the uIPSC amplitude. In FSBC– and AAC–pyramidal cell pairs the reduction in the peak amplitude could be restored by an M2-receptor-preferring antagonist AF/DX 116 (10 μM), while a CB_1 cannabinoid receptor antagonist AM251 (1 μM) reversed the suppression of uIPSC amplitude in RSBC–pyramidal cell pairs. (B) Average of five uIPSCs evoked by single presynaptic action potentials taken at the labelled time points. (C) Summary data of all pairs. Each square represents a mean value of IPSC amplitude from individual cell pairs under a given condition. Asterisks indicate the significant differences. Note the different scales on *y* axis.

asynchronous transmitter release and, thus, could generate fluctuating and long-lasting inhibitory signals (Hefft & Jonas, 2005; Daw *et al.*, 2009). We also noticed in our experiments that the occurrence of IPSCs often increased after the action potential trains in RSBC–pyramidal cell pairs. Therefore, we investigated the magnitude of the asynchronous release as a function of the discharge frequency of the presynaptic RSBCs, and contrasted this with data obtained in FSBC– and AAC–pyramidal cell pairs. We compared the total charge transfer of spontaneous postsynaptic currents received by the pyramidal cells before and after the action potential trains elicited at different frequencies (Fig. 6). At RSBC–pyramidal cell synapses we observed robust asynchronous release that showed strong frequency dependence. While below 10 Hz no asynchronous release could be observed, at 15 Hz ($P = 0.02$) and at 30 Hz ($P = 0.0001$, $n = 14$) significant increases in the charge transfer could be detected (Fig. 6). We then examined the possibility of asynchronous release at the other two types of perisomatic inhibitory cell, but we did not find any significant change in the charge transfer following action potential trains tested at 30 Hz ($P = 0.17$ for FSBCs, $n = 17$; and $P = 0.05$ for AACs, $n = 18$), confirming that neither FSBCs nor AACs release transmitter in an

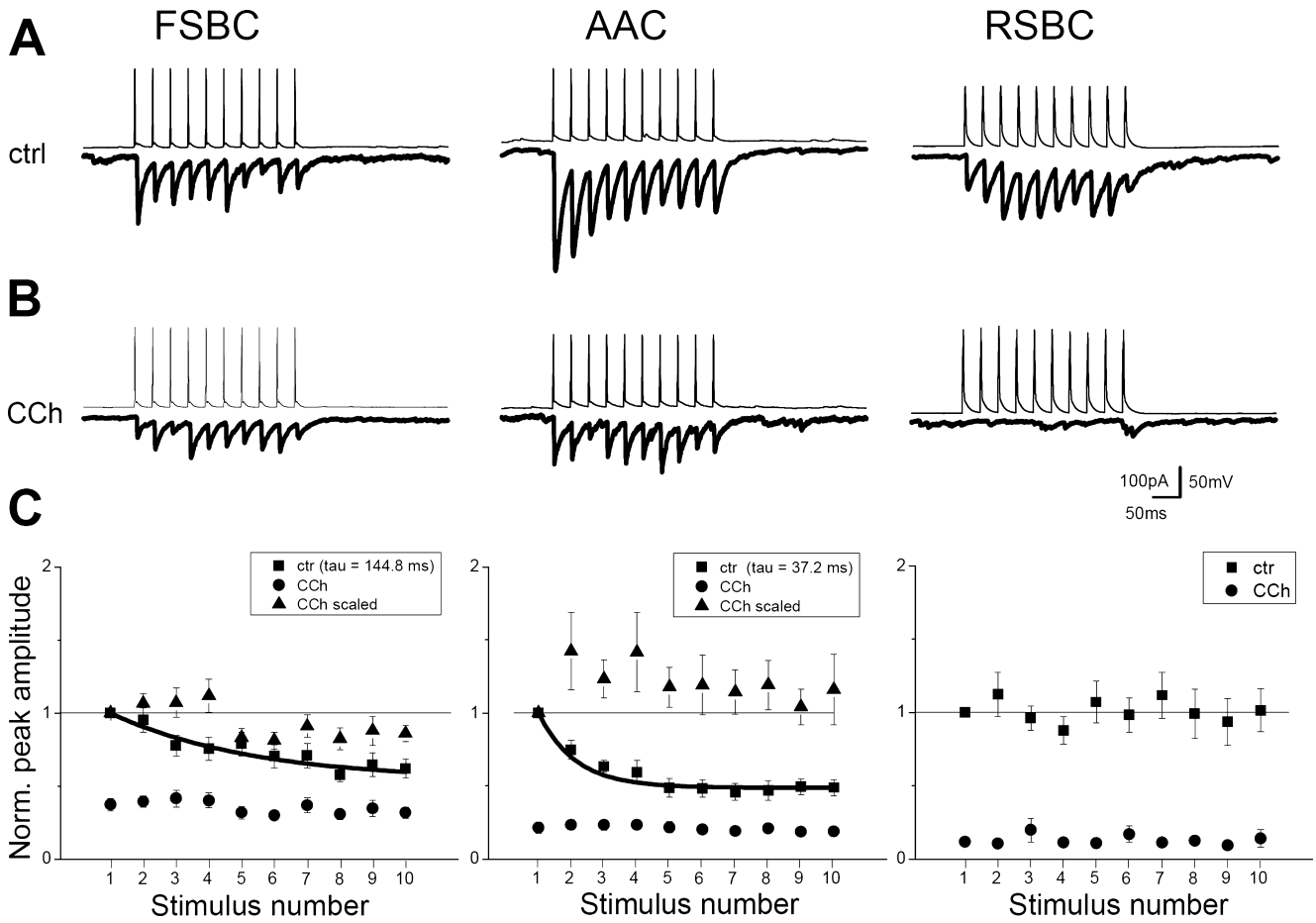

FIG. 4. Carbachol changed the short-term dynamics of transmitter release. (A) Representative averaged IPSCs in response to 10 action potentials at a frequency of 30 Hz in control conditions. (B) Responses in the same pairs in the presence of 5 μM carbachol. (C) Summary of changes in release dynamics effected by carbachol at 30 Hz recorded in FSBC– (n = 14), AAC– (n = 17) and RSBC–pyramidal cell pairs (n = 14). Filled squares represent normalized peak amplitudes in control conditions, circles show the same in carbachol, and triangles show data obtained in carbachol that were normalized to the first IPSC amplitude in carbachol. Amplitudes are plotted against time during trains. Curves represent exponential fit to control data points. Note that RSBC data were unsuitable for fitting with exponentials because of the lack of short-term plasticity.

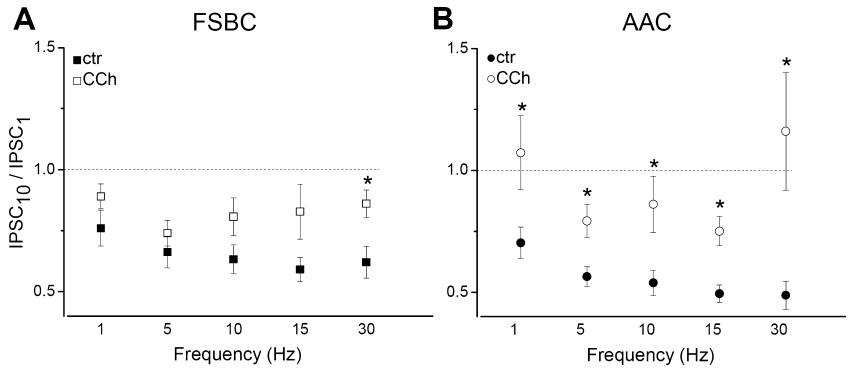

FIG. 5. Frequency-dependent changes in short-term plasticity of synaptic transmission in FSBC– and AAC–pyramidal cell pairs. (A) Ratio of $IPSC_{10}/IPSC_1$ is shown at different frequency values at FSBC–pyramidal cell pairs. (B) Same as in A, but for AAC–pyramidal cell pairs. Solid squares and circles represent control conditions, open symbols show data from carbachol-treated slices. All data are from 14 FSBC– and 17 AAC–pyramidal cell pairs; *P < 0.05.

asynchronous manner. In addition, we tested whether the asynchronous release from RSBC terminals was also sensitive to carbachol. At 30 Hz the amount of asynchronous release drastically decreased in the presence of carbachol (22.2 ± 34.1% of control charge; P = 0.001; n = 14).

These results indicate that, in contrast to FSBCs and AACs, RSBCs can release GABA asynchronously; the magnitude of this release increases with the firing frequency of the interneurons and this type of release is also suppressed by cholinergic receptor activation.

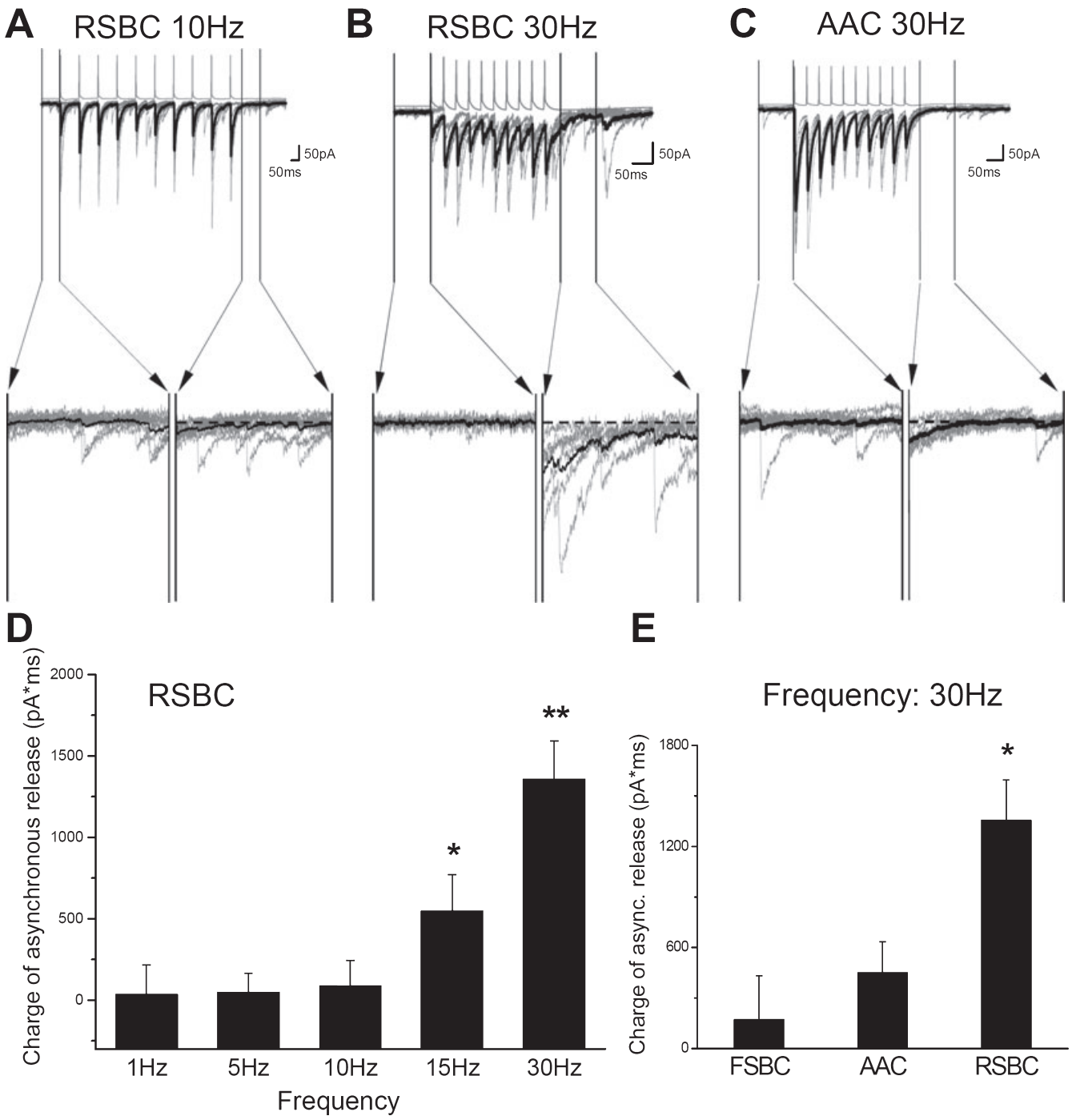

FIG. 6. Asynchronous transmitter release in perisomatic inhibitory interneuron–pyramidal cell pairs. Examples of IPSC trains in response to 10 action potentials evoked at (A) 10 Hz and at (B) 30 Hz in an RSBC–pyramidal cell pair, and (C) at 30 Hz in an AAC–pyramidal cell pair. Averages are shown in black and the individual traces in grey. The magnified 100-ms-long periods before and after the action potential trains were compared to estimate the amount of asynchronous release, demonstrating the presence of asynchronous release in the RSBC–pyramidal cell pair only at 30 Hz. (D) Summary of the frequency-dependent asynchronous release in RSBC–pyramidal cell pairs. A significant asynchronous release was found at 15 and 30 Hz (*$P < 0.05$ and **$P < 0.001$, respectively). (E) Summary of asynchronous release in the three types of perisomatic inhibitory interneuron–pyramidal cell pairs at the discharge frequency of 30 Hz.

Synaptic cross-talk between terminals of AACs may elongate the decay of synaptic currents

We observed different decay kinetics of postsynaptic currents originating from AACs than from basket cells (Fig. 2). As we obtained our experiments at room temperature, when the neurotransmitter uptake is reduced (Binda *et al.*, 2002), we wondered whether the slower decay of synaptic currents recorded in AAC–pyramidal cell pairs might be due to the spillover of GABA between release sites, as they are in a close proximity along the AIS of pyramidal cells (Fig. 1E), providing the structural basis for synaptic cross-talk. One way to test this assumption is to compare the decay of IPSCs evoked under conditions with high release probabilities with those that were recorded under reduced release probabilities. In the latter case, GABA has a lower chance of reaching its receptors in the neighbouring synapses so

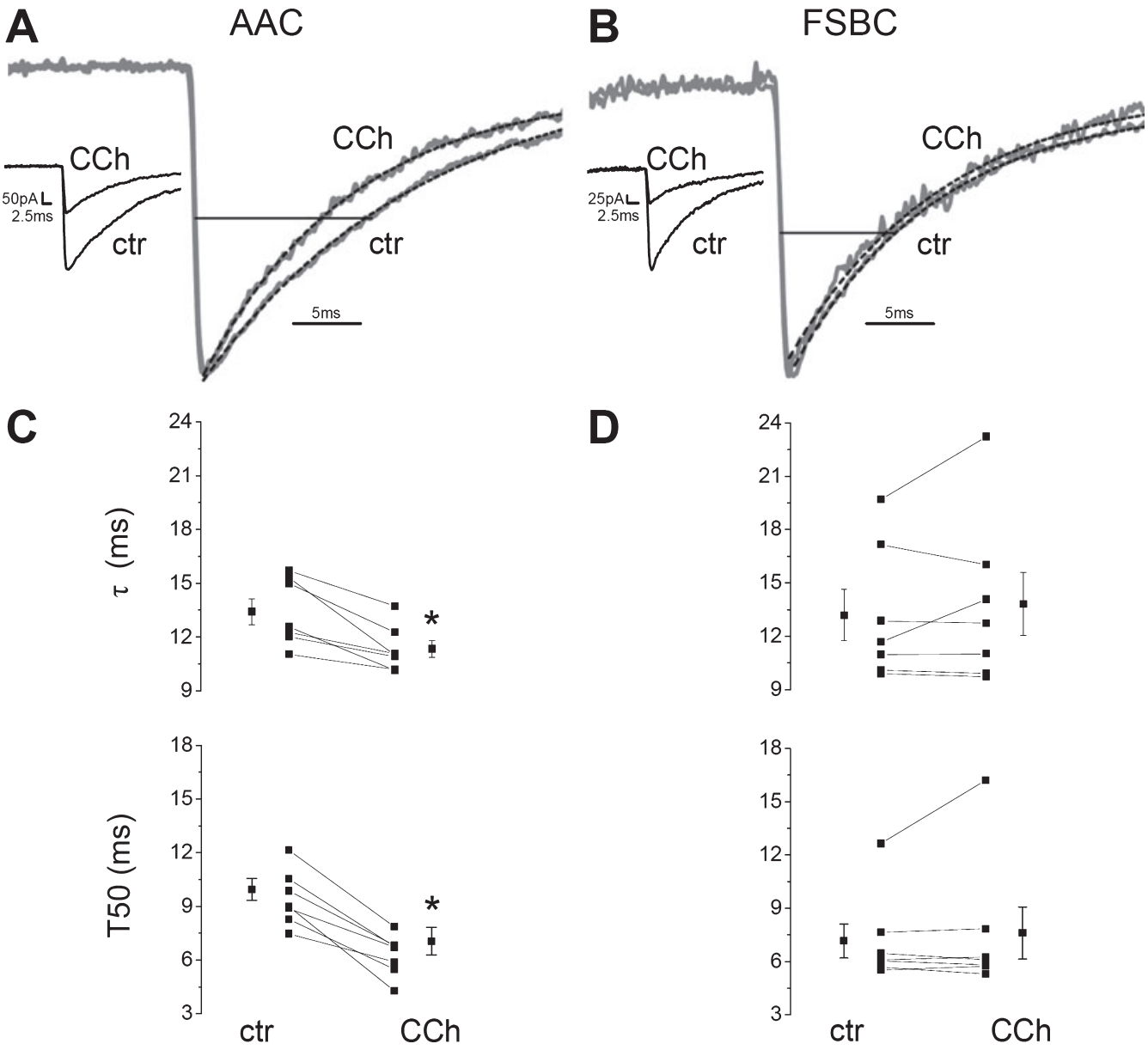

FIG. 7. Synaptic cross-talk between release sites of AACs, but not those of FSBCs, may explain the differences in decay kinetics. (A) Two representative superimposed IPSCs originating from an AAC–pyramidal cell pair in control conditions (ctr) and in the presence of carbachol (CCh). Dashed lines represent the exponential fits while the horizontal line illustrates the decay width at 50% (T50) of the peak amplitude. Note that the traces are normalized in order to visualize the changes in the decay. Original traces are shown in the inserts. (B) Same as in A, but with uIPSCs originating from an FSBC cell. (C) Summary of changes in decay time constants (τ) and T50 values at AAC–pyramidal cell pairs in response to carbachol. (D) Same as in C, but for FSBC–pyramidal cell pairs. Each data point represents a cell pair in the line series. Data calculated from seven paired recordings in each case; *$P < 0.01$.

the decay of IPSCs should be faster (Overstreet & Westbrook, 2003). Therefore, we determined the decay time constants (τ) by fitting an exponential to the averaged IPSCs in control conditions (i.e. with high release probability) and in the presence of carbachol (i.e. with lower release probability), as carbachol affects GABA release from the terminals without directly altering GABA receptor function (Behrends & ten Bruggencate, 1993). We found that the decay of uIPSCs was significantly faster at AAC–pyramidal cell synapses in the presence of carbachol than in control conditions ($P = 0.01$, $n = 7$, Fig. 7A and C; Table 2). Similar results were obtained by analyzing the half-width (T50) values of uIPSCs in control conditions and in the presence of carbachol ($P = 0.01$; $n = 7$, Fig. 7A and C; Table 2). In contrast, both types of analysis failed to detect any difference between the decay of uIPSCs recorded in FSBC–pyramidal cell pairs under conditions with high and low release probabilities ($P = 1.0$ and $P = 0.93$ for the comparison of τ and T50 values, respectively; $n = 7$; Fig. 7B and D; Table 2). The comparison of the uIPSC decays of AACs with that of FSBCs in the presence of carbachol revealed no difference ($P = 0.46$ for τ and T values, $n = 7$ for FSBC and AACs), suggesting that kinetics of GABA receptor operation might be similar at the two types of synapses if they are operating independently of each other.

These data are in line with the hypothesis that, when GABA uptake is compromised, synaptic cross-talk could significantly elongate the synaptic inhibition originating from AACs but not from FSBCs.

TABLE 2. Summary of uIPSC properties before and after carbachol treatment

	FSBC				AAC			
	Control	Carbachol	*P*-value	*n*	Control	Carbachol	*P*-value	*n*
Peak amplitude (pA)	367.4 ± 167.5	155.2 ± 78.7*	0.008	8	509.8 ± 103.7	116.5 ± 26.5*	0.004	9
Rise time (10–90%, ms)	1.2 ± 0.2	1.9 ± 0.6*	0.04	8	0.9 ± 0.1	1.2 ± 0.3	0.07	9
T50 (ms)	7.1 ± 1.0	7.6 ± 1.5	0.94	7	9.5 ± 0.6	6.3 ± 0.4*	0.02	7
Decay τ (ms)	13.2 ± 1.4	13.8 ± 1.8	0.74	7	13.4 ± 0.7	11.3 ± 0.5*	0.008	7
Probability of failure	0.089 ± 0.049	0.194 ± 0.069	0.06	8	0.027 ± 0.022	0.258 ± 0.064*	0.008	9
Latency (ms)	1.5 ± 0.1	1.4 ± 0.1	0.15	8	1.6 ± 0.2	1.8 ± 0.2	1.0	9

*Statistical significance obtained by Wilcoxon signed-rank paired test. AAC, axo-axonic cell; FSBC, fast-spiking basket cell; uIPSC, unitary IPSC.

Discussion

In this study we showed that AACs can be unequivocally distinguished from basket cells at the light-microscopic level using double immunofluorescent staining to visualize biocytin-filled axon collaterals and AISs with ankyrin-G. Paired recordings obtained from perisomatic inhibitory cells and pyramidal neurons revealed that AACs produced uIPSCs with the largest amplitudes and with the longest decays, probably due to the spillover of GABA between release sites under our recording conditions. In contrast to AACs and FSBCs, RSBCs produced uIPSCs that had the longest latency, the probability of transmitter release was the lowest at these connections, and they could release GABA asynchronously, the magnitude of release increasing with the discharge frequency of RSBCs. Cholinergic receptor activation by carbachol reduced the amplitude of uIPSCs that were recorded in FSBC– and AAC–pyramidal cell pairs, an effect that could be fully restored by the M2-type muscarinic receptor-preferring antagonist. In contrast, carbachol muted the synaptic transmission in RSBC–pyramidal cell pairs via triggering endocannabinoid production, as antagonism of CB_1 cannabinoid receptors reversed the reduction in IPSC amplitude. In addition, the depressing nature of synaptic currents in FSBC– and AAC–pyramidal cell pairs were largely reduced, or even eliminated, by carbachol in a frequency-dependent manner.

As $GABA_A$ receptors present at the perisomatic inhibitory synapses consist of similar subunits (alpha 1, alpha 2, beta 2 and gamma 2; Nusser *et al.*, 1996; Nyiri *et al.*, 2001; Kasugai *et al.*, 2006), neither the larger amplitude nor the longer decay of uIPSCs in AAC–pyramidal cell pairs compared to those recorded in basket cell–pyramidal cell pairs could be the result of distinct subunit compositions. In addition to the similar subunit composition, the area of synapses formed by basket cells and AACs was found to be similar (Nusser *et al.*, 1998). Thus, the large amplitude might reflect the large number of synaptic contacts in these cell pairs. Although the number of axon terminals of AACs contacting CA3 pyramidal cells has not been studied specifically in CA3, basket cells preferentially innervate pyramidal cells in CA3 via two to six synapses (Miles *et al.*, 1996; Biro *et al.*, 2006). This number is lower than the observations obtained in other regions, for instance in CA1, where 10–12 synaptic contacts were identified between basket cells and pyramidal cells (Buhl *et al.*, 1994; Cobb *et al.*, 1997). In this region, AACs have been shown to innervate their targets via similar numbers of synapses (Maccaferri *et al.*, 2000), which is in agreement with physiological measurements showing that basket cells and AACs in CA1 produce uIPSCs with similar amplitude. If we assume that the sum of $GABA_A$ receptor conductances in a given synapse that originate from perisomatic inhibitory cells are similar in different regions, then in CA3 more synaptic contacts should be responsible for the larger IPSC amplitude in AAC–pyramidal cell pairs than in basket cell–pyramidal cell connections.

By reducing the GABA release from the axon terminals of both AACs and FSBCs, carbachol accelerated the decay of uIPSCs recorded only in AAC– but not in FSBC–pyramidal cell pairs. This finding agrees well with previous data showing that GABA molecules could spill over to neighbouring release sites in the case of AAC– but not in FSBC–pyramidal cell pairs when the transmitter uptake is blocked by uptake inhibitors (Overstreet & Westbrook, 2003). As we performed the experiments at room temperature, i.e. when uptake systems were largely altered (Binda *et al.*, 2002), the significantly longer decay time of uIPSCs of AACs observed in the present study could also be due to the cross-talk of neighbouring synapses. Under physiological conditions (i.e. at higher temperature), GABAergic synapses of AACs are not subject to cross-talk because produce IPSCs with similar kinetics to basket cells (Maccaferri *et al.*, 2000; Overstreet & Westbrook, 2003). Nevertheless the present observations might gain significance in pathological states in which the GABA uptake system is compromised (Volk *et al.*, 2001; Liu *et al.*, 2007).

We found that the synaptic depression at PV-containing interneuron–pyramidal cell connections observed under control conditions was largely reduced or even eliminated in the presence of carbachol. These results seemingly contradict those findings obtained in the dentate gyrus, where carbachol suppressed but did not abolish the depression (Hefft *et al.*, 2002). The major difference that could explain the disagreement between these two studies was the recording temperature. While we performed our experiments at room temperature, the study in the dentate gyrus was done at 34°C. As the vast majority of physiological processes, including the affinity of muscarinic acetylcholine receptors to their agonists (Aronstam & Narayanan, 1988), have been found to be altered by lowering the temperature, the higher affinity of carbachol with their receptors, causing more stable receptor–G-protein complex at room temperature, might produce a larger reduction in the release probability in parallel with the elimination of the depression (Brenowitz *et al.*, 1998). In agreement with this hypothesis, we observed a 70% reduction in the peak amplitude after carbachol application at room temperature, whereas at 34°C this agonist suppressed the first IPSC amplitude by only 30% (Hefft *et al.*, 2002). This temperature-dependent difference in the efficacy of carbachol in decreasing the initial release probability could account for its distinct effects on synaptic depression. Similarly, the slower decay of uIPSCs in our study compared to those values found at 33–34°C (Bartos *et al.*, 2002) is probably due to the difference in the recording temperature (Otis & Mody, 1992).

What could be the reason for the longer latency, lower release probability and asynchronous nature of GABA release characteristic of axon terminals originating from RSBCs than from PV-containing interneurons? Previous studies showed that Ca^{2+}enters the terminals of FSBCs via P/Q-type voltage-gated Ca^{2+}channels that are in the active

zone of presynaptic terminals, where vesicles filled with transmitter molecules are located (Wilson *et al.*, 2001; Hefft & Jonas, 2005; Bucurenciu *et al.*, 2008). This mechanism allows the axon endings of FSBCs (and probably of AACs as well) to release GABA upon action potential discharge with high probability and with precise timing. In contrast, the axon terminals of RSBCs are equipped with N-type voltage-gated Ca^{2+}channels that are probably located at a distance from active zone (Wilson *et al.*, 2001; Hefft & Jonas, 2005). The distant location of Ca^{2+}entry from the release site could cause larger jitter and longer delay in the time of transmitter release, lower chance of releasing vesicles, and a build-up of Ca^{2+}levels in the terminals that prolongs the transmitter release upon firing at high frequencies (present study; Rozov *et al.*, 2001; Wilson *et al.*, 2001; Hefft *et al.*, 2002; Hefft & Jonas, 2005; Daw *et al.*, 2009). These contrasting features in Ca^{2+}entry into the boutons of PV-containing interneurons vs. RSBCs might, at least in part, explain the observed differences in IPSC characteristics, which predict their functional differences in neuronal operation (Freund & Katona, 2007).

In addition to the Ca^{2+}entry, the signalling cascade triggered by cholinergic receptor activation that reduces GABA release from the axon terminals of PV-containing interneurons and RSBCs is also different. In the former case, the activation of M2-type muscarinic receptors located at the axon endings of FSBCs and AACs control GABA release (present study; Hajos *et al.*, 1998; Fukudome *et al.*, 2004). In contrast, carbachol has been shown to act on the postsynaptically located M1/M3 types of muscarinic receptors in pyramidal cells that triggers the synthesis of endocannabinoids, which act in a retrograde fashion via CB_1 cannabionoid receptors located on the terminals of RSBCs, resulting in reduced GABA release (present study; Fukudome *et al.*, 2004; Neu *et al.*, 2007). In summary, the different efficacies of carbachol in the suppression of synaptic inhibition generated by the three types of perisomatic GABAergic cells could be due to the distinct signalling machinery underlying the reduction in vesicular release.

Our observation that carbachol could massively reduce or even eliminate the depression of IPSC amplitude in a frequency-dependent manner suggests that cholinergic tone originating from the medial septum may change the dynamics of information processing in the neuronal networks by altering the efficacy of feed-forward inhibition (Pouille & Scanziani, 2004; Pouille *et al.*, 2009). The mechanism underlying the change in short-term dynamics of synapses is probably related to the reduction in the initial release probability, an adjustment that promotes information transfer at higher frequencies (Brenowitz *et al.*, 1998).

Functional implications

Although the three types of GABAergic cells investigated in this study innervate the perisomatic region of pyramidal cells, their function might be very different in neuronal information processing. This assumption is strongly supported by *in vivo* experiments which revealed that FSBCs, RSBCs and AACs discharged dissimilarly during different types of network oscillations in the CA1 region (Klausberger *et al.*, 2003, 2005), providing a temporal frame for dividing the labour among these inteneurons. The input and output properties of FSBCs are designed to respond and follow faithfully the ongoing network events (Hefft & Jonas, 2005; Doischer *et al.*, 2008; Hu *et al.*, 2010). For instance, by participating in both feed-forward and feed-back inhibition, they could set the dynamic range of cortical circuits or maintain oscillatory activities at different frequencies (Sik *et al.*, 1995; Freund & Katona, 2007; Pouille *et al.*, 2009). In contrast, RSBCs predominantly integrate the inputs from distinct sources and provide a prolonged, less precise GABAergic output that could modulate learning processes at cellular levels at different timescales (Carlson *et al.*, 2002; Hefft & Jonas, 2005; Glickfeld & Scanziani, 2006; Puighermanal *et al.*, 2009). As AACs specifically target AISs of principal cells, their role might be to regulate action potential generation directly. The fact that AACs are excitatory in cortex in certain states or inhibitory in others (Szabadics *et al.*, 2006), as in the hippocampus (Glickfeld *et al.*, 2009), does not influence the conclusion that they can play a role in rhythmic or intermittent synchronization of large pyramidal cell populations. As our data indicate, cholinergic input could affect the outputs of these GABAergic cells differently, so it is likely that this subcortical impact might also alter the network dynamics by controlling the inhibitory clamp provided by the functionally distinct types of perisomatic inhibitory cells.

Acknowledgements

We are grateful to Professors Hannah Monyer, Gábor Szabó and Ferenc Erdélyi for providing transgenic animals. We thank Erzsébet Gregori, Katalin Lengyel and Emőke Simon for their excellent technical assistance. This work was supported by the Wellcome Trust, the Hungarian Scientific Research Funds (OTKA T049517, K60927 and NKTH-OTKA CNK 77793), the National Office for Research and Technology (OMFB-01678/2009) and the Howard Hughes International Program.

Abbreviations

AAC, axo-axonic cell; AIS, axon initial segment; CCK, cholecystokinin; eGFP, enhanced green fluorescent protein; FSBC, fast-spiking basket cell; GAD65, glutamate decarboxylase 65; IPSC, inhibitory postsynaptic current; PV, parvalbumin; RSBC, regular-spiking basket cell; uIPSC, unitary IPSC.

References

Aronstam, R.S. & Narayanan, T.K. (1988) Temperature effect on the detection of muscarinic receptor-G protein interactions in ligand binding assays. *Biochem. Pharmacol.*, **37**, 1045–1049.

Bartos, M., Vida, I., Frotscher, M., Meyer, A., Monyer, H., Geiger, J.R. & Jonas, P. (2002) Fast synaptic inhibition promotes synchronized gamma oscillations in hippocampal interneuron networks. *Proc. Natl Acad. Sci. USA*, **99**, 13222–13227.

Behrends, J.C. & ten Bruggencate, G. (1993) Cholinergic modulation of synaptic inhibition in the guinea pig hippocampus in vitro: excitation of GABAergic interneurons and inhibition of GABA-release. *J. Neurophysiol.*, **69**, 626–629.

Binda, F., Bossi, E., Giovannardi, S., Forlani, G. & Peres, A. (2002) Temperature effects on the presteady-state and transport-associated currents of GABA cotransporter rGAT1. *FEBS Lett.*, **512**, 303–307.

Biro, A.A., Holderith, N.B. & Nusser, Z. (2006) Release probability-dependent scaling of the postsynaptic responses at single hippocampal GABAergic synapses. *J. Neurosci.*, **26**, 12487–12496.

Blackstad, T.W. & Flood, P.R. (1963) Ultrastructure of hippocampal axo-somatic synapses. *Nature*, **198**, 542–543.

Boiko, T., Vakulenko, M., Ewers, H., Yap, C.C., Norden, C. & Winckler, B. (2007) Ankyrin-dependent and -independent mechanisms orchestrate axonal compartmentalization of L1 family members neurofascin and L1/neuron-glia cell adhesion molecule. *J. Neurosci.*, **27**, 590–603.

Brenowitz, S., David, J. & Trussell, L. (1998) Enhancement of synaptic efficacy by presynaptic GABA(B) receptors. *Neuron*, **20**, 135–141.

Bucurenciu, I., Kulik, A., Schwaller, B., Frotscher, M. & Jonas, P. (2008) Nanodomain coupling between Ca^{2+} channels and Ca^{2+} sensors promotes fast and efficient transmitter release at a cortical GABAergic synapse. *Neuron*, **57**, 536–545.

Buhl, E.H., Halasy, K. & Somogyi, P. (1994) Diverse sources of hippocampal unitary inhibitory postsynaptic potentials and the number of synaptic release sites. *Nature*, **368**, 823–828.

Carlson, G., Wang, Y. & Alger, B.E. (2002) Endocannabinoids facilitate the induction of LTP in the hippocampus. *Nat. Neurosci.*, **5**, 723–724.

Cobb, S.R., Buhl, E.H., Halasy, K., Paulsen, O. & Somogyi, P. (1995) Synchronization of neuronal activity in hippocampus by individual GABAergic interneurons. *Nature*, **378**, 75–78.

Cobb, S.R., Halasy, K., Vida, I., Nyiri, G., Tamas, G., Buhl, E.H. & Somogyi, P. (1997) Synaptic effects of identified interneurons innervating both interneurons and pyramidal cells in the rat hippocampus. *Neuroscience*, **79**, 629–648.

Daw, M.I., Tricoire, L., Erdelyi, F., Szabo, G. & McBain, C.J. (2009) Asynchronous transmitter release from cholecystokinin-containing inhibitory interneurons is widespread and target-cell independent. *J. Neurosci.*, **29**, 11112–11122.

Doischer, D., Hosp, J.A., Yanagawa, Y., Obata, K., Jonas, P., Vida, I. & Bartos, M. (2008) Postnatal differentiation of basket cells from slow to fast signaling devices. *J. Neurosci.*, **28**, 12956–12968.

Freund, T.F. & Buzsaki, G. (1996) Interneurons of the hippocampus. *Hippocampus*, **6**, 347–470.

Freund, T.F. & Katona, I. (2007) Perisomatic inhibition. *Neuron*, **56**, 33–42.

Fukudome, Y., Ohno-Shosaku, T., Matsui, M., Omori, Y., Fukaya, M., Tsubokawa, H., Taketo, M.M., Watanabe, M., Manabe, T. & Kano, M. (2004) Two distinct classes of muscarinic action on hippocampal inhibitory synapses: M2-mediated direct suppression and M1/M3-mediated indirect suppression through endocannabinoid signalling. *Eur. J. Neurosci.*, **19**, 2682–2692.

Glickfeld, L.L. & Scanziani, M. (2006) Distinct timing in the activity of cannabinoid-sensitive and cannabinoid-insensitive basket cells. *Nat. Neurosci.*, **9**, 807–815.

Glickfeld, L.L., Roberts, J.D., Somogyi, P. & Scanziani, M. (2009) Interneurons hyperpolarize pyramidal cells along their entire somatodendritic axis. *Nat. Neurosci.*, **12**, 21–23.

Gulyas, A.I., Miles, R., Hajos, N. & Freund, T.F. (1993) Precision and variability in postsynaptic target selection of inhibitory cells in the hippocampal CA3 region. *Eur. J. Neurosci.*, **5**, 1729–1751.

Hajos, N., Papp, E.C., Acsady, L., Levey, A.I. & Freund, T.F. (1998) Distinct interneuron types express m2 muscarinic receptor immunoreactivity on their dendrites or axon terminals in the hippocampus. *Neuroscience*, **82**, 355–376.

Hasselmo, M.E. (2006) The role of acetylcholine in learning and memory. *Curr. Opin. Neurobiol.*, **16**, 710–715.

Hefft, S. & Jonas, P. (2005) Asynchronous GABA release generates long-lasting inhibition at a hippocampal interneuron-principal neuron synapse. *Nat. Neurosci.*, **8**, 1319–1328.

Hefft, S., Kraushaar, U., Geiger, J.R. & Jonas, P. (2002) Presynaptic short-term depression is maintained during regulation of transmitter release at a GABAergic synapse in rat hippocampus. *J. Physiol.*, **539**, 201–208.

Hu, H., Martina, M. & Jonas, P. (2010) Dendritic mechanisms underlying rapid synaptic activation of fast-spiking hippocampal interneurons. *Science*, **327**, 52–58.

Jenkins, S.M. & Bennett, V. (2001) Ankyrin-G coordinates assembly of the spectrin-based membrane skeleton, voltage-gated sodium channels, and L1 CAMs at Purkinje neuron initial segments. *J. Cell Biol.*, **155**, 739–746.

Kasugai, Y., Fukazawa, Y., Roberts, J.D.B., Somogyi, P., Sieghart, W. & Shigemoto, R. (2006) Localization of $GABA_A$ receptor subunits on rat hippocampal pyramidal cells by freeze-fracture replica immunolabeling. *Soc. Neurosci. Abstr.*, 527.18.

Katsumaru, H., Kosaka, T., Heizmann, C.W. & Hama, K. (1988) Immunocytochemical study of GABAergic neurons containing the calcium-binding protein parvalbumin in the rat hippocampus. *Exp. Brain Res.*, **72**, 347–362.

Kawaguchi, Y. & Kubota, Y. (1997) GABAergic cell subtypes and their synaptic connections in rat frontal cortex. *Cereb. Cortex*, **7**, 476–486.

Klausberger, T. & Somogyi, P. (2008) Neuronal diversity and temporal dynamics: the unity of hippocampal circuit operations. *Science*, **321**, 53–57.

Klausberger, T., Magill, P.J., Marton, L.F., Roberts, J.D., Cobden, P.M., Buzsaki, G. & Somogyi, P. (2003) Brain-state- and cell-type-specific firing of hippocampal interneurons in vivo. *Nature*, **421**, 844–848.

Klausberger, T., Marton, L.F., O'Neill, J., Huck, J.H., Dalezios, Y., Fuentealba, P., Suen, W.Y., Papp, E., Kaneko, T., Watanabe, M., Csicsvari, J. & Somogyi, P. (2005) Complementary roles of cholecystokinin- and parvalbumin-expressing GABAergic neurons in hippocampal network oscillations. *J. Neurosci.*, **25**, 9782–9793.

Lawrence, J.J. (2008) Cholinergic control of GABA release: emerging parallels between neocortex and hippocampus. *TINS*, **31**, 317–327.

Liu, G.X., Cai, G.Q., Cai, Y.Q., Sheng, Z.J., Jiang, J., Mei, Z., Wang, Z.G., Guo, L. & Fei, J. (2007) Reduced anxiety and depression-like behaviors in mice lacking GABA transporter subtype 1. *Neuropsychopharmacology*, **32**, 1531–1539.

Lopez-Benedito, G., Sugress, K., Erdélyi, F., Szabó, G., Molnár, Z. & Paulsen, O. (2004) Preferential Origin and layer destination of GAD65-GFP cortical interneurons. *Cereb. Cortex*, **14**, 1122–1133.

Maccaferri, G., Roberts, J.D., Szucs, P., Cottingham, C.A. & Somogyi, P. (2000) Cell surface domain specific postsynaptic currents evoked by identified GABAergic neurones in rat hippocampus in vitro. *J. Physiol.*, **524**, 91–116.

Meyer, A.H., Katona, I., Blatow, M., Rozov, A. & Monyer, H. (2002) In vivo labeling of parvalbumin-positive interneurons and analysis of electrical coupling in identified neurons. *J. Neurosci.*, **22**, 7055–7064.

Miles, R., Toth, K., Gulyas, A.I., Hajos, N. & Freund, T.F. (1996) Differences between somatic and dendritic inhibition in the hippocampus. *Neuron*, **16**, 815–823.

Neu, A., Foldy, C. & Soltesz, I. (2007) Postsynaptic origin of CB1-dependent tonic inhibition of GABA release at cholecystokinin-positive basket cell to pyramidal cell synapses in the CA1 region of the rat hippocampus. *J. Physiol.*, **578**, 233–247.

Nusser, Z., Sieghart, W., Benke, D., Fritschy, J.M. & Somogyi, P. (1996) Differential synaptic localization of two major gamma-aminobutyric acid type A receptor alpha subunits on hippocampal pyramidal cells. *Proc. Natl Acad. Sci. USA*, **93**, 11939–11944.

Nusser, Z., Hajos, N., Somogyi, P. & Mody, I. (1998) Increased number of synaptic GABA(A) receptors underlies potentiation at hippocampal inhibitory synapses. *Nature*, **395**, 172–177.

Nyiri, G., Freund, T.F. & Somogyi, P. (2001) Input-dependent synaptic targeting of alpha(2)-subunit-containing GABA(A) receptors in synapses of hippocampal pyramidal cells of the rat. *Eur. J. Neurosci.*, **13**, 428–442.

Otis, T.S. & Mody, I. (1992) Modulation of decay kinetics and frequency of GABAA receptor-mediated spontaneous inhibitory postsynaptic currents in hippocampal neurons. *Neuroscience*, **49**, 13–32.

Overstreet, L.S. & Westbrook, G.L. (2003) Synapse density regulates independence at unitary inhibitory synapses. *J. Neurosci.*, **23**, 2618–2626.

Pawelzik, H., Hughes, D.I. & Thomson, A.M. (2002) Physiological and morphological diversity of immunocytochemically defined parvalbumin- and cholecystokinin-positive interneurones in CA1 of the adult rat hippocampus. *J. Comp. Neurol.*, **443**, 346–367.

Pouille, F. & Scanziani, M. (2004) Routing of spike series by dynamic circuits in the hippocampus. *Nature*, **429**, 717–723.

Pouille, F., Marin-Burgin, A., Adesnik, H., Atallah, B.V. & Scanziani, M. (2009) Input normalization by global feedforward inhibition expands cortical dynamic range. *Nat. Neurosci.*, **12**, 1577–1585.

Puighermanal, E., Marsicano, G., Busquets-Garcia, A., Lutz, B., Maldonado, R. & Ozaita, A. (2009) Cannabinoid modulation of hippocampal long-term memory is mediated by mTOR signaling. *Nat. Neurosci.*, **12**, 1152–1158.

Rozov, A., Burnashev, N., Sakmann, B. & Neher, E. (2001) Transmitter release modulation by intracellular Ca^{2+} buffers in facilitating and depressing nerve terminals of pyramidal cells in layer 2/3 of the rat neocortex indicates a target cell-specific difference in presynaptic calcium dynamics. *J. Physiol.*, **531**, 807–826.

Sik, A., Penttonen, M., Ylinen, A. & Buzsaki, G. (1995) Hippocampal CA1 interneurons: an in vivo intracellular labeling study. *J. Neurosci.*, **15**, 6651–6665.

Somogyi, P. (1977) A specific 'axo-axonal' interneuron in the visual cortex of the rat. *Brain Res.*, **136**, 345–350.

Somogyi, P., Tamas, G., Lujan, R. & Buhl, E.H. (1998) Salient features of synaptic organisation in the cerebral cortex. *Brain Res. Brain Res. Rev.*, **26**, 113–135.

Szabadics, J., Varga, C., Molnar, G., Olah, S., Barzo, P. & Tamas, G. (2006) Excitatory effect of GABAergic axo-axonic cells in cortical microcircuits. *Science*, **311**, 233–235.

Volk, D., Austin, M., Pierri, J., Sampson, A. & Lewis, D. (2001) GABA transporter-1 mRNA in the prefrontal cortex in schizophrenia: decreased expression in a subset of neurons. *Am. J. Psychiatry*, **158**, 256–265.

Wainer, B.H., Levey, A.I., Rye, D.B., Mesulam, M.M. & Mufson, E.J. (1985) Cholinergic and non-cholinergic septohippocampal pathways. *Neurosci. Lett.*, **54**, 45–52.

Watanabe, M., Fukaya, M., Sakimura, K., Manabe, T., Mishina, M. & Inoue, Y. (1998) Selective scarcity of NMDA receptor channel subunits in the stratum lucidum (mossy fibre-recipient layer) of the mouse hippocampal CA3 subfield. *Eur. J. Neurosci.*, **10**, 478–487.

Wenk, H., Ritter, J. & Meyer, U. (1975) Histochemistry of cholinergic systems in the CNS. I. Topochemical and quantitative changes in acetylcholinesterase activity in the limbic cortex after septal lesions in the rat. *Acta Histochem.*, **53**, 77–92.

Wilson, R.I., Kunos, G. & Nicoll, R.A. (2001) Presynaptic specificity of endocannabinoid signaling in the hippocampus. *Neuron*, **31**, 453–462.

dc_71_10

18. számú melléklet

dc_71_10

The Journal of Neuroscience

http://jneurosci.msubmit.net

Parvalbumin-containing fast-spiking basket cells generate the field potential oscillations induced by cholinergic receptor activation in the hippocampus

JN-RM-4104-10

Norbert Hajos, Inst Exp Med Hungarian Acad Sci

Attila Gulyas, Institute of Experimental Medicine

Gergely Szabo, Institute of Experimental Medicine, Hungarian Academy of Sciences

Istvan Ulbert, MTA

Noemi Holderith,

Ferenc Erdelyi, Institute of Experimental Medicine

Hannah Monyer, University Hospital for Neurology

Gabor Szabo, Institute of Experimental Medicine

Tamas Freund, Inst. Exp. Med., Budapest

Commercial Interest: No

Cellular/Molecular
Senior Editor: Chris J. McBain

Parvalbumin-containing fast-spiking basket cells generate the field potential oscillations induced by cholinergic receptor activation in the hippocampus

Attila I. Gulyás[1], Gergely G. Szabó[1], István Ulbert[2,3] Noémi Holderith[1], Hannah Monyer[4], Ferenc Erdélyi[1], Gábor Szabó[1], Tamás F. Freund[1,3] and Norbert Hájos[1]

[1] Institute of Experimental Medicine, Hungarian Academy of Sciences, H-1083 Budapest, Hungary
[2] Institute for Psychology, Hungarian Academy of Sciences, Budapest, Hungary
[3] Péter Pázmány Catholic University, Faculty of Information Technology, Budapest, Hungary
[4] Department of Clinical Neurobiology, University Hospital of Neurology, 69120 Heidelberg, Germany

Number of figures: 8
Number of tables: 1
Supplementary material contains 9 supplementary figures
Number of pages: 37
Number of words for Abstract 245; Introduction: 499; Discussion: 1497

Corresponding authors:
Norbert Hájos
Laboratory of Network Neurophysiology
Institute of Experimental Medicine
Hungarian Academy of Sciences
Szigony u. 43, Budapest
1083 Hungary
Phone: 36-1-2109400/387, Fax: 36-1-2109412
Email: hajos@koki.hu

Abbreviated title: Perisomatic interneurons in network oscillations.
Keywords: inhibition, rhythm, μ-opioid receptor, gamma oscillations, in vivo, in vitro

Acknowledgements
We are grateful to Prof. B.L. Kieffer for providing MOR KO mice for our study. This work was supported by the Wellcome Trust, the Hungarian Scientific Research Fund (OTKA T049517, NNF78917, K 060927, K 81357), the National Office for Research and Technology (OMFB-01678/2009, NKTH-ANR Neurogen), the European Union (LSHM-CT-2004-005166), and the Howard Hunghes Medical Institute. We also thank Erzsébet Gregori, Emőke Szépné Simon, Zoltánné Lengyel, and Győző Godaa, Richárd Fiáth and Bálint P. Kerekes for their excellent technical assistance.

Abstract

Gamma frequency oscillations in cortical regions can be recorded during cognitive processes, including attention or memory tasks. These oscillations are generated locally as a result of reciprocal interactions between excitatory pyramidal cells and perisomatic inhibitory interneurons. Here, we examined the contribution of the three perisomatic interneuron types – the parvalbumin-containing fast-spiking basket (FSBC) and axo-axonic (AAC) cells, as well as the cholecystokinin-containing regular-spiking basket cells (RSBC) to cholinergically induced oscillations in hippocampal slices, a rhythmic activity that captures several features of the gamma oscillations recorded in vivo. By analyzing the spiking activities of single neurons recorded in parallel with local field potentials, we found that all three cell types fired phase-locked to the carbachol-induced oscillations, although with different frequencies and precision. During these oscillations FSBCs fired the most with the highest accuracy compared to the discharge of AACs and RSBCs. In further experiments we showed that activation of μ-opioid receptors by DAMGO, which significantly reduced the inhibitory, but not excitatory transmission, suppressed or even blocked network oscillations both in vitro and in vivo, leading to the desynchronization of pyramidal cell firing. Using paired recordings we demonstrated that carbachol application blocked GABA release from RSBCs and reduced it from FSBCs and AACs, whereas DAMGO further suppressed the GABA release only from FSBCs, but not from AACs.

These results collectively suggest that the rhythmic perisomatic inhibition, generating oscillatory fluctuation in local field potentials after carbachol treatment of hippocampal slices, is the result of periodic GABA release from FSBCs.

Introduction

Cortical activities are organized and temporally segmented by several overlaid and embedded oscillations with different frequencies (Steriade, 2006). In awake brain, oscillations at gamma frequencies (30-100 Hz) recorded in different cortical areas have been found to emerge during sensory encoding, neuronal assembly formation, or memory storage and retrieval (Tiitinen et al., 1993; Sederberg et al., 2003; Montgomery and Buzsaki, 2007). The importance of gamma oscillations has been emphasized in cognitive processes such as feature binding (Singer, 1993), and in changes of synaptic weights, since they could provide a temporal frame for spike time-dependent plasticity (Paulsen and Moser, 1998). Although some insights into mechanisms of these rhythmic activities have been recently achieved (Hájos and Paulsen, 2009), the identity of inhibitory neuron types involved in the oscillogenesis is not yet established unequivocally.

One of the most studied in vitro models of gamma oscillations is the carbachol (CCh)-induced network oscillation in the CA3 area of the hippocampus, that is a brain region capable of intrinsically generating rhythmic activities in vivo and in slices (Fisahn et al., 1998; Csicsvari et al., 2003; Maier et al., 2003). It was proposed that gamma oscillations are the result of the precisely timed feedback interaction among pyramidal cells and GABAergic interneurons (Hájos et al., 2004; Mann et al., 2005; Oren et al., 2006). Current source density analysis combined with imaging of membrane potential fluctuation of pyramidal cells revealed that local field potentials are primarily generated by perisomatic inhibitory currents (Mann et al., 2005).

Perisomatic inhibitory interneurons (Freund and Katona, 2007; Klausberger and Somogyi, 2008) that synapse on the proximal dendrites and somatas of principal neurons or on their axon initial segments, are in strategic position to control action potential generation (Cobb et al., 1995; Miles et al., 1996). In cortical structures, three types of these GABAergic

cells can be identified: the parvalbumin (PV) containing fast-spiking basket cells (FSBCs) and axo-axonic cells (AACs), as well as the cholecystokinin (CCK) expressing regular-spiking basket cells (RSBCs, Freund and Katona, 2007). Any of them could potentially contribute to oscillogenesis at gamma frequencies. Recent studies modifying the behavior of PV-containing inhibitory neurons using molecular biological techniques demonstrated the importance of these GABAergic cells in the generation of gamma oscillation (Fuchs et al., 2007; Cardin et al., 2009). However neither approach could differentiate between the contribution of FSBCs and AACs, since both cell types express PV. In addition, the participation of CCK-expressing RSBCs to oscillogenesis has not been addressed either.

In this study, we aimed to clarify the involvement of these three types of interneurons in the generation of CCh-induced network oscillation (Oren et al., 2010). To reveal the firing properties of distinct neuron types during oscillation, we recorded local field potentials and spiking activity of identified inhibitory neurons from hippocampal slices. Using paired recordings from perisomatic inhibitory interneurons and pyramidal cells as well as pharmacological manipulations of oscillation, we found that FSBCs are responsible for most of the perisomatic inhibitory currents during the CCh-induced oscillations in the CA3 region of the hippocampus.

Materials and Methods

All experiments were carried out in accordance with the Hungarian Act of Animal Care and Experimentation (1998. XXVIII. section 243/1998), and with the guidelines of the institutional ethical code.

Transgenic animals: Two transgenic mouse strains were used to selectively obtain recordings from perisomatic inhibitory cells. FSBCs and AACs were sampled in a strain, where EGFP expression was controlled by PV promoter (Meyer et al., 2002), whereas RSBCs were recorded in another strain, where EGFP was expressed under GAD65 promoter (López-Bendito et al., 2004). In addition, μ-opiate receptor (MOR) knockout mice (Matthes et al., 1996) were used to test the specificity of DAMGO effects, which were compared to the effects obtained in their wild-type littermates.

In vitro electrophysiological experiments: C57/Bl6 mice of both sexes (P15-22) were deeply anaesthetized with isoflurane and decapitated. Following decapitation, the brain was quickly removed into ice-cold cutting solution containing (in mM): sucrose, 252; KCl, 2.5; $NaHCO_3$, 26; $CaCl_2$, 1; $MgCl_2$, 5; NaH_2PO_4, 1.25; glucose, 10, bubbled with carbogen gas. Horizontal hippocampal slices were prepared using a Leica VT1000S or VT1200S microtome (Leica, Nussloch, Germany), and placed into an interface-type holding chamber containing standard ACSF at 35 ºC that gradually cooled down to room temperature (~1-1.5 h). To induce oscillations with carbachol (CCh), 300-350 μm thick slices were cut. To characterize cellular interactions from identified cell pairs or other mechanisms of DAMGO actions, we cut 200-250 μm thick slices to reduce the connectivity in the slice, since the high spontaneous activity evoked by CCh could have influenced the analysis of synaptic events.

The standard ACSF had the following composition (in mM): 126 NaCl, 2.5 KCl, 1.25 NaH_2PO_4, 2 $MgCl_2$, 2 $CaCl_2$, 26 $NaHCO_3$, and 10 glucose, prepared with ultra pure water and bubbled with 95% O_2/ 5% CO_2 (carbogen gas), pH 7.2-7.4. Recordings from cell pairs and the measurements of synaptic currents were made in a submerged-type slice chambers (Luigs & Neumann, Ratingen, Germany), while oscillations were induced in a dual-superfusion chamber (Supertech Ltd., Pecs, Hungary) at room temperature with a flow rate of 2-4 ml/min.

Oscillations were induced by bath application of 5 μM CCh. Patch pipettes (≈ 4-6 MΩ) filled with ACSF were used to monitor local field potentials and action potentials extracellularly. The field pipette was placed in str. pyramidale of CA3. To record from identified interneuron subtypes slices were cut from transgenic animals. EGFP-expressing neurons were identified using epifluorescence and differential interference contrast on an Olympus BX61 (Japan) microscope. A second pipette was used to record spiking activity in a loose patch configuration from the visually identified neurons. Action potentials were recorded for at least 60 s. The pipette was then withdrawn from the slice, and the same cell was patched with a new pipette filled with intrapipette solution containing (in mM): K-gluconate 138; CsCl 3; phosphocreatine 10; ATP 4; GTP 0.4; HEPES 10; QX-314 0.2; biocytin 3 mg/ml, adjusted to pH 7.3-7.35 using KOH (285-290 mOsm/l). Whole-cell series resistance was in the range of 5-15 MΩ. Both extracellular and whole-cell recordings were done with a Multiclamp 700B amplifier (Axon Instruments, Foster City, California), with exception of experiments presented in Supplementary fig. 7, where field potentials were recorded with a BioAmp amplifier (Supertech Ltd., Pecs, Hungary). To detect EPSCs more reliably in pyramidal cells during oscillation, picrotoxin (600-650 μM) was included in the pipette solution (Nelson et al., 1994). Voltage measurements were not corrected for a junction potential. Both field and unit recordings were low-pass filtered at 2 kHz using the built-in Bessel filter of the amplifier. Data was digitized at 6 kHz with a PCI-6042E board (National

instruments, Austin, Texas) and recorded with EVAN 1.3 software (courtesy of Prof. I Mody, UCLA, CA). All data was analyzed off-line using custom-made programs written in MATLAB 7.0.4 (Natick, MA) and Delphi 6.0.

Calculating peak-to-peak amplitude of the oscillation: To calculate the amplitude of the oscillation, an amplitude distribution histogram was made on a 60 second 1 Hz high-pass filtered section of the recording. The voltage range containing 95% of the points were used as peak-to-peak amplitude.

Firing phase calculation: A custom written firing phase detection algorithm was used. Spikes recorded in a loose patch mode were detected by manually setting threshold on unfiltered trace. The negative peak of the trough of the oscillation was considered as phase zero. However, the position of the negative trough of an oscillation depends on how the original signal is filtered. In in vivo studies (Buzsaki et al., 2003) for gamma detection the field potential is filtered with a relatively narrow (30-80 Hz) band-pass filter. Filtering at such a low frequency distorts the shape of the gamma oscillation, makes the original asymmetric wave shape symmetric, similar to a harmonic oscillation (Supplementary fig. 4b). We, therefore detected the negative peak of the oscillation on field potentials band-pass filtered with an RC filter between 5 and 500 Hz.. We chose the negative peak of the oscillation as zero, because it has functional significance. Pyramidal cells start to fire in high synchrony in this phase (Hájos et al., 2004; Mann et al., 2005; Oren et al., 2006). Also at this point the extracellular potential rises very quickly and defines phase zero very well. If the signal is low-pass filtered at gamma frequencies (as in the in vivo studies), this sharp negative peak will disappear and the position of the zero phase will be influenced by potential changes

throughout the full cycle as well as by variable gamma cycle length (Atallah and Scanziani, 2009) all spoiling functionally meaningful zero phase definition.

The phase of individual spikes was specified by calculating the position of the unit spikes in relation to two subsequent negative phase time. Here again care has to be taken, since the amplitude and the instantaneous frequency of the oscillation vary, and often the detection algorithm might skip one or more oscillation cycles. This would result in an erroneous shift in spiking phase towards zero.

Therefore, our spike phase detection algorithm checked for the actual detected cycle length and assigned a phase to a spike only, if the actual cycle length did not differ from the mean of the average cycle length more than a chosen fraction of the standard deviation of the cycle length. Heuristically we found that if we chose 0.3 STD, we get feasible phase calculation. If there is no oscillation length checking, as a result of the skipped cycles, firing phase is shifted toward zero. If the detection algorithm is too strict (not allowing jitter) spikes during short or long oscillatory cycles are discarded (can be rather high portion), the phase coupling will be very high, but does not represent physiological values.

Since the oscillations in our experiments had the mean frequency of 15.2 ± 0.5 Hz (n=15) at room temperature, to relate our results to in vivo data we mimicked the narrow BP filtering with a 5-30 Hz BP filter and calculated the phase of the spikes this way, too. The cell groups showed the same overlap in their phase but firing phase were shifted in the positive direction (due to the fact that low-pass filtering of the saw teeth like oscillations shifts the negative peak to the negative direction).

In vivo recordings: Adult mice (n=4) were used for the in vivo experiments. In each animal, injections of DAMGO and saline were made into the CA3 area of the hippocampus in approximate stereotactic AP and ML coordinates: 3.0 and 3.0 mm. DV position (usually 3.0

mm) was identified by the electrophysiological recordings, guided by the appearance of the large amplitude gamma oscillations in local field potential (LFP) recordings. At the end of the experiments the animals were sacrificed and the brain was removed, histology confirmed the localization of the electrodes.

Anesthesia was induced in isoflurane atmosphere followed by the intramuscular injection of a mixture of ketamine and xylazine (100 mg/kg and 10 mg/kg respectively), maintained by repeated (approximately every 30 min) intramuscular administration of the same substance. Body temperature was kept at 37 °C with a heating pad. The head was held by a mouse adaptor affixed to a stereotaxic frame (David Kopf Instruments, Tujunga, CA, USA). Midline incision was made on the scalp exposing the skull, followed by retraction of the skin and craniotomy to expose a part of the left hemisphere. The dura was left intact and room temperature saline solution was used to prevent desiccation.

16 channel laminar multielectrodes equipped with two inner cannulae (40 µm diameter glass capillaries) were used to record field potentials and to deliver DAMGO and saline solution. The injector electrode was lowered through the intact dura to target the CA3 region using a microdrive. Interelectrode spacing was 100 µm, electrode site diameter was 25 µm, shaft diameter was 350 µm, the drug delivery site was located between contacts 10 and 11. The cannulae were attached to two calibrated micrometer driven 10 µL Hamilton syringes (Hamilton Company, Reno, NV) via a 250 µm inner diameter Tygon tube (Saint-Gobain, Akron, OH, USA). Separate cannulae were carefully forward and back filled with DAMGO and saline to avoid air bubbles in the tubes.

LFP (0.03 Hz-5000 Hz) was recorded from each of the 16 contacts, sampled at 20 kHz/channel rate with 16 bit precision (LabView, National Instruments, Austin, TX, USA) and stored on hard drive for off-line analysis. Current source density analysis (CSD) identifies synaptic/transmembrane generators of LFP, using high-resolution maps of simultaneously

recorded field potentials obtained across a laminated neural structure. Inhomogeneous conductivity was not taken into account, second spatial derivative was calculated by the nearest neighbor method, and high spatial frequency noise was reduced by Hamming-window smoothing (Ulbert et al., 2001). Artifact free single sweep CSD epochs (1024 ms long) were averaged (n>300) in the frequency domain to obtain the power spectrum. The spatial location of the largest CSD sinks in the gamma band was regarded as the indicator of the pyramidal layer. CSD power spectra before and after DAMGO (1 mM) and saline pressure injection (200-400 nl) were compared at this location using Student's paired t-test, significance level was set to p=0.001 (Scan4.3 Edit, Compumedics, Charlotte, NC, USA).

Paired recordings: The intrapipette solution used for the presynaptic perisomatic inhibitory cells contained (in mM): potassium-gluconate 110, NaCl 4, Mg-ATP 2, HEPES 40, GTP 0.3, 0.2% biocytin, adjusted to pH 7.3 using KOH (290 mOsm/l). Intracellular solution used for the postsynaptic pyramidal cells contained (in mM): CsCl 80, Cs-gluconate 60, $MgCl_2$ 1, Mg-ATP 2, NaCl 3, HEPES 10, and QX-314 5, adjusted to pH 7.3 with CsOH (295 mOsm/l). Presynaptic interneurons were held in a current clamp mode around -65 mV, and stimulated by brief current pulses (1.5 ms, 1-2 nA). Pyramidal cells were held in a voltage-clamp mode at a potential of -65 mV. Access resistance was frequently monitored and compensated between 65–75%, and cells that changed more than 25% substantially during recording were discarded from further analyzes. In experiments with CCh, occasionally 5 µM NBQX was added to the bath solution to reduce the high background activity, or eliminate oscillations. The effect of CCh on inhibitory transmission was tested at 2 and 5 µM in the pairs of fast-spiking interneurons and pyramidal cells, whereas CCh was added only in 5 µM for the pairs of RSBCs and pyramidal cells. We found that CCh in 2 µM and 5 µM indistinguishably reduced the IPSC amplitude compared to the control values for both FSBCs and AACs

(FSBC in 2 µM: 49.1 ± 6.9 % of control, n=6; in 5 µM: 42.3 ± 2.4 % of control, n=8, p=0.32; AAC in 2 µM: 31.9 ± 3.2 % of control, n=9; in 5 µM: 36.5 ± 5.8 % of control, n=8, p=0.49; t-test), therefore data within each group were pooled and compared with those data obtained in experiments of RSBC-pyramidal cell pairs.

Measurements of evoked and miniature events: In the presence of CCh, electrically-evoked or miniature IPSCs were pharmacologically isolated by bath application of 3 mM kynurenic acid to block ionotropic glutamate receptors. To isolate evoked EPSCs and to prevent epileptiform discharges in CA3, $GABA_A$ receptor-mediated currents were blocked intracellularly by including picrotoxin (600-650 µM) in the pipette solution. We experienced that 10-15 min was enough after break-in to eliminate IPSCs. To measure miniature events, 0.5 µM tetrodotoxin (TTX) was included in the bath solution.

Drugs: All salts and drugs were obtained from Sigma-Aldrich, except TTX, CTAP (d-Phe-Cys-Tyr-d-Trp-Arg-Thr-Pen-Thr-NH2) and DAMGO ([D-Ala^2,N-Me-Phe^4,Gly^5-ol]enkephalin acetate) that were purchased from Tocris. TTX, CTAP and DAMGO was dissolved in water in 100 mM concentration, and stored at -20 ºC.

Statistical analysis: Unless it is indicated, Student's paired t-test was used to compare the changes in IPSC amplitude, firing characteristics, cell membrane property parameters and oscillations power after drug application. Data are presented as mean ± SEM. The Kolmogorov–Smirnov (K–S) test was used to compare two cumulative distributions. Circular statistics was used to calculate cell firing phase and phase coupling. ANOVA was used to compare multiple data sets.

Anatomical identification of biocytin filled neurons. After intracellular recording and biocytin filling, the slices was fixed in 4 % paraformaldehyde in 0.1 M phosphate buffer (PB; pH 7.4) for at least 30 min, followed by washout with PB several times, and incubation in cryoprotecting solution (30 % sucrose in 0.01 M PB) for 2 hrs. Slices were then freeze-thawed three times above liquid nitrogen and treated with 1 % H_2O_2 in PB for 15 min to reduce endogenous peroxidase activity. For single stainings, filled cells were visualized using avidin-biotinylated horseradish peroxidase complex reaction (ABC; Vector Laboratories, Burlingame, CA) with nickel intensified with 3–3-diaminobenzidine tetrahydrochloride (0.05% solution in Tris buffer, pH 7.4; Sigma) as a chromogen giving a dark reaction product. After dehydration and embedding in Durcupan (Fluka), neurons were identified based on their dendritic and axonal arborization and some representative cells were reconstructed with the aid of a drawing tube using a 40x objective.

Fluorescent immunohistochemistry and electron microscopy: After recordings, the slices were fixed in a fixative containing 4% paraformaldehyde (PFA), in 0.1 M phosphate buffer (PB), pH 7.4, at 4°C. Before processing, the fixative was thoroughly washed out with 0.1 M PB. Slices were then cryoprotected in 30% sucrose, freeze-thawed over liquid nitrogen, embedded in agar, and re-sectioned at 60 µm thickness. Every third section was processed for electron microscopy: biocytin was visualized using the avidin–biotinylated–HRP complex (Vector Laboratories, Burlingame, CA) and 3–3-diaminobenzidine tetrahydrochloride (0.05% solution in Tris buffer, pH 7.4) as a chromogen. Sections were then postfixed in 1% OsO_4, stained in 1% uranyl acetate, dehydrated in a graded series of ethanol, and embedded in epoxy resin (Durcupan; Sigma). Ultrathin sections of 60 nm thickness were cut for EM, and the postsynaptic target of 5-10 boutons of each recorded cells were identified. The remaining sections were processed for fluorescent double labeling (see in detail in Lorincz and Nusser,

2008). They were treated with 0.2 mg/ml pepsin (Cat. No.: S3002; Dako) in 0.2 M HCl at 37°C for 5 min and were washed in 0.1 M PB. Sections were blocked in normal goat serum (NGS, 10%) made up in Tris-buffered saline (TBS, pH=7.4) followed by incubations in mouse anti-Ankyrin G (1:100, Santa Cruz Biotechnology) diluted in TBS containing 2% NGS and 0.3% Triton X-100. Following several washes in TBS, Cy3 conjugated goat anti-mouse(1:500, Jackson) was used to visualize the immunoreactions, and Alexa488 conjugated strepavidin (1:500; Molecular Probes) to visualize the biocytin. Sections were then mounted on slides in Vectashield (Vector Laboratories). Images were taken using an AxioImager.Z1. All interneurons recorded in PV-EGFP mice were identified with this method.

Results

Identification of inhibitory neurons innervating the perisomatic area of CA3 pyramidal cells using EGFP-expressing transgenic mice and immunostaining for ankyrin G

To study the role of the three types of perisomatic inhibitory interneurons (Figure 1) in the generation of CCh-induced oscillation, we used transgenic mice strains in which these neurons were selectively labeled with enhanced green fluorescent protein (EGFP). PV-containing interneurons (FSBCs and AACs) were identified in slices from mice, where EGFP expression was driven by PV promoter (Meyer et al., 2002), whereas RSBCs were targeted in slices from animals, where GAD65 promoter regulated the expression of EGFP (López-Bendito et al., 2004). During recordings all neurons were filled with biocytin and visualized *post hoc*. Only interneurons with axonal arbor restricted to the stratum (str.) pyramidale and inner str. radiatum and oriens were included in this study (Figure 1a). To unequivocally distinguish the FSBCs and AACs, we performed *post hoc* double immunofluorescent labeling for biocytin and the scaffolding protein ankyrin G. This protein anchors different channels,

including voltage-gated sodium channels (Nav1.2 and 1.6) in the axon initial segments (AIS) of neurons, allowing their selective visualization at light microscopic level (Jenkins and Bennett, 2001).

From a total number of 61 PV-EGFP cells recorded in different sets of experiments, in 30 cases the biocytin filled boutons were localized to str. pyramidale and only rarely approached ankyrin G-stained profiles (Figure 1c_{1-3}) suggesting their FSBC origin. Conversely, in the remaining 31 cases the axonal arbor was densest in the str. pyramidale and neighboring str. oriens border, and the boutons formed close appositions with ankyrin G-immunoreactive segments, often in climbing-fiber manner, alike to AAC's axon terminals (Figure 1d_{1-2}). To identify the postsynaptic target of these cells, we performed electron microscopic examination on consecutive sections. In those cases where the immunofluorescent reaction showed only rare appositions, boutons mostly synapsed on pyramidal cell soma and proximal dendrites (n=5; Figure 1c_4, and Supplementary fig. 1), whereas in those cases where tight appositions were visible, boutons synapsed exclusively on AISs of the principal neurons (n=5; Figure 1d_{3-4}, and Supplementary fig. 1) that can be unequivocally identified upon having membrane undercoating and microtubule fascicles (Somogyi et al., 1983). As electron microscopic examination verified the double immunofluorescent labeling as a powerful tool for the identification of FSBCs and AACs, the remaining 25 FSBCs and 26 AACs were identified only with this method.

Perisomatic inhibitory cell types have distinct firing characteristics during CCh-induced network oscillations

To induce oscillatory activity 5 µM CCh was bath applied and the local field potential was monitored extracellularly with an electrode placed in str. pyramidale. After a 10-15 min-long period, necessary for the full development of oscillations (Hájos et al., 2009), the local

field potentials were recorded. To achieve necessary oxygenation of neurons, experiments were conducted at room temperature. Under these conditions, the peak-to-peak amplitude of the CCh-induced oscillations was 147.6±7.12 μV with a power peak at 15.2±0.5 Hz (n=15). Although the frequency of CCh-induced oscillations at room temperature is in the beta frequency band (13-30 Hz), it falls into the gamma frequency range if recorded at higher temperature (see Supplementary fig. 2, 3) (Fisahn et al., 1998; Hájos et al., 2004). All other features of CCh-induced oscillations at room temperature and during temperatrure transitions resemble gamma oscillations recorded in vitro at 30-35 ºC or in vivo (Csicsvari et al., 2003; Mann et al., 2005; Hájos and Paulsen, 2009).

First, we examined the firing properties of the three types of perisomatic inhibitory interneurons in CA3 during cholinergically-induced oscillatory activities. We recorded the spontaneous firing properties of EGFP expressing neurons in a loose patch mode (Figure 2a, b). Using a whole-cell configuration, the same cell was then re-patched and filled with biocytin for *post hoc* identification. Analysis of the results revealed that during oscillations the firing of the three cell types differed (Figure 2b-f, Table 1). FSBCs fired single spikes almost at each oscillation cycle, in contrast to AACs and RSBCs that often skipped cycles (Figure 2b, c). On average, FSBCs discharged two action potentials (i.e. doublets) in every tenth cycle, AACs only occasionally fired doublets, while RSBCs very rarely did so (Figure 2d). The phase of the action potentials (zero set to the negative peak of the oscillation recorded in str. pyramidale) of different cell types did not prove to be a distinguishing feature, since cells fired on the ascending phase of oscillations with their preferred phase varying within overlapping ranges (Figure 2e see also Supplementary fig. 4a). In contrast, there was a difference in the phase-coupling strength of the three cell types (Figure 2f). FSBCs fired with high accuracy around the phase characteristic for the individual cells. The firing of AACs was

less coupled to the oscillation, and RSBCs proved to be significantly less accurate in their firing than the other two cell types.

In summary, during CCh-induced synchronous activities in hippocampal slices, FSBCs were the most active perisomatic inhibitory cells, often fired doublets in a cycle, and their action potentials were the most strongly coupled to the oscillation.

DAMGO reduces CCh-induced network oscillations via μ-opioid receptors

Previous data showed that morphine could disrupt long-range synchrony of gamma oscillations in hippocampal slices via μ-opioid receptors (MOR)(Whittington et al., 1998). Since this type of opioid receptors are selectively expressed on PV-immunopositive axon terminals (Drake and Milner, 2002) and their activation effectively reduced GABA release from fast-spiking interneurons with a much smaller effect on the inhibitory transmission of RSBCs (Glickfeld et al., 2008), activation of MORs could be a useful tool to separate the contribution of RSBCs from that of PV-containing perisomatic inhibitory cells in oscillogenesis.

First, we tested whether the activation of MORs could interfere with gamma oscillation recorded in vivo. To this end, we monitored local field potentials in anesthetized mice using a 16 channel laminar multielectrode equipped with two inner cannulae for solution applications. After obtaining the control period, 200-400 nl of saline or DAMGO (1 mM) was applied. Following DAMGO application occasional interictal like activity appeared with variable delays (10-60sec) in the recordings. Analysing sections free of interictal episodes we found that DAMGO significantly ($p<0.001$) reduced the CSD gamma band power in the pyramidal cell layer, while saline did not induce significant changes (Figure 3). These results indicate that DAMGO can effectively reduce gamma oscillations in the CA3 region of the intact hippocampus.

Next, we aimed to clarify how the MOR activation by DAMGO leads to the suppression of gamma oscillations. Therefore, we induced network oscillations by bath application of 5 µM CCh in hippocampal slices. To reproduce our in vivo findings, 1 µM DAMGO was added to the superfusate. This treatment effectively reduced the power or even fully eliminated the CCh-induced oscillations within 2-8 minutes both at room temperature (Figure 4, left) or at 32-34 ºC (Supplementary fig. 5). To test the specificity of DAMGO action, CTAP, a MOR antagonist was applied (200 nM) for 5 minutes preceding DAMGO. CTAP alone did not change the parameters of the oscillation, suggesting the lack of tonic MOR activation in our slice preparations, but prevented the effect of subsequently applied DAMGO (Supplementary fig. 6). If CTAP was applied after DAMGO-induced drop in oscillation power, it could fully reverse the effect of DAMGO in 5-10 minutes (Supplementary fig. 6). To further confirm that DAMGO acted exclusively via MORs, we repeated the experiments in MOR knockout mice. We found no difference in the peak power (WT: 164.9±26.3 μV^2/Hz, n=44; KO: 161.17±38.2 μV^2/Hz, n=19; Mann-Whitney test; p=0.98) or in the frequency of network oscillations (WT: 15.1±0.7 Hz, n=44; KO: 16.5±0.8 Hz, n=19; Mann-Whitney test; p=0.12) between the KO and wild-type animals. In mice lacking MORs, DAMGO application had no detectable effect on the power and the frequency of the oscillations (Figure 4, right). Thus, these data showed that DAMGO could effectively suppress CCh-induced oscillation, an effect that was mediated solely via MORs.

DAMGO application suppresses synaptic inhibition, which desynchronizes, but does not decrease pyramidal cell activity

Field oscillations can break down either because the activity of neurons decreases and thus, currents responsible for the generation of the rhythmic field potentials disappear; or the firing of neurons desynchronizes and the currents do not sum up to give a detectable field

signal. To get a deeper insight into the mechanisms how DAMGO blocks oscillations and to distinguish these two possibilities, first we recorded local field potentials in str. pyramidale and simultaneously monitored multiunit activity that reflects mostly pyramidal cell firing (Figure 5). Whilst the peak power of oscillations was significantly reduced by DAMGO application (CCh: 86.4 ± 17.8 μV^2/Hz, CCh+DAMGO: 18.6 ± 5.4 Hz, n=5, p=0.006), the frequency of multiunit firing did not change (CCh: 26.2 ± 9.3 Hz, CCh+DAMGO: 24.2 ± 9.1 Hz, n=5, p=0.54), but remarkably, unit synchrony disappeared as shown by the multiunit autocorrelograms (Figure 5). Though we could not identify the neurons participating in the multiunit spike assembly, they fired earlier in the oscillation phase (Phase: 2.96 ± 1.13 degree, Phase-coupling strength: 0.67 ± 0.054, n=5) than the interneurons (see Table 1), indicating that they were pyramidal cells (Hájos et al., 2004).

In the next set of experiments, we monitored local field potentials in str. pyramidale as well as excitatory (EPSCs) and inhibitory postsynaptic currents (IPSCs) from two pyramidal cells (Supplementary fig. 7). The originally synchronized, phase-locked, large amplitude compound IPSCs decreased, or, as in the experiment shown in Supplementary fig. 7, largely fell below the detection threshold by DAMGO application (Supplementary fig. 7, bottom). Since the currents generating CCh-induced oscillations in the hippocampus predominantly originate from perisomatic inhibitory synapses (Mann et al., 2005; Oren et al., 2010), parallel to the IPSC amplitude decrease, the power of the oscillations also dropped, or completely disappeared (Supplementary fig. 7, top). During this transition, there was a much smaller change in the amplitude or in the frequency of EPSCs (or in the charge per cycle). However, the synchrony of the excitatory events decreased and disappeared as shown on autocorrelograms (Supplementary fig. 7, middle).

These results together suggest that after the suppression of CCh-induced oscillations caused by DAMGO, pyramidal cell activity is mostly maintained, but their spikes are no

longer phase locked to the oscillations due to the disappearance of periodic inhibitory control. Thus, the reduction of synaptic inhibition by DAMGO could decrease or abolish CCh-induced network oscillations.

DAMGO exerts its effect by reducing inhibitory transmission, but leaves excitatory transmission and pyramidal cell properties intact

The finding that DAMGO reduces synaptic inhibition is in agreement with earlier results (Cohen et al., 1992; Masukawa and Prince, 1982). However, to clarify the mechanisms underlying the effect of MOR activation on oscillation, we aimed to determine whether DAMGO exerts additional effects on the elements of CA3 neuronal network. First, we tested the effects of DAMGO on the basic properties of CA3 pyramidal cells. These neurons showed no significant change in their input resistance (in CCh: 370.0±25.5 MOhm, in CCh + DAMGO: 355.5 ± 9.83 MOhm; n=5; p=0.53) or in their membrane time constant (in CCh: 88.6 ± 8.58 ms, in CCh + DAMGO: 90.5 ± 16.0 ms, n=5; p=0.89). We then examined the effects of DAMGO on evoked and miniature postsynaptic currents. As shown in Figure 6, in CA3 pyramidal cells DAMGO application caused a significant reduction in the amplitude of IPSCs evoked by electrical stimulation of fibers in str. pyramidale or at the border of strata pyramidale and lucidum. In contrast, MOR activation had no effect on EPSC amplitude evoked with the stimulation of fibers in str. radiatum. Similarly, in CA3 pyarmidal cells a decrease was detected in the frequency of miniature IPSCs (mIPSCs) following DAMGO application, without a change in their amplitude distribution. No change could be detected in the frequency or amplitude of miniature EPSCs (mEPSCs). For more details see Supplementary fig. 8. Last, we examined whether the excitatory input on interneurons expressing PV could be affected by DAMGO. Similarly to the results obtained in CA3 pyramidal cells, the activation of MORs had no effect on the amplitude of evoked EPSCs

recorded in three fast spiking basket cells and two axoaxonic cells (in CCh: 202.7 ± 59.1 pA, in CCh + DAMGO: 214.8 ± 73.3, n=5, p=0.72).

These results collectively demonstrated that DAMGO suppresses only inhibitory transmission, without affecting the excitatory synaptic communication and pyramidal cell excitability in the presence of CCh.

Cholinergic receptor activation differentially decreases transmitter release from perisomatic inhibitory cells

Our pharmacological experiments strengthened the hypothesis that PV-immunopositive perisomatic inhibitory cells expressing MORs could have a role in oscillogenesis. However, DAMGO caused a small, but significant reduction in the IPSC amplitude recorded in RSBC-pyramidal cell pairs (Glickfeld et al., 2008), thus the contribution of IPSCs to the perisomatic inhibitory currents generating CCh-induced network oscillations cannot be completely ruled out. Since all three types of perisomatic inhibitory interneurons fired at a similar phase of the oscillation cycles (though with different frequency and precision, Table 1), each cell group, in principle, could indeed contribute to the inhibitory currents, if GABA were released from their axon terminals under the conditions of CCh-induced oscillation. To address the question to what extent IPSCs originating from the three interneuron types might contribute to active current sources in the pyramidal cell layer (Mann et al., 2005), we examined their release properties in the presence of 5 μM CCh used to induce oscillations in this study.

We performed paired whole-cell recordings from presynaptic interneurons and postsynaptic pyramidal cells in the CA3 region (Figure 7a). Regardless of the cell type, CCh application decreased the amplitude of postsynaptic currents. In the absence of CCh the IPSCs of FSBCs and AACs showed short-term depression, the IPSCs of RSBCs did not. To

approximate the conditions to continuous firing during on-going oscillation, we compared the amplitude of the last five IPSCs, when the synaptic depression in FSBC- and AAC-pyramidal cell pairs reached steady state levels (Figure 7b). Statistical analysis revealed that CCh significantly ($p<0.001$) suppressed the amplitude of the last five IPSCs in a cell-type specific manner (Figure 7c). Almost full reduction of IPSC amplitude was observed in RSBC-pyramidal cell pairs, whereas CCh exerted a smaller inhibition on the amplitude of IPSCs of AACs and FSBCs. The degree of reduction was significantly different among cell types ($p<0.001$).

In line with earlier data (Neu et al., 2007; Fukudome et al., 2004), depression at synapses between RSBCs and pyramidal cells by CCh was the result of the activation of CB_1 cannabinoid receptors (CB_1R), since bath application of a CB_1R antagonist, AM251 (1 μM) reversed the silencing effect of cholinergic receptor activation on IPSC amplitude (in CCh: 23.6±16.1 % of control; in CCh + AM251: 89. 4±19.5 % of control, n= 4, p=0.04).

These results suggest that, while RSBCs do fire during CCh-induced network oscillation, the GABA release from their axon terminals is almost completely muted as a result of CB_1R activation. Thus, the IPSCs originating from RSBCs can only minimally contribute to active current sources, therefore, these perisomatic inhibitory cells do not play an active role in the generation of synchronous activities induced by cholinergic receptor activation.

DAMGO differentially affects GABA release from FSBCs and AACs in the presence of CCh

Immunocytochemical results showed that MORs are expressed in PV-immunopositive axon terminals synapsing on the somata or on the proximal dendrites of hippocampal pyramidal cells, but in the axon endings contacting axon initial segments the presence of

MORs is questionable, as stated by Drake and Milner (2002). Since RSBCs do not participate in perisomatic current generation here, these data propose that the effect of DAMGO on oscillation could be due to the reduction of GABA release predominantly, if not exclusively from the axon terminals of FSBCs.

To separate the possible contribution of FSBCs and AACs to oscillation generation, we subsequently applied DAMGO (together with CCh) after CCh treatment in paired recordings (see above). The amplitude of the last five IPSC in FSBC-pyramidal cell pairs were significantly depressed compared to the amplitude in the presence of CCh, but there was no further reduction in IPSC amplitudes observed in AAC-pyramidal pairs (Figure 8a,b). Interestingly, the IPSC amplitude of FSBCs in the mixture of CCh and DAMGO was not significantly different from the IPSC amplitude of AACs in the presence of CCh or in CCh plus DAMGO ($p=0.15$, Figure 8c).

These data demonstrate that in the presence of CCh DAMGO selectively suppressed GABA release from axon terminals of FSBCs, but not of AACs, and thus, synaptic output of FSBCs is the major source of the perisomatic inhibitory currents, which generates CCh-induced field oscillation.

Discussion

In the present study we provided several lines of evidence converging to the conclusion that FSBCs, but not RSBCs or AACs, play a central role in the generation of rhythmic field activities induced by CCh in hippocampal slices: 1) during CCh-induced network oscillations FSBCs fired the most with the highest accuracy compared to the discharge of AACs and RSBCs; 2) at the CCh concentration used to induce network oscillations, IPSCs of RSBCs were nearly completely eliminated, while IPSCs exerted by FSBCs and AACs were also reduced to a different extent; 3) the MOR agonist DAMGO,

which effectively blocked oscillations in vitro and in vivo, selectively reduced inhibitory currents of FSBCs, but not of AACs in the presence of CCh.

The three types of perisomatic inhibitory interneurons fire within the same time window, but with different phase coupling precision during CCh-induced network oscillation

The analysis of the firing phases of cells (Figure 2) showed that there is a considerable variation in the preferred firing phase of individual neurons within each type and thus, activity of the populations overlap. Most of the cells fire 0 to 60 degrees after the negative peak of the oscillations (i.e. in the ascending phase, measured in str. pyramidale), following the discharge of pyramidal cells, consistently with the synaptic feedback model of pharmacologically-induced oscillations in CA3 either in hippocampal slices (Hájos et al., 2004; Gloveli et al., 2005; Mann et al., 2005; Hájos and Paulsen, 2009) or in in vivo gamma (Csicsvari et al., 2003; Atallah and Scanziani, 2009). Based on population averages, FSBCs fired somewhat earlier, but the differences did not reach significance level. While the phase of firing did not differ among the three cell groups, their phase locking was distinct. FSBCs showed the strongest phase locking (0.8 ± 0.04) and RSBCs the weakest (0.49 ± 0.06). These differences found in the spiking accuracy of the two basket cell types match earlier findings. PV-containing basket cells (FSBCs) have a narrow input integration window, precise input-output relationship, and synchronized transmitter release, in contrast to CCK-immunopositive basket cells (RSBCs) that have a wider input integration window, their firing is less accurate, and show asynchronous, delayed GABA release (Glickfeld and Scanziani, 2006; Hefft and Jonas, 2005; Daw et al., 2009). Regardless whether the cells fire with high accuracy or not, since the preferred phase of individual cells within each population overlap, and a large number of perisomatic inhibitory cells converge onto a single pyramidal cell, principal neurons receive

inhibitory currents during the first half of the gamma cycle both in vitro and in vivo (Atallah and Scanziani, 2009; Hájos and Paulsen, 2009)

We found that the phase coupling of the three types of perisomatic inhibitory interneurons in CA3 was considerably higher (0.80-0.49) than measured in the CA1 area in vivo during gamma oscillations (0.23-0.07)(Klausberger and Somogyi, 2008)·(Tukker et al., 2007). Still, the relative modulation depth of firing of these cell types is similar in vivo and in vitro, since FSBC had the highest modulation, while RSBCs the lowest.

Several explanations can be proposed for the difference in the modulation depths: 1) In vitro the strength of gamma modulation of interneuronal firing in the CA1 area is weaker than in the CA3 area (unpublished observations), most probably because gamma activity is generated in CA3 and only spreads into CA1 (Csicsvari et al., 2003); 2) Differences in the recording and signal processing methods used in in vivo and in this study; 3) In vivo there are several network activity patterns embedded in each other that might result in weaker modulation of neuronal activity in the gamma band, since subsequent gamma cycles are occurring at different phases of the carrier activities; 4) Though, we induced CCh-evoked network oscillations with a lower concentration of agonist than in earlier studies, in our slices the synchrony of oscillations and therefore, the accuracy of cell firing can be still higher than in vivo.

Activation of cholinergic and MORs differentially regulates synaptic inhibition mediated by GABAergic cells

Our experiments revealed that during CCh-induced network oscillations in slices, the inhibitory transmission of the three types of perisomatic inhibitory cells (and of different other inhibitory cell types) is modulated to a different extent. Application of CCh mimics high cholinergic tone present during theta-associated behavior with theta-embedded gamma

oscillations (Marrosu et al., 1995; Buzsaki et al., 2003). Thus, the demonstrated tuning of different inhibitory circuits, among other effects, might play an important role in switching the hippocampal network from one state to another.

In addition to perisomatic inhibitory cells, a dendrite-targeting GABAergic cell type, the bistratified cells had been suggested to contribute to oscillogenesis, since their firing was found to be highly modulated by gamma oscillations in in vivo recordings (Tukker et al., 2007). However, it is a question whether bistratified cells release transmitter at elevated cholinergic tone and thus participate in the generation of CCh-induced oscillations? To examine this issue directly, we recorded synaptically coupled bistratified cell-pyramidal cell pairs in the CA3 region of the hippocampus. The bath application of 5 µM CCh profoundly reduced the IPSC amplitude measured in these pairs (11.9 ± 7.4 % of control amplitude, n=5, $p < 0.001$), showing that in cholinergically-induced oscillations in hippocampal slices bistratified cells cannot significantly contribute to the oscillogenesis.

In line with previous findings (Neu et al., 2007; Fukudome et al., 2004), CCh application largely eliminated GABA release from axon terminals of RSBCs, an effect that was mediated via CB_1Rs. These data suggest that IPSCs from RSBCs are not crucial for oscillogenesis, at least in oscillations generated with high cholinergic tone in vitro. This suggestion is consistent with the idea that the imprecise input-output function of RSBCs are poorly suited to operate at high frequencies (Hefft and Jonas, 2005; Glickfeld and Scanziani, 2006). The reduction of IPSC amplitude from FSBCs and AACs after CCh application is likely due to the activation of M2 cholinergic receptors located on their presynaptic terminals (Hájos et al., 1998; Fukudome et al., 2004).

Our data obtained from paired recordings showed that MOR activation further reduced the GABA release from FSBCs, but did not influence the release of AACs in the presence of CCh. These electrophysiological data agree with the results obtained with

immunocytochemistry, showing the presence of MORs at the axon terminals of FSBCs, but their lack at the axon endings of AACs (Drake and Milner, 2002).

FSBCs are responsible for most of the perisomatic rhythmic currents generating CCh-induced network oscillations

Since high cholinergic tone mutes GABA release from the axon terminals of RSBCs, the rhythmic discharge of PV-containing perisomatic inhibitory cells remains the only possible source for perisomatic inhibitory currents generating oscillations in local field potentials. This conclusion is supported by recent experiments in vivo, in which optically driven PV-containing interneurons in neocortex amplified gamma oscillations (Cardin et al., 2009). Our experiments with DAMGO further differentiated the role of PV-containing FSBCs and AACs in oscillogenesis. The fact, that DAMGO potently blocks network oscillation, by selectively reducing GABA release from the axon terminals of FSBCs in the presence of CCh, supports the key role of FSBCs in the generation of rhythmic inhibitory currents that temporally structure the oscillation in CCh-induced synchronous activities in CA3.

The question arises whether DAMGO would be able to suppress the CCh-induced oscillation, if the GABA release was normal from the axon terminals of RSBCs, i.e. when the firing of RSBCs would give rise to IPSCs during oscillations. To clarify this issue, we induced oscillations with CCh in hippocampal slices prepared from CB_1R knockout mice, where CCh does not alter the GABA release of RSBCs (Neu et al., 2007). Comparable to those results obtained in wild type mice, DAMGO could reduce, or even eliminate the CCh-induced oscillations in slices from these knockouts (Supplementary fig. 9). This finding further supports our main conclusion that fast spiking basket cells alone can generate oscillations in the cholinergic model of oscillations, even if the function of RSBCs is intact.

As DAMGO suppressed the oscillation, the pyramidal cell firing and consequently the EPSCs became desynchronized as a result of elimination of phasic inhibition originating from FSBCs. Thus, DAMGO did not diminish activity in the CA3 network, only let pyramidal cells to discharge without rhythmic entrainment, i.e. out of synchrony. This observation suggests that endogenously released opioids might set the level of synchrony and thereby the mode of information processing in the hippocampus. Since dynorphin is present in the mossy terminals of dentate granule cells (Torres-Reveron et al., 2009), that are located adjacent to the MOR-expressing axon terminals of FSBCs, one might speculate that dynorphin release during highly synchronized activities in the dentate gyrus might contribute to the feed-forward suppression of oscillations in CA3 (Bragin et al., 1995b, 1995a).

In conclusion, our data indicate that FSBCs represent the most important inhibitory component of the network that generates oscillation in the presence of CCh. Our experiments also revealed a possible mechanism how opiates interfere with oscillogenesis and thus with cognitive functions (Smith et al., 1962; Braida et al., 1994; Whittington et al., 1998).

LIST OF REFERENCES

Atallah BV, Scanziani M (2009) Instantaneous Modulation of Gamma Oscillation Frequency by Balancing Excitation with Inhibition. Neuron 62:566-577

Bragin A, Jandó G, Nádasdy Z, van Landeghem M, Buzsáki G (1995a) Dentate EEG spikes and associated interneuronal population bursts in the hippocampal hilar region of the rat. J. Neurophysiol 73:1691-1705

Bragin A, Jandó G, Nádasdy Z, Hetke J, Wise K, Buzsáki G (1995b) Gamma (40-100 Hz) oscillation in the hippocampus of the behaving rat. J Neurosci 15:47-60

Braida D, Gori E, Sala M (1994) Relationship between morphine and etonitazene-induced working memory impairment and analgesia. Eur. J. Pharmacol 271:497-504

Buzsaki G, Buhl D, Harris K, Csicsvari J, Czeh B, Morozov A (2003) Hippocampal network patterns of activity in the mouse. Neuroscience 116:201-11

Cardin JA, Carlén M, Meletis K, Knoblich U, Zhang F, Deisseroth K, Tsai L, Moore CI (2009) Driving fast-spiking cells induces gamma rhythm and controls sensory responses. Nature Available at: http://www.ncbi.nlm.nih.gov/pubmed/19396156 [Accessed May 11, 2009].

Cobb S, Buhl E, Halasy K, Paulsen O, Somogyi P (1995) Synchronization of neuronal activity in hippocampus by individual GABAergic interneurons. Nature 378:75-8

Cohen GA, Doze VA, Madison DV (1992) Opioid inhibition of GABA release from presynaptic terminals of rat hippocampal interneurons. Neuron 9:325-335

Csicsvari J, Jamieson B, Wise K, Buzsaki G (2003) Mechanisms of gamma oscillations in the hippocampus of the behaving rat. Neuron 37:311-22

Daw MI, Tricoire L, Erdelyi F, Szabo G, McBain CJ (2009) Asynchronous transmitter release from cholecystokinin-containing inhibitory interneurons is widespread and target-cell independent. J. Neurosci 29:11112-11122

Drake C, Milner T (2002) Mu opioid receptors are in discrete hippocampal interneuron subpopulations. Hippocampus 12:119-36

Fisahn A, Pike F, Buhl E, Paulsen O (1998) Cholinergic induction of network oscillations at 40 Hz in the hippocampus in vitro. Nature 394:186-9

Freund T, Katona I (2007) Perisomatic inhibition. Neuron 56:33-42

Fuchs EC, Zivkovic AR, Cunningham MO, Middleton S, Lebeau FEN, Bannerman DM, Rozov A, Whittington MA, Traub RD, Rawlins JNP, Monyer H (2007) Recruitment of parvalbumin-positive interneurons determines hippocampal function and associated behavior. Neuron 53:591-604

Fukudome Y, Ohno-Shosaku T, Matsui M, Omori Y, Fukaya M, Tsubokawa H, Taketo MM,

Watanabe M, Manabe T, Kano M (2004) Two distinct classes of muscarinic action on hippocampal inhibitory synapses: M2-mediated direct suppression and M1/M3-mediated indirect suppression through endocannabinoid signalling. Eur. J. Neurosci 19:2682-2692

Glickfeld L, Atallah B, Scanziani M (2008) Complementary modulation of somatic inhibition by opioids and cannabinoids. J Neurosci 28:1824-32

Glickfeld L, Scanziani M (2006) Distinct timing in the activity of cannabinoid-sensitive and cannabinoid-insensitive basket cells. Nat Neurosci 9:807-15

Gloveli T, Dugladze T, Saha S, Monyer H, Heinemann U, Traub R, Whittington M, Buhl E (2005) Differential involvement of oriens/pyramidale interneurones in hippocampal network oscillations in vitro. J Physiol 562:131-47

Hájos N, Pálhalmi J, Mann E, Nemeth B, Paulsen O, Freund T (2004) Spike timing of distinct types of GABAergic interneuron during hippocampal gamma oscillations in vitro. J Neurosci 24:9127-37

Hájos N, Papp E, Acsády L, Levey A, Freund T (1998) Distinct interneuron types express m2 muscarinic receptor immunoreactivity on their dendrites or axon terminals in the hippocampus. Neuroscience 82:355-76

Hájos N, Ellender TJ, Zemankovics R, Mann EO, Exley R, Cragg SJ, Freund TF, Paulsen O (2009) Maintaining network activity in submerged hippocampal slices: importance of oxygen supply. Eur. J. Neurosci 29:319-327

Hájos N, Paulsen O (2009) Network mechanisms of gamma oscillations in the CA3 region of the hippocampus. Neural Netw 22:1113-1119

Hefft S, Jonas P (2005) Asynchronous GABA release generates long-lasting inhibition at a hippocampal interneuron-principal neuron synapse. Nat Neurosci 8:1319-28

Jenkins SM, Bennett V (2001) Ankyrin-G coordinates assembly of the spectrin-based membrane skeleton, voltage-gated sodium channels, and L1 CAMs at Purkinje neuron initial segments. J. Cell Biol 155:739-746

Klausberger T, Somogyi P (2008) Neuronal diversity and temporal dynamics: the unity of hippocampal circuit operations. Science 321:53-7

López-Bendito G, Sturgess K, Erdélyi F, Szabó G, Molnár Z, Paulsen O (2004) Preferential origin and layer destination of GAD65-GFP cortical interneurons. Cereb. Cortex 14:1122-1133

Lorincz A, Nusser Z (2008) Cell-type-dependent molecular composition of the axon initial segment. J. Neurosci 28:14329-14340

Maier N, Nimmrich V, Draguhn A (2003) Cellular and network mechanisms underlying spontaneous sharp wave-ripple complexes in mouse hippocampal slices. J Physiol 550:873-87

Mann E, Suckling J, Hajos N, Greenfield S, Paulsen O (2005) Perisomatic feedback

inhibition underlies cholinergically induced fast network oscillations in the rat hippocampus in vitro. Neuron 45:105-17

Marrosu F, Portas C, Mascia M, Casu M, Fa M, Giagheddu M, Imperato A, Gessa G (1995) Microdialysis measurement of cortical and hippocampal acetylcholine release during sleep-wake cycle in freely moving cats. Brain Res 671:329-32

Masukawa LM, Prince DA (1982) Enkephalin inhibition of inhibitory input to CA1 and CA3 pyramidal neurons in the hippocampus. Brain Res 249:271-280

Matthes HW, Maldonado R, Simonin F, Valverde O, Slowe S, Kitchen I, Befort K, Dierich A, Le Meur M, Dollé P, Tzavara E, Hanoune J, Roques BP, Kieffer BL (1996) Loss of morphine-induced analgesia, reward effect and withdrawal symptoms in mice lacking the mu-opioid-receptor gene. Nature 383:819-823

Meyer A, Katona I, Blatow M, Rozov A, Monyer H (2002) In vivo labeling of parvalbumin-positive interneurons and analysis of electrical coupling in identified neurons. J Neurosci 22:7055-64

Miles R, Toth K, Gulyas A, Hßjos N, Freund T (1996) Differences between somatic and dendritic inhibition in the hippocampus. Neuron 16:815-23

Montgomery S, Buzsaki G (2007) Gamma oscillations dynamically couple hippocampal CA3 and CA1 regions during memory task performance. Proc Natl Acad Sci U S A 104:14495-500

Nelson S, Toth L, Sheth B, Sur M (1994) Orientation selectivity of cortical neurons during intracellular blockade of inhibition. Science 265:774-777

Neu A, Földy C, Soltesz I (2007) Postsynaptic origin of CB1-dependent tonic inhibition of GABA release at cholecystokinin-positive basket cell to pyramidal cell synapses in the CA1 region of the rat hippocampus. J. Physiol. (Lond.) 578:233-247

Oren I, Mann E, Paulsen O, Hajos N (2006) Synaptic currents in anatomically identified CA3 neurons during hippocampal gamma oscillations in vitro. J Neurosci 26:9923-34

Oren I, Hajos N, Paulsen O (2010) Identification of the current generator underlying cholinergically-induced gamma frequency field potential oscillations in the hippocampal CA3 region. J Physiol Available at: http://www.ncbi.nlm.nih.gov/pubmed/20051494 [Accessed February 3, 2010].

Paulsen O, Moser E (1998) A model of hippocampal memory encoding and retrieval: GABAergic control of synaptic plasticity. Trends Neurosci 21:273-8

Sederberg PB, Kahana MJ, Howard MW, Donner EJ, Madsen JR (2003) Theta and gamma oscillations during encoding predict subsequent recall. J. Neurosci 23:10809-10814

Singer W (1993) Synchronization of cortical activity and its putative role in information processing and learning. Annu. Rev. Physiol 55:349-374

Smith GM, Semke CW, Beecher HK (1962) Objective evidence of mental effects of heroin, morphine and placebo in normal subjects. J. Pharmacol. Exp. Ther 136:53-58

Somogyi P, Smith A, Nunzi M, Gorio A, Takagi H, Wu J (1983) Glutamate decarboxylase immunoreactivity in the hippocampus of the cat. Distribution of immunoreactive terminals with special reference to the axon initial segment of pyramidal neurons. J.Neurosci. 3PBS Record: 1676:1450-1468

Steriade M (2006) Grouping of brain rhythms in corticothalamic systems. Neuroscience 137:1087-106

Tiitinen H, Sinkkonen J, Reinikainen K, Alho K, Lavikainen J, Naatanen R (1993) Selective attention enhances the auditory 40-hz transient response in humans. Nature 364:59-60

Torres-Reveron A, Khalid S, Williams TJ, Waters EM, Jacome L, Luine VN, Drake CT, McEwen BS, Milner TA (2009) Hippocampal dynorphin immunoreactivity increases in response to gonadal steroids and is positioned for direct modulation by ovarian steroid receptors. Neuroscience 159:204-216

Tukker J, Fuentealba P, Hartwich K, Somogyi P, Klausberger T (2007) Cell type-specific tuning of hippocampal interneuron firing during gamma oscillations in vivo. J Neurosci 27:8184-9

Ulbert I, Halgren E, Heit G, Karmos G (2001) Multiple microelectrode-recording system for human intracortical applications. J. Neurosci. Methods 106:69-79

Whittington M, Traub R, Faulkner H, Jefferys J, Chettiar K (1998) Morphine disrupts long-range synchrony of gamma oscillations in hippocampal slices. Proc Natl Acad Sci U S A 95:5807-11

Figure legends

Figure 1. Three subsets of inhibitory neurons innervate the perisomatic region of CA3 pyramidal cells. (**a**) Parvalbumin (PV) containing fast-spiking basket cells (FSBC, orange) and axoaxonic cells (AAC, green) as well as cholecystokinin (CCK) containing regular-spiking basket cells (RSBC, blue). The axonal (in color) and dendritic (in black) arbor of the three cell types are shown together with, (**b**) their response to de- and hyperpolarizing current steps. Though the axonal arbor of the AACs is shifted towards stratum oriens compared to the axonal arbor of basket cells, it is difficult to reliably separate the two cell types. (**c, d**) Using double fluorescent staining against Ankyrin-G (selectively labeling axon initial segments (AIS)) and biocytin (visualizing the axons of the filled cells) the difference between the two cell types can be resolved. While there is no, or very little association between boutons of basket cells (green, $\mathbf{c}_{1\text{-}3}$) and the ankyrin G stained AISs of the pyramidal cells (yellow), bouton rows of the AACs (green, $\mathbf{d}_{1\text{-}2}$) outline the axon initial segments of pyramidal cells. The target selectivity of the two cell types had been confirmed in serially sectioned electron microscopical slices (for 5 cells of both types). Axon terminals of FSBCs ($\mathbf{c}_4$) contacted somata of pyramidal cells (arrow on inset shows synaptic specialization in higher magnification), while axon endings of AACs ($\mathbf{d}_3$) innervated the axon initial segments of the same cell type and formed symmetrical synapses (arrow on $\mathbf{d}_4$). Scales: $\mathbf{c}_1$, $\mathbf{d}_1$ = 20µm, $\mathbf{c}_{2\text{-}3}$, $\mathbf{d}_2$ = 5µm, $\mathbf{c}_4$, $\mathbf{d}_3$ = 0.5µm.

Figure 2. Subtypes of perisomatic inhibitory cells can be separated on the basis of their firing frequency, doublet incidence and phase coupling strength during CCh-induced network oscillations in vitro. Concomitant recording of field oscillations and spikes in a loose patch mode from different perisomatic inhibitory cells (**a**) showed that they fire phase

locked to oscillations induced by CCh (**b, c**). FSBC cells (orange) often fired doublets (asterisks). The spikes per cycle (**c**) and the doublet ratio (**d**) were significantly higher for FSBCs (n=13) than for AACs (n=12, green) and RSBCs (n=10, blue). Thus, FSBCs fired approximately once in every oscillation cycle. While the average phase of the individual cells varied around the ascending phase of the cycles (**f**, see also Supplementary fig. 4a), and cell types could not be separated on the basis of their firing phase (**e**), the phase coupling (**f**) of FSBCs and AACs was significantly (p=0.001 and p=0.023) higher than that of the RSBCs. Polar plot showing the firing accuracy and phase of each recorded neurons are shown in Supplementary fig. 4a. Here in **c-f**, and also in Figures 7 and 8, the mean (small open square), the median (midline of the big box), the interquartile range (large box), the 5/95% values (ends of bars), as well as the minimal/maximal values (bottom and top X) are shown on the charts.

Figure 3. μ-opioid receptor (MOR) activation suppresses gamma oscillations in vivo. (**a**) Band pass filtered (between 38 and 42 Hz) in vivo recordings from the CA3 region of the hippocampus and (**b**) the corresponding power spectra before and after DAMGO application. The mean frequency of oscillations was 41.5±2.9 Hz (n=4). Scale bars, 10 μV and 100 ms. (**c**) DAMGO significantly reduced the CSD gamma band power monitored in str. pyramidale (ctr, 0.217±0.073 μV^2/Hz; DAMGO, 0.091±0.045 μV^2/Hz, n=4, p<0.001). (**d**) In contrast, saline application caused no significant change (ctr, 0.235±0.115 μV^2/Hz; DAMGO, 0.231±0.121 μV^2/Hz, n=2).

Figure 4. μ-opioid receptor (MOR) activation blocks CCh-induced network oscillations in vitro. (**a**) CCh-induced oscillations (top row) were blocked by bath application of 1 μM DAMGO in the wild type mouse (WT, left), but not in MOR KO animals (KO, right), indicating the specific action of DAMGO on MORs. (**b**) Power spectral density plots from the same experiment show a decrease in the power following DAMGO application in WT (left),

but not in KO (right) animals. (**c**) Statistical analyses demonstrated a significant drop in the peak power in the WT (left, 164.9±26.7 μV^2/Hz vs. 46.7±11.6 μV^2/Hz, n=44, Wilcoxon Signed Ranks Test: $p<0.0001$), but not in the KO animals (right, 161.7±38.2 μV^2 /Hz vs. 127.3±34.4 μV^2/Hz, n=19, Wilcoxon Signed Ranks Test: $p=0.15$).

Figure 5. DAMGO application suppresses network oscillations: desynchronization of multiunit activity without changing firing frequency. The left column shows parallel recordings of field oscillations (top trace) and concomitant multiunit activity (filtered between 100 Hz - 2 kHz) during CCh-induced oscillation before and after DAMGO application. Scale bars, 50 µV and 0.1 s. The time course of the same experiment is shown in the right column (top). While the wash-in of DAMGO caused a fast drop in the peak power of the oscillation, the frequency of multiunit activity only slightly decreased, but their synchronization was abolished as indicated by the autocorrelograms (bottom).

Figure 6. DAMGO reduces the amplitude of inhibitory, but not excitatory synaptic currents evoked by electrical stimulation in CA3 pyramidal cells. (**a**) Two examples showing that the bath application of DAMGO reduced the peak amplitude of inhibitory synaptic currents (eIPSCs), leaving unaffected the amplitude of excitatory synaptic currents (eEPSCs). Recordings were done in the presence of 5 µM CCh. Example traces are averaged records of 6-8 consecutive events taken at the labeled time points. Scale bars, 10 pA and 10 ms. (**b**) In all tested cases, DAMGO application significantly reduced the amplitude of evoked IPSCs (left, 164.3±52.38 pA vs. 79.3±26.68 pA in DAMGO, n=7, p=0.017) recorded from CA3 pyramidal cells elicited by electrical stimulation in str. pyramidale or at the border of strata radiatum and lucidum. In contrast, EPSCs elicited by electrical stimulation in str.

radiatum showed no change following DAMGO application (right, 104.4±42.3 pA vs. 107.2±45.6 pA in DAMGO, n=4, p=0.45).

Figure 7. Cholinergic activation eliminates IPSCs originating from RSBCs and decreases synaptic inhibition mediated by FSBCs and AACs. Perisomatic inhibitory interneuron-pyramidal cell pairs had been recorded to test the effective inhibition exerted by different cell types on pyramidal cells, in conditions characteristic of CCh-induced network oscillation. Trains of ten action potentials were evoked in each interneuron at different frequencies to record unitary IPSCs in their postsynaptic pyramidal cells first under control conditions, followed by bath application of CCh. After *post hoc* analysis of the cell's identity, the properties of IPSCs at the characteristic frequencies at which the given cell type would have fired during CCh-induced oscillations were analyzed (Table 1; action potentials evoked at 15 Hz for FSBCs, and at 10 Hz for AACs and RSBCs). (**a**) Action potentials evoked in identified cells shown in Figure 1 at frequencies characteristic of their firing during oscillatory activities elicited IPSCs in their postsynaptic pyramidal cell. Application of CCh reduced or eliminated IPSCs (**a, c**) depending on the type of presynaptic inhibitory neurons. The GABA release from PV-containing neurons was depressing, which was decreased by CCh. RSBC synapses were facilitating-depressing, showing on average no short-term plasticity, and their release was almost completely blocked by CCh application. (**b**) To analyze the effect of CCh on steady-state release, from 6^{th} to 10^{th} of the evoked IPSCs were averaged and compared. (**c**) All reductions were significant (ANOVA, p=0.001) and differed from each-other. IPSCs evoked by the RSBCs were almost completely eliminated (9.9±3.8 % of control, n=10, p=0.001). In the case of PV-containing cells, where transmission persisted, there was a stronger reduction for AACs (34.1±3.1 % of control, n=17, p=0.001) than for FSBCs (45.2±3.3 % of control, n=14, p=0.001).

Figure 8. The μ-opiate receptor agonist DAMGO selectively reduces the residual inhibition of FSBCs, but not of AACs in the presence of CCh. (**a, b**) As demonstrated on the same cell pairs as in Figure 6, DAMGO application did not cause a noticeable decrease in synaptic inhibition of the AAC, but further suppressed the unitary IPSC amplitude of the FSBC. (**c**) While the addition of DAMGO has not significantly reduced further the amplitude of IPSCs in AAC-pyramidal cell pairs (90.4 ± 6.0 % of the amplitude in CCh, n=15, p=0.15), there was a significant reduction in the amplitude in FSBC-pyramidal cell pairs (62.3 ± 3.9 % of the amplitude in CCh, n=14, p=0.001), decreasing the current amplitudes down to the level of AAC-pyramidal cell pairs (p=0.15).

Tables

Table 1. **Firing properties of the three types of perisomatic inhibitory cells during CCh-induced network oscillation.**

	FSBC (n=13)	**AAC** (n=12)	**RSBC** (n=10)
Firing frequency (Hz)	15.01 ± 2.3	7.9 ± 1.3	9.42 ± 1.2
Spike/osc. cycle	0.86 ± 0.13	0.51 ± 0.09	0.52 ± 0.08
% of Doublets	11.6 ± 3.6	3.4 ± 1.4	0.4 ± 0.1
Phase (degree)	29.9 ± 7.8	36.3 ± 8.4	38.1 ± 6.5
Phase coupling strength	0.8 ± 0.04	0.69 ± 0.06	0.49 ± 0.06

Data are presented as mean ± SEM.

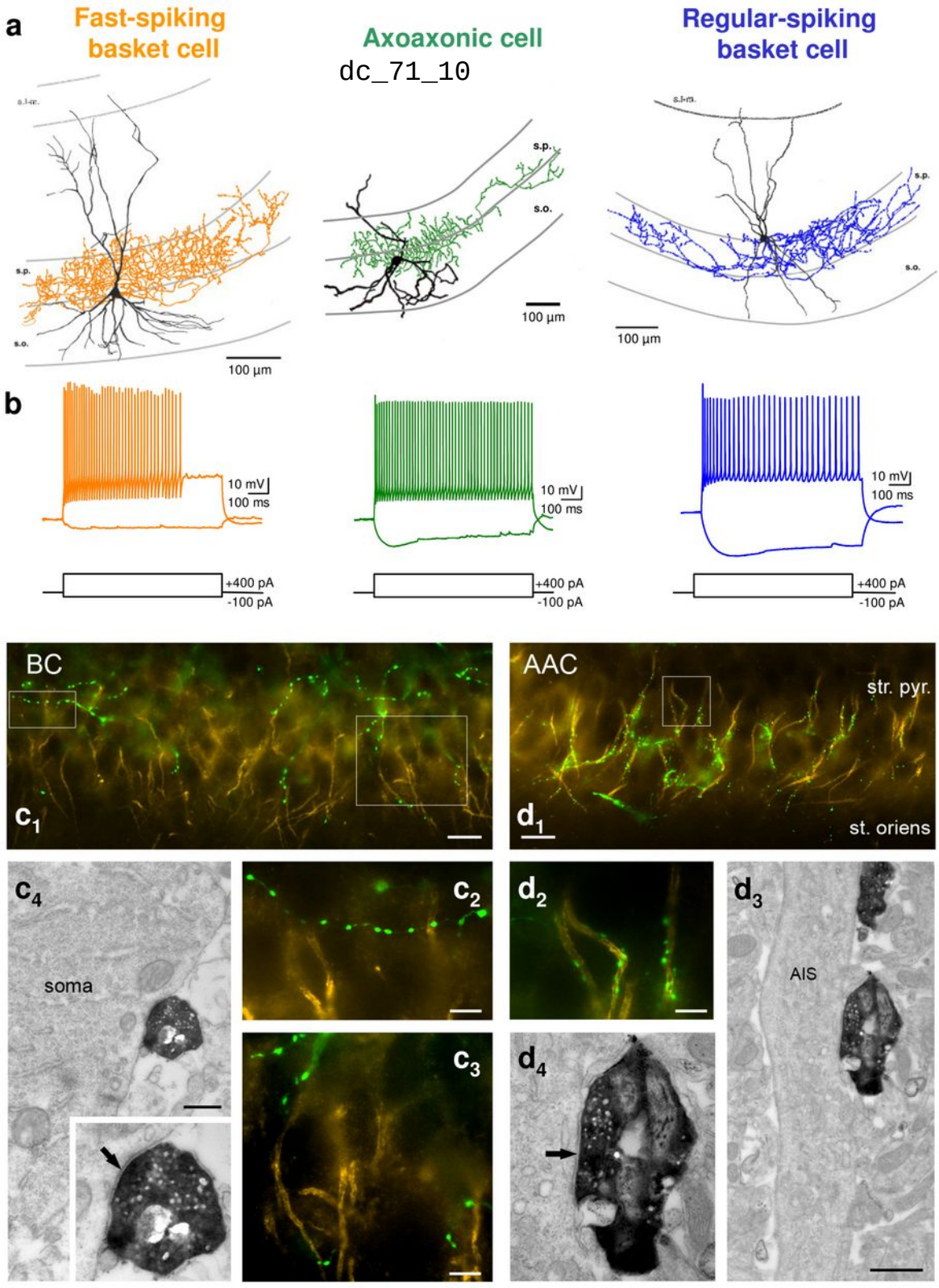
a
Fast-spiking basket cell
Axoaxonic cell
dc_71_10
Regular-spiking basket cell
s.l-m.
s.p.
s.o.
100 µm
b
10 mV
100 ms
+400 pA
-100 pA
BC
AAC
str. pyr.
st. oriens
c1
d1
c4
soma
c2
c3
d2
d3
AIS
d4

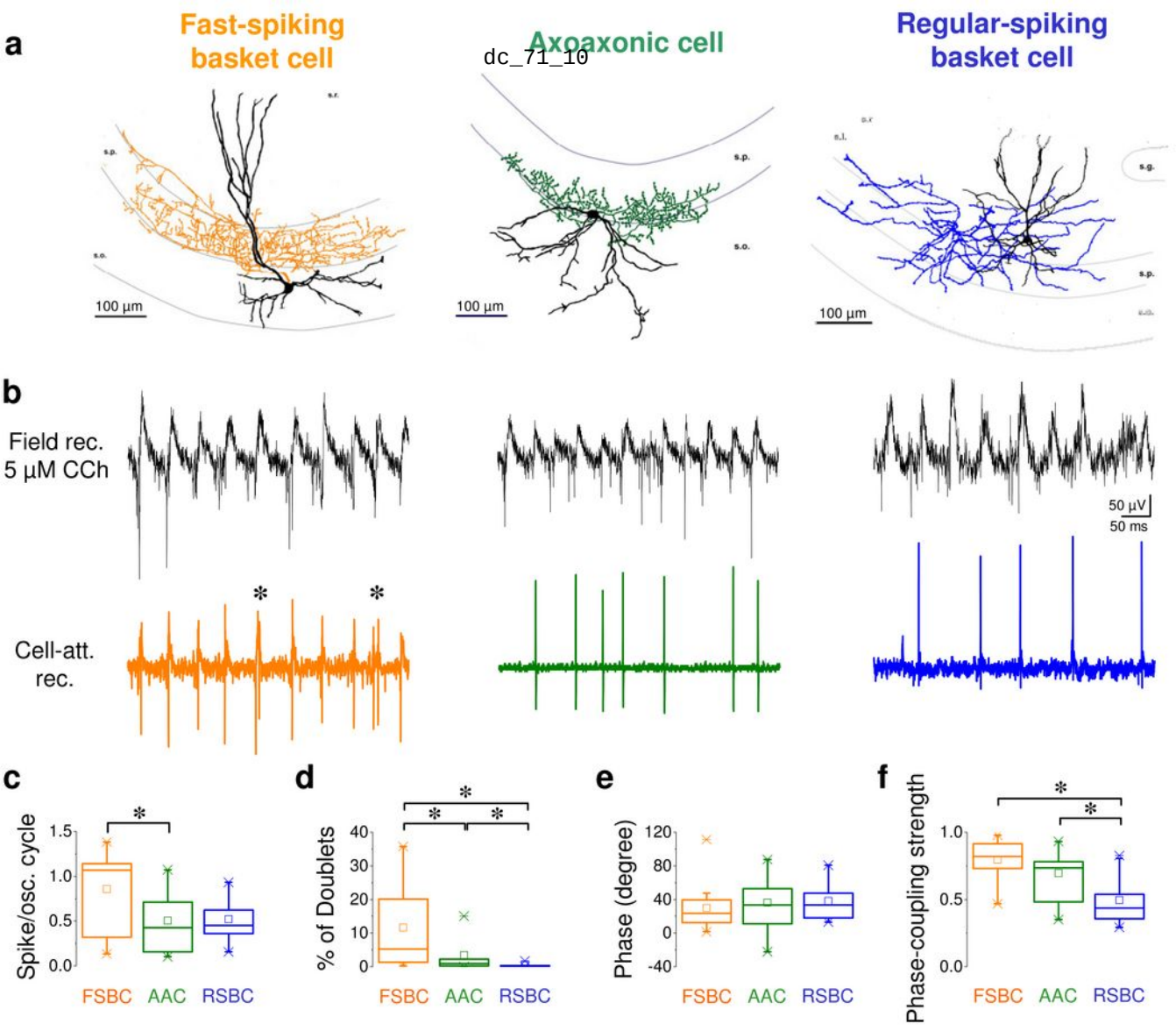
a
Fast-spiking basket cell
Axoaxonic cell
Regular-spiking basket cell
dc_71_10
s.r.
s.p.
s.o.
s.l.
s.g.
100 µm
b
Field rec.
5 µM CCh
Cell-att. rec.
50 µV
50 ms
c
Spike/osc. cycle
d
% of Doublets
e
Phase (degree)
f
Phase-coupling strength
FSBC
AAC
RSBC

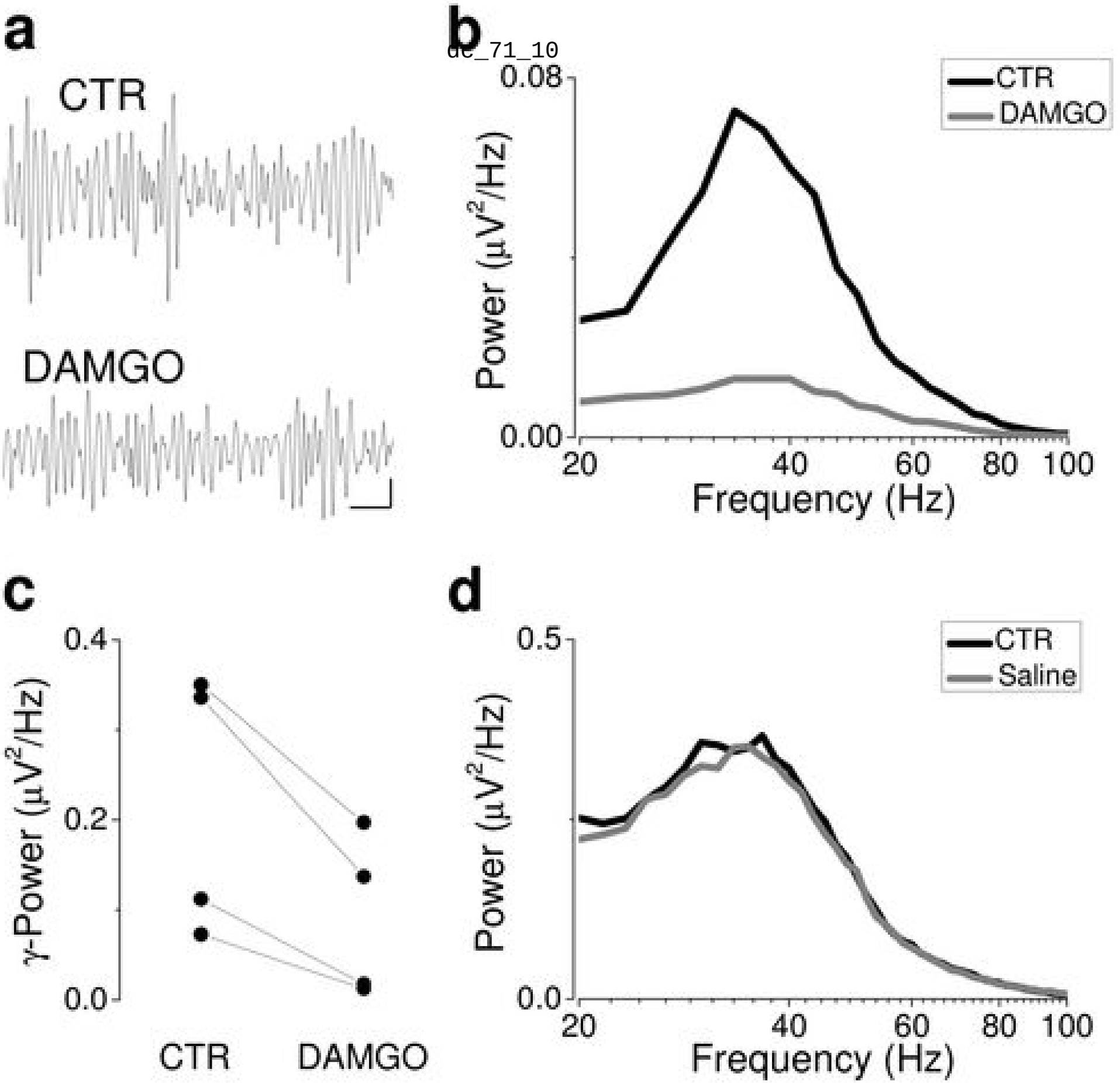
a
CTR
DAMGO
b
CTR
DAMGO
0.08
0.00
Power (μV²/Hz)
20
40
60
80
100
Frequency (Hz)
c
0.4
0.2
0.0
γ-Power (μV²/Hz)
CTR
DAMGO
d
CTR
Saline
0.5
0.0
Power (μV²/Hz)
20
40
60
80
100
Frequency (Hz)

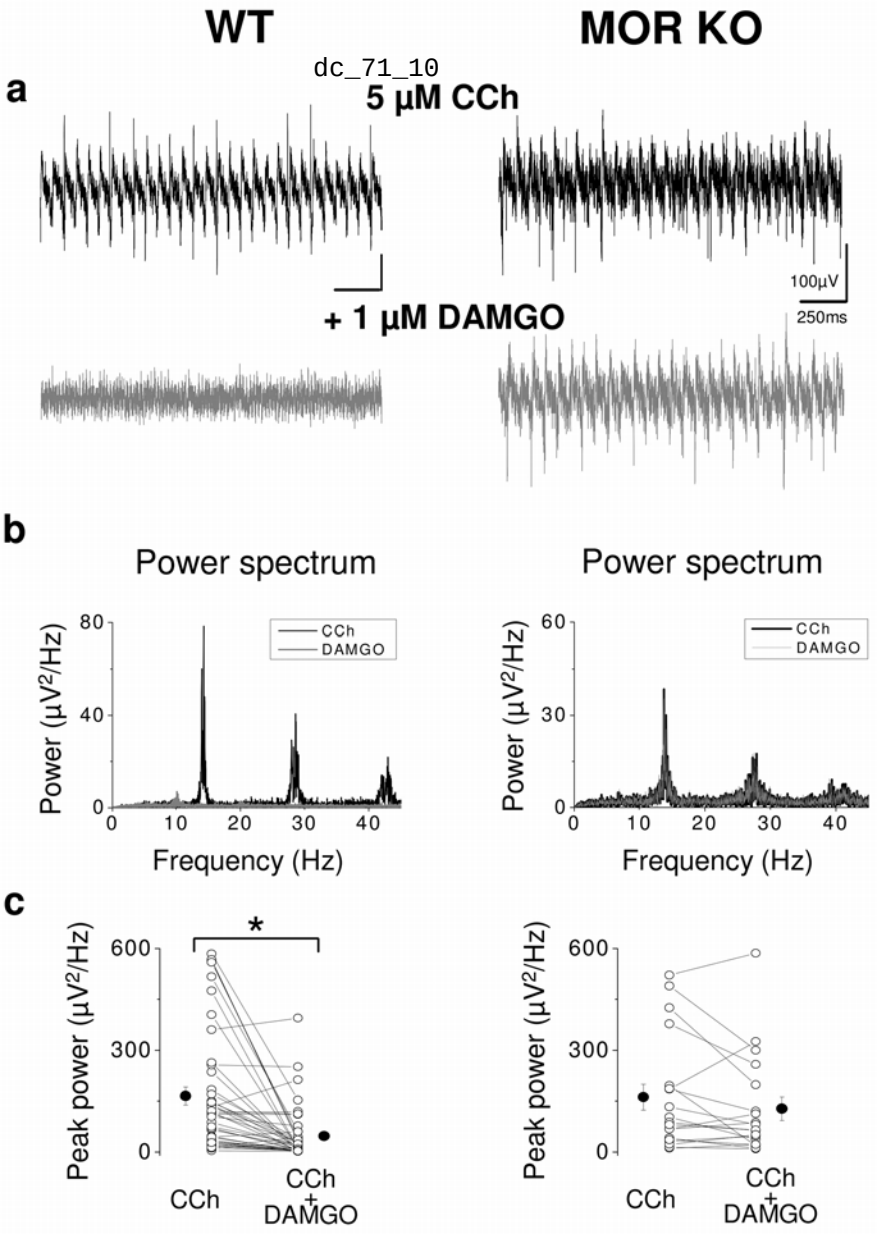
WT
MOR KO
dc_71_10
a
5 µM CCh
100µV
250ms
+ 1 µM DAMGO
b
Power spectrum
Power spectrum
CCh
DAMGO
Power (µV²/Hz)
Frequency (Hz)
c
Peak power (µV²/Hz)
*
CCh
CCh + DAMGO

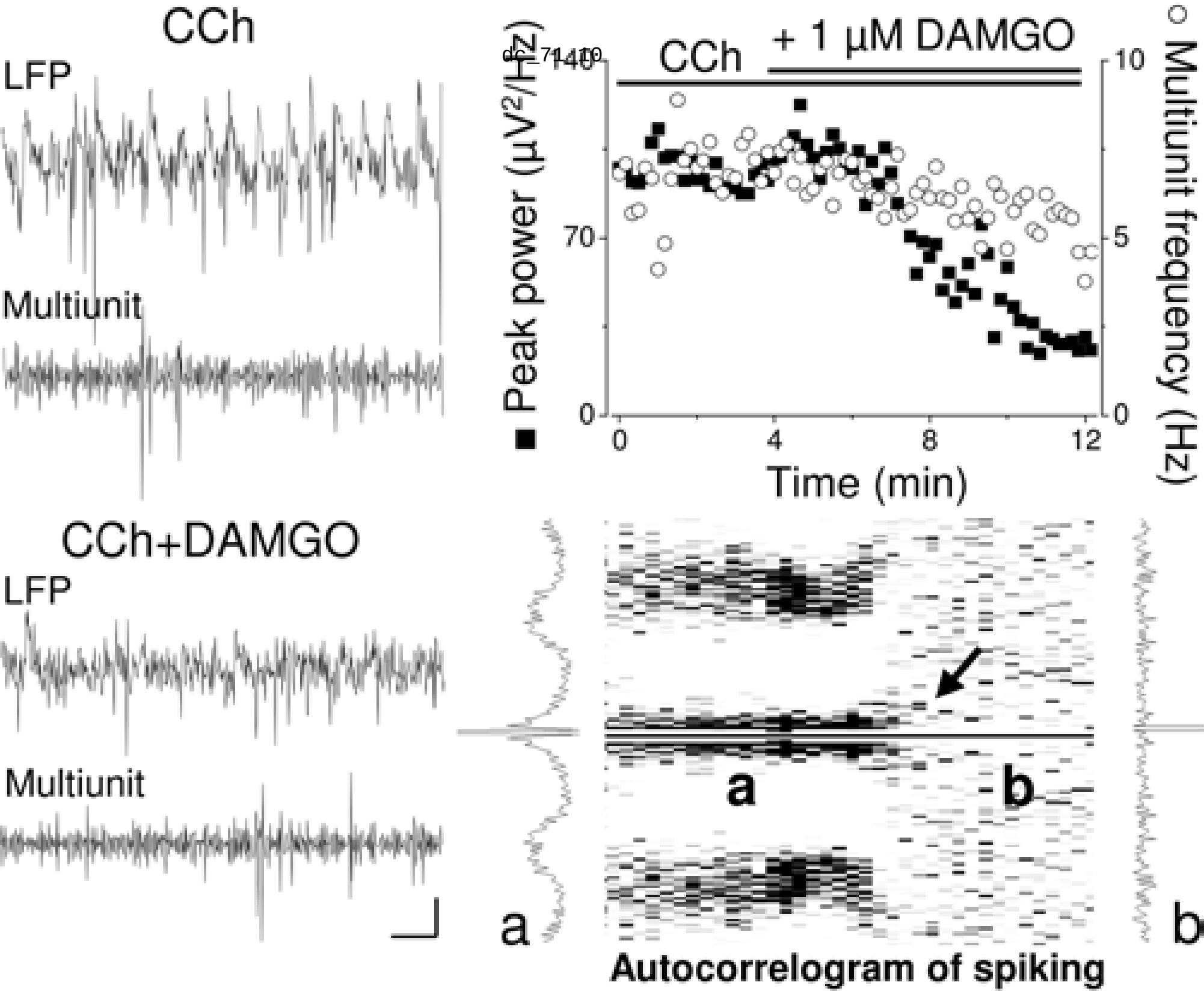
CCh
LFP
Multiunit
CCh+DAMGO
LFP
Multiunit
CCh
+ 1 μM DAMGO
■ Peak power (μV²/Hz)
○ Multiunit frequency (Hz)
Time (min)
0
4
8
12
70
140
5
10
a
b
Autocorrelogram of spiking

dc_71_10

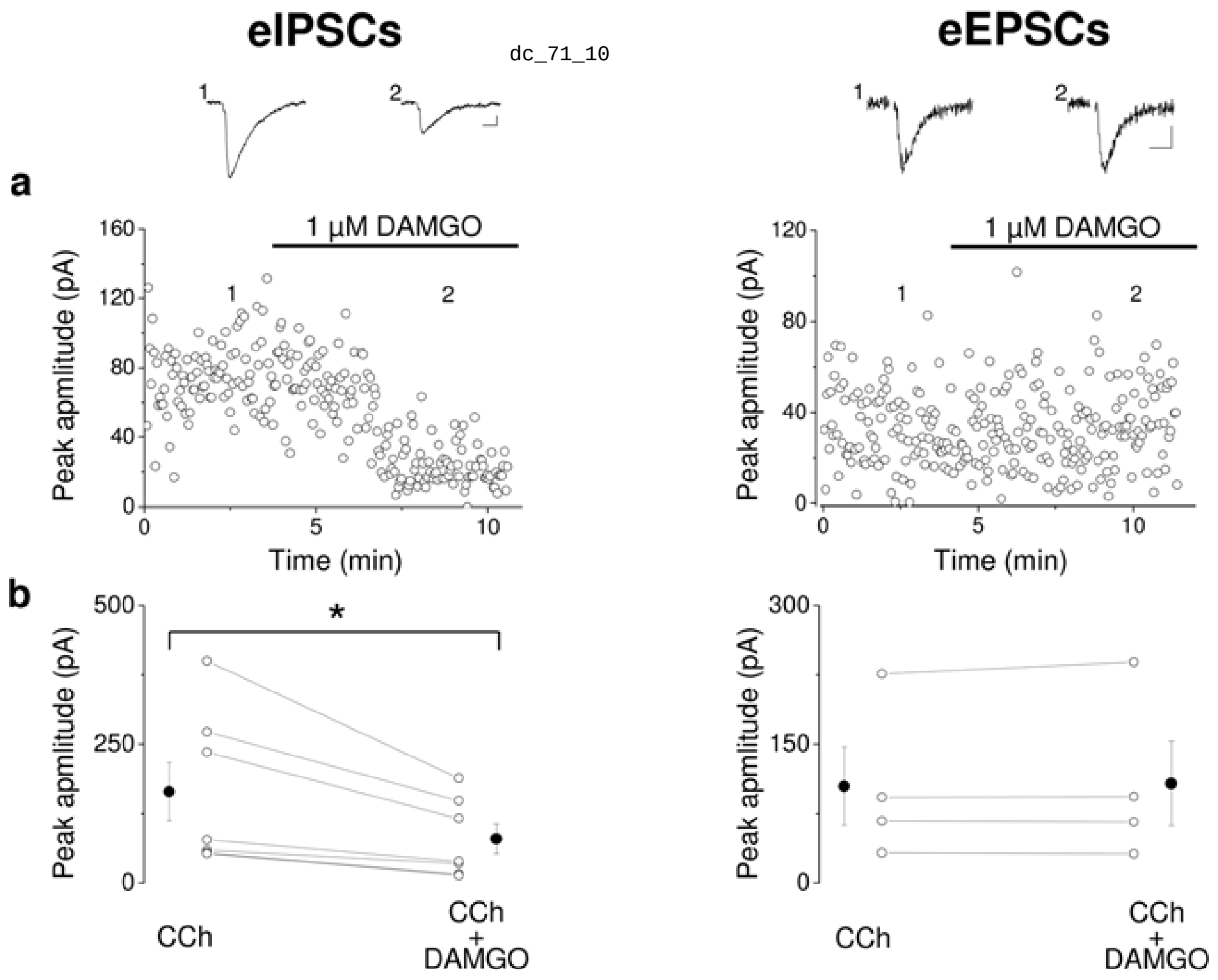
eIPSCs
eEPSCs
a
1
2
1 µM DAMGO
Peak apmlitude (pA)
Time (min)
160
120
80
40
0
5
10
b
500
250
300
150
*
CCh
CCh + DAMGO

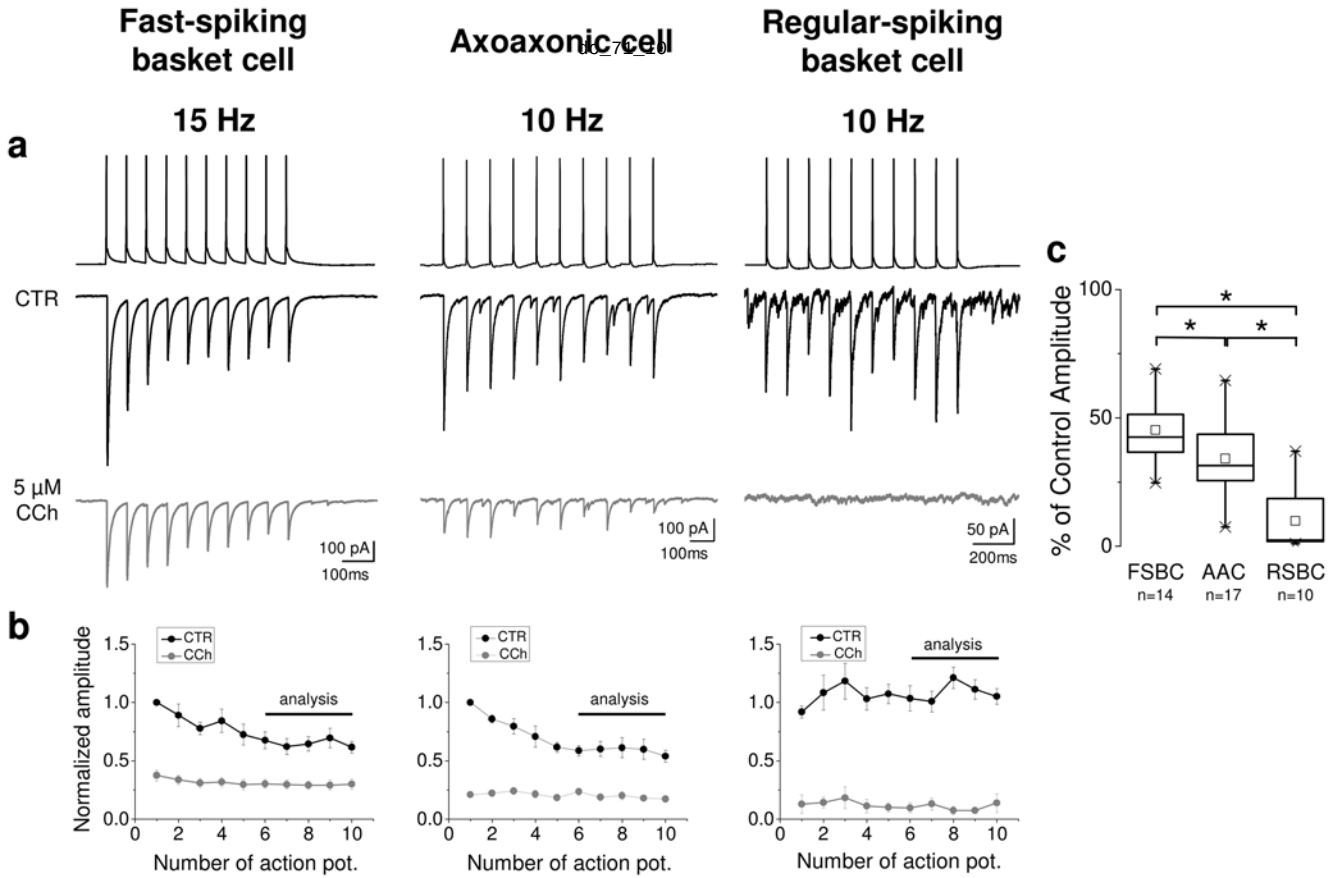
Fast-spiking basket cell
Axoaxonic cell
Regular-spiking basket cell
15 Hz
10 Hz
10 Hz
a
CTR
5 µM CCh
100 pA
100ms
100 pA
100ms
50 pA
200ms
b
Normalized amplitude
CTR
CCh
analysis
Number of action pot.
c
% of Control Amplitude
FSBC n=14
AAC n=17
RSBC n=10
*
*
*

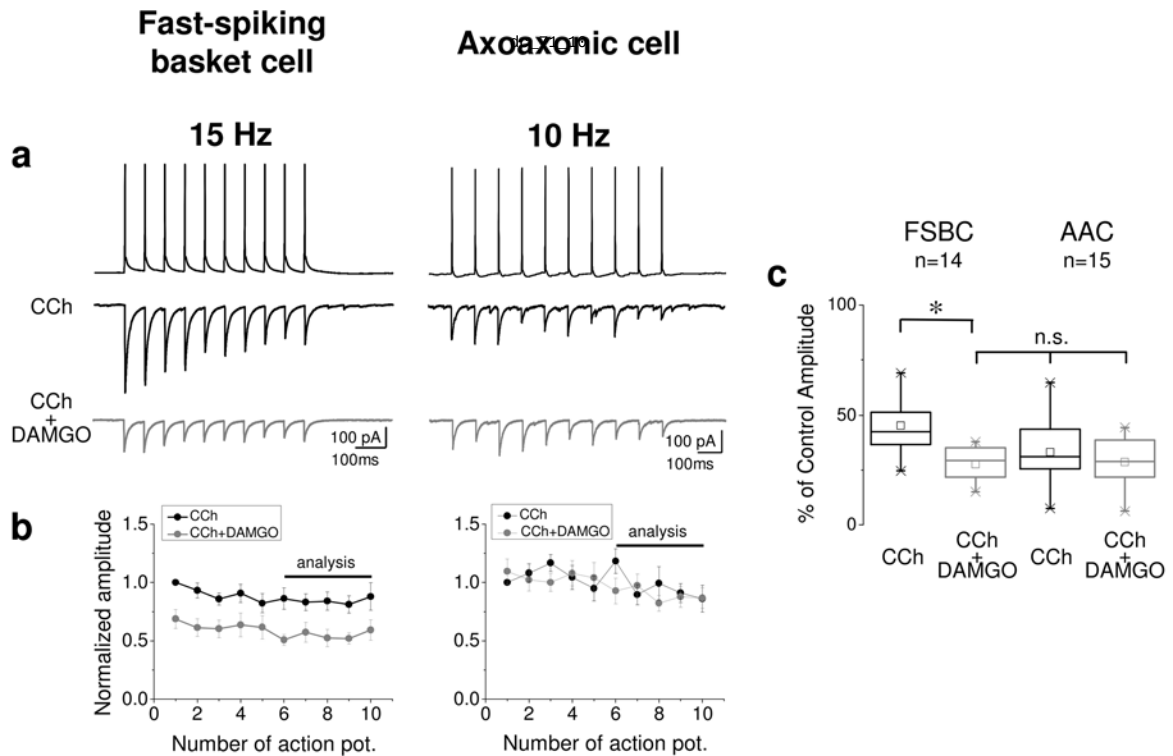
Fast-spiking basket cell
Axo-axonic cell
15 Hz
10 Hz
a
CCh
CCh + DAMGO
100 pA
100ms
100 pA
100ms
b
Normalized amplitude
CCh
CCh+DAMGO
analysis
Number of action pot.
CCh
CCh+DAMGO
analysis
Number of action pot.
c
FSBC
n=14
AAC
n=15
% of Control Amplitude
*
n.s.
CCh
CCh + DAMGO
CCh
CCh + DAMGO

dc_71_10

19. számú melléklet

Feed-forward inhibition underlies the propagation of cholinergically induced gamma oscillations from CA3 to CA1 hippocampal region

Rita Zemankovics[1], Judit Veres[1], Iris Oren[2] and Norbert Hájos[1]

[1] Department of Cellular and Network Neurobiology, Institute of Experimental Medicine, Hungarian Academy of Sciences, Budapest, Hungary
[2] Department of Clinical and Experimental Epilepsy, Institute of Neurology, University College London, London WC1N 3BG, UK

dc_71_10

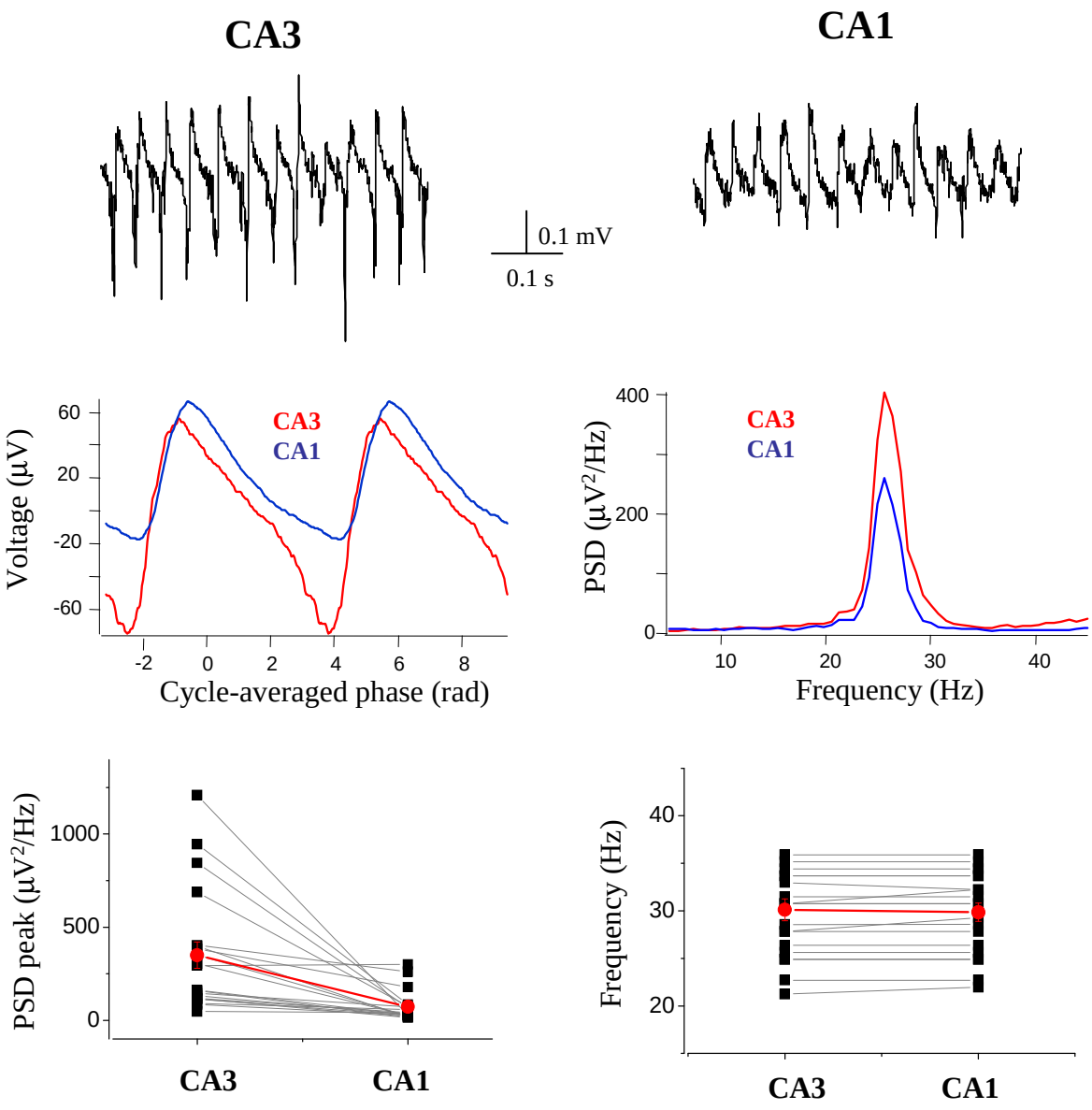

Fig. 1 Field oscillations recorded extracellularly from the stratum pyramidale of the CA3 and the CA1 region of the hippocampus after bath application of 20 µM carbachol. **B**, Cycle average of the field oscillations in *A*. **C**, Power spectral density function of the traces in *A* showing gamma frequency peak. Comparison of power (**D**) and frequency (**E**) of oscillations in CA3 and CA1.

dc_71_10

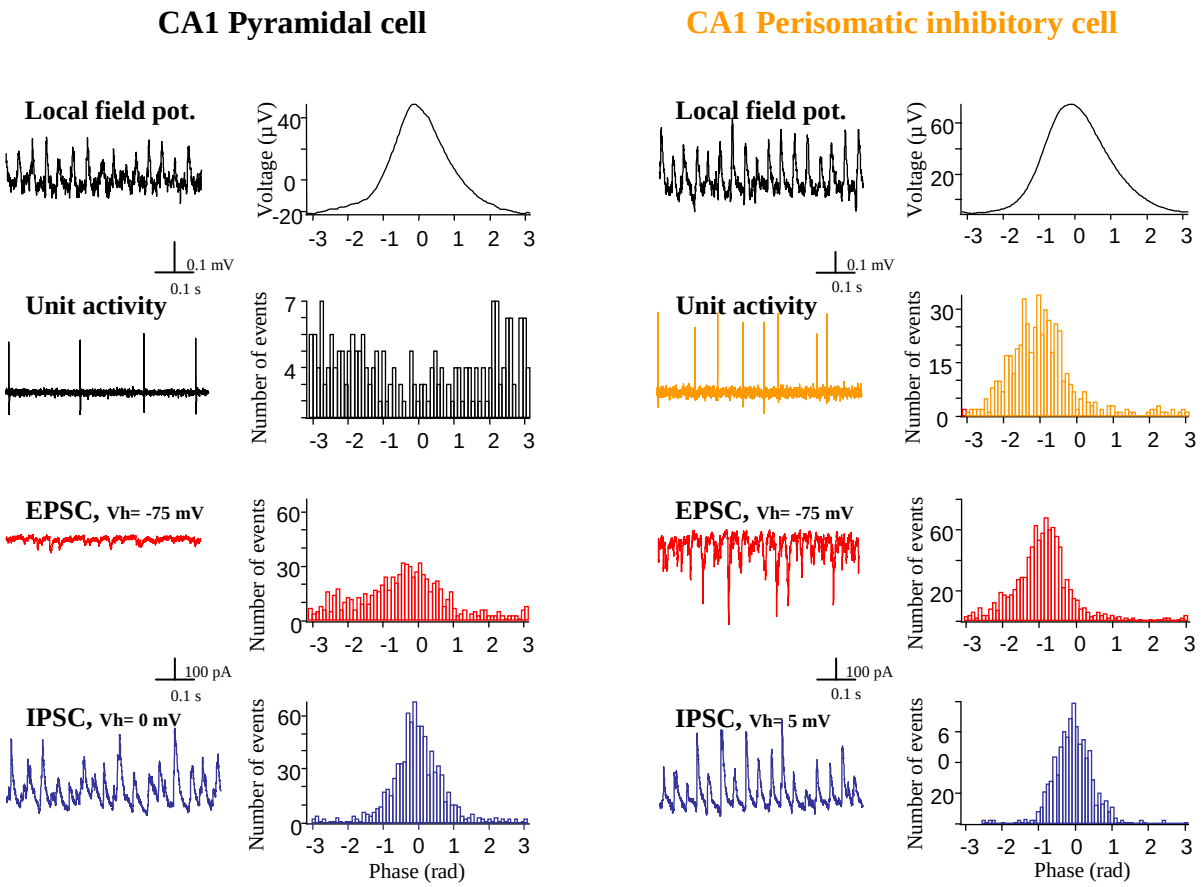

Fig. 2 Simultaneous extracellular recordings of field potentials and spike trains from a CA1 pyramidal cell and from a CA1 perisomatic-targeting interneuron. EPSCs and IPSCs recorded from the same pyramidal cell and the same interneuron at the estimated reversal potentials. Cycle averages of the field oscillations, spike-phase histograms of the recorded cells as well as the phase histograms of EPSCs and IPSCs of the same pyramidal cell and of the interneuron are shown.

dc_71_10

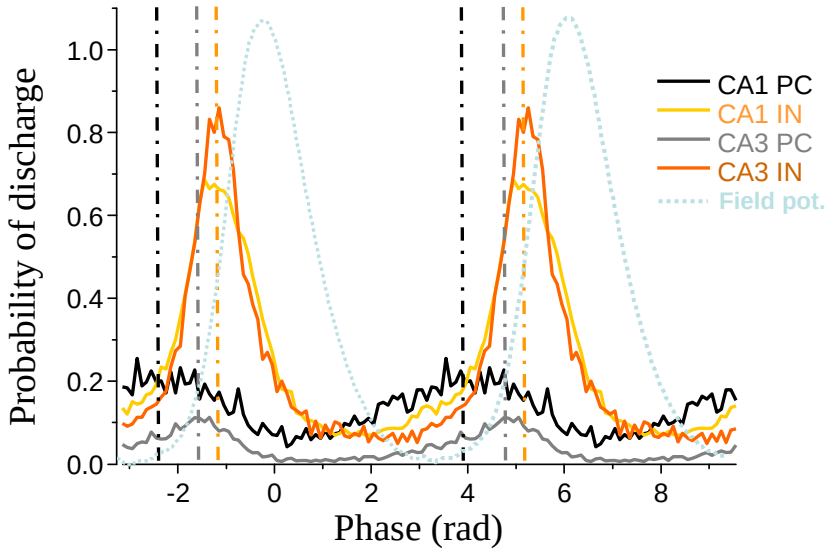

Fig. 3 Average phase histograms of unit activity during gamma oscillations showing that CA1 PC discharge much earlier than CA3 PCs. Note that CA3 PC discharge is followed by spiking of both CA1 and CA3 INs. Dotted vertical lines indicate the mean of the phase histograms. Dotted grey line shows the averaged field oscillation.

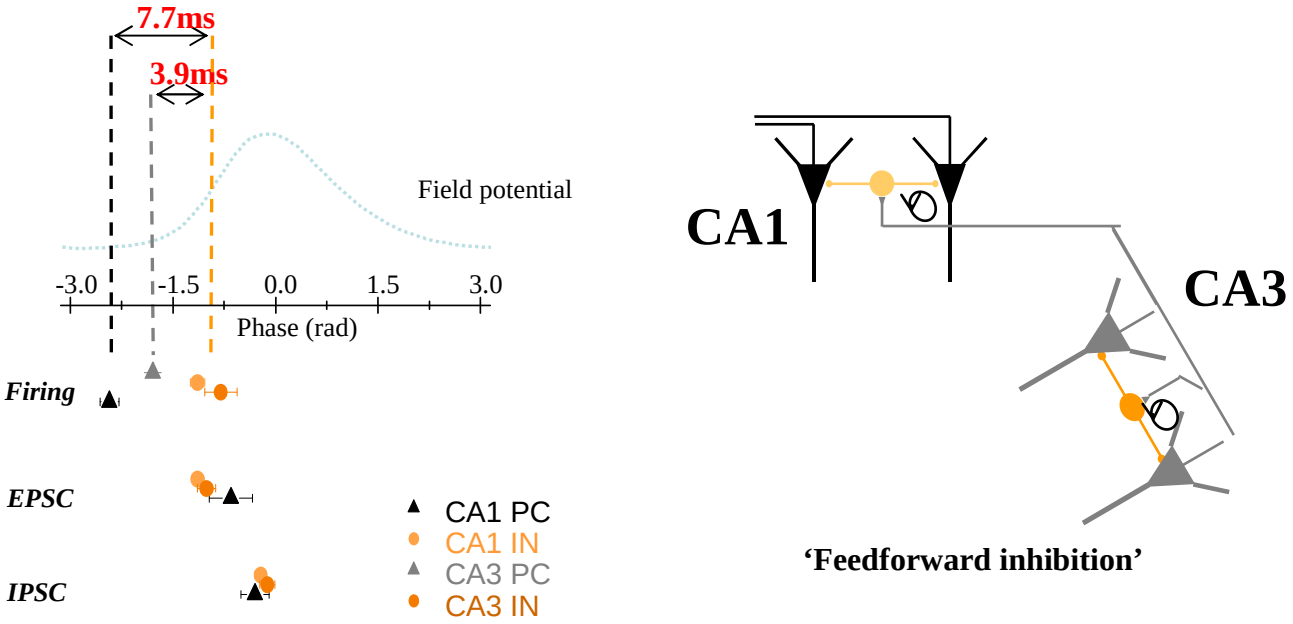

Fig. 4 Left, Our data combined with our previous results from the CA3 region of rat hippocampus (Oren et al. 2006. JNsci), suggest a model whereby CA3 PCs excite both CA3 and CA1 INs that fire at latencies indicative of monosynaptic connections. In contrast, the spike timing of CA1 PCs is controlled primarily by inhibition. These findings are consistent with *in vivo* recordings, suggesting that similar functional networks may underlie carbachol-induced oscillations *in vitro* and gamma frequency oscillations in the hippocampus of the behaving animal. Bars indicate the mean action potential phase (ΦAP) of the investigated cell types. PC: pyramidal cell, IN: interneurons. Right, Based on our data, we propose that the discharge of CA3 pyramidal cells during gamma oscillation drives the firing of local interneurons in CA1 in a feed forward manner, and the synaptic inhibition originating from the rhythmic firing of CA1 interneurons generates the oscillation in this hippocampal region.

dc_71_10

20. számú melléklet

Impairment of gamma oscillation by cannabinoids is due to a mutual suppression of excitatory inputs onto CA3 pyramidal cells and fast spiking interneurons

Noémi Holderith, Beáta Németh, Judit Veres, Gergely A. Nagy, Gergely G. Szabó and Norbert Hájos

Laboratory of Network Neurophysiology Institute of Experimental Medicine, Hungarian Academy of Sciences, H-1083 Budapest, Hungary

dc_71_10

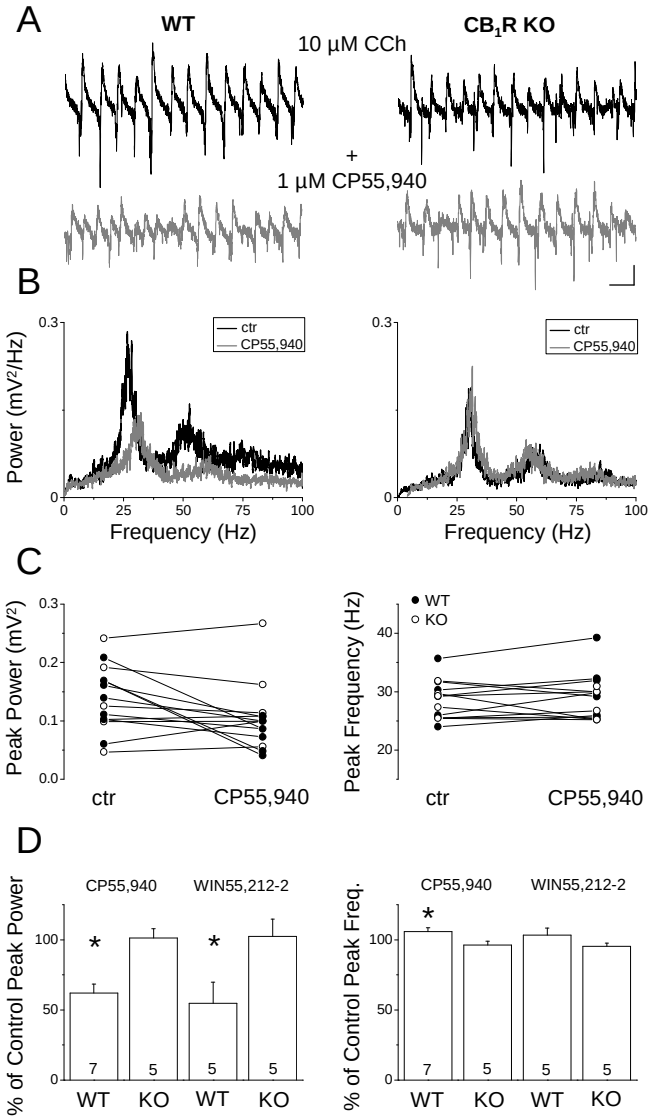

Fig 1. CB1 receptor activation reduces the power of the cholinergically induced gamma oscillation in the CA3 region of the hippocampus. ***A,*** Example traces of extracellular field recordings of cholinergically induced oscillations (10µM carbachol) in the pyramidal cell layer of the CA3 in a wild type (WT, left traces) and in a CB1 receptor knock out (CB1R KO, right traces) before (upper black traces) and after (lower grey traces) a cannabinoid receptor agonist CP55,940 (1µM) bath application. ***B,*** Power spectral density functions of the traces in ***A*** showing similar gamma-frequency peaks at 25Hz (black) both in the WT and in the CB1R KO animals. CB1R agonist application reduces the peak power and shifts the peak frequency to larger values (grey). No change was detected in the CB1R KO animals (right). ***C,*** Comparison of the peak power (left) and peak frequency (right) change in wild type (filled black circles) and CB1R KO (empty circles). ***D,*** Summary graphs showing a reduction of the peak power (left) due to the bath application of both CP55,940 and WIN55,212-2 (1µM, asterisks indicates $p<0.05$) and an increase in the peak frequency (right) of the oscillation in case of CP55,940 in wild type and no change in either of them in CB1R KO animals.

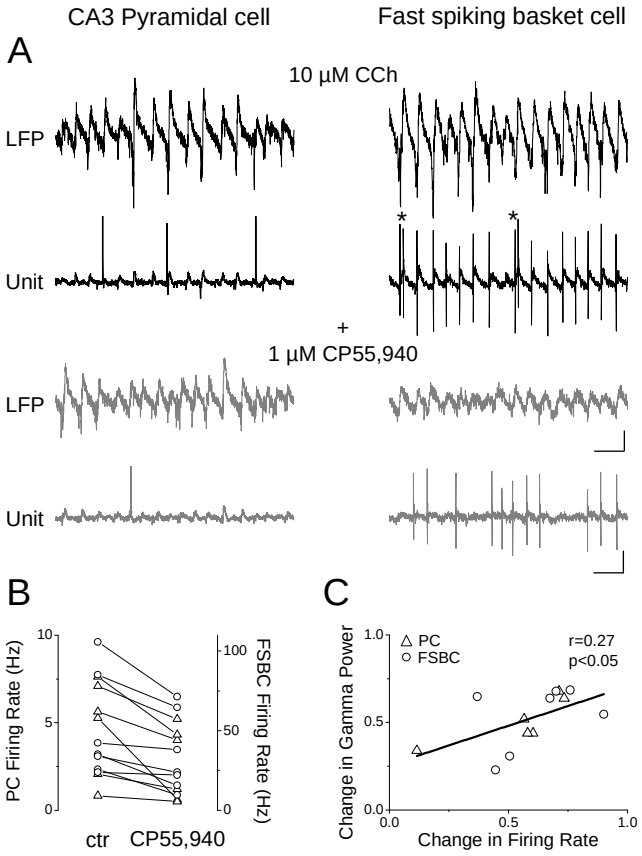

Fig 2. Effect of CB1R activation on the firing frequency of CA3 pyramidal cells and fast spiking basket cells during CCh-induced gamma oscillation. **A,** Simultaneous extracellular recordings of field potentials in the str. pyramidale of the CA3 (top black traces) during CCh-induced oscillations and spike trains recorded in cell attached mode (bottom black traces) from an anatomically identified CA3 PC (left) and a fast spiking basket cell (right). CB1R agonist CP55,940 (1µM) reduces the firing frequency of both cell types (lower grey traces) along with the power of the oscillation (upper grey traces). ***B,*** Summary of the effect of the CP55,940 application on the firing rate of each measured CA3 PCs (triangle) and FS BCs (circle) showing a clear reduction in every cell. ***C,*** A linear relationship was found between the change in the power of the oscillation and the in the firing rate of the recorded cells.

dc_71_10

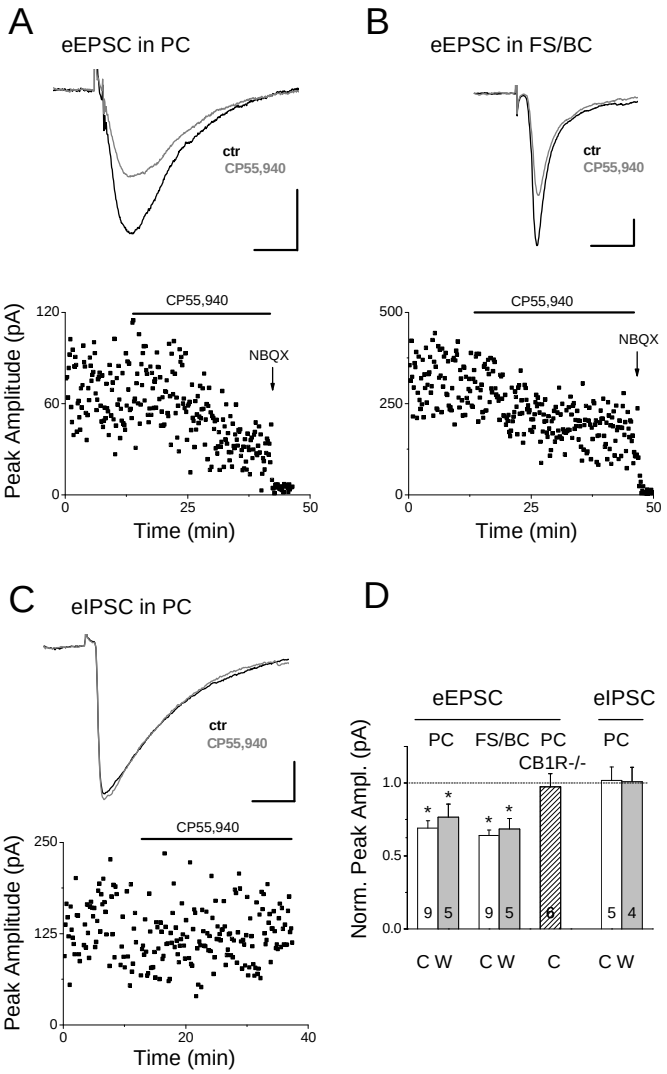

Fig 3. Cannabinoid agonists reduce only the monosynaptically evoked EPSCs both on CA3 PCs and FS BCs but have no effect on IPSCs on CA3PCs in the presence of 10 µM CCh. ***A-B,*** Upper traces show typical mean EPSCs evoked in the str. radiatum of the CA3 recorded in a CA3 PC (A) or in a FS BC (B) in control (black) and after CP55,940 (1µM, grey) application. Amplitude plots (lower panels) show the reduction of the amplitude of eEPSCs upon CP55,940 application (black lines indicate the wash in period of the drug). The excitatory nature of the evoked currents were tested in each case by the application of an antagonist of the AMPA and NMDA-type glutamate receptors, NBQX. ***C,*** Typical mean IPSC (upper panel) recorded in a CA3 PC before (black trace) and after (grey trace) application of CP55,940 (1µM). Lower panel shows the amplitude plot of eIPSCs. No change in the amplitude can be detected after the application of the agonist (black line). **D,** Graph summarizing the effect of CP55,940 (C, white columns) and WIN55,212-2 (W, grey columns) application on the evoked excitatory and inhibitory PSCs. Data shows the normalized peak amplitudes after drug application compared to control (dashed line). Dashed column represents the control measured in CB1R knock out animal. Scale: 10ms 30pA